TUHH
Hamburg University of Technology

Simulation of Time Dependent Degradation of Porous Materials

Final Report on Priority Program 1122
Funded by the German Research Foundation DFG

Edited by

L. Franke
G. Deckelmann
R. Espinosa-Marzal

Simulation of Time Dependent Degradation of Porous Materials

TUHH
Hamburg University of Technology

Simulation of Time Dependent Degradation of Porous Materials

Final Report on Priority Program 1122
Funded by the German Research Foundation DFG

Edited by

L. Franke
G. Deckelmann
R. Espinosa-Marzal

Cuvillier Verlag Göttingen
Internationaler wissenschaftlicher Fachverlag

Bibliografische Information der Deutschen Nationalbibliothek
Die Deutsche Nationalbibliothek verzeichnet diese Publikation in der Deutschen Nationalbibliografie; detaillierte bibliografische Daten sind im Internet über http://dnb.ddb.de abrufbar.
1. Aufl. - Göttingen : Cuvillier, 2009

978-3-86727-902-4

Nonnenstieg 8, 37075 Göttingen
Telefon: 0551-54724-0
Telefax: 0551-54724-21
www.cuvillier.de

1. Auflage, 2009
Gedruckt auf säurefreiem Papier

978-3-86727-902-4

Foreword

Porous mineral materials can be damaged by both physical and chemical attack. The presence of an aggressive solution in the pores may induce dissolution of the porous substrate and precipitation of damaging solids, cause chemical changes, or induce swelling processes, all of which lead to damaging mechanical stresses and substrate loss. These damage mechanisms can be denoted altogether as *corrosion*. Corrosive processes are dependent on the moisture, the temperature, and the concentration and nature of the carried species in the solution as well as on the flux rate at variable concentration and other boundary conditions.

From 2002 until 2009 the DFG has financially supported our research in the field of materials science in civil engineering, which is focused on the time-dependent description and prediction of the cited damage mechanisms of porous mineral materials by using numerical simulation under real field conditions. Hereby, the modeling of microstructures and transport processes has been extensively studied.

The present book holds the reports published by the involved institutes. Each report contains a summary of the main results achieved in their research. High mathematical complexity and computing cost linked to thorough knowledge of physical chemistry has been required for the successful achievement of the research goals.

Indeed, the implemented numerical models and simulation programs, some of which are in ongoing development, provide for an increasingly useful tool to predict the described corrosive processes in engineering and underground constructions as well as in historic buildings.

Reviewer:

First Funding-Period:

Prof. Dr.-Ing. Manfred Curbach
Prof. Dr.-Ing. Manfred Ehlers
Prof. Dr.-Ing. Hubert K. Hilsdorf
Prof. Dr. Dietbert Knöfel
Prof. Dr.-Ing. Hans-Wolf Reinhardt
Prof. Dr. J.C. Walraven

Second Funding-Period:

Prof. Dr.-Ing. Rolf Breitenbücher
Prof. Dr.-Ing. Hubert K. Hilsdorf
Prof. Dr. Dietbert Knöfel
Prof. Dr. Jan G.M. van Mier
Prof. Dr.-Ing. Hans-Wolf Reinhardt
Prof. Dr. Robert Svensen
Prof. Dr. J.C. Walraven

Third Funding-Period:

Prof. Dr.-Ing. Rolf Breitenbücher
Prof. Dr.-Ing. Frank Dehn
Prof. Dr.-Ing. Josef Hegger
Prof. Dr.-Ing. Ludger Lohaus
Prof. Dr.-Ing. Hans-Wolf Reinhardt
Prof. Dr.-Ing. Michael Schmidt
Prof. Dr.-Ing. Albrecht Wolter

Contents

B. Microstructure, Crystallization and Hydration

C. Corrosion and Degradation

Matthias Koster
Dr.-Ing. Dipl. Phys.

Wolfgang Brameshuber
Univ.-Prof. Dr.-Ing.

Institute of Building Materials Research (ibac), RWTH Aachen University, Aachen, Germany

Simulation of the Microstructure of Cement-Based Materials
- 3D-Simulation of Moisture Transport -

Summary

The research project focuses on simulating the moisture transport processes permeation, diffusion and capillary absorption in hardened cement pastes and mortars as the first two scale levels of a multi-scale model for describing the hygric properties of concrete. On the basis of three-dimensional representations of the microstructure of the hardened cement pastes and the mortars the various moisture transport coefficients are calculated with finite element methods. The generation of a moisture distribution in the materials serves as a prerequisite for simulating frost attack of concrete tackled by a companion project.

Keywords: *moisture transport, hardened cement paste, mortar, permeation, diffusion, capillary absorption, finite element method*

1 Introduction

The durability of porous building materials is significantly affected by their capabilities to transport moisture. This results from the fact that most of the damaging reagents (e.g. sulphates, chlorides) enter the material solved in water or by the so-called “piggyback transport”. The prediction of the durability of the building materials is therefore closely connected to the question of their hygric properties. This is especially true for the damaging of concrete due to frost which was the subject of the cooperation of the Institute of Building Materials Research, RWTH Aachen University (ibac) and the Institute of Mechanics and Computational Mechanics, Leibniz University Hannover (ibnm). The part of the project dealt with at the ibac encompass the simulation of moisture transport and the derivation of the hygric material properties whereas the ibnm was engaged in the mechanical modeling with the goal to deduce the mechanical properties of the materials and to simulate the arising stresses due to frost attack.

Since the building material “concrete” covers several length scales starting from the nano level of the gel phases up to the macro level of the construction component, the limited computational power of today’s data processing equipments prohibits the use of one all-encompassing model. In fact, multi-scale models have to be used to capture the complex nature of concrete. The workings so far dealt with the micro level of the hardened cement paste (typical length scale:

100 µm) and the meso level of the mortar (typical length scale: 10 mm) representing the first steps towards a multi-scale model of concrete.

The approach chosen aimed for calculating the hygric and mechanical properties of hardened cement pastes and mortars on the basis of three-dimensional representations of their microstructure without further assumptions or empirical parameters that would have to be determined experimentally.

In the following the generation of the 3D microstructure of the materials and the simulation of the moisture transport are presented. The transport processes considered encompass the water vapor diffusion, the water permeation and the capillary absorption in hardened cement pastes and mortars. The overall procedure with respect to hardened cement pastes and sandstones is described in detail in [1], [2] .

2 Generation of the 3D microstructures of the hardened cement pastes

The first step of the simulation of moisture transport at the micro level of the multi-scale model of concrete consists in generating a three-dimensional representation of the microstructure of the hardened cement pastes which serves as basis for the later calculations. This aim is achieved by two ways: Firstly, by using the simulation software CEMHYD3D ([3][4]), and secondly, by generating microtomographic images on the basis of the real material.

2.1 Used cements

The base material for the hardened cement pastes was a micro-milled Portland cement with a median grain size d_{50} of approximately 3.4 µm and a Blaine value of 10300 cm^2/g. A fine-ground cement was used in order to keep the representative volume element for the simulation with CEMHYD3D as small as possible in order to reduce the computational power needed. Furthermore, since in CEMHYD3D no diffusion through a closed surface of hydration products is implemented, smaller cement grains are able to hydrate up to a higher degree than larger grains.
The production and preparation of the samples for the microtomographic images (cf. Sect. 2.3) is described in [5].

2.2 Simulation of the microstructure of the hardened cement paste with CEMHYD3D

The computer program CEMHYD3D simulates the development of a three-dimensional microstructure of Portland cement with time during hydration. The software was developed by Bentz et al. at the National Institute of Standards and Technology (NIST), USA.

Starting from SEM (scanning electron microscopy) images of the cement powder, its particle size distribution, and the selected water to cement ratio a three-dimensional computational model of the cement paste is generated by CEMHYD3D. On the basis of this 3D model the hy-

dration of the cement paste is simulated. At the end of the procedure a three-dimensional computational model of the hardened cement paste (hcp) is generated. Two hardened cement pastes were simulated. Their water to cement ratios and degrees of hydration are shown in Table 1.

Table 1: Water to cement ratios w/c and degrees of hydration α of the hardened cement pastes

Name	**w/c**	α
hcp-45	0.45	0.95
hcp-55	0.55	0.99

The initial microstructure of the cement paste generated with CEMHYD3D and the resulting microstructure of the hardened cement paste for the hcp-45 are displayed in Figure 1. The side length of the microstructures amounts to 256 voxels with a voxel length of 1 µm.

(a) Initial cement paste microstructure (b) Hardened cement paste (hcp-45)

Figure 1: Initial 3D microstructure of the cement paste and simulated hardened cement paste (hcp-45)

2.3 Microtomographic images of the hardened cement pastes

In order to decide whether the simulated microstructures are realistic microtomographic images of real hcp samples with a resolution of about 1 µm/voxel were made. After acquisition of the microtomographic data sets, noise was removed by applying a median filter. Subsequently, the microtomographic images were segmented in unhydrated clinker phases, hydration products and pores by thresholding, making use of the cement hydration model of Powers [6]. The microtomographic images of both hardened cement pastes hcp-45 and hcp-55 are depicted in Figure 2.

(a) hcp-45 (b) hcp-55

Figure 2: µCT images of the hardened cement pastes hcp-45 and hcp-55 after segmentation

2.4 Rescaling of the resolution of the microstructures

Both the microstructures simulated with CEMHYD3D and the microtomographic images of the hardened cement pastes have a resolution of about 1 µm/voxel. Hence the submicron part of the pore space, which is significant for the moisture transport, is not captured. In Figure 3 the results of the mercury intrusion porosimetry (MIP) of the hcp-45 are shown.

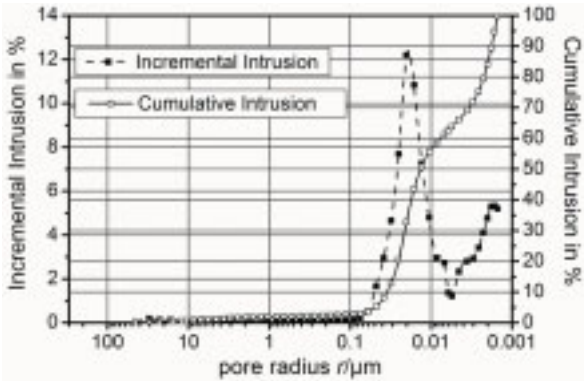

Figure 3: MIP curves of the hcp-45

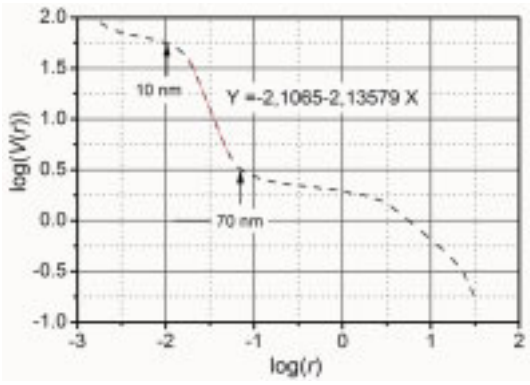

Figure 4: log(V(r)-log(r) plot of the cumulative MIP curve of the hcp-45

According to [7], pores with radii larger than the critical radius r_c, defined by the inflection point of the cumulative intrusion curve, do not form a connected network but are linked by smaller pore channels which act as bottle necks with respect to moisture transport. The critical radii of the hardened cement pastes cover a range between 10 nm and 30 nm. In Figure 4 the log(V(r))-log(r) plot of the cumulative MIP curve in Figure 3 is displayed. Linear segments of the curve represent domains of self-similarity with a fractal dimension defined by the slope of the segment. In case of the hcp-45 the fractal dimension amounts to 2.14 in the range of r_c. The pore space of the corresponding microtomographic image of the hcp-45 also is self-similar with a fractal dimension of 2.12, calculated with a three-dimensional version of the box-counting method described in [8]. Due to the self-similarity of the pore space and accounting for the fact that the fractal dimension of the pore space of the microtomographic image is almost identical to that

of the real material the resolution of the simulated microstructures and the microtomographic data sets was scaled up to 20 nm/voxel assuming that pores with a smaller radius only make a minor contribution to the overall moisture transport.

The change of the resolution scale only affects the later simulation of the permeation and the capillary absorption. The diffusion is independent of the resolution.

3 Simulation of the moisture transport in the hardened cement pastes

The basic approach to simulate the moisture transport in the hardened cement pastes is to replace their pore spaces with networks of cylindrical tubes which possess the same moisture transport properties. On the basis of the transportation networks the moisture transport coefficients are calculated using finite element methods.

3.1 Generating of the moisture transport networks of the hardened cement pastes

The first step in generating the moisture transport networks consists in extracting the medial axis of the pore spaces of hardened cement pastes. This is achieved by a modified version of the “thinning algorithm” described in [9]: Starting with the solid – pore interface all pore voxels that fulfill certain adjacency relations to their neighbor voxels are deleted until the medial axis remains. In a second step all dead end branches and isolated parts of the medial axis, i.e. parts that are not linked to the surface of the microstructures, are removed. Afterwards all voxels where branches of the medial axis intersect are identified using the concept of λ-adjacency [10].

The transportation network is generated by replacing all branches of the medial axis by cylindrical tubes having the same moisture transport properties than the original pore channels. The starting and end points of the tubes are marked by the previously determined intersection points of the medial axis branches.

The diameters of the tubes are assigned in the following way: Each voxel of the medial axis is considered as center point of a sphere, which is steadily increased until it contacts the solid phase. The resulting radius of the sphere is afterwards assigned to the center voxel.

In case of simulating the water permeation the effective hydraulic radius of the pore channels enters the corresponding equations. The hydraulic radius for each voxel of the medial axis is determined by the area A and the perimeter P of the pore channel perpendicular to the medial axis through this voxel, according to

$$r_H = 2\frac{A}{P}. \tag{1}$$

Having assigned a diameter, the voxels of the medial axis are considered as small tubes. The radius of a tube in the transportation network then follows from the calculation of the radius of a serial connection of one voxel long tubes, namely the voxels of the medial axis it consists of.

In Figure 5 a part of the medial axis and the resulting transportation network of the pore space of the microtomographic data set of the hcp-45 are shown.

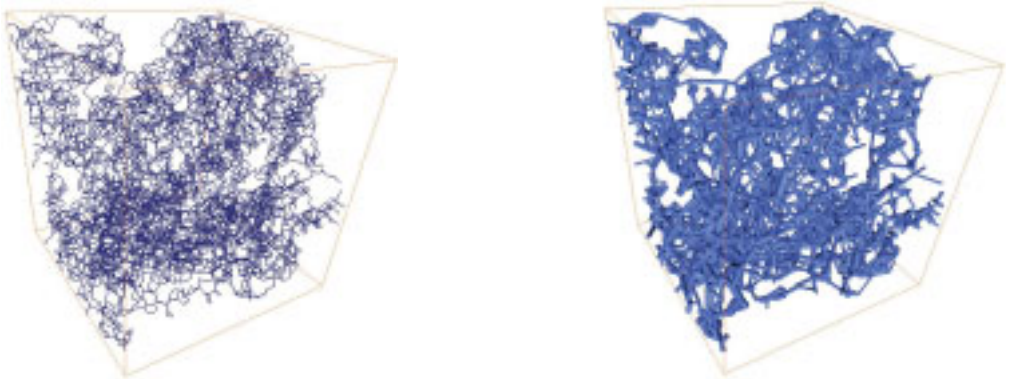

Figure 5: Medial axis and resulting transportation network of the pore space of the µCT image of the hcp-45 (the side length of the displayed volumes is 128 µm)

After generating of the transportation networks the different moisture transport processes (diffusion, permeation and capillary absorption) are simulated with finite element methods.

3.2 Water vapor diffusion of the hardened cement pastes

The simulation of the water vapor diffusion in the hardened cement pastes is carried out by replacing every tube of the transportation networks by one-dimensional heat conducting elements. The mass flow rate in a tube t_{ij} ranging from node i to node j is calculated by Fick's first law, i.e.

$$Q_{ij} = D_{air} \cdot A_{ij} \cdot \frac{\Delta c_{ij}}{L_{ij}} \tag{2}$$

where D_{air} is the diffusion coefficient of water vapor in air, A_{ij} is the cross section of the tube, L_{ij} its length and $\Delta c_{ij} = c_i - c_j$ the imposed water vapor concentration difference. Since the t_{ij} are serial connections of n one voxel long tubes the relations

$$\begin{aligned} Q_{ij} &= Q_k \\ \Delta c_{ij} &= \sum_{k=1}^{n} \Delta c_k \end{aligned} \tag{3}$$

hold. From Eqs. (2) and (3) the diameter of t_{ij} is calculated by

$$d_{ij} = \sqrt{\frac{L_{ij}}{\sum_{k=1}^{n} \frac{L_k}{d_k^2}}} \,. \tag{4}$$

The total mass flow rate within the microstructure is given by

$$Q = D_{hcp} \cdot A \cdot \frac{\Delta c}{L} = \sum_{j \in A_{out}} Q_{ij} \tag{5}$$

with D_{hcp} denoting the water vapor diffusion coefficient of the hardened cement paste, A the cross section, and L the length of the volume passed through by the water vapor, and Δc the imposed vapor concentration difference between inlet and outlet surface of the volume. Constant concentration boundary conditions were used for all nodes and no-flow boundary conditions for all end nodes of tubes not lying on the inlet or outlet surface. The mass flow rate within the porous medium is calculated by summation of the mass flow rates of all tubes crossing the outlet surface. The simulated water vapor diffusion coefficients of both hardened cement pastes are shown in Table 2. The degree of compliance between the water vapor coefficients of the microtomographic images and those of the simulated microstructures depends on the water to cement ratio, as can be seen from Table 2.

Table 2: Simulated water vapor diffusion coefficients of the hardened cement pastes

Hardened cement paste	**D_{hcp}**	
	µCT	**CEMHYD3D**
	10^{-7} m^2/s	
hcp-45	0.8	7.1
hcp-55	16.1	12.4

Unfortunately the water vapor diffusion coefficients of the hardened cement pastes could not be determined experimentally due to a pronounced tendency to form drying shrinkage cracks. For comparison experimental results of a hardened cement paste consisting of an ordinary Portland cement according to [11] are displayed in Table 3.

Table 3: Measured water vapor diffusion coefficients of hardened cement pastes made of ordinary Portland cement

w/z	**D_{hcp}**
	10^{-7} m^2/s
0.35	2.2
0.45	4.1
0.60	6.1

Even though, the water vapor diffusion coefficients of Table 3 cannot be compared directly to those in Table 2, because of different raw materials, the values lie in the same order of magnitude.

3.3 Water permeability of the hardened cement pastes

The simulation of water permeability is achieved by replacing every tube in the transportation network by a one-dimensional fluid conducting element for which Bernoulli's law is applied. The mass flow rate in a tube t_{ij} is calculated by

$$Q_{ij} = A_{ij}\sqrt{\frac{2\rho\,\Delta p_{ij}}{c_l}} \tag{6}$$

where ρ is the density of the fluid, c_l the loss coefficient and $\Delta p_{ij} = p_i - p_j$ the imposed pressure difference. The loss coefficient can be expressed by

$$c_l = \lambda\frac{L_{ij}}{D_{ij}} + \zeta \tag{7}$$

with λ denoting the friction factor and ζ accounting for hydraulic losses due to a variation of the diameter of t_{ij}, cross points with other tubes and the constriction of the tubes provoked by the "self-sealing" effect of hardened cement paste due to its distinct interaction with water [12]. Assuming laminar flow in the tubes the friction factor results from

$$\lambda = \frac{64}{Re} \tag{8}$$

where Re is the Reynolds number defined by

$$Re = \frac{Q_{ij}\cdot d_{ij}}{\eta\cdot A_{ij}} \tag{9}$$

with η the dynamic viscosity of the fluid.

Analogous to Eq. (4) the diameter of the tube t_{ij} is given by

$$d_{ij} = \sqrt[4]{\frac{L_{ij}}{\sum_{k=1}^{n}\frac{L_k}{d_k^4}}}\,. \tag{10}$$

The mass flow rate through the hardened cement pastes is calculated using Darcy's law:

$$Q = \frac{\rho k A}{\eta}\cdot\frac{\Delta p}{L} = \sum_{j\in A_{out}} Q_{ij}\,. \tag{11}$$

For the FE simulation constant pressure boundary conditions for all nodes and no-flow boundary conditions for all nodes at the end of dead end tubes were used.

The water permeability coefficients of the hardened cement pastes were measured using the triaxial flow cell described in [13].

In Table 4 the simulated permeability coefficients together with the experimental values are shown. In order to account for the already mentioned "self-sealing" effect of the hardened ce-

ment pastes the loss coefficient ζ in Eq. (7) was determined so that the measured permeability coefficient of the hcp-45 matches the simulated value of the µCT microstructure. The obtained value was afterwards also used for the hcp-55. It should be mentioned that the loss coefficient was only necessary for the hardened cement pastes. In case of sandstones which behave more or less inert with respect to water no loss coefficient was needed to match the experimental data [1].

Table 4: Water permeability coefficients of the hardened cement pastes

Hardened cement paste	**k**		
	µCT	**CEMHYD3D**	**Experiment**
		10^{-21} m^2	
hcp-45	3.6	9.2	3.5 ± 0.7
hcp-55	14.5	14.8	15.0 ± 1.7

3.4 Capillary water absorption of the hardened cement pastes

In order to simulate the capillary water absorption of the hardened the cement pastes every tube of the transportation network is replaced by a one-dimensional heat conducting element t_{ij} ranging from node i to node j. The relevant equations are deduced as follows: At time t = 0 the temperature at node i of t_{ij} is suddenly increased from 0 to 1. In node j adiabatic conditions shall prevail. The heat transfer in t_{ij} is then described by the heat conducting equation

$$\frac{\partial^2 T}{\partial x^2} - \frac{1}{a_{ij}} \frac{\partial T}{\partial t} = 0, \tag{12}$$

where T denotes the temperature and a_{ij} the temperature conductivity, together with the initial condition

$$T(x,0) = 0 \tag{13}$$

and the boundary conditions

$$\left.\frac{\partial T}{\partial x}\right|_{x=h} = 0$$
$$T(0, t \geq 0) = 1 \tag{14}$$

with h denoting the length of t_{ij}. The solution of Eq. (12) in conjunction with Eq. (13) and Eq. (14) for the time dependent temperature increase in node j is given by

$$T(h,t) = 2(\operatorname{erfc}(\xi) - \operatorname{erfc}(3\xi) + \operatorname{erfc}(5\xi) - \cdots \tag{15}$$

where erfc is the complementary error function

$$\mathrm{erfc}(\xi) = 1 - \frac{1}{2\pi}\int_0^{\xi} e^{-t^2} dt \tag{16}$$

and ξ is defined by

$$\xi = \frac{h}{2\sqrt{a_{ij}\, t}}\,. \tag{17}$$

If ξ is large, that is for small time periods t, the series on the right-hand side of Eq. (15) can be truncated after the first term. Setting T(h,t) = ε it follows from Eq. (15) that

$$\xi = \mathrm{erfc}^{-1}(\varepsilon / 2) \tag{18}$$

which inserted in Eq. (17) leads to

$$h = 2\sqrt{a_{ij}}\, \mathrm{erfc}^{-1}(\varepsilon / 2)\sqrt{t}\,. \tag{19}$$

On the other hand, if the maximum height of capillary rise is much larger than h, the capillary water absorption of a cylindrical tube t_{ij} is governed by the equation

$$h = \sqrt{\frac{\sigma \cos \vartheta r_{ij}}{2\eta} \cdot t}\,, \tag{20}$$

[14] where r_{ij} is the radius of the tube, σ the surface tension of water, and ϑ the contact angle. Equating Eq. (20) and Eq. (19) yields the following relation for the temperature conductivity of t_{ij}:

$$a_{ij} = \frac{1}{8}\frac{\sigma r_{ij} \cos \vartheta}{\eta(\mathrm{erfc}^{-1}(\varepsilon / 2))^2}\,. \tag{21}$$

The results so far can be summarized as follows:

When at node i of an heat conducting element t_{ij} of the transportation network the temperature is increased from 0 to 1 at time zero and its temperature conductivity satisfies Eq. (21), the time needed to increase the temperature at node j to ε matches the time needed by a water column to travel from i to j in case of capillary suction. Since this is only valid if adiabatic conditions prevail at j the temperature conductivity of the subsequent elements intersecting in j may not start until the temperature in j has reached ε. This means that the temperature conductivity of the heat conducting elements have to be changed continuously during the FE calculation.

Table 5 summarizes the simulated water absorption and water infiltration coefficients of the hardened cement pastes.

Table 5: Simulated water absorption and water infiltration coefficients of the hardened cement pastes

Hardened cement paste	**Porosity**	**A_w**		**E_w**	
		µCT	**CEMHYD3D**	**µCT**	**CEMHYD3D**
	%	kg/(m^2 h$^{0.5}$)		10^{-2} m/h$^{0.5}$	
hcp-45	14	0.4	2.1	1.0	1.3
hcp-55	22	1.5	3.4	1.5	1.4

Due to the already mentioned problem of drying shrinkage cracks the capillary absorption coefficient of the hardened cement pastes could not be measured. For comparison experimental values of various hardened cement pastes made of an ordinary Portland cement according to [15] are listed in Table 6 pointing out that the simulated water absorption coefficients lie in the same range. This indicates that the presented model is able to produce reliable results.

Table 6: Measured water absorption coefficients of hardened cement pastes made of ordinary Portland cement

Hardened cement paste	**Porosity**	**A_w**
	%	kg/(m^2 h$^{0.5}$)
0.35	14	0.5
0.45	25	0.6
0.60	32	2.0

4 Generation of the 3D microstructures of the mortars

4.1 Materials

At the meso level of the multi-scale model two mortars m47 and m57 with water to cement ratios of 0.47 and 0.57, respectively, were used. The mixture composition of the mortars shown in Table 7 complied with the requirement that the contained bulk matrix was identical to the hardened cement pastes already investigated at the micro level of the model. The necessary workability of the mortars was achieved by adding a superplasticizer on the basis of polycarboxylate ether.

Table 7: Mixture composition of the mortars m47 and m57

Mortar	Constituent	Density kg/m³	Net Weight g
m47	Cement	3113	248.4
	Sand 0.25/1.0	2650	634.3
	Water	1000	115.4
m57	Cement	3113	242.4
	Sand 0.25/1.0	2650	619.0
	Water	1000	137.1

4.2 Microtomographic images of the mortars

The preparation of the mortar samples for the microtomographic images is described in [16]. The resolution of the microtomographic data sets was 7.1 µm/voxel. In order to remove noise a median filter was applied. After that the images were segmented into the phases aggregates, matrix and pores by a threshold operation. Since the latter were few and far between they could safely be neglected.

Because of the limited resolution of the microtomographic data sets the interfacial transition zone (ITZ) could not be distinguished from the bulk matrix. The ITZ was therefore computationally generated. In accordance with experimental results from [17] its thickness was chosen to be 3 voxels (≈ 21.3 µm).

(a) Original µCT image

(b) µCT image after noise filtering, segmentation and generation of ITZ

Figure 6: Noise filtering and segmentation of the µCT data set of the mortar m47

5 Simulation of the moisture transport in the mortars

5.1 Generating of the moisture transport networks

The basic approach for simulating the different moisture transport processes in the mortars consists in replacing the bulk matrix and the ITZ by transportation networks much like in the case of the pore space of the hardened cement pastes depicted in Sec. 3.1. First the medial axis of the bulk matrix and the ITZ are extracted. Then both medial axes are transformed into transportation networks which are subsequently superposed to an overall transportation network. Afterwards, this transportation network forms the basis for calculating the moisture transport coefficients with finite element methods. In doing so the contained aggregates are assumed to be impermeable. For the contained bulk matrices in the mortars the calculated moisture transport coefficients of the corresponding hardened cement pastes based on the (more realistic) µCT images are used (cf. Chapt. 3). The moisture transport coefficients of the ITZs are inversely determined by comparing the calculated values of the mortars with experimental data. The whole procedure is described in [16].

5.2 Water vapor diffusion of the mortars

Analogous to Eq. (2) the mass flow rate in a tube t_{ij} of the transportation networks is calculated by

$$Q_{ij} = D \cdot A_{ij} \cdot \frac{\Delta c_{ij}}{L_{ij}} \tag{22}$$

where D is the water vapor diffusion coefficient of the phase represented by the network, i.e. $D = D_{hcp}$ in case of the bulk matrix and $D = D_{ITZ}$ for the ITZ. The value of D_{hcp} results from the simulation of the water vapor diffusion of the hardened cement pastes (cf. Table 2). The unknown diffusion coefficient D_{ITZ} was inversely determined so that the calculated water vapor diffusion coefficients of the mortars resulting from

$$Q = D_{mortar} \cdot A \cdot \frac{\Delta c}{L} = \sum_{j \in A_{out}} Q_{ij} \tag{23}$$

(cf. Eq. (5)) matched the experimental values. The measurement of the water vapor diffusion coefficients of the mortars were conducted according to the German standard DIN EN ISO 12572:2001-09. In order to avoid surface diffusion, not taken into account in the simulation, the maximum water vapor concentration was limited to 50 % r.h.

In Table 8 the simulated water vapor coefficients of the mortars together with the measured values are listed. As can be seen from the data, in order that the calculated water vapor diffusion coefficients of the mortars match the experimental values the diffusion coefficient of the ITZ has to be 180 times larger than that of the corresponding bulk matrix in case of the mortar m47 and 26 times larger in case of the mortar m57.

Table 8: Water vapor diffusion coefficients of the mortars and their constituents

Mortar	Constituent	D	
		Simulation	Experiment
		10^{-8} m^2/s	
m47		5.6	5.4 ± 0.7
	Bulk Matrix	8	
	ITZ	1450	
m57		16.0	17.0 ± 5.7
	Bulk Matrix	161	
	ITZ	4200	

5.3 Water permeability of the mortars

The water permeability of the mortars was simulated by starting with Eq. (6) for the mass flow rate Q_{ij} in a tube t_{ij} of the network. Since the "self-sealing" effect of the bulk matrix in the mortars is already included in the permeability coefficient of that phase the loss coefficient ζ in Eq. (7) is zero. Q_{ij} then simplifies to

$$Q_{ij} = \frac{\rho d_{ij}^2 A_{ij}}{32 \eta_{eff}} \cdot \frac{\Delta p_{ij}}{L_{ij}} \tag{24}$$

where η_{eff} is the effective dynamic viscosity of the fluid. Eq. (24) holds if the tubes in the transportation network are hollow. However, since the network represents the bulk matrix and the ITZ of the mortars the tubes are filled with the corresponding solid phase. This can be taken into account within the FE simulation by appropriately choosing η_{eff}. The mass flow rate in a cylinder of bulk matrix or ITZ is calculated by using Darcy's law:

$$Q_{ij} = \frac{\rho k A_{ij}}{\eta} \cdot \frac{\Delta p_{ij}}{L_{ij}} \tag{25}$$

with the permeability coefficient k of the corresponding solid phase (bulk matrix or ITZ). Equating Eq. (24) and Eq. (25) leads to

$$\eta_{eff} = \frac{\eta d_{ij}^2}{32 k}. \tag{26}$$

Thus, in order to account for the fact that the tubes in the network are not hollow but filled with a solid phase for every tube a particular viscosity of the transported fluid has to be assigned according to Eq. (26). Besides of that, the calculation of the permeability coefficients of the mortars is carried out in much the same way as described in Sec. 3.3. The permeability coefficients of the mortars k_{mortar} are calculated using Darcy's law:

$$Q = \frac{\rho k_{mortar} A}{\eta} \cdot \frac{\Delta p}{L} = \sum_{j \in A_{out}} Q_{ij} \,. \tag{27}$$

In Table 9 the simulated and the measured permeability coefficients are displayed.

Table 9: Water permeability coefficients of the mortars and their constituents

Mortar	**Constituent**	**k**	
		Simulation	**Experiment**
		10^{-21} m^2	
m47		3.2	3.2 ± 1.7
	Bulk Matrix	3.6	
	ITZ	18700	
m57		7.6	7.4 ± 3.5
	Bulk Matrix	14.5	
	ITZ	267000	

The permeability coefficients of the bulk matrices result from the simulation of the water permeation of the corresponding hardened cement pastes in Sec. 3.3. The permeability coefficients of the ITZs were inversely determined so that the simulated values of the mortars matched the experimental ones. The permeability coefficients were measured in accordance with the German standard DIN 18130-1:1998-05.

From Table 9 it follows that $k_{ITZ}/k_{bulk} \approx 5200$ for the mortar m47 and $k_{ITZ}/k_{bulk} \approx 18400$ for the mortar m57. These values appear to be somewhat high and further investigations are necessary in order to prove their validity.

5.4 Capillary water absorption of the mortars

The fact that the tubes in the transportation network are not hollow is taken into account by appropriately choosing the effective viscosity of the fluid as it was already done in case of the water permeation described in the previous section. The capillary water absorption of a circular tube t_{ij} is described by Eq. (20). On the other hand the water uptake of a cylinder of bulk matrix or ITZ is given by

$$h(t) = E_W \sqrt{t} \tag{28}$$

whereas E_W denotes the water infiltration coefficient of the corresponding solid phase (bulk matrix or ITZ). Equating Eq. (28) and Eq. (20) leads to

$$\eta_{eff} = \frac{\sigma \cos \vartheta \, d_{ij}}{4 E_W^2} \tag{29}$$

for the effective viscosity of the fluid. Inserting Eq. (29) into Eq. (21) yields

$$a_{ij} = \frac{E_W^2}{4(\mathrm{erfc}^{-1}(\varepsilon/2))^2} \tag{30}$$

for the temperature conductivity of t_{ij}.

The FE simulation of the capillary absorption of the mortars is based on the following assumptions: The porosity of the ITZ is twice as large as the porosity of the corresponding bulk matrix [17]. The water infiltration coefficients of the bulk matrices result from the simulation of the capillary absorption of the corresponding hardened cement pastes. A linear relationship between the porosity and the water infiltration coefficients of the hardened cement pastes is assumed and the water infiltration coefficients of the ITZs are then obtained by extrapolation.

The simulated water absorption coefficients of the mortars together with the experimental values, which were determined according to the German standard DIN EN ISO 15148:2003-03, are displayed in Table 10.

Table 10: Water absorption coefficients of the mortars and their constituents

Mortar	**Constituent**	**Porosity**	**E_W**	**A_W**	
			Simulation	**Simulation**	**Experiment**
		%	10^{-2} m/h$^{0.5}$	kg/(m^2 h$^{0.5}$)	
m47				0.14	0.50 ± 0.03
	Bulk Matrix	16	1.0	0.40	
	ITZ	32	1.9		
m57				0.24	1.22 ± 0.05
	Bulk Matrix	26	1.5	1.50	
	ITZ	52	2.9		

As can be seen, the experimental values are larger by a factor of 3.5 to 5 compared to the simulated ones. The main reason for this discrepancy is the formation of drying shrinkage cracks during specimen preparation for the capillary absorption tests which occurred despite drying the samples as gentle as possible. Furthermore, the transportation networks of the bulk matrix and the ITZ are disjoint, which also may have an influence on the simulation results.

6 Final comments and conclusions

On the basis of three-dimensional representations of the microstructure of hardened cement pastes and mortars their moisture transport coefficients were calculated with finite element methods. Starting point for the calculations were microtomographic images of the materials considered. In case of the hardened cement pastes additionally computationally generated microstructures with the aid of the simulation software CEMHYD3D were used. However, the

microtomographic images turned out to be closer to reality and therefore led to moisture transport coefficients which better match experimental values.

The pore space of the hardened cements pastes was replaced by a transportation network consisting of cylindrical tubes. The mortars were considered as three-phase systems consisting of aggregates, bulk matrix and interfacial transition zone. The aggregates were assumed to be impervious. The contained bulk matrix as well as the interfacial transition zone was replaced by a transportation network reflecting the moisture transport properties of the corresponding phase. On the basis of the generated transportation networks the various moisture transport processes were simulated with FEM. The calculated moisture transport coefficients of the hardened cement pastes entered the simulation of the moisture transport of the mortars as transport coefficients of the contained bulk matrices. By comparing the calculated moisture transport coefficients of the mortars with measured values the hygric properties of the included interfacial transition zones could be derived. However, the evaluation of the obtained results entails further experimental investigations of the moisture transport capabilities of the interfacial transition zone.

Financial support from the German Research Foundation DFG is gratefully appreciated.

7 References

[1] Koster, M.: Mikrostruktur-basierte Simulation des Feuchtetransports in Zement- und Sandstein, Aachen, RWTH Aachen University, Institute of Building Materials Research, PhD thesis, 2007 (in German)

[2] Koster, M. and Hannawald, J. and Brameshuber, W.: Simulation of Water Permeability and Water Vapor Diffusion Through Hardened Cement Paste, Computational Mechanics 37 (2) (2006), p. 163-172

[3] Bentz, D. P.: A Three-Dimensional Cement Hydration and Microstructure Program. I. Hydration Rate, Heat of Hydration and Chemical Shrinkage / NIST. U.S. Department of Commerce, Washington D.C., 1995 (NISTIR No. 5756) – Internal Report

[4] Bentz, D. P.: A Three-Dimensional Cement Hydration and Mircrostructure Development Modeling Package. Version 2.0 / NIST. U.S. Department of Commerce, Washington D.C., 2000 (NISTIR No. 6485) – Internal Report

[5] Koster, M. and Hannawald, J. and Brameshuber, W.: 3D Simulation of Moisture Transport in Porous Building Materials. Freiburg: AEDIFICATIO Publisher, 2007. - In: Transport in Concrete: Nano-to Macrostructure. TRANSCON 07. Proceedings of 5th International Essen Workshop, Duisburg-Essen, June 2007, p. 435-446

[6] Powers, T. C.: Physical properties of cement paste. Proceedings of the Forth International Symposium on the Chemistry of Cement. Washington D. C., 1960, p. 577 – 613

[7] Katz, A. J. and Thompson, A. H.: Quantitative Prediction of Permeability in Porous Rock, Physical Review B 34 (1986), No. 11, p. 8179-8181

[8] Hou, X.-J. et al.: An efficient algorithm for fast O(N ln(N)) box counting, Physics letters A 151 (1990), No. 1-2, p. 43-46

[9] Palágyi, K. et al.: A Sequential 3D Thinning Algorithm and Its Medical Applications, Insana, M. F. and Leahy, R. M. (Eds.), Proceedings of the 17th International Conference Information Processing in Medical Imaging, IPMI 2001, Davis, USA, p. 409-415

[10] Liang, Z. and Ioannidis, M. A. and Chatzis, I.: Geometric and Topological Analysis of Three-Dimensional Porous Media: Pore Space Partitioning Based on Morphological Skeletonization, Journal of Colloid Interface Science 221 (2000), p. 13-24

[11] Hedenblad, G.: The Use of Mercury Intrusion Porosimetry or Helium Porosimetry to Predict the Moisture Transport Properties of Hardened Cement Paste, Advanced Cement Based Materials 6 (1997), p. 123-129

[12] Rucker, P.: Moisture and Salt Transport in Concrete – A New Approach to Modeling, Walraven, J. et al. (Eds.), 5th Int. PhD Symposium in Civil Engineering, Delft, 16-19 June 2004, p. 111-118

[13] Schloemer, S. and Krooss, M.: Molecular transport of methane, ethane and nitrogen and the influence of diffusion on the chemical and isotopic composition of natural gas accumulations, Geofluids 4 (2004), p. 81-108

[14] Cammerer, W. F.: Die kapillare Flüssigkeitsbewegung in porösen Körpern, Düsseldorf: VDI-Verlag, VDI-Forschungshefte (1963), No. 500 (in German)

[15] Künzel, H. M. and Krus, M.: Pore Size Distribution and Transport Properties of Porous Building Materials, Fraunhofer Institute of Building Physics, Stuttgart, 1994 – Science Report

[16] Koster, M. and Hannawald, J. and Brameshuber, W.: 3D Simulation of Moisture Transport in Cement Mortars, Bagneux: RILEM, 2008. - In: Concrete Modelling CONMOD ´08 Proceedings of the International RILEM Symposium, Delft, The Netherlands, 26-28 May 2008, (Schlangen, E. ; Schutter De, G. (Eds.)), p. 511-520

[17] Scrivener, K.L.: Characterisation of the ITZ and its Quantification by Test Methods. Cachan Cedex : RILEM, RILEM Report 20, 1999. - In: Engineering and Transport Properties of the Interfacial Zone in Cementitious Composites, (Alexander, M.G. ; et al (Ed.)), p. 3-15

Christoph Liebrich *Dipl.-Ing.*
Regina Vogt *Dipl.-Ing.*
Ralf Kriegel *Dr. rer. nat.*
Christian Kaps *Prof. Dr. rer. nat. habil.*

Bauhaus-University Weimar, Germany

Modelling of diffusive transport of salt ions in porous, water-containing building materials and capillary transport behaviour of salt solutions, subject to building material, salt type, concentration and fluid content

Summary

A concept was developed for the modelling of the diffusion. This enabled the known influences on diffusive transport in free solution (salt type and concentration, temperature) to be presented in general quantitive contexts and in connection with the building-materials-specific parameters of the pore system (tortuosity, moisture exponent in accordance with influence on pore filling) which had been established by experiments. In order to produce a description of the advective fluid transport, the behaviour of the salt solutions was investigated on the basis of the standard suction experiments used to determine the water-absorption speed of capillary-porous building materials. This was then successfully reproduced in formulaic dependence of the essential influences, such as dynamic viscosity and the solution density of various salt concentrations. As a result of special drying experiments and the determination of the salt content distribution, it was possible to identify the break-off conditions for advective fluid transport.

Keywords: *diffusive transport of salt ions, effective diffusion coefficient in porous building materials, fluid transport of the pore solution, critical pore filling*

1 Modelling of the Diffusive Transport of Salt Ions in Porous Building Materials

1.1 Summary

In order to achieve a practically-applicable model of the diffusive transport of a dissolved salt in porous building materials (a corresponding cation-anion pair), it was necessary to carry out an assessment of several calculation methods with reference to the experimentally-proven diffusion coefficients $D_s(c_s,T)$ in free solution. An adequately accurate description of the concentration dependence of the diffusion $D_s(c_s)$ could only be achieved with an experimental reference curve dependent on salt type. It was possible to approximate the temperature dependence $D_s(T)$ by means of the Arrhenius method. The material parameters necessary for calculating the effective diffusion coefficient in porous building materials were determined by testing a selection of materials. The verified functional coherences and data fields were then integrated into

the simulation programme DELPHIN and successfully tested under laboratory conditions (the two-disc experiment). In addition to this, a method was developed and used which made it possible to simulate diffusive transport for complex ion- and salt mixtures. This method involved the use of ion-specific parameters and their combination with each other. Experiments into the hygric characteristics of porous building materials revealed that the sorption isotherms of building materials containing salts arise cumulatively from the sorption isotherm of the salt-free building material and the water sorption of the incorporated salt.

1.2 Dependencies of the Salt Diffusion Coefficient in Free Solution

Salt diffusion coefficients in free solution display, among other things, a pronounced dependence on salt concentration c_s and temperature T. The salts relevant to building materials differ mainly with regard to the concentration dependence (i.e. functional dependence) of the salt diffusion coefficient $D_{sol}(c_s)$. Although the models considered (Stokes-Einstein, Nernst-Einstein, Nernst-Planck) to some extent produce well-calculated diffusion coefficients for selected salts and concentration areas, they fail completely in the case of other contaminating salts or with high concentrations. The model assessment and the data found in the relevant literature have so far failed to produce a generally-applicable and sufficiently accurate calculation model for $D_{sol} = f(c_s,T)$.

On the other hand, the temperature dependence of the diffusion coefficient $D_{sol}(T)$ at constant concentration c_s can, like many other thermically active processes, be described with sufficient accuracy by the Arrhenius method.

$$D_{sol}(T) = D_0(c_s) \cdot \exp\left(-\frac{E_A(c_s)}{RT}\right)$$

D_0	diffusion coefficient at theoretically infinite temperature [cm²/s]
E_A	activation energy of the diffusion / conductivity [kJ/mol]
T	temperature [K]
R	gas constant

In addition, the dependence of the activation energy $E_A(c_s)$ and the pre-exponential factors $D_0(c_s)$ on the salt concentration is comparatively slight in the case of the salts considered. Starting from an experimental diffusion coefficient $D_{r,sol}(c_s)$ at a reference temperature T_r (value taken from the literature), the diffusion coefficient $D_{sol}(c_s,T)$ in free solution can thus be calculated even with a medium activation energy E_A for the underlying concentration c_s and a selected temperature T (Equation 1).

$$D_{sol}(c_s,T) = D_{r,sol}(c_s) \cdot \exp\left(\frac{E_A \cdot (T - T_r)}{R \cdot T \cdot T_r}\right) \quad (1)$$

If sufficient (possibly interpolated) data $D_{r,sol}(c_s)$ and $E_A(c_s)$ at a constant reference temperature T_r are available in the literature, it is possible to calculate the concentration-dependent salt-diffusion coefficient in free solution for a given temperature.

If one compares the diffusion of a salt in a building material with that of one in free solution, one achieves an effecive diffusion coefficient D_s lower than the diffusion coefficient in free solution

D_{sol}. This finding reflects the complex influence of the pore structure (elongated diffusion path, reduced width, pore connection) and can be summarised as so-called tortuosity τ. Tortuosity is determined by means of experiment and emerges from the relationship between the experimentally-efficient diffusion coefficient [1] of a model salt and the diffusion coefficient in free solution as a material-specific parameter which is independent of salt type [2]. Once the tortuosity of a building material is known, the effective diffusion coefficient of any contaminating salt can be calculated at moisture saturation point. This is assuming that the diffusion coefficient in free solution (for a given c_s, T) can be taken from the literature or calculated on the above basis.

Further to this, the effective diffusion coefficient D_s of a salt in a building material depends on its moisture content θ_l [3]. The form of functional dependence is clearly influenced by pore morphology and can be described in terms of the material-specific moisture exponent n (Equation 2).

$$D_s(\tau,\theta,c_s,T) = \frac{D_{sol}(c_s,T)}{\tau} \cdot \left(\frac{\theta_l}{\theta_{cap}}\right)^n \qquad (2)$$

θ_l	volumetric water content of material
θ_{cap}	water content of material at capillary saturation point
θ_l/θ_{cap}	relative moisture content of building material

The modelling of effective diffusion coefficients in building materials is shown schematically in Figure 1.

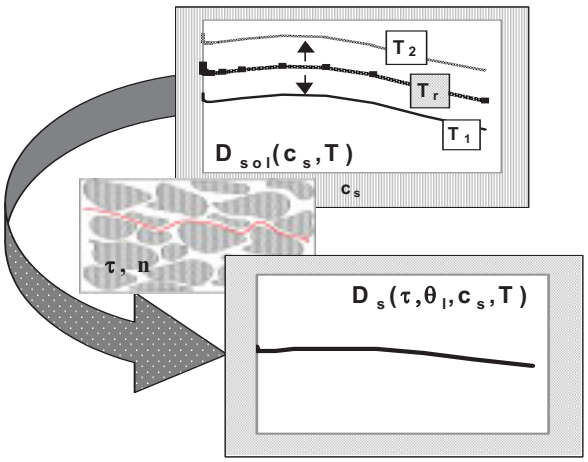

$D_{sol}(c_s)$	diffusion coefficient in free solution [cm²/s]
$E_A(c_s)$	molar intrinsic ionisation energy diffusion [kJ/mol]
T_r	temperature, reference temperature [K]
τ	tortuosity [-]
n	moisture exponent [-]

Figure 1: Diagram of the Modelling of the effective diffusion coefficient.

The material-specific parameters of various selected reference materials were determined by means of diffusion experiments. The salt-specific model parameters of the relevant contaminating salts were taken from data in the literature. This data was incorporated into the material- and salt data banks of the programme system. As a result of this, it is now possible to model changes in the diffusive transport characteristics, subject to electrolyte composition and temperature.

1.3 Two-Disc Experiment (Weimar) with Calcium Silicate

The two-disc experiment (Figure 1) serves to determine the material dependence of the diffusion coefficient. Two discs of the selected material are produced, measuring 47 mm in diameter and 10 mm in thickness. One disc is saturated with a 1-molar salt solution (in this case, Na_2SO_4) and the other with pure water. The two discs are then joined together (with high concentration to the left) and the outer surfaces sealed so that no external steam transport can take place. Owing to the salt concentration gradient, a diffusive salt transport takes place from the left-hand to the right-hand disc. Boreholes are then drilled at certain (temporal) intervals, and the salt distribution is determined by means of drill-powder analysis. These tests are carried out using a Jöns clay brick and calcium silicate as an internal sealing material. The test series are arithmetically simulated at the same time with a simulation time lasting 12 hours. The salt distributions are compared with the measured data after 3, 6 and 8 hours. In the case of calcium silicate, the initial moisture content measured 89 Vol.-%, which corresponds to the saturation moisture. The parameter τ of Equation 2 measures 0.85.

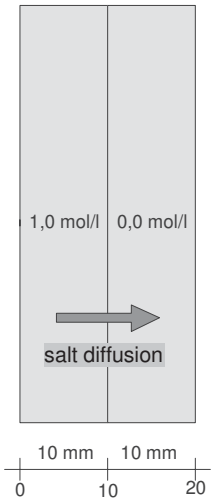

Figure 1: Test Structure.

Figure 3 shows a good measure of correlation between calculation and measurement. The exaggerated values on the left-hand side near the centre can probably be attributed to contact problems between the two discs.

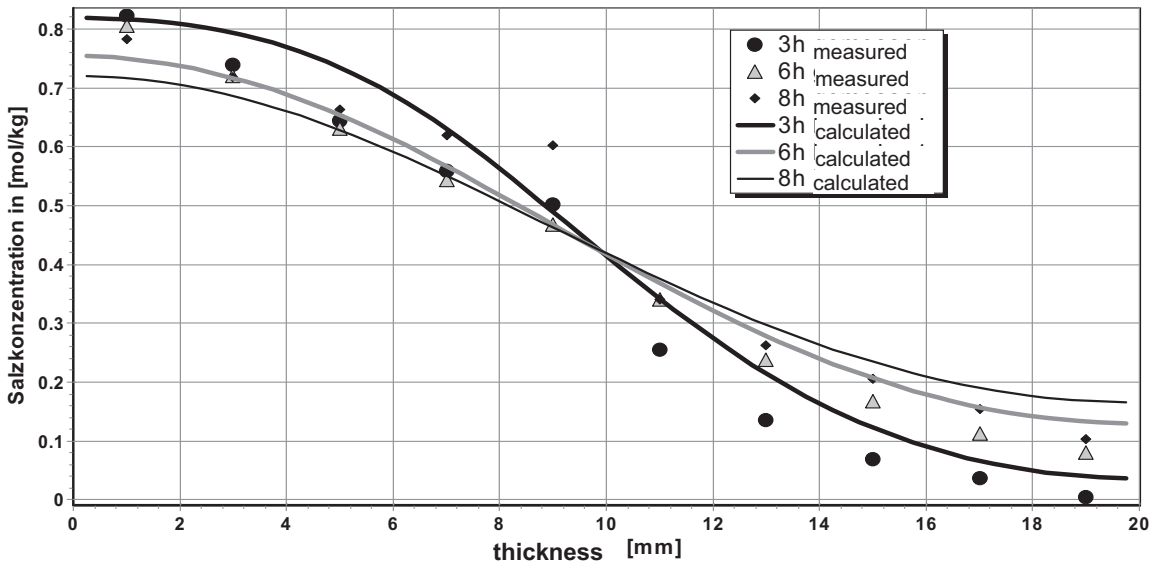

Figure 3: Comparison between calculated and measured salt concentrations after 3, 6 and 8 hours of testing for calcium silicate.

1.4 Concentration Dependence of the Diffusion Coefficient and of Diffusion Coefficients in Salt Mixtures

In order to calculate the diffusion in solution of various salts, the ions are considered separately. The method used is an extended Nernst-Planck Equation (Equation 4), which describes the mass flow of an ion in mol/(m²s).

$$J_i = D_{s,i}\left(\frac{\partial c_i}{\partial x} + \frac{z_i F}{RT} c_i \frac{\partial U}{\partial x} + c_i \frac{\partial(\ln \gamma_i)}{\partial x}\right) \tag{4}$$

J	- ion flow [mol/m²s]	R	- gas constant [J/Kmol]
D_s	- diffusion coefficient of ion in pore space [m²/s]	T	- temperature [K]
c	- concentration (molarity) [mol/m³]	U	- electrical potential [V]
z	- electrochemical valency of ion [-]	γ	- activity coefficient of ion [-]
F	- Faraday constant [As/mol]	x	- local components [m]

The influence of the pore structure and the moisture saturation degree in the effective diffusion coefficient $D_{i,s}$ is also included here - along the lines of the salt diffusion model used previously (Equation 5):

$$D_{s,i} = \frac{D_{i,sol}}{\tau} \cdot \left(\frac{\theta_l}{\theta_{cap}}\right)^n \tag{5}$$

The different diffusion speeds of the various ions of a dissolved salt can in principle lead either to the 'hurrying-ahead' or to the 'lagging behind' of certain ion types. The result of this would be the formation of a local charge field, which would in turn cause certain ions to be accelerated or decelerated due to the electrostatic coupling of the ion charges, depending on charge and mobility. The charges must therefore balance each other to such an extent that no noticeable charge separation results. The neutrality of the charge or zero-current condition must be numerically enforced by means of the Poisson Equation.

Alternatively, the use of our method slightly relaxes the prerequisite of charge neutrality and allows for a very small charge field to emerge. This means that the ion diffusion can be described in terms of two overlapping processes: one the one hand, diffusion takes place as a result of the concentration gradient and the gradient of the activity coefficient; on the other, compensating ion flows are created by the charge field which forms in the meantime. A coupling parameter now scales these compensating ion flows in such a way that the transport caused by the charge compensation is very considerable in relation to that of the diffusive transport. Accordingly, this scaling can even lead to significant ion flows in the case of the very small charge fields which emerge during the numerical simulation of the diffusion. These counteract the diffusive drifting-apart of ions of various degrees of mobility and the subsequent enlargement of local electric potentials. In principle, this method justifies the use of ion-specific parameters (diffusion coefficients, concentrations) and their linking with each other, thus making it possible to simulate diffusive transport even for complex ion mixtures (salt mixtures). Furthermore, one can manage with data from relatively few ions without needing to account for all the special salts.

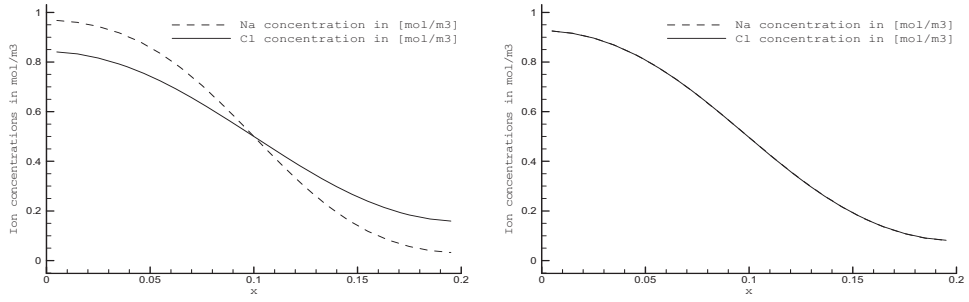

Two-disc diffusion experiment without charge-coupling Two-disc diffusion experiment with charge-coupling

Figure 4: Two-disc diffusion experiment with various (accepted) ion diffusivities after 100 hours, with and without charge-coupling.

The implementation of this method was tested. The results for the various coupling conditions between Na^+ and Cl^-, as shown in Figure 4, were as anticipated. In the case of neglected charge coupling, the ions diffuse at different speeds. This is due to their varying degrees of mobility or to the varying ion diffusion coefficients within the same period of time. This leads to significant differences in the concentration distribution of the ions, despite an identical initial concentration distribution (t = 0) and the same diffusion time. In the calculation using the charge-coupling, the concentration profiles of the ions are superimposed on each other. This is to be expected for NaCl diffusion.

As a result of the simplifications introduced, the convergent characteristics of this numerical process are very good and the deviations from the anticipated results minimal.

1.5 Storage Characteristics in a State of Equilibrium

The hygric characteristics of porous building materials change considerably as a result of dissolved or crystalline salts. The data measured in relation to twelve different porous materials,

$$\theta_l(\varphi, c_s, T) = \theta_l(\varphi) + c_s \cdot m_{sorp}(\varphi, T) \qquad (3)$$

$\theta_l(\varphi)$ – sorption isotherm of salt-free building material

m_{sorp} – water sorption of salt [kg / mol]

four different salts (of various concentrations) and four salt mixtures indicated that the sorption isotherms (adsorption and desorption) of building materials containing salts emerge additively from the sorption isotherm of the salt-free building material and the water sorption of the incorporated salt. This is shown schematically in Figure 5.

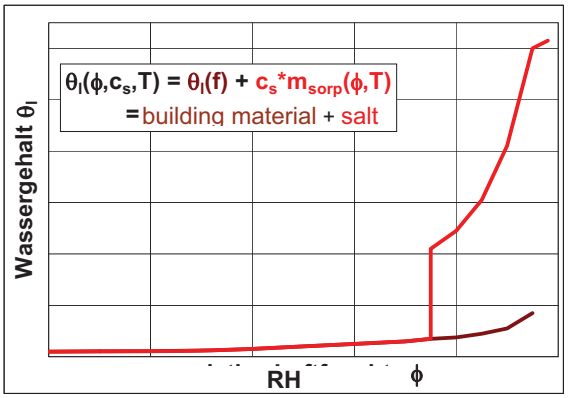

Figure 5: Schematic representation of the influence of salt content on the sorption isotherm

Magnesium sulphate is the only one of the contaminating salts examined to display a pronounced hysteresis between adsorption and desorption ($20 \leq RH \leq 85\%$). The measured data also showed that the speeds of adsorption and desorption, as well as the hydratation and dehydratation of the salt phases (in the building material), vary considerably. For this reason, the kinetics relating to the introduction of the sorption isotherm must continue to be tested.

2 Capillary Transport Behaviour Tests Carried Out on Salt Solutions, Subject to Building Material, Salt Type and Concentration and Fluid Content

2.1 Summary

If one is to use simulation programmes to describe the complex processes involved in the capillary transport of salt solutions in porous building materials, it is essential to show dependencies and correlations. The evaluation of an extensive series of tests carried out on materials with various salt types and concentrations indicated correlations of the capillary absorption coefficient to the dynamic viscosity η_L of the solution in question. The use of an adjustment function, which takes into account the experimentally-verified influence of the density ρ_L of the salt solution, was able to produce a sufficiently exact description of the relative absorption coefficient of all the salt solutions tested. As salts can only be transported in dissolved form, the determination of the pore filling at which capillary fluid transport beaks off and below which only steam transport takes place is of crucial importance. This critical pore filling of salt immobilisation $\theta_{L,krit.}$ could only be determined by using special drying experiments. The results show critical values of the fluid content of between approx. 2 and 14 Vol.-% (in relation to pore volumes). For the building materials tested, a definite material dependence could be proved, whereas influence on the part of the salt type could be largely excluded. The tendency of the slightest critical pore fillings to appear at high levels of capillary conductivity and at low levels of steam-diffusion resistance was also confirmed by the experiments.

2.2 Influence of the Viscosity of Capillary Transport in Porous Building Materials

The European norm DIN EN ISO 15148 [4] sets out a process to determine the water absorption coefficient for short periods of time. This involves partial submersion without temperature gradients. It serves to judge the intensity of water absorption as a result of capillary forces during periods of constant or driving rain. Water absorption due to partial submersion is determined by measuring the change in mass of a test specimen whose underside has usually been in contact with water over a period of at least 24 hours. Using this procedure, a water absorption coefficient A_W can be gauged. This describes the temporal dependence of the water absorption – using $\sqrt{t}$ according to the model – when the contact of the material with water is in the form of A_W [kg/(h^{0,5}·m^2)]. The salt solution absorption coefficient A_L can be produced along the same lines by immersing the test specimen in salt solutions. This proved to be of central importance to the project.

If the absorbing material surface F and the mass density ρ of the absorbed fluid remain constant throughout the suction test, the rate of rise can be deduced from the temporal change in the mass.

$$\mathrm{m(t)} \sim \mathrm{z(t)} \cdot \mathrm{F} \cdot \rho \quad \rightarrow \quad \Delta m(t) \sim \Delta z(t) \cdot const. \tag{6}$$

m	mass [kg]	F	capillary suction surface [m^2]
z	elevation of fluid [m]	ρ	fluid density [kg/m^3]

It cannot be discounted that, in certain gravitational circumstances, the capillary forces could gain in significance; this could happen if the local suction were to lead to a case of static balance, which would in turn lead to the mass density assuming influence. Be that as it may, no further movement of the capillary fluids would take place in these circumstances. Furthermore, the experimental tests are generally far removed from a case of static balance.

Equation 6 formulates a model for the water absorption coefficient A_W. The water absorption coefficient behaves like the rate of rise relationship.

$$A_W \sim \frac{z(t)}{\sqrt{t}} \sim \sqrt{\frac{\sigma_W \cos\delta_W}{2\eta_W} \cdot r_{äqu}} \text{ with } z(t) = \sqrt{\frac{\sigma_W \cos\delta_W}{2\eta_W} \cdot r_{äqu}} \cdot \sqrt{t} \tag{7}$$

A	absorption coefficient of fluid (W-water, L-solution) [kg/m^{2}s$^{0.5}$]	η	dynamic viscosity of fluid [Ns/m, kg/ms]
		r	equivalent capillary radius [m]
z	elevation of fluid [m]	t	time [s]
σ	surface tension of fluid [N/m]		
δ	contact angle of fluid [°]		

According to *SOMMER* [5], the concept shown in Equation 7 can be formulated for small elevations z(t). This concept incorporates, among other things, the surface tension σ_W, the contact angle δ_W and the dynamic viscosity η_W of the water. The relation shown in Equation 8 for the relative absorption coefficient A_L/A_W can be deduced from this, with the surface tension σ_L, contact angle δ_L and dynamic viscosity η_L of the salt solution influencing the relative absorption co-

efficient. These defining characteristics are in turn dependent on the salt solution tested and, by extension, on salt type, concentration and temperature.

$$\frac{A_L}{A_W} \sim \sqrt{\frac{\sigma_L}{\sigma_W} \cdot \frac{\cos\delta_L}{\cos\delta_W}} \cdot \sqrt{\frac{1}{\frac{\eta_L}{\eta_W}}} \quad \text{where} \quad \frac{A_L}{A_W} = f\left(\sigma_L, \delta_L, \eta_L\right) \tag{8}$$

For the salts used in the course of the project, the literature [6 - 8] was consulted to determine densities, surface tensions and dynamic viscosities subject to concentration and to combine them in relation to water. This is illustrated in Fig. 6.

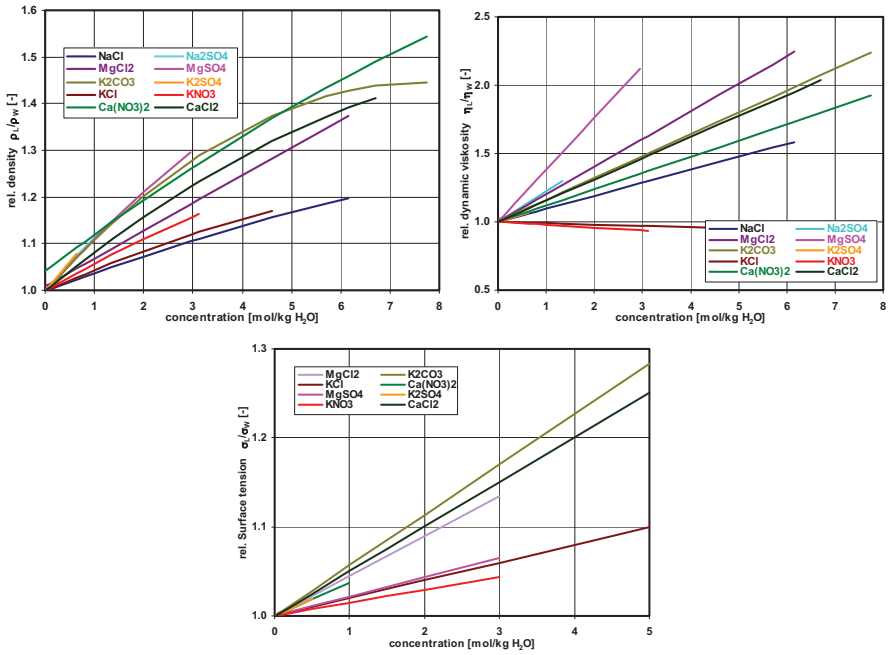

Figure 6: Relationship between the relative densities of salt solutions and water (ρ_L/ρ_W), surface tensions (σ_L/σ_W) and dynamic viscosities (η_L/η_W) subject to concentration.

It can be ascertained that the variation in relative densities and relative surface tensions above the concentration of the respective salt solution has a factor of 1.05 - 1.55. This is lower than that of the variation in dynamic viscosities, which is up to 2.3. Furthermore, the behaviour of the viscosity of the tested salt solutions can be divided into three groups; whilst KNO_3 and KCl display little or no concentration dependence, the salt solutions of K_2SO_4, $Ca(NO_3)_2$, Na_2SO_4 and NaCl behave similarly to each other, and $MgSO_4$ displays the greatest concentration dependence of all.

The relative absorption coefficients A_L/A_W established in the experiments carried out on various salts above the concentration of the respective solution and on various materials were then evaluated. This evaluation showed correlations with the behaviour of the viscosity of the respective salt species (a selection is shown in Figure 7). The absorption speeds of the solutions K_2SO_4, $Ca(NO_3)_2$, Na_2SO_4 and NaCl were reduced by up to 20 %. Hardly any or no change was shown in the cases of the solutions KCl and KNO_3. In contrast, $MgSO_4$ solutions with increasing concentrations showed a reduction in absorption speed of approx. 50 %. The results for some tested materials and salts are combined in Figure 8 with reference to the values for the saturation concentrations.

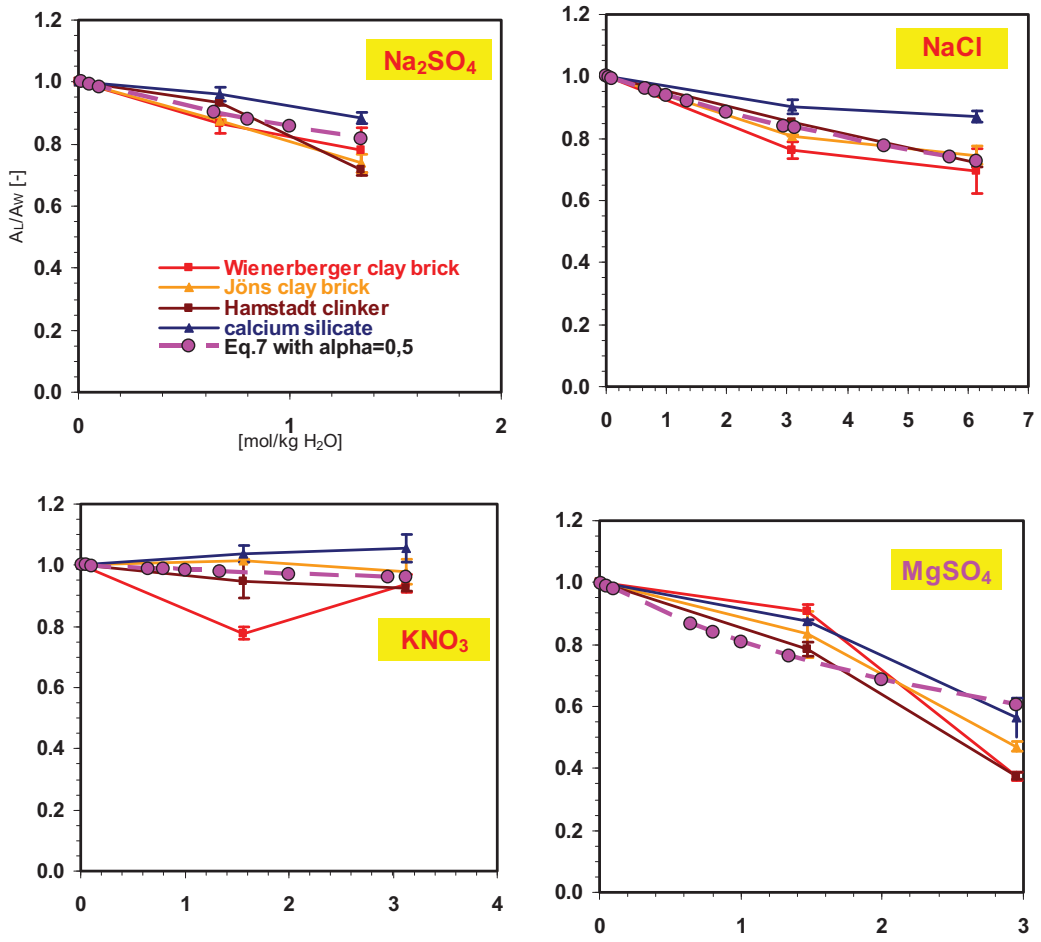

Figure 7: Relationship of the absorption coefficients A_L/A_W for Na_2SO_4, NaCl, KNO_3 and $MgSO_4$ above the concentration of the solution, tested on a selection of building materials.

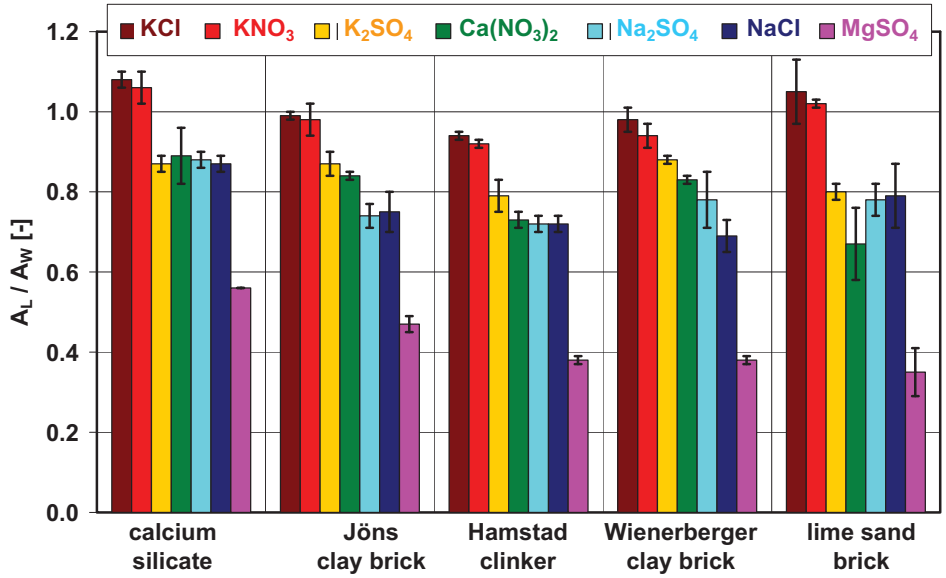

Figure 8: Relationship of the absorption coefficients for saturated salt soltions (A_L) to water (A_W) for each of the materials tested.

When comparing the relative solution absorption coefficients with the characteristics of the solutions themselves, a remarkable relationship (in other words a comparable sequence of dependencies) could be established, especially in relation to the viscosity of the solutions. This is shown by the following data:

KCl, KNO_3	$A_L \approx 0.92..1.08 \cdot A_W$	(viscosity 0.98..0.99 x)
K_2SO_4, $Ca(NO_3)_2$, Na_2SO_4, NaCl	$A_L \approx 0.67..0.89 \cdot A_W$	(viscosity 1.1..1.2 x)
$MgSO_4$	$A_L \approx 0.35..0.56 \cdot A_W$	(viscosity 1.4 x)

It is possible to introduce an approximate description of the contact angle of the solution, taken from the equilibrium relationship, into the method described in Equation 8 for the relative absorption coefficient (Eq. 9).

$$\cos\delta_L = \frac{\sigma_W}{\sigma_L} \cdot \frac{\rho_L}{\rho_W} \cdot \frac{h_L}{h_W} \tag{9}$$

In addition, a contact angle of water δ_W of 0° for mineral building materials is assumed. From Equations 8 and 9, this gives a simplified expression of the relative absorption coefficient (Equation 10), which is independent of concentration-dependent surface tensions. Correlations to the relationship of the density and viscosity of the solution to water can be formally excluded. However, the elevations of the respective solutions h_L remain undefined, with the result that even Equation 10 does not represent an arithmetical reference to the relationship A_L/A_W.

$$\frac{A_L}{A_W} \sim \sqrt{\frac{\rho_L}{\rho_W} \cdot \frac{h_L}{h_W}} \cdot \sqrt{\frac{1}{\frac{\eta_L}{\eta_W}}} \tag{10}$$

The experimental results as given in Figure 7 do, however, provide the empirical basis for a subsequent salt-solution-specific description of A_L/A_W, subject to the salt contents. Using an adjustment function $\overline{f}(\rho_L/\rho_W)$, a possible density influence could be accounted for and the dominant viscosity influence added in accordance with Equation 4. This produces Equation 11.

$$\frac{A_L}{A_W} \approx \overline{f}(\rho_L/\rho_W) \cdot \sqrt{\frac{1}{\frac{\eta_L}{\eta_W}}} \qquad \text{with } \overline{f}(\rho_L/\rho_W) \approx \frac{1}{\left(\frac{\rho_L}{\rho_W}\right)^{\alpha}} = \left(\frac{\rho_L}{\rho_W}\right)^{-\alpha} \tag{11}$$

The coefficients calculated in Equation 11 are also included in Figure 7 for purposes of comparison. The viscosities for concentrations > 1 mol/kg water were interpolated on a linear basis. Using an adjustment function with an adjustment parameter of $\alpha \approx 0{,}5$ (Eq. 11), a sufficiently accurate description of the relative absorption coefficient could be achieved for all the salt solutions tested. A later specification of α as somewhere between 0.45 and 0.65 in relation to salt type now appears possible. The evaluation of the experimental tests points in all aspects to correlations with the behaviour of the viscosity of the tested salt solutions. This correlation between the relative absorption coefficient and the behaviour of the viscosity of the respective salt solution is made clear in Equation 11. The density-dependent adjustment function takes into account the possible influence of gravity described in Equation 6, and thus the mass density. Embedded in the capillary fluid conductivity K_{cap} in accordance with Equation 12, which is discussed by GRUNEWALD ET AL. [9], one finds the method used by the simulation tool DELPHIN in accordance with Equation 13.

$$K_{cap,W} \approx k \cdot A_w^2 \qquad [\mathrm{m^2/s}] \tag{12}$$

$$\frac{K_{cap,L}}{K_{cap,W}} \approx k' \cdot \left(\frac{A_L}{A_W}\right)^2 \approx k' \cdot \frac{\eta_W}{\eta_L} \text{ with } k' = f(\bar{f}) \tag{13}$$

Thus the fluid conductivity of salt solutions can also be calculated with the aid of their calculated absorption coefficients.

2.3 Testing of the Critical Fluid Content of Salt Immobilisation

Water plays an important role as a transport medium not only in salt insertion, enrichment and mobilisation, but also in the after-effects of damage. It is well known that salts can only be transported in dissolved form in water – as a rule either diffusively (ion transport) or advectively (solution transport). Pure water transport, on the other hand, takes place in the fluid phase and

in the form of steam. If the capillary fluid transport of a pore fluid containing salts should for some reason be aborted, moisture transport can then only take place in the form of steam. The salt remains in the pores of the building material. The capillary fluid transport and the steam transport interfere with each other to various degrees, subject to the pore filling in the material, and they cannot be separated for experimental purposes. The pore filling under which only steam transport takes place with the salt remaining immobilised in the pores (transport abortion in the fluid phase) is denoted as the critical pore filling of salt immobilisation $\theta_{L,\,krit}$.

Initial tests carried out as part of the project have produced results which show a considerable influence of material and salt type on the critical pore filling. The values noted are, however, extremely widely dispersed and appear to have a very high upper limit in relation to the values found in the literature; Huinink et al. [10] put the critical pore filling at 0.1 - 0.3 times the overall porosity, whilst KRUS et al. [11, 12] estimate it to be under 10 Vol.-%, which is negligibly low.

Table 1: Characteristics of the building materials used.

material	calcium silicate	Jöns clay brick	Wienerberger clay brick	Hamstad clinker	lime sand brick
water absorption [Ma.-%]	323 (±4,0)	15.5 (±1,2)	16.9 (±0,7)	10.3 (±0,8)	13.8 (±0,4)
open porosity [Vol.-%]	91.4 (±1,8)	27.9 (±2,8)	29.5 (±1,3)	18.4 (±1,6)	23.1 (±0,5)
Max. pore radii [µm]	0.36	0.56 / 15,8	0.31 / 4.5	1.9	0.015 / 15.2
A_W – value [kg/m²h^{0,5}]	42.4 (±1,2)	10.5 (±1.0)	7.0 (±0.5)	4.4 (±0.4)	2.8 (±0.6)
µ-value (dry cup)	3..6	20	10..20	26	35
tortuosity	1.10 (±0,31)	2.85 (±0.18)	5.86 (±0.65)	3.12 (±0.11)	7.02 (±0.30)

The initial results nevertheless point to salt immobilisation values of between approx. 10 - 70 Vol.-% of the pore space filling. In order to be able to draw more secure conclusions on salt immobilisation, the drying tests on two materials and five salts (four hydrate-free plus Na_2SO_4) were repeated in a calculatedly modified form, using the initial experiments as a basis.

Table 2: Characteristics of the salts used.

salt	density [g/cm³]	solubility [mol/kg water]	deliquescence humidity [%]
NaCl	2.163	6.145 (25°C)	7.,4 (20°C)
Na_2SO_4	2.663	1.970 (25°C)	93.6 (20°C)
KCl	1.984	4.598 (20°C)	84.3 (25°C)
KNO_3	2.109	3.118 (20°C)	94.6 (20°C)
K_2SO_4	2.662	0.637 (20°C)	97.0 (25°C)
$Ca(NO_3)_2 \cdot 4\ H_2O$	-	-	47.0 (30°C)
$Ca(NO_3)_2$	2.504	7.749 (20°C)	13.2 (30°C)
$MgSO_4 \cdot 7\ H_2O$	-	-	90.1 (20°C)
$MgSO_4 \cdot 4\ H_2O$	-	-	37.0 (20°C)
$MgSO_4$	2.960	2.797 (20°C)	21.0 (20°C)

Particular attention was paid in the course of these experiments to achieving results which could be reproduced later. The constant climatic parameters were raised to ± 2 K and ± 4 % RH, and the 'uniaxial' drying experiments were carried out in two directions (instead of one) to achieve moisture discharge. The aim was to clarify the dimensions of the critical pore filling and to establish whether it can be disregarded in future simulation calculations on salt transport. In addition, the question of material and salt-type dependence had to be clarified. In the drying experiments which were developed especially for this project, test specimens of various building materials in the form of prisms and cylinders (cf. Table 1) were loaded with saturated salt solutions up to moisture saturation levels. The circumferential surfaces were gas-proofed and subsequently dried under temporally constant climatic conditions across one or two end faces until moisture equilibrium (constant mass) was reached.

In order to prevent the formation of hydrate phases, a temperature of 30 °C and an air humidity of 40 % were selected. In order to lessen the influence of self-sealing salt crusts and to unify the evaporation area for all test specimens, a standard 2-3 cm strong bentonite-sand-cellulose compress was applied to the open end faces. After moisture equilibrium had been achieved, the salt profile which was beginning to form in the test specimens was established by sawing-off five to seven sections and producing eluates of their interiors. The original volume of the saturated salt solution could then be calculated back from the solid salt content. Evaporation crystallisation then set in at this volume of saturated solution; this was because, apart from the steam transport, no further fluid transport was still taking place. If one relates this calculated volume of saturated salt solution to the overall porosity of the building material, one arrives the critical pore filling at which the fluid transport (capillary solution transport) - and with it the salt transport - came to a standstill. Because saturated salt solutions are used, the initial salt and moisture contents (or concentrations) can be precisely identified (cf. Table 2).

As fluid transport dominates at moisture contents of over 10% pore filling – the speed being several times that of steam transport – a supersaturation of the solutions in the building materials up to this moisture content level through the evacuation of water in gaseous form can largely

be discounted. In addition to this, a defined deliquescence humidity establishes itself above a saturated salt solution, with the result that, during the drying process, no locally-variable partial steam pressures should appear. No additional impetus is thus provided for moisture transport in the building materials themselves. There is also no concentration gradient of the salt ions to be found in the saturated pore solution. For these reasons, the idea that a diffusion of the salt ions might interfere with the moisture transport can be discounted.

Figure 9 shows examples of the critical pore filling $\theta_{L,\,krit}$ achieved for lime sand brick and Hamstadt clinker when saturated solutions of Na_2SO_4, NaCl, KNO_3, KCl and K_2SO_4 are added. The results shown have been confirmed three times over and display only slight deviations. The climatic conditions applied during the test period were able to maintained at constant levels. Figure 9 clearly shows the influence of the material, although there is a difference between the two; for lime sand brick, the critical pore fillings lie between 8.5 and 14.1 Vol.-%, whilst for Hamstadt clinker they vary at a lower level between 1.7 and 4.6 Vol.-%. These results from the second series of tests display considerably lower critical pore fillings than those from the first series. Furthermore, in the case of lime sand brick the influence of the salts used can be clearly divided into to two categories: NaCl, KNO_3 and KCl, with 8.5 - 9.9 Vol.-% critical pore filling; and Na_2SO_4 and K_2SO_4, with 13.9 and 14.1 Vol.-% critical pore filling. In the case of Hamstadt clinker, no relevant salt-specific influence can be detected, except for Na_2SO_4 (with 4.6 Vol.-%).

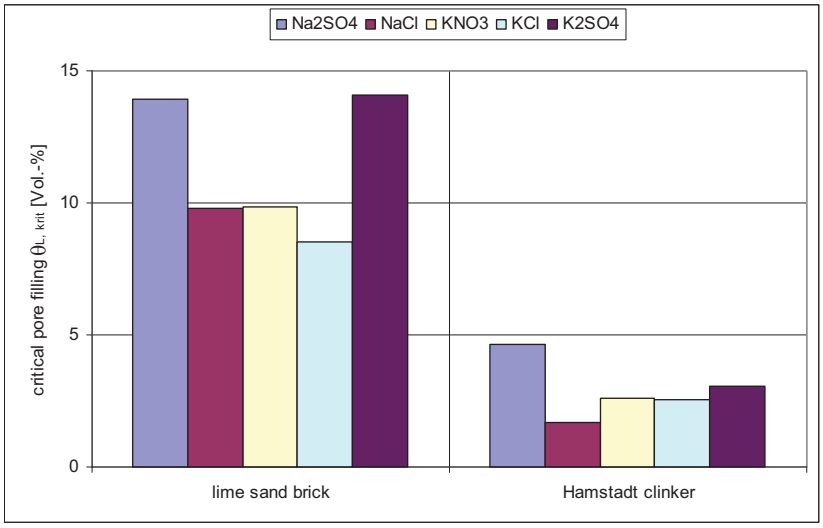

Figure 9: Critical pore filling of salt immobilisation $\theta_{L,\,krit}$ subject to salt type and building material.

The influence of the material is equally evident in the salt discharge towards the evaporation zones. Whilst this led to clear concentrations on the test surfaces with lime sand brick, only a slight concentration gradient over the entire sample length could be detected with Hamstadt clinker (cf. Fig. 10) The displacement of the evaporation and crystallisation zones into the applied compress material can be explained by a better contact between the compress material and Hamstadt clinker or by a lower resistance from the building material to the compress material than with lime sand brick. This had already become manifest before the experiments were concluded.

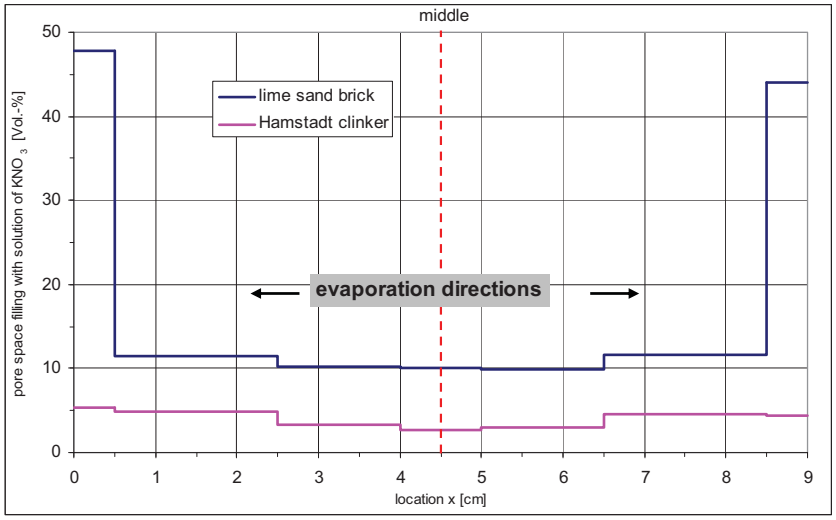

Figure 10: KNO_3 content in lime sand brick and Hamstadt clinker after storage at 30 °C and 40 % RH.

A striking dependence of the critical pore filling on the type of building material (pore system) could thus be proved. Considering the low values obtained for the critical pore filling, the influence of the salt itself can be discounted. The tendency of the slightest critical pore fillings to establish themselves at high levels of capillary conductivity and low levels of steam diffusion resistance could also be confirmed. Further tests on other building materials with even higher capillary conductivity or lower steam diffusion resistance should confirm this trend. When using these materials, therefore, simulation calculations should account for salt transport down to very low levels of moisture content. The salt species used were qualitatively verified within the framework of the accompanying X-ray analysis. There was no evidence of the formation of a hydrate phase in the case of Na_2SO_4.

3 References

[1] Kriegel, R.; Kaps Ch.: *Bestimmung geometrieunabhängiger Stofftransportgrößen - ausgewählte Beispiele aus der Werkstoffchemie* in *Beiträge der 3. Tagung Bauchemie, GDCh-Monographie 15,* pp. 231-235 (1999).

[2] Buchwald, A.: *Ionentransportprozesse zur Verminderung von Schadsalzgehalten in porösen, feuchten Mauerwerksbaustoffen.* Dissertation, Bauhaus-Universität Weimar (2000).

[3] Buchwald, A.; Kaps Ch.: *The ion mobility of deteriorating salts in masonry materials of different moisture content* in *Euromat 99 6* (2000), pp. 157-162.

[4] DIN EN ISO 15148: Hygrothermal performance of building materials and products - Determination of water absorption coefficient by partial immersion. EUROPEAN COMMITTEE FOR STANDARDIZATION (March 2003).

[5] Sommer, E.: *Beitrag zur Frage der kapillaren Flüssigkeitsbewegung in porösen Stoffen bei Be- und Entfeuchtungsvorgängen* Dissertation, TH Darmstadt (1971).

[6] D‘ Ans; Lax: *Taschenbuch für Chemiker und Physiker. Band I Physikalisch chemische Daten,* 4th ed, Springer-Verlag, Berlin.

[7] Gmelin: *Handbuch der anorganischen Chemie*.Vol. 21 - 1928, Vol. 22 - 1938, Vol. 27 - 1939, Vol. 28 B - 1957, Verlag Chemie GmbH Weinheim - Berlin.

[8] Lobo, V. M. M.: *Handbook of Electrolyte Solutions*, Amsterdam Elsevier (1989).

[9] Grunewald, J.; Funk, M.; Scheffler, G.: *Das Simulationsprogramm Delphin4 für gekoppelten Feuchte, Luft, Salz und Wärmetransport in kapillarporösen Baustoffen. Physikalische Grundlagen und Anwendungsbeispiele*, TU Dresden (2002).

[10] Huinink, H. P.; Pel, L.; Michels, M. A. J.: *How ions distribute in a drying porous medium, Phys. Fluids*, 14(4), pp.1389-1395,(2002).

[11] Krus, M.: verbal discussion on DFG-Kolloquium SPP 1122 19th April, München (2004).

[12] Krus, M., Holm, A.: *Approximationsverfahren für die Bestimmung feuchtetechnischer Materialkennwerte. Proceedings* 10. Bauklimatisches Symposium Dresden, 27th-29th September 1999, pp. 423-432.

Petra Rucker-Gramm,
Dr.-Ing.

Managing partner
Concrete concepts
Ingenieurgesellschaft mbH
Munich, Germany

Robin E. Beddoe,
Dr. BSc PhD

Centre for Building Materials,
Technische Universität München,
Munich, Germany

Concrete Self-Sealing Mechanisms against Penetrating Water

Summary

^{1}H NMR and suction experiments with mortar (w/c=0.6) were used to study the effect of liquid properties, moisture content and water pressure on the self-sealing of concrete against penetrating water. Capillary penetration is determined by surface tension and viscosity. The redistribution of the penetrating liquid into gel pores results in internal swelling which reduces the connectivity of the capillary pore system. The ongoing redistribution process results in the self-sealing effect characterized by deviation of penetration depth from $\sqrt{t}$ behaviour. The strength of self-sealing depends on the specific surface of the cement gel, the dipole concentration of the liquid and the concentration of dissolved ions which affect the disjoining pressure exerted by water molecules in gel pores. Dissolution and precipitation of phases in the pore system affect capillary transport and occur alongside redistribution and self-sealing. The results are being implemented in a model for the prediction of moisture and salt transport in concrete components under service conditions.

Keywords: *self-sealing, water uptake*

1 Introduction

Moisture and salt penetration can lead to significant damage in reinforced concrete structures. Thus a realistic calculation of the evolution of moisture and salt distributions in cementitious building materials exposed to service conditions is essential for the estimation of the service life of reinforced concrete structures. In the course of the present project, the main mechanisms and interactions affecting moisture and salt transport in cementitious building materials were observed and described mathematically with the aim of developing a numerical model which is described in detail in [1]. The mechanisms include the transport of chlorides by ionic diffusion, capillary suction and internal redistribution of water with advection of chlorides, water vapour

diffusion, binding of chlorides, thermal transport and crystallization of salt. The effect of dissolved chlorides on the capillary transport of water and water vapour diffusion is also included in the model. The penetration of water and salt was studied using nuclear magnetic resonance (NMR) and gamma ray absorption. Transport coefficients for the model were determined for over 20 different concrete compositions. The kinetics and concentration dependence of chloride binding was investigated by expressing pore solutions from specimens after different storage periods. Diffusion coefficients were determined using thin mortar disks in a diffusion cell and rapid chloride migration tests. The effect of chloride concentration on the water-vapour sorption isotherm of concrete was investigated. The experimental methods and results are described in detail in [1].

The present contribution focuses on the explanation of the self-sealing mechanism and its causes. In the last decade it has been recognised that the uptake and penetration depth of water and thus chlorides in concrete is restricted by a self-sealing effect, [2, 3, 4, 5]. Although of great practical importance, the self-sealing effect is not well understood and current explanations of it varied, see [4]. The self-sealing effect is also of consequence regarding the design of concrete structures in contact with water and has, based on the work in [3], been considered in a German guide line [6] specifying concrete thickness for structures exposed to ground and seepage water.

The driving force for water uptake by suction is the action of surface tension σ at the wall of capillary pores which results in a capillary pressure $p_K = 2\sigma/R$ depending on pore radius R. Especially in small pores, capillary pressure is opposed by viscous flow so that uptake and depth of penetration x increase with the square root of time t.

$$x = c\sqrt{\frac{\sigma}{\eta}t} \tag{1}$$

Here, the constant c is a function of porosity, pore size distribution and tortuosity of the material. Linear $\sqrt{t}$ behaviour has often been observed for the uptake of water in non-cementitious materials containing predominantly large capillary pores. The self-sealing effect is manifested in the non-linear $\sqrt{t}$ water uptake by cementitious building materials which contain small gel pores. Krus et al. [5] suggested that self-sealing is caused by the swelling of cement gel during water penetration because the uptake of non-polar hexane is linear with $\sqrt{t}$ conforming to (1) and the saturation of hardened cement paste with hexane does not cause swelling - as opposed to strongly polar water. Swelling occurs owing to the interaction forces between gel pore water molecules and the gel matrix across the liquid/solid interface. Consequently, self-sealing may be explained by the redistribution of part of the water penetrating the material in capillary pores into small gel pores which expand and reduce the connectivity of the capillary pore system, see [2]. Since the gel pore water is strongly bound it no longer takes part in capillary transport.

In view of this, swelling and the deviation of uptake from $\sqrt{t}$ behaviour should be related to the physical properties of the penetrating liquid, in particular, its dipole moment. However, there is

evidence that self-sealing occurs with liquids which have dissolving reactions with the hydration products and not with liquids such as hexane in which, for example, $Ca(OH)_2$ is insoluble. Sosoro [7] attributed the deviation of the uptake of water and ethylene glycol from $\sqrt{t}$ behaviour to the dissolution of $Ca(OH)_2$ in these liquids. Obviously, the effect must be caused by subsequent precipitation processes - presumably involving alkalis which reduce $Ca(OH)_2$ solubility - or other mechanisms since dissolution alone would tend to increase pore space and thus permeability. Hearn and Morley [4] considered dissolution and deposition processes responsible for the reduction in permeability observed for supply water passed under pressure (10 bar, 320 h) through concrete disks in a simple water permeameter [8]. Chemical analysis revealed systematic changes in the composition of the outflow water. The opposition of capillary pressure by osmotic pressure has also been suggested as a cause of the self-sealing effect. Investigations by Edwardsen [9] indicate that calcium carbonate formation is the main reason for the self-healing of cracks in concrete. However, this mechanism may be excluded as the cause of self-sealing because, as opposed transport in open cracks, insufficient CO_2 is able to reach the binder matrix inside concrete.

The present work aims at shedding light on the self-sealing effect, i.e. non-$\sqrt{t}$ uptake, by considering the results of different experimental investigations on the effect of liquid properties and pressure on the uptake and penetration of water in mortar. As well as a number of organic solvents, NaCl solutions were also investigated on account of their relevance to the corrosion of steel reinforcement in concrete exposed to marine environments or deicing salt. Results are also presented on the effect of initial concrete moisture content and water pressure on self-sealing.

2 Experimental Investigations

2.1 Sample Preparation

Slabs measuring 700×150×150 mm^3 were cast from mortar prepared with 515 kg/m^3 German Portland cement CEM I 42.5 R at a water cement ratio of 0.60 and local 0/4 mm Munich sand. After 24 hours the slabs were demoulded and stored in water at 20 °C for three months. Prisms with a cross sectional area of 45×45 mm^2 and lengths between 120 and 240 mm were sawn out of the centre of the slabs. The prisms were then oven-dried for three months at 50°C and stored at 23°C and 50% RH until use. Several weeks before measuring, the rectangular surfaces of the prisms were coated several times with epoxy resin to minimize moisture loss through the sides of the prisms during the suction experiments and ensure predominantly one dimensional liquid transport along the length of the prisms. The uncoated 45×45 mm^2 end surfaces were roughened with wire brush. The specimens were at least one year old when the experiments were performed. To investigate the effect of initial moisture content on self-sealing, additional prisms were stored in desiccators to constant weight at a relative humidity of 80% RH.

2.2 Measurements

In the suction experiments, dry mortar prisms were placed end down in different liquids and the uptake monitored by weighing. The total volume of liquid taken up through the surface at different times was calculated using the density of the particular liquid. In the case of specimens exposed to water, salt solutions and hexane, the liquid penetration was also followed using ^{1}H NMR. A detailed description of the experimental procedure is in [1]. After weighing, each prism was placed on a carriage which moved it in 1 mm steps through the sensitive region of a 0.47 tesla magnetic field positioned across the width of the prism. In this manner, step-scans of ^{1}H signal strength along the length of each prism were recorded. A more detailed description of the equipment is in [10]. The specimens were also weighed on completion of each scan; the total procedure requiring 10 minutes. No discernible change in weight was observed between the beginning and end of each scan. In order to calculate profiles of liquid content from the NMR scans, the signal intensity recorded at each step was corrected with the appropriate background value from an initial dry scan and then multiplied by a factor *F* to obtain the amount of liquid in litre/m^3. *F* was calculated from the weight gain due to liquid uptake and the corresponding total NMR signal intensity obtained by integration of signal strength over prism length. The factor was determined using prisms at a suction time of one hour where it was assumed that mainly capillary pores were filled after this short time. The resulting value was used for later scans. To determine the maximum possible uptake, additional uncoated mortar specimens were immersed in water until no appreciable change in weight was measured. A free saturation of 146 litre/m^3 was calculated from the weight gain of the specimens previously stored at 50% RH. The relevant physical properties of the liquids used in the investigations are listed in Table 1. The solubility of $Ca(OH)_2$ in ethylene glycol and methanol was determined experimentally.

Table 1: Physical properties of liquids affecting transport in porous materials. The dipole concentration is calculated using the density and molecular weight of the liquid. The mean molecular size is estimated from density and molar mass.

Solvent	Molar mass M_r [g/mol]	Density ρ [g/cm³]	Surface tension σ [mN/m]	Viscosity η [mPa s]	$(\sigma/\eta)^{0.5}$ [m$^{0.5}$/s$^{0.5}$]	Dipole moment μ_D [D]	Dipole conc. c_D [D/nm^3]	Mol. size a_m [nm]	$Ca(OH)_2$ solubility [g/l]
Water	18.0	0.998	72.8	1.002	8.52	1.85	61.8	0.31	1.2
n-hexane	86.2	0.66	18.43	0.326	7.5	0.00	0	0.60	0
Methanol	32.0	0.79	22.61	0.57	6.3	1.71	25.4	0.41	0.2
Ethanol	46.1	0.79	22.75	1.2	4.2	1.70	17.5	0.46	0
Isopropanol	60.1	0.79	21.7	2.27	3.1	1.69	13.4	0.50	0
Ethylene glycol	62.1	1.11	47.7	21	1.5	2.28	24.5	0.45	3
3.3 wt.% NaCl	-	1.02	73.8	1.064	8.33	-	-	-	1.7
8.7 wt.%	-	1.06	75.5	1.222	7.86	-	-	-	1.9
26.4 wt.%	-	1.20	82.8	2.831	5.41	-	-	-	2.0

The dipole concentration was calculated from the data in the table ($c_D = \mu_D \rho N_A/M_r$, N_A is Avogradro's constant). It is a measure of the dipole strength of the bulk liquid. The mean molecular size was estimated by $a_m = [M_r/(\rho N_A)]^{1/3}$.

3 Effect of Liquid Type

In Figure 1 the uptake of various organic solvents over a period of 80 days is compared with distilled water. The abrupt decrease in uptake rate at the end of each suction period for hexane, methanol, ethanol, isopropanol and ethylene glycol (after about 3600 h) occurred when the liquid reached the opposite end of the prism. In no case was the liquid uptake equivalent to free saturation of the specimen.

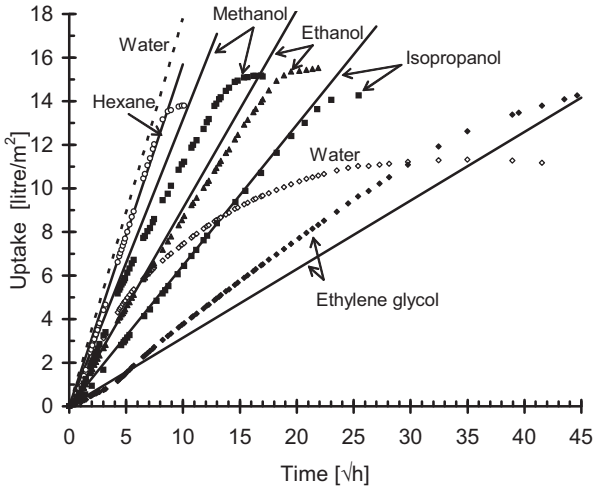

Figure 1: - Symbols: uptake of various organic solvents by mortar (w/c =0.60) over a period of 80 days. Lines: uptake expected due to action of surface tension and viscosity alone - based on fitted hexane data

As opposed to water where uptake deviates markedly from $\sqrt{t}$ behaviour, the uptake of hexane is linear with $\sqrt{t}$ indicating, as discussed above, that capillary forces control the penetration of hexane into the mortar. In order to compare the behaviour of the organic liquids, a straight line was fitted to the hexane data to determine the proportionality constant c of (1) which was then used with the values for $\sqrt{(\sigma/\eta)}$ in Table 1 to calculate the lines in Figure 1 for the other solvents, i.e. it is assumed that viscosity and capillary pressure alone govern uptake behaviour. The comparison of the straight lines with the measured data shows that the general rate of uptake of the organic liquids correlates with the values $\sqrt{(\sigma/\eta)}$ in Table 1. High capillary uptake rates were observed for water only at the very beginning of suction. The deviation of the measured uptake from the appropriate straight line becomes less moving across the liquids methanol, ethanol and isopropanol in Figure 1 - although these solvents possess similar dipole moments. Whereas a deviation from $\sqrt{t}$ behaviour is apparent for methanol, isopropanol appears to exhibit $\sqrt{t}$ behaviour in agreement with the effect of σ and η alone. Moreover, significant expansion and swelling

stress have been observed following the saturation of dry hardened cement paste with methanol or water, but not with isopropanol; swelling stresses of 6 and 4 MPa were measured for Portland cement (w/c = 0.5) with water and methanol, respectively, [11, 12]. On first sight, this suggests that self-sealing depends on molecular size, i.e. the ability of the solvent molecules to enter gel pores. However on comparing the penetration behaviour of, for example, ethylene glycol and ethanol whose molecules have similar mean sizes, it is apparent that the self-sealing effect is not determined by molecular size alone. The deviation of ethylene glycol from $\sqrt{t}$ uptake behaviour seems larger than for ethanol, as would be expected from the larger dipole moment of this molecule, but less than that of water whose dipole moment is smaller.

It is suggested that the saturation of gel pore volume with different liquids affects swelling, and consequently self-sealing, differently because the strength of the interaction between the liquid and the solid matrix depends on the dipole concentration of the liquid c_D. The values of dipole concentration together with σ and η in Table 1 explain the observed uptake behaviour for the liquids investigated. Like water, methanol and ethylene glycol are able to dissolve $Ca(OH)_2$ which can, in principle, lead to deposition. Since non-$\sqrt{t}$ uptake is observed with ethanol, despite its inability to dissolve $Ca(OH)_2$, it appears that dissolution and deposition processes involving $Ca(OH)_2$ do not cause self-sealing.

3.1 Calcium Hydroxide Solutions

The effect of $Ca(OH)_2$ dissolution in the penetrating liquid was investigated in more detail by performing suction experiments using water and ethylene glycol, both with and without $Ca(OH)_2$ saturation, see [7]. If $Ca(OH)_2$ dissolution is responsible for self-sealing then the effect should be larger for ethylene glycol which is able to dissolve 2.5 times more $Ca(OH)_2$ than water. The results are in Figure 2 where evidently self-sealing occurs both with and without saturation of the penetrating liquid with $Ca(OH)_2$. This provides more evidence that dissolution or precipitation processes involving $Ca(OH)_2$ do not cause the self-sealing effect.

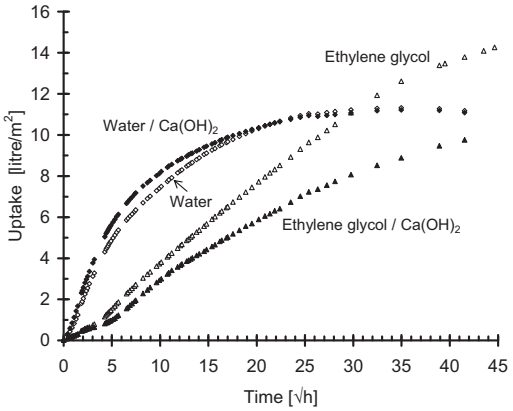

Figure 2 : Effect of saturation of water and ethylene glycol with $Ca(OH)_2$ on liquid uptake by mortar (w/c 0.6)

Nevertheless, the dissolution of $Ca(OH)_2$ contained in the hydration products of cement by the penetrating liquid may increase water uptake because even small amounts of dissolved $Ca(OH)_2$ can have a significant effect on the continuity and accessibility of the pore system for the liquid. Opposed to this, small amounts of $Ca(OH)_2$ may precipitate during the uptake of liquids saturated $Ca(OH)_2$ solution because alkalis enter the penetrating liquid disturbing the solubility equilibrium. In the case of penetrating aqueous $Ca(OH)_2$ solutions, the volume fraction of precipitate in the pore solution was estimated to be at most 0.05 vol.%. The reduction in $\sqrt{(\sigma/\eta)}$ due to $Ca(OH)_2$ saturation of ethylene glycol was estimated at 0.1% which therefore cannot explain the effect of dissolved $Ca(OH)_2$ on ethylene glycol uptake in Figure 2. It is perhaps due to due differences in $Ca(OH)_2$ dissolution and precipitation which superimpose on capillary suction and redistribution of water into gel pores.

In view of these results, the development of osmotic pressure due to gradients in Ca concentration is excluded as a cause of self-sealing. Owing to the high solubility of alkalis in the pore solution it is unlikely that spatial variations in the alkali concentration of the pore solution are high enough to generate osmotic pressures able to oppose capillary suction.

3.2 NaCl Solutions

The distributions of water content determined by NMR during the uptake of water and a solution containing 26.6 wt.% NaCl are shown in Figure 3 where the rate of penetration of the NaCl solution is clearly slower than that of water.

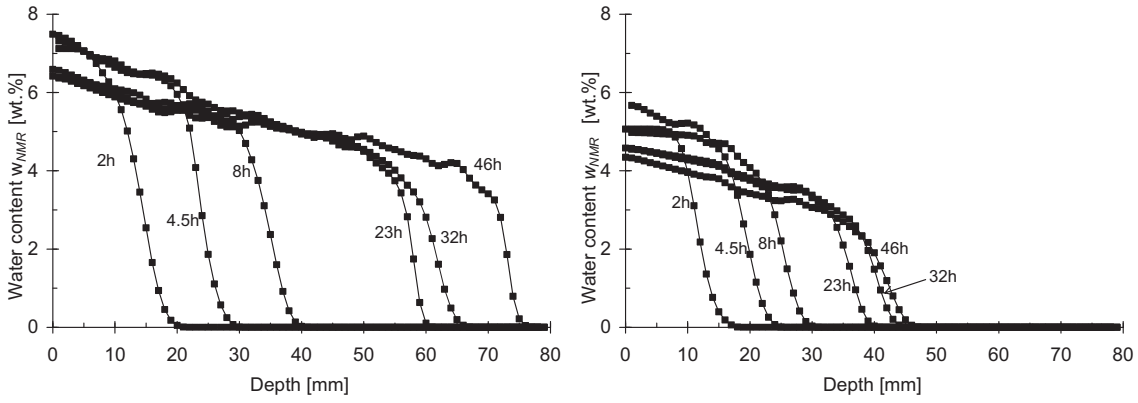

Figure 3: NMR Penetration profiles for water and 26.4 wt.% salt solution in mortar (w/c 0.6)

The gravimetric uptake of different salt solutions is plotted in Figure 4, left, as a function of $\sqrt{t}$ and is compared with the corresponding NMR penetration depths of water, Figure 4, right, estimated by extrapolating straight lines fitted to each leading NMR profile edge through the horizontal axis. Solution uptake and penetration depth both decrease with the concentration of salt and deviate from $\sqrt{t}$ behaviour in a similar way. In order to characterize the deviation of uptake from $\sqrt{t}$ behaviour, straight lines are drawn to extrapolate the uptake of solution measured after 4.5 hours, Figure 4, left. The reduction in slope of the lines corresponds to the change in $\sqrt{(\sigma/\eta)}$ with salt concentration (Table 1) and therefore uptake according to (1). Thus the rate of capillary

penetration of the NaCl solutions is governed by the surface tension and viscosity of the solution.

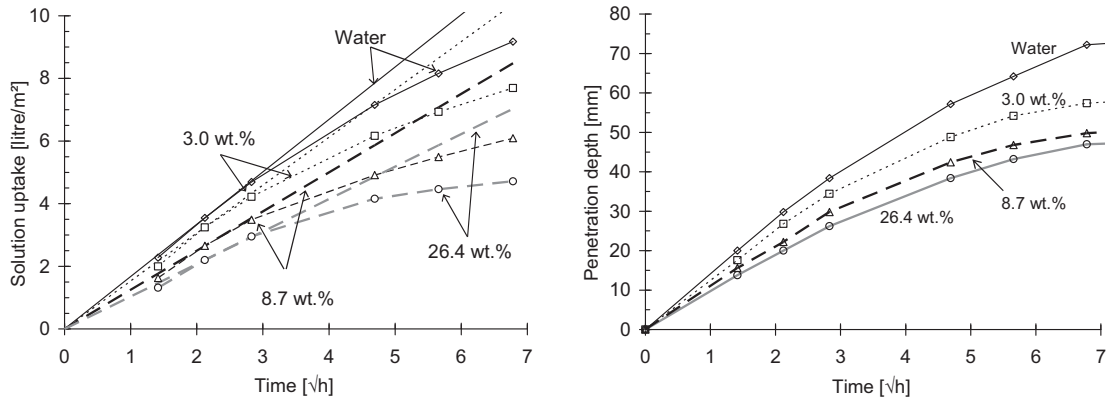

Figure 4: Effect of NaCl concentration on solution uptake and penetration depth. Average values taken over 5 individual measurements

Mortar specimens (45×45×15 mm^3) were stored at different relative humidities to determine the effect of pore size on NMR signal strength, see [1, 13]. It was found that the present NMR equipment does not register water in pores with diameters below roughly 10 nm, but essentially only water in larger capillary pores. This is because water in small gel pores is strongly affected by the interaction forces between water molecules and the gel pore surface which change the NMR relaxation time. In earlier work [2, 14], the proportion of water registered by the NMR equipment w_{NMR} with respect to actual gravimetric uptake w was observed to decrease with time indicating that more and more water moves from large capillary pores into small gel pores as penetration proceeds. Figure 5, left, shows the fraction of water registered by NMR during the uptake of the NaCl solutions in the present investigations. The gravimetric uptake of water w is calculated from the concentration of the NaCl solution used.

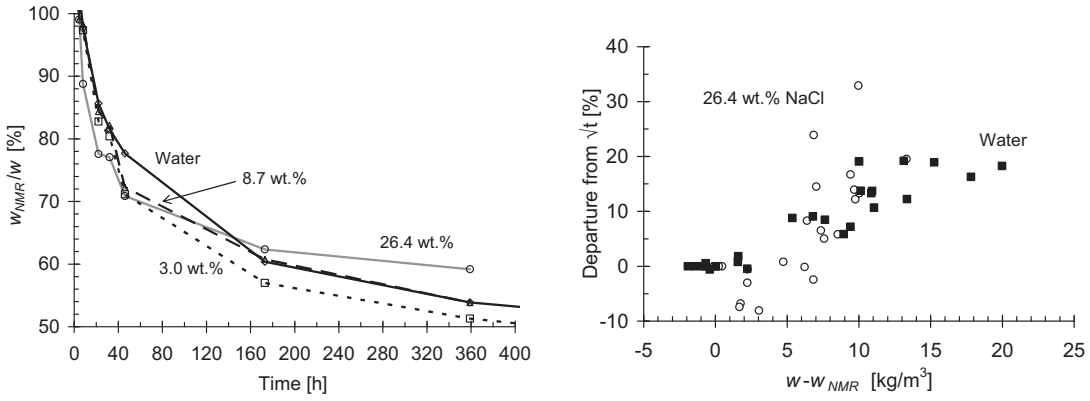

Figure 5: Left: Fraction of water measured by NMR during uptake of NaCl solutions by mortar (w/c 0.6). Average values taken over 5 individual measurements. Right: Effect of amount of redistributed water on departure of solution uptake from $\sqrt{t}$ behaviour

The redistribution of water in the penetrating NaCl solutions is similar to that of water. However, the actual amount of water in the pores is lowered due to the presence of dissolved salt in the penetrating solution. Thus for a given value of w_{NMR}/w the amount of water in gel pores will decrease with the concentration of the salt solution.

In [13], the departure of uptake from √t dependence is explained by the ongoing redistribution of water from capillary into gel pores during capillary suction. This could be verified by plotting the difference between the straight lines and the observed uptake in Figure 4 as a function of the amount of water which has undergone redistribution (w-w_{NMR}) for different suction times, Figure 5, right.

Thus capillary uptake slows down as more and more water enters the gel pores. In Figure 5, right, the departure from $\sqrt{t}$ uptake behaviour increases more rapidly with the amount of redistributed water if salt is present. This would indicate that the effect of water molecules in the gel pore solution on self-sealing is strengthened by salt ions. Such an effect is expected if self-sealing is due to internal swelling of the gel pores because dissolved ions modify the interaction between gel pore water and the solid matrix, see [15]. Since the present specimens were prestored at a relative humidity of 50%, water uptake will lead primarily to an increase in disjoining pressure and consequently internal swelling as gel pores are saturated with water. Measurements of the separation between quartz spheres have shown that dissolved NaCl is able to increase the disjoining pressure considerably due to DLVO repulsion or ion solvation [16].

It is postulated that the combination of two effects which occur simultaneously explain the data in Figure 5, left. (a) w_{NMR}/w decreases in the presence of salt because the dissolved ions modify the interaction of the water molecules with the gel pore surface and thus the proton environment. (b) w_{NMR}/w tends to increase because dissolved salt slows down the movement of water from the capillary into the gel pores. Whereas mechanism (a) dominates at the beginning of suction, mechanism (b) becomes more important after longer times which could explain the cross-over effect in the figure.

3.3 Effect of Initial Moisture Content

If the redistribution of water from capillary pores into gel pores is the reason for self-sealing, then initial moisture content ought to affect liquid uptake because at higher initial moisture contents the gel pores contain more water. Since the effect of initial moisture content on uptake and penetration of water and hexane is dealt with in [13] only the relevant results are presented here. The water content of prisms equilibrated at 80% RH was found to be 59 litre/m^3 with respect to storage at 50% RH (zero condition) which corresponds to a surface uptake of 13.5 litre/m^2 by the prisms used. The uptake and penetration of water and hexane were followed gravimetrically and using NMR as already described, Figure 6.

Non-$\sqrt{t}$ uptake behaviour is evident for water penetration as well as uptake and occurs for both initial moisture contents. For the reasons already discussed, self-sealing does not occur during

hexane penetration which is faster than water, but nevertheless dependent on initial moisture content.

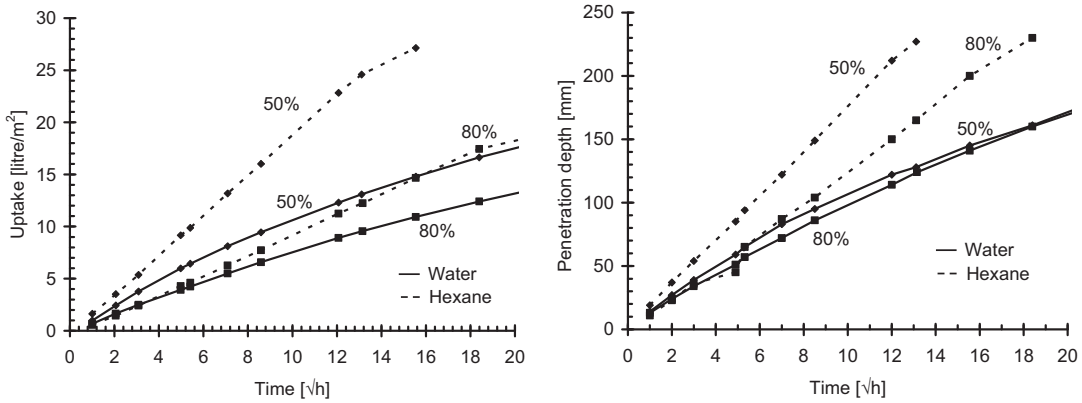

Figure 6: Left: uptake of water and hexane through the surface of mortar prisms (w/c=0.6) after storage at 50 and 80% RH. Right: corresponding NMR penetration depths

The higher moisture content following storage at 80% RH results in a slower penetration rate and uptake of hexane. The increase in moisture content between 50% and 80% RH is due to capillary condensation of water in pores with Kelvin radii between 1.5 and 4.7 nm. Thus hexane penetration in much larger capillary pores is reduced by small water-filled gel pores. It therefore appears that internal gel swelling produced by the initial gel pore water content reduces hexane transport. The initial water content has, so to speak, already undergone redistribution and restricts uptake and penetration in (linear) dependence of $\sqrt{t}$. The fraction of water registered by NMR w_{NMR}/w with respect gravimetric uptake is shown on the left of Figure 7. The absence of redistribution for hexane provides evidence that self-sealing is due to redistribution of water into gel pores.

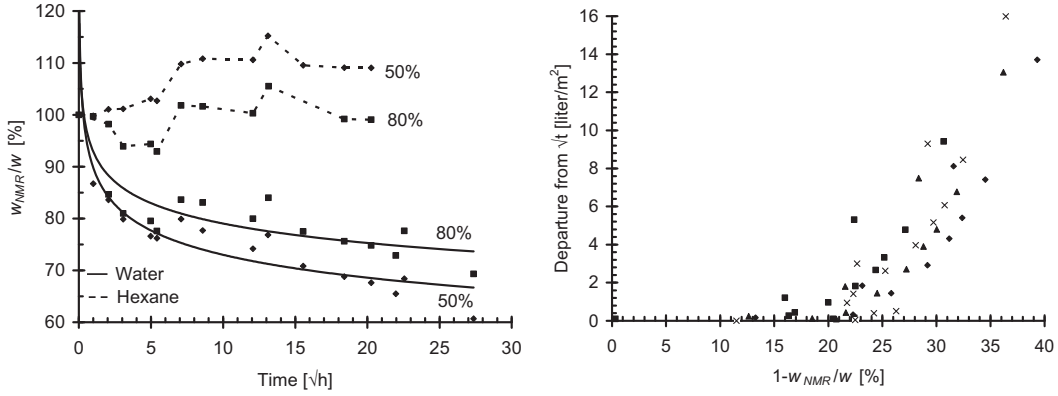

Figure 7: Left: fraction of hexane and water measured by NMR during capillary suction by mortar prisms. Right: Departure of capillary uptake of water from initial $\sqrt{t}$ behaviour as a function of weight fraction of redistributed water. Additional values for specimens equilibrated at 65 (▲) and 75 % RH (×) are also included.

The departure of water uptake from initial $\sqrt{t}$ behaviour was estimated by fitting straight lines through data for the first nine hours in Figure 6, left. The difference between the fitted lines and

the measured uptake is plotted in Figure 7, right, as a function of the weight fraction of redistributed water from the NMR data, i.e. (1-w_{NMR}/w). The departure of capillary uptake from $\sqrt{t}$ behaviour correlates well with the amount of redistributed water.

3.4 Reversibility

If the redistribution of water into gel pores during suction leads to self-sealing then, as opposed to precipitation, deposition or particle clogging, the self-sealing effect should be reversed to a high degree by drying which will remove redistributed gel pore water. This aspect was investigated by observing water uptake and penetration before and after second drying. In a first cycle, an end face of a mortar prism equilibrated at 50% RH was placed in contact with water and uptake and penetration followed over 48 hours. The prism was then dried at 50% RH for 535 days and uptake and penetration measured again. The amount of water taken up during first suction was not completely removed during the second drying period, Figure 8. This is why the penetration profiles uniformly shift to lower depths during the second suction period.

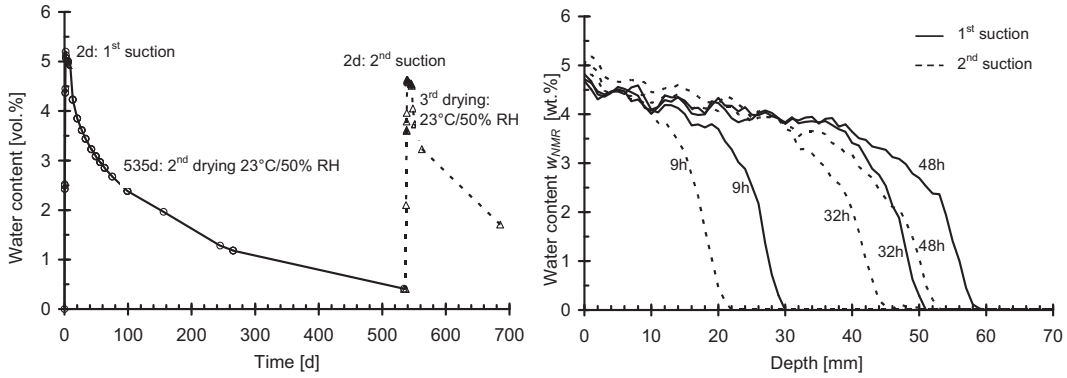

Figure 8: Left : water content during repeated suction and drying. Right: NMR penetration profiles for suction with intermediate drying

The uptake and penetration of water during the first and second suction periods increase in a parallel manner after 9 hours and have not been affected by intermediate drying, Figure 9.

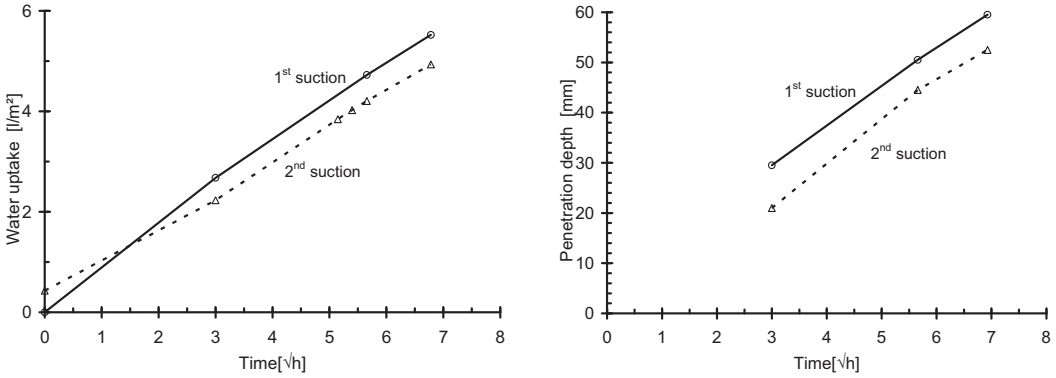

Figure 9: Water uptake and NMR penetration depth for suction with intermediate drying

The lower values observed during the second suction period are due to the small amount of water which remained after drying. The results show that the self-sealing effect can be reversed

by water removal. This would not occur if non-$\sqrt{t}$ behaviour is due to pore blocking by deposition or clogging during suction.

3.5 Effect of Water Pressure

The results of extensive investigations on the effect of water pressure and self-sealing on moisture transport in mortar and concrete designed for high water impermeability have been recently published, [2]. The results relevant to the self-sealing mechanism are outlined here. A special apparatus was constructed with which water pressures up to 1 bar were applied to the end faces of mortar prisms. The results for water uptake and NMR penetration depth at pressures of 0, 0.5 and 1.0 bar are shown in Figure 10.

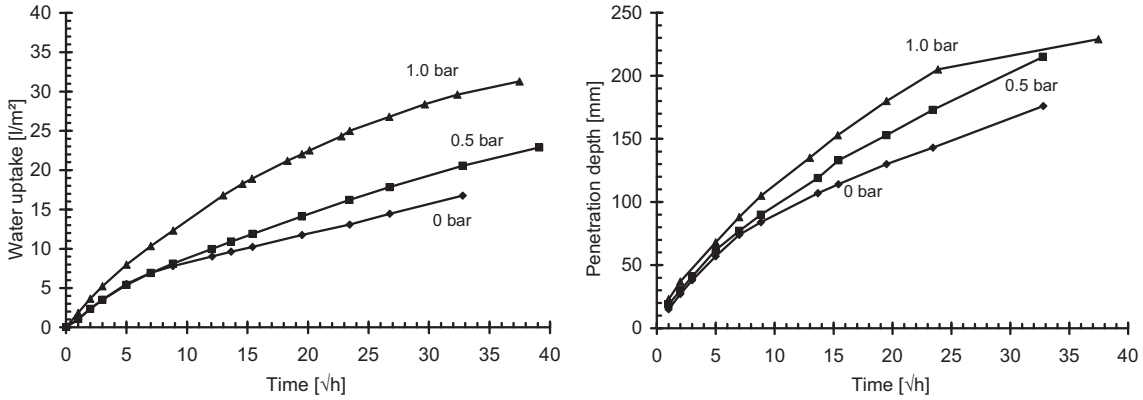

Figure 10: Effect of water pressure on uptake and NMR penetration depth in mortar (w/c=0.6). Prism length: 225 mm

As would be expected, water uptake and depth of penetration increase with water pressure. The non-linear $\sqrt{t}$ behaviour proves that the penetration water under pressure is also reduced by the self-sealing effect. At the same time, the proportion of water being redistributed from capillary into gel pores during penetration increases with pressure, Figure 11.

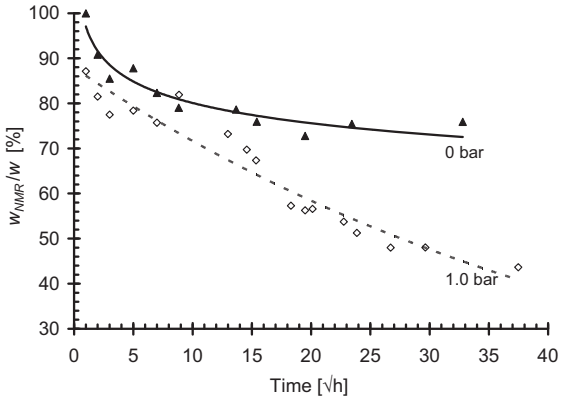

Figure 11: Effect of pressure on fraction of water measured by NMR during water penetration uptake and NMR penetration depth in mortar (w/c=0.6)

The external application of pressure causes pores which are otherwise not accessible by capillary suction to be filled by water. Thus pressure not only leads to a greater penetration depth, but also to higher degree of saturation, as may be calculated from the water uptake and penetration depths in Figure 10, see [2]. Since the proportion of redistributed water increases with pressure, the higher saturation of the pore system due to pressure makes more gel pores available for the redistribution process causing the self-sealing effect to set in faster. Thus while pressure accelerates water penetration due to its direct action in capillary pores it also slows down penetration by increasing water redistribution and self-sealing.

3.6 Effect of Specific Surface

It is well-known that the interaction of gel pore water molecules with the solid gel matrix across the liquid/solid phase boundary in hardened cement paste results in swelling or shrinkage of concrete due to moisture absorption or loss, see [17]. The degree of swelling or shrinkage increases with the specific surface of hardened cement paste [18]. Figure 12 shows the effect of the specific surface of hardened cement paste in concrete on the departure of uptake from $\sqrt{t}$ behaviour after a suction time of 188 hours for more than 20 different concrete compositions. The specific surface of the hardened paste was estimated from measurements of water vapour adsorption by concrete specimens equilibrated at 22% RH, the thickness of the adsorbed layer on open surfaces at this humidity and the volume fraction of hardened paste in the concrete, see [1].

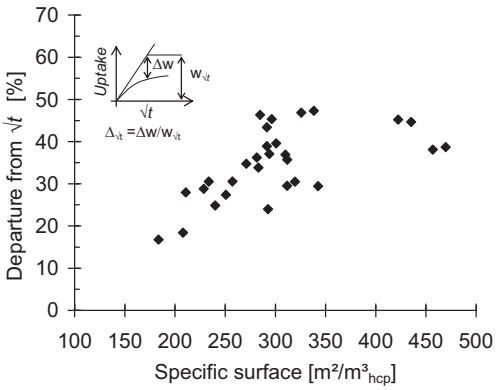

Figure 12: Effect of specific surface of hardened cement paste on departure of water uptake from $\sqrt{t}$ behaviour

It is evident that the departure of uptake from $\sqrt{t}$ behaviour is more pronounced at larger specific surface areas. This indicates that the self-sealing effect is mainly caused by the interaction between gel pore water molecules and the solid matrix which leads to internal swelling. A larger specific surface means a stronger interaction per unit volume of cement gel and thus greater deviation from $\sqrt{t}$ behaviour during uptake, i.e. the self-sealing effect is stronger.

4 Computer Modelling

The results presented here and in [1] are being implemented at the Fraunhofer Institute for Building Physics, Holzkirchen in a computer model for the simulation of moisture and salt penetration in concrete exposed to a varying climate (temperature, relative humidity, wetting with water or salt solution). The model simulates the transport of chlorides by ionic diffusion, capillary suction and redistribution of water in capillary pores with advection of chlorides, water vapour diffusion, binding of chlorides, thermal transport, crystallization of salt and wash-off of surface salt. The effect of dissolved chlorides on capillary transport and water vapour diffusion are included. The self-sealing effect is described by the redistribution rate of capillary pore water into gel pores - which are non-active in capillary transport - and the effect of gel pore water on the rate of capillary suction. In addition, the effect of dissolved chlorides on self-sealing is also considered. The computer model is based on the modelling language Modelica.

At first, the coupled heat- and moisture transport processes were implemented and validated by comparing simulation results of the model with well-established simulation tools [19, 20]. Afterwards, the effects concerning the self-sealing mechanism were included in the model. Figure 13 shows some simulation results for the uptake of water by 12 cm thick concrete with and without the self-sealing effect. As expected without the self-sealing effect, the water uptake increases approximately linearly with the square root of time whereas the uptake is reduced if self-sealing is considered. After reaching a maximum, the uptake decreases slightly despite continuous exposure of a surface to water. The reason for this is drying on the opposite side due to vapour diffusion.

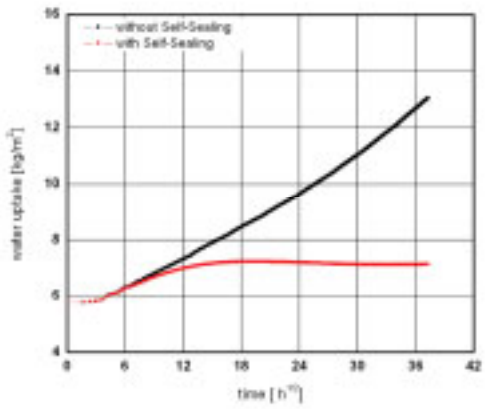

Figure 13: Simulation of the water uptake in concrete with and without self-sealing effect

Currently, the effects due to salt are being integrated in the model. Details on the model may be found in [1].

5 Conclusions

When dry concrete is exposed to water, NaCl solutions or an organic solvent, the rate of penetration and, correspondingly, the surface uptake are determined by the action of surface tension and viscosity in the capillary pore system as well the external pressure exerted on the liquid. As the liquid penetrates deeper into the concrete, part of it undergoes redistribution into gel pores which leads to swelling of the cement gel. The degree of swelling is determined by the specific surface of the cement gel, the dipole concentration of the liquid and the concentration of dissolved ions which affect the disjoining pressure exerted by water molecules in gel pores. The expansion of the cement gel reduces the connectivity of the capillary pore system and thus the rate of capillary transport. The ongoing redistribution process results in a deviation of both uptake and penetration depth from $\sqrt{t}$ behaviour - otherwise characteristic for unrestricted capillary transport of liquids. Dissolution and precipitation of phases in the pore system affect capillary transport and occur alongside redistribution and self-sealing. A computer model is being developed for the simulation of heat, moisture and salt transport in concrete under real service conditions.

An additional aspect of the research project was modelling the damage in sand stone caused by the crystallisation and dissolution of sodium sulphate phases in pores during climatic variation. The main results of are available in [21].

6 Acknowledgements

The authors express their thanks to the German Research Foundation (DFG) for sponsoring the research.

7 References

[1] Rucker-Gramm, P.: Modellierung des Feuchte- und Salztransports unter Berücksichtigung der Selbstabdichtung in zementgebundenen Baustoffen. Dissertation Technische Universität München, eingereicht im Juni 2008

[2] Rucker, P., Beddoe, R.E.: Transport von drückendem Wasser in Betonbauteilen. In: Beton und Stahlbeton 102, S.414-426, 2007

[3] Beddoe, R.E., Springenschmid, R.: Feuchtetransport durch Bauteile aus Beton. In: Beton- und Stahlbetonbau 94,S.158-166, 1997

[4] Hearn, N., C.T. Morley, C.T.: Self-sealing property of concrete - experimental evidence. Mater. Struct. 30, pp.404-411, 1997

[5] Krus, M., Hansen, K.K. and H.M. Künzel, H.M.: Porosity and liquid absorption of cement paste. In: Mater. Struct. 30, pp.394-398, 1997

[6] Wasserundurchlässige Bauwerke aus Beton (WU-Richtlinie), Deutscher Ausschuss für Stahlbeton – DAfStb, 2003

[7] Sosoro, M.: Transport of organic fluids through concrete. In: Mater. Struct. 31, pp.162-169, 1998

[8] Hearn, N. and Mills, R.H.: A simple permeameter for water or gas flow. In: Cem. Concr. Res. 21, pp. 257-261, 1997

[9] Edvardsen, C.K.: Wasserundurchlässigkeit und Selbstheilung von Trennrissen in Beton, Beuth Verlag Berlin, Schriftenreihe des Deutschen Ausschuss für Stahlbeton Heft 455, 1996

[10] Krus, M: Moisture transport and storage coefficients of porous mineral building materials, theoretical principles and new test methods, PhD Thesis. University of Stuttgart, Fraunhofer IRB Verlag, 1996, ISBN 3-8167-4535-0

[11] Beddoe, R.E., Lippok, R.: Hygral stress in hardened cement paste. In: Materials and Structures. 32, pp. 627-634, 1999

[12] Beddoe, R.E.: Einfluss von organischen Flüssigkeiten auf Zementstein. In: DFG Abschlussbericht R. Springenschmidt, R.E. Beddoe Sp 174/28, 2002

[13] Rucker, P., Beddoe, R.E., Effect of moisture content of concrete on water uptake. Submitted for publication in Cem. Concr. Res., 2007

[14] Rucker, P., Beddoe, R.E., P. Schießl, P.: Wasser- und Salzhaushalt im Gefüge zementgebundener Baustoffe – Modellierung der auftretenden Mechanismen. In: Beton- und Stahlbetonbau 6, S.402-412, 2006

[15] Churaev, N.V., Setzer, M.J., Wowra, O., Reick, M.: Electrolytes in narrow pores. In: Int. Z. für Bauinstandsetzen und Baudenkmalpflege 6, S.87-102, 2000

[16] Beltzung,F., Wittmann, F.H.: Role of disjoining pressure in cement based materials. In: Cem. Concr. Res. 35, S.2364-2370, 2005

[17] Setzer, M.J. Einfluss des Wassergehalts auf die Eigenschaften des erhärteten Betons. In: Schriften reihe Deutscher Ausschuss für Stahlbeton Heft 280, 1977

[18] Feldman, R.F., Swenson, E.G.: Volume change on first drying of hydrated Portland cement with and without admixtures. In: Cem. Concr. Res. 5, pp.25-35, 1975

[19] Nouidui, T.: Entwicklung einer objektorientierten Modellbibliothek zur Ermittlung und Optimierung des hygrothermischen und hygienischen Komforts in Räumen. Dissertation Universität Stuttgart, eingereicht im Juni 2008

[20] Holm, A., Krus M., Künzel H.M.: Feuchtetransport über Materialgrenzen im Mauerwerk. In: Internationale Zeitschrift für Bauinstandsetzen 2, H. 5, S.375-396, 1966.

[21] Rucker, P., Becker, J., Schießl, P.: Gefügeschädigung tonhaltiger Sandsteine infolge Feuchte und Salzbelastung - Modell der Schädigung bei Trocknung. In: Bauinstandsetzen und Denkmalpflege 13, Heft 5, S.293-304, 2007

Adrian Muntean
Dr.

Centre for Analysis, Scientific computing and Applications (CASA)
Department of Mathematics and Computer Science
Eindhoven University of Technology,
The Netherlands

Michael Böhm
Prof. Dr.

Alfred Schmidt
Prof. Dr.

Centre for Industrial Mathematics (ZeTeM)
Department of Mathematics and Computer Science
University of Bremen,
Germany

On the motion of internal carbonation layers

Summary

Carbonation is the reaction of environmental carbon dioxide with alkaline species in concrete. It is one of the major processes affecting the concrete durability. In this note, we review a few modelling strategies that are behind conceptually different carbonation models which are all able to capture the formation and propagation of internal layers hosting fast reaction(s).

Keywords: *fast reaction, internal reaction layers, moving-interface methodology, multiscale, matched-asymptotic expansions, complex vs. reduced chemistry, isolines method*

Acknowledgement: *The authors wish to express their deep gratitude to their colleagues Prof. Malte Peter (Auckland (New Zealand)/Augsburg (Germany)) and Dr. Sebastian Meier (Bremen (Germany)) for their substantial contributions to this project*.

1 Introduction

In general terms, carbonation is the reaction of environmental carbon dioxide, CO_2, with carbonatable species in concrete, hydration in- or excluded. It is one of the main players influencing the service life of steel-reinforced concrete by changing the alkalinity in the proximity of the steel bars. Rather than going into detail we refer to some of the (standard) references (see, for instance, [33], [13]). There is a multitude of approaches aimed at describing carbonation – some of them very involved connecting many reactions and others focussed on some particular aspects and thus neglecting part of the transport or involved chemistry.

In general one has several options of how to model carbonation:

- The **moving-boundary approach**: A particular phenomenological feature of carbonation is the formation of reaction surfaces and/or layers that progress into the concrete-based materials[1]. From a more mathematical point of view the formation of such, more or less, *thin* layers is the result of an ongoing co-existence between slow diffusion and fast reaction of the reacting substance, here: Carbon dioxide. The deeper cause for the formation of these patterns is not completely clear, although the major chemical and physical reasons seem to be known [33], [13], [3]. The reaction layer is idealized as a time dependent interface, $\Gamma = \Gamma(t)$, and moves as into the interior of the concrete sample Ω as time goes on. Γ separates the carbonated and the uncarbonated parts of Ω from each other. In this approach the bulk-reaction as well as precipitation are concentrated on Γ.

- The **classical isolines approach**: The whole carbonation process is modeled in terms of partial (mainly parabolic) or ordinary differential equations accompanied by algebraic equations *if* some of the involved chemical reactions are considered in thermodynamic equilibrium. The model equations are supposed to hold on the whole concrete sample, Ω. Material and/or process parameters (such as reaction coefficients, diffusion coefficients and others) might depend on some of the concentrations involved, including humidity. The reaction layer mentioned above is determined by isolines of the participating concentrations such as the ones of $Ca(OH)_2$ or CO_2.

- The **phase-field approach**: Here one introduces an additional order parameter which equals 1 in the carbonated zone, zero in the non-carbonated zone and which is between zero and one in the bulk-reaction zone. For this approach one needs an a-priori guess about the width ε of the reaction layer. The phase-field equations determine the position of the bulk-reaction layer.

In section 2 we make some remarks on the second approach. The isolines approach does not play a role in this paper - with the exception that information about the width ε in phase field approaches plays a role in the moving-boundary approach. From section 4 on our focus is on the moving-boundary strategy for reaction (*) below (in detail) and on results obtained for a more complex carbonation setting based on the isolines approach.

To this end we formulate the concrete carbonation as a whole, first as a one-dimensional, then as a two-dimensional process. The result of this is a coupled system of non-linear partial differential equations in fixed or moving domains. The most important sub-processes we are dealing with are the carbonation kinetics, the changes in the pore configurations induced by reaction and the transfer of humidity. Monitoring of such processes enables conclusions about moving

[1] This paper and the underlying project has been heavily motivated by this feature.

reaction-front behavior and can lead to a better prediction of penetration depths and of the corrosion initiation time.

2 Carbonation models with complex chemistry

In the preliminary study [27] we examined which of the many reactions contributing to carbonation are of essential relevance with respect of the advance of the carbonation layer. The following is a short summary of the processes we were looking at[2]: As atmospheric carbon dioxide enters the pore space Ω_p of the unsaturated concrete sample Ω, it diffuses through the air-filled pore space Ω_a, enters the water filled pore space Ω_{pw}, and reacts there with the available carbonatable species to form carbonates.

Commonly the *main* reaction is the one with calcium hydroxide, roughly summarized as

$$\mathrm{CO_2(g \rightarrow aq) + Ca(OH)_2(s \rightarrow aq) \rightarrow CaCO_3(aq \rightarrow s) + H_2O} \qquad (*)$$

One observes a relatively steep gradient of the concentration of $c_{Ca(OH)_2}$. The gradient of c_{CO_2} is less pronounced since CO_2 has to move to the location of the bulk reaction before it starts reacting. In concrete there is more carbonatable material such as the C-S-H phases (calcium-silicate-hydrates) in various stoichiometric variants. Moreover there are hydration products like C_2S and C_3S which compete for $Ca(OH)_2$. In this note, we disregard the other carbonatable species such as $Mg(OH)_2$, KOH, aluminate phases or NaOH (see [5], [7], [32] for more details). The reactions involving the latter species follow a similar scenario as the ones with C-S-H and $Ca(OH)_2$, but their overall contribution to the whole carbonation process is much lower. Once $Ca(OH)_2$ is used up, the C-S-H carbonation begins[3]. Around the same time, the reaction of C_2S and C_3S with water (i.e. a late hydration) produces new carbonatable material - $Ca(OH)_2$ and C-S-H, see [2], [33], [28], e.g. There are also reactions with sulphates and chlorides, which are relevant for the overall alkalinity. We disregard the latter ones and focus initially on the other ones. Beginning with section 3, we restrict ourselves to a slightly refined version of reaction (*) in the context of moving-boundary models.

In this note we exclusively concentrate on the propagation speed of the carbonation process, the calculation of concentrations profiles will be a by-product of the approach.

Most models for carbonation involve a relatively large number of material and process parameters. Many of these parameters are only incompletely known or stem from uncorrelated experiments, respectively. Therefore we performed (see [18,27], e.g.) parameter studies of the influence of the various parameters on the propagation speed. This study can be seen as a par-

[2] The full system of PDEs describing the model with complex chemistry is listed in [27].

[3] Once a critical low concentration of Ca(OH)2 is reached, the C-S-H carbonation begins.

tial justification of the simplified setting in section 3, although many other authors, who deal with just (*), do not attempt any such justification when restricting themselves to (*). One outcome of the results is: Regardless how many reactions are taken into account: At the qualitative level, the Thiele numbers (see section 3) play an essential role influencing the speed as well as the width of the carbonation layer.

3 Further notation

3.1 Concentrations

We define the concentrations (in grams per cm^3) by

$c_{CO_{2g}(g)}$	-	concentration of CO_2 in pore air,
c_{CO_2}	-	concentration of CO_2 in pore water,
$c_{Ca(OH)_2}$	-	concentration of $Ca(OH)_2$ in pore water,
c_{CaCO_3}	-	concentration of $CaCO_3$,
w	-	concentration of (mobile) moisture,
RH	-	relative humidity.

Similarly we proceed with the other reactants CSH, C_2S and C_3S.

We refer to w as total humidity, or simply, moisture – in all cases this variable incorporates the pore water *and* the water vapours from the air-filled parts of the pore. By means of this variable, we aim at describing the water produced via the carbonation reaction only.

3.2 Initial conditions

The whole process begins at time $t = 0$. All the concentrations introduced in section 3.1 are supposed to be given at that time, i.e. $c_l(x, t = 0) = c_{l0}$ for all $x \in \Omega$, where $l = water, Ca(OH)_2, CO_2(g), .., C_3S.$

3.3 Production- and exchange terms

Re. Moving-boundary approach (w/o. hydration):

- $f^{Henry} = C^{ex}(C^{Henry}\, c_{CO_{2g}(g)} - c_{CO_2})$ - the Henry exchange term. C^{ex} is the interfacial mass-transfer coefficient. The Henry-like constant is chosen as $C^{Henry} = 0.82,$

- $g^{hum}(RH) := \begin{cases} 0 & if \quad RH \le 0.5, \\ \frac{5}{2}(RH - 0.5) & if \quad 0.5 < RH \le 0.9, \\ 1 & if \quad 0.9 < RH \le 1. \end{cases}$ - a humidity factor,

- $f^{reac}_{Ca(OH)_2} = C^{reac}_{Ca(OH)_2} g^{hum}(c_{C0_2})^p (c_{Ca(OH)_2})^p$ - with some exponents $p, q \ge 1$. $C^{reac}_{Ca(OH)_2}$ is the reaction constant for the reaction (*). For the sake of simplicity we have also used

$f^{reac} = C^{reac}_{Ca(OH)_2} (c_{C0_2})^p (c_{Ca(OH)_2})^p$ thus disregarding the influence of the relative humidity on the reaction rate.

Sometimes we write η instead of f^{reac}.

- m_l denotes the molecular weight of species $l, l = CO_2, Ca(OH)_2$ etc.,

- ϕ, ϕ^w, ϕ^a stand for the porosity, the fraction of water-filled pores and the fraction of air-filled pores, respectively. In particular: $\phi^w + \phi^a = 1$.

- $-m_{CO_2} \phi \phi^w f^{reac}$ is the pore averaged production rate for carbon dioxide; here: loss due to reaction.

- $-m_{Ca(OH)_2} \phi \phi^w f^{reac}$ is the pore averaged production rate for calcium hydroxide; here: loss due to reaction.

- $+m_w \phi \phi^w f^{reac}$ is the pore averaged production rate for calcium hydroxide, here: gain due to reaction.

- Whenever non-instantaneous dissolution or precipitation of species l is assumed, we use the source law $f_l^{diss/prec} = \pm S_{diss/prec}(c_{l,eq} - c_l)$, where "+" relates to dissolution and "-" to precipitation. $c_{l,eq}$ is the corresponding equilibrium concentration of species l.

Re. Hydration, C_2S and C_3S:

In this subsection, the index l refers to C_2S and C_3S.

- f_l^{hydr} denotes the hydration production rate. Following [24], we choose $f_l^{hydr} = C_l^{hydr} c_l$ with the hydration constant $C_l^{hydr} = k_l^{hydr} / (c_{l0})^{p_l - 1}$. c_{0l} is the initial concentration of species l, k_l^{hydr} is the reaction constant (re. reaction with water).

- The rates for the reaction with CO_2 are given by $f_l^{reac} = C_l^{reac} c_{CO_2}$, where $C_l^{reac} = k_l^{reac} A_l$. k_l^{reac} is the reaction rate, A_l is the average water-exposed surface of species l. The literature yields only a lower estimate for $k_l^{reac} / k_{Ca(OH)_2}^{reac} > 2.4 \times 10^{-3}$. For a systematic study of the impact of changing this quotient, we refer to [18].

3.4 Fluxes

Employing Fick's law, we have the following fluxes of concentrations:

- $-D_{CO_2(g)}\phi\phi^a\nabla c_{CO_2(g)}$ - carbon dioxide flux in the air-filled part Ω^a of the pores,
- $-D_{CO_2}\phi\phi^w\nabla c_{CO_2}$ - carbon dioxide flux in the water-filled part Ω^w of the pores,
- $-D_{Ca(OH)_2}\phi\phi^w\nabla c_{Ca(OH)_2}$ - calcium hydroxide flux in Ω^w,
- $-D_w\phi\nabla w(x,t)$ - humidity flux in Ω^w,

with corresponding diffusion coefficients $D_{CO_2},..,D_w$.

3.5 Boundary conditions

The CO_2(g)- influx through the exterior boundary is modeled by Robin-boundary conditions:

$-D_{CO_2(g)}\phi\phi^a\nabla c_{CO_2(g)}\bullet n = f^{Rob}_{CO_2(g)} := C^{Rob}_{CO_2(g)}(c_{CO_2(g)} - c^{ext}_{CO_2(g)})$.

n is the unit outward normal, $C^{Rob}_{CO_2(g)}$ is the exchange coefficient, while $c^{ext}_{CO_2(g)}$ is the exterior concentration. All the other fluxes are assumed to be zero.

4 Capturing moving reaction fronts via a moving-interface methodology

4.1 Problem statement

A natural way to describe fast reaction-slow transport scenarios in porous media such as carbonation in concrete is to employ a so-called *moving-interface model*. Introductory examples of moving-interface models are given, for instance, in [9] and references cited therein. Such a model consists of a system of mass-balance equations whose main feature is that it describes the (carbonation) reaction concentrated at the moving *interface* (or, following the case, near a thin layer, or within a larger strip). The position of the moving layer is *a priori unknown*. Therefore, this needs to be determined simultaneously together with the concentration profiles of the involved chemical species. One of the most important questions that we wish to address within this frame is "*How fast does carbonation penetrate the cement-based material?*" Note that, in general, one can distinguish between two different classes of moving-interface models. Following the terminology from [37]), we have

- Models with *equilibrium conditions at the moving interface:* [36], [6];
- Models with *non-equilibrium conditions at the moving interface:* [19].

In this section, we focus on a particular model belonging to the latter class. We refer to it as moving-interface model with kinetic condition. The word "kinetic" means here that an explicit expression of the normal component of the velocity of the moving interface (where the bulk of the carbonation reaction is concentrated) is given as a function of the carbonation-reaction rate. Kinetic conditions have been originally derived to describe the non-equilibrium interface kinetics during rapid solidification, [1], [37], where deviations from the local equilibrium occur at a rapidly

moving solid-liquid interface. This is a typical situation where phase diagram information cannot describe in an accurate manner the thermodynamics at the moving interface. As far as we are aware, there are at least two alternative modelling strategies replacing (in some sense) the use of the kinetic condition. One of them relies on switching on/off conditions at the moving interface (or on unilateral conditions of Signorini type), [23], while the other one involves two-steps matched-asymptotic expansions, [11]. In what follows, we concentrate a moving-interface model with kinetic condition for a carbonation model with reduced chemistry. With very few modifications, a somewhat similar PDE model can be written for a model with complex chemistry.

4.2 The 1D-moving interface model

Within this section, we recall a one-dimensional moving-interface model [19,21] describing the carbonation of $Ca(OH)_2$ only and focus the attention on the interface conditions.

Our sample is a cylinder exposed at the top and bottom to the environment and otherwise isolated. We assume symmetries across all cross sections of Ω such that the whole process is 1D. We choose the middle line of the cylinder as reference line and put on this line the x-axis. x = 0 and x = 2L denote the position of the beginning and the end of the middle line. $\Omega_1(t) := (0, s(t))$ refers to the fully carbonated region at time t, while $\Omega_2(t) := (s(t), L)$ is the yet uncarbonated part. x = L is a symmetry point (e.g. situated in the centre of the middle line of our cylindrical sample). The averaged equations read as follows:

Mass-balance equation for CO_2(g)*:*

$$\partial_t\left(\phi\phi^a c_{CO_2(g)}(x,t)\right) - \nabla\cdot\left(D_{CO_2(g)}\phi\phi^a \nabla c_{CO_2(g)}(x,t)\right) = -f^{Henry}(x,t), x\in\Omega_1(t)$$

Mass-balance equation for CO_2*:*

$$\partial_t\left(\phi\phi^w c_{CO_2}(x,t)\right) - \nabla\cdot\left(D_{CO_2}\phi\phi^w \nabla c_{CO_2}(x,t)\right) = +f^{Henry}(x,t) - m_{CO_2}\phi\phi^w f^{reac}, x\in\Omega_1(t)$$

Mass-balance equation for $Ca(OH)_2$*:*

$$\partial_t\left(\phi\phi^w c_{Ca(OH)_2}(x,t)\right) - \nabla\cdot\left(D_{Ca(OH)_2}\phi\phi^w \nabla c_{Ca(OH)_2}(x,t)\right) = -m_{Ca(OH)_2}\phi\phi^w f^{reac}, x\in\Omega_2(t)$$

Mass-balance equation for $CaCO_3$*:*

$$\partial_t\left(\phi\phi^w c_{CaCO_3}(x,t)\right) = +m_{CaCO_3}\phi\phi^w f^{reac}, x\in\Omega_1(t)$$

Mass-balance equation for w:

$$\partial_t\left(\phi w(x,t)\right) - \nabla\cdot\left(D_w\phi\nabla w(x,t)\right) = +m_w\phi f^{reac}, x\in\Omega_1(t)\cup\Omega_2(t).$$

Initial and boundary conditions describe the chemical composition at time $t = 0$ of the material as well as the exchange through the exterior boundaries of Ω with the ambient.

In order to be able to determine the position of the moving interface at each moment t, two additional boundary conditions are needed. The first one is standard - the mass of the involved chemical species has to be conserved across the evolving interface. This fact is expressed by means of Rankine-Hugoniot conditions. Denoting by $s(t)$ the position of the moving interface and by $s'(t)$ the corresponding one-dimensional velocity, the Rankine-Hugoniot conditions read:

$$
\begin{aligned}
&-D_{CO_2(g)}\nabla c_{CO_2(g)}(s(t),t)\cdot n = \eta\big(s(t),t\big)+ s'(t)c_{CO_2(g)}(s(t),t)\\
&-D_{CO_2}\nabla c_{CO_2}(s(t),t)\cdot n = s'(t)c_{CO_2}(s(t),t)\\
&-D_{Ca(OH)_2}\nabla c_{Ca(OH)_2}(s(t),t)\cdot n = -\eta\big(s(t),t\big)+ s'(t)c_{Ca(OH)_2}(s(t),t)\\
&\big[-D_w\nabla w\cdot n\big]_{\Gamma(t)} = \eta(s(t),t), \quad \big[w\big]_{\Gamma(t)} = 0.
\end{aligned}
$$

For the sake of clearness we use the gradient symbol, ∇, rather than its 1D pendant, the partial derivative. n stands for the unit outward normal – i.e. *n = -1* if *x = 0* and *n= + 1* if *x = L*.

The second condition is the kinetic condition

$$s'(t) = \alpha\frac{\eta(s(t),t)}{c_{Ca(OH)_2}(s(t),t)}.$$

It points out that the speed $s'(t)$ of the interface $\Gamma(t)$ is directly proportional to the strength of the reaction and inversely proportional to the amount of $Ca(OH)_2$ still available at that interface. α is a proportionality factor.

Note: A special role in investigating carbonation is played by semi-theoretical models. Using a technique inspired by [4] an approach via matched-asymptotic expansions is proposed in [22], [20] to show the occurrence of two distinct characteristic length scales in the carbonation process corresponding to the characteristic time scales of diffusion of the fastest species and that of the carbonation reaction. The separation of these scales arises due to the strong competition between reaction and transport effects. It has been shown that, for sufficiently large times *t,* the width of the carbonation region is proportional to $t^{\frac{p-1}{2(p+1)}}$ for carbonation reaction rates with a power-law structure like $k\big[\mathrm{CO}_2\big]^p\big[\mathrm{Ca(OH)}_2\big]^q$, where $k>0, p, q>1$ and when $Ca(OH)_2$ is assumed to be static. Furthermore, in this case the proportionality coefficient is obtained by solving a nonlinear algebraic equation instead of the usual fitting procedure. Interestingly, the asymptotic penetration depth is in the same range with the asymptotic penetration depth obtained in [24]. Related asymptotic studies are reported in [14], [34], e.g.

5 Numerical examples

In this section we illustrate the accelerated penetration of carbonation described in [24], [35] following the approaches developed in [27], [29] and [21] (i.e. the moving-interface model presented in section 4).

5.1 Internal layers and effect of complex chemistry. One-dimensional motion of the moving interface

Compared with simplified models which neglect CSH, C_2S, and C_3S, we observed in [27] that for the accelerated carbonation test described in [24] (OPC sample, w/c=0.5, a/c=3, RH about 65%, exposed to 50% CO_2) the two silicate phases only have a small influence on the total outcome in the late stage of hydration, which is particularly important in what the carbonation process is concerned. Note that for a large range of parameters, different reaction layers are formed; see Figure 1 and also [18]. Each of them is associated with the several competing reactions.

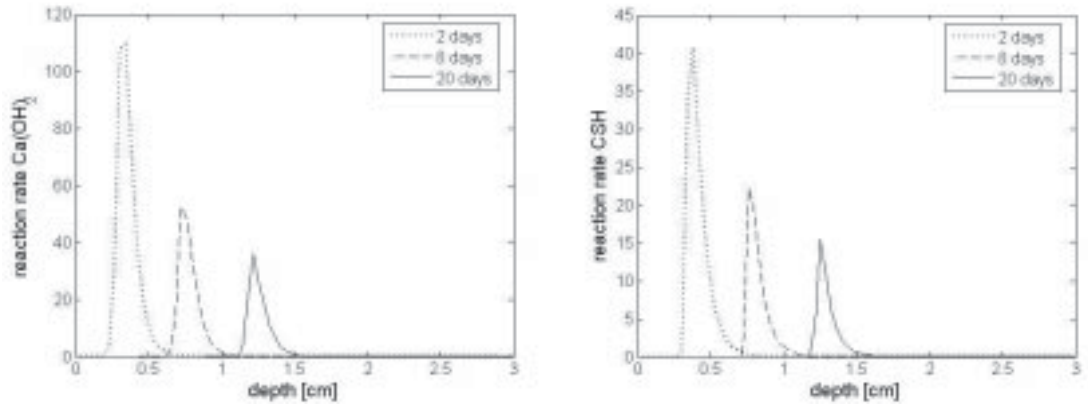

Figure 1: Internal layers associated to the fast CH and CSH carbonation.

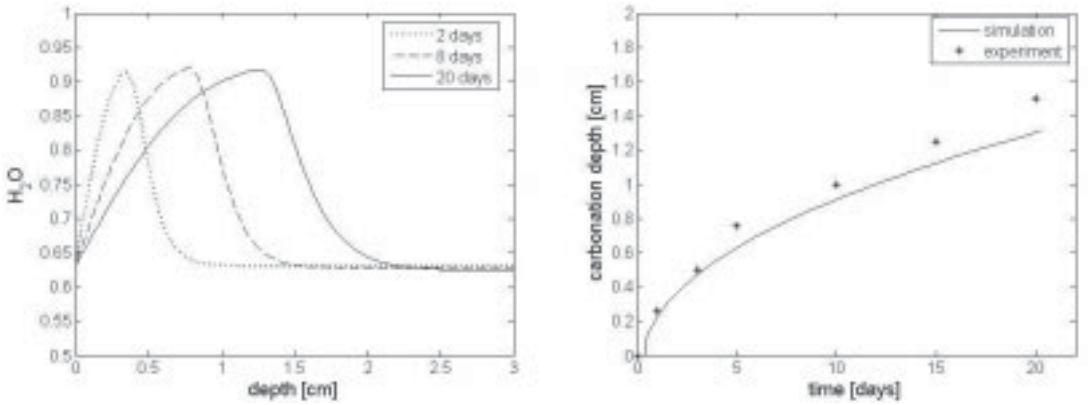

Figure 2: Left: Formation of a water barrier near the exposed boundary. Right: Typical penetration depth curve vs. time. One notices that the simulated penetration depth is close to the measured one.

The internal layers corresponding to CH and CSH are partially overlapping. It seems however that the layer associated to CH is somewhat faster. Figure 2 (left) points out a nonlinear effect arising in accelerated tests (especially if 50% CO_2 is entering the material). Namely, a water barrier is initially formed and travels inside the material possibly hindering the penetration of gaseous CO_2. The major output of carbonation models (with moving interfaces or not) is the penetration depth vs. time curve. Pictures like Figure 2 (right) are the natural outcome of moving-interface models (see [21] or section 4, e.g.), but can also be obtained by means of isolines models employing a suitable concept for the degree of carbonation. The reader is referred to [18] for more details.

5.2 Motion of the moving interface around a corner

In order to test the self-adaptive numerical isolines method that we developed (in [29]) a carbonation test on samples under controlled laboratory conditions (cf. [32], [19]) has been used. In [35], the authors consider the case of a poor OPC concrete with 1 day of curing and estimated w/c=0.7. The cement has a 65% CaO content and a density of about 300 kg/m^3. We assume that the concrete sample presenting corners is entirely exposed to the increased CO_2 concentration of an industrial site. In this setting, the concentration of CO_2(g) is kept at 0.0001 kg/m^3. The relative humidity in the structure and outside is assumed to be 65%. The rest of the model parameters are identical with the reference set of parameters employed in [29].

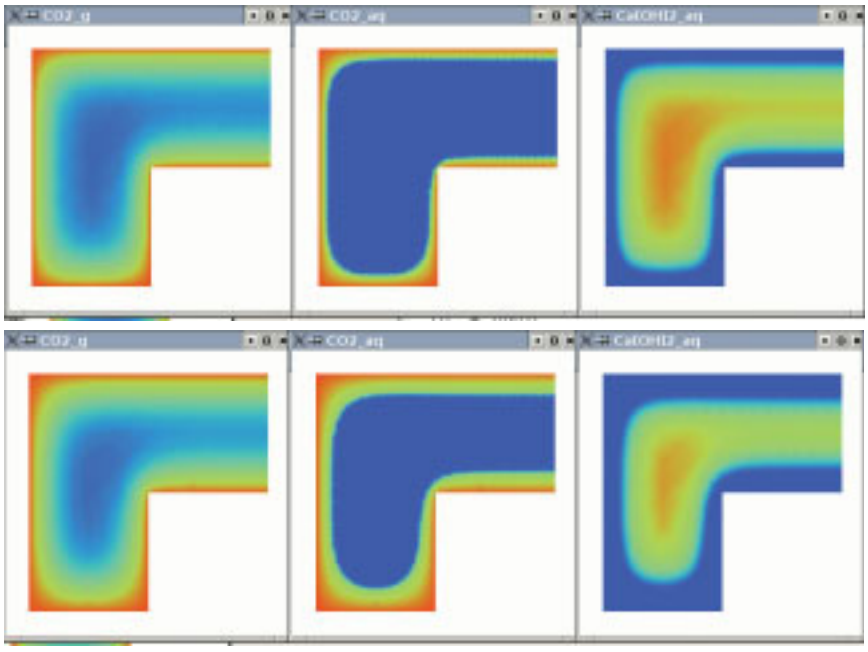

Figure 3: Concentration profiles of active species at two different times. One can see that the reactants separate in space and that the reaction front progresses inwards the material.

The basic geometry is depicted in Figure 3. It is basically an L-shaped domain with one symmetry boundary edge (on the right). Besides the symmetry boundary edge, the boundary conditions on all other parts of the boundary are the same. Due to the L shape, we observe the behavior of the reaction front near three convex corners and near a single concave corner. Figure 3 also shows the concentrations fields of the active species. After a short transient time, the carbonation front is formed and a zone separating the reactants occurs. Near convex corners a faster carbonation is noticed. Figure 4 points out meshes corresponding to two different times.

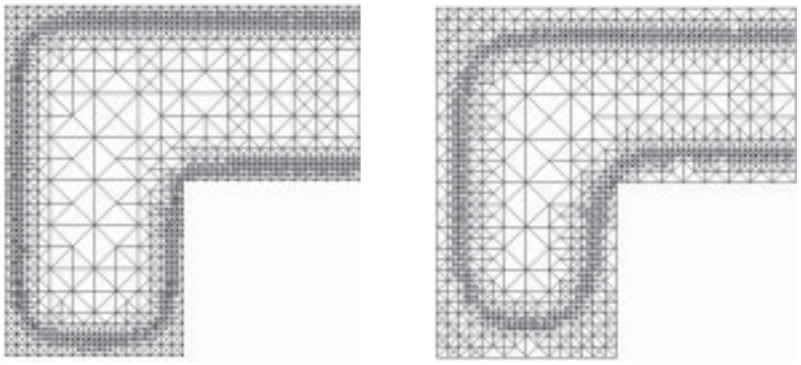

Figure 4: Automatically adapted meshes at two different times corresponding to concentrations fields in Fig. 1. After a transient time, an internal reaction layer is formed and progresses into the material. This moving reaction layer is automatically captured by the self-adaptive mesh refinement method.

Figures 3-4 show the presence of two distinct length scales- one is relevant for reaction and the second one is relevant for the transport. This observation is in agreement with the theoretical observations in [20,22] and also with Figure 1. Figures 3-4 motivate the application of phase-field-based modeling strategies to the carbonation problem; see sections 1 and 6.

6 Perspectives

There are three methodological aspects that we would like to mention:

(1) The phase-field method (see [25], [8], [10], e.g.) has recently emerged as a powerful computational approach to modeling and predicting mesostructure and microstructure evolution in complex materials. It describes the physico-chemical processes using a set of conserved and non-conserved field variables that are continuous across the interfacial regions. The temporal and spatial evolution of the field variables is governed by the Cahn-Hilliard nonlinear diffusion equation and the Allen-Cahn relaxation equation. With the fundamental thermodynamic and kinetic information as the input, the phase-field method is able to predict the evolution of arbitrary morphologies and complex geometries without explicitly tracking the positions of interfaces. An important advantage of the phase-field method, as opposed to a moving-interface strategy, is that its extension to multidimensional situations is conceptually easy to be done,

whilst the second approach leads to tremendous mathematical difficulties at both modeling and computational levels.

(2) Recently, two-scale models and related computational schemes involving local representative unit-cells have succeeded to capture quite well the multi-scale behaviour of concrete materials from the mechanical point of view [12], but also from the reaction and transport perspective [15], [26]. For the case of concrete carbonation a few steps in this direction were already performed in [16] and [17]. However, many newly arisen aspects need to be further investigated.

(3) A challenge is to understand the large-time behaviour of the active concentration profiles and corresponding penetration depth position for models of type (1) and (2) in connection with the *extrapolation* of accelerated carbonation tests results to what happens in natural carbonation scenarios. A simple upscaling does not work. A suitable combination of formal and rigorous asymptotic methods needs to be found (for related matter in a different context, see [11], [30]).

7 References

[1] Aziz, M.J.: Non-equilibrium interface kinetics during rapid solidification. In: Materials Science and Engineering 98, pp.369-372, 1988.

[2] Babushkin, V. I., Matveyev, G. M, Mchedlov-Petrossyan, O. P.: Thermodynamics of Silicates, Springer, 1985.

[3] Bary, B.; Selier, A.: Coupled moisture-carbon dioxide calcium transfer model for carbonation of concrete. In: Cement and Concrete Research 34, pp. 1859-1872, 2004.

[4] Bazant, M. Z., Stone, H. A.: Asymptotics of reaction-diffusion fronts with one static and one-diffusing reactant. In: Physica D 147, pp. 95-121, 2000.

[5] Bier, T. A.: Karbonatisierung und Realkalisierung von Zementstein und Beton, PhD thesis, University Fridericiana in Karlsruhe, Schriftenreihe des Instituts für Massivbau und Baustofftechnologie. Editors: J. Eibl, H. K. Hilsdorf, 1988.

[6] Brieger, L. M., Wittmann, F. H.: Numerical simulation of concrete carbonation. In: F. H. Wittmann (Ed.), Werkstoffwissenschaften und Bausanierung. Int. Koll. Technische Akademie Esslingen.

[7] Bunte, D.: Zum Karbonatisierungsbedingten Verlust der Dauerhaftigkeit von Aussenbauteilen aus Stahlbeton, Ph.D.-thesis, Technical University of Braunschweig, 1994.

[8] Chen, L.-Q.: Phase-field models for microstructure evolution. Annual Review of Materials Research 32, pp. 113-140, 2002.

[9] Crank, J.: Free and Moving Boundary Problems. Clarendon, Oxford, 1984.

[10] Emmerich, H.: The Diffuse Interface Approach in Materials Science, Springer, 2003.

[11] Evans, J.D., King, J. R.: On the derivation of heterogeneous reaction kinetics from a homogeneous reaction model. SIAM Journal of Applied Mathematics 60, 6, pp. 1977-1996, 2000.

[12] Geers, M.: Aspects of microstructural evolution. EM lecture notes in micromechanics, TU Eindhoven, 2008.

[13] Kropp, J.: Relations between transport characteristics and durability. In: J. Kropp, H. K., Hilsdorf (Eds.), Performance Criteria for Concrete Durability, RILEM Report 12, E and FN Spon editions, pp. 97-137, 1995.

[14] Mainguy, M., Coussy, O.: Propagation fronts during calcium leaching and chloride penetration In ASCE J. Engineering Mechanics 3, pp. 252-257, 2000.

[15] Meier, S. A.: Two-scale models for reactive transport and evolving microstructure, PhD thesis, University of Bremen, Germany, 2008.

[16] Meier, S. A., Muntean, A.: A two-scale reaction–diffusion system with micro-cell reaction concentrated on a free boundary, Comptes Rendus Mecanique 336, 6, pp. 481-486, 2008.

[17] Meier, S. A., Peter, M. A., Muntean, A., Böhm, M., Kropp, J.: A two-scale approach to concrete carbonation. In: Intl. RILEM Workshop on Integral Service Life Modeling of Concrete Structures, Guimaraes, Portugal, 2007.

[18] Meier, S. A., Peter, M. A., Muntean, A., Böhm, M.: Dynamics of the internal reaction layer arising during carbonation of concrete, Chemical Engineering Science 62, pp. 1125- 1137, 2007.

[19] Muntean, A.: A moving-boundary problem: modeling, analysis and simulation of concrete carbonation, PhD thesis, University of Bremen, Cuvillier, Göttingen, 2006.

[20] Muntean, A.: On the interplay between fast reaction and slow diffusion in the concrete carbonation process: a matched-asymptotics approach, Meccanica, published online, 2008.

[21] Muntean, A., Böhm, M.,, Kropp, J.; Moving carbonation fronts in concrete: a moving-interface approach. Submitted for publication, 2007.

[22] Muntean, A., Böhm, M.: Length scales in the concrete carbonation process and water barrier effect: a matched-asymptotics approach, Berichte aus der Technomathematik, 07-06, 2006.

[23] Muntean, A., Böhm, M., Meier, S. A.: A moving-boundary model with Stefan-Signorini conditions to predict service life of concrete structures. In: Int. RILEM Workshop on Integral Service Life Modeling of Concrete Structures, Guimaraes, Portugal, 2007.

[24] Papadakis, V.G., Vayenas, C. G., Fardis, M. N.; A reaction engineering approach to the problem of concrete carbonation, AIChE Journal 35, 1639-1650, 1989.

[25] Penrose, O, Fife, P.C: Thermodynamically consistent models of phase-field type for the kinetics of phase transitions. In: Physica D 43, pp. 44-62, 1990.

[26] Peter, M. A.: Coupled reaction-diffusion systems and evolving microstructure: mathematical modeling and homogenization, Ph.D.-thesis, University of Bremen, Logos Verlag, 2007.

[27] Peter, M. A., Muntean, A., Meier, S. A., Böhm, M.: Parametric study of the competition of several carbonation reactions in concrete. Submitted for publication, 2007.

[28] Ramachandran, V. S.: Concrete Science. In: V. S. Ramachandran, J.J. Beaudoin (Eds.), Handbook of Analytical Techniques in Concrete Science and Technology, Nyoes Publications, pp. 1-62, 2001.

[29] Schmidt, A., Muntean, A., Böhm, M.: Numerical experiments with self-adaptive finite element simulations in 2D for the carbonation of concrete, Berichte aus der Technomathematik, Report 05-01, University of Bremen, 2005.

[30] Seidman, T., Kalachev, L.: A one-dimensional reaction/diffusion system with fast reaction, Jour nal of Mathematical Analysis and Applications 209, pp. 392-414, 1997.

[31] Sisomphon, K.: Influence of pozzolanic material additions on the development of the alkalinity and the carbonation of composite cement pastes and concretes, PhD thesis, TU Hamburg-Harburg, 2004.

[32] Steffens, A., Dinkler, D., Ahrens, H.: Modelling carbonation for corrosion risk prediction of concrete structures, Cem. Concr. Res. 32, pp. 935-941, 2002.

[33] Taylor, H. F. W.: Cement Chemistry, Thomas Telford, London, 1997.

[34] Thiery, M., Villain, G., Dangla, P., Platret, G.: Investigation of the carbonation front shape on cementitious materials: effects of the chemical kinetics, Cement and Concrete Research 37, pp. 1947-1058, 2007.

[35] Thomas, M. D. A., Matthews, J. D.: Carbonation of fly ash concrete, Magazine of Concrete Research 44, 160, 1992.

[36] Tuutti, K.: Corrosion of steel in concrete, Swedish Cement and Concrete Research Institute (CBI), Stockhom, 1982.

[37] Visintin, A.: Models of Phase Transitions, Birkhäuser, Boston, 1996.

Andreas Nicolai	***Gregor A. Scheffler***	***John Grunewald***	***Rudolf Plagge***
Dr.	*Dipl.-Ing.*	*Prof. Dr.-Ing.*	*Dr.-Ing.*

Institute of Building Climatology, TU Dresden, Germany

Development of a Combined Heat, Moisture, and Salt Transport Model for Unsaturated Porous Building Materials

Summary

This article describes a comprehensive model for the prediction of the coupled heat, air, moisture, and salt transport in porous building materials. First, the state-of-the-art in hygrothermal material modeling and coupled heat and moisture transport models is reviewed. The article then presents and discusses different fundamental model components incorporated into the framework of the transport model, such as the models for salt solution properties, solution transport, and salt phase transitions. Particular focus lies on the salt and moisture interaction related to the salt solution and to phase transitions of hydrate phases, and the description of a consistent calculation algorithm. The capabilities of the model are demonstrated in simulations of laboratory experiments and application cases.

Keywords: *coupled, heat, moisture, salt, transport, porous material, phase transitions*

1 Background and Motivation

Annual damage to valuable building materials and built structures has a significant financial impact worldwide. To a large extent such damage is related to increased content of harmful salts within building materials. Examples of damage caused by salt-related chemical reactions in or with building materials are degradation of road surfaces caused by de-icing salts, erosion of concrete in sewer systems, salt efflorescence on surfaces of buildings, degradation of painted surfaces in historical buildings, and many others. For new structures and materials, but also for restoration and preservation of historical building, predictions of service life in the presence of salt become increasingly important.

Comprehensive and accurate models are prerequisites for reliably predicting the durability of materials and constructions. The transport and phase transition model described in this article was developed with the central motivation to provide the means for understanding the complex interconnected processes. Also, the model and simulation tool should be capable to answer a number of questions from researchers and practitioners, of which some are listed below.

- Why and under which conditions are salts mobilized and transported in the material?
- What conditions do salt phase transitions, crystallization, dissolution, hydration, dehydration and deliquescence depend on and how can they be described in a model?
- What impact has salt on the moisture transport and storage in materials and related hygrothermal problems?
- How do salt mixtures behave in porous materials? What is the impact of salt mixtures on location and frequency of salt phase transitions and related durability concerns?

Questions also arise from the field of restoration and preservation of historical building, monuments, and structures. Particularly, the various preservation measures could be improved with knowledge of the internal processes occurring in salt containing materials as response to a change of conditions or applied desalination actions.

Investigating these questions for the large range of building materials is not feasible. Therefore, the scope of this research was limited to masonry structures, and thus brick and natural stone materials. Also, the primary focus in model development was on accurately describing the coupled transport and phase transition processes inside such materials, and creating a comprehensive simulation tool for analyzing salt related effects.

Developing a model and simulation program, and obtaining the various model parameters in experiments was a complex task that could only be solved in close cooperation with research partners; the Bauhaus University in Weimar, University of Hamburg and Hamburg University of Technology (TUHH). At Bauhaus University Weimar the primary research interest was to investigate salt migration and the interaction of salt and moisture transport [1]. Models and parameterization for describing thermodynamic properties of salt solutions and the solution-crystal interface were derived at the University of Hamburg [2]. At TUHH an experimental investigation of phase transition kinetics along with the development of suitable models for such processes were at the center of the research activity [3].

The different stages in developing an integrated model that encapsulates the research results of the project partners and an accurate hygrothermal material model developed at Dresden University of Technology will be described and discussed in the following sections.

2 Model Development

The work is based on the combined heat, air and moisture transport model by Grunewald [5] and follows the state-of-the-art in modeling combined heat and mass transfer in porous materials. It is a macroscopic approach considering the material as homogeneous medium. Liquid and vapor transport are described separately whereas for the latter vapor diffusion and vapor convection are taken into account as means of transport. The associated enthalpy transported with the phases is included in the energy balance equation, thus enabling the model to capture evaporation cooling and condensation heating effects.

Before discussing the various extensions made to the model to sufficiently incorporate salt transport and phase transitions, a quick review of the moisture transport and storage characteristics will be given. Moisture, being the transport medium for salt, must be accurately described by the model and the relevant equations must be suited for extension to salt.

2.1 Moisture Transport and Storage Model

Regarding the moisture transport, equations (1) and (2) are the constitutive equations for liquid capillary transport and water vapor diffusion respectively. They describe mass flux densities of the liquid phase ℓ and water vapor v.

$$j_{conv,k}^{m_\ell} = -K_\ell \frac{\partial p_\ell}{\partial x_k} \tag{1}$$

$$j_{diff,k}^{m_v} = -\frac{D_v}{R_v T} \frac{\partial p_v}{\partial x_k} \tag{2}$$

It can be noted here, that the driving potentials (gradient of liquid pressure p_l and gradient of vapor pressure p_v) are independent of salt.

On the moisture storage side, the moisture retention curve $\theta_\ell = \theta_\ell \left(p_c \right)$ gives the equilibrium relation between the capillary pressure p_c (moisture potential) and the moisture content θ_ℓ (extensive quantity). The potentials capillary pressure and relative humidity are related through the Kelvin equation (3). This relation essentially describes the effect of the pore system on the water vapor – liquid phase equilibrium of water.

$$\varphi = \exp\left(\frac{p_c}{\rho_w R_w T} \right) \tag{3}$$

A detailed review of moisture transport and storage models, and methods of obtaining suitable parameterization can be found in [6]. The heat and moisture transport model was implemented into the computer code DELPHIN which has been successfully used in a large number of different application scenarios (see [5],[7] for examples).

In the past years we made extensive research efforts to improve the hygrothermal material model and the procedure to obtain material functions suitable for simulations. The focus of this research was primarily on:

- Designing reliable and accurate experimental setups for storage and transport parameter deterimination,
- Improving the material model and its calibration procedure by using data from moisture adsorption and drying experiments, and
- Describing and using hysteretic moisture storage functions to reproduce experimental results.

Scheffler [8] provides a detailed discussion about the listed advances in hygrothermal material modeling. Using the new calibration procedure a set of very accurate moisture transport and storage functions could be defined and adjusted that are a key requirement for any model describing salt transport in porous media. The fundamental heat and moisture transport model was gradually extended to incorporate salt related effects as described below.

2.2 Salt Diffusion in Moisture-Saturated Materials

Salt transport in porous materials can be studied experimentally in a number of different ways, depending on initial and boundary conditions. The least complex are experiments where specimens are saturated with salt solution, because defined initial conditions (moisture and salt distribution) can be easily created. Two typical experiments with moisture-saturated materials are Tracer experiments [9],[10] and diffusion cell [10] or multi-layer diffusion experiments [11]. The latter were investigated extensively at the Bauhaus University Weimar where a salt diffusion model, initially proposed by Buchwald [12], was extended and parameterized.

According to Vogt [11], diffusion of a binary salts in a moisture-saturated medium can be described by equation (4), where the concentration-dependent diffusion coefficient for a free solution D_{sol} is reduced by the tortuosity τ of the medium. The driving potential for salt diffusion is hereby the gradient of the molarity $c_{m,s}$.

$$j_{diff,k}^{m_s} = -\frac{D_{sol}}{\tau}\frac{\partial c_{m,s}}{\partial x_k} \tag{4}$$

Using a similar expression and an additional coupling equation ensuring electro-neutrality of the solution, the diffusion of individual ions in the solution is described in the model (see [9] and [10] for details).

2.3 Salt Diffusion in Unsaturated Porous Materials

For materials in the unsaturated moisture range an additional term needs to be added which describes effects illustrated in Figure 1, which shows the possible salt migration paths for various moisture saturation levels of the porous material.

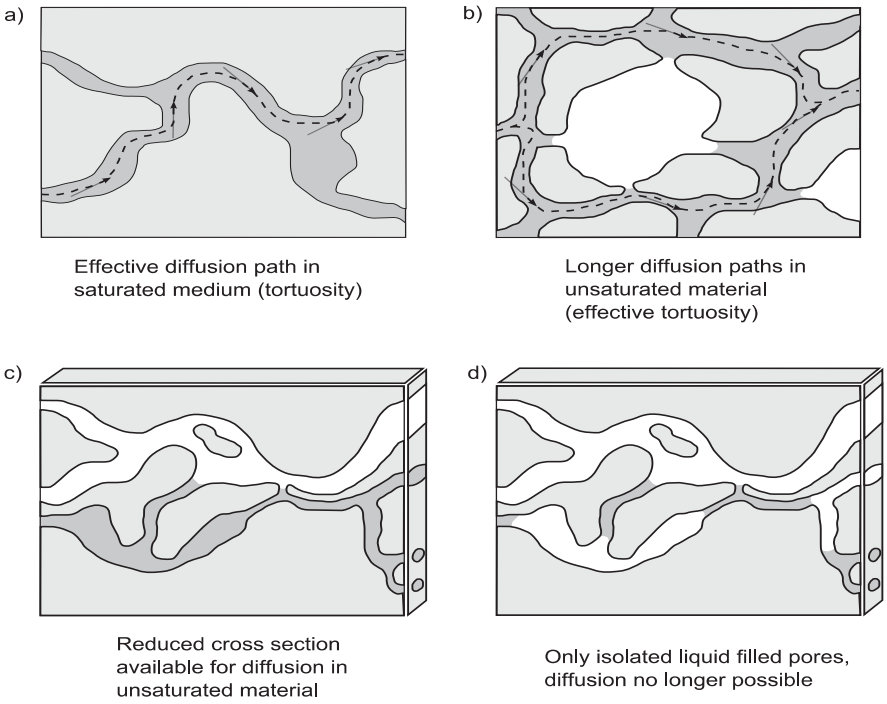

Figure 1: Influence of Moisture Saturation on Salt Diffusion

In the model given by Buchwald and Vogt [11] the effect of the unsaturated porous medium is considered through an additional factor in (5).

$$D_s = \frac{D_{sol}}{\tau}\left(\frac{\theta_\ell}{\theta_{\ell,eff}}\right)^n \tag{5}$$

This factor effectively decreases the diffusion coefficient with decreasing moisture saturation. The moisture exponent *n* is hereby a material dependent fitting parameter. The model of the diffusion coefficient may be enhanced further by adding an Arrhenius term to account for the temperature dependency of the diffusion coefficient [11].

While the tortuosity of the material can be obtained from diffusion cell experiments in moisture-saturated materials [10], the moisture exponent needs to be fitted using simulations of experiments with materials exposed to drying or wetting conditions [13].

2.4 Salt Solution Uptake into Dry Materials

One example of such experiments is the moisture or salt solution uptake experiment. Dry materials are brought in contact with water or salt solution and capillary suction will result in solution/moisture uptake, gravimetrically monitored and plotted in absorption curves.

Depending on the concentration and composition of the salt mixture, the solution properties contact angle, surface tension, viscosity, and density differ substantially from those of pure wa-

ter. Experiments done at the Bauhaus University Weimar showed a notable difference between solution absorption curves and water absorption curves [1]. To capture this effect the model was extended in two ways.

First, a thermodynamic description for the density of salt solutions was incorporated. This Pitzer-based model was derived by Steiger from University of Hamburg, who also generated an accurate parameterization for salt mixtures of the system Na-K-Mg-Ca-NO3-Cl-SO4. The calculation-intensive model was implemented at TU Dresden and TUHH into the high-performance calculation library JADE and incorporated into the transport model. The key advantage of the model is its ability to predict solution densities for salt mixtures of variable composition and wide concentration range including super-saturated solutions, and a large temperature range beginning from sub-zero temperatures.

Secondly, the liquid transport equation (1) was extended by a salt concentration dependent factor $f_{K,\ell}$ that combines the effects of the concentration dependent contact angle, surface tension and viscosity of salt solutions [14].

$$j_{conv,k}^{m_\ell} = -f_{K,\ell} K_\ell \frac{\partial p_\ell}{\partial x_k} \tag{6}$$

With these extensions of the model, the salt solution absorption experiments could be reproduced with satisfactory agreement.

2.5 Influence of Salt on Hygroscopic Moisture Uptake

Salt does not only influence uptake of liquid salt solutions, it also affects the moisture content of materials. The hygroscopicity of salt results in increased uptake of moisture into salt containing materials up to a point, where materials will remain moist and may no longer dry out. This effect can be explained by the reduced equilibrium vapor pressure above salt solutions, expressed by the water activity a_{H2O} for free salt solutions. Inside the porous system this effect becomes combined with the reduction of vapor pressure above a capillary, expressed by the Kelvin equation previously given in (3). The vapor pressure inside the porous system is now influenced by both effects individually, which is expressed in equation (7).

$$\begin{aligned} \varphi &= \exp\left(\frac{p_c}{\rho_w R_w T}\right) a_{H2O} \\ \varphi &= \varphi(\theta_\ell)\ a_{H2O} \end{aligned} \tag{7}$$

The second row in equation (7) shows the same relationship but using the reverse sorption isotherm. Using this formulation, the equilibrium relation between moisture content θ_ℓ and relative humidity φ obtained for the salt-free material can be used, and the effect of the salt is enclosed in the additional factor.

Essentially the equation expresses that above salt solutions with a water activity of less than unity the relative humidity is lowered. In order for the material to remain in equilibrium with its surroundings it must compensate the lowered relative humidity. According to Equation (7) this can only be done by increasing the first factor, which effectively requires higher moisture contents. Until the material has gained enough moisture to compensate the vapor pressure reduction above the salt solution, a vapor pressure difference exists between the material and the ambient which causes vapor diffusion from the environment into the material.

The calculation of the water activity demands a comprehensive model for thermodynamic properties of salt mixtures. Again, a Pitzer-based model was composed, extended and parameterized by Steiger from University of Hamburg [15]. The model does not only provide water activities, but also ion activities, needed for the ion diffusion model, and saturation ratios, required for phase transitions as described below. The model was implemented into the high-performance calculation library JAC [15] and included into the transport model. The parameterization for salt mixtures of the system Na-K-Cl-NO3-SO4 already includes many salts commonly found in building materials.

With the knowledge of the water activity and the corresponding water vapor reduction above the pore solution, the model can now reproduce the observable increased hygroscopic moisture contents of salt containing materials compared to salt free materials.

2.6 Drying Processes and Phase Transitions

In addition to these effects, also drying processes are influenced by salt and effectively slowed down. While equation (7) describes the reduction of drying potential, i.e. the difference in vapor pressure in the material and the environment, sufficiently well, drying processes are significantly more complex. In particular, drying processes involving salt solutions will inevitably lead to salt crystallization and potentially subsequent dehydration phase transitions.

Following the model of Espinosa [18] the phase transitions crystallization and dissolution are considered in the model as kinetic reactions, and hence, are described by kinetic source and sink terms in the balance equations of the different salt phases. Also, phase transitions between solid salt phases, hydration and dehydration, are described as kinetic reactions.

An example shall illustrate the need for modeling phase transitions as kinetic reactions. Consider a salt crystal that is completely submerged in a saturated salt solution. If a pressure was now exerted on the crystal, this would affect the equilibrium between crystal and solution and the crystal would dissolve to evade the stress, even though the solution is saturated. In turn this requires a sufficiently super-saturated solution for the crystal to grow *against* pressure. The super-saturation of the solution becomes essentially an indicator for the damage potential of a crystal, because for higher super-saturations the crystal could grow against higher pressures and exert larger force on the material matrix.

This example also illustrates why quickly changing conditions, like fast drying or cooling, may result in larger stresses and strains. With equilibrium models it is not possible to calculate super-saturated solutions and this effect could not be described or modeled. In general, equilibrium crystallization models are not suitable to distinguish between slow and harmless crystal growth and fast and damaging phase transitions. Therefore, it is important to use a kinetic crystallization model in order to predict durability-related stresses and strains in the material, as it was incorporated in the present model.

$$\sigma_p = K_p \left(U - 1\right)^{g_p} \tag{8}$$

$$\sigma_{sol} = K_{sol} \left(1 - U\right)^{g_{sol}} \tag{9}$$

The equations describing crystallization (8) and dissolution (9) reaction rates require the saturation ratio *U* as driving force for the reaction, whereas the parameters *K* and *g* (with the indices *p* and *sol* for precipitation and dissolution respectively) are fitting parameters obtained in phase transition experiments [11],[19]. Regarding hydration and dehydration processes, a similar formulation is used, however the process direction and rate is hereby only influenced by the water activity (see [17], pp. 69 for a detailed discussion).

With models for phase transitions, salt-dependent moisture storage and transport properties, solution properties, and appropriate parameterization, it is now possible to describe and simulate drying experiments. And, together with wetting processes, the dynamic processes in salt containing porous materials exposed to the climate can be captured and explained.

2.7 Combined Heat, Moisture, and Salt Transport Model

The combination and integration of all previously described models in a consistent and closed-form model was a central research objective at TU Dresden. Based on the original balance equation system for the combined heat and moisture transport, an extended balance equation system for the complete model was developed.

2.7.1 Balance Equations

The system of balance equations consists of an energy conservation equation and several mass balances. Following the state-of-the-art in hygrothermal modeling, the energy balance describes the conservation of internal energy U, but restricted to thermal oscillation and binding energies. Based on the assumption of slow, laminar movement of fluids through the porous medium, the kinetic energy of fluids and other energies of small magnitude are neglected. A balance equation for the moisture mass m_{w+v}, being the sum of liquid water and water vapor, several mass balances for dissolved ions $m_{s,i}$ and several mass balance equations for precipitated salts $m_{p,j}$ are formulated. Mass and energy can change in time due to spatial fluxes de-

noted as j^E and source or sink terms σ^E, wherein E represents one of the previously introduced mass or energy quantities (10).

$$E = \left\{ U, m_{w+v}, m_{s,i}, m_{p,j} \right\} \tag{10}$$

Using a generalized formulation the set of balance equations can be expressed as shown in Equation (11).

$$\frac{\partial \rho^E}{\partial t} = -\frac{\partial}{\partial x_k}\left(j^E_{conv,k} + j^E_{diff,k} \right) + \sigma^E \tag{11}$$

Here, the Einstein summation convention is used, k is hereby the directional index. Other subscripts denote convective and diffusive transport mechanisms. A detailed list of all specific equations with all terms can be found in reference [17].

2.7.2 Calculation Algorithm

Using the quantities in the vector *E* as extensive variables of state, a consistent algorithm must be formulated to calculate intensive state variables, such as temperature, pressures, concentrations, and material functions. In the calculation algorithm depicted in Figure 2, a series of calculations leads to a set of intensive variables and driving potentials that are required for the calculation of the remaining material functions and quantities (see [17] for a description of symbols and an in-depth discussion of the algorithm).

JADE and JAC refer hereby to the previously discussed encapsulated calculation algorithms. The Pitzer-based models are also used for binary solutions, which are modeled slightly different than salt mixtures. The model distinguishes between salt mixtures and binary solutions. In the case of salt mixtures (more than three different ions) it uses one conservation variable for each dissolved ion. In the case of binary solutions only a single conservation variable for the dissolved salt is used. This has mainly an impact on description of diffusive and convective salt transport, however, for the other components of the model the same formulation based on salt mixtures is used.

The algorithm begins with a set of conserved quantities (energy density, total moisture mass density, mass densities of dissolved ions or mass density of dissolved salt, and mass densities of crystalline salt phases).

First, the liquid water mass is estimated from the total moisture mass by neglecting the mass of the vapor component. Now the molalities of the dissolved ions can be calculated, using different equations for whether salt mixtures or a binary solution is modeled.

Depending on the required accuracy, the temperature estimate equation only considers the dry material matrix and the water component of the liquid phase, or in an extended form, also include latent heat of crystallization/dissolution. This is, for instance, necessary to reproduce measurements as done by Espinosa [11],[19], where the rate of crystallization is quantified

through measured differences in temperature between salt-free and salt-containing specimen during crystallization reactions as result of latent heat of the phase transition.

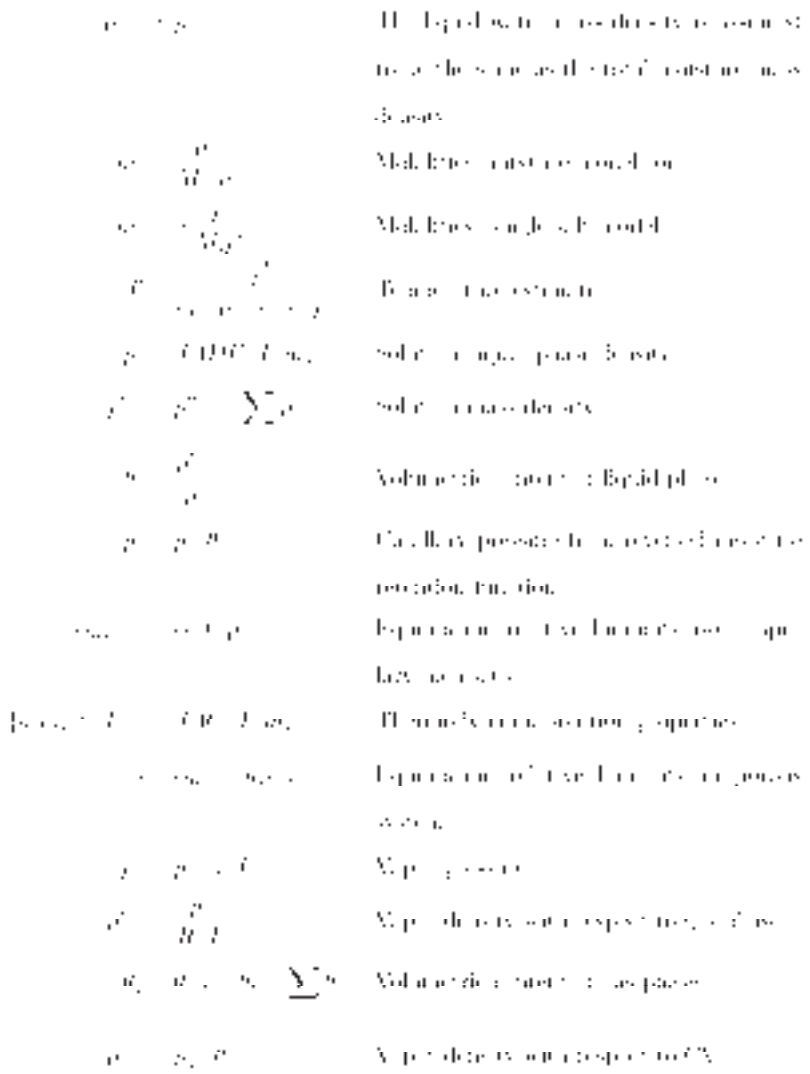

Figure 2: Central Calculation Algorithm (Decomposition of Extensive Quantities)

With temperature and ion molalities the intrinsic density of the solution can be calculated using the JADE model. In the next two steps the solution mass density and the volumetric content of the solution in the porous system is calculated.

The use of the liquid volume fraction is a central and important aspect of this model. It is used in order to arrive at a consistent moisture and salt transport model. Independent of the salt in the solution, the maximum amount of liquid in the porous system is defined by the accessible *pore volume*. Therefore, all material properties and functions must be defined in the range between zero and maximum volume fraction of the liquid phase, whereas the latter corresponds to moisture saturation. Considering that the density of salt solutions can be well above 1000 kg/m³, for example the density of a saturated NaCl solution at 25°C is 1230 kg/m³, material functions

which use gravimetrical quantities are no longer usable, for instance the moisture retention curve in the format w(pc) (moisture mass versus capillary pressure).

In the next calculation step, the reversed moisture retention curve is used to obtain the capillary pressure corresponding to the previously calculated liquid volume fraction. With the Kelvin equation the relative humidity inside the porous medium, yet without salt influence, is calculated.

The remaining thermodynamic solution properties are obtained from the JAC model, which provides the water activity, ion activities and saturation ratios. Now the relative humidity inside the pore space is calculated as result of the combined effect of the pore system and vapor pressure reduction above the pore solution. The remaining calculation steps are required to quantify the vapor pressure and vapor mass density of the gas phase, which in turn could be used to iteratively improve the estimate made in step 1 of the algorithm.

Knowledge of all intensive quantities of the system permits evaluation of all required material functions, such as transport and storage functions. Also, the algorithm provides all driving potentials for liquid flow (the capillary pressure), salt diffusion (molalities) and salt phase transitions (saturation ratios from the JAC model). The calculation of the various transport and source and sink terms of the balance equations is now easily possible.

The described algorithm has the central advantage that by using the liquid volume fraction as primary parameter, material functions obtained for the salt-free material, such as the moisture retention curve, can still be used unmodified in salt calculations because the effect of salt on moisture storage and transport is considered separately.

2.8 Numerical Solution

The presented algorithm uses a sequential calculation scheme. Except for trivial numerical solution schemes, such as the explicit first-order Euler integration method, special calculation methods have to be used. In general, if an efficient solution is required, explicit schemes cannot be used since the system of balance equations contains convection-diffusion equations. However, traditional implicit iteration methods, such as the Picard iteration scheme, will also fail to provide accurate results in reasonable time, particularly when considering two-dimensional problems.

If properly formulated, the class of fast converging implicit Newton-Raphson iteration schemes permits the use of sequential algorithms as presented above, while providing results in reasonable computational time.

For the solution of the model presented here, a numerical solution method of Newton-Raphson type was developed, using a variable-order, variable-step, multi-step integration scheme, which was implemented into the comprehensive simulation program DELPHIN 5 [20]. A detailed discussion of this numerical calculation algorithm for the solution of the tightly coupled system of balance equations can be found in [2].

3 Demonstration of Model Capabilities

The described heat, moisture, and salt transport model includes many coupled effects to describe the complex phenomena occurring in salt-containing materials under climatic loads. A set of example simulations shall demonstrate the capabilities of the model to reproduce and predict processes observed in laboratory experiments.

Several laboratory experiments have been used in the past to investigate the salt migration in porous materials and the salt-moisture interaction. Out of the variety of experiments, the following experiments will be simulated:

- hygroscopic uptake experiment, illustrates hygroscopicity and the phase transitions deliquescence, hydration and dissolution
- drying experiment, illustrates concurrent convection and diffusion of salt, and phase transitions crystallization and dehydration

3.1 Hygroscopic Moisture Uptake

Consider a cubic specimen, initially conditioned at low relative humidity, with initially uniformly distributed salt contents. The specimen is sealed at all but one side and then exposed to step-wise increasing humidity levels. The weight gain is monitored. Each humidity level is maintained until the specimen weight is no longer increasing, thus forming characteristic plateaus. For salt-free materials the plateaus of the curve are expected to match the points in the sorption isotherm.

In salt-containing materials a number of concurrent phase transitions are possible. Depending on the salt, either deliquescence/dissolution or hydration reactions are possible. Once all salt has hydrated to the highest stable hydrate phase of the salt, a further increase of humidity above the deliquescence humidity will result in deliquescence or dissolution of this hydrate phase. Hereby it is difficult to clearly distinguish between deliquescence and dissolution, since inside porous media capillary condensation may already occur well below the deliquescence humidity of a salt. In this case, some crystals may be already in contact with liquid pore solution and dissolve, while others are isolated from the liquid phase, possibly in the larger pores, and can only take up moisture from the gas phase (deliquescence).

Two simulations demonstrate how the model captures the hygroscopic moisture uptake under the influence of salt. Figure 3 shows the results for simulations with different initial contents of crystalline sodium chloride. The ambient relative humidity was increased step-wise in the simulation as shown in the figures. As long as the relative humidity remains below the deliquescence humidity of 75% for NaCl at 20°C, the increase in relative humidity only results in moisture uptake and partial dissolution of the sodium chloride crystals. Regardless of the initial salt content, the process is the same in the first 5 days for each simulation case, and the moisture uptake is only governed by the vapor diffusion and moisture sorption properties of the material. Once the deliquescence humidity has been exceeded, the solution properties determine the process. As

long as enough crystalline salt is present that can dissolve and maintain a saturated solution, the water activity of the solution will correspond to the deliquescence humidity. Therefore, the humidity inside the pores may not increase above this humidity, and vapor diffusion into the material continues until *all* salt is dissolved. The simulation cases with different initial salt contents illustrate this behavior. It has to be noted that in reality not all salt may dissolve, because some fractions of the pore space may not be accessible, or the process may be very slow in some parts of the material. This deviation from the assumed perfectly homogenous and interconnected pore space cannot be described with the current model.

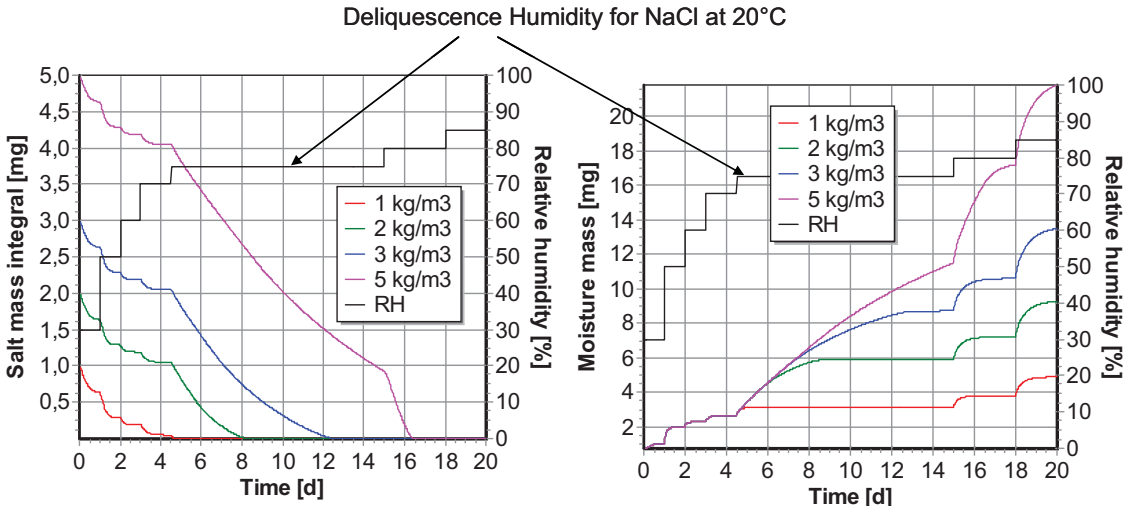

Figure 3: Hygroscopic Moisture Uptake for Different Initial Contents of NaCl (the black line shows the step-wise adjustment of ambient relative humidity)

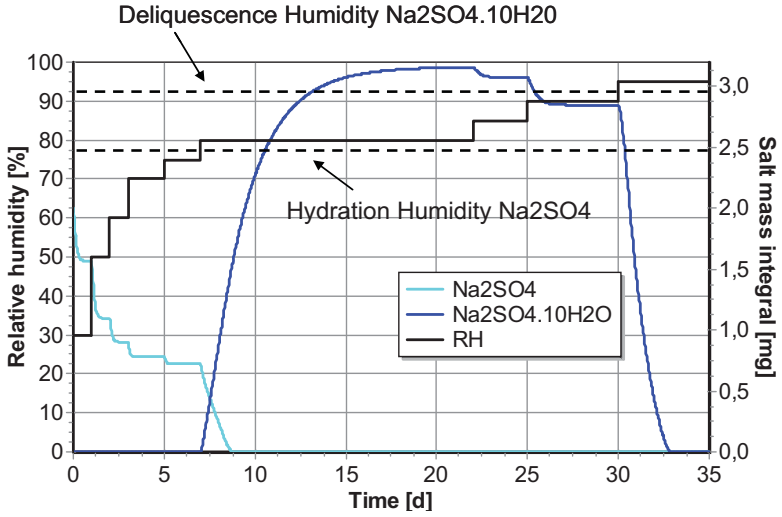

Figure 4: Hygroscopic Moisture Uptake for Na2SO4

In the second simulation case (Figure 4) an initial content of sodium sulfate was assumed and the simulation was done at 23°C. At this temperature, the water free thenardite is only stable below the hydration humidity 79%. Therefore, the simulation was begun at low relative humidity

and in the first few steps a similar process as for the sodium chloride case is observed. However, as soon as the hydration enthalpy is exceeded hydration of the water free salt begins and all thenardite is transformed gradually into mirabilite. This process is a kinetic process and aside from the vapor diffusion and moisture sorption in the material, also the kinetic phase transition parameters used in the simulation determine now the rate of this transition process. During the hydration a significant amount of water is incorporated into the salt crystal, visible in the salt mass integral shown in Figure 4. Once all salt has hydrated into the thermodynamically stable hydrate phase, the process continues as in the first simulation case. Once the deliquescence humidity of Na2SO4.10H2O (94% at 23°C) has been exceeded, all salt dissolves.

3.2 Drying Simulation

Drying experiments with salts have previously been done with emphasis on extension measurements [10]. Here, the transport processes and interactions between moisture and salt shall receive focus. Surface effects, such as efflorescence and related change of transfer coefficients are neglected in the following simulations, as are clogging effects due to crystallization within the material matrix.

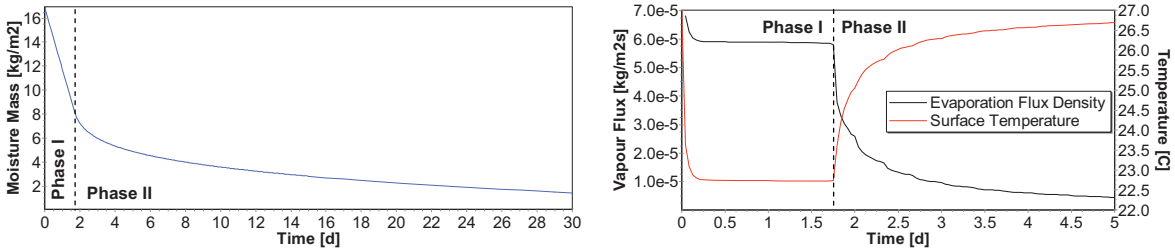

Figure 5: Drying Simulation with Pure Water, Left: Drying Curve, Right: Surface Temperature and Evaporation Flux

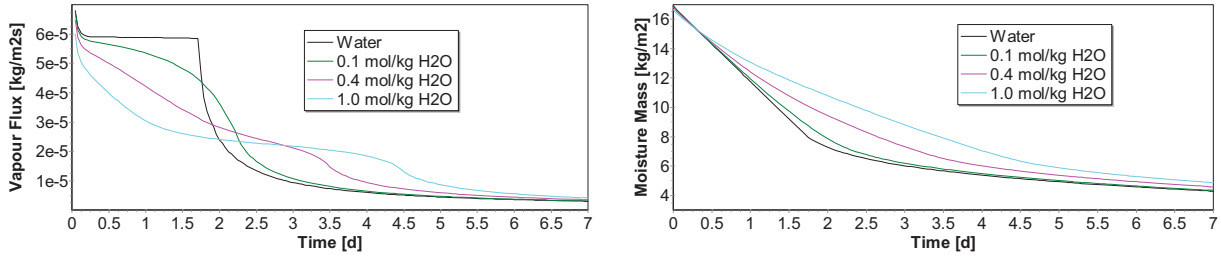

Figure 6: Evaporation Flux (left) and Integral Moisture Masses (right)

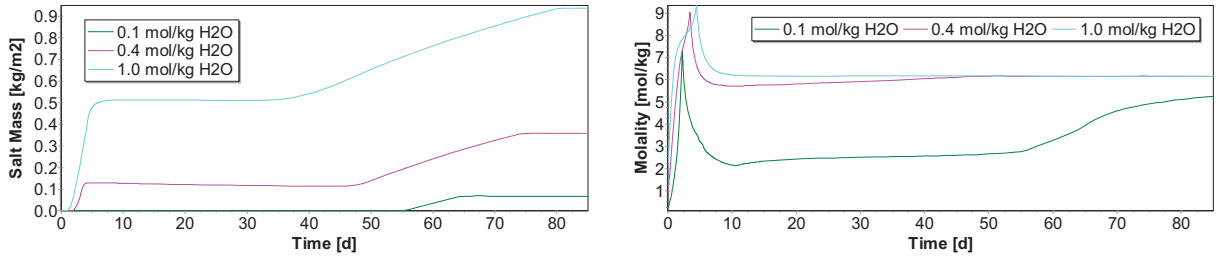

Figure 7: Crystalline Salt Mass Integrals (left) and Solution Concentrations at the Surface (right)

One-dimensional drying experiments are done with specimens saturated with pure water or salt solutions and sealed at all but one side. The specimens are then dried under controlled conditions (constant temperature, relative humidity, air velocity over evaporation side), and the weight loss and surface temperature are monitored. In drying experiments with pure water two distinct phases can be observed. While the drying rate in the first phase is nearly constant, the second phase is a long term process with decreasing drying rate. In the first phase the process is controlled only by transfer conditions at the evaporation surface. Moisture transport from the inside of the moist material to the evaporation side is fast and air movement over the evaporation surface, which is considered in the model through the heat and vapor transfer coefficients, dictates the kinetics of the process. In the second phase the moisture transport to the evaporation side decreases and the drying rate is limited by liquid and vapor transport properties of the material. Figure 5 shows the integral of the moisture mass in the material. The constant rate of drying in the first phase of the experiment is clearly visible in this chart. Figure 6 shows the simulated evaporation flux density and surface temperature. The latter decreases in phase I substantially, as result of the evaporation cooling effect. The simulations were done for a 5 cm brick material (one-dimensional simulations). The material properties and moisture transport and storage characteristics of the brick were obtained by Scheffler [8].

If the same simulation is repeated with specimens initially saturated with salt solution the drying process becomes significantly more complex and the following processes occur simultaneously.

- Salt convection along with the liquid phase from the inside of the material to the evaporation side,
- Increase of solution concentration at the evaporation side,
- Back-diffusion of salt into the material as result of the concentration gradient,
- Reduction of evaporation rate due to reduction of vapor pressure above the increasingly concentrated pore solution at the evaporation side,
- Crystallization of salt near the evaporation surface once the solution is sufficiently super-saturated, and
- Movement of the crystallization zone into the material in the second phase of drying

Figures 6 and 7 show the results of the simulations with NaCl solutions. The simulations were done with different initial concentrations of the salt solution. With increasing solution concentration, the accumulation of salt near the surface in phase I leads to higher surface concentrations. Consequently, the drying rate is reduced because of the vapor pressure reduction. This overall reduction in drying rate is best seen in Figure 6.

The initial solution concentration also results in different maximum solution concentrations near the evaporation surface. The characteristic peak visible in Figure 7 (right) hereby marks the end of drying phase I. In the cases with 0.4 mol/kg H2O and 1 mol/kg H2O initial concentrations, the solution becomes super-saturated already in the first drying phase. In these cases, crystallization occurs in the first phase, followed by a redistribution of salt due to back-diffusion and reduc-

tion of solution concentration near the surface. Later, the remaining pore liquid becomes gradually more saturated and eventually the remaining salt crystallizes inside the material.

4 Conclusions and Outlook

This article discusses a comprehensive model for the coupled heat, moisture, and salt transport including phase transitions in porous media. The described model is applicable for inert masonry materials and constructions, and in particular for bricks and natural stones. Salt transport is considered through convection with the liquid phase and salt diffusion. Thermodynamic properties of salt solutions, for example density, ion activities, and water activity are modeled using a Pitzer-based ion-interaction model. Interactions between salt and moisture transport are considered, including vapor pressure reduction above salt solutions, reduction of mobility of the liquid phase as result of increased viscosity, and salt diffusion depending on moisture saturation. Phase transitions are incorporated into the model using kinetic reactions. Concurrent phase transitions are possible by the use of independent balance equations for the solid phases.

The model is implemented in a highly efficient numerical solver program that permits multi-year simulations of real-life application cases under realistic climatic boundary conditions within few minutes and hours. The ability of the simulation model to predict coupled transport processes has been demonstrated in example cases.

While the model is already applicable to a number of real-life simulation cases, further research work is still needed. In particular, the model needs to be extended to account for pore clogging, the moisture transport model needs to be enhanced with respect to hysteretic behavior and additional moisture-salt interactions. Also, the extension to reactive materials is envisioned. This, however, implies the development of a complex model for the change of moisture transport and storage properties as result of chemical reactions. Aside from model extensions, much experimental work is needed to obtain the required parameters and provide calibration cases for the model. This will help to increase the confidence in the model and help to draw conclusions from model predictions for different applications.

The authors would like to thank the German Research Council (DFG) for the financial support of this project.

5 References

[1] Liebrich Ch., Vogt R., Kriegel R., Kaps Ch., 2008, Modelling of diffusive transport of salt ions in porous, water-containing building materials and capillary transport behaviour of salt solutions, subject to building material, salt type, concentration and fluid content, DFG SPP 1122 Research Report (this volume), ed. L. Franke

[2] Linnow K. & Steiger M., 2008, Modeling the properties of pore solutions in porous building materials, DFG SPP 1122 Research Report (this volume), ed. L. Franke

[3] Espinosa R., Deckelmann G. & Franke L., 2008, Kinetics of phase changes of salts in porous materials: crystallization, hydration and deliquescence, DFG SPP 1122 Research Report (this volume), ed. L. Franke

[4] Nicolai A., Grunewald J. & Fechner H., 2008, An Efficient Numerical Solution Method and Implementation for the Coupled Heat, Moisture, and Salt Transport, DFG SPP 1122 Research Report (this volume), ed. L. Franke

[5] Grunewald J., 1997, Diffusiver und konvektiver Stoff- und En-ergietransport in kapillarporösen Baustoffen, PhD thesis, Dresden University of Technology, Institute of Building Climatology

[6] Grunewald J., Häupl P. & Bomberg, M. 2003, Towards an Engineering Model of Material Characteristics for Input to Ham Transport Simulations - Part 1: An Approach, Journal of Thermal Envelope & Building Science, Vol. 26 No. 4, 343-366

[7] Fechner H., Häupl P, Martin, Neue & Petzold H., 1998, Thermische Sanierung von Fachwerkbauten mittels Innendämmung- ein Vergleich zwischen Messungen und numerischer Simulation, Dresdner Bauklimatische Hefte #2

[8] Scheffler G.A., 2008, Validation of hygrothermal material modelling under consideration of the hysteresis of moisture storage, PhD thesis at Dresden University of Technology, Institute of Building Climatology, Dresden

[9] Plagge R. & Grunewald J., Determination of Solute Transport from Laboratory Tracer Experiments, Proc. Of the 6th Nordic Symposium of Building Physics, Session 12: Hygrothermal Properties of Materials p. 531-538.

[10] Poupeleer A.-S., 2007, Transport and crystallization of dis-solved salts in cracked porous building materials, PhD the-sis at Katholic University of Leuven, ISBN 978-90-5682-797-7

[11] Grunewald J., Deckelmann G., Kaps C., Steiger M., Vogt R., Espinosa R., Nicolai A. & Scheffler G.A., 2005, Mo-dellierung, Software-Implementation and Verifikation des Feuchte- und Salztransportes, der Salzkristallisation und -schädigung in kapillar-porösen Mauerwerksbaustoffen, DFG SPP 1122: Vorhersage des zeitlichen Verlaufs von physikalisch-chemischen Schädigungsprozessen an minera-lischen Werkstoffen, Report Nr. 2

[12] Buchwald A., 2000, Ionentransportprozesse zur Verminderung von Schadsalzgehalten in porösen, feuchten Mauerwerks-baustoffen. PhD thesis at Bauhaus University of Weimar, Shaker Verlag, ISBN 3-8265-8282-9

[13] Buchwald A., 2000, Determination of the Ion Diffusion Coefficient in Moisture and Salt Loaded Masonry Materials by Impedance Spectroscopy, Proceedings of 3rd Int. PhD Symposium, Vienna, Vol 2 (2000) 475-482

[14] Nicolai A., Grunewald J. & Zhang, J.S., 2007, Salztransport und Phasenumwandlung – Modellierung und numerische Lösung im Simulationsprogramm Delphin 5, Bauphysik, #613

[15] Nicolai A. & Grunewald J., 2008, Parametric Study of Salt Transport and Phase Transition Parameters in Simulations of Porous Materials Saturated with Salt Solutions under Drying Conditions, Proceedings of the 8th Symposium for Building Physics in the Nordic Countries, Vol. I, p. 299-306

[16] Nicolai A., Grunewald J. & Zhang J.S., 2007, Salt transport and phase transitions, modeling and numerical solution in the simulation code Delphin 5 / CHAMPS-BES, Proceedings for the 12th Symposium for Building Physics, Dresden, Germany

[17] Nicolai A., 2007, Modeling and Numerical Simulation of Salt Transport and Phase Transitions in Unsaturated Porous Building Materials, PhD thesis, Syracuse University

[18] Steiger M., Kiekbusch J. & Nicolai A., 2007, An improved model incorporating Pitzer's equations for calculation of thermodynamic properties of pore solutions implemented into an efficient program code ,Construction and Building Materials, 22 (2008) 1841–1850

[19] Espinosa R., Franke L. & Deckelmann G., 2007, Phase changes of salts in porous materials: Crystallization, hydration and deliquescence, Construction and Building Materials, 22 (2008) 1758-1773

[20] Nicolai A., 2008, Delphin 5 Simulation Software, Webpage: http://www.bauklimatik-dresden.de/delphin

Andreas Nicolai *Dr.*
Gregor A. Scheffler *Dipl.-Ing.*
John Grunewald *Prof. Dr.-Ing.*
Rudolf Plagge *Dr.-Ing.*

Institute of Building Climatology, TU Dresden, Germany

An Efficient Numerical Solution Method and Implementation for Coupled Heat, Moisture, and Salt Transport: The DELPHIN Simulation Program

Summary

This article introduces a highly-efficient numerical solution method for the combined heat, moisture and salt transport in porous media, that permits parameter variation and sensitivity studies in short time. The general solution strategy for this type of coupled partial differential convection-diffusion equations with source terms is presented, including an overview of the Newton-Raphson iteration scheme. Various improvements of the numerical method, such as the value extrapolation and modified Newton method that lead to a robust, accurate and fast solver implementation are discussed in detail. Performance comparisons are shown for different simulation cases, and the capabilities and numerical efficiency of the DELPHIN simulation program are illustrated with a 2D simulation example.

Keywords: *numerical solution, coupled heat and moisture transport, porous material, performance, simulation, salt transport*

1 Introduction

The complexity of simulation models for the coupled energy and mass transport in porous media has significantly increased in the past years [1],[2]. The development of such models is mainly motivated through the large number of combinations for material properties, climatic scenarios (which structures are exposed to), and possible salts and salt mixtures in varying distributions and amounts. Classical laboratory testing methods can only be applied to a limited subset of these combinations. Consequently, models are being developed and continuously improved to allow predictions and analyses for structures, materials, and conditions that have not been tested previously.

With respect to salt, the new models allow investigation of the influence of different initial salt distributions, concentrations and mixture compositions, and can provide predictions about the influence of ambient climate on salt migration and phase transitions. In order to capture many different effects, the models have been continuously improved and extended. In the research

field dealing with coupled transport of heat, moisture and salt in porous media, the models have recently reached a complexity that requires significant computational efforts.

Efficient numerical solution methods are required in order to use the new models in research and engineering applications. At first, salt transport models are typically applied for long-term simulations which are necessary to obtain predictions for the behavior of materials and structures over the course of several years. Furthermore, several simulation runs are required for different initial conditions, climates, materials, and salt mixtures to evaluate the influence of the numerous parameters. Particularly when investigating construction details in 2D simulations, computational costs can be significant. It is therefore desirable to use a solution method that provides simulation results quickly.

The use of realistic climate, including short and long wave radiation, and driving rain, can lead to strong variations and gradients to the solution. In conjunction with equations containing convective transport terms, such as they are found in the salt balance equations, special care has to be taken to obtain an accurate solution and to prevent numerical instability or large approximation errors.

The aforementioned demands on the solution method can be summarized in a list of important desirable properties:

- Fast calculation performance,
- Defined and controlled accuracy,
- Applicable to a range of problems, and usable with different material parameters, climatic data, different geometries,
- Reasonable effort to develop, test and extend the model and program code.

In this article a numerical method will be presented that was successfully applied to solve the system of non-linear coupled partial differential equations that describe the combined heat, moisture and salt transport, accurately and very efficiently.

2 Discussion of the Numerical Method

The core of the HAM+SP model (Heat, Air, Moisture, and Salt transport and Phase transitions) is a set of balance equations, complemented by several transport and phase transition equations, see [1] for details. They are briefly reviewed as follows.

2.1 Governing Equations

Leaving the air flow calculation out of the scope, the quantities to balance are the internal Energy U, the total moisture mass m_{w+v} (as the sum of liquid water and water vapor), the mass balances for all dissolved ions $m_{s,i}$, or the single mass balance for the dissolved salt m_s if the

binary solution model is used. Finally mass balances are needed for the masses $m_{p,j}$ of all crystalline salt phases. These quantities can be summarized in the vector E, according to Eq. (1)

$$E = \left\{ U, m_{w+v}, m_{s,i}, m_{p,j} \right\} \tag{1}$$

For each conserved quantity a generic balance equation can be given, in the general form of Eq. (2), where the index k is used to indicate the actual transport direction.

$$\frac{\partial \rho^E}{\partial t} = -\frac{\partial}{\partial x_k}\left(j^E_{conv,k} + j^E_{diff,k} \right) + \sigma^E \tag{2}$$

The equations are conservation equations for the quantity densities to arrive at a volume-independent formulation. As shown in Eq. (2), the quantity of a substance can change due to convective transport $j^E_{conv,k}$, diffusion $j^E_{diff,k}$ or sources and sinks, which can also be coupling terms between equations. This will be illustrated briefly using the mass balances of crystalline and dissolved salt.

Consider the specific mass balance equation for a dissolved salt (binary solution model) given in Equation (3).

$$\frac{\partial \rho^{m_s}}{\partial t} = -\frac{\partial}{\partial x_k}\left(-c_s K_{\ell,s} \frac{\partial p_\ell}{\partial x_k} - M_s D_s \frac{\partial c_m}{\partial x_k} \right) - M_s \sum_j \nu_j \frac{\sigma^{m_{p,j}}}{M_{p,j}} \tag{3}$$

The left-hand-side of the equation describes the change of dissolved salt mass. On the right-hand-side of Equation (3) we have the convection term

$$j^{m_s}_{conv,k} = -c_s K_{\ell,s} \frac{\partial p_\ell}{\partial x_k}$$

given as mass flux of the liquid phase multiplied with the mass fraction of the dissolved salt with respect to the liquid phase $c_s = m_s / m_\ell$. Secondly, we have the mass diffusion flux:

$$j^{m_s}_{diff,k} = -M_s D_s \frac{\partial c_m}{\partial x_k}$$

Salt diffusion is driven by a gradient of salt concentration (in this case gradient of molarity c_m). Finally, we have the source/sink term in the equation that summarizes the gain or loss of dissolved salt mass as result of phase transitions:

$$\sigma^{m_s} = -M_s \sum_j \nu_j \frac{\sigma^{m_{p,j}}}{M_{p,j}}$$

The source term contains a sum over all solid species that are considered. The stoichiometric factors ν_j are used to relate the molar change rates of the solid species to the molar change rate of the dissolved salt. The summation over all solid phases j is necessary, for instance,

when we want to describe Na2SO4(aq) with its two possible solid phases Na2SO4 and Na2SO4.10H2O. Here, both solid phases could concurrently crystallize, dissolve, or undergo other phase transitions. The respective mass change rates $\sigma^{m_{p,j}}$ of the solid salts is reflected in the mass balance of the dissolved salt through the source term σ^{m_s}, which is the aforementioned coupling term.

A detailed description of all symbols used in the equations above can be found in reference [2]. Equation (3) already indicates that a numerical solution of these coupled equations may require special care, since convection and source terms are included. A suitable numerical method is presented in the following sections.

2.2 Solution Strategy for the System of PDE

The system of partial differential equations (PDE) to be solved is highly non-linear. In addition, all equations are strongly coupled with each other. Almost all transport and phase transition terms for a conserved quantity depend directly or indirectly on the quantity itself and other balanced quantities. Also, the transport coefficients are functions of one or more conserved quantities or related intrinsic properties. For example, the liquid conductivity is a function of the moisture content and may vary over 10 orders (!) of magnitude. A similar non-linearity is found in the moisture retention function, which describes the relation between the moisture content and the capillary pressures.

Analytical solutions for this set of PDE cannot be given. Several choices exist for the numerical methods. However, to obtain the desired solver performance, a form of a Newton-iteration is required, because:

1. Explicit solution schemes are not suitable. Both, the convective terms in the dissolved salt mass and the energy balance equations, and the source terms impose limitations on the time step to be used to avoid numerical instabilities. Such time step constraints are hard to quantify and generally lead to extremely poor performance.
2. For implicit schemes, an iteration method needs to be used. Partly because of the non-linearities, but mostly because of different time scales for the evolution of energy and masses, the system of equations is stiff. Traditional methods such as the Picard scheme converge very slowly when used for stiff systems.

For completeness, the derivation of a Newton-Raphson scheme for the system of equations (2) is sketched out below.

2.3 Newton-Raphson Iteration Scheme

The system of equations (2) can be rearranged to Eq. (4),

$$G(y) = 0 = \left\{ \frac{\partial \rho^E}{\partial t} + \frac{\partial}{\partial x_k} \left(j^E_{conv,k} + j^E_{diff,k} \right) - \sigma^E \right. \tag{4}$$

and be written more formally as $G(y) = 0$, where G is the vector of equations and y is the vector of unknowns. In this case y corresponds to the densities of the conserved quantities. Note that the right-hand-side of equation (4) actually contains as many partial differential equations as in the vector E, see Eq. (1). After spatial discretization of the equations (4) using the control volume technique, the vector y holds the whole set of conservative variables multiplied with the number of elements.

The non-linear system of ODE, written as $G(y) = 0$, can be solved with a standard Newton-Raphson algorithm, shown in equation (5).

$$\left.\frac{\partial G}{\partial y}\right|_m \Delta y^{m+1} = -G\left(y\right)^m \tag{5}$$

Here, m and $m+1$ indicate iteration levels. Since it is an implicit scheme, the iteration levels are defined at the yet-unknown time level $n+1$, with n being the most recently known solution to the system of ODE. However, just applying a standard algorithm will not lead to a robust and efficient solver implementation. Some specific modifications and improvements are necessary to achieve the initially set objectives.

2.4 Specific Method Improvements

In order to improve the standard solution and obtain a suitable algorithm for the coupled HAM+SP model, all parts of the numerical method where investigated and improved. The principle integration and time stepping scheme is illustrated in Figure 1.

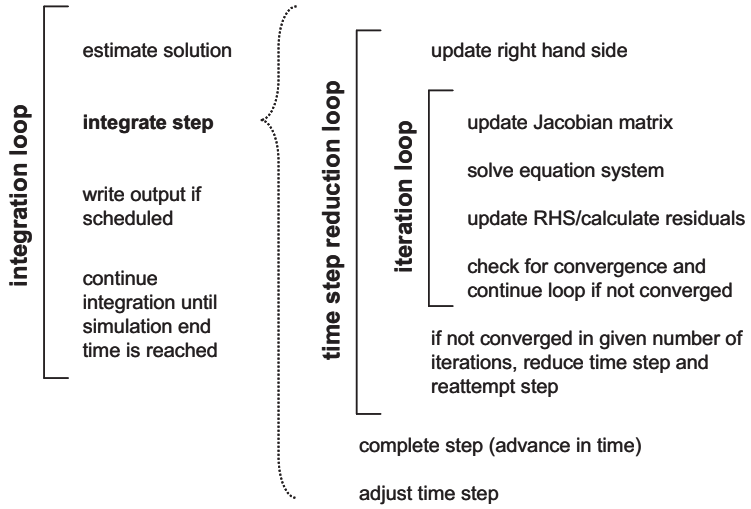

Figure 1: Integration and Time Stepping Scheme

Among the many tasks involved in the scheme, the following were investigated and fine-tuned in order to achieve better performance.

- The estimation of the solution at next time step,
- Number of Jacobian evaluations and factorizations, and the
- The time step adjustment strategy.

2.4.1 Estimation of the Solution at Next Time Step

As shown in Figure 1, each integration step begins with an evaluation of the right hand side function *G(y)*. Hereby, the initial guess $y^{n+1,(m=0)}$ for the new solution at time level n+1 is needed. It is possible to assume that the previously calculated values will remain constant (no change of solution = steady-state) and therefore set $y^{n+1,(0)} = y^n$. However, mostly the transient processes are of interest and it is more feasible to assume a changing solution. If the solution changes smoothly, linearly extrapolated values may yield a solution much closer to the final, iterated results. Equation (6) is used to obtain the extrapolated initial estimate of the solution at the next time level $n+1$. It uses the current time step Δt_n and the time step used in the previous integration step Δt_{n-1} as well as the respective solutions.

$$y^{n+1,(0)} = y^n + \left(y^n - y^{n-1}\right)\frac{\Delta t_n}{\Delta t_{n-1}} \tag{6}$$

2.4.2 Modified Newton-Raphson Algorithm

Particularly for 2D simulations, the most time consuming part of the numerical method is the solution of the equation system (5) for the unknown Δy^{m+1}. To solve the equation system, first a LU-factorization (lower-upper triangular matrix decomposition) of the Jacobian matrix is done followed by a back-solving step.

The modified Newton-Raphson algorithm makes use of the fact, that the Jacobian matrix $\partial G / \partial y$ does little change near convergence. In order to improve the performance, the LU-factorization is only done in the first iterations. Afterwards, only back-solving is used to iterate the solution further. However, it is generally difficult to determine the number of complete Newton iterations before stopping the LU factorizations.

A meaningful way to determine this iteration level is to use the residuals of the rearranged balance equations (4). It was found, that the best results could be obtained, when the residuals *G(y)* of the balance equations were monitored and the Jacobian matrix updates were stopped, once the residuals were small enough. This method can be formalized by Eg. (7) using the max norm of the vector of residuals $\max_i \left|G_i\right|$.

$$\max_i \left|G_i\right| < \varepsilon \tag{7}$$

This essentially requires that the Jacobian matrix is updated until the residuals in *all* control volumes become smaller than the limit ε. For the remaining iterations the last factorized Jacobian matrix is used unchanged and only the relatively inexpensive back-solving algorithm is needed.

2.4.3 Dynamic Time Step Adjustment Strategy

Many application cases for the combined heat, moisture, and salt transport simulation require the use of realistic climatic conditions, including weathering due to driving rain, and quickly changing ambient temperature and relative humidity. Rapidly changing surface conditions can lead to steep gradients in the solution. In order to solve the equations correctly, the time step sizes have to be reduced quickly. Once redistribution and smooth processes dominate the numerical solution, the time steps can be gradually enlarged again.

The new time step can be calculated based on the number of iterations needed for the last step. A small number of iterations results in growing of the time step, a large number results in a smaller time step. In Equation (8) i indicates the number of iterations, whereas $i_{\max}$ indicates the maximum number of allowed iterations.

$$\Delta t_{new} = \left(1.5 - \frac{i}{i_{\max}}\right) \Delta t_{old} \tag{8}$$

If the number of allowed iterations is exceeded or the solution diverges, the time step is halved. With this dynamic time step adjustment strategy, the solver can quickly react to changing gradients. An example of the course of the changing time step over the course of the simulation is given in Figure 2. The ability of the solver to quickly reduce the time steps when demanded by accuracy and convergence criteria and increase them again afterwards is the key to good overall performance.

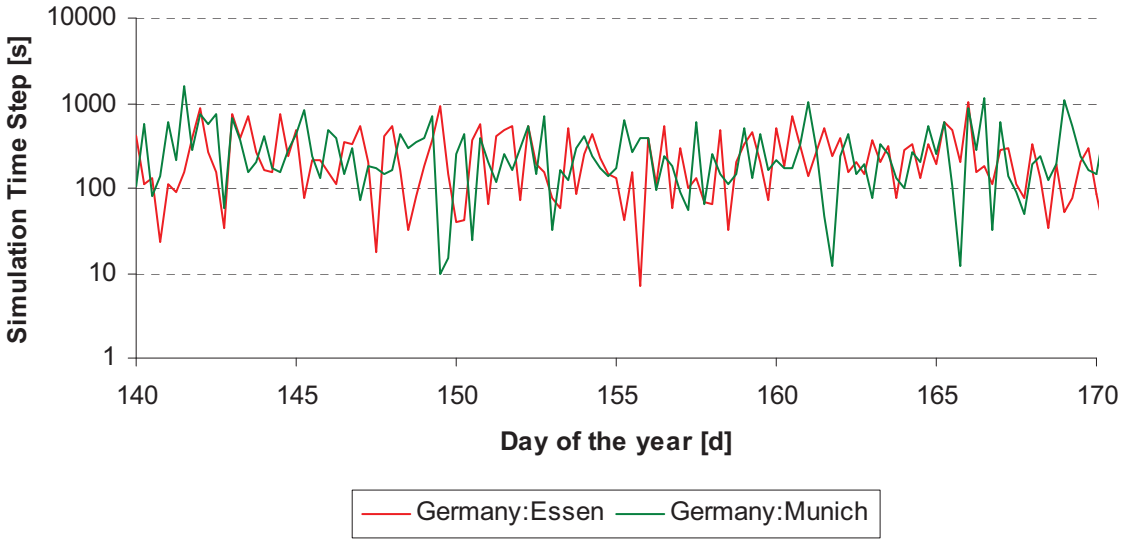

Figure 2: Dynamically Adjusted Time Steps for Different Boundary Condition Scenarios

The consideration of output time points is related to the time step adjustment strategy. The optimal performance can be expected if the solver were allowed to select the time step without the need to match output time points. This can be accomplished by allowing the solver to over-step an output time point and interpolate the solution variables at the requested output time. Details of this procedure can be found in reference [2], pp. 106.

2.5 Overall Effect of Improvements on Solver Performance

The combination of the various solver improvements results in a much more efficient solution method. The following steps of improvements are tested:

I standard implementation
II I + linear extrapolation
III II + output interpolation (no time step restraints)
IV III + modified Newton-Raphson method

Table 1 shows the simulation statistics obtained for a benchmark case with strong variations in boundary conditions. The 1D simulation scenario emulates a weathered brick wall exposed to driving rain and solar radiation.

Table 1: Solver Statistics for the Improved Implementations

Method	RHS evaluations		Jacobian evaluations		Simulation Time [s]	
I	100007	100.0%	95998	100.00%	48.4	100.0%
II	48217	48.2%	44862	46.70%	25.0	51.5%
III	9929	9.9%	8154	8.50%	8.5	17.5%
IV	9742	9.7%	1459	1.50%	6.9	14.2%

Of course, the statistics in Table 1 may vary significantly depending on the grid, the number of elements, the material functions, the boundary conditions, and other model and simulation parameters. However, it is apparent that the combination of the different improvements can lead to dramatically reduced number of iterations and thus calculation time. Also, the number of required Jacobian matrix compositions can be greatly reduced. This is particularly important for 2D simulations, since the computation time spend in the LU factorization of the Jacobian matrix typically amounts to about 70% of the total computational costs in 2D simulations.

2.6 The CVODE Integrator and the DELPHIN Simulation Program

The performance investigation and implementation tests of the various solver improvements were first done using a heat and moisture transport solver alone. After the initial analysis using two different implementations, one with a first-order Euler backward difference equation, and the other using the CVODE integrator, the latter code was selected for extension to salt. The CVODE integrator [3] is an implementation of a variable-order, variable-step, multi-step method (BDE formulation), which also includes the improvements mentioned above. The main reason

for the decision to use CVODE as core solver component was the estimated effort to implement, test, and debug the complex salt transport simulation code. In the case of the first solver implementation, the effort was evaluated as much higher.

The DELPHIN simulation program in its 5th version was created using this solver component (see [2], chapter 4 for details). However, despite the high performance achieved for purely heat, air, and moisture transport problems, the observed performance for salt simulations (HAM+SP) was much lower. This could be attributed to two difficulties:

1. The size of the equation system increases with each additional balance equation significantly,
2. Crystallization and dissolution reactions may cause weak discontinuities which result in poor convergence and small time steps.

Particularly the second problem needed to be addressed.

2.6.1 Treatment of Discontinuities Resulting from Phase Transitions

The weak discontinuity in the solution stems from the source term related to dissolution reactions of solid salts. In the HAM+SP model, the dissolution rates are calculated according to Espinosa et al. [4]. The saturation ratio required for this calculation is determined from water and ion activities, calculated with the Pitzer model and parametrization by Steiger et al. [5]. Once the solution becomes sub-saturated, salt crystals can dissolve. Hereby, the kinetic dissolution rate depends only on the sub-saturation of the solution and not on the amount of available crystalline salt. In the moment that the complete amount of crystalline salt has dissolved, the phase transition rate suddenly drops to zero. This jump corresponds to a discontinuity in the first derivative of the salt mass balances and, if a hydrate phase is involved, also in the derivative of the water mass balance. If simulations with realistic boundary conditions, for instance for weathering applications, are done, such crystallization and complete dissolution processes can occur very frequently in some parts of the simulation domain. The result of these accumulated discontinuities is very poor calculation speed.

To avoid these discontinuities a special ramping function was introduced, that gradually reduces the phase transition rate once the amount of salt becomes very small. The threshold is hereby selected such that the results will only marginally be affected, but a large gain in performance is achieved.

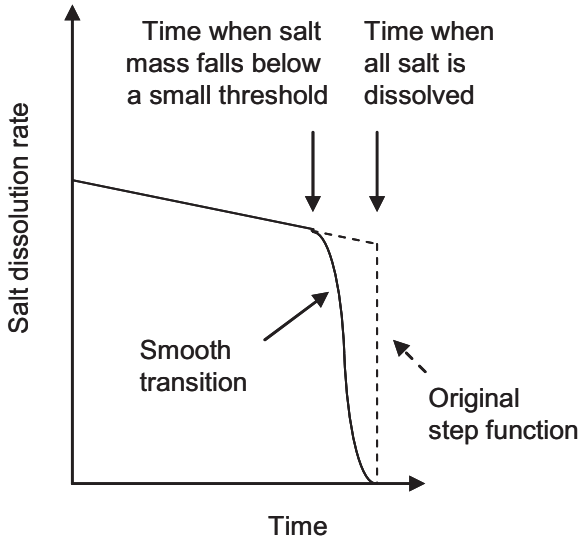

Figure 3: Dynamically Adjusted Time Steps for Different Boundary Condition Scenarios

The ramping function for this case is given in Equation (9).

$$f\left(\frac{\rho^{m_p}}{\rho^{m_p}_{\lim}}\right) = 0.5\left(1-\cos\pi\frac{\rho^{m_p}}{\rho^{m_p}_{\lim}}\right) \qquad \text{with} \qquad \rho^{m_p} \le \rho^{m_p}_{\lim} \tag{9}$$

The function value is multiplied with the calculated phase transition rate. This phase transition rate is reduced once the available salt mass density ρ^{m_p} falls below the threshold, of the salt mass density, taken as $\rho^{m_p}_{\lim} = 10^{-4}\ \mathrm{kg/m^3}$.

Several other improvements were included in the combined heat, moisture, and salt transport program DELPHIN (see [2], chapter 5) in order to reduce the simulation time further.

Table 2 shows simulation times of example simulations done with the final simulation program and different salts. In this benchmark a brick wall is exposed to realistic climatic conditions including driving rain, short and long wave radiation, relative humidity and temperature. The first case shown is the pure heat and moisture transport simulation with a very fast simulation speed of about 150 hours per second (Intel Core 2, 2.67 GHz). For the second case, the number of balance equations (BE) increases to 4: energy, moisture mass, dissolved salt mass, crystalline salt mass. This, in addition to the increased computational effort needed to calculate the solution properties, results in the observed reduction of computation speed. Figure 4 illustrates that the weathering of the construction results in frequent phase transitions. Depending on the rain penetration depths, in some sections of the material the salt dissolves completely and crystallizes again. The ability of the solver to capture these effects is an important feature that can provide criteria for damage and durability assessment.

Table 2: Solver Statistics for 5-Year Simulations (1D)

Model	Solid Salts	BE	Sim. Time [min]	Speed [h/s]	Iterations	Iter-Speed [1/s]
HM	-	2	4.9	149	4551639	15482
HMS	NaCl	4	17.8	41	2608630	2443
HMS*	NaCl	4	225.7	3	17759913	1311
HMS	Na2SO4, Na2SO4.10H2O	5	39.1	19	2412242	1028

The third case HMS* is the same problem as for case 2, but simulated with a standard solver implementation that had not been optimized yet (only first order, no discontinuity treatment). The optimized solver variant in case 2 runs more than 12 times faster!

In the last benchmark case with sodium sulfate that also includes hydration and dehydration reactions between thernardite and mirabilite, the calculation time increases further compared to case 2. However, the improvements in the solver still allow simulation with sufficient computational speed. If the non-optimized solver variant is used for the last case, the frequent phase transitions (see Figure 4) result in excessive simulation times of several days that are no longer acceptable.

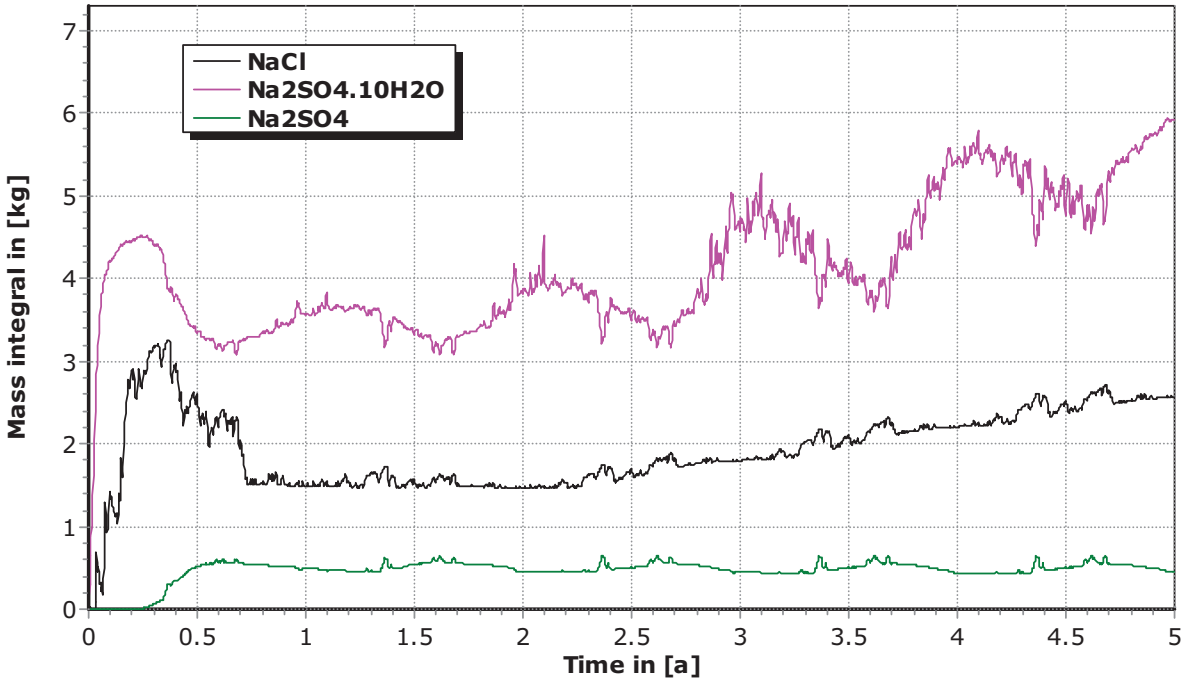

Figure 4: Integral Salt Masses in the Construction for the Simulation Cases 2 and 4.

3 Application of the DELPHIN Simulation Program for 2D Problems

A main concern in developing the DELPHIN simulation program was to achieve sufficient performance for 2D simulation cases. Such simulations are required for a number of applications, for instance for evaluating the effectiveness of desalination procedures in brick walls, investi-

gate corner effects, and in general for all application cases where the initial salt distribution is not uniformly distributed in all but one direction.

The simulation case shown below represents a weathered brick wall where salt originates from the mortar and is migrating through bricks and mortar to the surfaces of the construction. Figure 5 shows the model in the DELPHIN user interface.

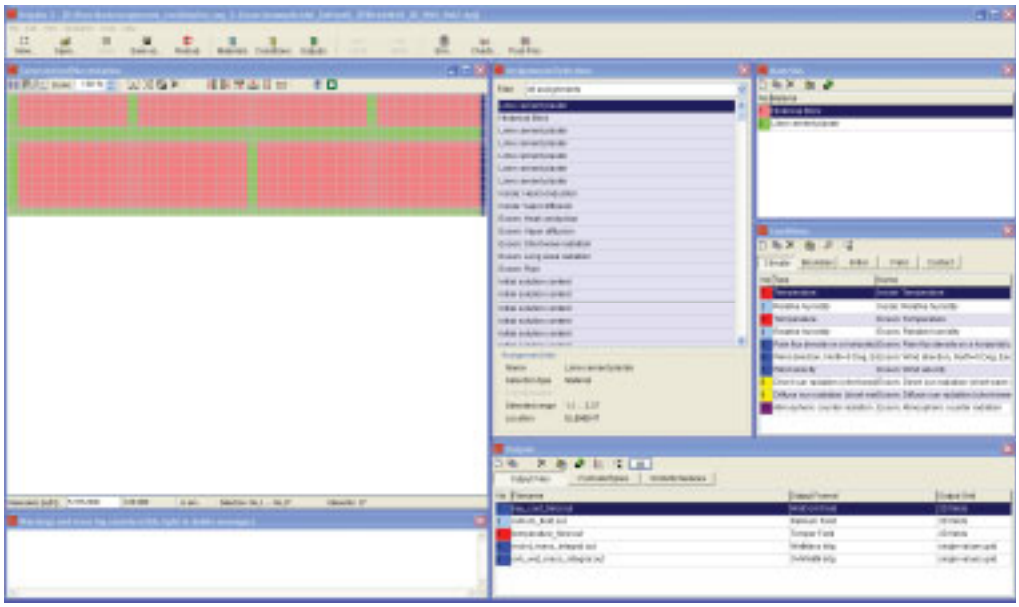

Figure 5: User Interface of the DELPHIN Software with 2D Brick Wall Model

The primary use of the interface of the DELPHIN program is the input of the large number of simulation parameters with the necessary error checking regarding initial and boundary conditions, material and salt properties, and simulation model options.

The simulation results in Figure 6 a-f are shown as example for the coupled processes described with the model. The fields shown were obtained for one point in time during the weathering of the construction.

Figure 6a shows the moisture content field after some driving rain events and several days of drying. The moisture contents near the external surface (right side) is lower than further inside of the construction, indicating the drying process taking place directly at the surface.

The drying process results in super-saturation of the solution near the surface (see Figure 6b), that correlates with the water activity (Figure 6c) and molality (Figure 6d) of the solution.

The actual distribution of the salt in the construction is visible from Figures 6e and 6f, where the masses of the dissolved salt and the crystalline salt are shown. In Figure 6f most crystalline salt is found near the inside of the construction. The driving rain from the outside will dissolve and mobilize the salt near the external surface and gradually with increasing number of driving rain events and progressing moisture front into the construction, also the salt near the middle and inside of the construction will be dissolved and transported.

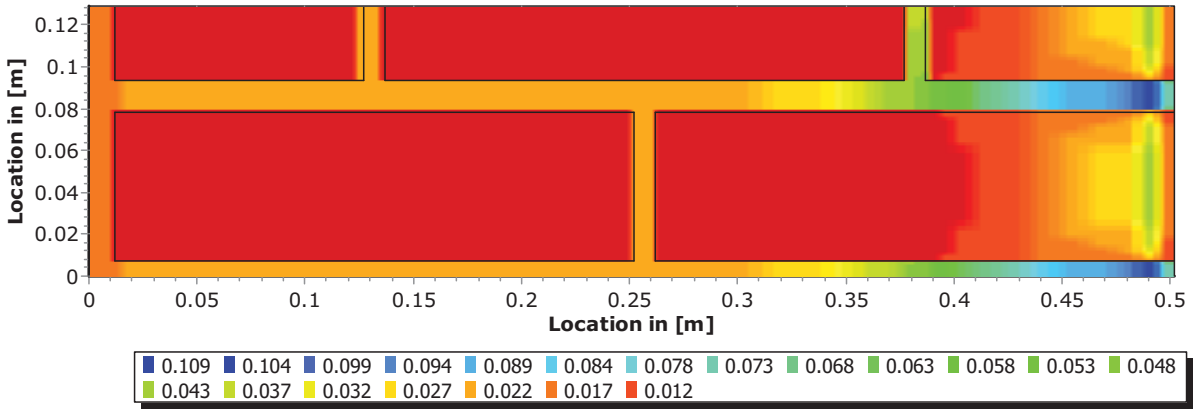

Figure 6 a: Liquid Moisture Content [m3/m3]

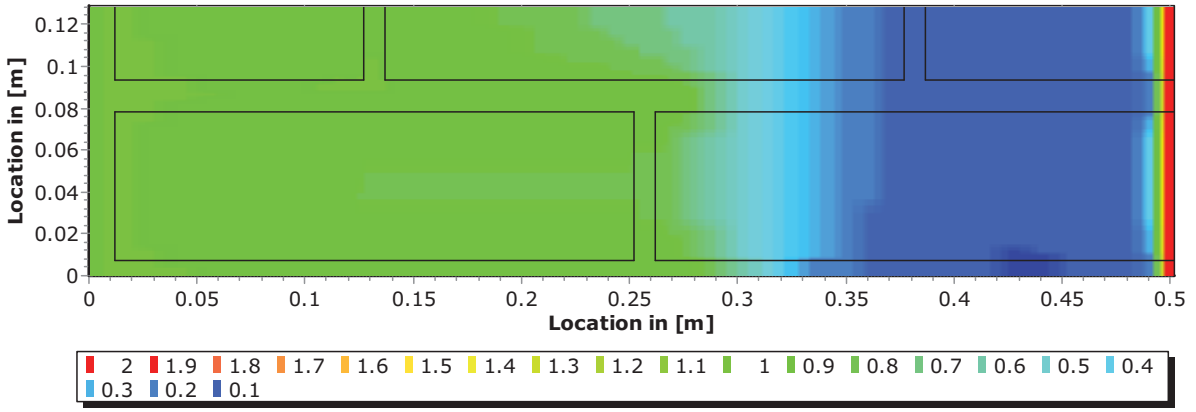

Figure 6 b: Saturation Ratio [-]

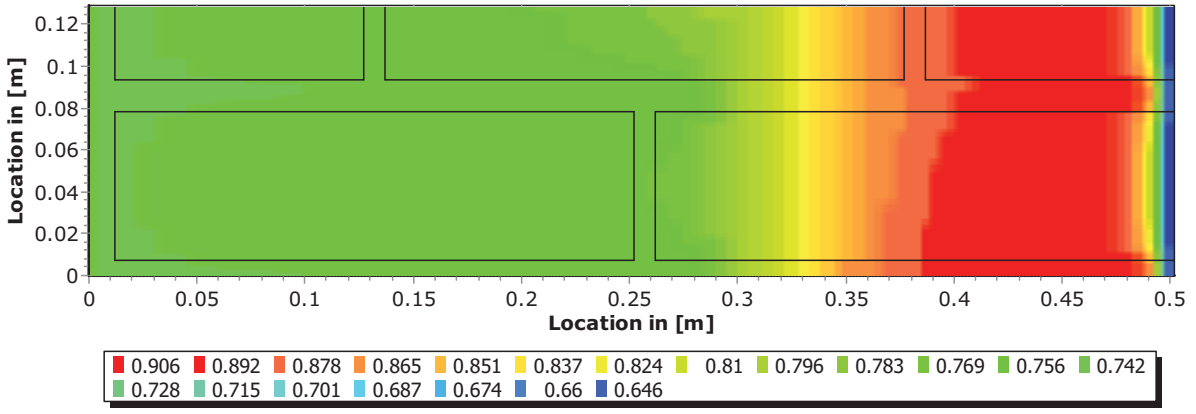

Figure 6 c: Water Activity [-]

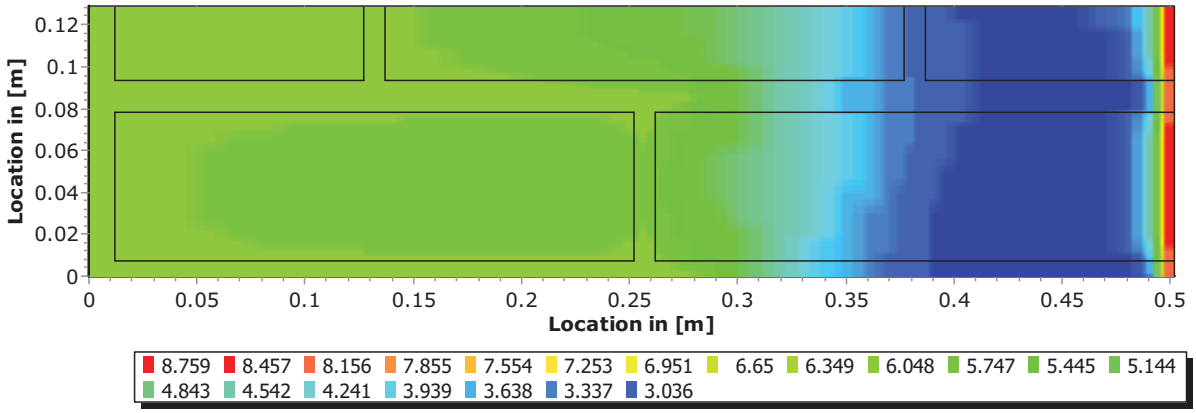

Figure 6 d: Molality [mol/kg]

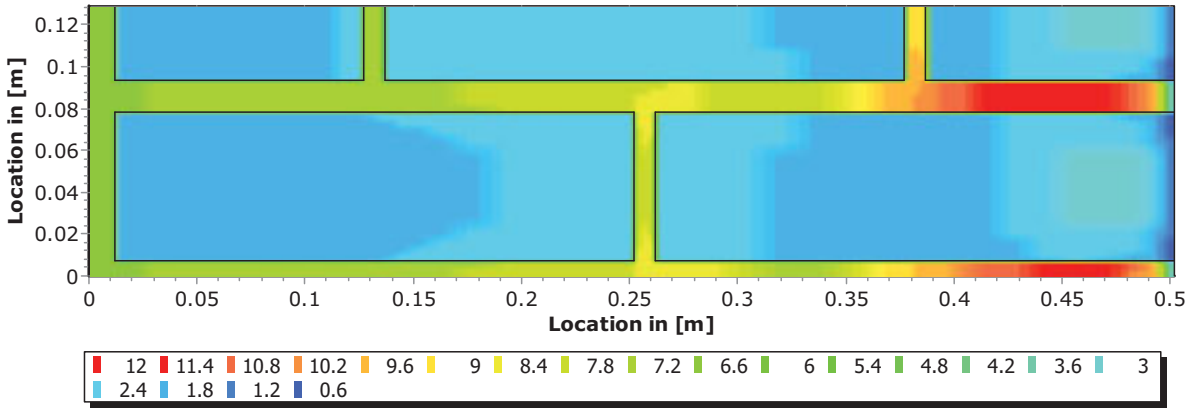

Figure 6 e: Dissolved Salt Mass Content NaCl(aq) [kg/m3]

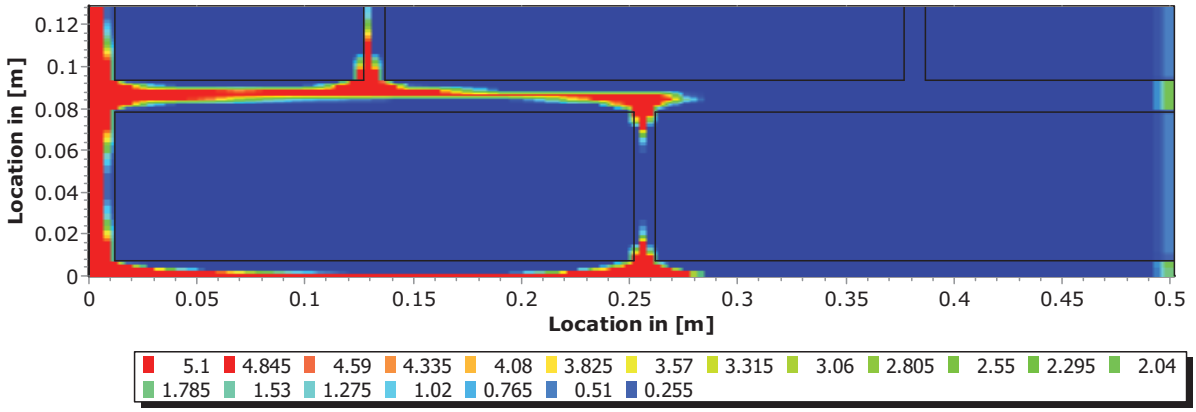

Figure 6 f: Crystalline Salt Mass Content NaCl [kg/m3]

The results shown above are only a very small excerpt of the results obtained in the multi-year simulation. The amount of output data created by 2D salt simulations also requires a suitable post-processing tool that assists in the physical and chemical analysis of the results.

4 Conclusions

The task of solving the complex coupled differential equations describing the combined heat, moisture, and salt transport with phase transitions (HAM+SP) in porous media requires besides a thermodynamically and physically sound model also an efficient solution method. Considering the complexity of the equations and the number of variables and parameters, a fast numerical solution method is imperative.

The DELPHIN simulation program incorporates a highly efficient solver for the HAM+SP equations. The solver implements a variable-order variable-step multistep method with Newton iteration. Specific optimizations are tested and investigated in detail using a custom heat and moisture transport solver implementation. It is found that by combining a number of optimizations, such as

- Extrapolation of the solution to obtain a good estimate for the next step,
- Dynamic time step control to balance accuracy with performance,
- Output interpolation to avoid sub-optimal time step adjustments,
- Modified Newton method to reduce the number of Jacobian matrix decompositions,
- Discontinuity treatment and others,

the calculation speed of the solver can be increased to an acceptable performance. Making use of these improvements, typical 1D simulation scenarios with realistic boundary conditions and simulation times of several years can be simulated with the DELPHIN solver within a few minutes. More complex cases with strongly changing boundary conditions or several hydrate phases that may concurrently precipitate can be calculated within few hours. 2D simulations can be run depending in grid size and simulation duration with calculation speeds of about 30 min/s (minutes simulation time per second real time).

The achieved solver performance is satisfactory for sensitivity studies and inverse parametrization, which are ultimately required for heat, moisture, and salt transport models. Many model parameters can only be determined indirectly from experiments and through inverse fitting using the numerical simulation. Also, for many application cases the uncertainties of initial conditions, particularly the initial distribution of salts in the construction may require many simulations in order to evaluate the effectiveness of restoration measures.

The DELPHIN simulation program and the implemented transport model is the fastest currently available simulation program for the coupled heat, moisture, and salt transport and phase transition model with such complexity and physical detail.

However, while the implemented transport and phase transition model contains already numerous effects and physical properties, including the Pitzer-model for prediction of thermodynamic solution properties, a number of processes are not captured, yet. Among these are efflorescence of salt, pore clogging, and change of pore structure as result of salt crystallization. These processes are subject of ongoing research at the Institute of Building Climatology at Dresden University of Technology.

5 References

[1] Nicolai A., Grunewald J., Plagge R. & Scheffler G., 2008, Development of a Combined Heat, Moisture, and Salt Transport Model for Unsaturated Porous Building Materials, DFG SPP 1122 Research Report, ed. L. Franke

[2] Nicolai A., 2007, Modeling and Numerical Simulation of Salt Transport and Phase Transitions in Unsaturated Porous Building Materials, PhD thesis, Syracuse University

[3] Hindmarsh A. C., Brown P. N., Grant K. E., Lee S. L., Serban R., Shumaker D. E. & Woodward C. S., 2005, "SUNDIALS: Suite of Nonlinear and Differential/Algebraic Equation Solvers," ACM Transactions on Mathematical Software, 31(3), pp. 363-396, Also available as LLNL technical report UCRL-JP-200037.

[4] Espinosa R., Franke L. & Deckelmann G., 2007, Phase changes of salts in porous materials: crystallization, hydration and deliquescence, Construction and Building Materials

[5] Steiger M., Kiekbusch J. & Nicolai A., 2007, An improved model incorporating Pitzer's equations for calculation of thermodynamic properties of pore solutions implemented into an efficient program code, Construction and Building Materials

Engin Kotan
Dipl.-Ing.

Harald S. Müller
Prof. Dr.-Ing.

Institute of Concrete Structures and Building Materials, Universität Karlsruhe (TH), Germany

Prediction model for the weathering of sandstone under ambient climate actions

Summary

Detailed analyses of the weathering processes indicate that the decomposition of sandstone can mainly be attributed to continuously changing temperature and moisture gradients, partly in conjunction with frost and ice formation as well as to partially arising crystallisation processes of solved salts in the stone. For the description of the deterioration process due to these main actions, which lead to a gradual failure of the grain bonding proceeding from the surface to inner parts of the cross section, an appropriate model for the weathering of sandstone is presently being developed.

Keywords: *sandstone, weathering model, durability, fatigue behaviour, finite element methods*

1 Introduction

1.1 Background

Sandstone is the most commonly kind of natural stone used for historical buildings in Central Europe. During the past century a dramatic increase of damages on historical buildings, monuments and sculptures made from natural stone has been observed. Due to these circumstances the weathering of sandstone and appropriate counter measures have been major aspects in numerous investigations in recent years. However, the past research work on natural stone weathering was primarily concentrated on the documentation of the deterioration process considering different attack conditions as well as on the investigations of chemical, mineralogical and physical sub-processes. So far analyses on theoretical aspects of strength loss and degradation during the decay processes have only been carried out to a very limited stage. Hence, no service life prediction models or similar approaches are available so far.

1.2 Target of this project

The weathering behaviour determined in standardized laboratory tests under accelerated and extreme boundary conditions can only be transferred qualitatively to the stone behaviour during natural weathering, due to the lack of exact deterioration time laws and prediction models, respectively. The aim of this research project was to develop an appropriate model to describe the

weathering of sandstone as a result of thermal and hygral actions. The principal idea of the proposed sandstone weathering model consists in the basic hypothesis that the weathering is primarily a result of a fatigue loading resulting from climate actions. In this approach the climatic induced strain gradients, which are determined by numerical-analytical investigations, have to be converted into external load induced strains, whose cyclic deterioration effect can be described on the basis of experimentally determined fatigue laws.

1.3 Approach

Physical deterioration processes have a significant influence on the weathering of sandstone. Often they exclusively determine the chronological development of the deterioration and the characteristic of the damage pattern. It is possible to differentiate and evaluate the weathering of sandstone from different varieties via accelerated laboratory tests. However there is a lack of models which enable the transfer of other exposure conditions and thereby permit the evaluation of realistic weathering behaviour under standard climate conditions. To close this gap and in order to develop a prediction model the concept presented in Figure 1 was pursued within the scope of this research project.

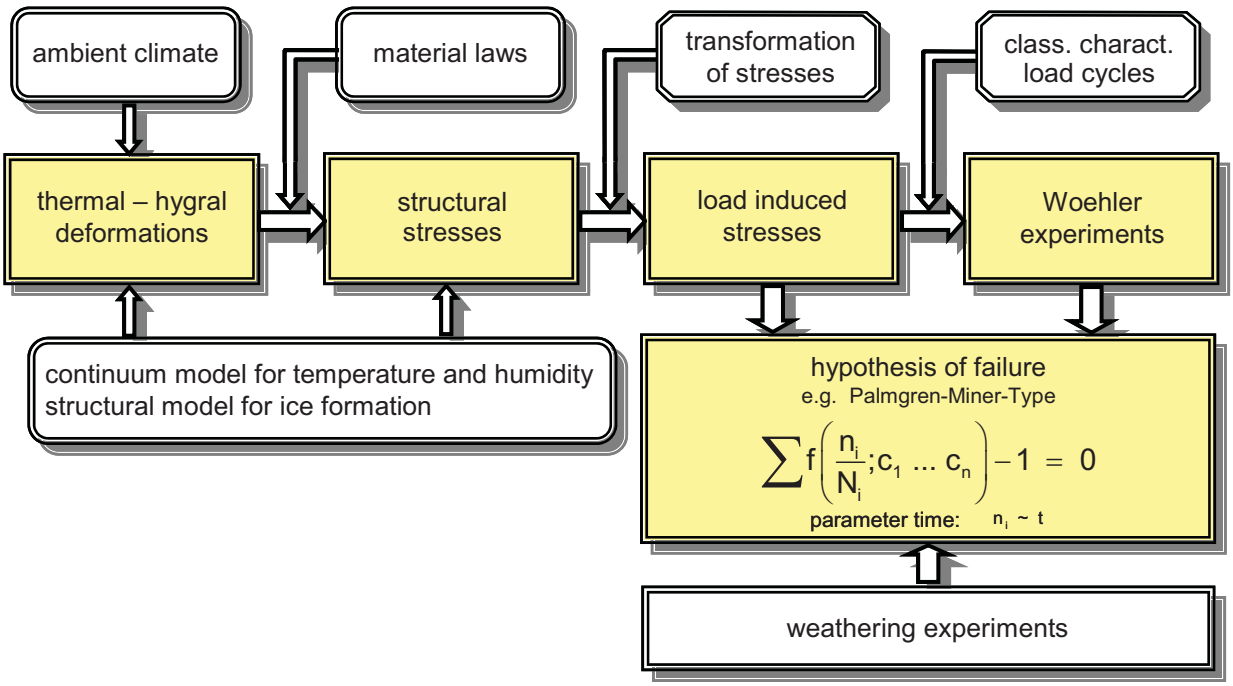

Figure 1: Concept of the research project for the development of a prediction model

The main target of the project was to describe the chronological progress of the weathering process of sandstone under ambient climate actions as a function of climate parameters and material properties using a mathematical-physical model. First a numerical analysis investigating the loading in the surface zone of the sandstone was computed. Further the stochastical distribution of the grains, grain bridges and structural pores was implemented in a structural

model. Finally material laws were developed in order to formulate the mechanically induced softening due to fatigue loading.

For construction materials like sandstone the loading due to the action of climatical ambient conditions can be securely assessed based on a continuum-mechanical approach using numerical methods. The prior target within the scope of this research project was to determine initial values for moisture and temperature gradients, in particular for the resulting stresses and strains caused by different climate actions.

A structural model which displays the mesostructure of sandstone – quartz grains, grain bondings and structural pores – was developed within a successive design step. On the basis of porosity values as well as other structural parameters a stochastical model was derived. The main objective of this model is the investigation of ice pressure and its transformation into load induced stresses in order to be able to superpose them with the results achieved by means of the continuum model.

Particular attention was hereby given to the numerical analysis was the development of adequate numerical models which allow for a quantitative analysis of the seasonally appearing textural strains in particular in the surface zones of sandstone. Based on these models the climatically induced actions can be combined into load collectives, whose cyclic deterioration effect depending on the fatigue behaviour of sandstone promises the formulation of a deterioration-time law.

The accuracy of such numerical calculations primarily depends on the precision and the soundness of the material laws. The required material characteristics for sandstone like structural data, strength values, weathering data were obtained in numerous own laboratory tests. In addition to that static tensile tests were performed at different temperatures (2, 20 and 50 °C, respectively) and humidity conditions (33, 65 and 94 % r. h., respectively) in order to be able to consider a possible variance of the relevant material parameters such as the tensile strength, Young's modulus, fracture energy and stress-crack width relation due to the alternating ambient conditions.

The main objective of the experimental tests however consisted in the determination of the dynamic tensile-strength of sandstone using centric Woehler tests. The intention of these tests was to derive Woehler curves which, in combination with an adequate failure-accumulation hypothesis allow for the specification of the intended prediction model.

2 Experimental analysis

2.1 Introduction

The implementation of realistic material characteristics and laws into the numerical analysis is essential for a realistic simulation of the deterioration process. Besides structural data and strength values, particularly material relations which describe e. g. the crack development in

sandstone are necessary. Therefore centric statical tensile tests were carried out under realistic boundary conditions. Furthermore the dynamic tensile-strength behaviour of sandstone was examined by means of centric fatigue tests (Woehler Tests).

2.2 Sample material

For all samples “Postaer” sandstone of the variety “Mühlleite” was used, as this material had been extensively investigated in a previous research project [1]. The analysed sandstone can be characterized as a medium grained siliceous bonded Elb sandstone with beige till light brown colour. Furthermore, irregular distributed iron bands as well as partially and cumulatively appearing iron-oxide stains are typical for this sandstone.

2.3 General material examination

The total porosity was determined according to DIN 52103 [2]. The porosity averages approx. 20 vol. % for the investigated sandstone and indicates a sandstone with a comparatively high porosity. In order to determine the pore size distribution, mercury intrusion porosimetry was applied. Further the grain size distribution was determined using thin sections which were microscopally examined as shown in Figure 2. A statistical evaluation of these results was finally applied for the geometry of the model to be implemented in the numerical analysis (structural model).

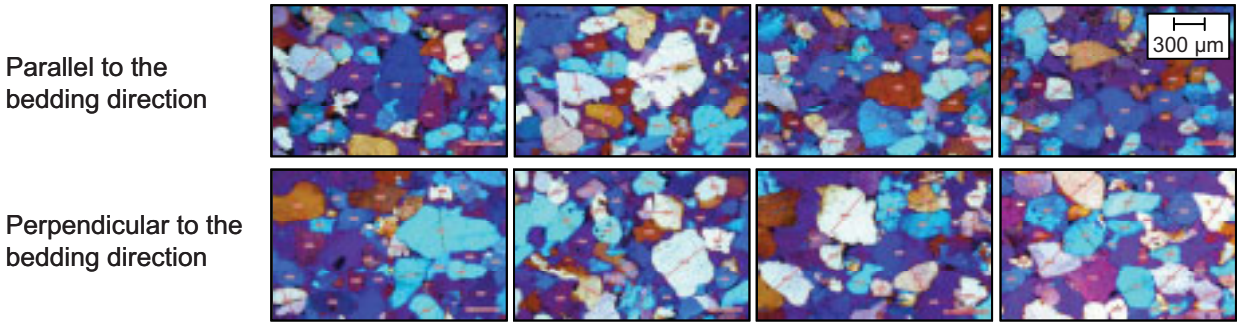

Figure 2: Microscopic analysis of sandstone for the determination of the grain size distribution

Further required parameters for the numerical analysis are temperature and moisture dependent storage and conductivity values as well as parameters to describe the deformation due to temperature, shrinkage and moisture expansion. These were deduced from adequate bibliographical references e.g. [1], [3] and [4].

2.4 Methods for the determination of the mechanical properties

2.4.1 Compressive strength

The compressive strength of the investigated sandstone was determined according to DIN 52105 [5] on cubes with an edge length of l = 50 mm. The specimens were loaded deformation controlled until failure. The results of these investigations are illustrated in Table 1.

2.4.2 Tensile strength

The tensile strength of the sandstone was determined on cylinders with a height of h = 150 mm and a diameter of d = 50 mm. The loading was applied by steel plungers which were glued to the front surfaces of the cylinders. The tensile strength values, which were determined according to [1], are shown in Table 1.

2.4.3 Young's modulus

The static Young's modulus was ascertained by the gradient of the tangent at the stress-strain relation within the linear-elastic range. The values [1] for the static Young's modulus of the Postaer sandstone of the variety Mühlleite that were determined via compressive tests are given in Table 1.

2.4.4 Fracture mechanical analysis

Within the tests for the determination of the centric tensile strength a softening behaviour after reaching the failure load could not be detected. In order to be able to record the entire stress-deformation behaviour also after reaching the ultimate load, notched specimens (Figure 3) were chosen in accordance with recommendations from the relevant literature [6]. The load application (v = 0,05 mm/min) occurs via stiff, rotation impeding steel plates between which the notched sandstone prisms were glued by a rapid hardening two-component adhesive on the basis of methacrylat. By means of the chosen impediment a stabile crack development was achieved over the specimens entire cross section (Figure 3 right). Thereby the required fracture mechanical properties e. g. the fracture energy G_F and the stress-crack-width relation σ-δ could be obtained.

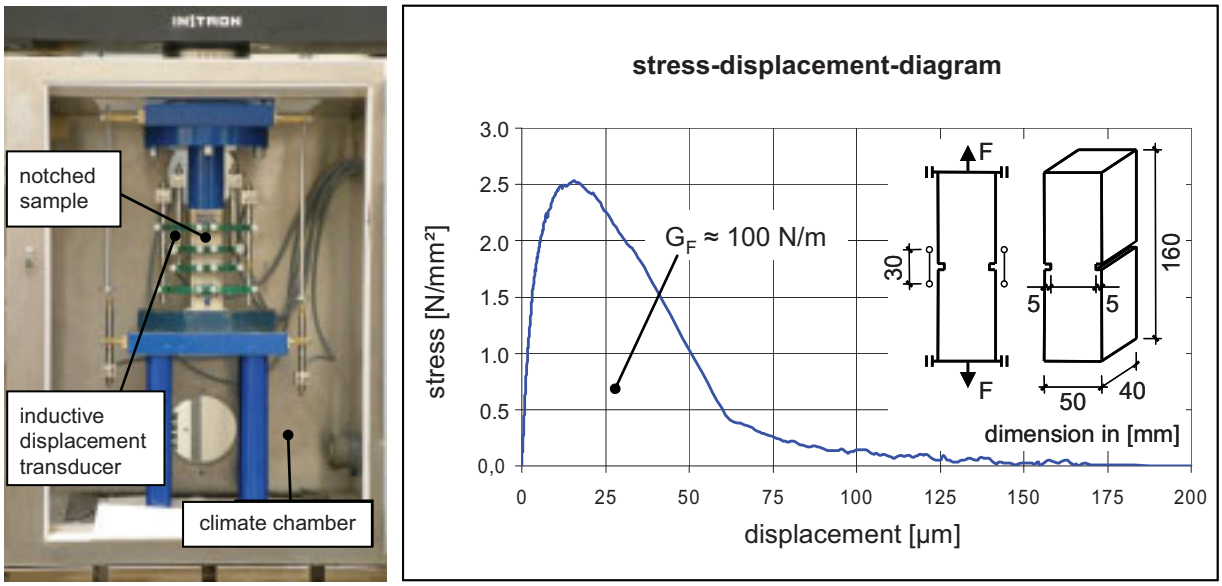

Figure 3: Experimental setup, characteristic curve progression and geometry of the notched samples

Figure 3 right shows a stress-strain relation obtained in the mentioned tests. The analysis of the illustrated curve leads to a fracture energy G_F of about 100 N/m for a sample strained parallel to

its layering. An about 10 % lower fracture energy was determined from corresponding tensile tests which were performed on notched specimens strained perpendicular to their layering.

Furthermore centric tensile tests were carried out on notched samples at different temperature and moisture conditions in order to be able to consider a possible variance of the relevant material parameters as a result of different ambient conditions. This variation is of relevance for the numerical analysis. For this purpose the tests were carried out in an air-conditioned box (see also Figure 3). The essential results regarding the fracture mechanical investigations are summarised in Table 1.

Table 1: Summary of mechanical properties

	Average value	Standard deviation	Coefficient of variation [%]
Compressive strength [N/mm²]			
to layering / ⊥ to layering	59.2 / 61.2	4.83 / 2.87	8.2 / 4.7
Tensile strength [N/mm²]			
to layering / ⊥ to layering	2.61 / 2.19	0.14 / 0.23	5.4 / 10.7
Modulus of Elasticity [N/mm²]			
to layering / ⊥ to layering	11.185 / 12.314	827 / 424	7.4 / 3.4
Poisson's ratio [-]	0.2	-	-
Net tensile strength [N/mm²]			
to layering / ⊥ to layering			
20 °C / 33 % r. h.	2.16 / 1.85	0.07 / 0.13	3.3 / 7.0
20 °C / 65 % r. h.	2.30 / 1.73	0.13 / 0.17	5.6 / 9.6
20 °C / 94 % r. h.	2.25 / 1.64	0.09 / 0.16	4.0 / 9.9
2 °C / 65 % r. h.	1.86 / 1.62	0.16 / 0.29	8.4 / 17.9
50 °C / 65 % r. h.	1.84 / 1.93	0.27 / 0.17	14.6 / 8.9
Fracture energy [N/m]			
to layering / ⊥ to layering			
20 °C / 33 % r. h.	98 / 86	3.06 / 10.2	3.1 / 11.9
20 °C / 65 % r. h.	106 / 91	7.13 / 8.5	6.7 / 9.3
20 °C / 94 % r. h.	100 / 86	8.54 / 9.3	8.5 / 11.5
2 °C / 65 % r. h.	100 / 88	5.72 / 9.5	5.7 / 10.8
50 °C / 65 % r. h.	94 / 92	11.35 / 6.5	12.1 / 7.1

2.5 Fatigue tests

A key part of the experimental analysis was the determination of the dynamic tensile strength of sandstone by means of centric Woehler tests. Thereby preferably largely identical specimens were exposed to appropriately scaled vibration stresses in order to determine the related load cycles to failure N_i (Figure 4). During the performance of the tests the lower stress σ_u was kept

constant for all specimens of a Woehler series while the upper stress σ_o was phased from specimen to specimen so that during the course of the tests not only the descending straight line (curve) of the Woehler curve could be specified but also the fatigue resistance depending on the limit-load cycles N_{max} could be evaluated. This proceedure was chosen since the compressive strength of approx. 60 N/mm² is absolutely a lot greater than the degree of the loading observed in corresponding fatigue tests, which have been determined to 1 to 2 N/mm² in numerical investigations. Hence it is assumed that the deterioration contribution due to corresponding compressive loads is insignificantly small.

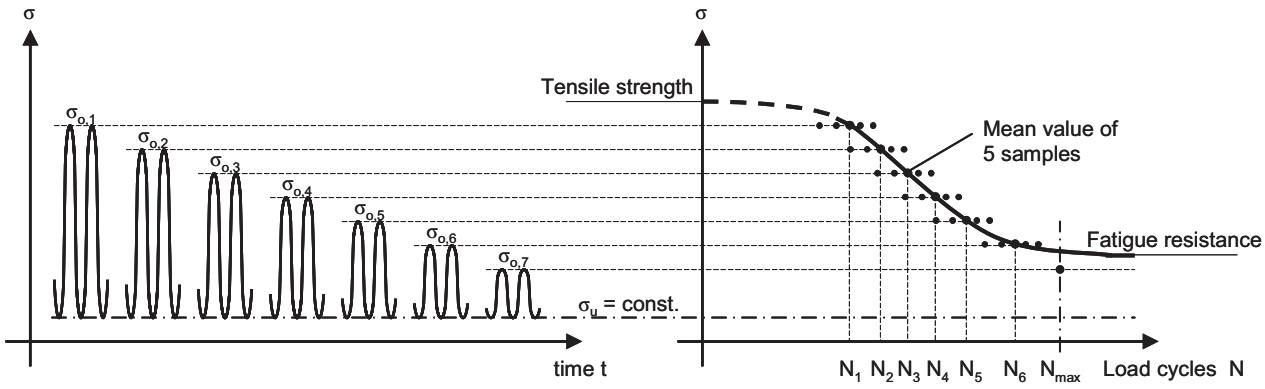

Figure 4: Evaluation of the Woehler curve with constant lower stress σ_u

According to the static tensile tests notched sandstone prisms with the dimensions 50x40x160 mm³ were used. As ambient condition a controlled reference atmosphere of 20°C / 65% r. h. was maintained. In order to balance material-dependent variations 5 tests per specimen series and direction of stratification were conducted. With regard to the test duration an upper limit of 2 million cycles was defined.

It is known for various materials that the fatigue behaviour depends only slightly on the frequency of the load cycles. However as the acceleration in the tests is of significant importance in order to develop a prediction model and therewith the possible long-range prognosis respectively, this hypothesis was experimentally verified. For the derivation of the mentioned Woehler curves a constant testing frequency of 5 Hz was chosen. The frequency was varied between 1 and 10 Hz for some representative upper stress/failure-cycle combinations. Within the examined scope the test frequency had negligible influence on the number of load cycles until failure. Therefore all following fatigue tests were performed at 5 Hz.

Figure 5 shows the result of the dynamic tensile tests. The diagram on the left represents the material behaviour for dynamic loadings applied parallel to the layering of the sandstone material. At a loading degree of 80 % of the static tensile strength of the sandstone the samples could withstand an average of 8.745 load cycles until failure. An average number of almost 200.000 load cycles was reached at a loading degree of 70 %. Finally the sample could resist 2 million load cycles without failure at a loading degree of 60 %. Five single tests per loading degree were performed. They are displayed as rhombi depending on their attained number of load

cycles in the diagram. The circles represent the average value per loading degree. The static tensile strength as well as a linear relationship between the loading degree and the number of load cycles (logarithmically scaled) was taken into account in order to determine the presented best fit straight line.

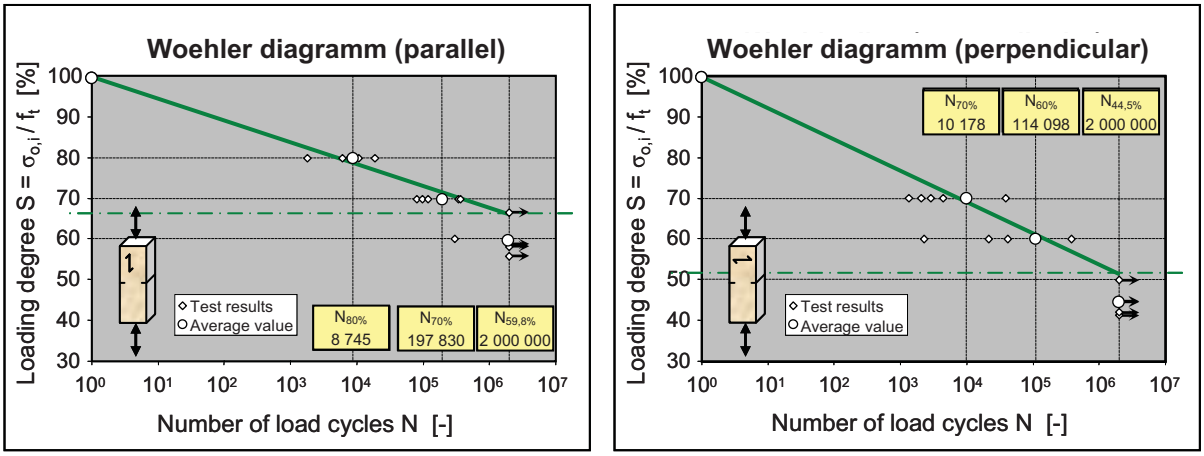

Figure 5: Test results of the dynamic tensile tests

The diagram on the right of Figure 5 shows the results for loadings applied perpendicular to the layering. The higher gradient of the Woehler curve for a loading perpendicular to the stratification is statistically significant and proves an increased fatigue sensitivity in this load direction. This goes along with a reduction in load cycles from > 2 million down to 114,000 at a loading degree of 60 %.

These Woehler curves provide essential information regarding the materials fatigue resistance. Based on the working hypothesis that the weathering – excluding an entire saturation with water – represents a cumulative mechanical softening process, failure criterions due to fatigue (Woehler, Palmgren-Miner a. o.) can now be utilised. They deliver a correlation between the loading degree, which can be considerably smaller than the strength, and the time span until failure occurs. Now a prediction model can be formulated which enables to forecast of the gradual destabilization under arbitrary ambient conditions. The effect of these conditions on sandstone still has to be quantified by numerical analysis.

3 Numerical investigations

In order to quantify the loads resulting from climatical conditions, adequate numerical models are used. The quantitative determination of loads resulting from seasonal variations of temperature and moisture is carried out by a continuum model. Hereby the temperature and moisture distribution, structural stresses and potential crack development can be analysed, amongst others. The simulation of pore pressures due to frost loadings and accordingly the textural loading on the granular structure are investigated by means of a structural model. Contrary to the continuum model in this case the mesostructure of the sandstone (grains, grain bondings and struc-

tural pores) is being reproduced. The finite element program DIANA [7] is applied for the numerical analysis.

3.1 Continuum model

The first step for developing the model consists in numerically analysing the deformations and stresses in the peripheral zones resulting from characteristic changes of temperature and humidity. With the help of the FE programme DIANA a FE net of a continuum model (macro level) was generated and tested. The main target of the numeric computation was to gain initial values of temperature and humidity gradients and in particular to determine the resulting tensions and deformations under different climate actions.

In a first step a freely deformable sandstone block was examined. Hereby the moisture and temperature transport were considered decoupled. To record realistic diffusion and capillary transport characteristics of the sandstone, the humidity dependent storage and conductivity characteristics for the humidity transport were considered in the computation. Furthermore appropriate convection elements were used to simulate the thermal and humidity transition between the ambient air and the sandstone surface.

In order to compute the deformations caused by temperature, shrinkage and swelling, which are actuated by temperature or humidity changes, respectively, the respective thermal and hygral strain functions are considered. The strain functions were derived from literature data [1], [3], [4] and cover the entire spectrum of possible moisture contents.

The calculative set of climate actions includes the usual climates as well as extreme effects like thermal shock (thundershower) and driving rain. Since the natural climate conditions do not only vary over long periods, it was necessary to run seperate long-term calculations (observation period: one to several years) as well as short-time calculations (observation period: one to several hours).

The extensive computer-aided simulations on the continuum that have been performed so far provide the calculative structural stresses, type and number of the tension alternations depending on the selected characteristic values, geometrical boundary conditions as well as the simulated influences of the weather. It is also essential to record the moisture distributions, which are later used to estimate the pore saturation degree in the peripheral zone.

Due to constantly changing climate conditions a steady alternation of both humidity and temperature is observed in the stones surface. The resulting moisture and temperature gradients cause distinct deformations of the sandstone, which strongly vary locally. This deformation tendency generates structural stresses, which can lead to a gradual failure of the grain bonding of the sandstone structure and finally to damages [8].

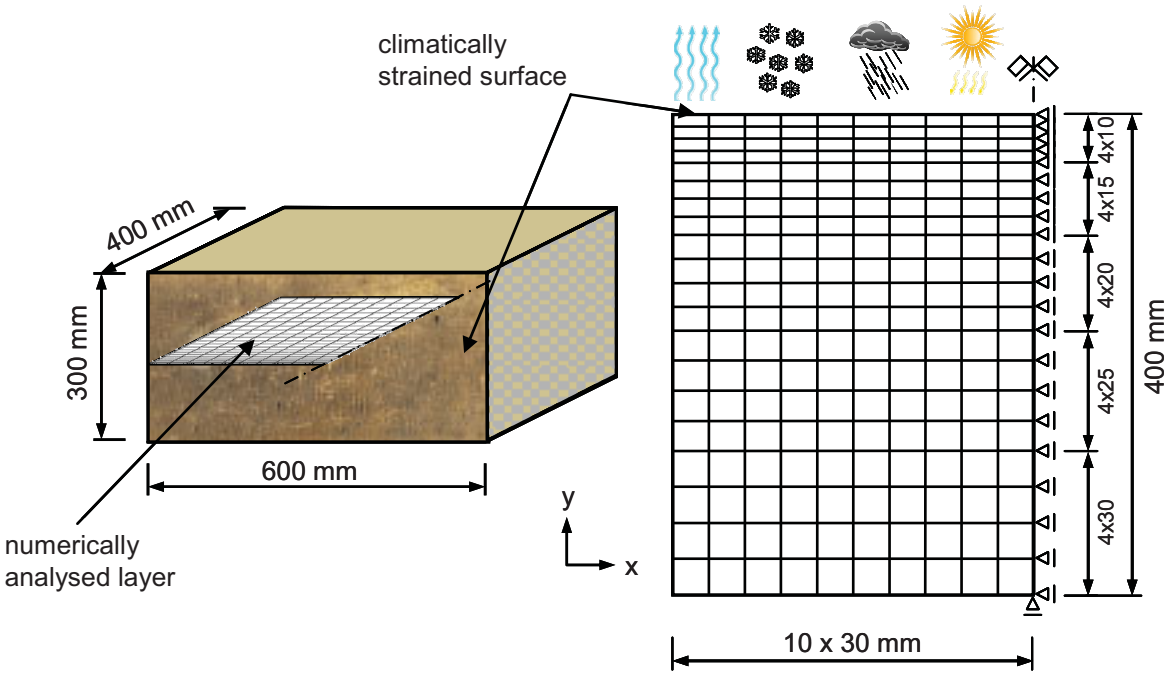

Figure 6: Numerically analysed layer of the sandstone continuum and discretised system

In order to analyse the structural stresses, a sandstone continuum, as it is represented in Figure 6, was examined in detail. Due to the fact that the deterioration process mainly takes place on the layers close to the surface, two-dimensional numerical investigations were carried out for the calculation of the determining stresses. As an example of the calculation results, Figure 7 shows the moisture distribution in the sandstone. In this case a sandstone which was dry in the beginning due to a long period of dry weather is suddenly exposed to a 6 hour period of wetting. The humidity penetration behaviour in the sandstone, being observed during the wetting, is characterised by a sharply marked sloping moisture front. In this case the penetration depth amounts to a depth of 75 mm into the stone. The following drying behaviour shows the typical well-known correlation that the drying of the material demands a multiple of the time compared to the humidification. Furthermore the calculated results show, that depending on prevalent drying possibilities at the sandstone surface, a part of the humidity is emited in the form of evaporation back to the ambient air. At the same time a rearrangement of moisture can be observed at the moisture front within the stone. Thus a part of the humidity continues to penetrate into the stone.

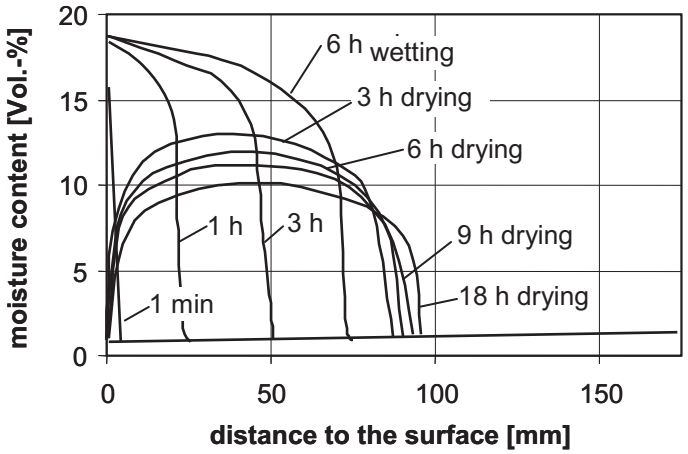

Figure 7: Moisture distribution in the stone – 6 hours of wetting followed by 18 hours of drying

In order to draw conclusions about the structural stresses due to moisture and temperature gradients adequate material laws have to be implemented into the FE model. The material behavior of the sandstone was modelled using the Crack Band Model developed by Bažant and Oh (Figure 8, left). The heterogeneity of the sandstone was taken into account by a variance of the material properties via a statistical distribution of the material parameters in particular a variation of the tensile strength and the fracture energy for each single element. Therefore nine material classes were defined and assigned randomly according to a Gaussian distribution to the finite elements (Figure 8, right).

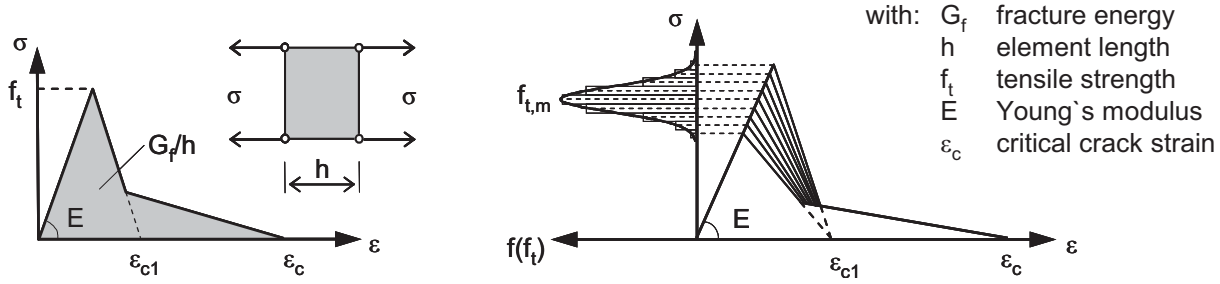

Figure 8: Implementation of the Crack Band Model in the finite element model (left) and consideration of the heterogeneity of the sandstone (right)

On the basis of numerous analyses, Figure 9 shows exemplarily the self-equilibrating stresses as a result of a chosen hygral strain over a period of 24 hours. For simplification purposes the temperature conditions were assumed to be constant. The left illustration shows explicitly the self-equilibrating stresses appearing after irrigating a sandstone which was completely dry to start off with. The diagram on the right hand side points out the stress ratio during the following 21 hour drying process.

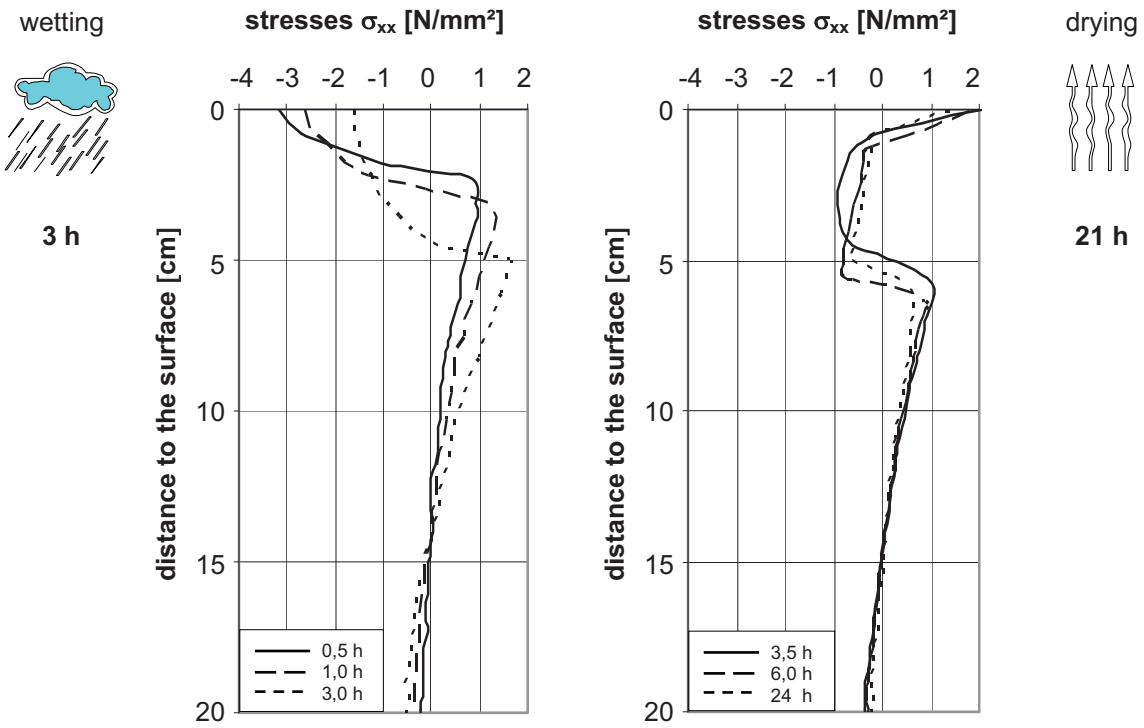

Figure 9: Self-equilibrating stresses due to hygral strain. Left picture: during three hours of wetting. Right picture: during 21 hours of drying

As expected, compressive stresses in the already humid stone are observed as a result of the moisture absorption. At the moisture front the signal of the stress changes from pressure to tension. This fact is a result of the restrained deformation caused by the lower and drier stone layers. Due to a further ingress of moisture into the stones interior the tensile stresses arise and can exceed the material strength (see Table 1).

The following 21 hour drying period cause the stress distribution illustrated on the right hand side of Figure 9. Due to moisture dissipation the layers close to the surface tend to exhibit shrinkage deformations. However, this deformation tendency is being restrained by the more humid lower layers. Thus, tensile stresses in layers close to the surface occur. Especially at the beginning of the drying process, when the moisture gradient is high, the tensile stresses can almost reach the material strength.

The quantitative survey of the stress alteration on the individual stone-layers is essential in order to investigate the fatigue behaviour due to climatical influence. Therefore seasonal climate actions (temperature and moisture) were examined and corresponding seasonal distributions of stress were determined. These distributions were subsequently evaluated by using statistical counting procedures (rainflow and reservoir counting method). Frequency distributions were developed and finally compiled in a profile of stress collectives (Figure 10).

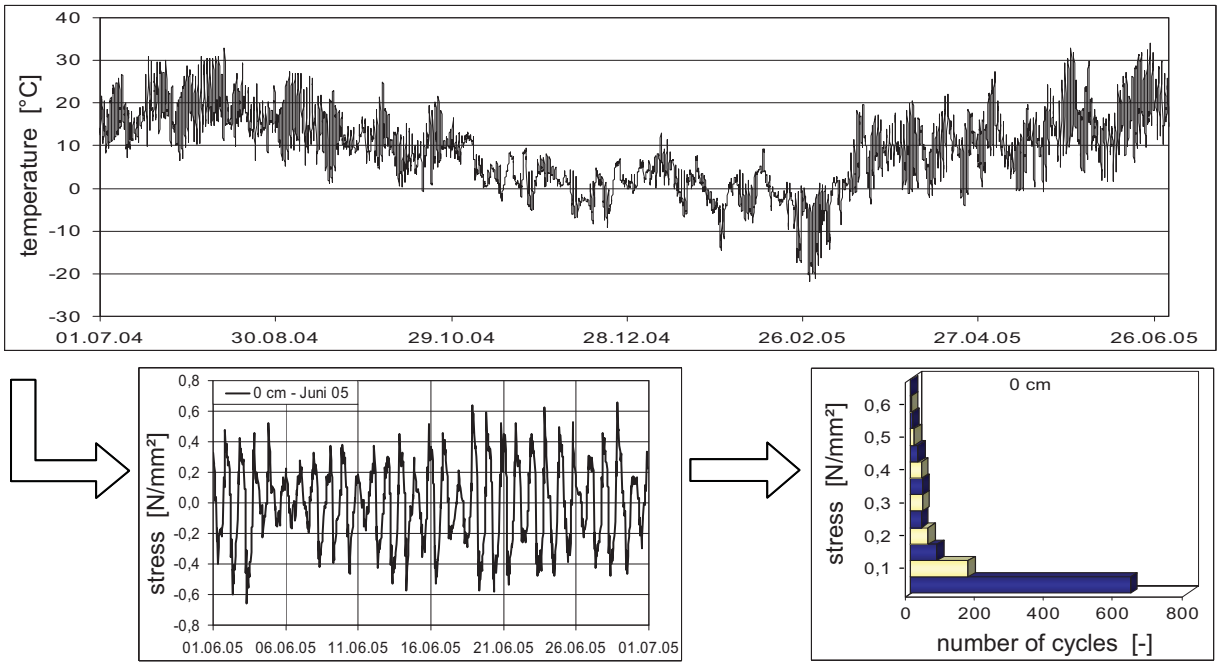

Stress magnitude on various levels of the specimen can be determined by means of numerical analysis on the continuum model (the variation of stress on the stone surface is exemplarily shown for a period of one month)

Seasonal tensile stresses presented as stress collectives (the results of the thermal stresses at the stone surface over a period of one year; exemplarily)

Figure 10: Presentation of exemplary test results on the continuum model

The stresses given in Figure 10 have to be superposed with the stresses due to seasonal hygral actions. Furthermore structural stresses as a result of a frost attack have to be taken into account by load collectives. For this purpose the investigations are performed on the structural model, which is specified in the following.

3.2 Structural model

The degree of pore saturation with water is of major relevance for the weathering during a frost attack. While the formation of ice for low degrees of saturation leads to reversible structural deformations irreversible deformations appear during saturated conditions due to the bursting pressure of the freezing water. Until now a quantitative investigation of these structural loadings within the texture of the sandstone has only been carried out rudimentarily. In particular the level of the arising stresses and the stress cycles require a quantitative analysis, in order to be able to reproduce the deterioration potential during the frost loading by means of a model.

For this purpose a two-dimensional structural model that takes the structural data of the real sandstone (porosity, grain size distribution) into account was generated and tested. Primary target of the numerical analysis was a quantitative evaluation of external dummy loads (load stresses). The stress condition due to these external loads has to be equal with the bursting effect due to icing in the pores (Figure 11).

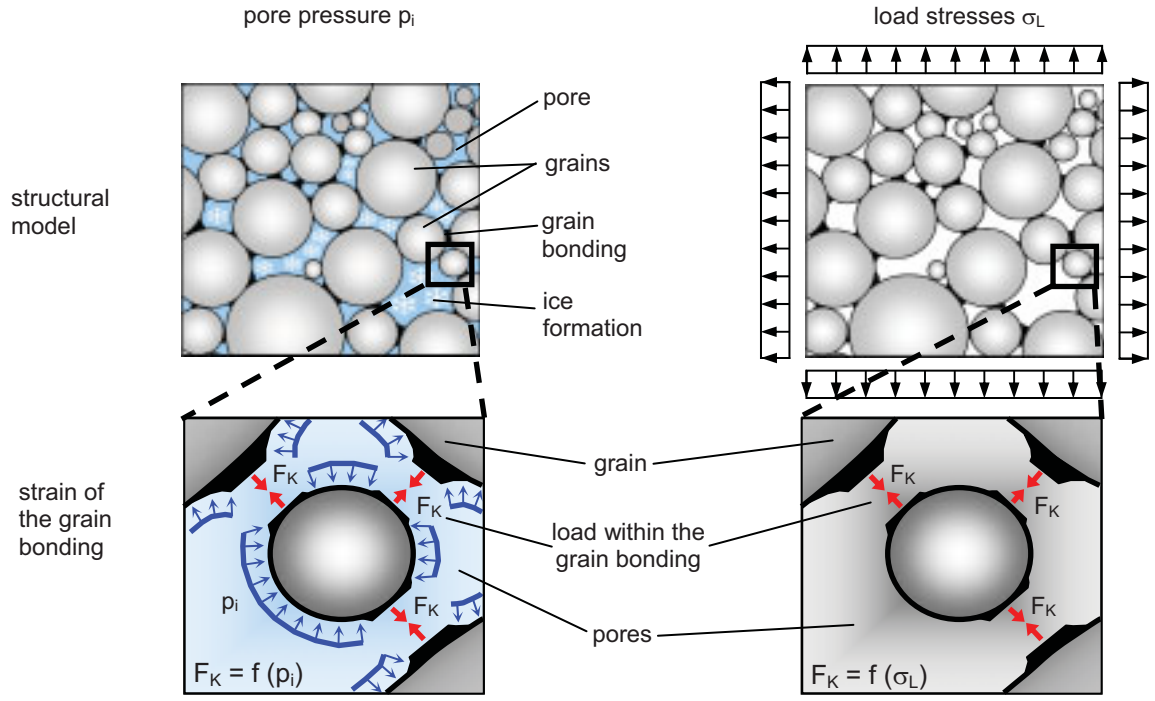

Figure 11: Exposure of the structural model to the effect of pore pressure due to ice formation (left) and load stresses (right)

Figure 12 (left) shows exemplarily one of the applied finite element meshes which are randomly generated corresponding to the total porosity and the grain size distribution. The variation of the material properties is included via a statistical distribution of characteristic values (tensile strength, fracture energy) for each single element. In order to be able to reproduce a realistic crack development the cohesive crack model is applied for the material behaviour of the grain matrix and implemented in the numerical model respectively. In order to simulate the bursting pressure due to the formation of ice, the pores within the numerical model are filled with an adequate material. This material has equal mechanical properties as ice and reproduces the volumetric expansion during icing by an adequate temperature-strain curve. Thereby also the degree of pore saturation is considered as a major influence.

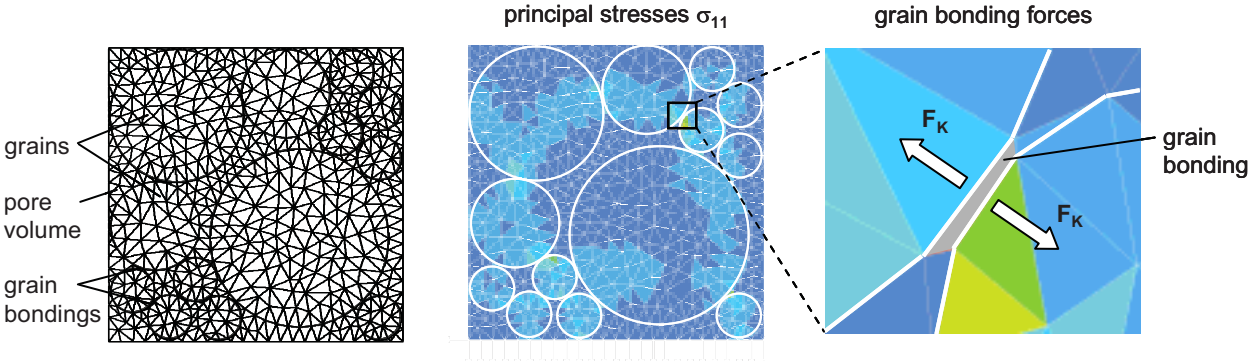

Figure 12: Randomly generated structural model depending on porosity and grain size distribution of the real sandstone (left) and exemplary presentation of computation results of grain bonding forces (right)

Structural stresses as well as crack development due to icing can be analysed by means of the described model. The effective grain bonding forces can be determined via an integral examination of the stresses within the grain bondings (Figure 12, right).

According to the principle idea for the development of the prediction model, the structural stresses due to the formation of ice are transformed into load induced stresses. Their cyclic deterioration effect is to be described on the basis of fatigue laws. However the performed calculations indicated that the transformation of the computed structural stresses into external load induced stresses is more extensive than estimated. The approach using grain bonding forces seems to be feasible but requires high efforts. Therefore the investigations concerning the possibility of transformation are not yet accomplished and continue at the present time.

4 Ongoing research and outlook

The exemplarily shown calculation results of chapter 3 still have to be expanded with regard to the total bandwidth of the seasonally prevalent climatic conditions. In this context, not only the maximum occurring stresses but also and more important, the acquisition of the stress changes, number and duration of the single stress amounts have to be surveyed. This is necessary to be finally able to acquire the mechanical fatigue load – i.e. the actual reason for the crack initiation, respectively decompression, even caused by stresses far below the short-term strength – occurring on the edge zone during a long period of time.

The conversion of the structural stresses into load-induced stresses takes place according to the principle that stresses acting in the internal profiles are attached as external loads by taking equilibrium conditions into account. In an integral consideration this is equivalent to external loads producing the same stresses as the self-equilibrating stress condition. In this context, fundamental considerations have to be taken into account as far as depth-dependent stresses and the corresponding load distributions – in particular due to frost actions –, respectively, are concerned.

Constantly changing climate conditions create variable structural stresses. Upon completion of the simulation calculations, all the calculated stresses (due to thermal, hygral and frost actions) have to be summarized in classes like incidence, frequency, medium stress amount and amplitude via the established mathematical methods. An important parameter for this is the influence of the depth on the stresses below the surface.

Finally bursting pressures during ice forming and their transformation into load-induced stresses have to be investigated. These stresses then must be superimposed to the frequency distributeion of the single stress amounts. Using the stochastically generated structural model (meso level), which is capable of representing grains, grain bondings and structural pores, it is also possible to transform the internal disruption forces between grains due to the ice formation into load induced stresses. On the basis of the hypothesis that the thermal and hygral induced weathering takes place in a first approximation as a mechanical fatigue process, the formulation

of a life time prediction model may be derived in conjunction with a damage accumulation hypothesis like e.g. the Palmgren-Miner rule. Finally the parameters of the weathering model of sandstone can be calibrated on the basis of already existing experimental results on the durability of sandstones.

5 Summary and Conclusions

Within the framework of this research project, the physically dependent stone weathering, is investigated. The target is to describe the time development of the sandstone weathering process depending on climatic parameters and material properties, finally ending up in a lifetime prediction model.

The time-dependent prediction of deteriorations, respectively the possibly remaining useful life expectancy of a building, is of very large economic importance for the scheduling of repair works. In case of a well-timed implementation of appropriate precautionary measures, the repair costs can be kept to a minimum. By creating an almost realistic forecast model for the time-dependent physical deterioration process of sandstone it will be possible to set up an evaluation of the “lifetime” of the most commonly used natural stones in Central Europe. Also it has to be taken into account that due to such a model the considerable consequential costs of an existing building can be estimated.

6 References

[1] Müller, H. S.; Hörenbaum, W.: Modellhafte Untersuchungen zu Fugenverbindungen von Alt- und Neusteinen am Beispiel der Frauenkirche Dresden unter dem Gesichtspunkt der Ressourcenschonung und der Verhinderung von Umweltschäden. Abschlussbericht zum Forschungsvorhaben, Institut für Massivbau und Baustofftechnologie, Universität Karlsruhe (TH), 2002.

[2] DIN 52103: Bestimmung von Wasseraufnahme und Sättigungswert. Beuth Verlag, Berlin, Oktober 1988.

[3] Schießl, P.; Alfes, C.: Festigkeiten und Verformbarkeit von Sandstein, Bedeutung für die Verwitterungsresistenz und Meßmethoden. In: Bautenschutz + Bausanierung, Band 14, 1991.

[4] Möller, U.: Thermo-hygrische Formänderungen und Eigenspannungen von natürlichen und künstlichen Mauersteinen. Dissertation, Lehrstuhl Konstruktive Bauphysik, Universität Stuttgart, 1993.

[5] DIN 52105: Prüfung von Naturstein. Druckversuch. Beuth Verlag, Berlin, August 1998.

[6] Mechtcherine, V.: Bruchmechanische und fraktologische Untersuchungen zur Rissausbreitung in Beton. Dissertation, Institut für Massivbau und Baustofftechnologie, Universität Karlsruhe (TH), 2000.

[7] DIANA, Finite Element Analysis: User’s Manuals release 7.2, TNO Building and Construction Research. Delft, 2001.

[8] Müller, H. S.; Garrecht, H.: Die Frauenkirche zu Dresden – Untersuchungen zur Dauerhaftigkeit der steinsichtigen Kuppel. Sonderforschungsbericht 315, Arbeitsheft 16, Universität Karlsruhe (TH), 1999.

Alexandra Schubert
Dipl.-Ing.

Klaus P. Großkurth
Prof. Dr.-Ing.

TU Braunschweig iBMB, Braunschweig, Germany

Development of a model for the homogenising description of the deformation behavior of concrete due to sulfate expansion

Summary

The center of this project was to determine the structure of specific parameters for the development of a model, which describes the deformation behaviour of concrete due to expansive reactions on the basis of a sulfate attack in the pore area. Thereby knowledge of the damage process of sulfate conditioned expansive reactions in the concrete structure is to be broadened on a quantitative level, so that it is possible to make forecasts on the course and the associated damage processes resulting from these expansive reactions.

1 Introduction

The phenomenon of mortar and concrete degradation due to sulfate attack is known since more than 100 years. In spite of extensive researches and analyses there are different views about the causes and the mechanisms of action of this important corrosive process, which depends both on chemical and on physical thermodynamical parameters. From the scientific point of view, new approaches are therefore required to elucidate completely the manifold dependences as well as to verify the different existing hypotheses.

Thus the purpose of this research project was the determination of the chemical, macro- and microstructural input data to develop a model describing the deformation behavior of concrete due the expansive reactions based upon sulfate attack in the pore area and external stress conditions. Within the framework of the collaboration in Research Unit 2 (SPP 1122) numeric analyses should be confronted to extensive experimental microstructure analyses. Thereby the model should be verified and validated as well as possible to couple the sulfate transport in concrete with the mechanical behavior and the damage process.

2 Materials and methods

The samples were manufactured according to DIN EN 196-1 [1]. Table 1 gives an overview about the sample spectrum as well as the testing solutions used. Because of time considerations the storage within 0.1 % sulfate solution took place at a temperature of 8°C, since it is known that the ettringite formation is accelerated by low temperatures.

Table 1: Sample spectrum overview

Type of samples		Hard. cement paste	Mortar	Concrete
Dimensions of cylindrical samples	[mm]	25 x 25	50 x 50	50 x 50
Dimensions of prisms	[mm]	-	160 x 160 x 40	160 x 160 x 40
Cement content	[kg/m³]	-	450	400
Max. aggregate size	[mm]	-	2	8
Cement type	[-]	CEM I 32.5R CEM I 42.5R CEM I 42.5R-white CEM I 42.5R-HS	CEM I 32.5R CEM I 42.5R CEM I 42.5R-white CEM I 42.5R-HS	CEM I 32.5R CEM I 42.5R CEM I 42.5R-white CEM I 42.5R-HS
w/c-ratio	[-]	0.4 0.5 0.6	0.4 0.5 0.6	0.4 0.5 0.6
Type of solution	[-]	Na_2SO_4 - 5% Na_2SO_4 - 0.1% Dist. H_2O	Na_2SO_4 - 5% Na2SO4 - 0.1% Dist. H_2O	Na_2SO_4 - 5% Na2SO4 - 0.1% Dist. H_2O

3 Experimental procedure

Before storage the samples were checked visually regarding damages e.g. due to shrinkage etc. to avoid incorrect statements. In the course of storage further test-accompanying measurements were conducted. At this all 14 days the heights and masses of the samples subjected to sulfate and water were determined in order to qualify the sulfate solution absorption of the samples and the variation of their water content due to the salt impact. The crack formation and propagation as well as the resulting sample damage on the course of the sulfate weathering were documented by a series of photographs and video recording.

The microstructure investigations took place on the basis of an extensive analysis scenario, which combined scanning electron microscopy, particle analysis and energy-dispersive X-ray analysis. The spotlight of the conducted investigations was first the pore system and its ettringite growth as well as its variation on the course of the sulfate attack. Mercury intrusion porosimetry was used as a complementarily analysis for the determination of the influence on the sulfate conditioned expansions to the pore. The investigations took all place at defined time periods, to guarantee the comparability of the results. To support the interpretation of the results, as well as the visualization of the strength reduction in the course of the sulfate attack, compressive and flexural tests were conducted on references and sulfate weathered prisms with dimensions 4 cm x 4 cm x 16 cm.

4 Results

4.1 Compressive and flexural strength

Within grant duration compressive and flexural strength were tested according to DIN 18555-3 [2] first on hardened cement paste prisms subjected to sulfate attack over a period of 56 days. To determine the influence of the varying mix-composition and the duration of the sulfate weathering, strength tests were additionally conducted in the last period of the grant on reference (climate 23/50) and sulfate attacked as well as water stored mortar prisms over a period of 91 days. The following conclusions can be derived from the results of these tests regarding the influence of sulfate attack on the strength of the microstructure whereas the results of the compressive and flexural strength tests have to be analyzed separately, because different dependences can be identified:

Compressive strength:

- The compressive strength of the uncontaminated as well as the water and sulfate stored mortar and hardened cement paste prisms increases with decreasing w/c-ratio and increasing cement grinding fineness.
- The compressive strength of the climatic, water and sulfate stored mortar prisms is approximately equal and shows a comparatively constant curve shape over the time of weathering observed, while the sulfate stored hardened cement paste samples show tendentious an increase of the compressive strength during the 56 weathering days independent of the cement type. This increase can be especially observed within the first 28 weathering days. The curve shapes of the water stored mortar and hardened cement paste samples are approximately identical.

Flexural strength:

- The flexural strength of the uncontaminated as well as the water and sulfate stored mortar and hardened cement paste prisms increases with decreasing w/c ratio and increasing grinding fineness of the cement.
- In the case of the mortar prisms stored in climate a light increase of the curve can be noticed and with sulfate and water weathering a constant curve shape during storage. These observations are independent from the type of cement used.
- The flexural strength of the sulfate stored specimen is somewhat higher compared to climatic and water weathering. However a decrease of the flexural strength for prisms made of white cement between 56 and 91 days is to be observed.

4.2 Porosity

Until now, there are many varying opinions in the literature regarding the topic of porosity, especially with respect to the pore size areas, as illustrated in table 2.

Table 2: Classification of the pores by different authors

References	Romberg [3]; Schneider [4]	Böttger [5]	Setzer [6]
Gel pores [µm]	0.001 – 0.01	> 0.03	0.002 – 0.05
Capillary pores [µm]	0.01 – 10	0.03 – 10	0.05 – 50
Air voids [µm]	1 – 1000	> 10	50 – 2000

To get information about the influence of the pore structure, particularly the porosity and the pore size distribution, in the course of the storage, porosity measurements were conducted on hardened cement paste, mortar and concrete samples after a storage duration of 100, 200 and 300 days. From this the following results depending on the composition, the kind of the solution and the duration of storage can be deduced:

- In the course of the storage the overall porosity of the hardened cement paste samples decreases faster than those of mortar and concrete due to closing of the pores with the crystal growth due the effect of the Na_2SO_4-solution. An increasing porosity within the investigation period indicates the beginning of a sample destruction caused by the increasing crystallization pressure. This phenomenon occurs much earlier in the case of the hardened cement paste specimen than in the case of the mortar and concrete specimen. Analogously, the development of the pore size distribution proceeds to it. In the case of the hardened cement paste specimen it shifts the fastest towards smaller pore radii in the course of storage.
- The overall porosity is reduced by storage in a solution with 5% Na_2SO_4 substantially faster than when the 0.1% test liquid is applied to the specimen.

4.3 Crack development and propagation

With the following of the cracks development and their propagation in the course of the storage the following differences were observed between hardened cement paste -, mortar and concrete specimen:

- In the case of hardened cement paste specimen the crack development occurred each starting from the sulfate weathered front, in which the crack further propagated and afterwards continued in the lateral surface of the specimen (fig. 1). Spalling due to salt crystallization of the sodium sulfate transported capillary through the specimen and the related crystallization pressure occurred on the specimen face outside of the test liquid (fig. 2).
- For the mortar and concrete specimen, first cracks were always to be observed within the sulfate weathered specimen front, though exclusively in the border region. However, compared to the hardened cement paste specimen, the cracks propagated here limited first in the specimen front located in the test liquid more or less radially and on the area

in the vicinity of the lateral surface and proceeded in the lateral surface of the specimen without any further propagation in the front surface (fig. 3).

- Independently of the concentration of the test liquid, the degradation of hardened cement paste during sulfate weathering takes place substantially faster than with mortar and concrete, whereby first cracks appeared earlier in the mortar specimen as in the concrete cylinders.
- The duration of the sulfate weathering also affects the degree of damages: The longer the specimen are subjected to the sulfate attack, the more severe the degree of damages.

Figure 1: Crack development and propagation in hardened cement paste specimen

Figure 2: Specimen spalling related to crystallization pressure (cement paste)

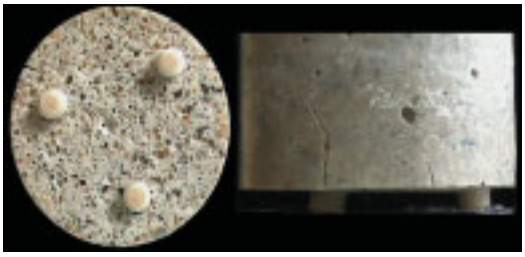

Figure 3: Crack development and propagation in mortar and concrete specimen

4.4 Results of the measurements accompanying the storage

The results of the measurements accompanying the storage of the first specimen batch, which were mainly manufactured for the definition of discrete moments for the scanning electron microscopic microstructure investigations of the second specimen batch, were verified on the basis of the second specimen batch.

Mass

In the course of the measurements accompanying the storage the maximum liquid absorption took place independently of the mixture composition and the weathering solution within the first 14 storage days for hardened cement paste, mortar and concrete specimen. Fig. 4 illustrates this with the example of a hardened cement paste specimen made of CEM I 32.5R, which had been produced with a w/c ratio 0.50 and stored in a solution with 5% Na_2SO_4. Since the mass altered only insignificantly from this moment, it can be assumed that an equilibrium between capillary water absorption and the evaporation at the specimen has adjusted itself this period.

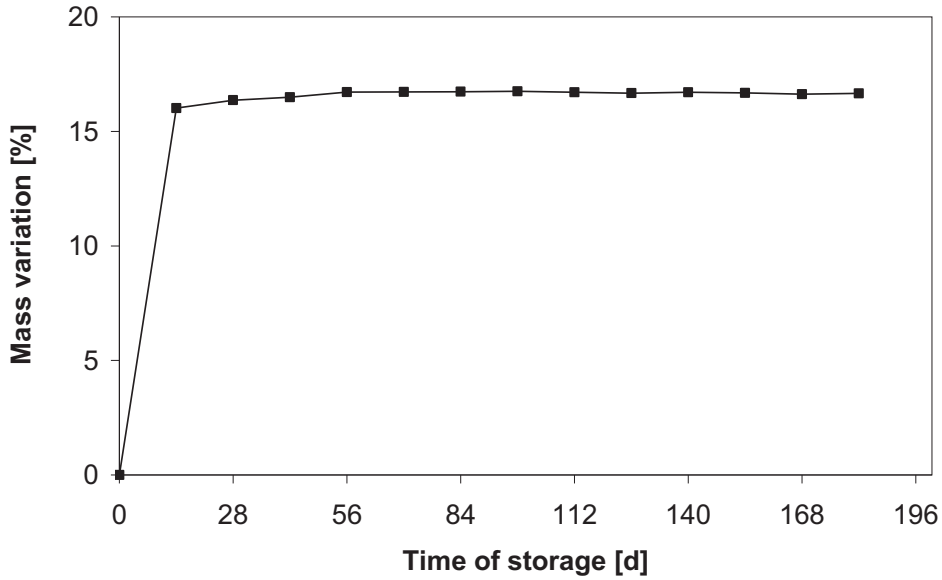

Figure 4: Typical progress of the mass variation as a function of the storage duration for the example of a hardened cement paste specimen made of CEM I 32.5R; w/c=0.50; solution with 5% Na2SO4

The proportional mass increase at this does not show any unique dependence on the cement type used and the test liquid. The proportional moisture absorption increases as expected with increasing w/c ratio and the related expansion of the capillary pore system. The maximum moisture absorption of the mortar and concrete specimen also takes place within the first 14 weathering days, it drops however substantially less than for the hardened cement paste specimen and amounts to 3 and 5 m.-% depending on the water cement ratio.

Strain

The following conclusions can be derived from the progress of the axial specimen strains:

- An increase of the w/c ratio leads to higher strains.
- The concentration of the test liquids has likewise a significant influence on the course of the strain (fig. 5). The specimen stored in a solution with 0.1 % Na_2SO_4 and the ones stored in water exhibit a similar, almost synchronous strain behavior. This is characterized by a strain increase at the beginning of the stored, which correlates with the mass increase of the specimen up to achieving moisture equilibrium, and a following constant strain course, on a somewhat higher level in the case of the solution with 0.1% Na_2SO_4. For the specimen stored in a solution with 5 % Na_2SO_4 the initial strain behavior is similar, whereby the duration of this interval depends on the composition of the specimen. A parabolic shaped strain increase follows, which only stops with the destruction of the specimen.
- The cement type used also determines the characteristic of the strain course. As illustrated in fig. 6, the beginning strain behavior is nearly independent of the cement type and corresponds to the beginning strain behavior described before. An approximately linear and only more slightly strain increase follows in the case of the specimen made of HS cement. In the case of the other cement types it gets in first with one of this depen-

dent latency-time to the parabolic shaped increase of strain ending with the destruction of the specimen as described before.

- Clear differences in the strain course between hardened cement paste, mortar and concrete specimen made of the same cement type and the same w/c ratio appeared (fig. 7). A significant accelerating strain increase was already to be observed after 90 days on hardened cement paste specimen made of white cement with a w/c ratio of 0.50 after a weathering with a solution with 5 % Na_2SO_4. In comparison with this, following the initial strain, the mortar and concrete specimen of the same w/c ratio showed up a largely linear, but only weakly pronounced increase of strain, which is larger for the mortar specimen than in the case of concrete, over the entire storage period of 400 days.

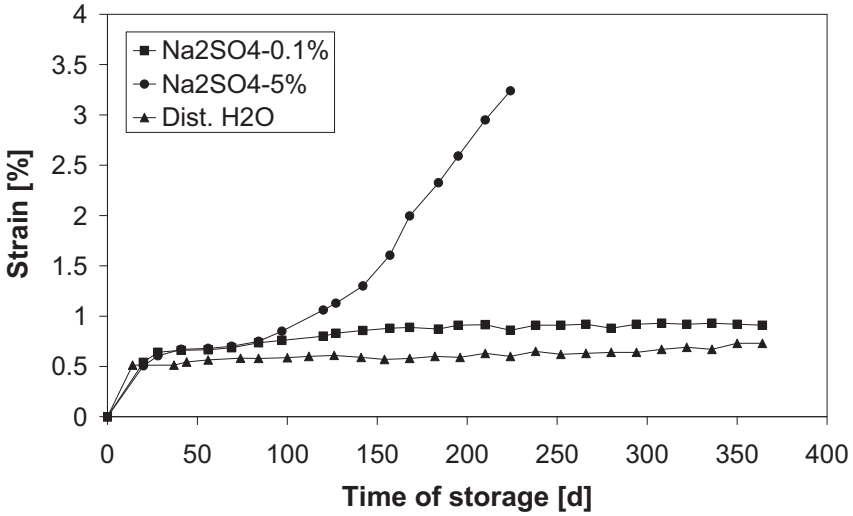

Figure 5: Strain developments as a function of the storage duration depending on the test liquid (hardened cement paste; CEM I 42.5R white; w/c = 0.50)

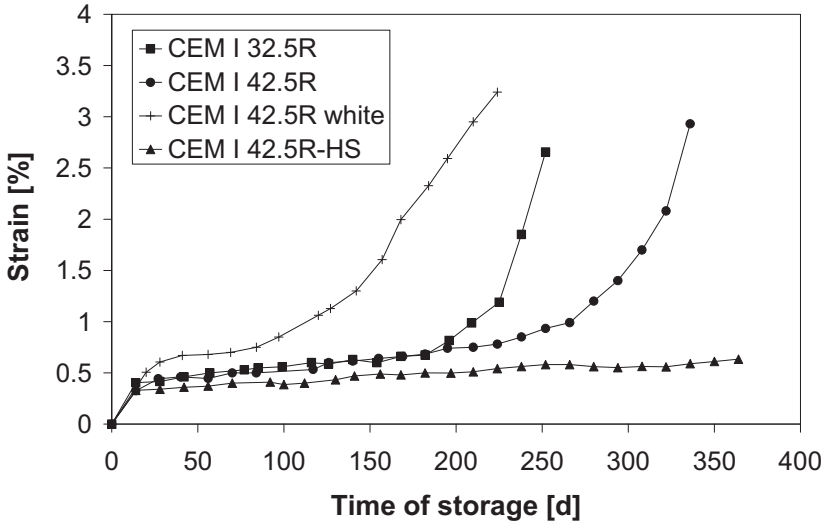

Figure 6: Strain developments as a function of the storage duration depending on the cement type in the case of storage in a solution with 5 % Na_2SO_4 (hard. cement paste; w/c = 0.50)

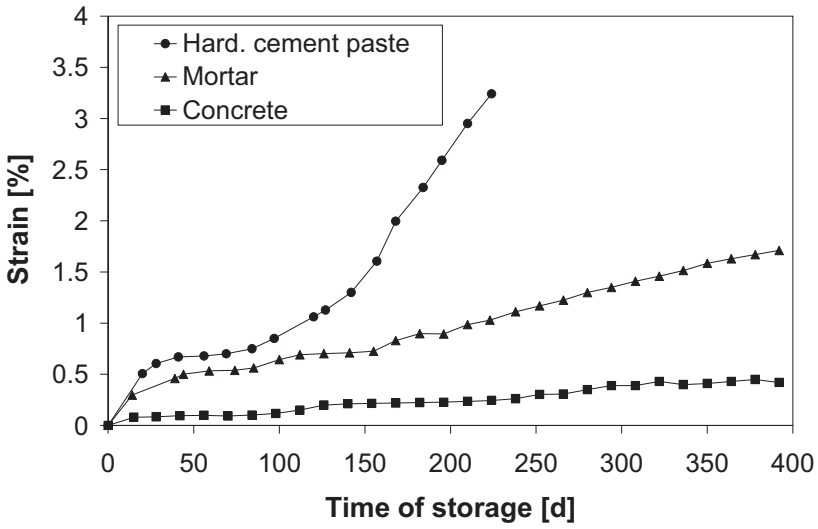

Figure 7: Strain developments as a function of the weathering duration depending on the type of specimen in the case of storage in a solution with 5 % Na_2SO_4 (CEM I 42.5R white; w/c = 0.50)

4.5 Ettringite growth

In order to investigate the ettringite growth in the course of sulfate weathering, a wide specimen spectrum was analyzed in regular intervals on the microscopic level during the weathering. On the basis of the conducted investigations, which are based upon the coupling of scanning electron microscopy, particle analysis and energy dispersive X-ray microanalysis, the following statements regarding ettringite growth within the pore volume of the structure can be done:

- Very varying ettringite shapes appear in dependence of the different parameter combinations. Examples of sphere and pin shaped ettringite formations are shown in fig.8, whereas non-directional and directional growth can be observed in the latter.
- The velocity and the intensity of the new formation of ettringite are dependent on the cement type, whereas in each case the specimen made of white cement showed the fastest ettringite growth due to their comparatively higher C_3A content, which correlates to the statements regarding crack, strain and porosity development (fig. 9).
- The higher the water cement ratio, the more rapidly and more intensively the process of ettringite new formation takes place (fig. 10).
- The higher the sulfate concentration of the weathering solution, the higher the ettringite growth velocity is (fig. 11).
- The size of those pores, in which ettringite growth is observed, is reduced with increasing storage duration.
- The ettringite growth takes mainly place in pores with a size starting from 10 µm. No ettringite growth was observed in pores within the nanometer range (fig. 12).

- The new formation of ettringite and the accrue of the pores in the case of hardened cement paste specimen take place substantially faster than for mortar and concrete. The slowest ettringite growth was to be observed at concrete specimen.

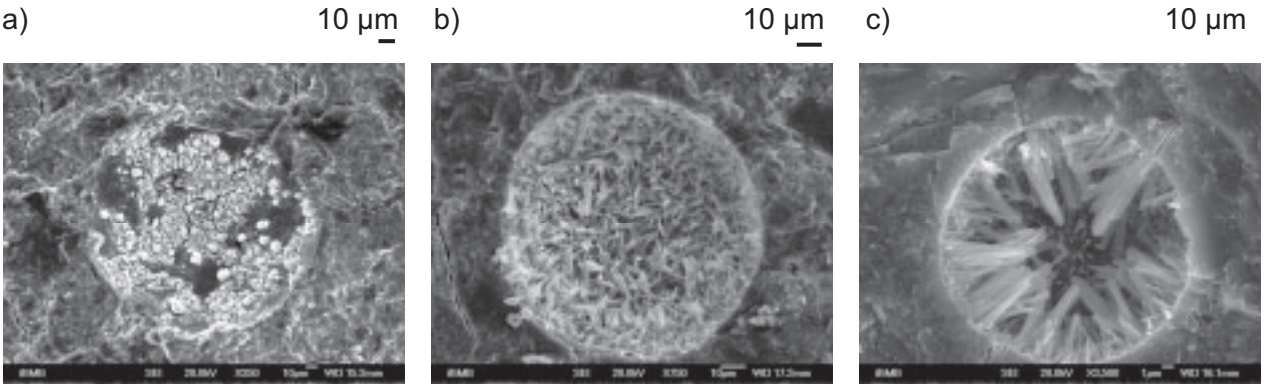

Figure 8: Examples for ettringite formations

a) Sphere shaped ettringite formations
b) Pin shaped ettringite formations (non directional growth)
c) Pin shaped ettringite formations (directional growth)

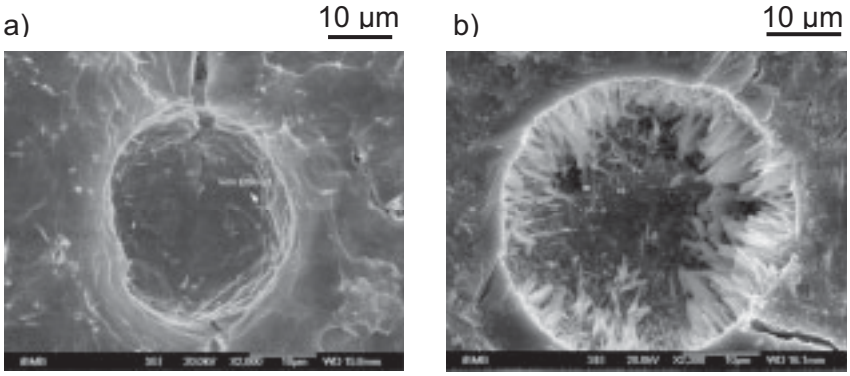

Figure 9: Cement type dependent ettringite growth
(56d storage in a solution with 5 % Na_2SO_4)

a) CEM I 42.5R-HS; w/c=0.40 - no new ettringite formation in a pore
b) CEM I 42.5R white; w/c = 0.40 - new ettringite formation in a pore

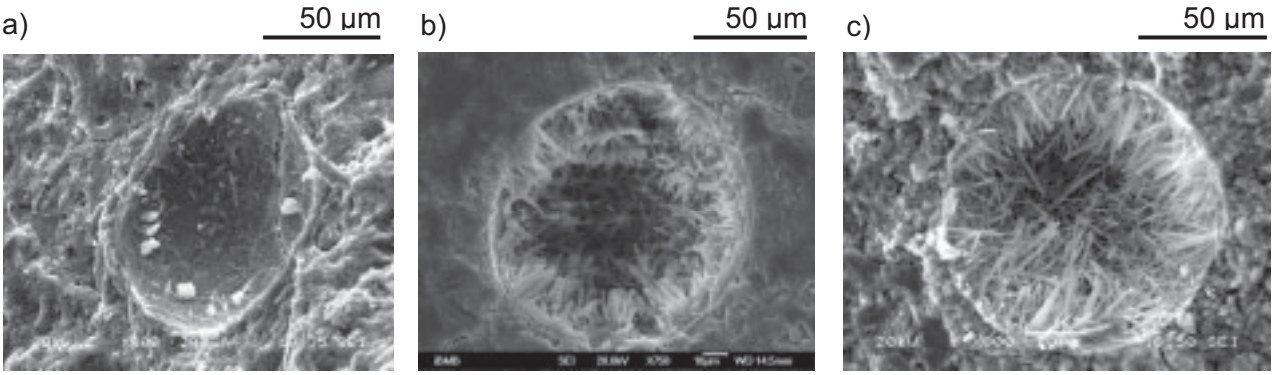

Figure 10: Water cement ratio dependent ettringite growth
(CEM I 42.5R white; 56d storage in a solution with 5 % Na_2SO_4)

a) w/z = 0.40 – isolated new ettringite formation in a pore
b) w/z = 0.50 – increased new ettringite formation in a pore
c) w/z = 0.60 – pronounced new ettringite formation in a pore

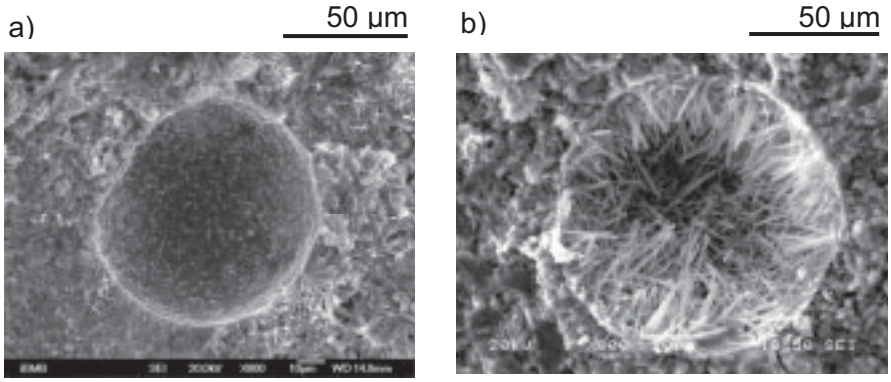

Figure 11: Ettringite growth vs. Sulfate concentration of the storage medium
(CEM I 42.5R white; w/c = 0.6; 56d storage)

a) Solution with 0.1 % Na_2SO_4 - no new ettringite formation in a pore
b) Solution with 5 % Na_2SO_4 - new ettringite formation in a pore

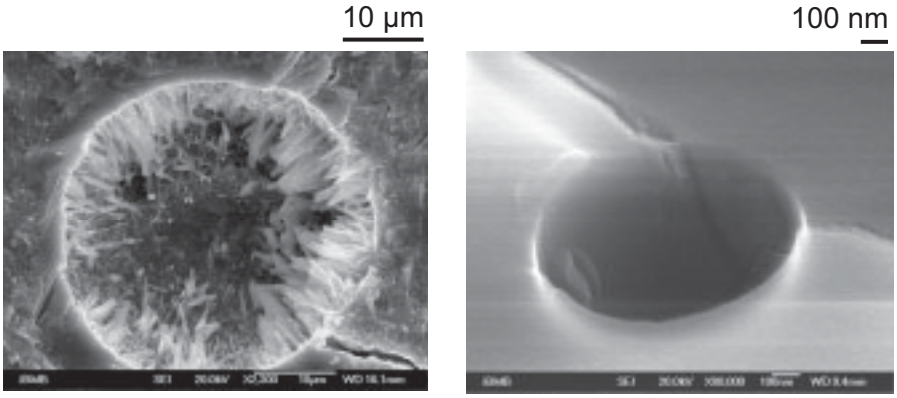

Figure 12: Pore size dependent ettringite growth (hardened cement paste CEM I 42.5R white; w/c=0.40; 56d in solution with 5% Na_2SO_4)

5 Discussion and outlook

The spotlight of this research project was the determination of chemical, macro and micro structural input data for the validation and the verification of a model, which describes the deformations resulting from a sulfate attack due to new formation of crystals in the pore volume of the microstructure. For the determination of these input data an extensive investigation scenario was developed and conducted, which provides the following results with renouncement of the presentation of quantitative structural data, since these are not yet sufficiently throve due to the not approved proposal of the third funding period:

Compressive and flexural strength

The compressive strength is as far as possible independent of the species of the applied medium within the regarded storage period of 91 days. Differences were to be determined here primarily between the strength development hardened cement paste and mortar specimen. Due to their mixture composition the mortar specimen exhibited higher compressive strengths within the test period than the prisms made of hardened cement paste. Clear differences showed also up in particular with the sulfate stored specimen with regard to the strength development. The significant rise of the compressive strength, as observed after 28 days in the case of the hardened cement paste specimen, did not arise for the mortar specimen. Here the strength development was approximately constant during weathering. Probably this behavior can be attributed to the higher porosity of the hardened cement paste, since the ettringite formation in the pore volume leads first to an increase of compressive strength. This assumption is confirmed by the observation of the strength development during immersion in water, where this significant increase was not to be observed.

While the climatic storage leads to an increase of strength at the beginning of the test period, an approximately constant course could be observed with the storage in the solutions. The strength

was there higher during water and sulfate storage at the beginning the test period than during climatic weathering. The immersion in water apparently causes a re-hydration and the sulfate storage additionally also causes a strength increase as a consequence of the crystallization in the pore volume of the microstructure. While the flexural strength values of the specimen stored in water remain constant, they are decreasing in the course of the sulfate storage, with exception of the samples made of HS cement. An increasing crystallization pressure in the course of the storage, which entails microstructure damages and finally losses of strength, follows the initially positive effect of a sulfate storage on the strength of the microstructure with somewhat higher strength values than during the immersion in water.

On the basis of the results of flexural and compressive strength, it becomes apparent that with the focus on the flexural strength, the influence of a sulfate attack on the specimen strength emerges more clearly than compared to the evaluation of the compressive strength development. That is confirmed by the statements of Stark et al. [7], who likewise connect a strength decrease caused by structure damages with a decreasing flexural strength, while they assign a more subsidiary role to the determination of the compressive strength. Mulenga [8] also comes to fruition that the determination of the compressive strength is not suitable for the evaluation of the sulfate stability.

Porosity

There is a good correlation between the results of the porosity measurements and the strength tests, with which the mortar prisms already showed a higher resistance against the sulfate action. That is confirmed by means of the porosity measurements. After an initial decrease of the porosity due to the ettringite formation starting in the pore volume, an increase of the overall porosity for hardened cement paste in the course of the sulfate storage starting earlier as in the case of mortar and concrete appeared on the one hand. This indicates a starting specimen destruction. On the other hand the faster decrease of the average pore radius refers to a quick crystal growth and an associated increased destruction velocity. Similarly to the results of the flexural strength the porosity investigations signal that the specimen made of white cement exhibit the slightest resistance against the attacking medium due to the comparatively high C_3A-content for hardened cement paste, mortar and concrete specimen.

The variation of the porosity parameters within the considered period of 300 weathering days indicates structural changes due to the sulfate action. No significant differences were observed regarding the measured porosity parameters of investigated specimen made of CEM I 32.5R after 300 days in the experiments conducted by Schmidt-Döhl [9]. Only for a w/c ratio of 0.60 an increased porosity was determined after the weathering with a Na_2SO_4 solution of approximately the same concentration.

Crack formation and propagation

The statements for the crack formation and propagation corroborate the preceding investigation results. While the crack formation of e.g. hardened cement paste specimen made of white ce-

ment with a w/c ratio of 0.60 already began after approximately 40 days storage in a solution with 5% sulfate, first cracks were observed at mortar and concrete specimen of comparable composition only after approximately the quadruple storage time. This fact can be explained by the higher porosity resulting in an increased salt transport and a more rapid crystal growth and the lower strength of the hardened cement paste compared to mortar and concrete.

The cement type likewise has influence on the damage process. In good agreement with the results reported by Malorny [10], the destruction process begins earlier for specimen made of white cement, due to comparatively high C_3A-content as with the other cement types, whereby the damages with continuous sulfate action lead to the complete decay of the specimen. Whereas a self strengthening effect resulting from the initial cracking, as it appears in the strain developments. To such an extent the statement of Stark et al. [7], after what the cracking comes along with partly extreme length variations, can be confirmed on the basis of the own investigations.

The duration of the sulfate attack has influence on the degree of damages by the continuous provision of the reaction partners and the constant crystallization coming along with it. The longer the specimen are subjected to a sulfate attack, the more intensive the damages are, which can lead to the complete destruction of the specimen, which is confirmed by Mulenga [8]. Thereby the specimen made of HS cement form an exception by the limited provision of calcium aluminates hydrates, which are likewise needed beside the sulfate ions as reaction partners for the ettringite formation.

Measurement accompanying the storage

The discrete investigation sections for the timing optimization of the scanning electron microscopic analyses were determined at a first specimen batch by means of the measurements accompanying the storage, which covered the regular determination of the specimen strain as well as the specimen mass in the course of the storage. The already available results of the first specimen batch could be verified on the basis a second batch. According to the results of the strain measurements the specimen strain depends on the cement type, the water cement ratio, the concentration of the sulfate solution and the specimen time.

Thus the specimen made of white cement showed the highest strains each due to their high C_3A content, whereby the statements regarding porosity and crack growth are supported. In the case of specimen made of sulfate resistant (HS) cement no significant strain increase appeared in the course of the sulfate weathering despite an ettringite formation in the pore volume of the microstructure. In his investigations Gasser [11] also already determined expansion phenomena when using white cement and the absence of such strain processes when using cements containing C_4AF (HS). The specimen made of CEM I 32.5R and CEM I 42.5R likewise reacted to the sulfate action with expansion strains, however with a temporal delay compared with the specimen made of white cement. Schmidt-Döhl [9] also determined such expansion strains with specimen made of CEM I 32.5R with varying w/c ratios.

The enlargement of the capillary pore system due to an increasing w/c ratio entails an increased sulfate transport in the microstructure of the specimen and thus earlier starting of noticeable strains. This corresponds with strain increase of the specimen made of CEM I 32.5 R with increasing w/c ratio, as observed by Schmidt-Döhl [9]. Bollmann [12] identifies the water cement ratio as a crucial factor of influence regarding ettringite formation in hardened concrete, since a more dense structure and higher strengths are related to a lower w/c ratio.

Considering the influence of the sulfate ion concentration the comparatively unstable hardened cement paste specimen made of white cement showed no significant increase in the strain development also after one year storage in the solution with 0.1% sulfate, while with the specimen of identical composition weathered with the solution with 5% sulfate showed such strain already after 90 days. Those confirm investigations of Mulenga [8], whereas specimen even weathered with a solution with 0.22% sulfate still did not exhibit any damages after one year. However the specimen tested there are mortar prisms, which experiential prove to be as more resistant. Nevertheless no damages could also be determined with the mortar specimen tested here after one year weathering with the low concentrated solution.

Investigations of the microstructure

The microstructure investigations of hardened cement paste, mortar and concrete specimen, which covered the coupling of scanning electron microscopy, energy dispersive X-ray microanalysis (EDX) and particle analysis, were differentiated regarding the varying specimen composition, the concentration of the weathering solution and the storage time. The ettringite growth located in the pore volume of the microstructure was in the spotlight of the investigations. As in the case of investigation methodologies already described, it also appeared here that the effects of a sulfate attack are depending on varying factors considering the ettringite growth.

Thus the high C_3A-content of the white cement, which is classified as the substantial cement component for the late formation of ettringite according to [7], leads to a more rapid ettringite growth, which explains the comparatively quicker crack growth and the results of the porosity measurements. On the other hand despites ettringite growth there were no damages to be determined in the case of the specimen made of HS cement in the course of the storage. The test results of Schmidt-Döhl [9] and Schröder/Hallauer [13] support this just like the statements of Stark et al. [7].

The increase of capillary porosity due to an increasing w/c ratio leads to an increased new formation of ettringite, which is confirmed by the higher strains, the smaller strengths and the increased crack growth.

As already determined in [14], the concentration of the sulfate solution likewise has an influence on the process of the formation of new ettringite and the associated expansion phenomena. Both the microstructure investigations as well as all other investigations conducted within the framework of this research project identify the sulfate concentration of the solution as an important variable influencing the crystal growth. This influence results from the increasing of the po-

tential of the reaction partner coupled with higher sulfate ion concentration and the increase of the velocity of the ettringite formation following.

After the results of the scanning electron microscopic investigations the structure destruction is caused mainly by the crystal growth in pores with a pore size starting from approx. 10 µm. On the one hand it was found in this connection it that no ettringite is situated in pores of the nanometer range, on the other hand that the crystal growth increases with increasing pore size. According to Malorny [10] new formations of ettringite were found mainly in larger air voids in the pore volume of the microstructure. The results of the microstructure investigations confirm the statement of Schmidt-Döhl [9] according to which it is not necessary to fill out the entire pore volume of the building material with solid material in order to generate expansion.

As the scanning electron microscopic investigations conducted by Stark et al. [7] already have shown, very varying forms of the ettringite occur, which extend from spherical aggregations up to felt like or parallel arranged prismatic crystals of varying size. However the cause for these varying morphologic phenomena could not be clarified so far.

As the results of the strength tests, porosities and strain measurements as well as crack growth already make clear, the velocity of the formation of new ettringite also depends on the specimen type. Thus the concrete specimen showed the most resistant behavior against sulfate action for all investigations, while the lowest resistance against the attacking medium was registered in the case of hardened cement paste specimen. This connection correlates with the results of the microstructure investigations. Afterwards due to the comparatively higher porosity the new formation of crystal takes place within the hardened cement paste specimen in the fastest way and the most slowly within the concrete samples.

The following points are of interest regarding the future research requirement:

- Apart from the past investigations regarding the growth of ettringite in the pore volume of the microstructure of concrete is to be aimed to also identify the various phases of the bonding agents as well as to characterize the spatial arrangement of the pore system and the solid structural constituents, in order to be able to make statements about variations of the microstructure and about the variation of the ratio matrix, pore system and clinker residues in the course of sulfate weathering.
- Since the transport and crystallization processes primarily take place in the capillary pore volume, the recording of its physical structure is a substantial condition both for the micromechanical observations to local deformations on the micro scale as well as to macroscopic structural variations, which in particular concern the cracking and the crack propagation processes. By the gradual uptake of defined sample sections in combination with the following degradation of the sample surface in each case so called image field stacks can be generated, which step instead of individual pictures and so make the transition possible from the two-dimensional image of the structure to the three-dimensional record and representation of the microstructure.

- Further clarifying requirement exist due to the lack of sufficient knowledge about the cause and the effect of the occurrence of varying ettringite formations.

6 References

[1] DIN EN 196-1: Prüfverfahren für Zement – Teil 1: Bestimmung der Festigkeit; Ausgabe Mai 1995

[2] DIN 18555-3: Prüfung von Mörteln mit mineralischen Bindemitteln – Teil 3: Festmörtel, Bestimmung der Biegezugfestigkeit, Druckfestigkeit und Rohdichte, Ausgabe September 1982

[3] Romberg, H. : Zementsteinporen und Betoneigenschaften, Beton-Information 5 (1978), S. 50-55

[4] Schneider, U.; Herbst, H. J.: Porositätskennwerte von Beton, TIZ-International 113,

(4 / 1989), S. 311-321

[5] Böttger, K. G.: Einfluss der Präparation auf die Ergebnisse der Hg-Druckporosimetrie von Zementmörteln und Beton, Symposium Mercury intrusion porosimetry of building materials, Bundesanstalt für Materialforschung und –prüfung, 2000

[6] Setzer, M.J.: Einwirkung von Kohlendioxid, Schwefeldioxid und Wasser auf Beton, Fachragung Langzeitverhalten und Instandsetzen von Ingenieurbauwerken aus Beton, München 1987, Hrsg. R. Springschmidt, München: Baustoffinstitut, S. 1-4, 1987,

[7] Stark, J., Wicht, B.: Dauerhaftigkeit von Beton – Der Baustoff als Werkstoff, F. A. Finger-Institut Weimar, Basel, Boston, Berlin: Birkhäuser, 2001

[8] Mulenga, D. M.: Zum Sulfatangriff auf Beton und Mörtel einschließlich der Thaumasitbildung, Dissertation, Bauhaus-Universität Weimar, 2002

[9] Schmidt-Döhl, F.: Materialschädigung durch Phasenneubildungen in mineralischen Baustoffen, Final project of research report, DFG, 2001

[10] Malorny, W.: Mikrostrukturuntersuchungen zum Sulfatangriff bei Beton, Dissertation, Technische Universität Braunschweig, 1996

[11] Gasser, M.: Untersuchungen über das Zustandekommen des Sulfattreibens, Dissertation, Technische Universität Clausthal, 17. 1987

[12] Bollmann, K.: Ettringitbildung in nicht wärmebehandelten Betonen, Dissertation, Weimar, 2000

[13] Schröder, H. T., Hallauer, O.: Beständigkeit verschiedener Betonarten im Meerwasser und in sulfathaltigem Wasser, Deutscher Ausschuss für Stahlbeton, Volume Nr. 252, Berlin 1975

[14] Bellmann, F.: Gefährdungspotential der betonschädigenden Thaumasitbildung, scientific report, F. A. Finger-Institut Weimar, 2004

Ralph Haberkern
Dr. rer. nat.

Heike Emmerich
Prof. Dr.-Ing. Dr. rer. nat. habil.

RWTH Aachen University, Aachen, Germany

A Hybrid Simulation Approach to Simulate Micro-Structural Dynamics in Cement

Summary

To model jointly microstructure evolution, chemical kinetics and relevant transport processes in cementitious materials, we developed a coupled phasefield-cellular automaton approach. Here we demonstrate the capability of the approach for two phenomena relevant in the processing of cement, namely sorption and microstructure evolution during hydration.

Keywords: *hybrid simulation approach, micro-structural dynamics, cement*

1 Motivation

The microstructure evolution of cementitious materials strongly influences the material properties of the hardened product. Already, several tools exist for the dynamic prediction of this microstructure evolution, e.g. [1], [2]. These cellular automata based methods offer a good description of the structure evolution. However, the diffusion and transport of ions and water is hard to model within this framework. Phasefield methods [3] provide an elegant approach for the simulation of crystallisation and diffusion. However, the complexity of the processes in curing cement makes it hard to model all these effects within a partial differential equations framework. Therefore we suggest a handshake of methods, to combine the advantages of both methods. For testing of fresh cementitious materials, the simulation should not only compute the evolving microstructure, but should also return status parameters that can be verified in experiments. Whereas the temperature rise can be predicted very well from cellular automata setups, quantities like the electrical conductivity or porosity are not directly accessible to these methods. Similarly, the chloride adsorption of hardened cement is difficult to predict with CA techniques. Partial differential equation methods can produce these quantities more easily. Our phasefield description of the solid-fluid interface enables application of these methods regarding different physical questions.

2 Problem Description

The simulation of the cement structure in the mesoscopic neighbourhood of curing effects is set up as a simplified model of flow and flow-augmented diffusion. This two-stage model allows the prediction of the flow resistance for porous periodic structures and the cumulated emission of slowly solving ions or slowly adsorbed ions from the fluid. This approach applies to arbitrary ion flows on the solid-fluid interface. Therefore, the Gibbs-Thomson relation can be used to predict the growth or dissolution of crystal layers on the pore space interface. When coupled with a time-stepping method, the evolution of the microstructure can be computed. However, this requires that the structure is described with a smooth boundary, such that the curvature of the structure exists for the Gibbs-Thomson relation to be well defined. This means that during time-stepping, the description of the structure has to be updated, accordingly. Moreover, chemical reactions can be considered by using cellular automata like Cemhyd3D or the G. Locher CA [1]. Thus our method is the first to simulate the transport of ions at the microscale coupled with the full chemical reactions scheme. It uses the phasefield concept [3] to apply partial differential equation techniques for diffusive processes, to obtain a hybrid CA. The simulation of the cement structure in the mesoscopic neighbourhood of curing effects is set up as a simplified model of flow and flow-augmented diffusion. This two-stage model allows the prediction of the flow resistance for porous periodic structures and the cumulated emission of slowly solving ions or slowly adsorbed ions from the fluid. This approach applies to arbitrary ion flows on the solid-fluid interface. Therefore, the Gibbs-Thomson relation can be used to predict the growth or dissolution of crystal layers on the pore space interface. When coupled with a time-stepping method, the evolution of the microstructure can be computed. However, this requires that the structure is described with a smooth boundary, such that the curvature of the structure exists for the Gibbs-Thomson relation to be well defined. This means that during time-stepping, the description of the structure has to be updated, accordingly. Moreover, chemical reactions can be considered by using cellular automata like Cemhyd3D or the G. Locher CA [1]. Thus our method is the first to simulate the transport of ions at the microscale coupled with the full chemical reactions scheme. It uses the phasefield concept [3] to apply partial differential equation techniques for diffusive processes, to obtain a hybrid CA.

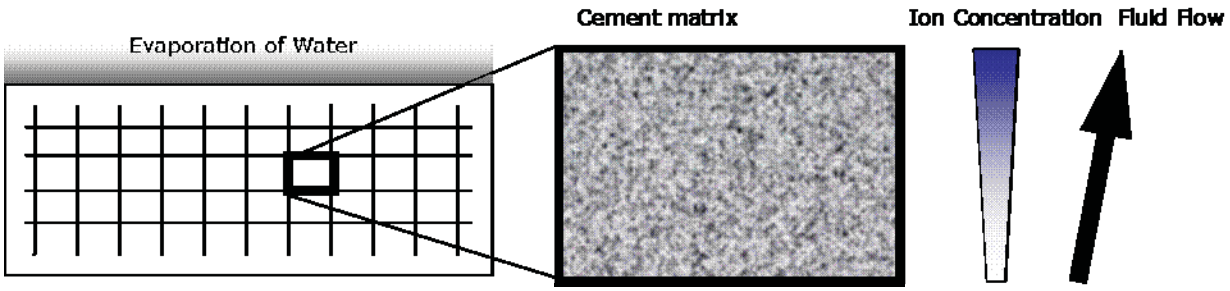

Figure 1: Problem description

On the free surface of curing cement, as you can see in Figure 1, water evaporates. A mesoscopic fluid flow to the surface competes with a developing concentration gradient on ion transport.

3 The Starting Point: The Cement Structure Simulated by Cellular Automata

First we describe the data produced by cellular automata [1], [2]. The bitmaps returned by these methods require special treatment to be processed with phasefield methods for the simulation of flow and diffusion.

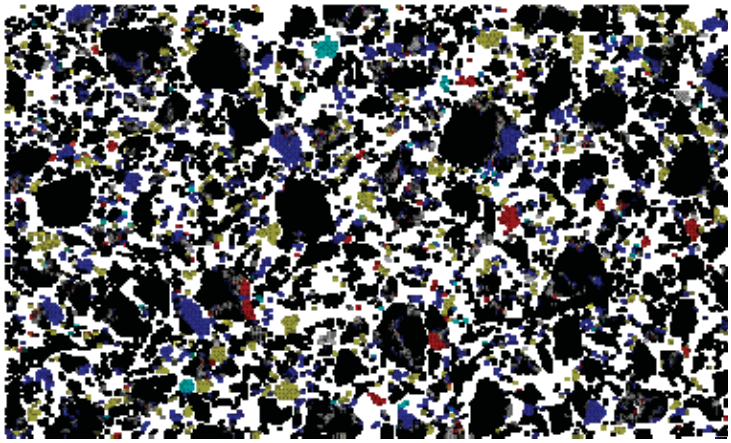

Figure 2: Cement paste structure at time index zero [2]. Beginning with real cement powder images, cemhyd3d generates an artificial cement powder distribution of spheres of different size. Several statistical properties like particle diameter and correlations are conserved.

For the virtual cement matrix, all ingredients like clinker and anhydride particles are simulated as spheres. Chemical composition, particle size distribution and neighbour correlations and the water to cement ratio are reproduced in statistically correct manner. Based on this artificial periodic microstructure, cellular automata compute the evolution of the microstructure. Both Cemhyd3D and the cellular automata of G. Locher are based on voxels and yield dithered images with large high frequency contents for the ongoing hydration process (Figure 3).

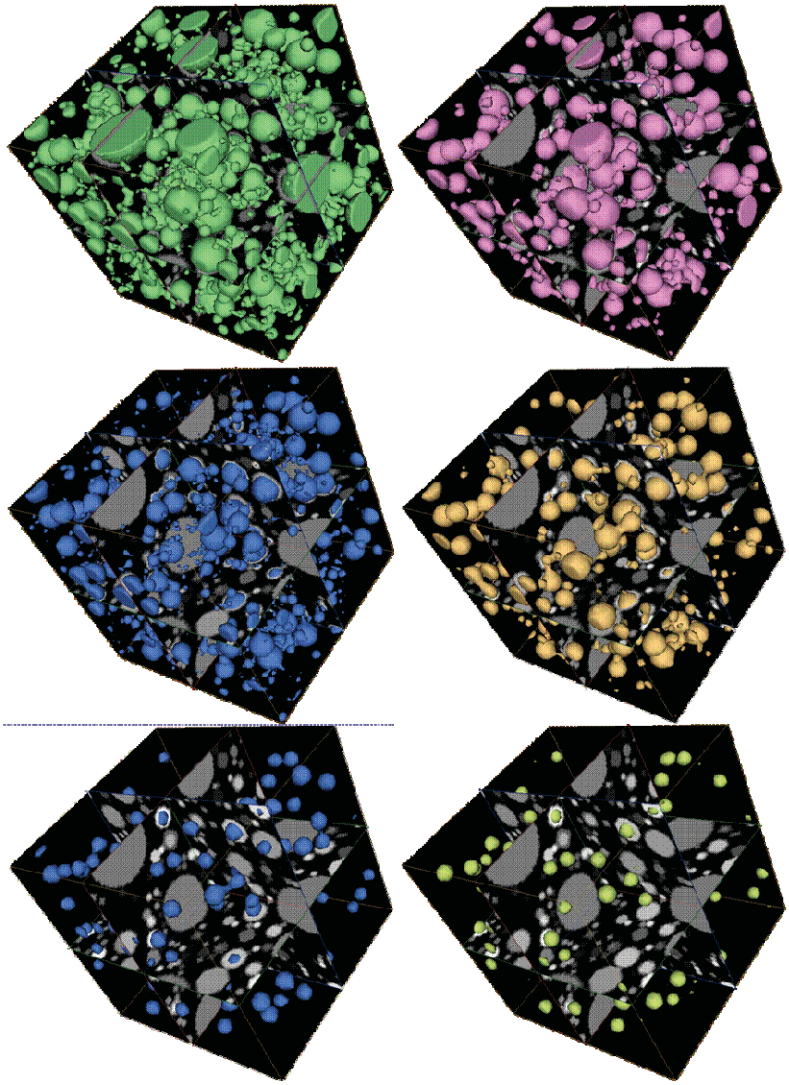

Figure 3: Evolution of cement matrix according to simulations developed for display in the CME of RWTH Aachen

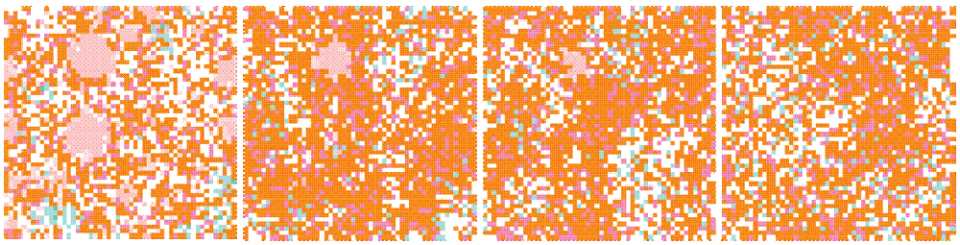

Figure 4: Cement Hydration from the G. Locher CA [2]. The cement microstructure evolution for CA steps 10, 100, 200 and 500

The bitmaps of indexed cellular automata are not directly suited for treatment with partial differential equation techniques. Smoothing is required to obtain a suitable solid-fluid interface.

4 The Methodological Modules

4.1 Survey on the Modules of the Hybrid Phasefield-CA Approach

In figure 5, we present the details of the hydrodynamic transport model of this combined ansatz. The early stage of CS dissolution and the growth of CSH crystals as a major mechanism of cement structure evolution can be simulated. Furthermore, as a particularly import application, the model can describe the adsorption of chloride ions by hardened cement paste. The hydrodynamic simulation consists of a time-stepping module, which computes the velocity and concentration fields, and a material parameters model, that processes the results to specific effective material parameters of the fresh cementitious slurp (FCS). This enables the prediction of both structure evolution and the dynamics of key material properties during the hardening of the cement paste. This model also allows the prediction of chloride absorption.

4.2 Module I: The Cellular-Automata-Phasefield Interface

The general technique is the spline approximation of the characteristic of a bitmap. That is, e.g. Cemhyd3D data is given as bitmap with values in a range {0..n}. The indices of water and ions are mapped to 0 (black), solid components are mapped to 1 (white), yielding a b/w bitmap. The characteristic Ξ of the bitmap is the discontinuous function returning -1 or 1 if r is inside the solid or fluid. This discontinuous function is not suited for smooth spline approximation.

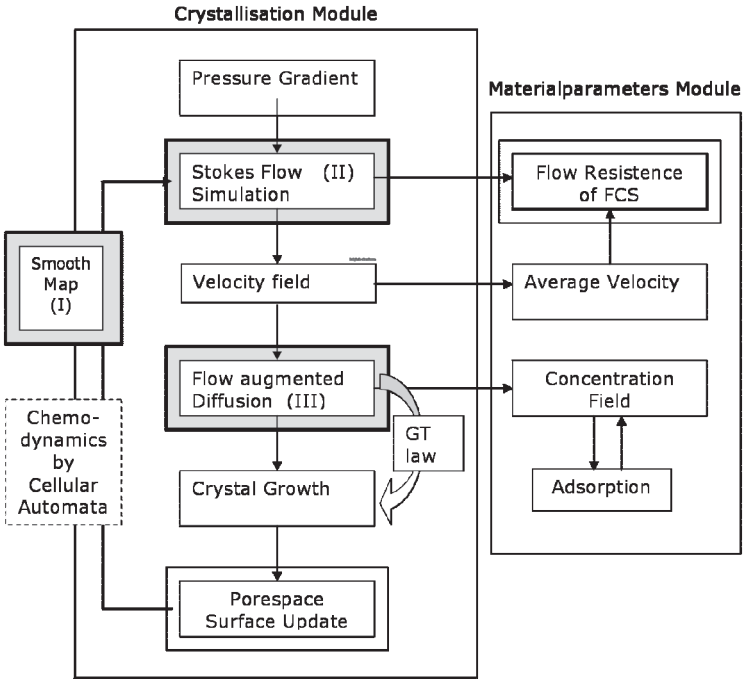

Figure 5: The methodical setup of this method. Subsequently, the Modules I, II and III are inspected in more detail. They form the key modules of this approach.

However the ±1 bitmap entries can now be interpreted as the coefficients of a spline of quadratic degree (general: degree q). For a single step in one dimension, this smoothing operation

$\Xi \rightarrow \Xi(\Xi_q)$ does not change the step. In two or three dimensions it provides a smoothing map from a bitmap - to the phasefield-representation of solid-fluid interfaces.

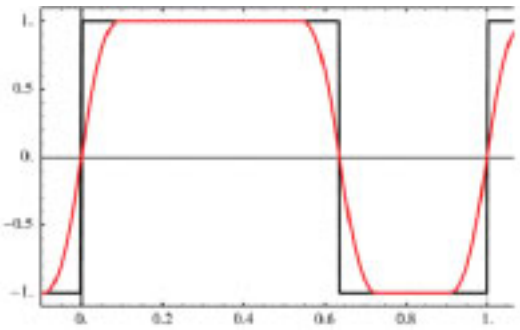

Figure 6: Spline smoothing of 1d-bitmap (1,1,1,1,1,1,1,0,0,0,0)

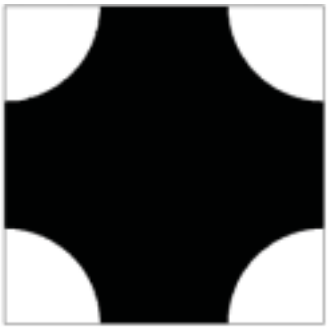

Figure 7: Simplified model geometry

With this technique, the geometries from e.g. Figure 2 can be imported from the cellular automata**.** Simple model geometry in affiliation to Figure 2 is given by the periodic lattice of equidistant spheres in 2D. Though simple in structure, it contains all elements to develop and test the partial differential equation modules of this method. The two-dimensional unit cell for a periodic lattice of size 1x1m is set as a square domain with solid spheres of radius 0.3 in the centres of the lattice. The pore space is represented in black. This model geometry is a simple prototype for the artificial periodic structures that e.g. Cemhyd3d generate as the initial solid-fluid geometry of the cement paste hydration simulation at time index 0.

4.3 Module II: Stokes Flow through periodic structures

At the free faces of a volume of curing cement water evaporates into the air. On a mesoscopic scale, this causes a flow of water to the outer regions of cement. Near the surface, this flow is normal to the free surface (that is horizontal for fresh cementitious materials). This flow of water is important for the structure evolution near the surface as it causes a transport of ions through the cement paste.

The flow of water through the periodic lattice of the cement paste is driven by a mesoscopic pressure gradient P_{mes} . The solution is described by the pressure distribution p and the velocity u inside the pore space Ω. considering the mesoscopic pressure gradient, the pressure can be written as sum of the linear mesoscopic field $p_{mes} = P_{mes} \cdot r$ and a periodic microscopic field: $p = P_{mes} \cdot r + p_{mic}$ The velocity u is periodic, as the driving pressure gradient is the same for each cell.

As the pore space of fresh cementitious materials is filled with water, the system is governed by the Stokes equation for incompressible flow:

$$\Delta u + \nabla p = 0, \qquad \operatorname{div} u = 0$$

We can assume that the fluid sticks to the pore space surface $\partial\Omega$. Then the problem can be formulated mathematically as the Saddle point problem ([6], p.138, c.f. [5])

Find u,p_2 in $H_0^1(\Omega)\otimes H_0^0(\Omega)/1$: (or equivalently)

$$\int_\Omega \left[\nabla u \nabla v + p_2 \operatorname{div} v\right] dV = -\int_\Omega P_1 v\, dV \qquad a(u,v)+b(v,p)=(-P_1,v)_0$$

$$\int_\Omega \left(\operatorname{div} u\right) q\, dV = 0 \qquad b(u,q)=0$$

The velocity field depends linearly on the macroscopic pressure gradient P_1. It is sufficient to solve the problem for each unit direction $P_1=e_i$.

The following examples show the pressure and velocity fields for P_1=(1,2), computed with the FE Software Package NGSolve [4] for the model geometry of Figure 6. Due to the incompressibility of the fluid, the average volume flow rate F through the pore space equals the average velocity <v>. There is a linear dependency between the average volume flow rate F and the pressure gradient P_1: $F=R\,P_1$, where the matrix R is the resistance to flow of the structure. This method can be applied to the complex geometries encountered in the Cemhyd3d simulation. This software operates on indexed bitmap structures. Once the pore space is identified as a Boolean bitmap, it is useful to smooth this rough and pixeled structure by transformation into an implicitly given surface to a smooth function, e.g. by Fourier or spline approximations.

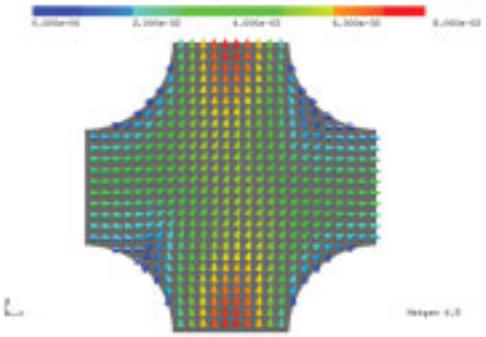

Figure 8: Vector field of velocity u

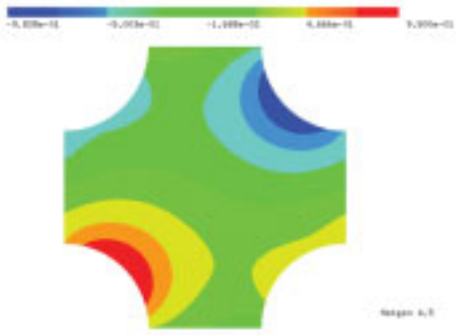

Figure 9: Pressure-distribution p_2

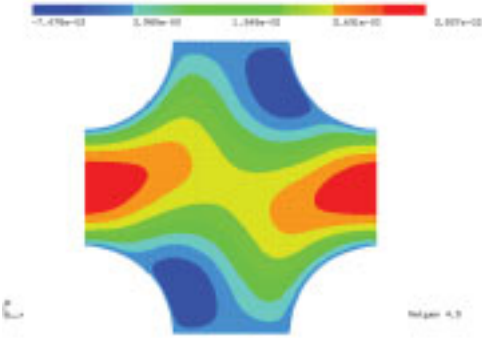

Figure 10: X-component of u

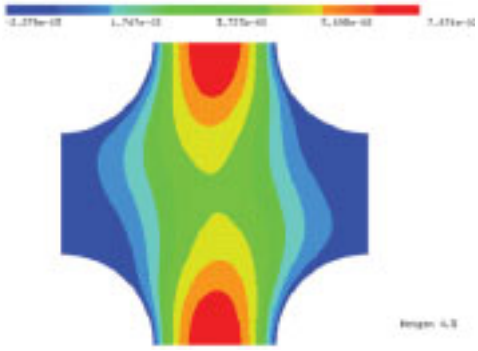

Figure 11: Y-component of u

This procedure operates on the scale of the approximation error of the cellular automata. It eliminates disturbing pixel effects on the boundary. This procedure is necessary to compute the curvature (and the true normal vector) of the surface. Then we can apply the partial differential equation methods to compute the quasi static approximation, and with time-stepping, the development of flow resistance over time for arbitrary solid-fluid structures.

4.4 Module III: The Flow-augmented Diffusive Transport

The surface of a single cement clinker particle exchanges ions with the fluid. If a mesoscopic flow is present, then the transport of ions is directed. Subsequently, a relative concentration plume will develop in the flow. This anisotropy should cause a directivity in the porosity of the evolving cement structure. Therefore, the curing conditions are important for the cement microstructure. In our simplified model, we consider the transport of a pure salt. The flow-augmented diffusive transport equations are

$$J = -D\nabla C + C \cdot v, \qquad \dot{C} = -\nabla J + f \tag{1}$$

The salt is gradually washed out by the fluid flow through the structure. It can be assumed that for the range of unit cells considered, the dissolution rate is independent of the concentration, as long as the concentration is well below the concentration of saturation and for the section of unit cells considered, the change of concentration is still small. Then a linearization of the physical setup can be made, and (for the finite neighbourhood of cells in a periodic grid) it can be assumed that a quasi static, mesoscopically linear concentration field $C = C_p + c_1 \cdot r$ will develop. In each cell, the same amount of ions is solved. Already for the problem without flow, a mesoscopically linear concentration field can be present. Then, an ion flow $J_{mac} = \vec{j}_0 + (\hat{j}_1 r)\vec{j}_2$ of constant direction but linear increasing size is present. If we assume a half space of the periodic structure, then ions are transported to the free surface. The ions will be transported in a direction somewhere between the primary orientation of the pore space and the normal $n = \hat{j}_1$ to the half space. Hence, the scalar product between the normal and the diffusive ion flow is positive: $n \cdot j_2 > 0$. The flow needs to transport both the ions that came from the diffusive flow and its own generated ions. Hence the flow is linear on mesoscopic scale.

On microscopic scale, the developing ion flow field j is divergence-free, as there are no ion sources inside the fluid of the pore space. However, for the linear mesoscopic pressure field J_{mes}, the pore space boundaries contribute a distributed flow of ions to the fluid. Hence, the mesoscopic ion flow is not divergence free. The ion flow from the microscopic boundaries is averaged to a mesoscopically homogeneous ion flow source density f_{mes} and it holds

$$J_{mes} = -D\nabla C_{mes} + C_{mes} \cdot v_{mes}, \qquad 0 = -\nabla J_{mes} + f_{mes}. \tag{2}$$

This equation results from (1) by volume averaging: all mesoscopic elements persist, whereas microscopically periodic quantities drop out. Due to the definition of the linear mesoscopic

pressure field J_{mes}, the mesoscopic ion source density is $f_{mes} = \hat{j}_1 \vec{j}_2 > 0$ and is positive, as it contributes ions to the flow.

Hence, the mesoscopic ion flow obeys the equation $0 = \nabla J_{mac} + \hat{j}_1 \vec{j}_2$.

Subsequently, the microscopic ion flow is divergence free: $0 = -\nabla J + f \to 0 = \operatorname{div} J_p$.

From the concentration law of (1), we can determine the quantitative size of J_{mes}:

$$J_{mes} = -Dc_1 + (c_1 r) \cdot v_{mes}, \text{ such that } j_0 = -Dc_1, \vec{j}_1 = \vec{c}_1, j_2 = \mid c_1 \mid \vec{v}_{mes}. \tag{3}$$

The mesoscopic ion flow is parallel to the constant mesoscopic velocity of fluid flow, but rises linearly in strength along with the rise of the concentration field. For the microscopic quantities, this result leads to the microscopic equation

$$J = -D\nabla C + Cv \to J_p + j_0 + (\hat{j}_1 r)\vec{j}_2 = (-D\nabla + v)(C_p + c_1 r)$$
$$\to J_p + j_0 + (\hat{j}_1 r)\vec{j}_2 = (-D\nabla + v)C_p - Dc_1 + v(c_1 r) \to J_p + (c_1 r)v_{mac} = (-D\nabla + v)(C_p + c_1 r)v$$

This implies $v_{mac} = \langle v \rangle$: The mesoscopic velocity encountered for the mesoscopic fields is the volume average of the fluid velocity v. In continuous continuation, v be zero not only on the boundary of the pore space, but also, formally, inside the solid.

Hence we get the following equation coupling the periodic microscopic concentration fluctuation and the periodic microscopic ion flow fluctuation:

$$J_p = (-D\nabla + v)C_p + (c_1 r)(v - \langle v \rangle) \tag{4}$$

As the mesoscopic ion flow has been expressed in terms of the mesoscopic fluid velocity and the concentration gradient c_1, this equation also only depends on c_1. The next question is how to determine c_1? Due to the conservation of particles, the ion flow is mesoscopically linked with the mesoscopical ion source density f_{me} :

$$J = -D\nabla C + Cv \to \int_{\partial\Omega} JdS = \int_{\Omega} divJdV = \int_{\Omega} fdV = \int_{\Omega} \hat{j}_1 \vec{j}_2 dV = \int_{\Omega} c_1 \langle v \rangle dV$$

On the other hand, microscopically, the ions originate from the pore space surface. Substituting the known ion flow on the boundary yields (*I* is the pore surface of the unit cell, *II* is the unit cell surface of the pore space)

$$\int_{\partial\Omega} wJdS = \int_{\partial\Omega} w\left[J_p + j_0 + (\hat{j}_1 r)\vec{j}_2\right]dS = \int_{\partial\Omega} w\left[(c_1 r)\vec{v}_{mac}\right]dS$$

$$\to \int_{I} w\left[(c_1 r)\vec{v}_{mac}\right]dS = \int_{I} wj_p dS$$

$$\int_{\partial\Omega} wJdS = \int_{I} wj_p dS + \int_{II} wJdS = \int_{I} wj_p dS + \int_{II} w(c_1 r)\vec{v}_{mac} dS$$

This condition holds for arbitrary constant vectors w. The flow balance holds for each direction $w = e_j$, $j = 1...d$: The conditions to uniquely determine c_1 are

$$\int_I (c_1 r) \langle v_i \rangle n_i \, dS = \int_I j_p n_i dS \tag{5}$$

This procedure works for arbitrary ion flow j_p on the boundary!

The ion flow on the boundary determines the local dissolution or the growth of the structure or initiates chemical transformations. When the concentration of the solute is known on the fluid interface, the rules inside the cellular automata of e.g. cemhyd3D determine the sorption rate of the ions for the current time step. Hence the quasi static flow-augmented diffusion computation can be initiated to compute the change of the concentration field during this time window. Also, the solid-fluid interface will be subjected to change due to the transport of chemical elements.

5 Structure Evolution: The Gibbs-Thomson Driven Crystallisation/Dissolution

The following boundary condition is the most important application with regard to the microstructure evolution of fresh cementitious pastes.

The growth of colloid layers obeys the Gibbs-Thomson relation [5, 6]:

$$j = -\max(C, \varepsilon(C - C_r)), \; C_r = \exp(-A\kappa) C_s$$

where C_s is the saturation concentration, which determines on crystal growth of dissolution. Depending on the local curvature of the surface, the Gibbs-Thomson relation returns a reduced concentration that decides upon the local crystallisation / dissolution speed on the solid-fluid interface. The microscopic crystallisation of minerals in cement can be described by isotropic Gibbs-Thomson conditions: a surface element with high curvature forming a surface tip is disproportionately involved in crystal growth, as ions can reach surface points with a higher probability than those points with the negative curvature of a cavity. In application to cement hydration, the microscopic ion flow on the pore space interface can be computed a priori from the known macroscopic concentration C. The local curvature of the surface then is responsible for the $\exp(-A\kappa)$ fluctuations of the ion flow on the boundary. In order to calculate the Gibbs-Thomson driven surface evolution, we can use the flow-augmented diffusion approach (III) based on the computed Stokes flow (II). In order to link this method with cellular automata, the phasefield map (I) enables the Geometry-Import from the CA. Then, the combined the results of the last paragraph combined with the CA allow the computation of the changing concentration fields and the microstructure evolution. A Note on Chloride Absorption: Taking a constant ion flow, one can predict the mesoscopic chloride adsorption of the porous structure. Inverse determination of the ion flow can be used to determine the chloride adsorption coefficients compared to measurements.

6 Application to Sorption Processes

Cement in its early stages is an aqueous suspension of different clinker particles. Reactions take place between the water and the individual chemical components of the admixture, such that the clinker particles become hydrated, substances are dissolved into the water and chemically adsorbed at the surface of other particles. Hence this is a highly complex dynamical system of hydration, diffusion and chemical reactions. When finally hardened, the focus of chemical reactions within the pore space is shifted to damaging mechanisms like carbonisation due to the chemical adsorption of carbon dioxide or reactions due to entering sodium chloride or sulphates. Again, solutes from the pore space solution react with the surface now of the cement stone matrix. Goal of our investigations is the setup of a simulation scheme that takes into account sources of ions, diffusion transport and adsorbing drains. It uses a porous periodic microstructure with a chemical solution in the pore space and different chemically active surfaces of the pore space to model the time-dynamic evolution of the ion concentration in the pore space and the dissolution and adsorption rates of the substances on the chemically active inner boundary.

6.1 The Basic Diffusion Model

We restrict our considerations to the ion concentration of one substance. Hence, the ion concentration in the pore space is determined by the basic diffusion equation

$$\dot{C} = \nabla(D\nabla C) \tag{1}$$

The concept of this work can be extended to chemical multi component systems in that C becomes a vector of concentrations and D a matrix of diffusion constants in the most simple case. However, the basic characteristics of the system can already be seen for a chemical system of one species. Then, the following boundary conditions can be applied:

total adsorption on the boundary	$C = 0$	(2a)
inert boundary	$C_{,n} = 0$	(2b)
Robin adsorption	$C_{,n} = -\alpha C^{+}$	(2c)
prescribed ion flow	$C_{,n} = const$	(2d)
Gibbs-Thomson relation	$C_{,n} = -\exp(A\kappa)C$	(2e)

This means that a) all ions are adsorbed on this boundary such that the concentration on the surface is zero, b) nothing happens on an inert boundary such that the ion flow normal to the boundary is zero, c) the ion adsorption is proportional to the concentration, d) a given dissolution rate is prescribed, e) the Gibbs-Thomson relation gives a curvature-dependant adsorption rate on the boundary.

6.2 Smoothed Geometrical Modelling

The diffusion in the pore space solution for structured periodic media, e.g. with a concentration-driven adsorption on the pore space surface, requires the normal vectors of the structure to be known. However, from practical measurements like CT or simulation models like cellular automata, only bitmap raster image representations of the pore space are available. Therefore, general smoothing techniques are needed to get a quantitative approximation of the geometric surface properties as far as possible. An implicit phasefield function [3] is used for this purpose. This also allows for models like the Gibbs-Thomson relation [5] for crystallisation to be applied.

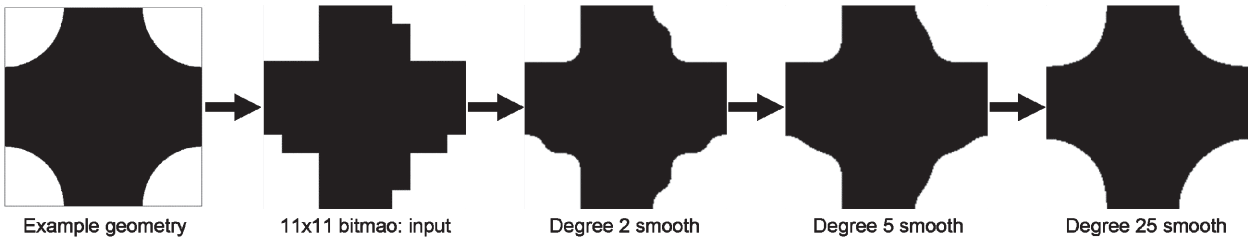

Figure 12: A two-dimensional example geometry (left)

In Figure 12 a two-dimensional example geometry (left) is approximated for input by an 11x11 bitmap. The next row shows successive smooth of degree 2, 5 and 25 by an implicit phasefield function. Now, the normal derivatives can be computed, reasonably.

6.3 Discretisation for Finite Differences

In order to apply the finite difference method to our problem, a discretisation method is needed to convert the smooth geometric description of pore space into a connected grid of points, with the pore space surface given as oriented points. In this model, a uniform rectangular grid is used for the mesh inside the pore space, with refined gridline-surface intersection knots to catch the surface. These are oriented analytically as obtained from the implicit phasefield description of the smoothed geometry.

6.4 Examples

First, we consider a simple, one-dimensional diffusion problem with totally inert boundaries, but an almost linear (actually, slowly exponential) initial concentration profile on [0.135, 0.365]. An infinitely extended linear concentration profile is static, as its Laplacian is zero. However, at isolating boundaries, there is no normal flow to keep up this profile. So considering diffusion only, in a totally isolating case, the concentration profile develops slowly towards a constant average concentration and the wall concentration changes most. Second, we consider the same problem for the two-dimensional, periodic case with a general slowly exponential slope. However, due to periodicity, the initial linear slope has a jump on each virtual domain boundary (see figure 13).

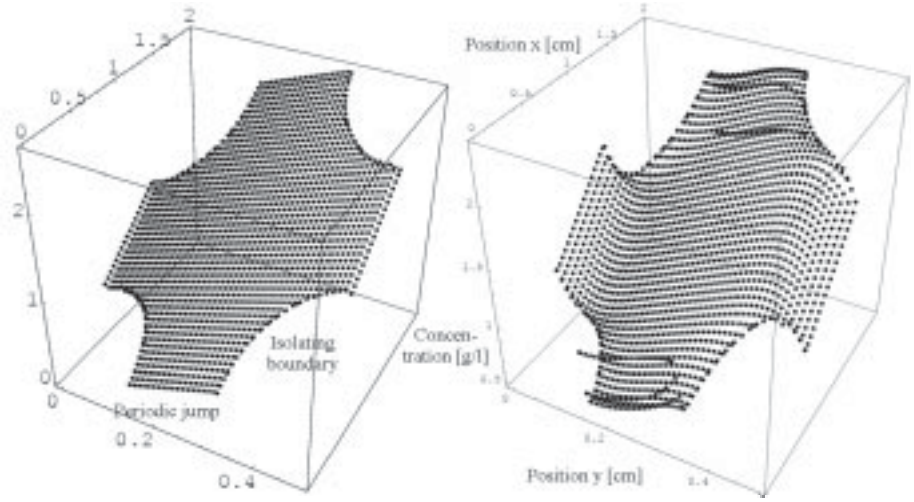

Figure 13: two-dimensionally periodic example with isolating boundaries for the arcs in the corners and jump in initial concentration, which dominates the simulation. Left: after one time step, Right: after 99 time steps. The time step-control is essential to get stable results.

6.5 The Asymptotic Adsorption

The case of adsorption is studied for an initially constant concentration. It is found that the concentration on the boundary drops very fast as the selected adsorption is almost as strong as total adsorption would be. Then the profile slowly changes to a sinusoid profile, which is preserved over time except for its exponentially decaying magnitude.

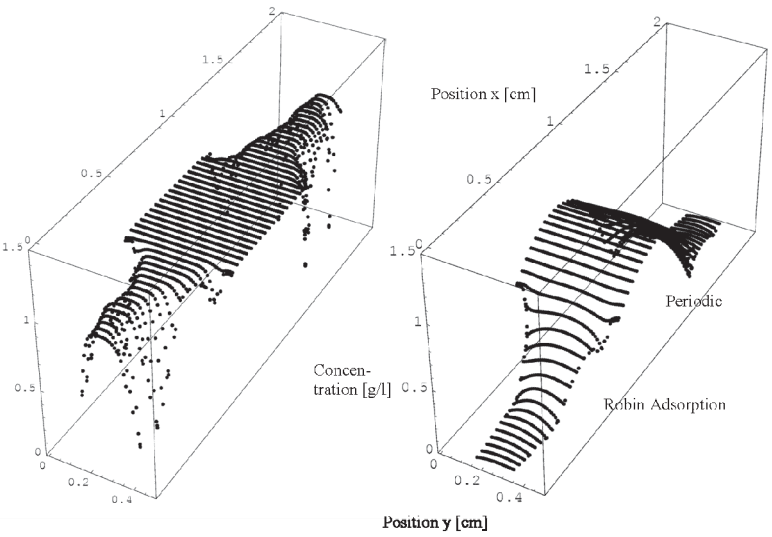

Figure 14: Robin Adsorption with initial start concentration constant 1. On the left after 129 time steps, on the right after 3999 time steps.

These two situations differ from each other in that on the left, the available concentration is almost one in a small neighbourhood to each surface knot, whereas on the right, the concentration has dropped in the narrow valley between the ellipsoids. Hence, the transport mechanisms in both situations differ: In the beginning, the adsorption on the surface is matched by diffusive

transport from the nearest neighbourhood. Hence, the adsorption rate is high. Later on, the characteristic concentration profile changes drastically to an asymptotic shape. In this case, diffusive transport has to take place over larger distances, and adsorption is no longer homogeneous throughout the surface. Hence, the ratio between the total mass of ions available and the cumulated adsorption flow throughout the surface is fundamentally different and depends on the geometry.

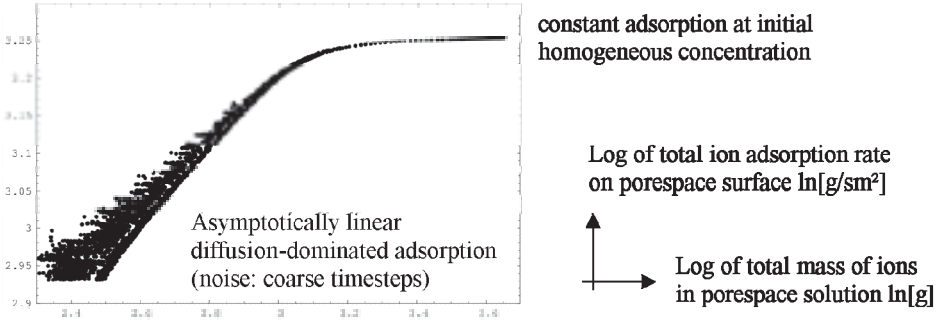

Figure 15: log-log Plot of cumulated adsorption by surface knots vs. total volume of ions

6.6 Building a Hybrid Simulation Tool for Cement Hydration

The basic concept for a phasefield description of cement hydration is founded on the description of the dry clinker, the hydrate layers and the aqueous solution by means of implicit phasefield functions. The transport of ions can be derived from the diffusion equation, possibly extended for reactions inside the hydrates [6]. The first step towards a dynamic problem of ion adsorption with boundary growth is to model the evolution of the geometry for given growth. The phasefield function is set as a B-spline function of a certain degree. Its coefficients are taken from [0, 1] and represent the bitmap of the initial material distribution. The adsorption of ions on the boundary causes growth of the microstructure. Therefore the phasefield function needs to be updated for the next time step. This is done in an active zone scheme by selecting those basis functions of the phasefield ansatz space that are next to the phase boundary and not already 1. From the finite difference discretisation of the problem, which is finer than the initial phasefield resolution, one gets a set of boundary knots resembling the phase boundary as a set of oriented points, as the normal of the phase boundary are known. If the phasefield function φ is varied by the basis function ψ in the active zone, i.e. $\varphi \rightarrow \varphi+\varepsilon\psi$, then the phase boundary at the boundary knot z propagates by $L=\varepsilon\psi\, d\varphi/dn$. For a given small positive growth g for all boundary knots, a best fit of this growth can be achieved by the solution of the nonnegative constrained least squares problem: For selected basis ψ_i find coefficients $\varepsilon_i \geq 0$: $|L_j-g(z_i)|^2=\min$. The solution of this problem for constant g is shown in figure 16. The circular disks of different size represent the size of the coefficients ε_i. It can be seen that the coefficients with horizontal normal are respectively smaller than those with vertical normal, which resembles the distortion of the aspect ratio of 4:1. These results can be compared with the case where the unit cell is square, as displayed

in figure 17. This ansatz has currently being extended from infinitesimal to real growth to obtain a working time-dynamic micro structural dynamics simulation of ion adsorption in porous media.

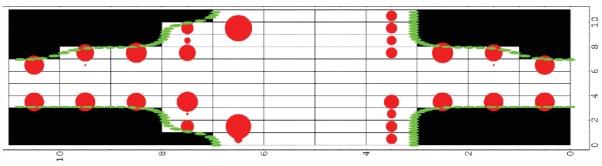

Figure 16: The uniform infinitesimal growth of the phasefield function for degree 4

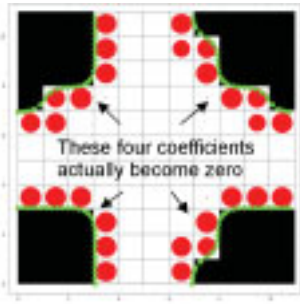

Figure 17: The uniform infinitesimal growth when the dimensions of the unit cell are 1:1.

The phasefield function mesh is shown. The small equal-sized elliptical disks resemble the phase boundary knots. The circular disks show the basis function updates for the phasefield function to resemble a uniform growth in the least squares sense. The dimensions of the unit cell are 4:1.

7 Conclusion and Outlook

The presented methods of quasi static flow and flow-augmented diffusion allow the prediction of quasi static fluid and ion flows viewed on mesoscopic scale. Different types of boundary conditions have been presented to reflect the different dissolution / growth / adsorption situations encountered in the simulation of cement hydration on microscopic scale. By theoretical considerations with our quasi static ansatz for incompressible stokes flow and diffusion, we have shown how to quantitatively determine the following dependencies: The mesoscopic fluid flow and the ion flow are linearly related to the pressure gradient, depending on the pore space geometry, and the ion flow boundary conditions. First results have been presented for the computation of flow through periodic structures.

With our method we can predict the ion concentrations in fresh cementitious pastes near curing interfaces. These results can thus be used for the advanced testing of fresh cementitious materials, by investigating e.g. the electrical conductivity, or individual ion concentrations near the free faces of cement. Furthermore, we compute the evolving resistance to flow, which can be measured in comparison. A second application proves the capacity of the method of model sorption processes.

8 References

[1] Locher, G.; Locher, F.W.: Contribution to the modelling of cement hydration. Cement International 04/2004, pp. 104-117.

[2] CEMHYD3D: A Three-Dimensional Cement Hydration and Microstructure Development Modeling Package. Version 3.0. National Institute of Standards and Technology Interagency Report 7232, Technology Administration, US Department of Commerce, June 2005.

[3] Emmerich, H.: The Diffuse Interface Approach in Materials Science: Thermodynamic Concepts and Applications of Phasefield Models. Lecture Notes in Physics monograph 73, 2003.

[4] Schoeberl, J.: NETGEN – An advancing front 2D/3D-mesh generator based on abstract rules. Comput. Visual. Sci. 1:41-52, 1997. See also Schoeberl, J.: Netgen / NGSolve – Mesh Generator and Finite Element Solver. Eccomas Finnland, 2004.

[5] Motsinger et al.: The measurement of the steady flow resistance of porous materials. AIAA-1983-779

[6] Klein, P.: Kolloidchemische Untersuchungen. Univ. Diss., Berlin, 1922.

Reinhard Nothnagel
Dr.-Ing.

Harald Budelmann
Prof. Dr.-Ing.

iBMB, Department Building Materials and Reinforced Concrete, Braunschweig, Germany

Model for the Formation of Microstructure during Hydratation and the consequences for autogenous shrinkage of paste and mortar

Summary

The porous space of cement paste is formed during hydration. Processes of transport and chemical reactions are proceeding in the capillaries influenced by the environmental conditions. Therefore the hydration process mainly determinates the state, the later behaviour and the durability of the material.

The model introduced here is delivering a description of the capillary pore space during hydration and of its state at the beginning of the period of use. The three-dimensional characterization of the porous structure of Portland cement paste and its development is based upon the constitutive volumetric approach of Powers & Brownyard. The process is described by means of finite elements. It contains the dissolution of non-hydrated cement and the formation of hydration products within the porous space. In opposite to existing models the model being developed is giving more detailed information on the local porosity distribution and the capillary microstructure.

Taking results of mercury intrusion into account the local porosity distribution can be transformed into a pore size distribution. By help of this procedure the detection of pores over a wide range of the capillary pore space can be put into practice.

In a first application of this model the consequences for autogenous shrinkage in cement paste and mortar will be figured out using a simple model based on the Laplace equation. The extension of the model to hydration under non-saturated conditions and the description of the interfacial transition zone was necessary to calculate the basic parameters and input data. The measurements, the results of the simulation and the restrictions of the simplified model will be presented.

Keywords: *hydration, microstructure, cement paste, mortar, autogenous shrinkage, numerical model*

1 Introduction

The porous space and the capillaries in particular influence the behaviour of the material. Chemical reactions and transport processes take place within the pore space and interact with the surrounding microstructure. Therefore the pore structure of hardened concrete, mortar and cement paste controls the material behaviour including the durability. The microstructure is formed during hydration. The initial state of the cement paste and the environmental conditions during the hardening period are governing the formation of the porous space. In transport and damage models which are often used for durability prediction the material status at the beginning of service life is not taken into consideration carefully. A more precise initial state description could lead to a more accurate prediction of the behaviour under service conditions.

In the model developed the hydration and the formation of the capillary pore space are considered as closely linked phenomena take into account the initial state of the fresh cement paste and the moisture and thermal conditions during hardening. The model introduced here differs in several parts from existing descriptions. It gives a more detailed information on the three-dimensional microstructure and describes the capillary pore space with a wider range of pore radii. A detailed schematic overview is given in figure 1.

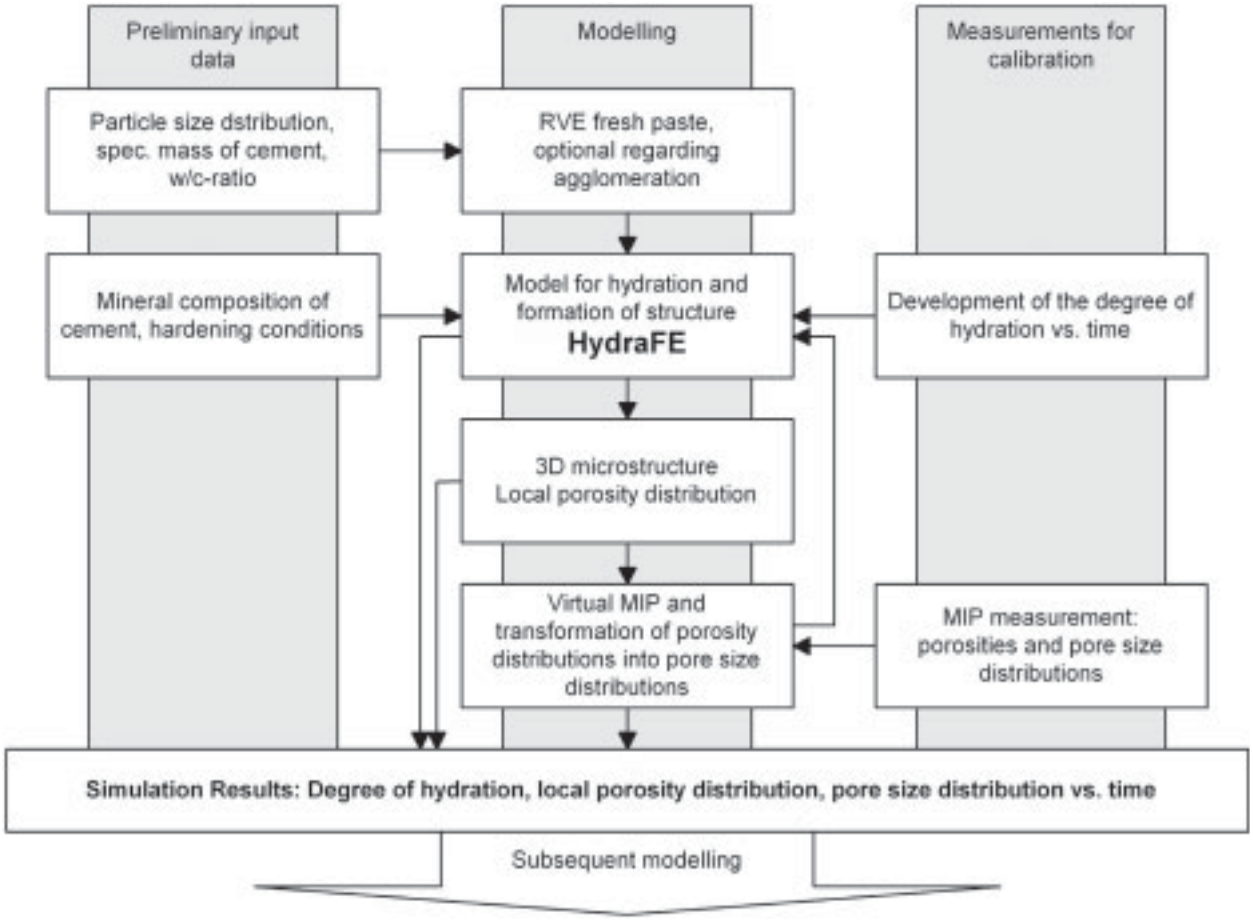

Figure 1: Overview – Modelling the hydration and the formation of microstructure

The proposal can be divided into three key aspects. First aspect is the modeling of the hydration and the formation of the microstructure. The second aspect is the description of the microstructure which is calculated by the numerical simulation. The result is the three dimensional local porosity distribution depending on the hydration time and the hardening conditions. This local porosity distribution can be transformed into a pore radii distribution by means of mercury intrusion measurements. The restrictions and the advantages of this description and of the transformation are discussed in the following. The third aspect is the test-application of the hydration model and the description of the microstructure. For this purpose the quite complex process of autogenous shrinkage of paste and mortar was chosen. The task was analysed step by step.
The first step is the application of the simulation results and the extension of the model to describe the formation of the structure under sealed conditions. Therefore the effect of self-desiccation is implemented. In the next steps the calculation of the autogenous shrinkage of cement paste using the simulated structure and moisture was tested. A simplified model based on the Laplace equation was used. The application will lead to several restrictions and uncertainties. This results will be discussed to show future areas of research. Furthermore the results of upscaling of autogenous shrinkage strains from paste to mortar using a finite element model will be presented.

2 The Hydration Model

The hydration model starts from a description of the initial state of the fresh cement paste. It describes the processes within a representative volume element (RVE). The hydration is modelled by three coupled main processes and implemented using the Finite-element-method.

2.1 Basis of the phase transition

The model uses a volumetric approach based on Powers & Brownyard [1]. The hardening reactions of the cement clinker are not considered in detail. Instead of this an overall balance is drawn up. It relates only the model phases unhydrated cement, free and bounded water and products respectively. During hydration the free capillary water is more and more bound physically and chemically. The hydration products are assumed to be uniform and gelporous. Therefore the ratio of chemically/physically bounded water to hydrated cement is constant. The values of this ratio, the gel porosity and the specific volume of the bound water can be determined using the mineral composition of the cement and the approach of Powers & Brownyard. Their work was published already 1947, however it was continuously enhanced by several authors (e.g. [2,3]).

2.2 Initial state of cement paste

The model takes into account the w/c-ratio and the particle size distribution. The particles are assumed to be spherical. They are placed randomly at first inside the representative volume

element (RVE). This procedure follows the approach of HYMOSTRUC [4], SPACE [5] and partially also CEMHYD3D [6].

The random placement does not match the situation inside the cement paste sufficiently. It is mentioned by several authors (e.g. [7]) that particles in Portland cement pastes are flocculated unless they are superplasticised. Furthermore in reality the particles shape is not spherical. In this approach the effect of flocculation is considered. The particles are moved by an iterative process towards neighbouring particles.

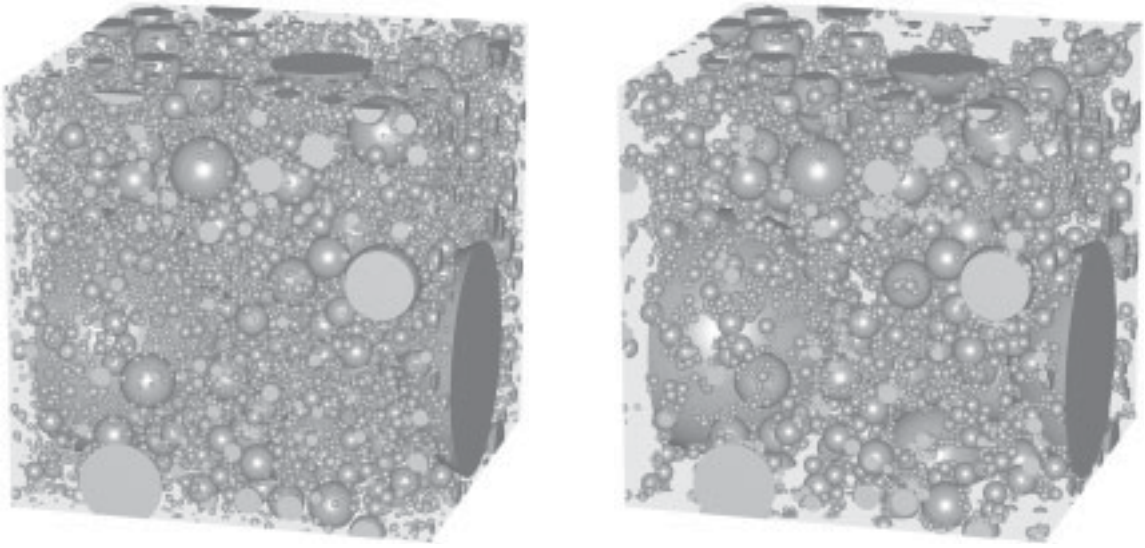

random flocculation

Figure 2: Spatial particle distribution in fresh cement paste (w/c=0.6)

In this approach attractive forces are assumed to let the particles form flocs and clusters. The attractive forces are calculated regarding the neighbourhood and assuming forces following a simplified electrostatic or gravitational model. The resulting spatial distribution of the solids differs from the more disperse random distribution and leads to a coarse and connected porous network structured by flocs. An example for the random distribution and the rearranged flocculated condition is shown in figure 2. Usually periodic boundary conditions are set for cement paste; regarded also in the boundary conditions in the FE system.

2.3 Description of the porous structure

Upon performing this particle arrangement inside the RVE the volume is transformed into a three dimensional lattice to start the FE simulation of the hydration process. Usually the RVE is cubical with edge length of around 100 µm for ordinary Portland cement to fit larger particles. The lattice is generated with a resolution of 1 µm edge length. In difference to other existing models every single subdivision of the volume may contain cement, pore space and later also products at the same time. This description as a kind of local porosity distribution has several advantages. With this approach no binary distinction of solids and pore space volumes is made. Therefore the model gives an additional information on the structure below the resolution of the

system which is useful further steps. In this proposal a transformation from local porosity distributions into pore size distributions accounting pore sizes below the resolution of the FE lattice is exemplified.

2.4 Hydration process

The hydration is described by several interacting model processes. A schematic representation of the model processes and phases is shown in figure 3.

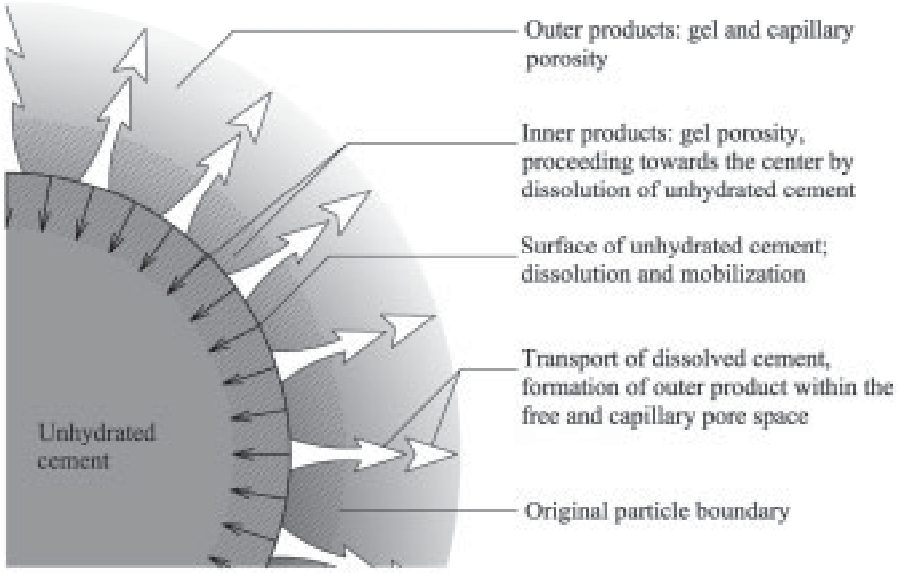

Figure 3: Scheme of the basic model processes and phases

The starting process is the dissolution of the unhydrated cement on the reactive surface of the particles. Instead of the dissolved cement volume gel-porous inner products are formed. The dissolved cement is transported by a diffusion process into the capillary pore space and outer products are formed there. The processes are coupled by the status variables of the system: supply and concentration of dissolved cement and the capillary microstructure formed by the hydration itself.

The implementation into a numerical simulation is performed on the basis of Fouriers law for diffusion processes extended by sources and sink terms. The basic efficiencies of the model processes are controlled by the model parameters. These parameters are independent of time and degree of hydration. They differ for various hardening temperatures and of course mineral compositions of the cement. The efficiency of the dissolution is directly coupled to the surface of the unhydrated cement and depends also on the concentration of the cement in the surrounding solution. The process is accounted as a source term in the model equation. The diffusion process is activated by the gradient of dissolved cement in the pore solution. The diffusion coefficient is determined by the porosity and the tortuosity (see e.g. [8]). The formation of products depends on the concentration of dissolved cement and on the free capillary pore space. This

process is dissipating the unreacted cement. It is implemented as a sink term in the model equation.

There are some model similarities with core-shell-models like HYMOSTRUC. But unlike this model the outer shell is not a homogenous layer of uniform porosity. The formation of products is controlled by the model processes and afford the formation of a diffuse capillary porous layer. The layers of adjacent particles are connected and interpenetrating, forming a capillary network. Another approach of smooth outer product shells containing capillary pores was used also in DUCOM [9]. In DUCOM the cement paste is substituted by the consideration of a single spherical particle in a cubical box.

As mentioned above the basic model parameters control the efficiency of the processes dissolution, diffusion and formation. These parameters must be calibrated for different cements and hardening temperatures. The calibration procedure cannot be executed comparing measured to simulated structures. There is no procedure or measurement method available which is suited to compare calculated and measured local porosities (or comparables) in hardening cement pastes. Some promising stochastic methods and approaches are given in [10,11]. For calibration of the parameters the comparison of the measured and calculated development of the degree of hydration depending on time was used. The hydration degree was measured in accordance to the approach of Powers & Brownyard on the basis of the amount of chemically bound water. As in their original approach and in the model proposed here the chemically bound water is assumed to be non-evaporable. The very early induction period was implemented by a blockade of the reactive surface decaying temporarily. Its duration can be obtained by measurement of the heat release in the early period.

2.5 Results

In figure 4 an example of the measured and calculated development of the degree of hydration is shown. A Portland cement paste (CEM I 32.5 R) with a w/c-ratio of 0.42 under saturated hardening conditions was tested. In the cross sections the decreasing capillary porosity at three different degrees of hydration is depicted. The formation of diffuse outer product layers can be observed. Finer capillaries are included in the diffuse layer replacing the continuous coarse pore network. The products of different adjacent particles interpenetrate and form large and dense areas.

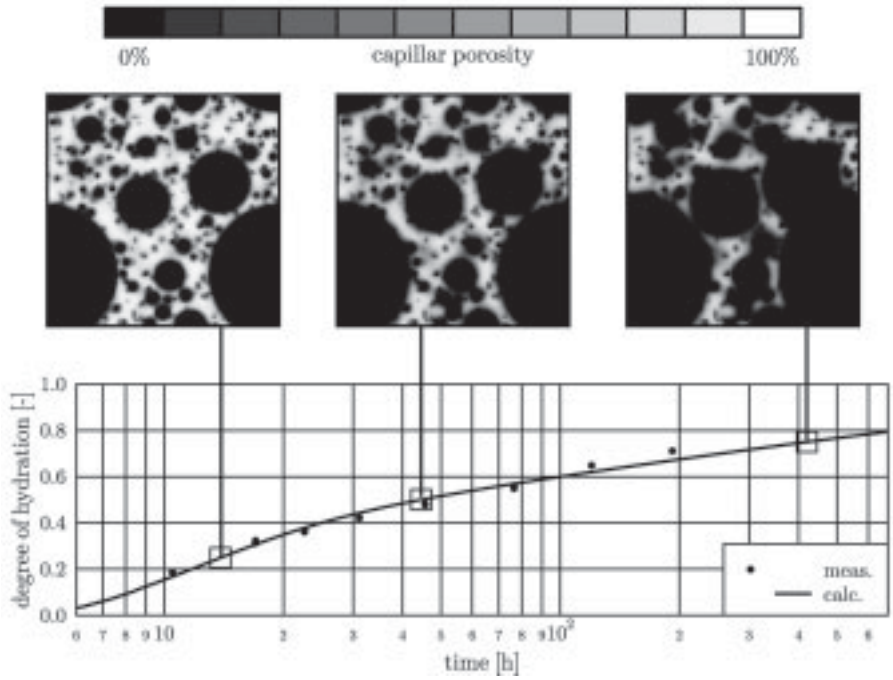

Figure 4: Development of the degree of hydration and capillary pore structure

3 Transformed Pore Size Distribution Representation and Application

3.1 Transformation of local porosities into pore radii

A transformation from local porosities to pore size distribution offers some certain advantages, for instance, for the description of transport processes or for other subsequent models which are using cylindrical pore descriptions. The calculated local porosity distributions can be transformed into local pore radius distributions. The idea underlying transformation is to assign a pore spectrum to the different element porosities, which is specific to this particular porosity. A direct approach is not available but can be derived from measured data on the basis of MIP. MIP is an often used experimental method for determination of the pore radius distribution. It supplies information on a wide spectrum of radiuses, but there are model limitations (parallel cylindrical pores) and some uncertainties. The sample preparation, here vacuum drying was used also to stop the hydration at certain points, is influencing the structure. Furthermore the measuring method itself is not as gentle. This side effects can not be neglected or corrected. In the approach introduced here the resulting differences from the MIP measurements are transformed also into the calculated pore size distributions because the measurement data are implemented to calibrate the transformation procedure.

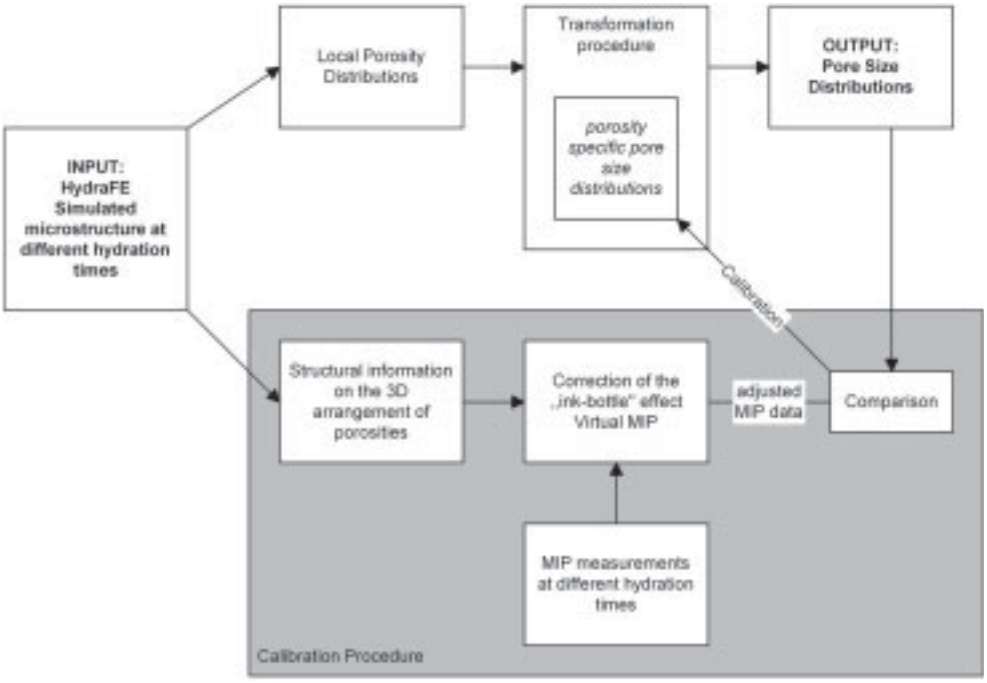

Figure 5: Transformation from local porosities into pore size distributions (schematic)

Furthermore the result is influenced by the effect of ink-bottle pores, due to the 3D pore arrangement. Large pore radiuses are often not correctly represented in the pore spectrum. In how far the larger pores are identified by smaller entrances can be determined approximately by a structural analysis of the calculated RVE, partly correcting the distortion produced by ink-bottle pores. This additional information is limited to the element level. Therefore the compensation is only an approximation. The details of this procedure called virtual MIP are not illustrated here (please ref. [12]). An schematic overview on the transformation and the calibration of the transformation is given in figure 5.

Thus cumulative radius distributions of the hardening cement paste can be determined, approximatively corrected by the effect of ink-bottle pores. Other effects that originate in the measuring process (MIP) and sample preparation cannot be eliminated. An example of calculated pore size distributions is given in figure 6. It can be seen that larger pore radiuses are disclosed by help of the correction of the ink-bottle effect.

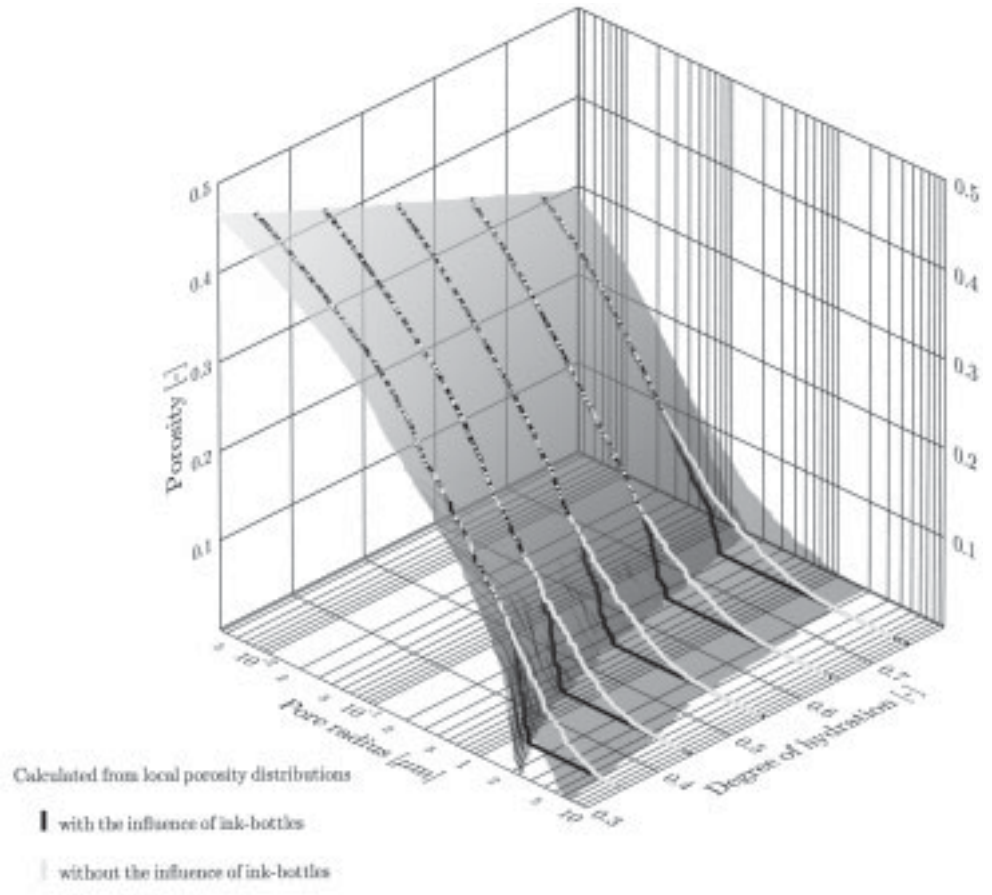

Figure 6: Calculated pore size distribution w/o the influence of ink-bottle pores (w/c=0.42, 20°C)

3.2 Application to sealed conditions and the interfacial transition zone

The model is applied to hardening under sealed conditions. Since the free water becomes bound in the course of hydration, the pore space is subject to a self-desiccation process. Pore desiccation starts at the large pore radiuses. To calculate the radiuses from the porosity distribution, the transformation procedure introduced before is calibrated and used. In the desiccated pores, the hydration sub-processes slow down and stop. Measured and calculated values are for the degree of hydration are to be seen in figure 7. The calculated values are the results of the simulation by HydraFE for a cement paste with w/c=0.3; 20°C under sealed and saturated conditions. Previously the model was calibrated to the Portland cement used here under different conditions – w/c=0.42 and saturated. This example demonstrates that the model once calibrated for the cement and the curing temperature can be applied to varied w/c-ratios and moisture conditions.

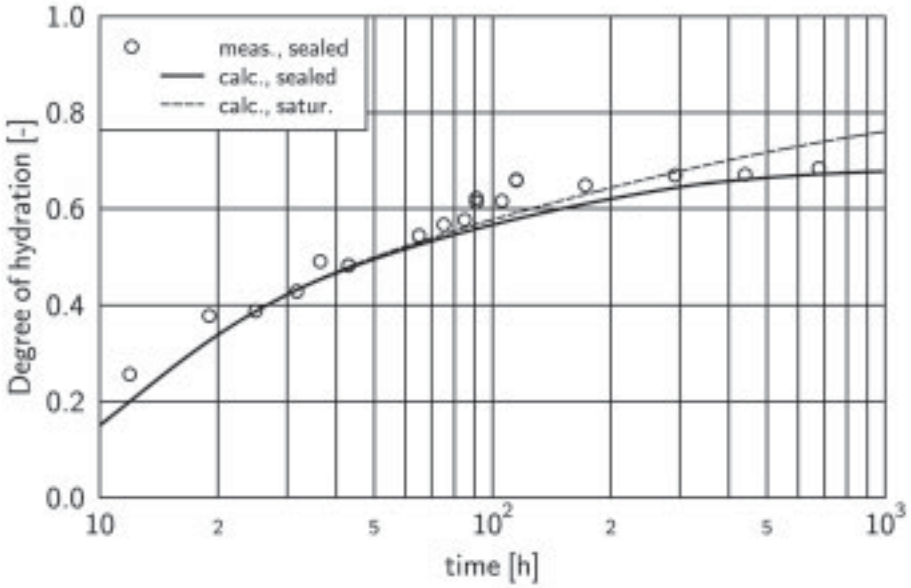

Figure 7: Development of the degree of hydration – measurements and simulation

Consequently these pores can not be filled with hydration products and fairly large interconnected capillary regions with large pore radiuses remain. The development is shown in the cross sections in figure 8.

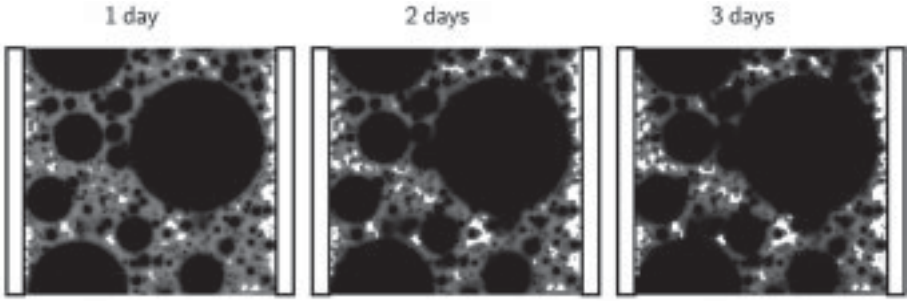

(white: empty capillary pore; grey: saturated capillaries; black: gelporous products and unhydrated cement)

Figure 8: Capillary porosity development at ITZ under sealed conditions (w/c=0.3; 20°C)

Furthermore in this application the formation of the microstructure within the interfacial transition zone (ITZ) was simulated. For this purpose, the wall effect in the ITZ was considered by means of an adjusted particle arrangement. From the start of the hardening phase the ITZ is characterized by a high porosity [13]. Results show that this zone is not completely filled with products throughout the entire hydration phase. In particular under sealed conditions, a high porosity in the ITZ has to be expected, since the larger pores are desiccating during the hydration phase inherently by the self-desiccation effect. Dependent on the w/c ratio the ITZ can be effective for several micrometers. Calculations have identified the ITZ to be a week point as confirmed under real conditions [14].

4 Modelling the Autogenous Shrinkage of Portland Cement Paste

4.1 Mechanism and model

The autogenous shrinkage is the macroscopic measurable strain as the result of the chemical shrinkage caused by the hydration of the cement. The chemical shrinkage leads to an internal self-desiccation. The occurring deformations can be illustrated by the three main models for the driving forces of shrinkage: surface tension, disjoining pressure, capillary tension.

In the last years several authors tried to calculate the autogenous shrinkage of cement pastes. Most of the approaches are using the Laplace law for the calculation of tensile stresses in cylindrical pores [e.g. 15,16,17]. Therefore the autogenous shrinkage models are reduced to the effect of capillary tension – also for the sake of simplicity. The capillary tension is applied to a solid skeleton of hydration products and unhydrated cement. Reviewing the approaches following this straight idea two main problems can be identified: How to obtain the saturated capillary radius and how to implement the non-linear and viscoelastic behaviour of the skeleton. In this study the main objective is to obtain the calculated (and measured) pore size distributions from the microstructure model as a parameter for the modelling of the autogenous shrinkage on the basis of the Laplace law assuming a linear elastic description of the material behaviour. Furthermore the autogenous shrinkage of Portland cement paste is measured at different w/c-ratios using an internal sensor with ,,zero'' stiffness based on displacement transducers. Some results are shown in figure 9.

4.2 Application

In [15] the basic model for autogenous shrinkage of cement paste regarding the capillary tension and linear elastic behaviour is given and explained. The model equations can be summed up to:

$$\varepsilon_{AS} = \frac{S\sigma_c}{3}\left(\frac{1}{K} - \frac{1}{K_s}\right) \qquad \sigma_c = \frac{2\gamma}{r};\ K = \frac{E}{3(1-2\mu)}$$

ε_{AS}: Autogenous shrinkage strain
σ_c: Capillary tension
S: Saturated pore volume fraction
K: Bulk modulus of the porous body
K_s: Bulk modulus of the solid skeleton

γ: Surface tension of the pore fluid
r: Radius of the saturated pore
E: Elastic modulus
μ: Poisson's ratio

The following state variables of the model for the hydration and formation of microstructure are known or calculable at each time step: degree of hydration, amount of hydrated cement, products, bound water, chemical shrinkage, porosity distribution and pore size distribution (using the MIP for calibration). Due to this the main parameters for the calculation of the capillary tension can be obtained. Additionally the pore size distribution and the chemical shrinkage according to different degrees of hydration can be controlled by measurements. The elastic modulus was measured directly and not calculated implementing existing models to keep the number of unknown model parameters and uncertainties as small as possible.

4.3 Results

In figure 10 the saturated radius vs. time calculated from the pore size distribution and the volume of the chemical shrinkage out of the hydration model is presented. It can be seen that the radius drops after 500 hours down to approximately 35 nm for w/c=0.3.

A much smaller radius than this cannot obtained out of the model because at this time free capillary water is not available – the hydration is stopped already however unreacted cement cores are still existing. The saturated radius is calculated using the pore size distribution and the volume of chemical shrinkage. The coarse pores are emptied first. The total porosity from the MIP or simulation contains the complete capillaries and approximately the half of the volume of the gel pores. This gel volume was dried during the sample preparation. Due to this modification also structural changes of the pores occurring and the volume is entrained by the MIP as well. This means the pore size distribution contains falsification - it cannot be retraced here which pore radii and volumes are affected. Therefore ideas for correction of this effect cannot be validated and should not be developed at this point.

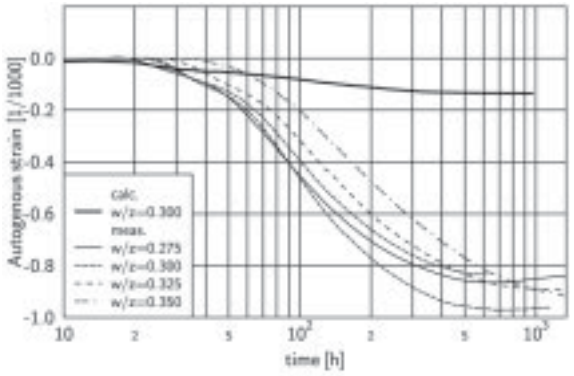

Figure 9: Calculated and measured autogenous strains (20°C)

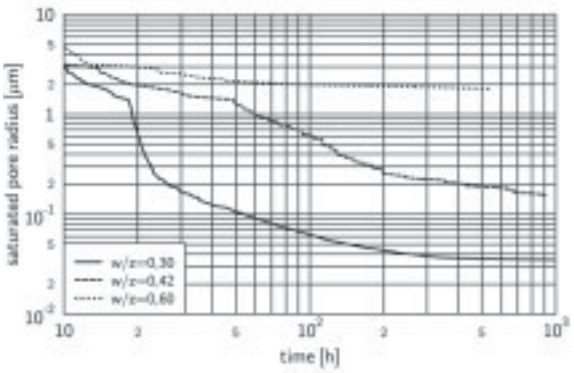

Figure 10: Calculated saturated pore radii vs. time under sealed conditions (20°C)

The calculated autogenous strains are in the order of 10 times smaller than the measured values (see fig. 9). Some reasons can be named to explain the differences between calculation and measurement. The underlying description of the microstructure must be improved to identify the saturated capillary radius more exactly. Furthermore the other driving forces and a viscoelastic mechanical behaviour must be regarded. To identify and explain the important parameters it would be better to divide, measure and validate the single effects. Therefore it seems to be recommended to focus some of the future work on a better description of the microstructure. The microstructure model should be validated using more precise and direct methods. Gathering a reliable structure - processes causing the shrinkage can be identified and modelled. Fitting the ,,virtual'' structure or other parameters to the measurements of effects like shrinkage will be an easier way – however this will not lead to a better understanding of the actually governing physical processes and not to a more generally applicable description of the

structure and subsequent solutions. Regardless of the differences between measurements and simulation in the next section the modelling of autogenous shrinkage for mortar is presented.

5 Modelling the Autogenous Shrinkage of Mortar

The autogenous shrinkage of mortar is described by a 2D finite element model. The material consist of three different phases: the hardening and shrinking paste, the less denser interfacial transition zone (ITZ) and the solid aggregates.

5.1 Setup and input data

To keep the influence of the aggregates in the numerical model and in the experimental observations manageable glass beads of two different diameters (0.5 and 1.0 mm) made of alkali-resistant glass are chosen. The elastic modulus and the autogenous shrinkage strain of the paste was obtained by the measurements directly (s. fig. 11). The thickness of the ITZ was estimated using the results of the simulation performed by the hydration model introduced in the first part. Three different contents of glass beads are examined for both aggregates diameter. The w/c-ratio was set to 0.3 at a hardening temperature of 20°C under sealed conditions.

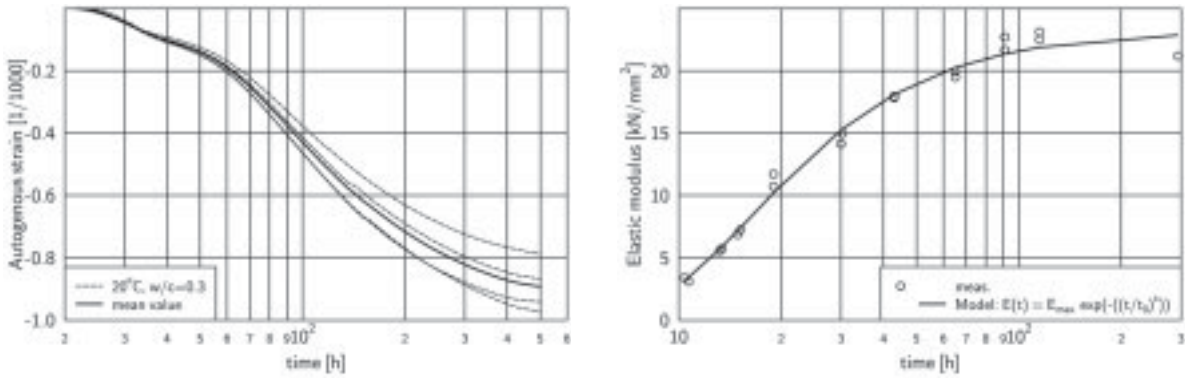

Figure 11: Measured autogenous strains (left) and elastic modulus (right) of the cement paste

5.2 Implementation

Two-dimensional cuts of 3D-mortar-RVEs are generated (fig. 15). The aggregates are placed randomly inside the volume and continued cyclically at the element boundary. The spherical aggregates are surrounded by an ITZ-shell with the thickness of 20 µm. The thickness is assumed to be constant after the first 20 hours of hydration when the calculation of the autogenous shrinkage starts. The thickness of the ITZ was estimated from the development of the capillary porosity during the hydration in a RVE regarding the wall effect which leads to a locally higher w/c-ratio (fig. 12). All mechanical material models are linear elastic. The elastic modulus of the ITZ is set to approximately 50% of the elastic modulus of the paste. The calculations are carried out using a two-dimensional finite element model. The measured autogenous shrinkage of the paste was applied as a load to the cement paste matrix only.

Additional studies are performed to calculate the resulting elastic modulus of the mortars for comparison with the measurements. A picture of a typical 2D-FE model can be seen in fig. 14. It was mentioned that an exact specification of the mechanical behaviour and of the thickness of the ITZ was not necessary in this study. The simulation results and the measurements are in a good agreement (s. fig. 13). The influence of variations of the ITZ-parameters is relatively low at low w/c-ratios with a dense matrix and solid aggregates dominating the system (ref. [18]).

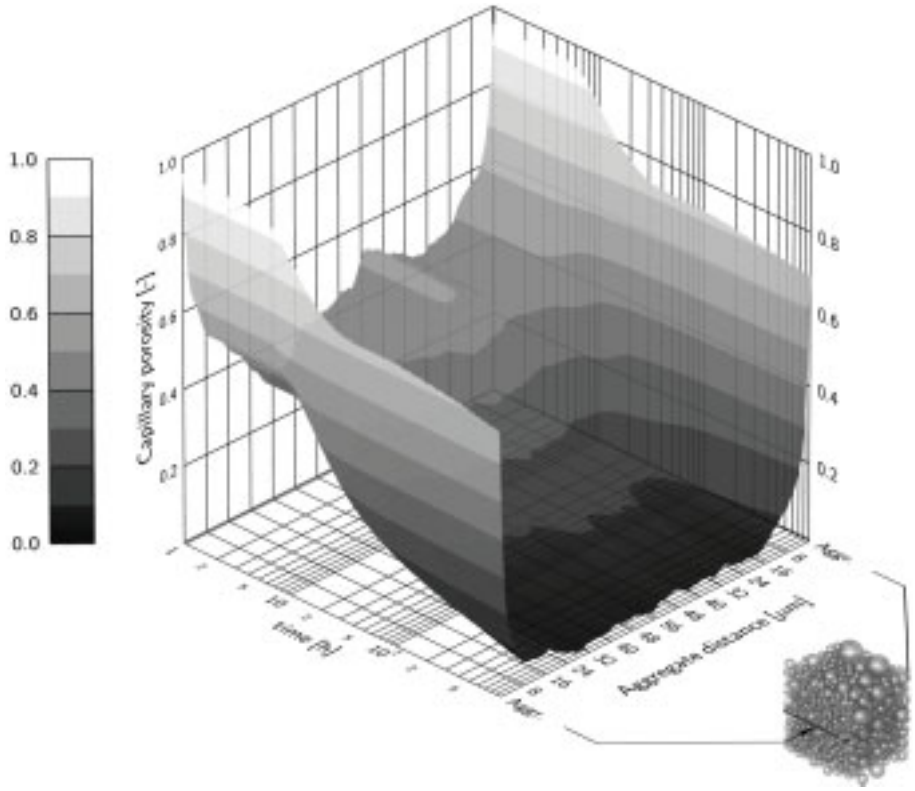

Figure 12: Development of the capillary porosity in the RVE vs. time and distance to modelled aggregate boundaries

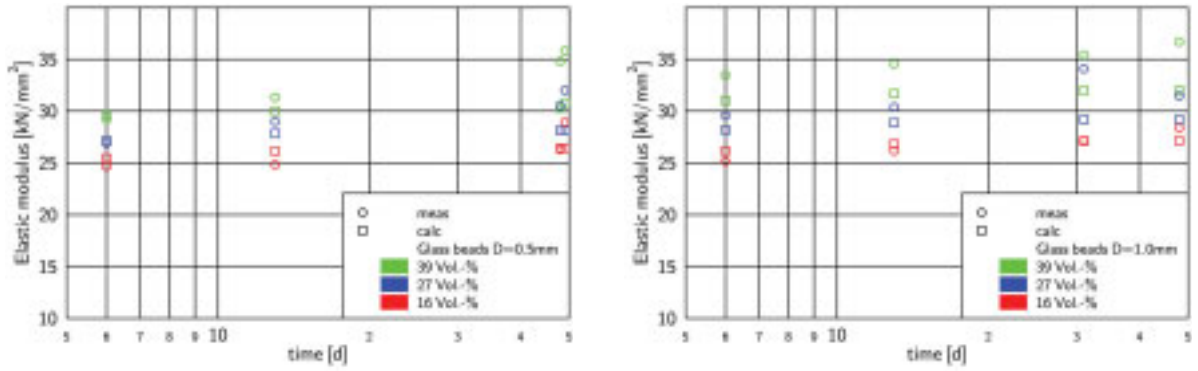

Figure 13: Measured and calculated elastic modulus of mortars (average values)

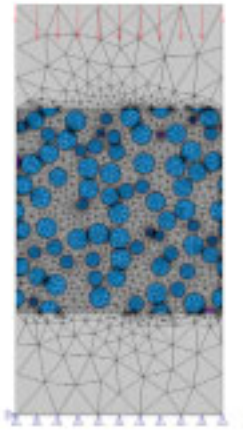

Figure 14: FE-model and mesh for the calculation of the elastic modulus

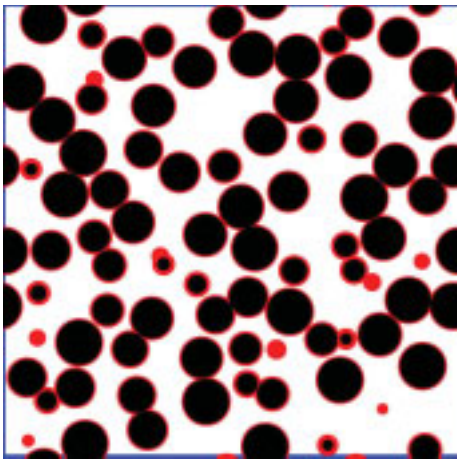

Figure 15: Typical cut of the 3 phases mesoscale mortar model regarding aggregates, ITZ and paste

5.3 Results

The measured and the calculated development of the autogenous shrinkage is to be seen in fig. 16. The absolute values are slightly overestimated by the calculations. However the characteristic development can be found in measurements and simulation as well. Furthermore the differences between the three different mortar compositions containing different volume fractions of aggregates are similarly reproduced by the model.

In comparison the mortars with 0.5 millimeter glass beads and with 1.0 millimeter glass beads at the same volume ratio of aggregates/total volume show no significant differences neither in measurements nor in the simulation. The mortar composition with the smaller 0.5 mm beads has got an ITZ-volume content which is approximately twice as the mortars with 1 mm glass beads. This supports the statement previously made that the variation of volume ratio of the ITZ at small ITZ-thickness and contents does not strongly influence the autogenous shrinkage.

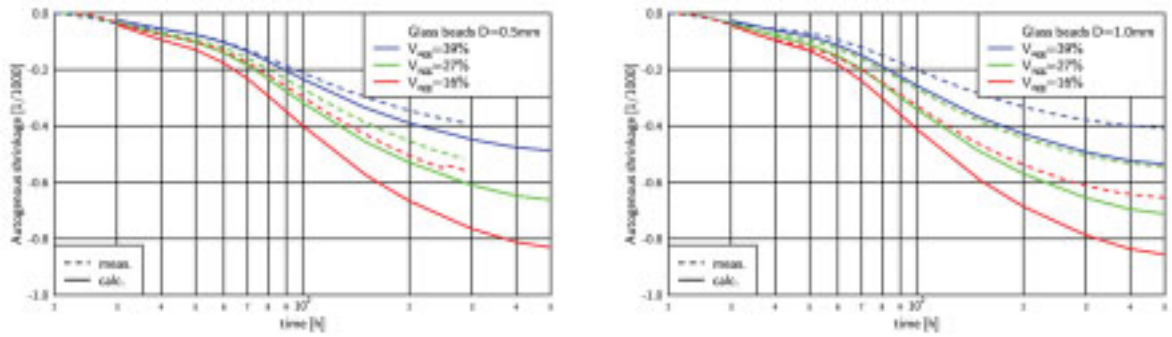

Figure 16: Measured and calculated autogenous shrinkage of mortars (average values)

The model is strictly linear elastic. Furthermore the local w/c-ratio of the paste is distorted by the spatial aggregate distribution. The calculation is not taking into account such local effects. Instead of this the average of previously measured values (fig. 11) of the autogenously shrinking paste was applied. Therefore several improvements can be implemented in future to correct this simple model and to sharpen the results.

6 Conclusions

6.1 Modelling the hydration and formation of microstructure

The proposed model allows a large part of the capillary porosity in the hardened cement paste to be shown as a three-dimensional structure. Starting from the fresh cement paste, the structure is calculated as a function of the hydration period regarding the initial and the hardening conditions (w/c ratio, particle size distribution, moisture saturation, temperature) using a discrete lattice by means of the FEM. The result is a 3D local porosity distribution. Although this distribution is linked to the dissolution of the FE lattice, it makes no clear distinction into solids or pore space. This is why individual elements differing in porosity and phase composition are possible.

In an additional computation process, the porosity distribution can be transformed to the distribution of radiuses. For this transformation the results of MIP measurements are used, partly corrected for the influence of ink-bottle pores.

The intention of this paper is to contribute to the development of a virtual laboratory for building material research. In particular the measuring instrumentation required to determine and describe the multi-scale pore structure is a field requiring additional effort. A more realistic and generally applicable micro-structure model could contribute enormously if it is applicable without limitation restrictions and permits validation on the structure level, which is not yet available without certain reservations.

6.2 Mesoscale modelling

With the need of a more generally applicable model of the microstructure of cement paste the next advancing steps are faced already to model the behaviour of mortar. In this approach the calculation of the elastic modulus and the development of the autogenous shrinkage are demonstrated. To keep the number of parameters as small as possible a simple linear elastic model was used. The description of behaviour on the mesoscale was implemented by means of a two-dimensional finite element model. The results were validated by means of measurements. It could be shown that the simulation fits the measurements well within certain limits. The accuracy depends on the model – for the sake of manageability a reduced approach was used here.

7 Acknowledgements

The presented research has been funded by the German Research Foundation (Deutsche Forschungsgemeinschaft) as a part of the program SPP 1122. The authors appreciate the financial support.

8 References

[1] Powers, T.C. ; Brownyard, T.L.: Studies of the Physical Properties of Hardened Portland Cement Paste. In: Bulletin 22, Research Laboratories of the Portland Cement Association (reprinted from Journal of the American Concrete Institute) 43 (1947), Part 1–9

[2] Brouwers, H.J.H.: The Work of Powers and Brownyard revisited: Part 1. In: Cement and Concrete Research 34 (2004), p. 1697–1716

[3] Copeland, L. E.: Specific Volume of Evaporable Water in Hardened Portland Cement Pastes. In: ACI Journal 27 (April 1956), p. 863 ff.

[4] Breugel, Klaas van: Simulation of hydration and formation of structure in hardening cement-based materials. The Netherlands, Delft, TU Delft, Dissertation, November 1991

[5] Stroeven, Martijn: Discrete Numerical Modelling of Composite Materials, TU Delft, Dissertation, November 1999

[6] Bentz, Dale P.: CEMHYD3D: A Three-Dimensional Cement Hydration and Microstructure Development Modelling Package. Version 2.0 / Building and Fire Research Laboratory – National Institute of Standards and Technology. Gaithersburg, MD, USA, April 2000 (6485). – NISTIR

[7] Diamond, Sidney: Particle Arrangement in Freshly-Mixed Mortars: Basis for Modelling. Journal of Advanced Concrete Technology 5 (3-2007), p. 277-283

[8] Snyder, K.A.: The relationship between the formation factor and the diffusion coefficient of porous materials saturated with concentrated electrolytes: theoretical and experimental considerations. In: Concrete Science and Engineering 3 (2001), p. 216–224

[9] Chaube, Rajesh P.: Simulation of Moisture, Transport, Hydration and Microstructure Formation in Cementitious Materials. Department of Civil Engineering, Tokyo, Japan, University of Tokyo, Dissertation, September 1996

[10] Berryman, James G.: Measurement of Spatial correlation functions using image processing techniques. In: Journal of Applied Physics 57 (7) (1985), p. 2374–2384

[11] Manwart, C. ; Torquato, S. ; Hilfer, R.: Stochastic reconstruction of sandstones. In: Physical Review E 62 (1) (2000), p. 893–899

[12] Nothnagel, R.: Hydratations- und Strukturmodell für Zementstein. TU Braunschweig, Dissertation, July 2007

[13] Scrivener, Karen L. ; Pratt, Peter L.: Characterisation of interfacial microstructure. In: Maso (Ed.): Interfacial Transition Zone in Concrete, E & FN Spon, London, 1996, p. 3–17

[14] Bentz, Dale P.: Effects of Cement PSD on Porosity Percolation and Self-Desiccation. In: Persson; Fagerlund (Ed.): Self-Desiccation and its Importance in Concrete Technology – Proceedings of 2nd International Research Seminar, Lund, Sweden, June 18, 1999, p. 127–134

[15] Lura, P.; Jensen, O.; van Breugel, K.: Autogenous shrinkage in high-performance cement paste: An evaluation of basic mechanisms. Cement and Concrete Research 33 (2003), p.223-232.

[16] Zhutkovsky, S.; Kovler, K.: Dependence between capillary stress and autogenous shrinkage for high-strength cement pastes. International RILEM Symposium on Concrete Modelling – CONMOD'08, Delft, Netherlands, 2008.

[17] Jaouadi, I.; Guidoum, A.; Scrivener, K.: Modelling autogenous shrinkage of hydrating cement paste. International RILEM Symposium on Concrete Modelling – CONMOD'08, Delft, Netherlands, 2008.

[18] Lee, K.M.; Park, J.H.: A numerical model for elastic modulus of concrete considering interfacial transition zone. Cement and Concrete Research 38 (2008), p.396-402.

Kirsten Linnow
Dr.

Michael Steiger
Dr.

University of Hamburg, Department of Chemistry, Inorganic and Applied Chemistry

Modeling the properties of pore solutions in porous building materials

Summary

Salts in porous building materials are not only a major cause of decay but also affect the hygric and capillary transport properties of such materials. The present paper reports the use of thermodynamic models to represent the properties of aqueous pore solutions that are required in humidity and moisture (HAM) transport models. The models are based on the Pitzer ion interaction approach and are used to predict the activities of water and dissolved ions, the density and the heat capacity of mixed electrolyte solutions that are typically found in building materials. Different levels of accuracy are required for these properties in HAM models. In the case of the activity calculations a high level of accuracy is required to guarantee an accurate prediction of phase equilibria in pore solutions and an extended Pitzer model had to be used. The calculation of solution densities is less critical and the use of a simplified Pitzer model neglecting the ion interactions in mixed solutions was possible. Finally, a further simplification of the Pitzer model equations proved to be sufficient for the calculation of heat capacities still leading to satisfactory model results for the use with HAM models.

Keywords: *thermodynamic modeling, pore solutions, water activity, activity coefficients, density, heat capacity*

1 Introduction

The crystal growth of salts in porous building materials is generally considered as a major cause of damage of such materials. Salts do also influence the hygric properties of building materials. For instance, due to their hygroscopicity salts strongly affect the sorption isotherm of a material and dissolved salts alter the capillary transport properties, e.g. solution density and viscosity, of the pore liquid. Finally, salts present in crystalline form change the pore structure, i.e. the pore size distribution and permeability of materials. Therefore, in heat, air and moisture transport models (HAM) for the evaluation of the hygric behavior of building materials and structures, an accurate representation of the behavior of salts and salt mixtures is required [1]. This includes (1) an appropriate model for the representation of the thermodynamic properties of aqueous pore solutions and (2) the ability to treat the relevant solid–liquid phase equilibria.

The relevant thermodynamic properties include the activities of water and dissolved ions and the solution density and thermal properties of pore solutions such as the heat capacity. In geochemical modeling the molality-based Pitzer formalism [2] was successfully applied in chemical equilibrium models [3] for the representation of thermodynamic properties of natural waters. Most of the available databases of model parameters are used to calculate sulfate and chloride solubilities in concentrated brines. However, only few models include nitrates which are quite often found as contaminant salts in building materials. It was shown previously that existing parameters may cause erroneous results if applied for the prediction of solubilities in mixed solutions containing chloride and nitrate at high ionic strength [4]. The ion interaction approach has been also used for the calculation of densities [5,6] and heat capacities [7,8] in electrolyte solutions.

In the present work we report on molality-based Pitzer models for the calculation of activities, densities and heat capacities in mixed electrolyte solutions. A highly accurate representation of activity coefficients and water activities in mixed solutions is required for an accurate prediction of phase equilibria in mixed solutions. Therefore, the model used is an extended Pitzer ion interaction model including the full set of binary and ternary parameters from the temperature of freezing to about 50 °C. No simplifications of the model to improve the computational efficiency could be introduced without significant loss of accuracy in the prediction of phase equilibria. In contrast, several simplifications of the original ion interaction equations were used while still allowing for a sufficiently accurate prediction of solution densities and heat capacities.

2 Theoretical background

2.1 Equilibrium constants and ion interaction approach

Given a salt of composition $M_{\nu M}X_{\nu X}\cdot \nu_0 H_2O$ consisting of ν_M positive ions M of charge z_M, ν_X negative ions X of charge z_X and ν_0 molecules of water the equilibrium constant K_{MX} of the dissolution reaction is given by

$$\ln K_{MX} = \nu_M \ln m_M + \nu_X \ln m_X + \nu_M \ln \gamma_M + \nu_X \ln \gamma_X + \nu_0 \ln a_w \tag{1}$$

where m_M, m_X, γ_M and γ_X represent the molalities and activity coefficients of the cations and anions, respectively, and a_w is the water activity defined as

$$\ln a_w = -\phi M_w \sum_i m_i \tag{2}$$

where ϕ is the osmotic coefficient and $M_w = 1.801528 \cdot 10^{-2}$ kg · mol^{-1} is the molar mass of water. Thus, the calculation of solubility equilibria requires the knowledge of the activity and osmotic coefficients as a function of composition and temperature. An appropriate thermodynamic model to calculate these properties of concentrated solutions is based on the ion interaction or Pitzer formalism.

Details of the model are not discussed here but may be found in reference [1]. Briefly, the Pitzer equations are used to represent the excess Gibbs energy of electrolyte solutions. The equations incorporate an extended Debye-Hückel limiting law and a virial expansion representing short range ionic interactions. In its original form only second and third virial coefficients are considered and the ionic strength dependence of the third virial coefficient is neglected. Expressions for activity and osmotic coefficients are obtained from appropriate derivatives of the Gibbs free energy equation. The equations are summarized in reference [4].

The virial coefficients are treated as empirical quantities, hence, they must be evaluated from experimental data. The adjustable parameters are the binary interaction parameters $\beta^{(i)}$ and C^{ϕ} and the ternary interaction parameters θ and ψ. The set of parameters $\beta^{(i)}$ represents the ionic strength dependence of the second virial coefficient. The binary interaction parameters are evaluated from thermodynamic data of binary solutions. The ternary interaction parameters are obtained from experimental data of simple mixtures containing only three different ions, i.e. mixtures of two salts with a common ion. Once all binary and ternary interaction parameters are evaluated, the equations may be used to predict activity and osmotic coefficients in mixed electrolyte solutions of any composition.

Comprehensive reviews of the Pitzer ion interaction approach and the form of the equations used for the calculation of volumetric quantities can be found elsewhere [5]. The total volume V of a multiple-solute electrolyte solution is given by

$$V = n_1 V_1^0 + \sum_i n_i \bar{V}_i^0 + V^{\text{ex}} \tag{3}$$

where V_1^{o} is the molar volume of water, $\bar{V}_i^0$ are the partial molal volumes of the ions i in solution at infinite dilution, n_1 and n_i are number of moles of water and dissolved ions, respectively, and V^{ex} is the excess volume of the mixed solution. Using the molal concentration scale

$$V = 1000 v_{\text{w}} + \sum_i m_i \bar{V}_i^0 + V^{\text{ex}} \tag{4}$$

where m_i are the molalities of the ions in solution, and v_{w} is the specific volume of water. The excess volume V^{ex} is the pressure derivative of the excess Gibbs energy. Hence, the ion interaction equations for volume calculations are obtained by taking the appropriate derivation of the interaction equation for the excess Gibbs energy [5]. These equations contain the empirical parameters for binary and ternary interactions which are given as the pressure derivatives of the binary ($\beta^{(i)}$ and C^{ϕ}) and the ternary (θ and ψ) interaction parameters as discussed before. Several authors have shown that there is only a small influence of the ternary interaction parameters [5,9]. Krumgalz et al. [9] also found that most of the available experimental data are not sufficiently reliable to allow for the determination of mixing parameters. Hence, for the purpose of the present work, it was decided to omit the mixing terms.

Using the full expression of the ion interaction model of mixed solutions with many different ions leads to a set of rather cumbersome equations that might affect computational efficiency which

is undesirable if this model is to be incorporated into a HAM model. It has been shown in previous work however, that the activity coefficient model cannot be simplified without considerable loss of accuracy in the prediction of phase equilibria. As the calculation of solubilities and freezing temperatures is the main purpose of the activity model, any loss of accuracy is not acceptable. The calculation of densities is much less critical in this respect and it will be shown below that there is still excellent agreement between experimental and calculated densities of multicomponent mixed solutions without using the mixing parameters.

HAM models also require the heat capacity of pore solutions. A review of the Pitzer ion interaction approach and the form of the equations used for the calculation of heat capacities can be found elsewhere [2,7,8]. Using the molal concentration scale the heat capacity c_P of a mixed solution is given by

$$c_P = \frac{1000 c^{\circ}_{P,\mathrm{w}} + \sum_i m_i \bar{C}^{\circ}_{P,i} + J}{1000 + \sum_i m_i M_i} \tag{5}$$

where $c^{\circ}_{P,\mathrm{w}}$ is the specific heat capacity of water, $C^{\circ}_{P,i}$ is the partial molar heat capacity of dissolved ions, M_i is the molar mass of the ions and J is the excess heat capacity calculated with the ion interaction approach [2,7,8]. Compared to other sources of error in HAM models, the modeling of heat capacities in mixed pore solutions is considered less critical. Therefore, a simplified model approach was selected in the present work for the calculation of heat capacities. First, the ternary parameters for the heat capacity were omitted. Second, considering the limited temperature range relevant to building materials, i.e. –40 to +40 °C, we decided to neglect the temperature dependence of the heat capacity parameters. As will be shown below however, there is still reasonable agreement of experimental heat capacities and the model predictions.

2.2 Determination of model parameters

The salt systems in building materials are complex mixtures typically containing the chlorides, nitrates and sulfates of sodium, potassium, magnesium and calcium. Hence, model parameters for the calculation of activities and solubilities are required for mixed solutions in the Na^+–K^+–Mg^{2+}–Ca^{2+}–Cl^-–NO_3^-–SO_4^{2-}–H_2O system from the temperature of freezing to about 40 °C. Apart from calcium sulfate all binary salts in this system are highly soluble. Because of its low solubility, calcium sulfate is far less mobile in building materials than any of the other commonly found soluble salts [10]. The mobility of a salt may be conveniently defined as the total amount of salt present in the pore space that can just be dissolved, if the pore space is completely filled with water. For example, in a natural stone with a water accessible porosity of 10%, the mobility of gypsum is only about 0.1 g kg^{-1} while, in the same material, the mobility of NaCl is 14 g kg^{-1} [11]. Typically, the concentration of calcium sulfate in historic masonry exceeds its mobility by several orders of magnitude. Hence, only a very small fraction of calcium sulfate present in the

pores can be dissolved, even if the pore space is saturated with water. In other words, gypsum once deposited in the pore space of a building material is essentially immobile.

In effect, high concentrations of calcium and sulfate in pore solutions cannot occur at the same time and the model system can be simplified assuming that only one of these ions, calcium or sulfate, can be present as a major constituent of the salt mixture in building materials. This results in two possible salt systems, the Na^+–K^+–Mg^{2+}–Cl^-–NO_3^-–SO_4^{2-}–H_2O system and the Na^+–K^+–Mg^{2+}–Ca^{2+}–Cl^-–NO_3^-–H_2O system, for which the ion interaction parameters were determined. The parameterization included both the determination of the Pitzer parameters for these systems in the temperature range of interest and the determination of the equilibrium constants in Eq. (1), i.e. the thermodynamic solubility products of all possible solid phases. These include simple anhydrous binary compounds such as KCl, different hydrated forms of these salts, e.g. the magnesium sulfate hydrates, and a large number of double salts such as darapskite ($Na_3NO_3(SO_4)\cdot H_2O$) schoenite ($K_2Mg(SO_4)_2\cdot 6H_2O$), glaserite ($K_3Na(SO_4)_2$) and astrakanite ($Na_2Mg(SO_4)_2\cdot 4H_2O$). Details of the determination of the model parameters are provided elsewhere [4,12].

To a large extent, the model parameters for the density model were taken from an earlier study that was based on a compilation of the experimental data available until about the end of 1996 [6]. The resulting database was very satisfactory in the case of the chlorides and sulfates. However, much less accurate data was available for the nitrates. This is the most likely reason why earlier models for the calculation of densities in mixed electrolyte solutions do not include nitrates. For the present study, we have updated the database of model parameters as new experimental data was available for aqueous $NaNO_3$, KNO_3 and $Mg(NO_3)_2$. It turned out that a significant improvement of the earlier treatment could only be achieved in the case of $NaNO_3$ and $Mg(NO_3)_2$. The parameterization included the determination of a consistent set of partial molar volumes at infinite dilution in the Na^+–K^+–Mg^{2+}–Ca^{2+}–Cl^-–NO_3^-–SO_4^{2-}–H_2O system and the binary interaction parameters for all possible binaries in this system. Details of the parameterization are provided elsewhere [12].

As pointed out before, a very simple, computationally efficient model for the calculation of heat capacities in mixed solutions was established. An equation given by Kell [13] was used to calculate the specific heat of water $c^\circ_{P,\mathrm{w}}$ as a function of temperature. The temperature dependence of the partial molar heat capacities of the dissolved ions, $C^\circ_{P,i}$, and of the interaction parameters in the excess heat capacity J was neglected. Values of $C^\circ_{P,i}$ at 25 °C were taken from Criss and Millero [7,8]. The binary interaction parameters for NaCl(aq), KCl(aq), KNO_3(aq), K_2SO_4(aq), $MgCl_2$(aq) and $CaCl_2$(aq) were taken from the compilations of the same authors. For the remaining salts the existing parameters could not be used as they are only valid for dilute solutions. Interaction parameters for $NaNO_3$(aq), Na_2SO_4(aq), $Mg(NO_3)_2$(aq), $MgSO_4$(aq) and $Ca(NO_3)_2$(aq) were determined from available experimental data together with the ionic partial molar heat capacities of Criss and Millero [7,8]. In this treatment the interaction equations were used in their conventional form as listed in reference [2]. Due to the low solubility of $CaSO_4$ its

contribution to the excess heat capacity is negligible and all interaction parameters were assigned a value of zero.

3 Results and discussion

The determination of the model parameters in a Pitzer type ion interaction model requires experimental data for binary electrolyte solutions and simple ternary mixtures, i.e. solutions containing only three different ions, to determine the binary and ternary model parameters. The particular strength of the model lies in the fact that, once the binary and ternary parameters are determined, the model can be used to predict the properties in mixed solutions of complex composition. In the following sections the ability of the various models for such calculations is demonstrated and a discussion of the model limitations is provided.

3.1 Calculation of activities and phase equilibria

A detailed discussion of the parameterization and validation of the model for the calculation of water and ion activities in binary and mixed electrolyte solutions is provided in references [4], [12] and [14]. As an example, Figure 1 depicts the results of the parameterization of the model for a ternary system, i.e. the solubilities in the $NaCl–NaNO_3–H_2O$ system. The symbols represent the literature data that were used for the determination of the ternary model parameters. There is very good agreement between calculated and experimental solubilities confirming that the model equations provide for an excellent reproduction of the activities in mixed solutions even at very high ionic strength.

The calculation of solubilities is based on the simultaneous solution of a set of mass action and mass balance equations. The mass action expressions are the solubility constants of the dissolution reactions (Eq. 1). The mass balance equations include the total charge balance:

$$\sum_{M} z_M m_M = \sum_{X} | z_X | m_X \tag{6}$$

The set of Eqs. (1) and (6) can be simultaneously solved for the unknown molalities by Newton-Raphson iteration yielding initial values $m_i^{(0)}$ for the equilibrium molalities of all ions i in the solution. At this point of the calculation the present ion interaction model is used to correct for the non-ideality, i.e. the calculation of activity coefficients γ_i and the water activity a_w.

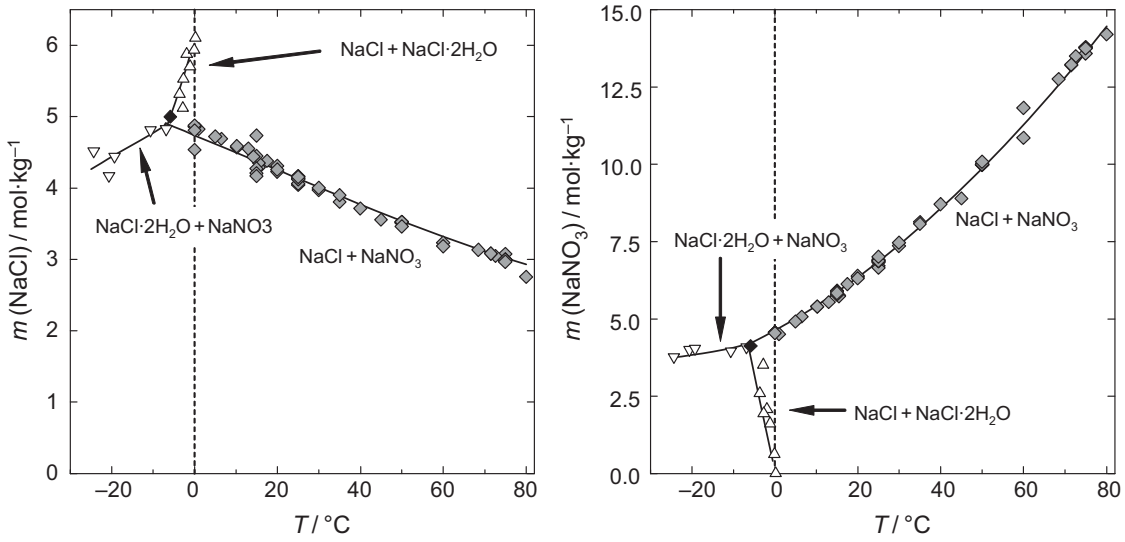

Figure 1: Solubilities of NaCl and $NaNO_3$ at the invariant points in the NaCl–$NaNO_3$–H_2O ternary system; symbols represent literature data, lines are calculated solubilities.

The Newton-Raphson iteration is repeated using the activities, $a_i^{(0)} = \gamma_i^{(0)} m_i^{(0)}$, and the water activity, $a_w^{(0)}$, as starting values, yielding new molalities $m_i^{(1)}$ which are used to calculate $\gamma_i^{(1)}$ and $a_w^{(1)}$. This procedure is repeated until satisfactory convergence in all γ_i and m_i is obtained.

While binary and common ion ternary experimental data are used to determine all model parameters, data from more complex systems are used to validate the model. Therefore, the model can be tested by comparing predicted solubilities with the available data of mixed systems containing more than three ions. We have used the model to calculate the solubilities at 25 °C in quaternary reciprocal systems for which experimental data are available. Figure 2 depicts a comparison of calculated and experimental solubility data in the systems Na^+–K^+–NO_3^-–SO_4^{2-}–H_2O and Na^+–K^+–Cl^-–NO_3^-–H_2O. All possible solution compositions in this system can be expressed as the contribution of each cation to the total amount of positive charges, e.g. $x(K^+)$, and the contribution of each anion to the total amount of negative charges, e.g. $x(NO_3^-)$ (Jaenecke projection). There is good agreement between the model calculations and the experimental data. It should be noted that the calculated solubilities are true model predictions since solubility data of reciprocal systems were not used in the parameterization of the model. The lines in the interior of the square diagram (Fig. 2) are the saturation curves for solutions coexisting with two solid phases. They define the crystallization fields of the stable solids at 25 °C, i.e. $NaNO_3$, KNO_3, $Na_2SO_4{\cdot}10H_2O$, Na_2SO_4 and the double salts $NaNO_3{\cdot}Na_2SO_4{\cdot}H_2O$ and $Na_2SO_4{\cdot}3K_2SO_4$. The intersections of the lines in Fig. 2 are the invariant points of the system representing the compositions of solutions in equilibrium with three solid phases, which is the maximum number according to the Gibbs phase rule.

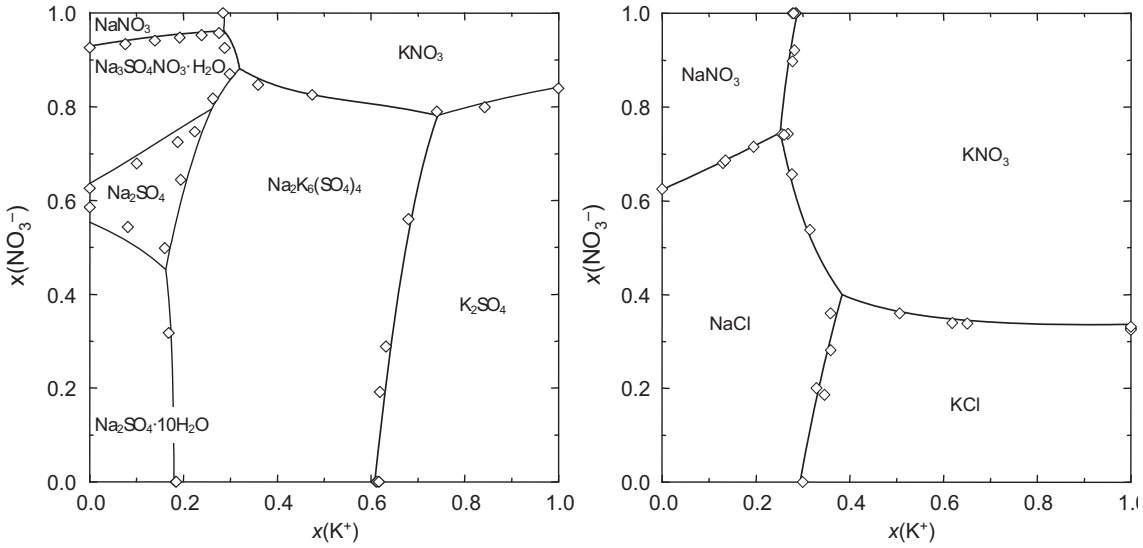

Figure 2: Calculated solubilities (—) in the Na^+–K^+–NO_3^-–SO_4^{2-}–H_2O (left) and in the Na^+–K^+–Cl^-–NO_3^-–H_2O (right) reciprocal systems at 25 °C compared to experimental data [15–18]; $x(K^+)$ and $x(NO_3^-)$ are charge equivalent fractions of K^+ and NO_3^- in saturated solutions (redrawn from reference [4]).

Excellent agreement of calculated and experimental solubilities is also obtained for the Na^+–K^+–Cl^-–NO_3^-–H_2O system at 25 °C. This system is considerably less complicated since there are no double salts that form in mixed solutions and none of the four salts forms hydrates at near ambient temperatures. The model performs very well for this system in the entire temperature range from –25 to +40 °C that is relevant to building materials. At higher temperatures, problems may arise if the model is used with highly concentrated solutions [4].

Another important application of the activity model is the calculation of freezing temperatures of pore solutions. A detailed description of the application of the model for such calculations is provided in reference [19]. Briefly, for ice and liquid water at equilibrium the equilibrium constant K_{ice} is given as:

$$K_{ice} = a_{w,ice} \tag{7}$$

where $a_{w,ice}$ is the water activity of a solution in equilibrium with ice. Freezing temperatures are used for the determination of the model parameters, thus, the model can be used for the prediction of the freezing temperatures in binary and mixed salt solutions. As an example, Fig. 3 depicts the results of freezing temperature calculations. The left diagram shows the freezing temperature curve and the saturation humidities of a number of salts that are commonly found in building materials. The shaded area represents the stability field of ice. A solution at subzero temperatures cannot exist at water activities above the saturation water activity, $a_{w,sat}$, of ice. The water activity of a salt solution decreases with increasing concentration, thus, there is a freezing temperature depression with increasing salt concentration.

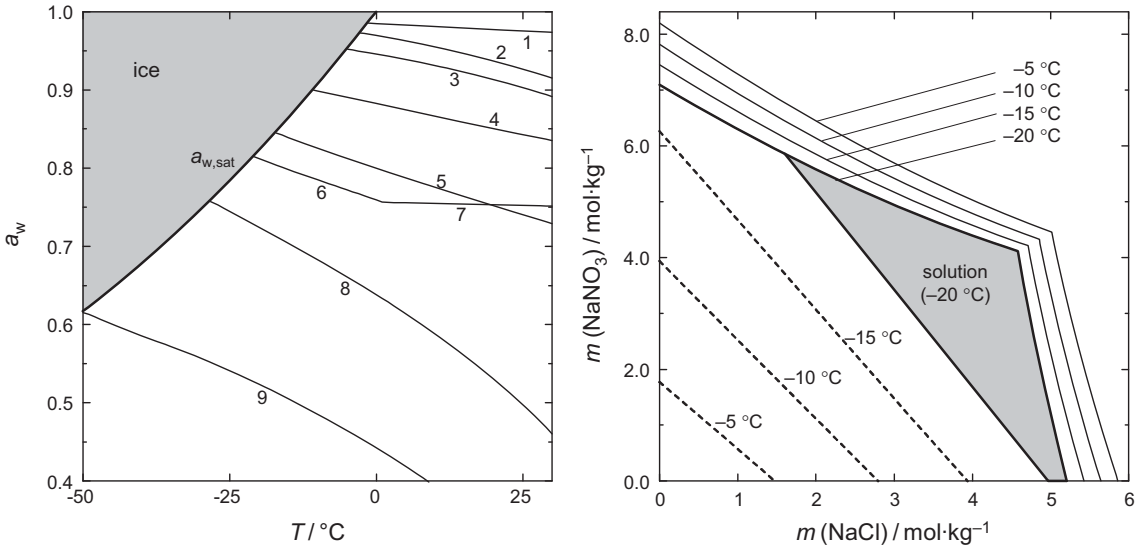

Figure 3: Freezing temperatures in salt solutions. Left diagram: freezing point depression and saturation humidities in binary salt solutions: (1) K_2SO_4, (2) KNO_3, (3) $MgSO_4{\cdot}7H_2O$, (4) KCl, (5) $NaNO_3$, (6) $NaCl{\cdot}2H_2O$, (7) NaCl, (8) $Ca(NO_3)_2{\cdot}4H_2O$, (9) $CaCl_2{\cdot}6H_2O$. Right diagram: solubilities (—) and freezing points (– – –) at –20, –15, –10 and –5 °C in mixed NaCl–$NaNO_3$ solutions (redrawn from reference [19]).

The maximum concentration or minimum water activity of a salt solution at a given temperature is limited by the solubility of the salt. The equilibrium humidities of the saturated solutions of several salts are also shown in Fig. 3 (curves 1–9). At relative humidities below these deliquescence curves the respective crystalline salts are stable, while above the deliquescence curve the solution is the stable phase. Due to their very high solubility the concentrated solutions of the calcium salts $Ca(NO_3)_2{\cdot}4H_2O$ and $CaCl_2{\cdot}6H_2O$ cause substantial depressions of freezing temperatures. In contrast, less soluble and less hygroscopic salts such as most sulfates, K_2SO_4 and $MgSO_4{\cdot}7H_2O$ in Fig. 3, only cause a minor freezing temperature depression.

The situation is slightly more complicated in salt mixtures as the water activity and, particularly, the saturation humidities of mixed solutions depend on the mixture composition. This is illustrated in the right diagram in Fig. 3 for a salt mixture containing NaCl and $NaNO_3$. The range of stable existence of a solution in this system is limited at low concentrations by the crystallization of ice (dashed freezing curves), and, at high concentrations by the crystallization of one of the two salts (thin black solubility isotherms). For instance, the hatched area in Fig. 3 indicates the range of stable existence of a solution at –20 °C. With increasing temperature there is an increase in the solubility of both $NaNO_3$ and $NaCl{\cdot}H_2O$, hence the solution field extends to higher molalities m (cf. isotherms at –20 °, –15 °C, –10 ° and –5 °C). The limit to low molalities is given by the freezing temperatures which are decreasing with increasing molality as shown by the freezing curves at –5 °C, –10 °C, –15 °C and –20 °C.

3.2 Calculation of densities

In the parameterization of the density model we have only included the binary interaction parameters including their temperature dependence. The model parameters are valid to about 100 °C. The typical relative standard errors of the fit range from 0.01% for K_2SO_4(aq) to about 0.2% for $Mg(NO_3)_2$(aq). As typical examples, a comparison of calculated and experimental densities of solutions of KCl(aq) and $CaCl_2$(aq) are shown in Fig. 4. It is obvious that there is excellent agreement over the entire temperature and concentration range. In the case of $CaCl_2$(aq), there is some cyclic deviation of the residuals indicating a minor degree of systematic bias. However, for the purpose of the present study the quality of the fit is quite satisfying and any further improvement would unnecessarily complicate the equations.

Test calculations carried out for mixed solutions confirmed that the present density model, though omitting the mixing parameters, provides a very satisfactory reproduction of experimental densities of mixed solutions. Table 1 lists the standard errors of the calculated densities compared to available high quality experimental data for a number of mixed systems. In all cases the model predictions are very close to the experimental results and the standard errors are only slightly higher than for single electrolyte solutions. Nonetheless, closer inspection reveals a very small systematic deviation depending on the mixing ratio and indicating that the model might be further improved by the inclusion of mixing parameters. However, there is a lack of such accurate experimental data that are required for the parameterization of the large number of possible ternary subsystems in the Na^+–K^+–Mg^{2+}–Ca^{2+}–Cl^-–NO_3^-–SO_4^{2-}–H_2O system that is relevant to building materials. Also, for the purpose of this research, there is clearly no need for further refinement of the model.

Table 1: Standard errors of calculated densities in mixed solutions

mixed solution	σ / g·cm^{-3}	T / °C	source of data
NaCl–Na_2SO_4	4.28E-04	5–95	[20,21]
	1.61E-04	5–95	[22,23]
NaCl–KCl	8.72E-04	5–95	[20,21]
NaCl–$MgCl_2$	7.32E-05	5–95	[22,23]
Na_2SO_4–$MgSO_4$	1.69E-04	5–95	[22,23]
Na_2SO_4–K_2SO_4	1.52E-03		[20,21]
KCl–K_2SO_4	1.85E-04	5–95	[20,21]
$MgCl_2$–$MgSO_4$	1.46E-04		[22,23]
NaCl–K_2SO_4	2.89E-04	5–95	[20,21]
Na_2SO_4–KCl	2.94E-04	5–95	[20,21]
NaCl–$MgSO_4$	2.08E-04	5–95	[22,23]
Na_2SO_4–$MgCl_2$	1.76E-04	5–95	[22,23]
NaCl–KCl–$MgCl_2$–$CaCl_2$	1.56E-04	10–40	[24]

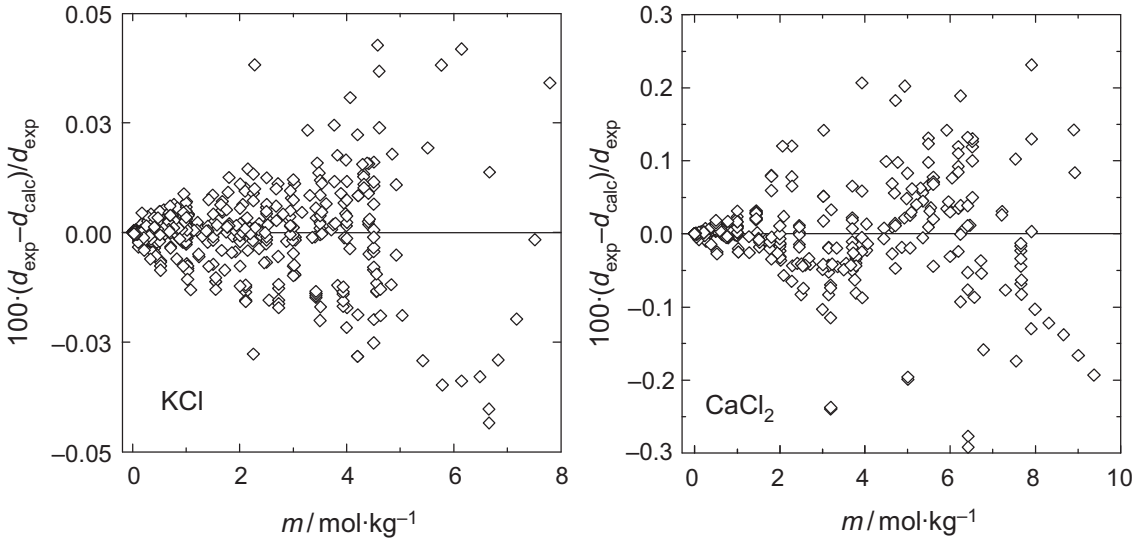

Figure 4: A comparison of experimental and calculated densities of binary aqueous solutions of KCl and $CaCl_2$.

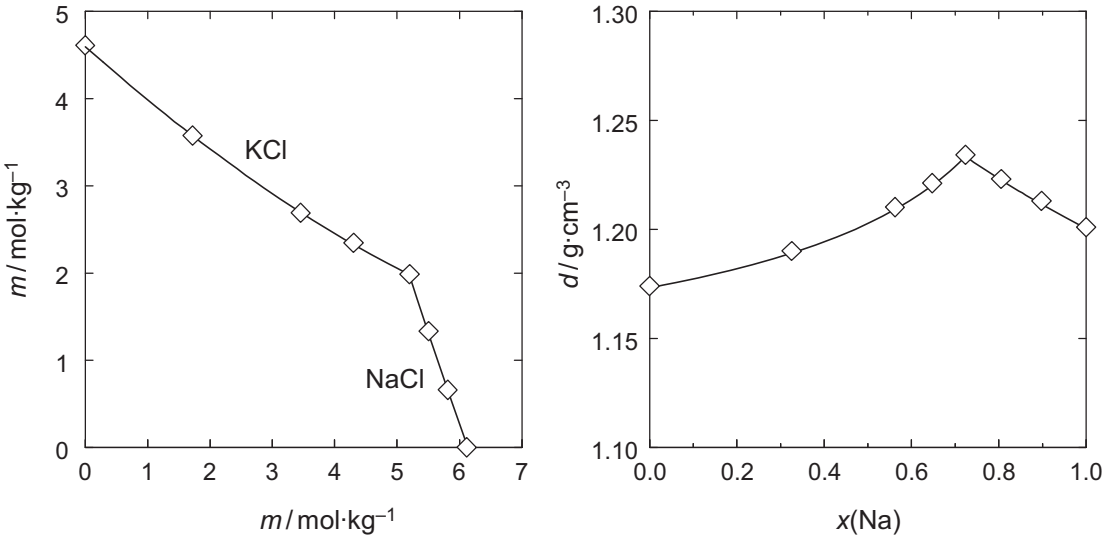

Figure 5: Calculated and experimental solubilities in the mixed system NaCl–KCl–H_2O (left) and densities *d* of saturated solutions (right) at 20 °C; *x*(Na) is the mole fraction of NaCl in the mixed saturated solutions; symbols represent experimental data [17].

Combining the density model and the activity model it is possible to calculate both solubilities and densities in mixed solutions. As an example, the results of such calculations for mixtures of aqueous NaCl and KCl at 20 °C are shown in Fig. 5. Symbols represent experimental data [17]. The curves are calculated solubilities and densities using the activity and the volumetric model, respectively. In both cases, there is excellent agreement with the experimental data. In the case of the activity data, the experimental data shown were used in the model parameterization since the ternary interaction parameters are required for the accurate reproduction of activity coefficients in mixed solutions. However, the calculated densities are true model predictions and con-

firm that the models can be used for the prediction of both phase equilibria and volumetric properties of mixed pore solutions. Such calculations are helpful to assess the volume changes during phase transitions of salts in porous materials [25].

3.3 Calculation of heat capacities

Experimental heat capacities of single salt solutions are useful experimental data for the determination of the binary interaction parameters in the activity model. Hence, such data were also used in the parameterization of the present model. This is illustrated in Fig. 6 for aqueous sodium sulfate at various temperatures. The experimental heat capacities shown were used in the determination of the binary model parameters of Na_2SO_4(aq) as described in detail in reference [14]. It is obvious that the binary parameters provide an excellent reproduction of the experimental data over the entire range of temperature and composition.

The prediction of heat capacities in multicomponent solutions results in quite complicated equations very similar to the equations used for the calculation of activities and densities, i.e. including a large number of binary and ternary interaction parameters, the partial molar heat capacities of all dissolved ions, and, the temperature dependence of all model parameters. It has been shown in the case of the density model that simplifications of the interaction equations are possible without introducing unacceptable large error. Considering typical sources of error in HAM models, errors in the order of a few percent in the calculation of heat capacities of pore solutions appear to be unproblematic. On the other hand, a computational efficient algorithm is highly desirable if the model is to be implemented into a HAM model.

We have therefore tried to use a considerably simplified form of the heat capacity equations. First of all, due to the paucity of the available experimental data and the very small influence of triple ion interactions the ternary parameters were also neglected in the heat capacity model. Second, it can be seen from Fig. 6 that there is only a rather small influence of temperature on the heat capacity of aqueous Na_2SO_4. In fact, the change of the heat capacity of Na_2SO_4(aq) in the temperature range 25–100 °C does not exceed 1.5% at any concentration. Considering the rather limited temperature range relevant to building materials, we tested a model in which the temperature dependence of both the binary interaction parameters and the ionic partial molar heat capacities are neglected. The model was tested with available experimental data for mixed solutions in the Na^+–K^+–Mg^{2+}–Ca^{2+}–Cl^-–H_2O system at high concentration [26]. From the results of these calculations shown in Fig. 7 it is obvious that neglecting the mixing parameters and the temperature dependence of the binary model parameters introduces some error in the reproduction of the experimental data at high concentration. Nonetheless the maximum errors of the calculated heat capacities hardly exceed about 2% relative deviation which is still considered acceptable.

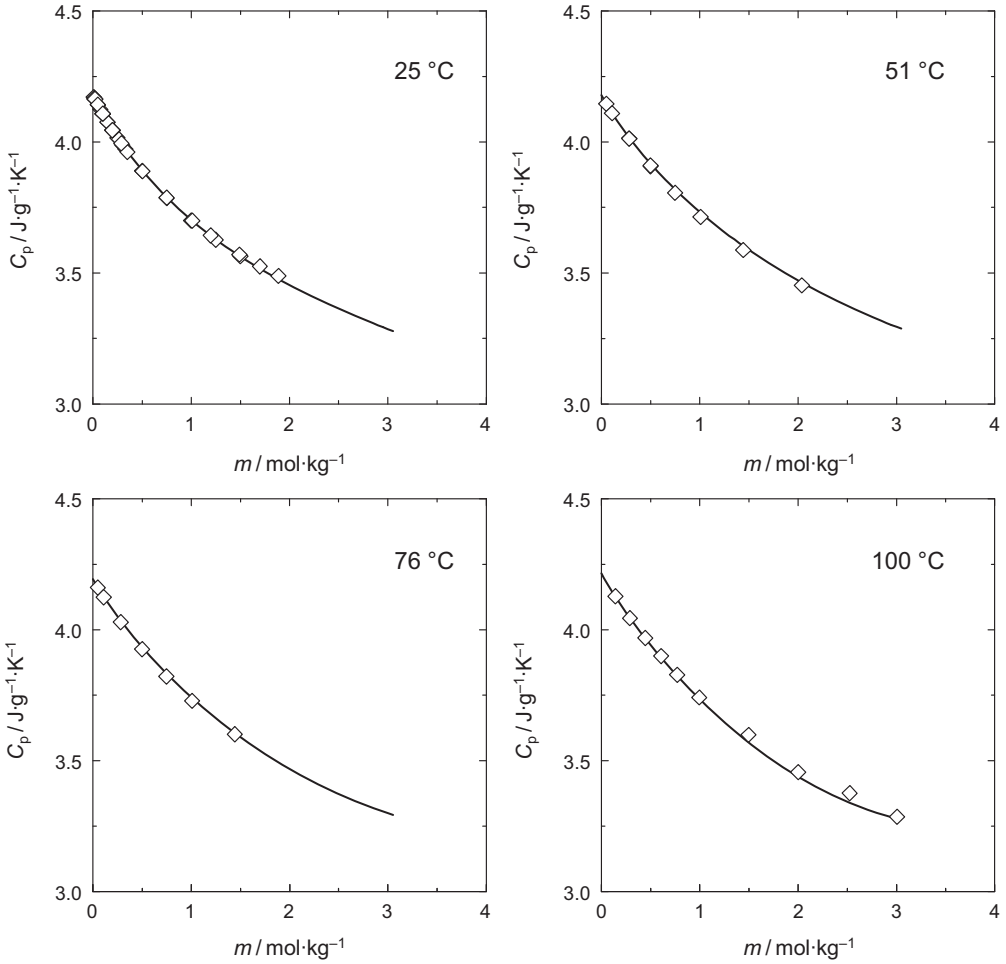

Figure 6: Heat capacities of aqueous sodium sulfate solutions at 25 °C, 51 °C, 76 °C and 100 °C; symbols are experimental data [27–[33]], lines are calculated using the binary model of Steiger and Asmussen [14].

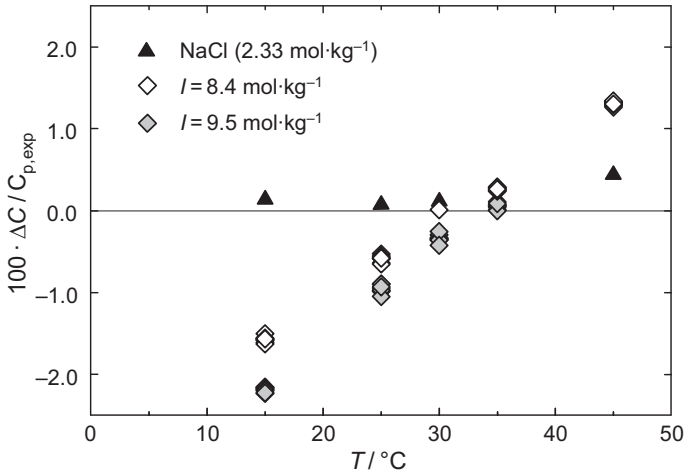

Figure 7: Percentage deviation of calculated from experimental [26] heat capacities in a NaCl reference solution (m = 2.33 mol·kg^{-1}) and in mixed solutions containing NaCl, KCl, $MgCl_2$ and $CaCl_2$ at two different ionic strengths I.

4 Conclusions

The Pitzer ion interaction equations provide an appropriate tool for the modeling of thermodynamic properties of multicomponent pore solutions in building materials. A model for the prediction of phase equilibria in such solutions requires the full parameter model including the binary and ternary interaction parameters. Such a model was parameterized in the present study and is now available for the accurate prediction of water and ion activities in mixed solutions. A slightly simplified yet still very accurate model for the calculation of densities of such solutions was also parameterized and validated. This model neglects ternary parameters. Finally, a very simple model is provided for the calculation of heat capacities in mixed pore solutions of building materials to within about 3%. All model parameters of the activity model and the density model are published [4] or will be available in the open literature in the near future [12]. Computer programs as C++ libraries and MS-Excel spreadsheets are also available (see references [4] and [14] and future publications) and are implemented in advanced models of our collaborators [1,34]. The parameters of the heat capacity model are available from the authors upon request.

5 References

[1] Nicolai A., Grunewald J., Plagge R., Scheffler G.: Development of a combined heat, moisture, and salt transport model for unsaturated porous building materials. This volume.

[2] Pitzer K. S.: Ion interaction approach: Theory and data correlation. In: Pitzer K. S. (ed.) Activity Coefficients in Electrolyte Solutions. CRC Press, Boca Raton, pp. 75–153, 1991.

[3] Harvie C. E., Møller N., Weare J. H.: The prediction of mineral solubilities in natural waters: The Na–K–Mg–Ca–H–Cl–SO_4–OH–HCO_3–CO_3–CO_2–H_2O system to high ionic strengths at 25°C. Geochimica et Cosmochimica Acta 48, pp. 723–751, 1984.

[4] Steiger M., Kiekbusch J., Nicolai A.: An improved model incorporating Pitzer's equations for calculation of thermodynamic properties of pore solutions implemented into an efficient program code. Construction and Building Materials, 22, pp. 1841–1850, 2008.

[5] Monnin, C: An ion interaction model for the volumetric properties of natural waters: densitiy of the solution and partial molal volumes of electrolytes to high concentration at 25 °C. Geochimica et Cosmochimica Acta 53, pp. 1177–1188, 1989.

[6] Steiger M.: Total volumes of crystalline solids and salt solutions. In: Price C. A. (ed.), An expert chemical model for determining the environmental conditions needed to prevent salt damage in porous materials. European Commission, Research Report 11, pp. 53–63, 2000.

[7] Criss C. M., Millero F. J.: Modeling the heat capacities of aqueous 1–1 electrolyte solutions with Pitzer's equations. Journal of Physical Chemistry 100, pp. 1288–1294, 1996.

[8] Criss C. M., Millero F. J.: Modeling heat capacities of high-valence type electrolyte solutions with Pitzer's equations. Journal of Solution Chemistry 28, 849–864, 1999.

[9] Krumgalz B. S., Pogorelsky R., Pitzer K. S.: Ion interaction approach to calculations of volumetric properties of aqueous multiple-solute electrolyte solutions. Journal of Solution Chemistry 24, pp. 1025–1038, 1995.

[10] Charola A. E., Pühringer J., Steiger M.: Gypsum: A review of its role in the deterioration of building materials. Environmental Geology 52, pp. 339–352, 2007.

[11] Steiger M.: Salts and Crusts. In: Brimblecombe P. (Hrsg.): Air Pollution Reviews – Vol. 2: The Effects of Air Pollution on the Built Environment. Imperial College Press, London, pp. 133–181, 2003.

[12] Steiger M., Linnow K.: manuscript in preparation.

[13] Kell G. S.: Density, thermal expansitivity, and compressibility of liquid water from 0° to 150°C: Correlations and tables for atmospheric pressure and saturation reviewed and expressed on 1968 temperature scale. Journal of Chemical and Engineering Data 20, pp. 97–105, 1975.

[14] Steiger M., Asmussen S.: Crystallization of sodium sulfate phases in porous materials: The phase diagram Na_2SO_4–H_2O and the generation of stress. Geochimica et Cosmochimica Acta 72, pp. 4291–4306, 2008.

[15] Jänecke E.: Über die Bildung von Konversionssalpeter vom Standpunkt der Phasenlehre. Zeitschrift für Anorganische Chemie 71, pp. 1–18, 1911.

[16] Reinders W.: Die reziproken Salzpaare KCl + $NaNO_3$ = KNO_3 + NaCl und die Bereitung von Konversionssalpeter. Zeitschrift für Anorganische Chemie 93, pp. 202–215, 1915.

[17] Cornec E., Krombach H.: Contribution a l'étude des équilibres entre l'eau, les nitrates, les chlorures et les sulfates de sodium et de potassium. Annales de Chimie 12, pp. 203–295, 1929.

[18] Cornec E, Krombach H, Spack A.: Nouvelle contribution a l'étude des équilibres entre l'eau, les nitrates, les chlorures et les sulfates de sodium et de potassium. Annales de Chimie 13, pp. 525–623, 1930.

[19] Steiger M.: Influence of salts on the freezing temperature of water: implications on frost damage to porous materials. In: D. Kwiatkowski, R. Löfvendahl (eds.): Proceedings of the 10th International Congress on Deterioration and Conservation of Stone, ICOMOS, Stockholm, pp. 179–186, 2004.

[20] Dedick E. A., Hershey J. P., Sotolongo S., Stade D. J., Millero F. J.: The PVT properties of concentrated aqueous electrolytes. IX. The volume properties of KCl and K_2SO_4 and their mixtures with NaCl and Na_2SO_4 as a function of temperature. Journal of Solution Chemistry 19, pp. 353–374, 1990.

[21] Millero F. J., Sotolongo S.: PVT properties of concentrated aqueous electrolytes. 7. The volumes of mixing of the reciprocal salt pairs KCl, K_2SO_4, NaCl, and Na_2SO_4 at 25 °C and I = 1.5m. Journal of Chemical and Engineering Data 31, pp. 470–472, 1986.

[22] Millero F. J., Connaughton L. M., Vinokurova F., Chetirkin P. V.: PVT properties of concentrated aqueous electrolytes. 3. Volume changes for mixing the major sea salts at I = 1.0 and 3.0 at 25 °C. Journal of Solution Chemistry 14, pp. 837–851, 1985.

[23] Connaughton L. M., Millero F. J.: The PVT properties of concentrated aqueous electrolytes. VIII. The volume changes for mixing the major sea salts at an ionic strength of 3.0 from 5–95°C. Journal of Solution Chemistry 16, pp. 491–502, 1987.

[24] Krumgalz B. S., Millero F. J.: Physico-chemical study of dead sea waters. II. Density measurements and equation of state of Dead Sea waters at 1 atm. Marine Chemistry 11, pp. 477–492, 1982.

[25] Steiger M.: Crystallization pressure: what is the effect of changes in total volume during phase transitions? In: Wittmann V. (ed.): Materials Science and Restoration MSR VI, Aedificatio Publishers, Freiburg, pp. 43-51, 2003.

[26] Krumgalz B. S., Malester I. A., Ostrich I. J., Millero F. J.: Heat capacities of concentrated multicomponent aqueous electrolyte solutions at various temperatures. Journal of Solution Chemistry 21, pp. 635–649, 1992.

[27] Randall M., Rossini F. D.: Heat capacities in aqueous salt solutions. Journal of the American Chemical Society 51, pp. 323–345, 1929.

[28] Likke S., Bromley L. A.: Heat Capacities of aqueous NaCl, KCl, $MgCl_2$, $MgSO_4$, and Na_2SO_4 solutions between 80° and 200° C. Journal of Chemical and Engineering Data 18, pp. 189–195, 1973.

[29] Desnoyers J. E., de Visser C., Perron G., Picker P. : Reexamination of the heat capacities obtained by flow microcalorimetry. Recommendation for the use of a chemical standard. Journal of Solution Chemistry 5, pp. 605–616, 1976.

[30] Olofsson I. V., Spitzer I. J., Hepler L. G.: Apparent molal heat capacities and volumes of aqueous electrolytes at 25°C: Na_2SO_4, K_2SO_4, $Na_2S_2O_3$, $Na_2S_2O_8$, $K_2S_2O_8$, K_2CrO_4, Na_2MoO_4, and Na_2WO_4. Canadian Journal of Chemistry 56, pp. 1871–1873, 1978.

[31] Rogers P. S. Z., Pitzer K. S.: High-temperature thermodynamic properties of aqueous sodium sulfate solutions. Journal of Physical Chemistry 85, pp. 2886–2895, 1981.

[32] Conti G., Gianni P., Tiné M. R.: Mixed interaction terms in the use of Pitzer equations: Application to the heat capacities of the reciprocal system Na^+–K^+–Cl^-–SO_4^{2-}–H_2O at high temperatures. Thermochimica Acta 145, 61–75, 1989.

[33] Magalhães M. C. F., Königsberger E., May P. M., Hefter G.: Heat capacities of concentrated aqueous solutions of sodium sulfate, sodium carbonate, and sodium hydroxide at 25°C. Journal of Chemical and Engineering Data 47, pp. 590–598, 2002.

[34] Espinosa R. M., Franke L., Deckelmann G.: Phase changes of salts in porous materials: Crystallization, hydration and deliquescence. Construction and Building Materials 22, pp. 1758–1773, 2008.

Michael Steiger
Dr.

Kirsten Linnow
Dr.

University of Hamburg, Department of Chemistry, Inorganic and Applied Chemistry

Phase equilibria in mesoporous materials

Summary

Phase equilibria in mesoporous materials are affected by the curvature of the vapor–solution and the crystal–solution interfaces. The present paper provides a discussion of the thermodynamic treatment of these influences in unsaturated small pores including equations for the calculation of vapor–liquid and solid–liquid phase equilibria. These equations are used together with an electrolyte solution model to predict the solubilities, freezing temperatures and saturation humidities of NaCl solutions in porous materials with different pore sizes. While there is a strong influence of pore size on the freezing temperature of the solvent and the saturation humidity, the influence on the solubility is less pronounced due to a partial compensating effect of the increased solubility of small crystals and the solubility decrease under conditions of low pressure as in unsaturated nanosized pores. It is also shown that the same model equations can be applied to predict the behavior of aerosol nanoparticles.

Keywords: *mesoporous materials, crystal size, pressure, unsaturated materials, interfacial energies, solubility calculation, nanoparticles*

1 Introduction

The pressure generated by crystal growth of salts in confined spaces of porous building materials such as stone, brick and concrete is generally recognized as a major cause of damage in ancient monuments and modern buildings. Crystal growth is also considered as an important weathering mechanism of natural rocks in a variety of environments not only on earth, e.g. in deserts, dry Antarctic valleys and tropical coastlines, but also on Mars. Crystal growth in porous materials is the result of phase changes that are induced by variation of ambient temperature and relative humidity, RH. Unfavorable conditions of temperature and RH may result in repeated cycles of freezing–thawing, crystallization–deliquescence and hydration–dehydration, respectively. Under such conditions, building materials and natural rocks are subject to rapid decay. The relevant phase equilibria in building materials can be modeled using a multicomponent electrolyte solution model such as the model presented in the previous chapter [1]. It is then possible to predict ambient conditions, i.e. temperature and relative humidity that minimize the frequency of occurrence of undesired phase changes inducing crystal growth in por-

ous materials. For instance, model simulations are particularly helpful to predict the influence of changes in the room climate to salt contaminated masonry [2].

The range of pore sizes found in various building materials extends from a few nanometers to hundreds of micrometers and it is important to consider possible effects of pore size on the various phase equilibria in these materials. Following the recommendations of IUPAC [3] pores with pore diameters exceeding about 50 nm are called macropores, while pores with diameters between 2 nm and 50 nm are called mesopores, and even smaller pores are called micropores. There is no restriction for the application of electrolyte solutions models and the calculation of phase equilibria in macroporous materials. However, in the small pores of mesoporous materials the situation becomes more complicated as the influence of interfaces can no longer be neglected. Such small pores are commonly found in concrete and sometimes in bricks and fine-grained natural stone materials. Phase equilibria in mesoporous materials are strongly affected by both the vapor–solution and the crystal–solution interfaces. Firstly, the available pore space limits the maximum size of growing crystals and the interfacial energy of the crystal–liquid interface affects the solubility of dissolved species [4]. Secondly, in an unsaturated porous material, a curved liquid-vapor interface is formed resulting in a substantial pressure decrease. Hence, in addition to crystal size effects the influence of low pressure on the various phase equilibria has to be considered. The present paper provides a discussion of the thermodynamic treatment of phase equilibria in unsaturated small pores including the vapor–liquid equilibrium, freezing temperatures and salt solubilities.

2 Theoretical background

2.1 Unsaturated porous materials

Phase equilibria in mesoporous materials are affected by the vapor–solution and the crystal-solution interface. Figure 1 depicts the situation of a crystal growing in idealized pores of cylindrical geometry. Considering a liquid in a porous material, it is important to distinguish the degree of saturation which is defined as the fraction of the pore space filled with liquid water. In a saturated material the liquid–vapor interface is flat (Fig. 1a) while, in an unsaturated porous material, a curved liquid–vapor interface is formed. For a wetting fluid such as in the case of water in building materials, the curvature of the liquid–vapor interface is concave as illustrated in Fig 1b. The curvature of the interface results in a pressure drop which is given by Laplace's law:

$$\Delta p = p_l - p_a = 2\gamma_{lv}/r_{lv} = -2\gamma_{lv}\cos\theta/r_P \quad (1)$$

Here, p_l is the pressure in the liquid phase, p_a is the ambient pressure, γ_{lv} and r_{lv} are the interfacial energy and the radius of curvature of the liquid–vapor interface, θ is the contact angle of water with the pore walls and r_p is the radius of a cylindrical pore. Note that by definition the radius of curvature of a concave surface is negative, hence, there is a pressure decrease in the liquid phase.

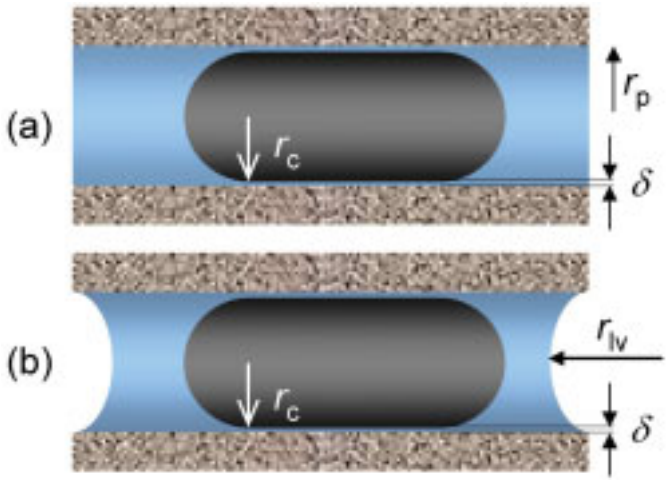

Figure 1: Liquid–vapor and crystal–liquid interface in a saturated (a) and unsaturated (b) porous material with cylindrical pore geometry; r_p is the pore radius, r_c is the radius of the cylindrical crystal, and, $\delta = r_p - r_c$ is the thickness of the liquid film between the pore wall and the crystal.

In contrast, for a convex interface such as in solution droplets there is a pressure increase in the liquid. Assuming that the liquid is perfectly wetting the pore wall (i.e. $\theta = 0$), which is a reasonable assumption for water in building materials, the Laplace law simplifies to $\Delta p = -2\gamma_{lv}/r_P$. For a pore radius of 5 nm, this yields a pressure of –29 MPa in the liquid phase.

2.2 Vapor–liquid equilibrium

Here, we follow the treatment in our previous work [5]. The standard states for pure solid phases and water are unit activity at any temperature and pressure. For the aqueous species other than H_2O, the standard state is unit activity in a hypothetical one molal ideal solution referenced to infinite dilution at any temperature and pressure. Then, equilibrium between water vapor and liquid water in an aqueous solution requires equality of the chemical potentials in the liquid phase (μ_l) and in the gas phase (μ_g). The chemical potentials of liquid water and water vapor are given by

$$\mu_l = \mu_l^\circ + RT \ln a_w = \mu_g = \mu_g^\circ + RT \ln(p_w / p_w^\circ) \tag{2}$$

where a_w is the water activity of the solution, p_w is the water vapor partial pressure over the solution, p_w° is the saturation vapor pressure and R and T are the gas constant and the absolute temperature, respectively. For a bulk sample of pure water at equilibrium we obtain $a_w = 1$ and $p_w = p_w^\circ$ In the case of a salt solution at equilibrium, the water activity equals the ratio p_w / p_w° which, by definition, is the relative humidity, RH.

For the chemical potential of liquid water under the reduced pressure p_l we obtain

$$\mu_l = \mu_l^\circ + RT \ln a_w + 2\gamma_{lv}\bar{V}_w / r_{lv} \tag{3}$$

where $\bar{V}_w$ is the partial molar volume of water in the solution. The pressure dependence of the partial volume of water is rather small and is neglected in this study. For more accurate calculations, an appropriate equation for the calculation of the pressure dependence may be found in reference [6]. In the derivation it is also assumed that a_w is not a function of pressure. Strictly, however,

$$d\ln a_w / dp = \left(\bar{V}_w - \bar{V}_w^\circ\right) \Delta p / RT \tag{4}$$

where $\bar{V}_w^\circ$ is the molar volume of pure water. It has been shown [7] that the quantity ($\bar{V}_w - \bar{V}_w^\circ$) is very small even at high solute concentrations. Therefore, the pressure dependence of a_w can be neglected and $\bar{V}_w$ in Eq. (3) may be replaced by $\bar{V}_w^\circ$. Values of the molar volume of water were taken from Kell [8].

Then, at equilibrium, the water vapor partial pressure over a solution in an unsaturated porous material is given by:

$$\ln\left(p_w / p_w^\circ\right) = \ln a_w + 2\gamma_{lv}\bar{V}_w^\circ / \left(r_{lv} RT\right) \tag{5}$$

Equation (5) yields the depression of the water vapor partial pressure due to the influence of both dissolved salts and the curvature of the liquid–vapor interface in small unsaturated pores. The influence of the solution composition on the water activity can be calculated by using the ion interaction model presented in the previous chapter [1] and in reference [9].

2.3 Solid–liquid equilibria

For the dissolution reaction of a salt of general composition $M_{\nu M}X_{\nu X} \cdot \nu_0 H_2O$

$$M_{\nu_M} X_{\nu_X} \cdot \nu_0 H_2O \rightleftharpoons M^{z+} + X^{z-} + \nu_0 H_2O \tag{6}$$

the thermodynamic solubility product is given by

$$\ln K = \nu_M \ln m_M + \nu_X \ln m_X + \nu_M \ln \gamma_M + \nu_X \ln \gamma_X + \nu_0 \ln a_w \tag{7}$$

where m_M, m_X, γ_M and γ_X represent the molalities and activity coefficients of the cations and anions, respectively. There are two influences that affect the solubility of a salt in a mesoporous material. First, there is an influence of crystal size as discussed in detail in reference [4]. Second there is an influence of the reduced pressure in an unsaturated material. The influence of crystal size on the solubility product in a cylindrical pore as shown in Fig. 1a is given by [4]:

$$\ln K_r^{(0)} = \ln K_\infty^{(0)} + \frac{2\gamma_{cl} V_m}{r_c RT} \tag{8}$$

where $K_r^{(0)}$ and $K_\infty^{(0)}$ are the thermodynamic solubility products at standard pressure (0.1 MPa) of the crystal with radius r_c and an infinitely large crystal, respectively; γ_{lc} is the interfacial free energy of the crystal–liquid interface and V_m is the molar volume of the solid.

The effect of pressure on the solubility is given by [10]:

$$\ln K_{\infty}^{(p)} = \ln K_{\infty}^{(0)} - \frac{\Delta \bar{V}^{\circ}}{RT}\Delta p + \frac{\Delta \bar{K}^{\circ}}{RT}(\Delta p)^2 \tag{9}$$

where $K_{\infty}^{(p)}$ is the thermodynamic solubility product at pressure p and $\Delta \bar{V}^{\circ}$ and $\Delta \bar{K}^{\circ}$ are the changes in molar volume and molar compressibility of the dissolution reaction at 0.1 MPa. For example, the change in molar volume for the dissolution reaction (6) is given by

$$\Delta \bar{V}^{\circ} = \sum_i \bar{V}_i^{\circ} + \nu_0 \bar{V}_{\mathrm{w}}^{\circ} - V_{\mathrm{m}} \tag{10}$$

where $\bar{V}_i^{\circ}$ are the partial molar volumes of the ions *i* at infinite dilution. An analogous expression holds for the change of standard compressibility. Combining Eqs. (8) and (9), yields an expression for the thermodynamic solubility product of a small crystal at pressure *p*:

$$\ln K_r^{(p)} = \ln K_{\infty}^{(0)} + \frac{2\gamma_{\mathrm{lc}} V_{\mathrm{m}}}{r_{\mathrm{c}} RT} - \frac{\Delta \bar{V}^{\circ}}{RT}\Delta p + \frac{\Delta \bar{K}^{\circ}}{RT}\Delta p^2 \tag{11}$$

The calculation of freezing temperatures of salt solutions using the ion interaction model was described in detail in reference [11]. The equilibrium constant in a bulk solution is given by:

$$\ln K_{\infty} = a_{\mathrm{w}} \tag{12}$$

Values of $\ln K_{\infty}$ at various temperatures were taken from reference [12]. An expression analogous to Eq. (11) can then be used for the calculation of freezing temperatures in small pores where the change in molar volume and compressibility is given as the difference of the molar volumes and compressibilities of ice and liquid water [5]. This yields

$$\ln K_r^{(p)} = \ln K_{\infty}^{(0)} + \frac{2\gamma_{\mathrm{lc}} V_{\mathrm{ice}}}{r_{\mathrm{c}} RT} - \frac{\bar{V}_{\mathrm{w}}^{\circ} - V_{\mathrm{ice}}}{RT}\Delta p + \frac{\bar{K}_{\mathrm{w}}^{\circ} - K_{\mathrm{ice}}}{RT}\Delta p^2 \tag{13}$$

where V_{ice} and K_{ice} are the molar volume and compressibility of ice. However, the compressibilities of water and ice were neglected in the present treatment.

3 Calculations

3.1 Liquid phase pressure and liquid–vapor equilibrium

The calculation of the liquid phase pressure in pore solutions requires values of the interfacial energy of the liquid–vapor interface γ_{lv}, i.e. the surface tension of the pore solutions. The available experimental surface tension data have been tabulated by Abramzon and Gaukhberg [13]. For most salts, the available data are quite scattered. The following very simple equation proved to be sufficient to reproduce most of the experimental data of γ_{lv} to within their respective uncertainties:

$$\gamma_{lv} = \gamma_{lv}^{\circ} + gm \tag{14}$$

Here, γ_{lv}° is the interfacial tension of pure water, m is the molality of the solution and g is an empirical parameter that is determined from experimental data for each salt. The interfacial tension of pure water at various temperatures has been calculated from the equation proposed by Cini et al. [14]. For the calculations with NaCl(aq) a temperature independent value of $g = 1.66 \pm 0.02$ J·kg·m^{-2}·mol^{-1} was used. Figure 2 depicts the calculated liquid phase pressures as a function of pore size for pure water and NaCl solutions. It is obvious that there is only a rather small influence of the surface tension of the solution on the liquid phase pressure. Hence, for binary solutions, our very simple approach for the calculation of interfacial tensions appears to be appropriate. For multicomponent systems, more complicated equations may be used such as, for example, provided in references [15] or [16].

The equilibrium of a salt solution of any composition in a porous material and the water vapor in the surrounding air can be treated using Eq. (5). For a bulk sample of pure water, i.e. RH = $a_w = 1$, it follows from Eq. (5) that the liquid–vapor interface is flat (i.e. $r_{lv} = \infty$). For water in a small cylindrical pore, the curvature of the liquid–air interface increases with decreasing RH. The maximum curvature is reached if $r_{lv} = -r_p$; any further decrease in RH will then cause the complete evaporation of the pore. In other words, if the relative humidity exceeds the critical value corresponding to the maximum curvature, capillary condensation occurs. Similar arguments apply to a salt solution in a small pore. In this case however, the water activity is lower and a flat surface is reached at a lower RH, namely at RH = a_w.

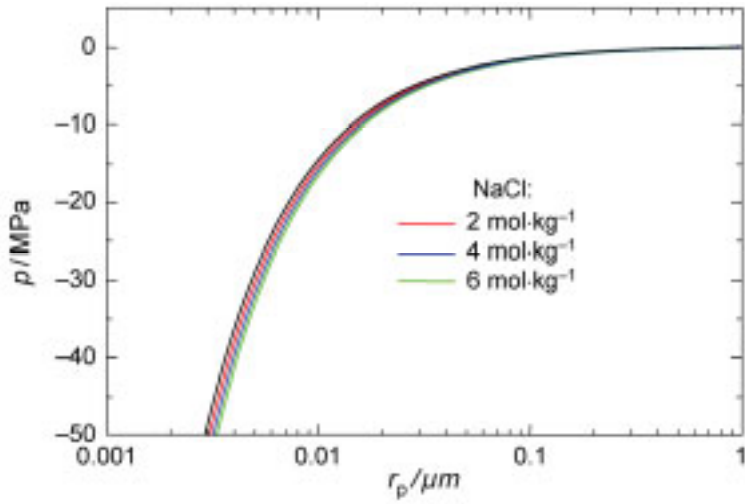

Figure 2: Liquid phase pressure as a function of pore size for pure water and NaCl solutions with molalities 2 mol·kg^{-1}, 4 mol·kg^{-1} and 6 mol·kg^{-1}.

3.2 Solubility of NaCl in mesoporous materials

It follows from Eq. (8) that there is an increase in solubility with decreasing crystal size. Therefore, salt solubilities in a saturated mesoporous material are higher than in a macroporous material. This is the theoretical basis of the equilibrium crystallization pressure that is generated by crystals that are confined in very small pores [4,17,18]. The additional influence of pressure in an unsaturated material is controlled by the change in molar volume and compressibility. Both, the values of $\Delta\overline{V}^{\circ}$ and Δp are negative resulting in a solubility decrease at low pressure. Since the values of $\Delta\overline{K}^{\circ}$ are also negative, it is expected that the solubility increase is less pronounced at very low pressures, i.e. in very small pores. A comparison of the two competing influences, i.e. crystal size and low pressure, on the solubility of NaCl is illustrated in Fig. 3.

In these calculations, a value of the molar volume of NaCl of 27.02 $cm^3 \cdot mol^{-1}$ was used. A compilation of the molar volumes of other salt minerals relevant to building materials is provided in reference [19]. Values of the partial molar volumes of the ions *i* at infinite dilution were taken from our density model [1]. Values of the partial molar compressibilities at infinite dilution were taken from Millero [10]. There is a lack of reliable data for the compressibilities of the solid phases. However, compressibilities of solids are typically low relative to the partial compressibilities of the respective ions at infinite dilution [20]. Therefore, we have neglected the compressibilities of the solid phases yielding a value of -0.047 $cm^3 \cdot mol^{-1} \cdot MPa^{-1}$ for the change of the compressibility in the dissolution reaction of halite (NaCl).

The crystal size influence is largely controlled by the value of the crystal–liquid free energy γ_{lc}. Unfortunately, no reliable experimental data of interfacial energies are available. In the case of NaCl(cr), we have adopted the value of $\gamma_{lc} = 30$ $mJ \cdot m^{-2}$ given by Wu and Nancollas [21]. These authors also discuss the difficulties in the measurement of interfacial energies. The shaded area in Fig. 3a indicates the range of uncertainty in the solubility product that arises from an arbitrarily estimated uncertainty in the γ_{lc} value of ± 20 $mJ \cdot m^{-2}$. This confirms the rather strong influence of the interfacial energy on the solubilities of very small crystals. There is a strong decrease of the NaCl solubility with decreasing pressure in small pores of unsaturated materials (Fig. 3b). As expected, the influence of compressibility is only significant at very low pressure, i.e. in very small pores.

Figure 4 depicts the combined influence of crystal size and the reduced liquid phase pressure in an unsaturated material, again calculated with different values of γ_{lc}. The activity coefficients and water activities required for the calculation of solubilities were taken from the electrolyte solution model presented in the previous chapter [1,9]. The thickness of the solution film was assumed as $\delta = 0.5$ nm. The very small influence of pressure on the activity coefficients of NaCl(aq) and the water activity were neglected.

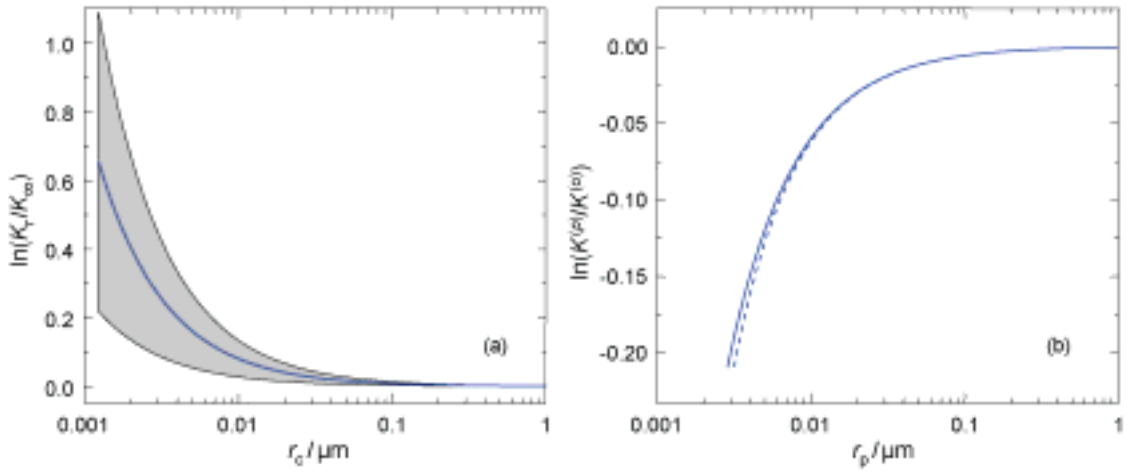

Figure 3: Solubility of NaCl in mesoporous materials (25 °C): (a) influence of crystal size in a saturated material at 0.1 MPa calculated with $\gamma_{lc} = 30$ mJ·m^{-2} (the shaded area indicates the influence of an uncertainty in this value of ± 20 mJ·m^{-2}); (b) influence of reduced pressure in small pores of an unsaturated material with (—) and without (---) inclusion of the compressibility term.

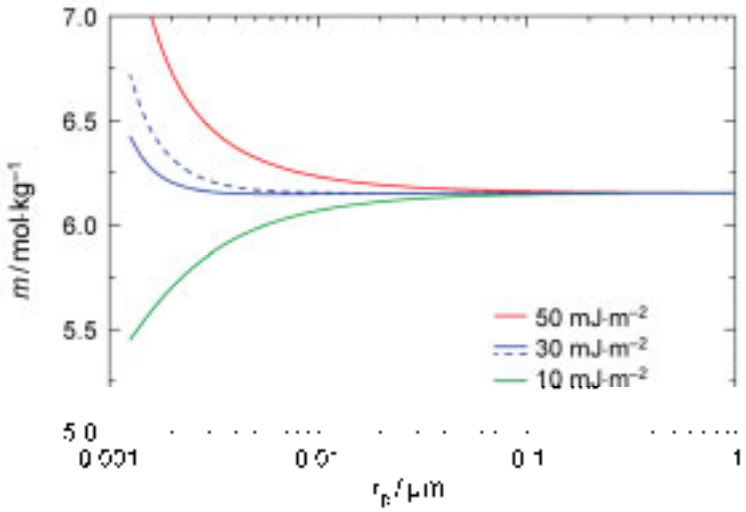

Figure 4: Solubility of NaCl as a function of pore size in mesoporous materials at 25 °C; with the exception of the dashed blue curve, all solubilities were calculated with the compressibility term in Eq. (11) included.

It is obvious from Fig. 4 that the pressure effect and the crystal size effect partly compensate each other. Even assuming significantly different values of γ_{lc}, the influence on the solubility of NaCl crystals does not exceed about 10% down to pore radii of about 2 nm.

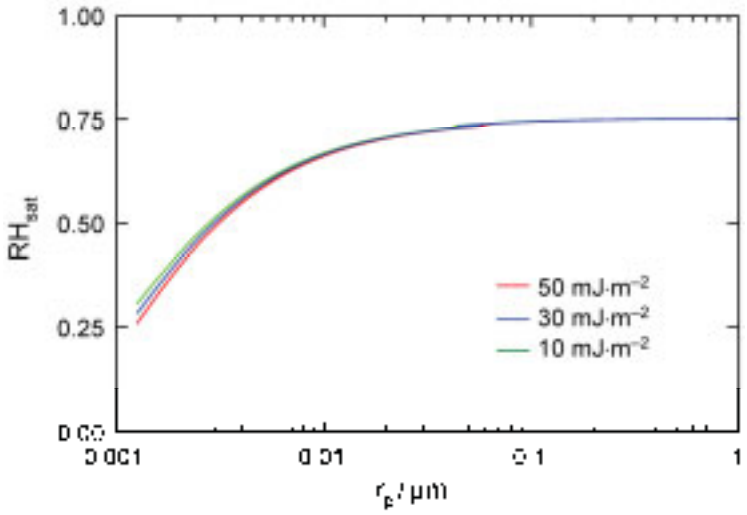

Figure 5: Saturation humidities RH_{sat} of saturated solutions of NaCl in unsaturated porous material at 25 °C; all calculations with inclusion of compressibility term.

More important than the solubility of NaCl is the saturation humidity, i.e. the relative humidity of the surrounding air that is in equilibrium with the saturated solution. Only if the relative humidity drops below the saturation humidity, the respective salt will crystallize out. Hence, no crystallization damage can occur at relative humidities above the saturation humidity. Figure 5 depicts the relative humidities in equilibrium with saturated NaCl solutions as a function of pore size. Using Eq. (5), calculations were carried out for the saturated solutions at different pore sizes as shown in Fig. 4. The water activities required in Eq. (5) were calculated with the electrolyte solution model [9]. It is obvious that there is a strong influence of pore size on the saturation humidities. Due to the curvature of the interface between the saturated solution and the air there is a substantial decrease in the saturation humidities. Sodium chloride in an unsaturated mesoporous material crystallizes at lower relative humidities than in macroporous materials. For example, a saturation humidity of 59% RH is calculated for an unsaturated cylindrical pore with a pore diameter of 10 nm, a value much lower than the value of 75.3% in bulk solutions. Figure 5 also shows that the uncertainty in the values of the interfacial energy of NaCl crystals that caused some scatter in the calculation of the solubilities in small pores is less critical in the calculation of the saturation humidity.

There are no experimental data of saturation humidities in mesoporous materials available that could be used to validate these model predictions. However, experimental data are available for the deliquescence humidities of nanosized aerosol particles [22,23]. Aerosol particles play a fundamental role in the microphysics of clouds. They provide heterogeneous nucleation sites for the formation of droplets. Water soluble aerosols such as NaCl can deliquesce to form saturated solutions in the form of small droplets that play an important role in forming haze and clouds and can act as sites for heterogeneous chemical reactions. Also, the hygroscopic growth of particles has important consequences for the predicted atmospheric radiative transfer of aerosols and their effect on climate.

The deliquescence of aerosol nanoparticles and the calculation of solubilities in nanosized droplets is a problem similar to the calculation of solubilities in small capillaries. In both cases there is a convex crystal–liquid interface. In droplets however, the curvature of the vapor–liquid interface is convex while this interface is concave in the case of a wetting fluid in small capillaries. For a convex interface, r_{lv} is positive resulting in a pressure increase in aerosol droplets with decreasing droplet size. Using the present model, solubilities and saturation humidities of NaCl in small droplets have been calculated and compared to experimental values [22,23]. Due to the convex interface, the deliquescence humidities are higher than for large crystals. In all cases, our calculations agree with the experimental values to within their stated uncertainty and correctly predict an increase in the deliquescence for small particle sizes. For example, for a 10 nm sized NaCl particle a deliquescence humidity of 84.8% is predicted. Note that the deliquescence of a particle in a small pore of the same size (10 nm diameter) was calculated at 59% RH. Finally, the agreement of the present calculations with the experimental data is significantly better than earlier model calculations of Mirabel et al. [24] as well as Russel and Ming [25].

3.3 Freezing temperatures

Calculations of freezing temperatures in bulk electrolyte solutions and in saturated and unsaturated porous materials have been reported earlier [5,11]. As an example, Fig. 6 depicts calculated freezing temperatures in bulk NaCl solutions and in NaCl pore solutions of a saturated mesoporous material in comparison to available experimental data [26,27,28,29]. In the calculations cylindrical pore geometry was assumed. The thickness of the unfrozen liquid film was assumed as $\delta = 1$ nm. Molar volumes of supercooled water were taken from Kell [8] while the molar volume of ice was assumed to be independent of temperature ($V_s = 19.65\ \mathrm{cm^3\,mol^{-1}}$). Values of the ice–liquid water interfacial energy were taken from Brun et al. [28] and interfacial tensions and water activities of NaCl solutions were calculated as described before.

There is excellent agreement between experimental and calculated freezing temperatures in bulk solutions. It should be noted however, that freezing temperatures were used to determine the model parameters in the electrolyte solution model [9]. The pore size dependence of the freezing temperatures curves in Fig. 6 indicate that in pores larger than about 10 nm the freezing temperature depression is largely controlled by the presence of dissolved NaCl. In smaller pores the freezing temperature rapidly decreases mainly as a result of the small size of the ice crystals in these pores, i.e. the influence of the interfacial energy of the crystal–liquid interface. Also shown in Fig. 6b are experimental freezing temperatures of pure water in mesoporous materials [27–29].

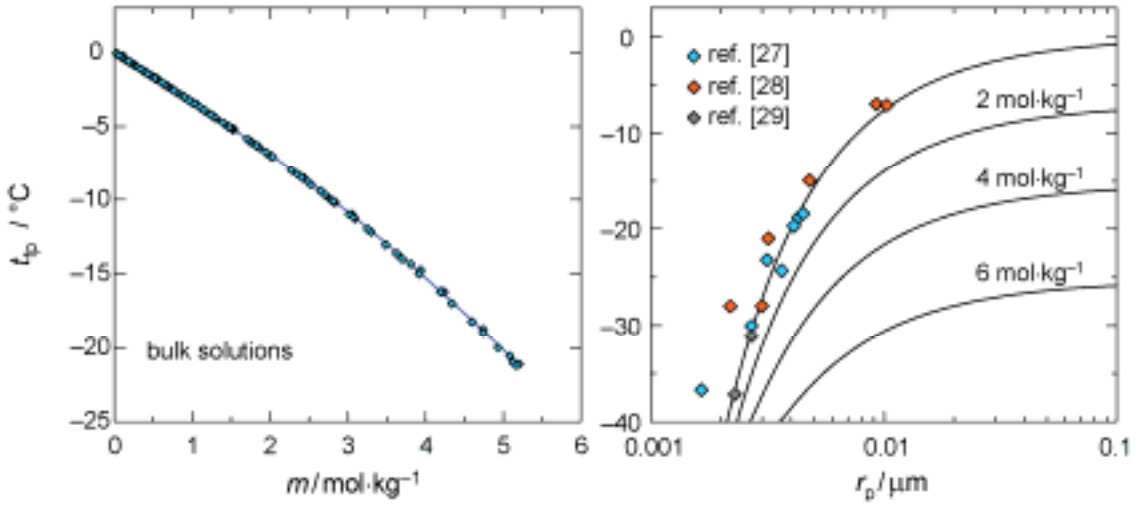

Figure 6: Freezing temperatures in NaCl solutions: (a) freezing temperatures in bulk solutions (symbols represent experimental data [26]); (b) freezing temperatures in saturated porous materials of pure water and NaCl solutions with 2 mol·kg^{-1}, 4 mol·kg^{-1} and 6 mol·kg^{-1} (symbols are experimental for pure water [27–29]).

Though these data are somewhat scattered, there is reasonable agreement with the calculated freezing temperatures. It has been shown in reference [5] that the pressure decrease in the liquid phase of unsaturated pores causes a minor increase in the freezing temperature in comparison to a saturated material. The resulting freezing temperature curves in unsaturated mesoporous materials are very similar to those shown in Fig. 6b. This is due to the fact that the difference in the molar volumes of liquid water and ice entering the second term on right-hand side of Eq. (13) is small.

4 Conclusions

Phase equilibria in mesoporous materials are affected by the curvature of the vapor–solution and the crystal–solution interfaces. Using Eqs. (5), (11) and (13) together with our model of the thermodynamic properties of bulk solutions, it is possible to predict phase equilibria in small pores. The parameters that are required in addition to the models presented in the previous chapter [1], are the surface tensions of salt solutions, the crystal–liquid interfacial energies of the solid phases and the ionic partial molar compressibilities at infinite dilution. As long as calculations are only required for single salts, a very simple equation can be used to calculate surface tensions in salt solutions with sufficient accuracy. Somewhat more complicated equations will be required in future work with mixed salt solutions. Accurate experimental data for the crystal–liquid interfacial energies of the solid phases are not available, hence, these values have to be estimated using equations available in the literature. Fortunately, the test calculations for NaCl carried out in this study indicate that the uncertainty in the γ_{cl} values may not cause unacceptable large errors at realistic pore sizes.

The calculated solubilities imply that there is not such a strong change in solubilities of salts in very small pores. A partial compensation of the competing influences of crystal size and liquid phase pressure in unsaturated mesoporous materials is the main reason for this behavior. In contrast to the solubilities, the saturation humidities in unsaturated materials are strongly affected by the pore size, i.e. there is a significant decrease in the saturation humidity with decreasing pore size. It is important to note, that the uncertainties in the interfacial energies of the solids do not introduce large error in the calculation of the saturation humidities.

Finally, it has been shown that the same model equations can be used to predict the behavior of aerosol particles in atmospheric applications where a convex solution–vapor interface causes a pressure increase in solution droplets. The resulting increase in the saturation or deliquescence humidities is accurately predicted by the present model.

5 References

[1] Linnow K., Steiger M.: Modeling the properties of pore solutions in porous building materials. This volume.

[2] Steiger M.: Salts in porous materials: Thermodynamics of phase transitions, modeling and preventive conservation. Restoration of Buildings and Monuments 11, pp. 419–431, 2005.

[3] Sing K. S. W., Everett D. H., Haul R. A. W., Moscou L., Pierotti R. A., Rouquerol J., Siemieniewska T.: Reporting physisorption data for gas/solid system with special reference to the determination of surface area and porosity. Pure & Applied Chemistry 57, pp. 603–619, 1985.

[4] Steiger M.: Crystal growth in porous materials:—II. The influence of crystal size. Journal of Crystal Growth 282, pp. 470–481, 2005.

[5] Steiger M.: Freezing of salt solutions in small pores. In: M.S. Konsta-Gdoutos (ed.): Measuring, Monitoring and Modelling Concrete Properties, Springer, Dordrecht, pp. 661–668, 2006.

[6] Mercury L., Tardy Y.: Negative pressure of stretched liquid water. Geochemistry of soil capillaries. Geochimica et Cosmochimica Acta 65, pp. 3391–3408, 2001.

[7] Monnin C.: The influence of pressure on the activity coefficients of the solutes and the solubility of minerals in the system Na–Ca–Cl–SO_4–H_2O to 200 °C and 1 kbar, and to high NaCl concentration. Geochimica et Cosmochimica Acta, 54, pp. 3265–3282, 1990.

[8] Kell G. S.: Effects of isotopic composition, temperature, pressure, and dissolved gases on the density of liquid water. Journal of Physical and Chemical Reference Data 6, pp. 1109–1131, 1977.

[9] Steiger M., Kiekbusch J., Nicolai A.: An improved model incorporating Pitzer's equations for calculation of thermodynamic properties of pore solutions implemented into an efficient program code. Construction and Building Materials 22, pp. 1841–1850, 2008.

[10] Millero F. J.: The effect of pressure on the solubility of minerals in water and seawater. Geochimica et Cosmochimica Acta 46, pp. 11–22, 1982.

[11] Steiger M.: Influence of salts on the freezing temperature of water: implications on frost damage to porous materials. In: D. Kwiatkowski, R. Löfvendahl (eds.): Proceedings of the 10th International Congress on Deterioration and Conservation of Stone, ICOMOS, Stockholm, 2004, pp. 179–186, 2004.

[12] Klotz I. M., Rosenberg R. M.: Chemical thermodynamics, basic theory and methods. Benjamin/Cunnings, Menlo Park CA, 3rd ed., pp. 374–378, 1972.

[13] Abramzon A. A., Gaukhberg R. D.: Surface tension of salt solutions. Russian Journal of Applied Chemistry 66, pp. 1139–1146, pp. 1315–1320, pp. 1473–1480, 1993.

[14] Cini R., Loglio G., Ficalbi A.: Temperature dependence of the surface tension of water by the equilibrium ring method. Journal of Colloid and Interface Science 41, pp. 287–297, 1972.

[15] Li Z., Lu B. Z.-Y.: Surface tension of aqueous electrolyte solutions at high concentrations - representation and prediction. Chemical and Engineering Science 56, pp. 2879–2888, 2001.

[16] Hu Y.-F., Lee H.: Prediction of the surface tension of mixed electrolyte solutions based on the equation of Patwardhan and Kumar and the fundamental Butler equation. Journal of Colloid and Interface Science 269, pp. 442–448, 2004.

[17] Everett D. H.: The thermodynamics of frost damage to porous solids. Transactions of the Faraday Society 57, pp. 1541–1551, 1961.

[18] Scherer G. W.: Crystallization in pores. Cement and Concrete Research 29, 1347–1358.

[19] Steiger M.: Total volumes of crystalline solids and salt solutions. In: Price C. A. (ed.), An expert chemical model for determining the environmental conditions needed to prevent salt damage in porous materials. European Commission, Research Report 11, pp. 53–63, 2000.

[20] Marion G.M., Kargel J. S., Catling D. C., Jakubowski S. D.: Effects of pressure on aqueous chemical equilibria at subzero temperatures with applications to Europa. Geochimica et Cosmochimica Acta 69, pp. 259–274, 1982.

[21] Wu W., Nancollas G. H.: Determination of interfacial tension from crystallization and dissolution data: a comparison with other methods. Advances in Colloid and Interface Science 79, pp. 229–279, 1999.

[22] Hämeri K., Laaksonen A., Väkevä M., Suni T.: Hygroscopic growth of ultrafine sodium chloride particles. Journal of Geophysical Research 106, pp. 20749–20757, 2001.

[23] Biskos G., Malinowksi A., Russell L. M., Buseck P. R., Martin S. T.: Nanosize effect on the deliquescence and the efflorescence of sodium chloride particles. Aerosol Science and Technology 40, pp. 97–106, 2006.

[24] Mirabel P., Reiss H., Bowles R. K. : A theory for the deliquescence of small particles. Journal of Chemical Physics 113, pp. 8200–8205, 2000.

[25] Russel L. M., Ming Y.: Deliquescence of small particles. Journal of Chemical Physics 116, pp. 311–321, 2002.

[26] Cohen-Adad R., Lorimer P. W: Alkali metal and ammonium chlorides in water and heavy water (binary systems). Solubility Data Series, International Union of Pure and Applied Chemistry, Pergamon Press, Oxford, pp. 80–84, 1991

[27] Schreiber A., Ketelsen I., Findenegg G. H.: Melting and freezing of water in ordered mesoporous silica materials. Physical Chemistry and Chemical Physics 3, pp. 1185–1195, 2001.

[28] Brun M., Lallemand A., Quinson J.-F., Eyraud C.: A new method for the simultaneous determination of the size and the shape of pores: The thermoporometry. Thermochimica Acta 21, pp. 59–88, 1977.

[29] Morishige K., Kawano K.: Freezing and melting of water in a single cylindrical pore: The pore-size dependence of freezing and melting behavior. Journal of Chemical Physics 110, pp. 4867–4872,

Rosa M. Espinosa-Marzal *Dr.-Ing.*
Gernod Deckelmann *Dr.-Ing.*
Lutz Franke *Prof. Dr. -Ing.*

Institute of Building Materials, Physics and Chemistry of Buildings
Hamburg University of Technology, Germany

Kinetics of phase changes of salts in porous materials: crystallization, hydration and deliquescence

Summary

The objective of this work was to deduce a mathematical model for the kinetics of phase changes of salts in pores to be coupled with a simulation program for heat, moisture and salt transport in capillary porous materials.

It could be proven that a unique equation describes the kinetics of all possible phase changes. This equation is based on the fact that the driving force for any phase change is the difference between the chemical potentials of the start and end phases. The difference in chemical potentials is described by means of the thermodynamic supersaturation ratio of the pore solution U^P_a. The time-dependent phase change of salts in porous materials was investigated experimentally by means of measuring temperature differences (crystallization and dissolution) and weight differences (hydration, dehydration and deliquescence). In all cases a supersaturation ratio greater than 1 is necessary for the phase change to start. In case of the crystallization, a "starting supersaturation ratio" $U^P_{a,start}$ larger than 1 was found for each material and salt. Furthermore two kinetic parameters K and g are also necessary to describe the phase change. The values of K and g were obtained by fitting the experimental results to the proposed equation for kinetics. It was found that the kinetics of each phase change generally depends on both salt and porosity.

Keywords: *salt crystallization, material pores, crystallization kinetics, supersaturation ratio, hydration, dehydration, dissolution, deliquescence.*

1 Introduction and backgrounds

The simulation of heat coupled with moisture, and salt transport in capillary porous materials has become possible since a couple of years due to the great development of computer technology. The reliability of simulation calculations depends on the quality of both input parameters and models for transport, storage and phase changes of salts and water processes. In this paper we will deal with the kinetics of phase changes of salts in pores. The extension to salt mix-

tures and the resulting mechanical stress due to crystallization pressure will be described in further papers.

Three classes of equilibrium between water and salt have to be considered depending on the bounding conditions:

- Equilibrium between water vapor and salt solution
- Equilibrium between salt solution and salt crystal
- Equilibrium between salt crystal and water vapor:
    - Hydration of salt crystals by bonding water vapor molecules or dehydration by loosing hydrate water
    - Deliquescence of a salt crystal by adsorption of water vapor molecules

According to Gibbs' theory, a supersaturation of the salt solution is thermodynamically necessary for nucleation [6]. The driving force for crystallization is the difference between the chemical potentials of solution and nuclei $\Delta\mu$:

$$\frac{\Delta\mu}{RT} = \upsilon \cdot \ln\left(\frac{a_{\pm}}{a_{\pm}^{*}}\right) = \ln U_a \rightarrow \text{with } U_a = \left(\frac{a_{\pm}}{a_{\pm}^{*}}\right)^{\nu}$$

$a_{\pm}^{*}$ = average ion activity of saturated solution
$a_{\pm}$ = average ion activity of given solution,
$\upsilon=\upsilon^{+}+\upsilon^{-}$ = ion mole number per mole solution
R = gas constant in J/Kmol
T= temperature in K

(1)

U_a is called the super saturation ratio of a salt in the solution. If a salt contains hydrate water, the supersaturation ratio is given by:

$$U_a = \left(\frac{a_{\pm}}{a_{\pm}^{*}}\right)^{\nu} \cdot \left(\frac{a_w}{a^{*}_{w}}\right)^{\nu_0}$$

a_w = water activity
a^{*}_w = water activity at equilibrium
υ_0 =number of water molecules per salt mol

(2)

If the supersaturation ratio U_a is larger than 1, the solution is metastable and crystallization can begin. But when U_a is larger than a determined valued $U_{a,start}>1$, nucleation starts abruptly. The start supersaturation ratio $U_{a,start}$ must obviously be larger than 1.

The value of $U_{a,start}$ depends on both salt and pore system. Moreover, the supersaturation determines the crystallization rate: the larger it is, the faster the crystallization proceeds.
Nucleation is said to be heterogeneous if a foreign substance is present in the solution. Since the pore system can be regarded as a foreign substance in contact with the pore solution, the crystallization in pore system will be regarded as heterogeneous. According to thermodynamics, the Gibbs energy necessary for heterogeneous nucleation is diminished by the presence of foreign substances so that the needed supersaturation is reduced, too. Thus, the start supersaturation that is necessary for nucleation in pore solutions is smaller than the one for nucleation in a free solution in absence of impurities: $U^{P}_{a,start} < U_{a,start}$.

When some salt crystals are still present in the pore system, a secondary crystallization of this salt takes place if the supersaturation is larger than 1 ($U_a^P > U^P_{a,start}=1$).

Supersaturation can be computed by means of the Pitzer model and/or its extensions, e.g. by Steiger [7][8][9]. Since equilibrium is reached after a relatively long time, kinetics of phase changes must be considered for calculating the salt crystallization during transport processes of salt and water.

So far, there are only few publications about kinetics of phase change of salts in pore system including experimental results [2]. Several empirical models for the description of kinetics of salt crystallization, dissolution, hydration and deliquescence can be found in [11][5]. Thereby, phase changes are investigated only in the bulk solution or in free salt crystals, and consequently the influence of pore system on the phase change is unknown as yet.

In this paper some experimental results will be discussed and mathematical models will be proposed for kinetics of phase changes of salts in porous material. Thus, it will be shown that kinetics of deliquescence, hydration/dehydration, solution and crystallization can be mathematically described using a very similar equation based on the difference of chemical potential, thus on the supersaturation ratio.

Furthermore, the phase change of salts causes often a damage of building materials. In a following paper, experimental results and mathematical model of the mechanical stress of the material due to crystallization processes will be dealt [2]. Hereby, it is proved that the mechanical stress is strongly affected by the kinetics of crystallization.

2 Description of experiments

The salts KNO_3, Na_2SO_4, KCl, $CaCl_2$, NaCl, $Ca(NO_3)_2$ and three building materials with different pore size distributions (see Figure 1) were selected for this work.

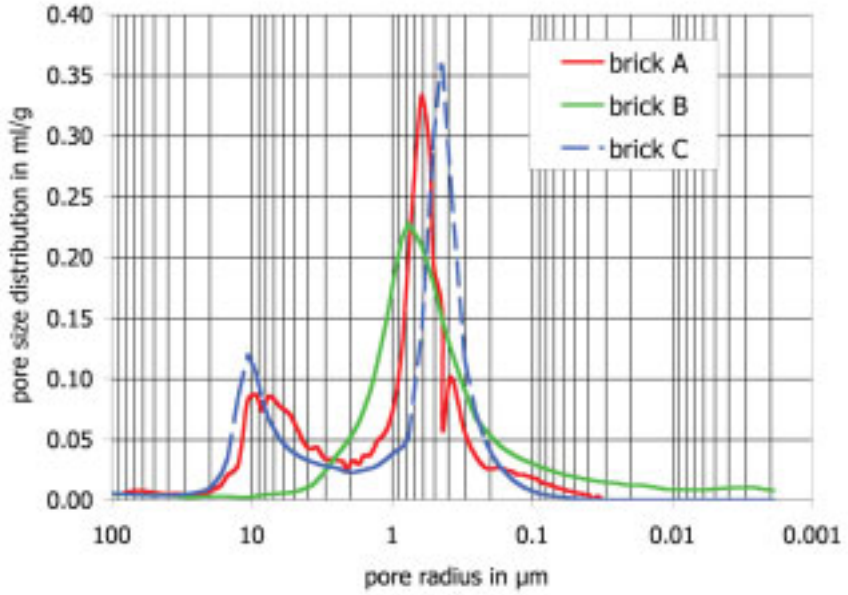

Figure 1: Porosity distribution of the selected materials measured by use of the mercury porosimetry.

The porosity of brick A is 34 %, of brick B, 32 % and of brick C, 31.5 %. The pore size distribution of brick A and C have two peaks (at around 10 and 0.8 µm). In contrast, the porosity of brick B has only one peak at around 0.9 µm. The amount of small pores (R<0.1 µm) in brick B is higher than in bricks A and C.

2.1 Crystallization and dissolution

Crystallization and dissolution of various salts in porous materials were investigated experimentally by means of a self-constructed device that measures temperature differences. The measuring principle is based on the enthalpy of crystallization and dissolution. A sealed sample is impregnated with salt solution (the reaction sample) at a known molality m_0 and placed into a container (the reaction container) which is filled with a mixture of water and glycerine to avoid ice formation at temperatures below 0 °C. The amount of dissolved salt in the pore solution $m_{sl,o}$ and the amount of water in the sample m_w are known.

A similar sealed sample is impregnated with water ($m_{w,0}$=water content in the reference sample) and located in a reference container, also filled with a mixture of water and glycerine. Both containers are located in a water bath with controllable temperature. The temperature in the middle of both samples is measured continuously be means of Platinum resistance thermometers (PT100) with an accuracy of 0.03 K at 0 °C (2·2.3·1.3 mm³). These sensors were manufactured specially for this kind of measurements and are watertight and resistant to a salt attack.

The purpose is to cause a supersaturation of the solution by cooling down the sample. Thus only salts, whose solubility depends on temperature, can be analyzed by use of this method.

When reaching a determined value of the supersaturation ratio $U^P_{a,start}$, crystallization starts. The temperature is maintained constant at 0 °C until crystallization has finalized. Afterwards the solution is heated up which leads to a gradual decrease of the supersaturation ratio and with it to a dissolution of the salt crystals in the unsaturated solution (U^P_a<1).

During crystallization, some amount of heat is released causing an increase of the sample temperature, thereby causing a difference temperature between reaction and reference samples. The temperature difference, which results from crystallization are often very small, so that a very precise measuring system is needed.

If the crystallization enthalpy is known, the time-dependent amount of salt crystals m_s can be estimated by means of an energy balance in the reaction sample according to following equation:

$$\frac{\partial}{\partial t}\left[\left(m_l \cdot c_{p,l} + m_s \cdot c_{p,s} + m_m \cdot c_{p,m}\right) T_s\right] = h_{crys} \cdot \frac{\partial m_s}{\partial t} + q_h$$

$$\text{with } q_h = H \cdot \left(T_s - T_{bath}\right)$$

m_m= mass of dried material
m_l=m_s+m_w mass of salt solution
c_p= specific heat capacity
T_s= temperature
h_{crys}= crystallization enthalpy
q_h= heat transfer with surroundings

(3)

The integration of (3 over the volume of the reaction sample at a given point of time t_i gives the amount of crystallized salt m_s in t_i:

$$m_s^{t_i} \cdot \left(h_{crys} - c_{p,s} \cdot \Delta T_s - c_{p,s} \cdot T_s\right) = m_s^{t_{i-1}} \cdot \left(h_{crys} + c_{p,s} \cdot T_s\right) + \left(c_{p,l} \cdot \left(m_{sl}^{t_i} + m_w^{t_i}\right) + c_{p,m} \cdot m_m\right) \Delta T_s - q_h \cdot \Delta t$$

(4)

The energy balance in the reference sample will be used for estimating the heat transfer constant H. Since no phase change takes place in the reference sample, the energy balance follows:

$$\frac{\partial}{\partial t}\left[\left(m_{w,0} \cdot c_{p,w} + m_m \cdot c_{p,m}\right) T_{ref}\right] = q_h$$

$$q_h = H \cdot \left(T_{ref} - T_{bath}\right)$$

H [J/sK] = constant of heat transfer, which depends on the surrounding conditions and sample properties but not on sample temperature.

(5)

The time-dependent concentration of the solution can be calculated with the amount of dissolved salt m_{sl}=$m_{sl,0}$-m_s and thereby the supersaturation ratio according to eq. (2).

However, it must be pointed out that this evaluation method for the crystallized salt amount in the material pores induces a maximal error of ±0.05 g. The maximal error is reached at constant temperature (0 °C). Hereby, the error involves a very pronounced variation of the supersaturation ratio (about ±0.5 [-]). Thus, the supersaturation ratio calculated at 0 °C, when crystallization has taken place, is submitted to a significant error. Therefore, it must be treated and interpreted

very carefully. In [2] an additional method to estimate the supersaturation ratio at 0 °C is described.

The analysis method is valid to investigate salt mixtures (more than two ions in solution), too. The Pitzer model and its modification [7][8][9] can be used to calculate the supersaturation ratio of each salt in the mixture as well as the density of the solution, the specific heat capacity of the solution and the crystallization enthalpy. Temperature and concentration of the solution must be known for the computation. The crystallization of salt mixtures will be dealt in future works.

Figure 2 shows the measured temperature in brick B, impregnated with a Na_2SO_4-solution (concentration=2.81 mol/kg) and cooling down at 0.01 K/min. The difference temperature between the reaction and reference samples increases about 11 K, when the sample temperature reaches 8 ºC. Hereby the crystallization of $Na_2SO_4.10H_2O$ (mirabilite) takes place in the materials pores according to the phase diagram of sodium sulphate. In case of brick A the maximal increase of the difference temperature is about 0.1 K.

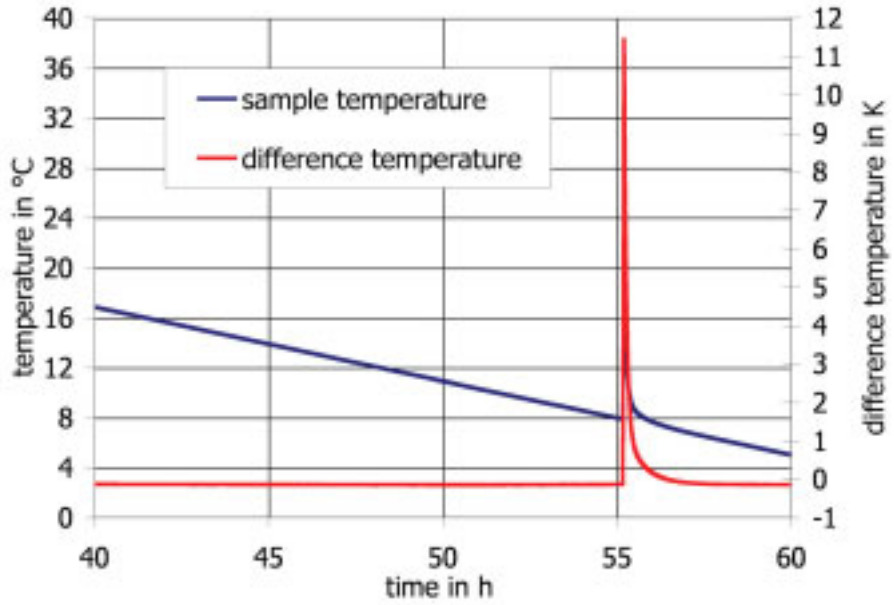

Figure 2: Time-dependent courses of sample temperature and difference temperature of brick B impregnated with Na_2SO_4-solution (2.81 mol/kg). Cooling rate=0.01 K/min.

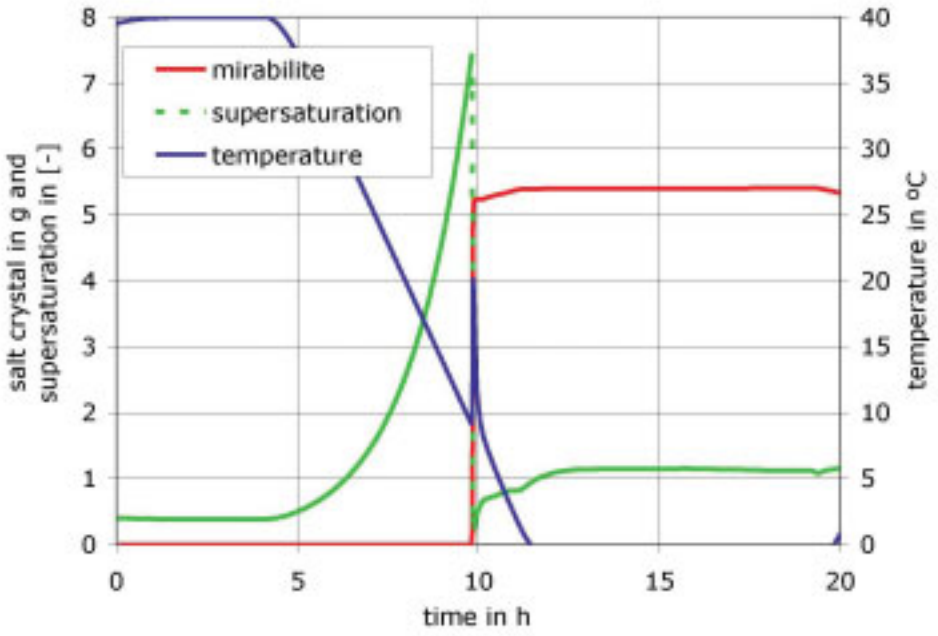

Figure 3: Time-dependent courses of sample temperature (right y-axis), salt crystal and supersaturation (left y-axe) in brick B ($U_{a,start}$ =7.5). Cooling rate=0.1 K/min.

The temperature increment measured on both bricks is caused by the salt crystallization, which is an exothermal process. Hereby the crystallization in brick A begins at a supersaturation equal to 1.8 ($U^{P}_{a,start}$ =1.8), while the required supersaturation for crystallization in brick B is much higher (7.5), which indicates that the crystallization is more inhibited in brick B.Our results show that the start supersaturation depends on the combination of salt and material. Taking into account that a heterogeneous nucleation takes place, this result is based on the different probability of nucleation sites on the pore surface of each particular material for the crystallization of each particular salt.

Thus, a high threshold supersaturation (e.g. 7.5) for nucleation indicates the lack of nucleation sites. In addition, it is important to remark that the largest values for the maximal supersaturation were obtained for the hydrated salts $Na_2SO_4.10H_20$ and $CaCl_2.6H_2O$ ($U_{a,start}$=2.5-10).

The crystallization rate was calculated using the method described in 2.1. The time-dependent supersaturation ratio was calculated according to [9]. Figure 3 shows the results for the crystallization rate of $Na_2SO_4.10H_2O$ in brick B.

In brick C, the crystallization starts also at a low supersaturation ratio and takes place very slowly, so that a larger supersaturation (ca. 10 [-]) is reached during the crystallization process, similarly to the crystallization in brick A, indeed. However, they differ strongly from the one in brick B though similar salt content (Na_2SO_4, 5.2 M.-%).

Indeed, the obtained supersaturation ratio gives an average value in the porous material. As discussed before, a higher supersaturation for crystallization is related with the lack of nuclea-

tion sites in brick B. In addition, crystallization in materials with a significant amount of small pores (<0.1 µm), needs a higher supersaturation ratio because of the higher energy of small crystals necessary to be stable. Brick B contains a significant amount of small pores, which explains the tendency for a higher start supersaturation, contrary to brick A and C.

The experimental results obtained on the investigated salts show that the crystallization rate depends strongly on the salt and on the material [3]. Moreover, the resulting mechanical stress also depends on the crystallization kinetics as it was discussed in [2].

2.2 Hydration/Dehydration

The salt hydration describes the absorption of water molecules in the salt crystal to build an hydrated salt, while the dehydration is the reverse process. Hydration and dehydration cannot be neglected in the numerical simulation of heat, moisture and salt transport, since the water uptake involves a considerable sink of the liquid water. Moreover, the damage pattern is influenced strongly by the formed hydrated phase of a salt and consequently, it is important to know which phase is filling the pores.

Water molecules can be uptake from vapor or from liquid water. If liquid water is used, the hydration proceeds quickly. Kinetics of this kind of hydration can be described as dissolution of an anhydrous salt and a crystallization of a hydrate. The hydration with water vapor takes place much slower. In this work we only investigated kinetics of this kind of hydration.

The phase diagrams of sodium sulphate and calcium nitrate (see e.g. www.salze-im-porenraum.de) show that both salts can be stable either as anhydrous or as different hydrates depending on temperature and on relative humidity. An increase of humidity or a temperature decrease leads to a hydration, while a decrease of the relative humidity or a temperature increase induces a dehydration.

Hydration and dehydration cause a weight change of the sample, since water molecules are adsorbed or lost, respectively. This fact was used for the experimental investigation of kinetics of hydration and dehydration. We used an automatic water adsorption measuring system (IGASorp, Hiden analytical) with a very sensitive balance (accuracy=±40 µg). The system controls both relative humidity and temperature in a sealed container where the sample is placed and records the time-dependent course of the sample weight.

The thickness of the used samples is equal to 1 mm in order to reduce the influence of the vapor transport on the measured time-dependent weight change. The same experiment was also carried out with a salt-free sample in order to get information about the vapor transport through the sample and the hygroscopic properties of the material. Thus, at a low pore filling ratio (<40 %) the influence of vapor transport is negligible but not at a higher pore filling ratio.

2.3 Deliquescence

The salt deliquescence describes the process where a soluble salt picks up water vapor from the air to form a solution. In order for deliquescence to proceed, the vapor pressure of the water in the air must be greater than the vapor pressure of the saturated solution. In this work, we only investigated the deliquescence at a constant temperature of 23 ºC.

Different steps can be distinguished during a deliquescence process. Firstly, water vapor is adsorbed on the crystal surface at each relative humidity building an adsorbent film (molecular adsorption). Nevertheless, if the deliquescence humidity is reached, the salt dissolves in the film and a saturated solution lies on the crystal surface. The progress of the deliquescence depends on kinetics of both adsorption of water molecules and solution of the rest crystal at the boundary phase between crystal and solution (interface). Finally, the slowest process determines the deliquescence rate.

Considering the thermodynamic equilibrium between water vapor and water in the solution at constant temperature it follows that the deliquescence humidity is equal to the water activity of the saturated solution at each temperature a^*_w. Thus, the value of the equilibrium deliquescence humidity can be calculated [9].

If the relative humidity is larger than the deliquescence humidity, both deliquescence and water condensation takes place to form an unsaturated solution at equilibrium.

The measured humidity at which the deliquescence begins is a little bit larger than the calculated one $a^*_{w.}$ This can be expected, since the vapor molecules diffuse from the gas phase to the salt crystals in order deliquescence to occur, therefore a gradient of partial pressure is necessary.

The deliquescence process of a salt in the pores causes a time-dependent weight change due to the water adsorption, as in case of hydration and dehydration. Thus, an automatic water adsorption measuring system (IGASorp, Hiden analytical) with a very sensitive balance was used for the experimental investigation of the deliquescence kinetics. The samples were impregnated with an unsaturated solution and then dried (by freeze drying). A similar amount of salt was contained in all materials.

Figure 4 shows the water vapor uptake of KCl (φ_{Del}=84.6 %) in brick A and B. The water vapor uptake of both salts was measured at a higher relative humidity (97 % and 92 % respectively). Therefore, not only deliquescence but also water condensation in the solution took place. From the experimental results, it follows that the water uptake rate in both bricks is very similar.

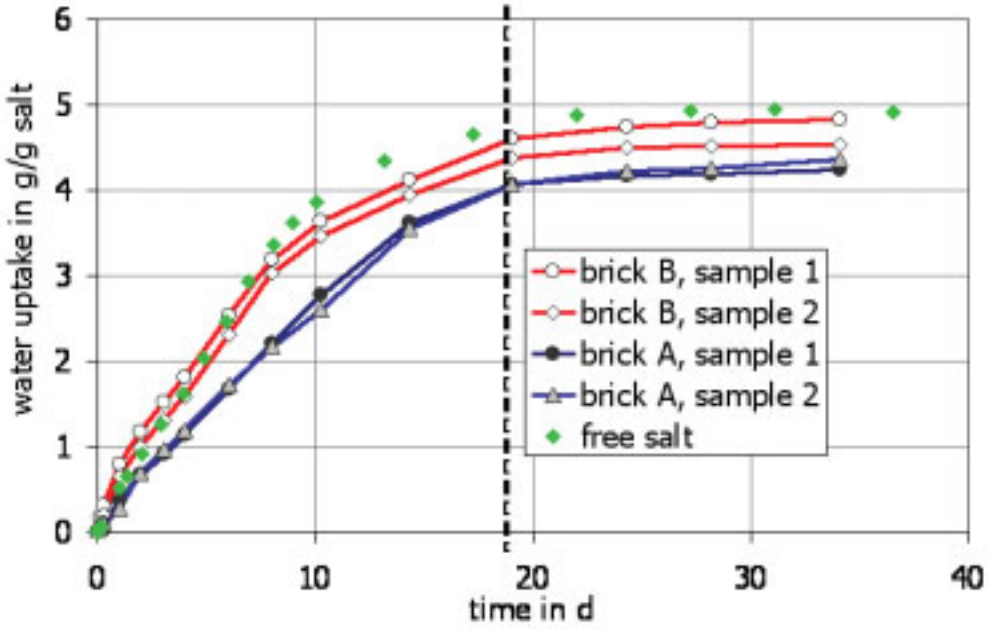

Figure 4: Measured water adsorption during the deliquescence of KCl in brick A (left, salt content=4.65 M.-%) and B (right, salt content=4.20 M.-%) at constant temperature 23 ºC compared to the water uptake of bulk KCl.

3 Mathematical model and validation

In this section, a mathematical model for kinetics of crystallization, dissolution, hydration, dehydration and deliquescence in porous materials will be discussed. The obtained parameters for the investigated materials and salts can be found in [3].

3.1 Crystallization and dissolution

In this work the diffusion-reaction model and its modification by Rocha and Martins [10] is used for the description of kinetics of crystallization and dissolution. Since the supersaturation ratio is the correct driving force for the crystallization and dissolution, the crystallization rate is better described as a function of the supersaturation ratio of the pore solution:

$$\sigma_s(t) = K_{cryst} \cdot \left(U_a^P - 1\right)^{g_{cryst}} \quad \text{for } U_a^P > U_{a,start}^P \tag{6}$$

where $U^P_{a,start}$ is the threshold supersaturation ratio for crystallization to start in the porous material and must be larger than one. This condition for the supersaturation ratio ($U^P_{a,start}$ >1) is only true in case of a primary crystallization, that is to say, if no salt crystals are present in the solution. Once crystals are present in the solution, the further crystallization (called secondary) begins at U_a^P>1.

In case of a small supersaturation, the crystal growth process is a diffusion-controlled process, while at high supersaturation ratios, the diffusion transport of the ions to the crystal surface takes place very fast and the crystal growth is determined by the integration reaction occurring on the crystal surface [1]. Furthermore, the parameter K_{cryst} is generally described according to the Arrhenius formulation as a function of the temperature [5].

The kinetics of salt dissolution can also be described by a similar equation:

$$\sigma_s(t) = K_{sol} \cdot \left(1 - U_a^P\right)^{g_{sol}} \quad \text{for } U_a^P < 1 \tag{7}$$

The experimental and theoretical method described in 2.1 was used to obtain the crystallization and dissolution rates in the selected materials. The kinetic parameters $U^P_{a,start,}$ K and g for crystallization and dissolution for each combination salt and material were obtained by means of an adaptation of equations 6 and 7 to the experimental data. The results obtained for the crystallization of sodium sulphate and potassium nitrate in brick C are displayed in figures 5 and 6.

The kinetics of crystallization of other salts like potassium chloride and calcium chloride was also investigated in both bricks (see [3] for more information). In case of potassium chloride the start supersaturation ratio for the beginning of the crystallization is very low (1.03), in contrast to calcium chloride or sodium sulphate. Thus, the driving force for crystallization (thus, the gradient U_a-1) is very weak and the crystallization proceeds slowly. The solubility of KCl is only slightly dependent on the temperature and this limits the maximal amount of KCl in the sample and with it the resulting stress. Besides, the crystallization enthalpy is not very large, which results in a small heat amount released during crystallization and with it a small difference temperature, too, which cannot be measured enough accurately. Even in this case it was possible to estimate the kinetic parameters for crystallization. However, this kind of crystallization behavior represents a limitation for the developed method.

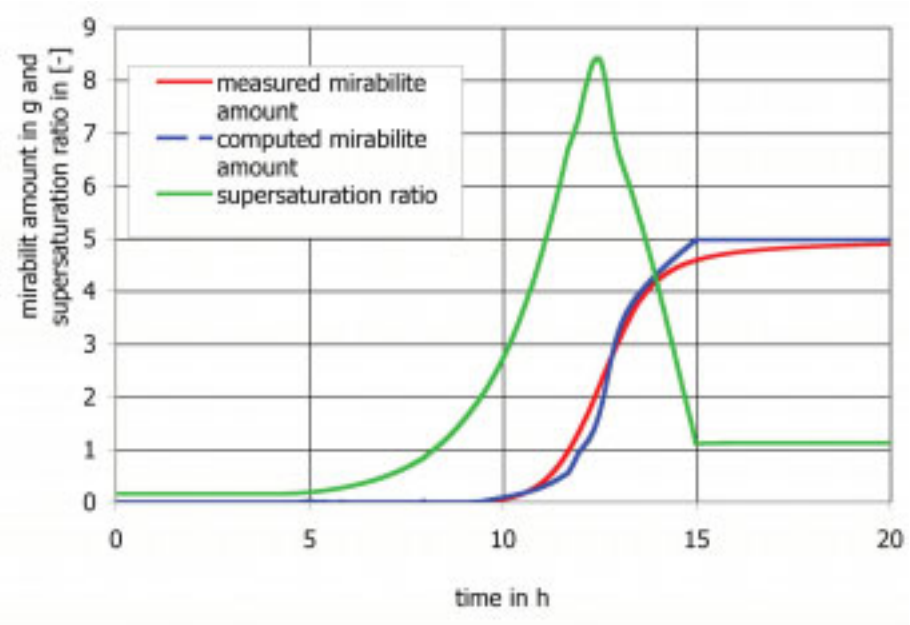

Figure 5: Measured and computed time-dependent course of crystallized mirabilite in brick C and supersaturation ratio in the pore solution. Solution molality=2.81 mol/kg. Salt amount=4.6 M.-%.

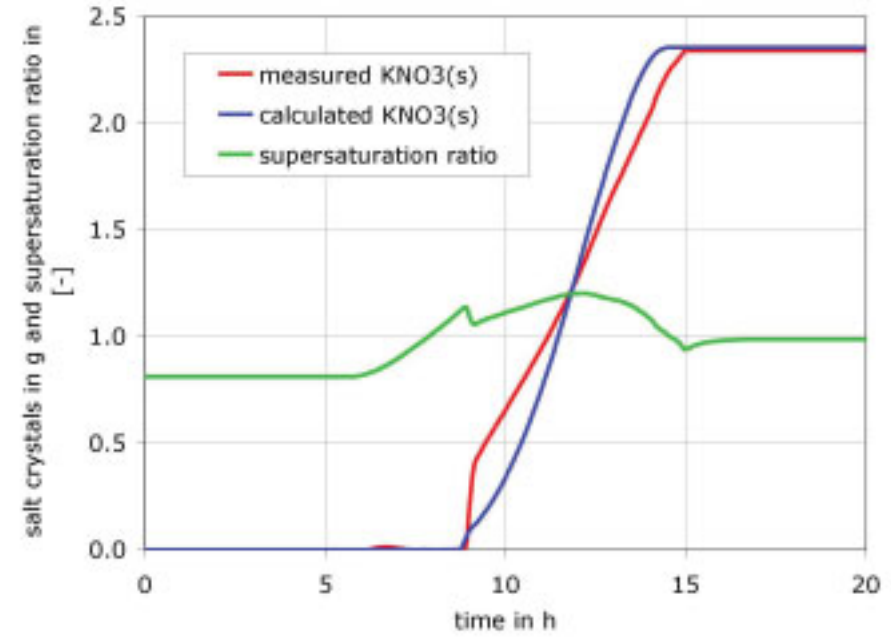

Figure 6: Measured and computed time-dependent course of crystallized potassium nitrate in brick C and supersaturation ratio of the pore solution. Solution molality=6.32 mol/kg. Salt amount=5.96 M.-%.

3.2 Hydration and Dehydration

The new model is based on a diffusion-forced reaction, assuming that hydration is induced by the difference between the actual relative humidity and the water activity of the saturated film on the crystal surface, which leads to an uptake of water molecules. This can be described by means of a supersaturation:

$$\sigma_{Hyd}(t) = x_{Dehy} \cdot K_{Hyd} \cdot (U_a - 1)^{g_{Hyd}} \text{ in g/m}^3\text{s mit } U_a = \varphi / a^*_H > U_{a,Hyd},\ g_{Hyd}=1 \quad (8)$$

where a^*_H gives the equilibrium humidity at which the phase change between hydrated and anhydrous salt (e.g. Na_2SO_4 and $Na_2SO_4.10H_2O$) starts and can be calculated using the computation model described in [7].

Similarly, it follows for the dehydration rate:

$$\sigma_{Dehyd}(t) = x_{Hyd} \cdot K_{,Dehyd} \cdot (1 - U_a)^{g_{Dehyd}} \text{ in g/m}^3\text{s mit } U_a = \varphi / a^*_H < U_{a,Hyd}, g_{Dehyd}=1 \quad (9)$$

This model can also be used when various hydration reactions of one salt are possible (as in case of $Ca(NO_3)_2$). The kinetic parameters $U_{a,Hyd}$, K_{Hyd} und K_{Dehyd} can be determined by means of a mathematical adaptation of eq. 8 (or 9) to experimental data. The method explained in 2.2 was used to get experimental data, in this case the weight change during the phase change $\Delta m_w(t)$. The hydration rate was calculated as $\sigma_{Hyd}=\Delta m_w(t)/\Delta t$.

Figure 8 shows the hydration rate of sodium sulphate in brick A at 80.5 % r.h.. At the beginning, the hydration proceeds very slowly, since the supersaturation is very small ($U_{a,Hyd}$=0.805/0.80). Before the salt hydration is completely finished, the relative humidity goes up to 85 %. Now the hydration proceeds much faster, since the supersaturation becomes higher ($U_{a,Hyd}$=0.85/0.80).
Our mathematical formulation for kinetics of hydration and dehydration has an important advantage in comparison with the classical formulations for kinetics. The kinetic parameters of the new model do not depend on the relative humidity during the phase change. Actually, the supersaturation U_a contains the influence of the environmental humidity.

3.3 Deliquescence

A new model was deduced based on a diffusion forced reaction similar to the hydration/dehydration model. Thus, the deliquescence rate is proportional to the gradient between relative humidity and the water activity of the saturated adsorbed film on the crystal surface $a^*_w(T)$. This assumption permits us to calculate the deliquescence rate by means of:

$$\sigma_{Del}(t) = x_{salt} \cdot K_{,Del} \cdot (1 - U_a)^{g_{Del}} \text{ in g/m}^3\text{s mit } U_a = \varphi / a^*_w < U_{a,Del}\ g_{Del}=1 \quad (9)$$

where x_{Salz} is the amount of salt crystal, U_a the actual supersaturation and $U_{a,Del}$ the necessary supersaturation for deliquescence to start.

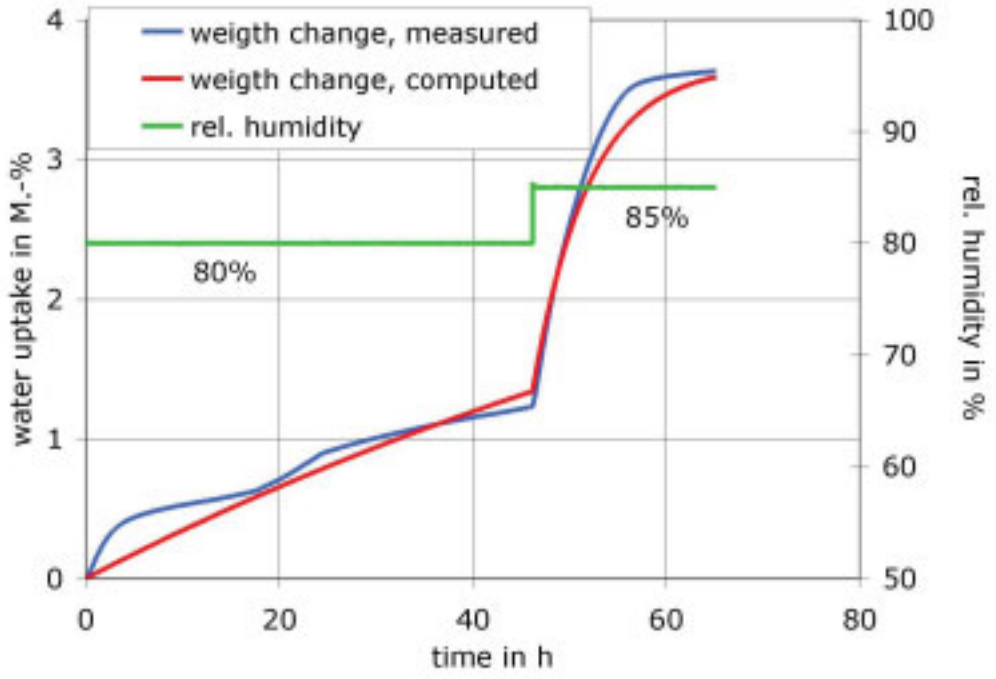

Figure 7: Hydration of Na_2SO_4 in brick A at 80 % and 85 % r.h at 23 ºC. Salt content=2.9 M.-%.

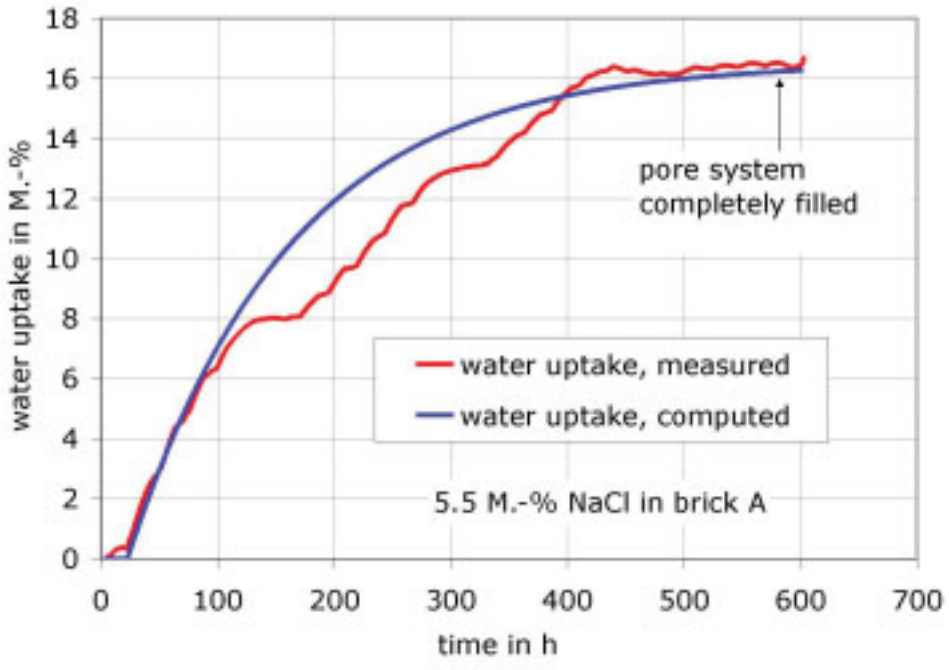

Figure 8: Calculated water uptake during deliquescence of NaCl in brick A at 75 % r.h. and 23 ºC. Salt content=5.5 M.-%.

The kinetic parameters K_{Del} and $U_{a,Del}$ have to be determined for each combination of material and salt by means of an approximation of experimental data with this equation. Experimental data were obtained using the method described in section 3.3.

Figure 9 shows the measured deliquescence of NaCl in the pores of brick A. The material was impregnated with a NaCl-solution and then dried (by freeze drying). The amount of salt in the pores was equal to 5.5 M.-% and with it, the pore-filling ratio equal to 14.5 %. The deliquescence starts at 75 % r.h., just above of the equilibrium deliquescence humidity at equilibrium (a_w*=0.74, 74 % r.h. at 23 ºC).

The difference between computed and experimental results is considerable after a pore-filling ratio of 40 % is reached. The reason is probably the increase of the vapor diffusion resistance coefficient due to the high pore-filling with solution. Moreover, a liquid moisture transport can also take place. Thus, the kinetic parameters for the deliquescence of a salt can only be determined at low pore-filling ratios to avoid the influence of moisture transport. In addition, as discussed in [3], the dependence of the kinetic parameters for the deliquescence on the material can be neglected, if the vapor diffusion is not hindered by crystals filling the pores.

4 Discussion

A mathematical model for the kinetics of phase changes of salts in pores was deduced, which can be coupled with a simulation program of heat, moisture and salt transport in capillary porous materials.

It could be proved that a unique equation describes the kinetics of all five phase changes. This equation is based on the fact that the driving force for any phase change is the difference between the chemical potentials of start and end phase. The difference between the chemical potentials is described by means of the supersaturation ratio. Furthermore, two kinetic parameters K and g are also involved in this equation.

Kinetics of crystallization and dissolution of salts in porous materials was investigated experimentally by means of a self-constructed device which measures temperature differences. Thus, only salts whose solubility depends on temperature can be analysed. Kinetics of hydration, dehydration and deliquescence of salts was investigated by measuring weight change due to the water uptake or lost.

In all cases a supersaturation ratio larger than 1 is necessary for the phase change to start. In case of the crystallization, a “start supersaturation ratio” $U^P_{a,start}$ larger than 1 was found for each material and salt. Hereby, the start supersaturation ratio for hydrated salts as sodium sulphate or calcium chloride is much higher than for anhydrous salts, indeed. The values of K and g were obtained by means of fitting the proposed equation for the phase change rate to the experimental results during phase change. It was found that the kinetic parameters for crystallization depend on both salt and porosity. Kinetics of hydration, dehydration and deliquescence (see

sections 3.2 and 3.3) are only strongly affected by the porosity, when the pore filling ratio with salt and solution is so high that the effectiveness of the vapor transport is reduced.

5 References

[1] Christian: The theory of transformation in metals and alloys, Part I, II, Ed. Elsevier, 1975.

[2] Espinosa, R. M., Franke L., Deckelmann, G: Model for the mechanical stress due to the salt crystallization in porous materials. Construction and Building Materials 22 pp. 1350–1367, 2008.

[3] Espinosa, R. M., Franke L., Deckelmann, G: Phase changes of salts in porous materials: Crystallization, hydration and deliquescence. Construction and Building Materials 22, pp. 1758–1773, 2008.

[4] Linnow K., Juling H., Steiger M.: Investigation of NaCl deliquescence in porous sub-strates using RH-XRD, International Journal of Geoscience, Environmental Geology, Salt Decay, Edited by S. Siegesmund & M. Steiger, Springer Verlag, 2007

[5] Mersmann, A:. Crystallization technology handbook. Marcel Dekker, 1995.

[6] Mullin, J. W.: Crystallization. Butterworth/Heinemann 3.ed. 1993

[7] Steiger M., Zeunert A:. Crystallization Properties of Salt Mixtures: Comparison of Experimental Results and Model Calculations. In: J. Riederer (ed.), International congress on deterioration and conservation of stone – proceedings, Möller Druck und Verlag GmbH, Berlin, pp. 535–544, 1996.

[8] Steiger M, Asmussen S.: Crystallization of sodium sulfate phases in porous materials: the phase diagram Na2SO4–H2O and the generation of stress. Accepted by Geochim Cosmochim Acta., 2008.

[9] Steiger, M.; Kiekbusch, J. & Nicolai, A.: "An improved model incorporating Pitzer's equations for calculation of thermodynamic properties of pore solutions implemented into an efficient program code", Construction and Building Materials, 22 pp. 1841–1850, 2008.

[10] Rocha F., Martins P.M.: Experimental investigation and kinetic modelling of crystal growth, 15th International Symposium on Industrial Crystallization, 2002.

[11] Zeunert, A.: Feuchtekontrollierte Rötgendiffraktometrie - Entwicklung und Anwendung zur Untersuchung verwitterungsrelevanter Salze und Salzsysteme, Diss. Universität Hamburg, 2000.

Rosa M. Espinosa-Marzal *Dr.-Ing.*
Gernod Deckelmann *Dr.-Ing.*
Lutz Franke *Prof. Dr.-Ing.*

Institute of Building Materials, Physics and Chemistry of Buildings
Hamburg University of Technology, Germany

Predicting efflorescence and subflorescence of salts in porous building materials

Summary

Crystallization of salts is a common cause of damage in porous building materials. Understanding of the crystallization mechanism of salts is important in order to prevent or avoid the problem. Subflorescence of salts (i.e., crystallization within the pores of the body) can induce scaling and cracking, while efflorescence (i.e., crystallization in a film of solution on the exterior surface of the body) does not generally affect the coherence and endurance of the building materials.

In this paper, we deal with the crystallization behavior of two salts, sodium sulfate and sodium chloride, in two bricks with different capillary porosity. The results reveal quite different crystallization behavior depending on salt and substrate.

The supersaturation of the solution is induced in our experiments by evaporation. Indeed, the main reason for the different behavior of these salts is their different ability to supersaturate. Thus, the sodium sulfate solution is prone to be much more supersaturated than the sodium chloride solution. Nucleation rate and crystal growth are both affected by the supersaturation leading to a different crystal morphology and distribution and as a consequence to a different the pore-clogging. Furthermore, the solution transport, which depends on salt properties, material porosity, pore-clogging and environmental conditions, affects the position of the drying front and, with it, the crystallization front, leading to the formation either of efflorescence or of subflorescence. Simulation of the experiments with the engineering tool ASTra is used to understand the effect of the influencing factors on the crystallization pattern. Therefore, considering both factors, supersaturation ratio and solution transport, it is possible to predict the different crystallization behaviors observed in the experiments.

1 Introduction

Efflorescence occurs in masonry construction, when water moving through a wall or other structure brings salts to the surface and evaporates there, causing salt to crystallize on the material surface. In some cases, salts crystallize beneath the material surface and build subflorescences (also called cryptoflorescence).

Although efflorescence does not generally affect the coherence and endurance of building materials, it impairs the surface appearance, which can be critical in the case of historical buildings. Indeed, there are some efforts to prevent the formation of efflorescence. For example, a penetrating sealer can help prevent or lessen the occurrence of efflorescence by soaking in and blocking the pores below the surface, thus preventing the water from moving to the surface bringing the salts with it. However, this process might lead to the crystallization of salts some millimeters beneath the surface (as subflorescence) or even deeper, causing possibly more severe damage.

In previous works [1], different crystallization behavior for sodium chloride and sodium sulfate was observed. To predict crystallization and, finally, to prevent material damage due to salt crystallization it is necessary to understand the crystallization mechanism within the pores as well as the interaction between the different involved processes. It is necessary to determine which properties both of the salts and of the materials influence the position of the crystallization front as well as the potential resulting stress, kind of damage and its intensity. Using the engineering tool ASTra [2][3], numerical simulation of experiments carried out in the laboratory is used to understand the interaction between some of the influencing factors on the crystallization process.

2 Experimental methods

Two different bricks (A and B) were selected for the experimental investigation of crystallization. A significant difference is the presence of large pores (~10 µm) in brick A, while most pores in brick B are smaller than 2 µm. Thus, the measured sorptivity of brick A is approximately 3 times larger than that of brick B: S_A=1.71 g^2/s and S_B=0.57 g^2/s.

Two kind of experiments were carried out:

- Drying experiments. Samples of brick A (prisms, 14 cm x 6 cm x 6 cm) were impregnated with sodium sulfate solution (1.61 mol/kg) or with sodium chloride solution (5.83 mol/kg). The evaporation occurred either through two opposite sides (14 cm x 6 cm) or through only one side under constant temperature (23 ºC) and relative humidity (50 %). The samples were placed in tubes where the air stream was maintained constant by means of small fans (see fig.1).

- Capillary rise tests were performed with samples of brick A and B in contact with sodium sulfate solution (1.61 mol/kg). The bottom side was immersed to a depth of 1 cm in the salt solution at known and constant concentration.

2.1 Drying Experiments

Figure 2 shows the measured weight change of the sample with respect to the dry and salt free sample, i.e. the total mass of solution and salt crystals (L+C) in the material pores. The drying

curve for the case of pure water is depicted in the same diagram. The significant difference of the starting point is given by the mass of salt.

Figure 1: Set up built for the drying experiments at 23ºC and 50% r.h.. The samples were placed in tubes where the air stream was maintained constant by means of small fans.

The samples impregnated with pure water are completely dry after 20 days, while the samples impregnated with sodium sulfate need around 40 days. In contrast, the water content in the sample impregnated with NaCl is still very high after 100 days. Thus, the drying process is strongly retarded due to the presence of salt and the intensity of the slowdown is strongly dependent on salt. Thus, the drying of the sample impregnated with sodium chloride is the most strongly hindered.

The kind of efflorescence is also quite dependent on salt (and substrate) and determines further evaporation rates, obviously affecting further crystallization. At the drying conditions of this experiment (50% r.h. and 21ºC), mirabilite precipitates directly from the solution and the first crystals are visible within the first hour. When mirabilite comes in contact with the air, it dehydrates to thenardite, which is accompanied by a significant reduction of the crystal volume. This dehydration open paths through the crystalline layer and provides for the continuous drying of the sample. Severe efflorescence of thenardite is visible after just 10 hours.

Thus, figure 2 (right) shows severe efflorescence of halite (right, top) and of thenardite (bottom). Indeed, efflorescence formation is expected since the capillary transport in brick A proceeds so fast, that the crystallization front is placed on the surface. While NaCl-crystals on the surface have a compact structure with high density, which impedes evaporation (see the inflection point

after 5 days), the thenardite crystals on the surface are thin prisms (acicular) and form a (vapor) permeable layer for the vapor.

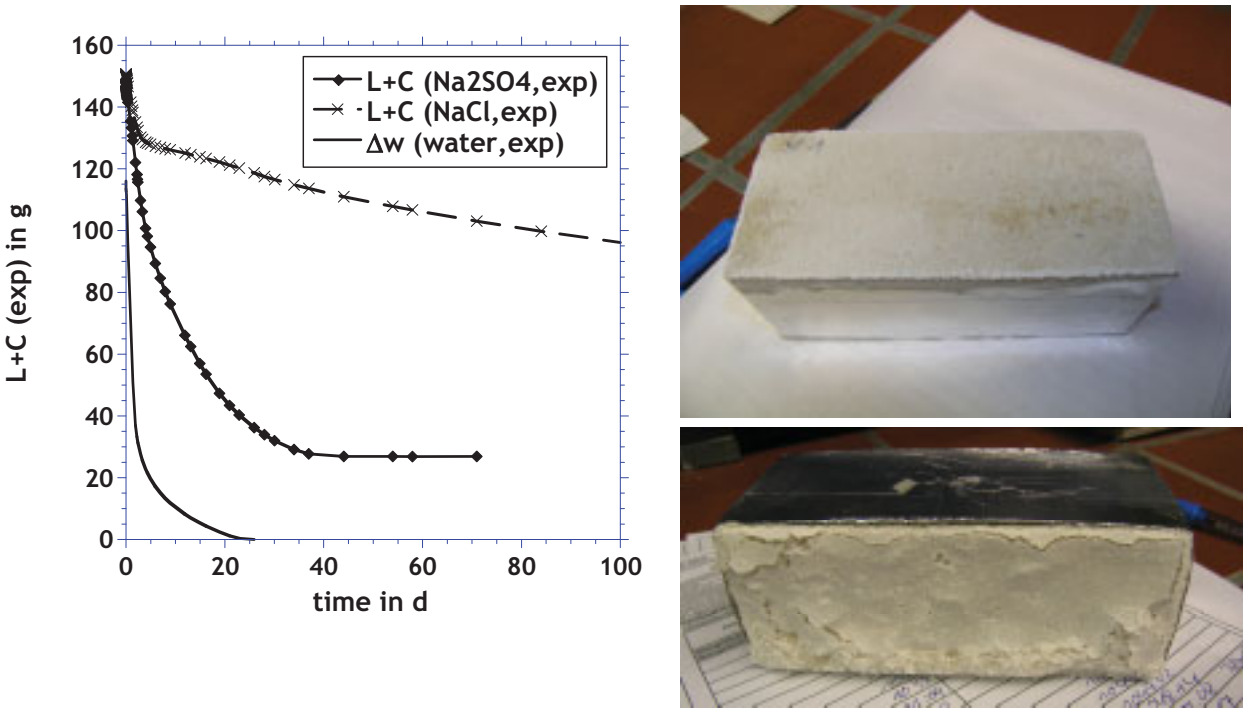

Figure 2: Left, weight loss due to evaporation of water in brick A impregnated with pure water, sodium sulfate or with sodium chloride solution. Evaporation takes place through one surface (14cm x 6cm). Efflorescence of halite (right, top) and of mirabilite (right bottom) after drying 24 hours at 50 % RH and 23 ºC.

2.1 Capillary rise test of sodium sulfate solution in brick A and B.

During the capillary rise of sodium sulphate solution the measured weight loss (figure 3) indicates that the evaporation in brick B is significantly slower, which can be expected because of its lower permeability. The change of the slope of the evaporation rate in brick B (approximately after 120 h) is due to the increase of the airflow velocity during the experiment.
In addition, the results show a considerably different crystallization behavior for mirabilite in those bricks. While severe efflorescence forms in brick A (fig.3, right top), it is negligible in brick B even after 2 weeks (fig.3, right left). Indeed, the transport properties of the porous material influence the position of the crystallization front, as will be described in the next sections.

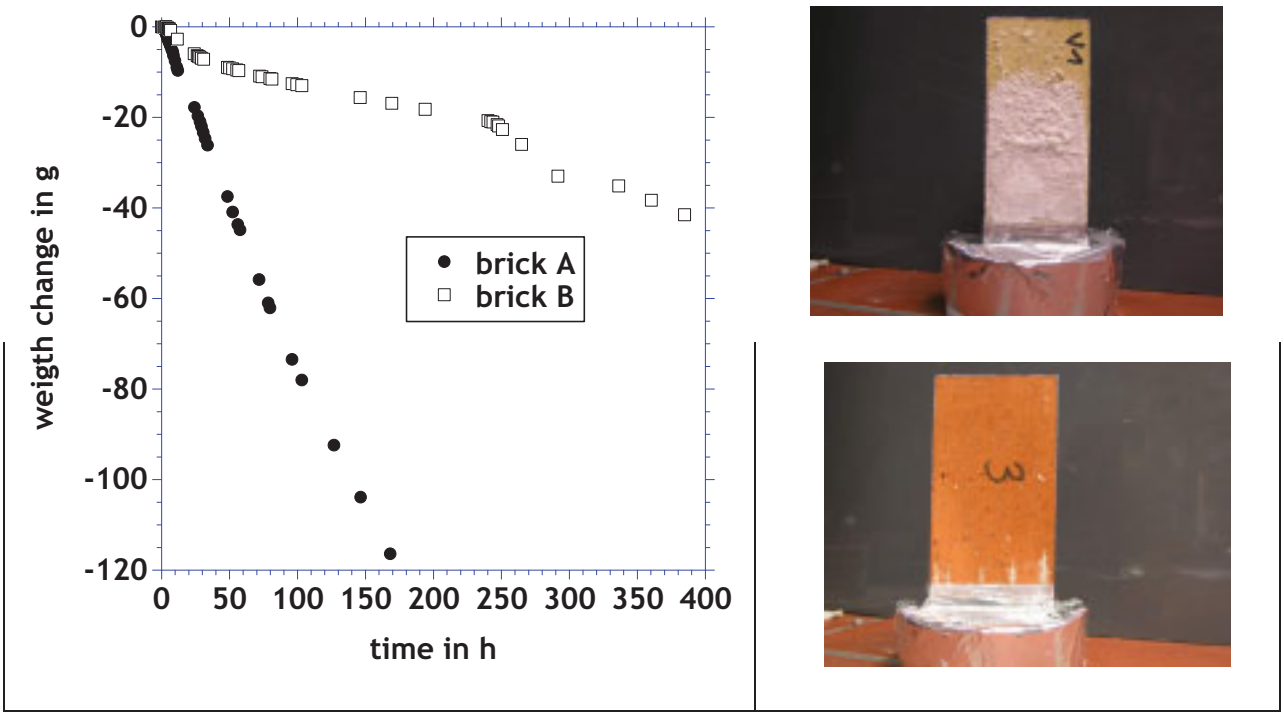

Figure 3: Left, evaporation rate of sodium sulfate solution (1.6 mol/kg) in bricks A and B during the capillary rise experiment at constant temperature (23°C) and relative humidity (50 % RH). Right, pictures of brick A (top) and brick B (bottom) at the end of the capillary rise experiment.

3 Mathematical model

The system of coupled partial differential equations that describe heat and water transport in porous materials subjected to climatic conditions, was derived from the thermodynamical point of view in [4]. For the prediction of salt crystallization in porous materials an additional model for the ion transport based on the Nernst-Plank-model [5][6] coupled with the kinetics of crystallization of salts in porous materials was developed. These models were implemented in an engineering tool, **ASTra** [2][3] to solve the coupled equations of heat, moisture, air and ion transport with the phase changes of salts in the material pores.

In a previous work [7] we investigated the phase change of salts (crystallization, dissolution, hydration, dehydration and deliquescence) in capillary porous materials and developed a model for the average rate. This model says that kinetics of crystallization in porous materials can be described using eq. (1). This equation is based on the fact that the driving force for crystallization is the supersaturation ratio of the solution with respect to a salt $U_{a,s}$:

$$\sigma_{c,s} = K_{c,s} \cdot \left(U_{a,s} - 1\right)^{g_{c,s}} \text{ with } U_{a,s} > U_{s,start} \text{ and } U_{a,s} = \frac{Q}{K} \tag{1}$$

with $\sigma_{c,s}$ the average rate of crystallization $K_{c,s}$ and $g_{c,s}$, kinetic parameters, $U_{s,start}$, the necessary supersaturation for crystallization to start, Q the ion activity product and K the solubility constant. For the dissolution, hydration, dehydration and deliquescence, similar equations were deduced.

Three kinetic parameters are necessary to calculate the crystallization rate ($K_{c,s}$, $g_{c,s}$, $U_{s,start}$), which generally depend on both the pore structure and salt and must be obtained experimentally. The starting supersaturation ratio gives the threshold condition for the phase change. Actually, it must be remarked that eq. (1) does not give the growth rate of a single crystal but the average crystallization rate per unit volume of liquid.

4 Discussion

In this section the influence of the nucleation, solution and material properties on the resulting crystallization pattern during the drying and capillary rise experiments is discussed. Further, the numerical simulation of those experiments is used to understand the effect of each of them.

4.1 Nucleation

The application of the theory of heterogeneous nucleation [8] to halite and mirabilite reveals the quite different behavior of these salts. Thus, the nucleation rate per unit surface and time ($I_{a,het}$) results from:

$$I_{a,het} = \frac{k_B T}{3\pi\eta\Omega^{5/2}} \exp\left(-\frac{f(\theta)\Delta F_i^*}{k_B T}\right)$$

$$\text{with } f(\theta) = \frac{(2 - 3\cdot\cos(\theta) + (\cos(\theta))^3)}{4}$$

$$\text{and } \Delta F_i^* = i^* \cdot k_B T \ln U_a + 4 i^{*2/3} \cdot \gamma_{cl} \cdot \Omega^{2/3} \qquad (2)$$

θ=contact angle
Ω = volume of a molecule
k_B=Boltzmann-constant
T=temperature
η=viscosity
ΔF_i^* = free energy barrier for nucleation
γ_{cl}=interface energy
i*=critical size of an embryo

The influence of the substrate, in this case the pore wall, on nucleation results from the surface area of the nucleating sites and the contact angle. Since we do not have any information about the contact angle, we assumed the same value for both bricks.

The computed nucleation rate per unit surface of the substrate as a function of the supersaturation ratio S is depicted in figure 4. While the nucleation of NaCl requires a low theoretical supersaturation (about 1.21 [-] for 1 nuclei/m^{2}s), the results show the mirabilite to first nucleate at a higher supersaturation (S=4.4 [-] for 1 nuclei/m^{2}s). Further, the nucleation rate of NaCl changes strongly at small variations of the supersaturation.

The ability of mirabilite to achieve a high supersaturation in the pores of these bricks was confirmed experimentally by Espinosa et al. [7]. Unfortunately it is not possible to measure the threshold supersaturation of NaCl according to the method explained in [7] since the solubility of

NaCl is not dependent on temperature. However the experimental results for other salts (like KNO_3, KCl, $CaCl_2.6H_2O$)[1], are also in agreement with the theoretical results from this model.

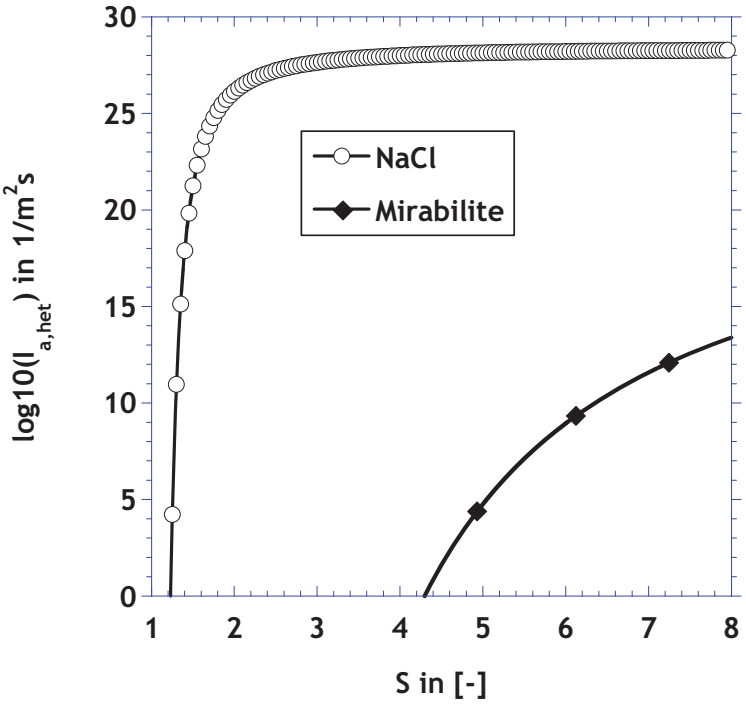

Figure 4: Heterogeneous nucleation rate per unit surface and time assuming a contact angle equal to 1.75 rad.

Since the necessary supersaturation of the solution for nucleation of both salts is so different, the crystal growth will take place in a different way, leading to equilibrium NaCl crystal morphology and non-equilibrium mirabilite crystal morphology (acicular) according to [9]. In fact, equilibrium NaCl-crystals in large pores are observed very often, while non-equilibrium mirabilite crystals are often reported in the pores [1]. These results suggest that the different crystal growth of both salts accounts for the different kind of pore clogging in this high permeable material.

To visualize the different morphology of the crystals that precipitate at the conditions of the drying experiments, evaporation of solution droplets was performed and observed with an optical microscope. Figure 5 (left) shows the thenardite crystals after complete drying of a droplet of solution (20 ml). The first crystals are observed after 1 hour of evaporation. Some crystals grow within the original droplet (marked by the circle) but also efflorescences has formed, leading to a low volume fraction of the droplet occupied by crystals which may explain the low intensity of the pore-clogging measured in the capillary rise experiment.

[1] Crystallization commences for $CaCl_2.6H_2O$ at high supersaturation and for KCl and KNO_3 at low supersaturation [

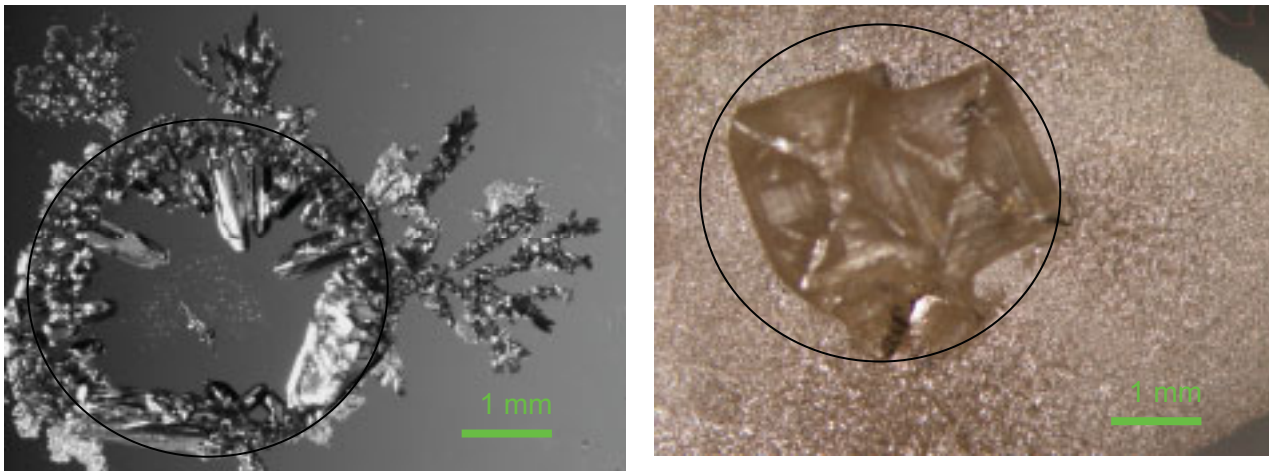

Figure 5: Left, thenardite crystals formed during the evaporation of a droplet of sodium sulphate solution (1.6 mol/kg). Right, halite crystals formed during the evaporation of a droplet of sodium sulphate solution (5.8 mol/kg).

The first halite crystals in the droplet form just after a few minutes after the beginning of the evaporation, which supports the lower supersaturation required for the nucleation of halite compared to that necessary for the nucleation of mirabilite/thenardite. The right picture in figure 5 shows that the original volume of the droplet (given by the circle) is almost completely filled by three halite crystals. As the crystals are just covered by a thin liquid film, the further evaporation leads to the formation of the white small compact crystalline layer surrounding the crystals.

Thus, the observed morphology of halite and thenardite supports the higher pore-clogging found on the crystallization of halite in the pores of our bricks.

4.2 Transport properties

The higher viscosity and surface energy of the solution compared to pure water leads to a slowdown of the capillary transport of the samples impregnated with the solution. Thus, the ratio of solution to pure water flow velocity v_{sol}/v_{H2O} is given by:

$$\frac{v_{sol}}{v_{H2O}} = \frac{\eta_{H2O}}{\eta_{sol}} \frac{\gamma_{sol}}{\gamma_{H2O}} \qquad (3)$$

γ=surface energy in N/m
η =viscosity in Pa•s
v=flow velocity in m/s

Experimental values for the viscosity were found in [11] and for the surface energy of the solution in [12]. Figure 6 shows the ratio v_{sol}/v_{H2O} for sodium sulfate and for sodium chloride solutions for different values of the ratio between concentration and solubility. This figure shows clearly that the flux of both solutions is slower than the flow of pure water, which explains at least partially the slowdown of the drying of the bricks in presence of salt.

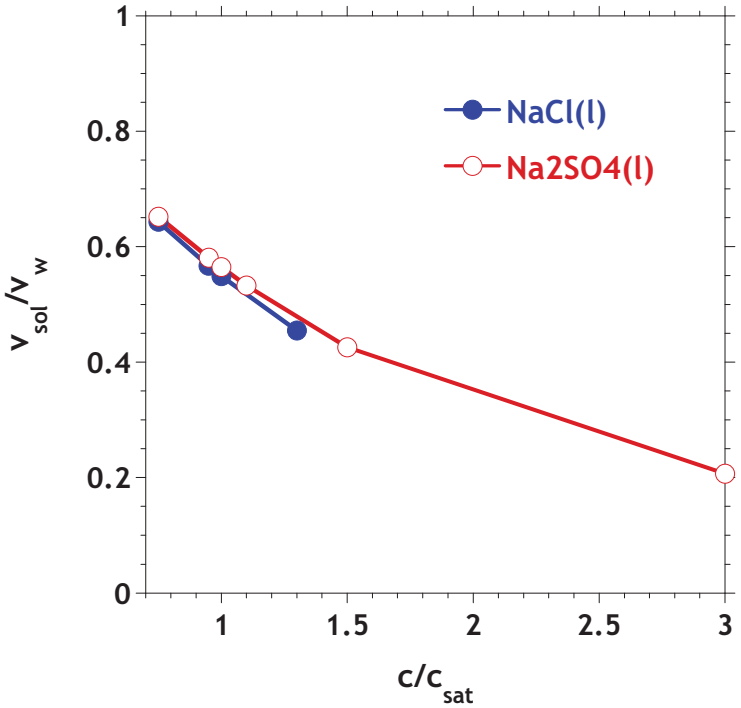

Figure 6: Ratio between the velocities of solution and pure water flow for sodium sulfate and sodium chloride solution at different values of the ratio between concentration and solubility c/c_{sat}, considering the influence of viscosity [11] and surface energy [12].

Further, within the usual range of values of the supersaturation ratio of halite and mirabilite, the flow velocity of sodium sulfate is slower. That means, the solution properties (viscosity and surface tension) do not explain the faster drying behavior of the sodium sulphate solution shown in figure 2. P*ore clogging* as well as the change of the surface properties due to efflorescence might account for the decrease of the drying rate.

In this work we assume that the crystals are distributed in all pore sizes. This leads to a reduction of the permeability k even at a low pore filling.

Figure 7 shows the assumed permeability of brick B as a function of the pore filling pf based on Brooks and Corey model:

$$k(pf) = k_0 \cdot g_p \text{ with } g_p = \left(1-(pf)^a\right)^b \text{ and } pf = \frac{\theta_s}{\Psi} \tag{4}$$

with k_0, the permeability of the salt-free material in m^2/s, θ_s, the volume of precipitated salt per unit volume (m^3/m^3) and ψ, the pore volume (m^3/m^3). The parameters for this model (a=2.77 and b=1.77 for mirabilite) were obtained empirically. Eq. (4) gives the resistance against the liquid transport due to the pore filling with crystals.

Further, at low water contents, the pores will depercolate and the liquid flow will be hindered. That happens in brick A at a saturation ratio of about 10 % and in brick B at about 18 %.

Therefore, it is assumed that the permeability tends to zero if salt crystals fill more than 90% of the total porosity of brick A and more than 80 % of the total porosity of brick B.

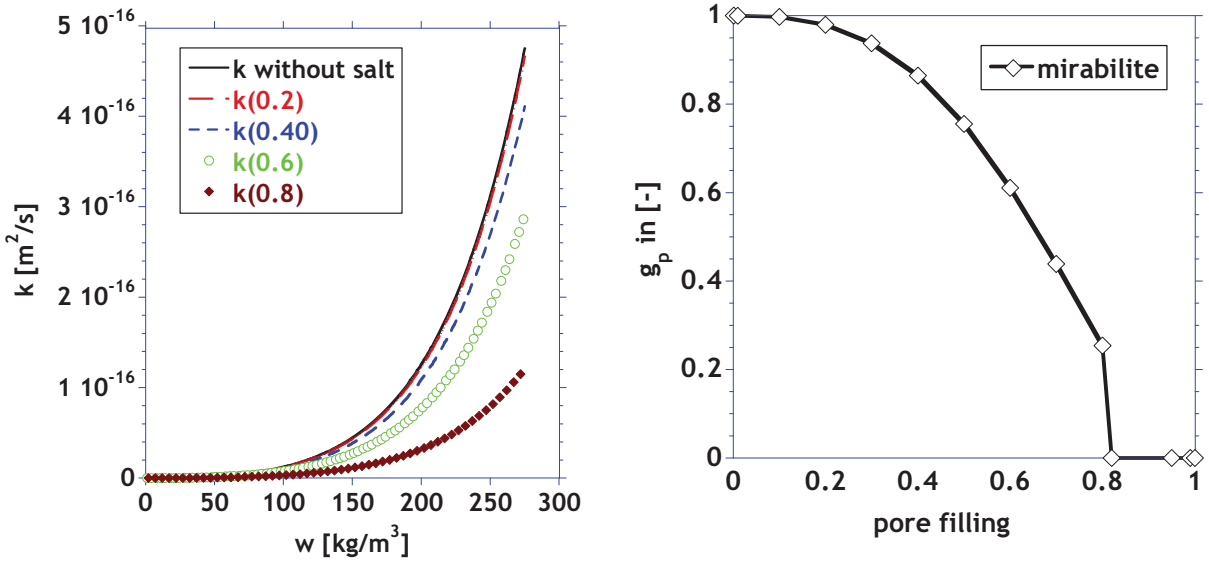

Figure 7: Left, liquid permeability k as a function of the water content (w) in brick B at different values of pore filling with salts (0.2, 0.4, 0.6 and 0.8). Right, resistance against liquid flow depending on pore filling given by g_p.

4.3 Numerical Simulation of capillary rise experiment

During capillary rise of sodium sulphate in brick A, the evaporation front is located at the surface because of the high capillarity of this material. The results of the simulation show the severe formation of efflorescence. Further, they show that there is no dehydration of mirabilite to thenardite in the simulated period of time (200 h) since the water content on the surface is still very high (70 % of saturation ratio) due to the steady water uptake. Thus, the rest of the pore volume is filled with salt, which grows from the solution into the surrounding air.

Apart from the differing permeability of bricks A and B, the distribution of nucleation sites may be also quite distinct in the bricks and with it the crystal distribution and the resulting pore clogging. Unfortunately, we do not have any information about the distribution of nucleation sites now. Therefore, the same resistance against the liquid flow as a function of the pore filling (see figure 7, right) is assumed for both bricks.

Figure 8 shows the computed distribution of mirabilite in brick B after 196 hours with the engineering tool **ASTra**. Due to the axisymmetric geometry, the simulation of the coupled transport with crystallization was performed only in the half of the sample. Thus, the x-axis goes from zero to 3 cm, the y-axis goes along the height of the sample (14 cm) and the computed mirabilite content is depicted on the z-axis.

The bottom 4 cm of the sample is placed inside of the pan, which contains the unsaturated solution that keeps the relative humidity constant at 95%. Therefore, the evaporation inside of the container is negligible and no crystallization takes place. Above this 4 cm, mirabilite precipitates.

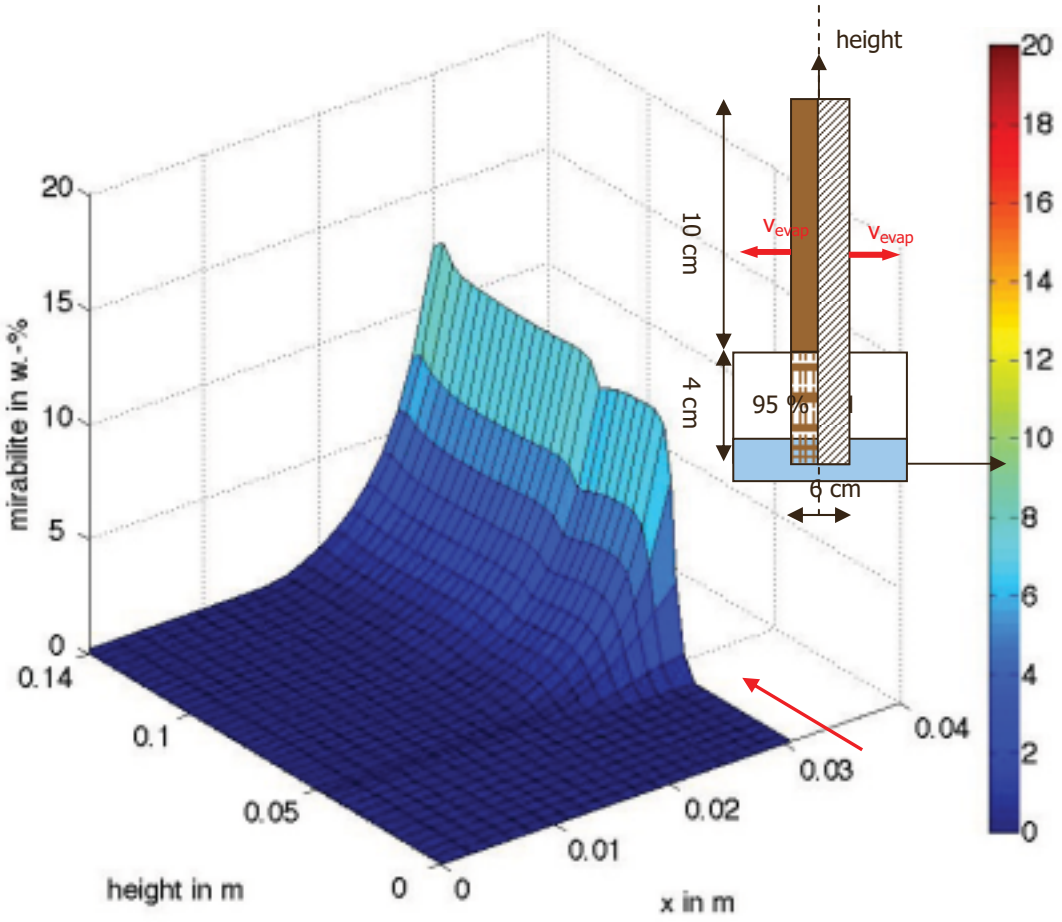

Figure 8: Computed distribution of the content of mirabilite (in w.-%) in brick B during the capillary rise experiment after 196 hours. Due to the axisymmetric geometry, the simulation was performed in the half of the sample (s. stripped surface in the sketch of the set up). Simulations performed with the engineering tool AStra.

The kinetic parameters $K_{c,s}$=0.0064 mol/m^{3}s and $g_{c,s}$=1 were determined experimentally [7]. Thus, the predicted width of the crystallization front is about 0.8 cm and no appreciable efflorescence forms according to the simulation. The pores on the sample surface (x=0.03 cm) contain salt crystals (≈15 w.-%) but there is no growth out of the pores (see arrow). Thus, the simulation with ASTra predicts just the formation of subflorescence, which is in agreement with the experimental results.

Further, the influence of the kinetic parameters on the computed results for brick B was examined. Figures 9 shows, how the average crystallization rate affects the results of the simulation. If crystallization takes place 3 times slower ($K_{c,s}$=0.002 mol/m^{3}s), both, the resulting

total amount of salt and the evaporation rate are larger. The reason for that is simply the reduction of the amount of crystals on the surface at the first drying stage due to the lower crystallization rate, which leads to a smaller reduction of the evaporation rate since pore clogging is less effective. Thus, the higher evaporation rate compared to the capillary transport moves the crystallization front into the interior of the sample of brick B. Thus, the right diagram shows that the amount of precipitated mirabilite is firstly smaller with $K_{c,s}$=0.002 mol/m^{3}s, as expected but after some hours the curves crossed each other and finally, more mirabilite precipitates in brick B at the low crystallization rate. Due to this, the width of the crystallization zone with $K_{c,s}$=0.002 mol/m^{3}s reaches 1.8 cm beneath the surface after 196 hours.

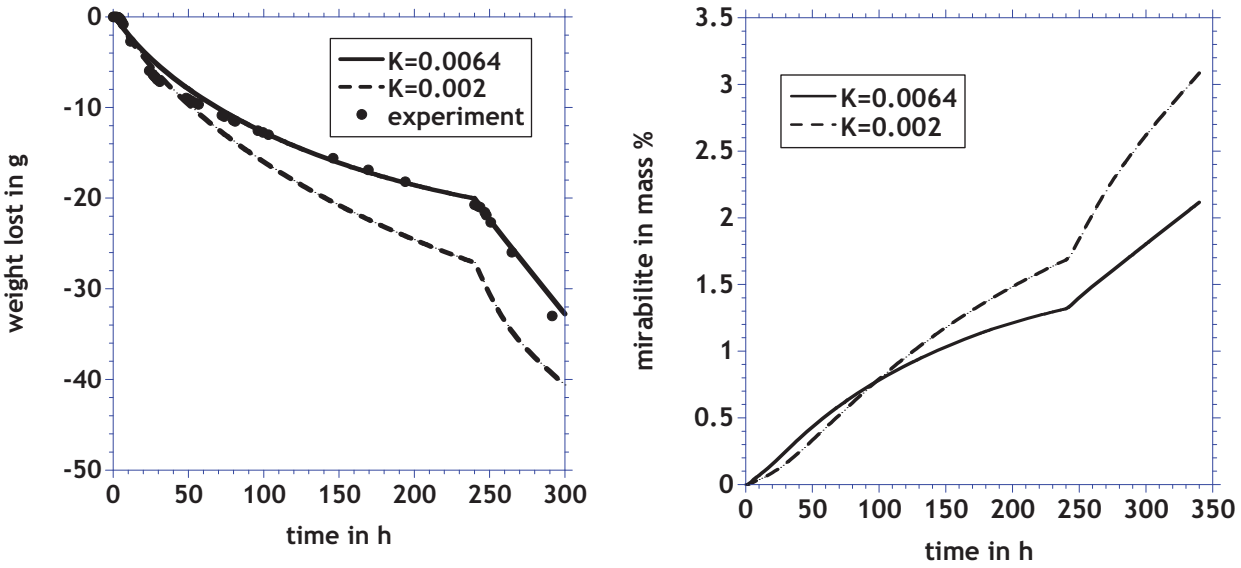

Figure 9: Evaporation rate (left) and total amount of mirabilite (right) in brick B at two different average crystallization rates ($K_{c,s}$=0.002 and $K_{c,s}$=0.0064). Simulations performed with the engineering tool AStra.

Thus, contrary to the expectations a lower crystallization rate might even cause more damage. However, this is not a general conclusion but only a result for this particular experiment. Indeed, the complexity of the coupled phenomena does not allow giving any general conclusion but the numerical simulation can help to understand the interaction between mechanisms under particular boundary conditions.

5 Conclusions

The model presented in this work reveals that the combination of salt crystal properties, solution transport and environmental conditions determines whether crystallization will result in damaging subflorescence or in efflorescence. The interaction between those factors can be examined and/or predicted with the help of the numerical simulation. We used the engineering

tool ASTra to perform the simulation of the coupled transport of heat, moisture, salt and air with salt crystallization in porous materials.

In particular, the ability of each salt to achieve high or low supersaturation determines the heterogeneous nucleation rate in the pores. Further, the rate of nucleation affects not only the crystal distribution in the pore network but also the resulting pore clogging.

Moreover, it was shown that liquid transport and crystallization processes will influence each other. Thus, liquid transport depends on the kind and intensity of pore clogging and determines the concentration gradient and supersaturation and with it the crystallization process at the same time.

Finally, it must be remarked that the average crystallization kinetics [7] does not say anything about the amount of crystals and the distribution in the pore structure. A high crystallization rate can be given by a large number of crystals, even if they have a low growth rate but also by a small number of crystals with a large growth rate caused by a high supersaturation. However the consequences on the pore clogging and on the damage of the materials are quite distinct depending on the crystal distribution. Therefore, the goal of future investigations is the study of the nucleation process and of the crystal distribution in the pores.

6 Acknowledgements

The authors thank DFG for financial support and Prof. Scherer, Princeton University for his comments, suggestions and helpful discussions.

7 References

[1] Rodriguez-Navarro C., Doehne E. Salt weathering: influence of evaporation rate, supersaturation and crystallization pattern. Earth Surface Processes and Landforms, 24 (1999) 191-209.

[2] Franke L., Espinosa R., Deckelmann G., Gunstmann C., Bandow D. AStra - Ein neues Berechnungswerkzeug zur Simulation des gekoppelten Wärme-, Feuchte- und Stoff-transports einschließlich der Korrosionsprozesse in porösen Baustoffen. Bauphysik 3/2007, Nr. 607.

[3] Espinosa-Marzal R.M, Kiekbusch J, Gunstmann C., Franke L. The program systems CeSa and AStra for cement and salt chemistry and the prediction of corrosion processes, in “Simulation of Time Dependent Degradation on Porous Materials”, in print, Franke et al., Cuvillier Verlag, 2009.

[4] Bear J. Dynamics of fluids in Porous Media. Dover Pub. Inc., 1988.

[5] Samson E. Marchand, J. Numeric Solution of the extended Nernst-Planck Model, In: Journal of colloid and interface science 215 (1999), pp. 1 – 8.

[6] Gunstmann C. Rechnerische Simulation von Säurekorrosionsprozessen zementgebundener Materialien. PhD, Hamburg University of Technology, 2007.

[7] Espinosa R. M., Franke L., Deckelmann G. Phase changes of salts in porous materials, Construction and Building Materials, 22, 1758–1773, 2008.

[8] Christian J.W., The theory of transformation in metals and alloys, Part I: Equilibrium and General Kinetic Theory, 2nd edition, Pergamon Press, Oxford, 1975.

[9] Sunagawa I. Crystals: growth, morphology and perfection. Cambridge University Press, 2005.

[10] Scherer, G. W.: Stress from crystallization of salt, Cement and Concrete Research 34 (2004) 1613-1624.

[11] CRC, Handbook of Chemistry and Physics, CRC Press, 83rd Edition, 2002-2003.

[12] Abramzon A., Gaukhberg R. Surface Tension of Salt solutions. Russian Journal of Applied Chemistry, Vol. 66 (6, 7 and 8), part 2, 1993.

Martin Fenchel
Dipl.-Ing.

Harald S. Müller
Prof. Dr.-Ing.

Institute of Concrete Structures and Building Materials, Universität Karlsruhe (TH), Germany

Prediction model for the degradation process of concrete due to the attack of sulphate-bearing water

Summary

This research project aims for the development of a realistic model to describe the degradation process of concrete due to the attack of sulphate-bearing water and its destructive potential. An essential part of the analytical-numerical approach consists in the separate analysis of processes on the micro, meso and macro level. Describing the hardened cement paste as a heterogeneous continuum with dispersed pores, the resulting stresses and cracks due to ettringite formation are simulated using fracture mechanics. Further numerical models for concrete are developed, taking into account the influence of aggregates and corrosion front induced strain gradients on the concrete damage. Related experimental investigations deliver the necessary characteristic values and also provide a basis for the validation of the model. The derivation of a simplified analytical prediction model for sulphate attack and its consequences on concrete complete the research study.

Keywords: *concrete, sulphate attack, degradation, fracture mechanics, prediction model, numerical simulation, FEM*

1 Introduction

The attack of sulphate-bearing water on cementitious materials has a great destructive potential which can result in a complete break-down of structural members. The origin of the sulphates can be soils rich of gypsum, industrial waste waters or aggregates containing sulphates or sulphides. Depending on the accompanying ion of the sulphate anion, different corrosion mechanisms occur:

- H_2SO_4: dissolving and expansive attack
- $CaSO_4$ and alkali sulphates: expansive attack
- $(NH)_4SO_4$ and $MgSO_4$: exchange of metal ions of salt with C-S-H-structure and expansive attack of sulphate

In the past 20 years, different imaging methods contributed to clarify the basic principle of the degradation mechanism considering the processes in the concrete pores and the change of phases. Sulphate ions ingress in the pore volume of the hardened cement paste due to capillary

suction and diffusion and react with AFm-phases forming ettringite. The expansive nature of the this reaction process results in the degradation of the cement paste microstructure. The macroscopic damage pattern is characterized by strains in the material along with crack formation on the surface. Here gypsum crusts can be found when high concentrations of sulphate ions are present in the solution [1]. With increasing content of aluminates in the AFm-phase, rising tensile strains evolve, whereas according to the literature only marginal volumetric expansions can be measured when ferrous ettringite is formed.

While previous studies mainly describe the encountered phenomena only qualitatively, this research project focuses on a quantitative description of the deterioration process with the intention to deduce a simplified analytical model in order to predict strength, deformation and cracking characteristics, i.e. the durability behaviour of concrete under sulphate attack.

2 Numerical Investigations

The numerical analyses are based on a finite element model of the deterioration process in the hardened cement paste and the concrete using statistical fracture mechanics. As key parameters this model primarily takes into account sulphate intensity, type and duration of the attack, porosity of the cementitious matrix, the material composition and geometry. An essential part of the approach consists in the separate analysis of processes on the micro, meso and macro level. In this consecutive analysis the results of the lower level will be integrated into the homogenised model of the next higher level.

So far two consecutive numerical models have been developed, describing the processes on the micro level (modelling of hardened cement paste) and the meso level (modelling of aggregates, matrix and interfacial transition zone). The calculations are carried out using the finite element code DIANA.

2.1 Numerical model on the micro level

2.1.1 Model geometry and pore size interval

The pore radii of hardened cement paste range from 10 nm to 1 mm. However, the modelling of pores within more than one order of magnitude in one model is not expedient for geometric reasons. Thus, to cover the whole spectrum of relevant pore radii, multiple calculations with consecutive pore radius magnitudes are needed. For each model, the calculated material behaviour is used as input data for the material properties of the finite element model of the next higher order.

According to Skalny et al. [2], pores in the range of several micrometers and smaller are highly responsible for the generation of cracks due to ettringite formation. Here heavy sulphate damages were observed as a consequence of ettringite formation although the latter could not be detected using scanning electron microscopy, which accounts for the formation of almost amorph ettringite structures in very small pores. On this background the modelling of the hard-

ened cement paste was started with a pore size interval from 100 nm to 1000 nm. Within this range, four pore size classes with similar class width were defined, using a logarithmic scale. The particular number of pores of one class was calculated from the differential pore volume of the hardened cement paste (CEM I cement, age 7 days, water-cement ratio w/c = 0.65). The principle of this approach and the distribution of pores are illustrated in Figure 1 and Table 1 respectively.

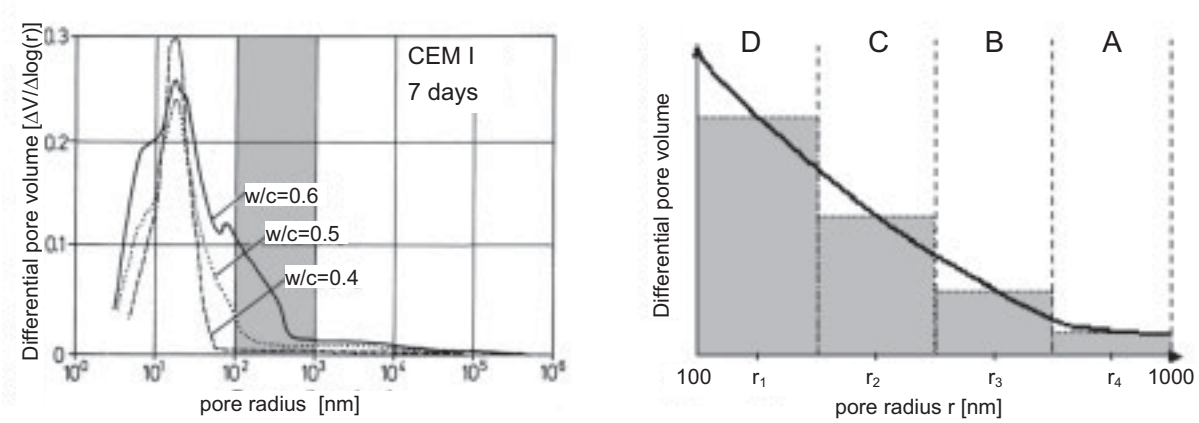

Figure 1: Differential pore volume of different hardened cement pastes; the modelled range of pores is marked in grey. Left: Pore size distribution. Right: Definition of four pore size classes with pores ranging from 100 to 1000 nm

Table 1: Number of pores in individual class, range from 100 to 1000 nm according to Figure 1 considering an area of 20 µm square

pore size class	**radius r_i [nm]**	**area of single pore [10^{-14} m^2]**	**area percentage [%]**	**number of pores n**
A	750	176.7	0.363	1
B	420	56.0	0.823	6
C	240	17.7	1.680	38
D	130	5.6	2.340	168

The statistical distribution of the pores in the model is assured by the use of a random number generator calculating the x- and y-coordinates of each pore centre. The biggest pores are calculated first, followed by the pores of the next smaller class until the smallest class in the end. In order to avoid too small spacing between pores or even overlapping, a concluding plausibility check with defined minimum values is carried out. Pores with interspaces below these values are finally eliminated. In the automated geometry generation the above generated data file of

pore distribution is implemented in DIANA applying a FORTRAN routine. Figure 2 shows the resulting model of hardened cement paste with an edge length of 20 µm.

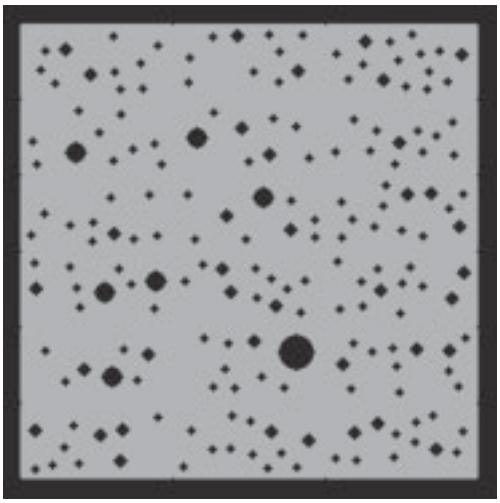

Figure 2: Geometry with pores in DIANA

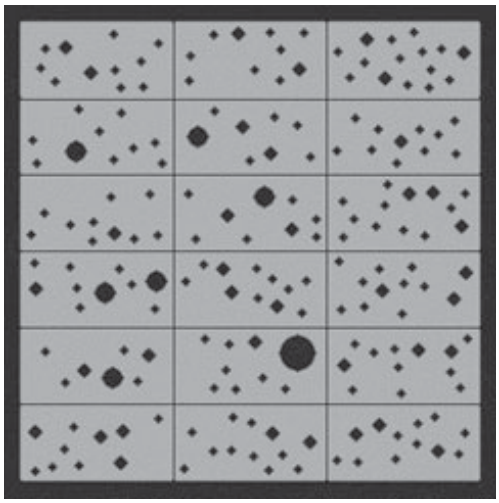

Figure 3: Geometry with pores and grid segmentation

2.1.2 Mesh generation

In the finite element model rectangular elements of second order are used, because triangular elements tend to exhibit stress locking and excessive stiffness. Because mesh generation in DIANA is done geometry-based (the geometry is generated first and meshing is done afterwards, starting from the edges), complex geometries with highly curved boundaries may induce problems in the automatic meshing routine if rectangular elements are used. Thus, heavily irregular meshes or programme termination may result.

In order to solve this problem, different approaches were tested whereof the idea of grid segmentation proved to be most effective (Figure 3).

Since this method still results in highly irregular meshes even with very small elements, additional auxiliary square boxes around the pores were introduced. These are generated as cut-outs around the pores within the routine of automatic pore generation. Hence, a separate mesh generation of the overall area with cut-outs and the cut-outs with pores themselves is possible. This technique now allows for a nearly fully automated mesh generation in combination with a high mesh quality. The only disadvantage is the increased required space for the square boxes compared to the circular pores, causing the need of a more strict plausibility control with respect to interspaces and overlapping of pores.

The effectiveness of this technique is illustrated in Figure 4, showing the differences in mesh geometry with and without applied auxiliary boxes. Figure 5 depicts the overall model with an edge length of 20 µm, composed of 18 single segments.

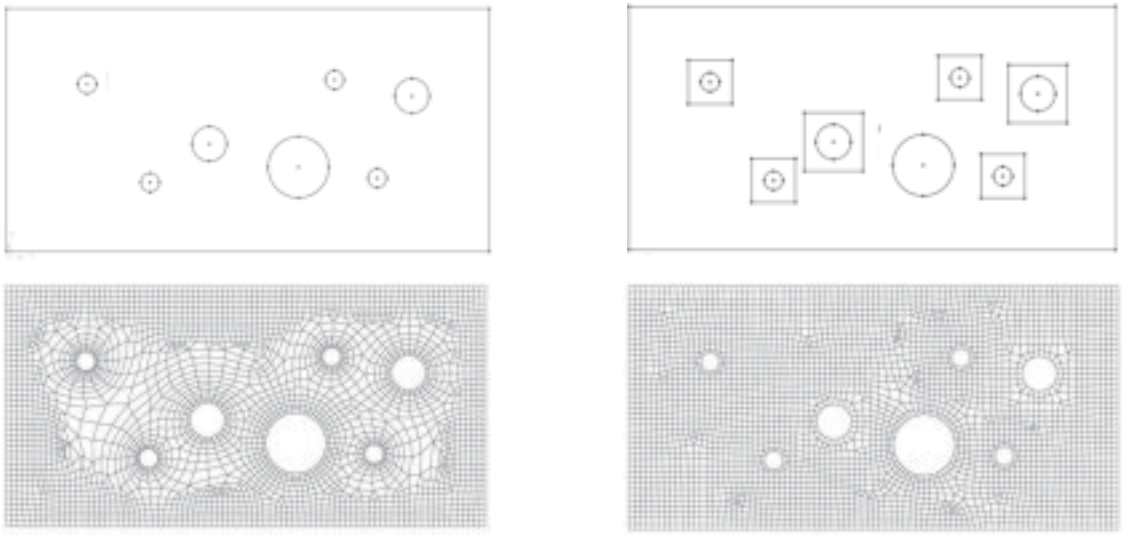

Figure 4: Segment without (left) and with (right) auxiliary square boxes. Top row: geometry. Bottom row: finite element mesh

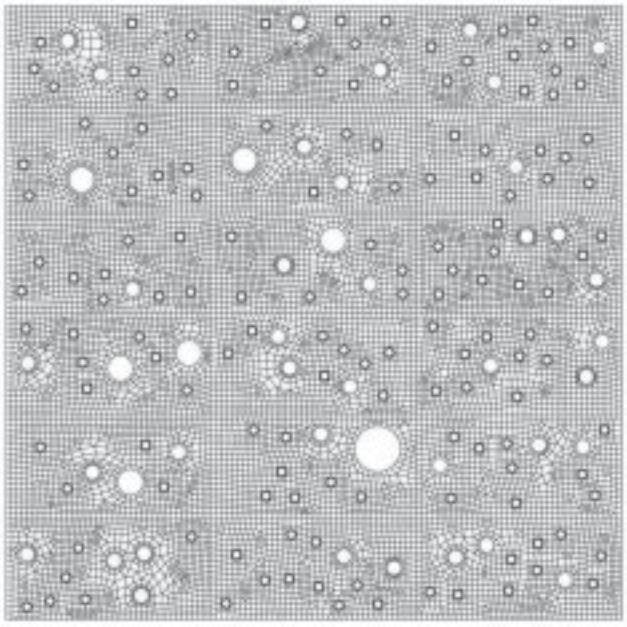

Figure 5: Finite element mesh of hardened cement paste containing circular pores within a pore size interval of 10^{-7} to 10^{-6} m and consisting of approx. 18000 elements

2.1.3 Material properties of hardened cement paste

The constitutive behaviour of the hardened cement paste was modelled using the “Crack Band Model” developed by Bažant and Oh [3] (see Figure 6) in order to facilitate the imaging of increasing crack formation and propagation. Within the numerical simulations the different cohesive crack models such as the Total Strain Rotating Crack, the Total Strain Fixed Crack as well as the Smeared Crack Model were investigated.

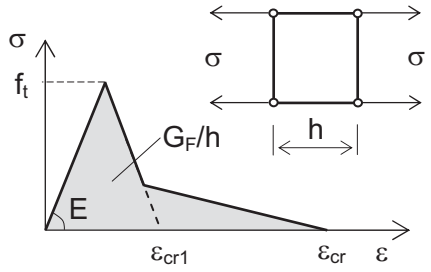

Figure 6: Crack Band Model implemented in the finite element model with:

- G_F fracture energy
- h characteristic element length
- f_t tensile strength
- E modulus of elasticity
- ε_{cr} critical crack strain

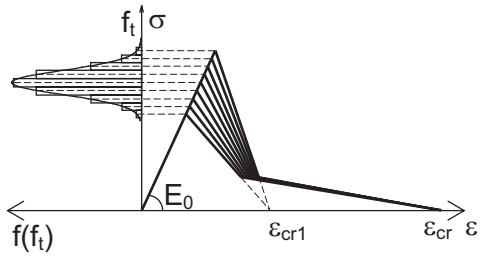

Figure 7: Implemented heterogeneity of hardened cement paste according to [4]

Furthermore, the heterogeneity of the material properties was taken into account by a Gaussian distribution of the material parameters (particularly tension strength and fracture energy, see Figure 7). For this purpose, material classes were defined and allocated randomly to the individual elements (Monte Carlo Method).

While recommended values for the strength and stiffness of the hardened cement paste were taken from literature, reliable magnitudes for the fracture energy of the mere matrix without pores could not be found. Hence, the fracture behaviour was modelled according to the concrete behaviour given in CEB Model Code 90 (see Figure 7). It was assumed that the strains ε_{cr1} and ε_{cr} correspond to crack widths of w_{c1} = 1 nm and w_c = 10 nm.

2.1.4 Modelling of sulphate attack

The propagation of the corrosion front was characterized in a first approach with the simplified empiric relation according to Atkinson and Hearne [5], whereas the corresponding pore stresses were estimated using the formula for linear crystallisation pressure p:

$$p = \frac{R \cdot T}{\nu} \cdot \ln\left(\frac{c}{c_s}\right) \tag{1}$$

where R represents the ideal gas constant, T the temperature, ν the molar volume of crystalline substance, c the actual concentration of the solute and c_s the saturation concentration.

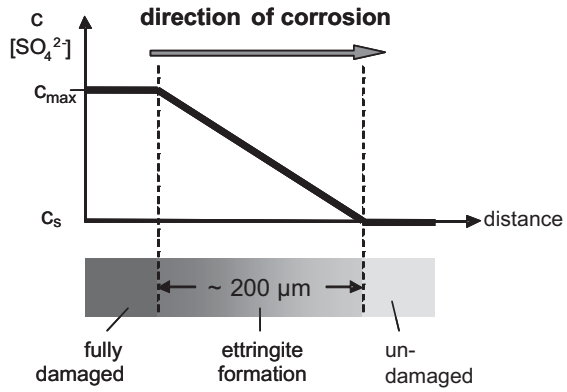

Figure 8: Sulphate concentration in hardened cement paste subjected to sulphate attack

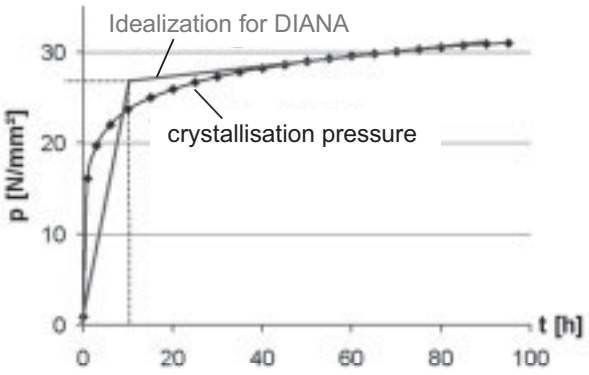

Figure 9: Effective and idealized development of crystallisation pressure with time

Assuming that ions not involved (K^+, Na^+, OH^- and others) do not have any influence on the solubility of sulphate, and that ettringite, monosulphate as well as portlandite are given as solid phases, a value of p = 31 MPa was calculated (T = 20 °C).

According to Gollop and Taylor [6], the thickness of the ettringite formation zone was set equal to 200 µm. To further minimise the extent of numerical calculations with DIANA, the course of crystallisation pressure over time was approximated with a bilinear function (see Figure 9).

2.1.5 Results of numerical investigations

Applying the derived model, numerous calculations were carried out to study the influence of different parameters and to verify the suitability of the model. Within these studies, simulations using the overall geometry, single segments as well as segment groups were conducted. The main problems in the finite element computations were numerical instabilities with increasing crack propagation as well as excessive calculation time using the overall model. The most important results are detailed below:

- The existing model constitutes a functional approach to describe the degradation process in hardened cement paste subjected to sulphate attack.

- A crack formation along crack paths can be reproduced with the model. The implemented heterogeneous material behaviour has a positive influence on the formation of distinct crack paths (see Figure 10).
- Considering the three cohesive models “Total Strain Rotating Crack”, “Total Strain Fixed Crack” and “Smeared Crack”, the Smeared Crack Model turned out to be the most suitable due to its significantly higher numerical stability and lower calculation costs.
- High calculation times are a core problem for models with more than 1000 to 1500 Elements. Lowering of the stipulated convergence criteria causes only limited reduction of calculation costs, but the convergence is improved.
- Against one’s expectations, increasing mesh refinement did not have significant influence on convergence. Partly, numerical instabilities occurred even earlier.
- Considering the applied iteration schemes (Newton-Raphson, modified Newton-Raphson, Constant Stiffness), the regular Newton-Raphson method together with a preceding line search scheme showed the best results.

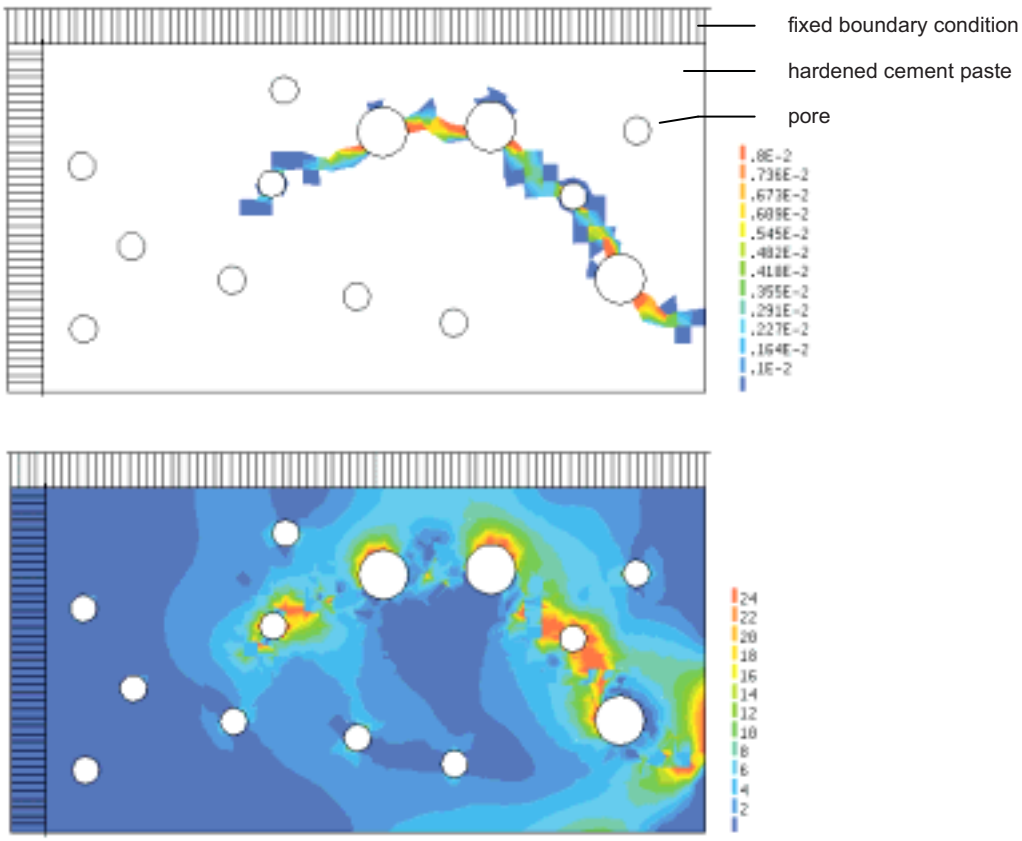

Figure 10: Critical crack strain ε_{cr} (top) and related main stress σ_{11} [MPa] (bottom) along a crack band for a segment of the overall model subjected to crystallization pressure in pores

2.2 Numerical investigations on the meso level

Parallel to the investigations on the material behaviour of hardened cement paste on the micro level, calculations on the meso level were carried out. The concrete was modelled as a three-phase-system consisting of aggregates, mortar matrix and interfacial transition zone.

2.2.1 Geometrical model

Similar to the proceeding for the distribution of the pores on the micro level, the aggregates with a maximum size of 8 mm (grading curve B8 of DIN 1045) were divided into four sub-classes sized 8, 4, 2 and 1 mm and statistically distributed using the already mentioned FORTRAN routine. In a first step a square shaped 40×40 mm^2 model was used which was later on reduced to 20×20 mm^2 due to high calculation times. The distribution of the aggregate sizes of both models is depicted in Table 2. The material behaviour of the aggregates was assumed to be linear elastic with an elastic modulus of E = 50000 MPa having no limiting tensile stress.

Table 2: Distribution of the aggregate sizes of the two models on the meso level with an edge length of 40 mm and 20 mm

aggregate class	aggregate diameter [mm]	volumetric content according to grading curve [%]	aggregate cross section area [mm^2]	number of aggregates for model 40 x 40 mm^2	number of aggregates for model 20 x 20 mm^2
A	8	26	50,265	4	1
B	4	21,5	12,566	14	3
C	2	16	3,141	42	11
D	1	14,5	0,785	158	38

The mortar matrix was reproduced using the approach of the heterogeneous continuum with variation of strength and stiffness values (see chapter 2.1). Mean values for strength and elastic modulus were adapted for the recomputation of given experiments with magnitudes at the time zero (start of sulphate attack) from 45 to 65 MPa (compressive strength) and 30000 to 36000 MPa (elastic modulus), respectively. In order to facilitate crack formation, the Cohesive Crack Model approach was applied, similar to the investigations on the micro level.

The interfacial transition zone between aggregate and matrix was taken into account by the implementation of an intermediate layer of elements. To start with, its thickness was set to 40 µm, independent from the aggregate diameter. However, the adaptation of the thickness of the transition zone to the corresponding aggregate size is easily possible and can be implemented in future calculations. The elastic modulus of the interfacial transition zone was coupled to the elastic modulus of the matrix elements with reduced values of 60 %.

2.2.2 Modelling of sulphate attack

The sulphate-induced expansion process was modelled via a volumetric expansion of the mortar matrix. Thus, measured volumetric strain values of mortar samples were specified in the model by applying a temporally and locally variant temperature field to the matrix with a linear correlation between temperature and strain values.

Furthermore, the decrease of the mortar strength and stiffness observed in experimental studies was taken into account by a variation of the model parameters over time. The corresponding values were adapted not only for the matrix but also for the interfacial transition zone in intervals of 30 days.

2.2.3 Recalculation of experiments

In order to verify the suitability of the deduced numerical concrete model, the experimentally measured deformation behaviour and the compressive strength of concrete samples were recalculated with DIANA for a period of 90 days and 120 days respectively. The essential material properties of the matrix were calibrated on mortar samples from the same test series. The calculated strains of three concretes with different types of cement (CEM I, CEM II and CEM I-HS) were in good agreement with the measured values (Figure 11) and the calculated compressive strengths could reproduce the right tendencies. Moreover, the computed crack formation pattern (Figure 12) is in accordance with the actual material behaviour. Thus, the deduced model is capable of calculating the degradation process in concrete subjected to sulphate attack in a realistic way.

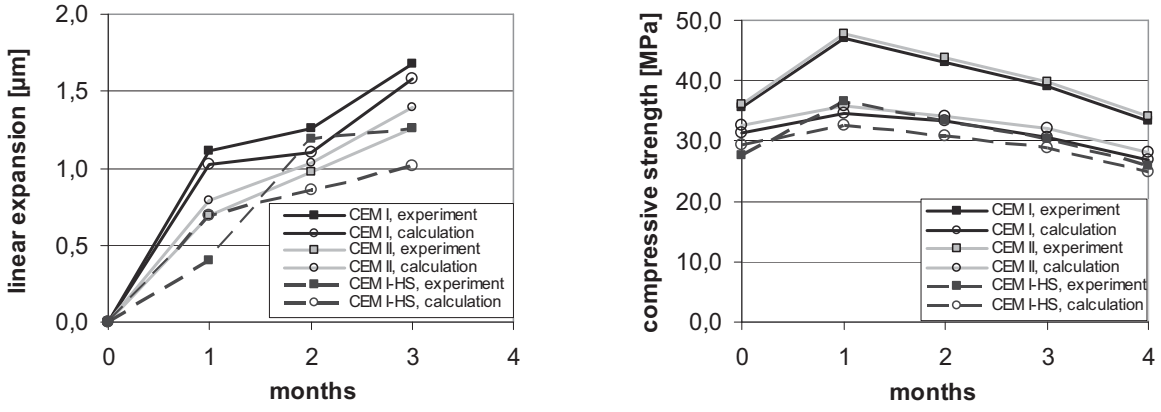

Figure 11: Linear expansion (left) and compressive strength (right) of three different concretes subjected to sulphate attack. Comparison of experimental and numerical results

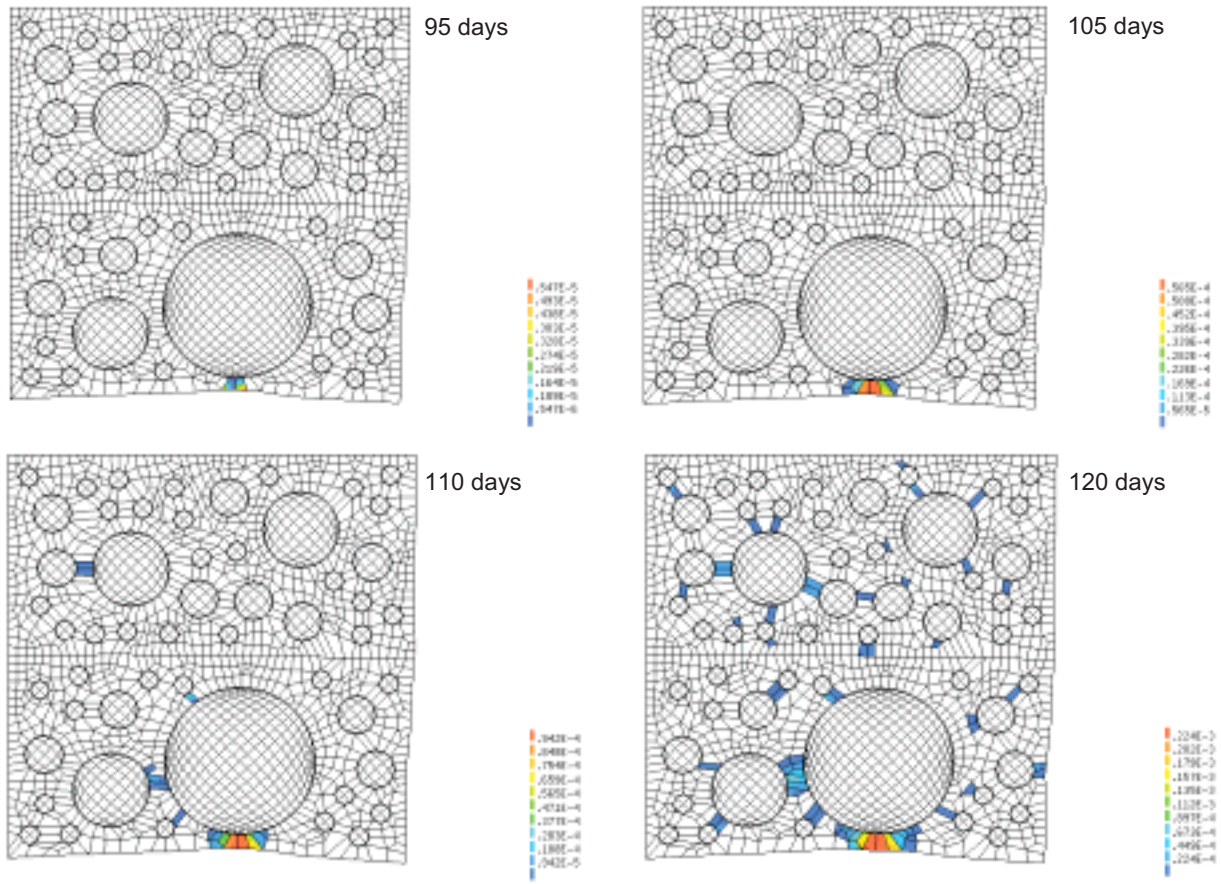

Figure 12: Calculated crack formation at the age of 95 days (top left), 105 days (top right), 110 days (bottom left) and 120 days (bottom right). Only strains higher than the critical strain are depicted ($\varepsilon > \varepsilon_{cr}$)

2.2.4 Parameter studies

In order to determine the influence of the different material parameters and geometry effects on the overall results, various parameter studies were carried out. In the following, the most important tendencies are illustrated.

The comparison of two different models with the same material parameters but differing maximum aggregate sizes and aggregate distribution (see Figure 13) shows a variation of calculated critical crack strains of more than factor two. Although bigger aggregates tend to create higher strains in their vicinity, the model to the right with a maximum aggregate size of 8 mm (left model: maximum aggregate size = 10 mm) shows much higher strains because of the location of the 8 mm aggregate close to a free boundary. Moreover, it can be seen that the neighbouring 4 mm and 8 mm aggregates generate higher stresses between themselves than between the 8 mm and a 1 mm aggregate with similar spacing. It can be concluded, that the geometric distribution of big aggregates is of a significantly higher importance than their maximum size and results in a considerable mesh dependence of the model.

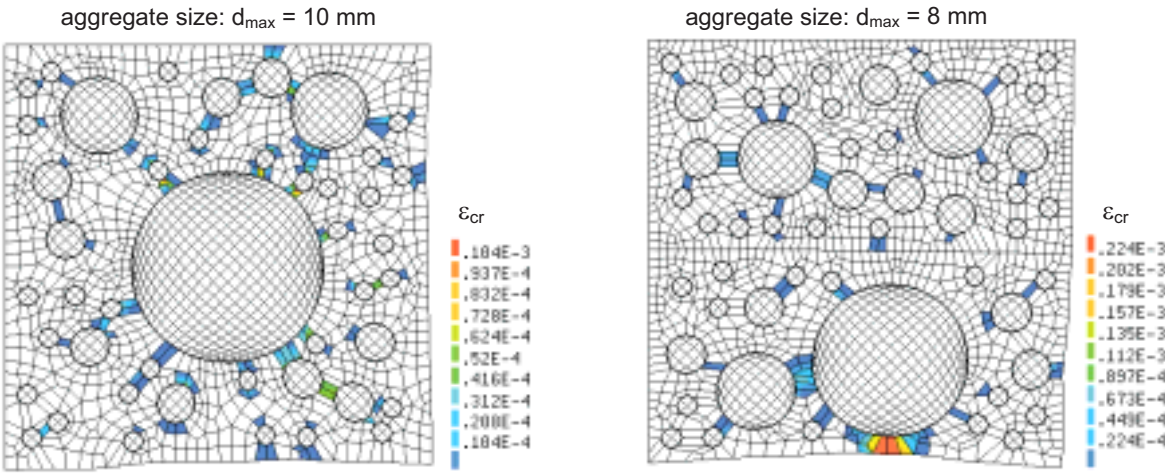

Figure 13: Influence of aggregate size and aggregate distribution on critical crack strains ε_{cr} after 120 days of sulphate attack

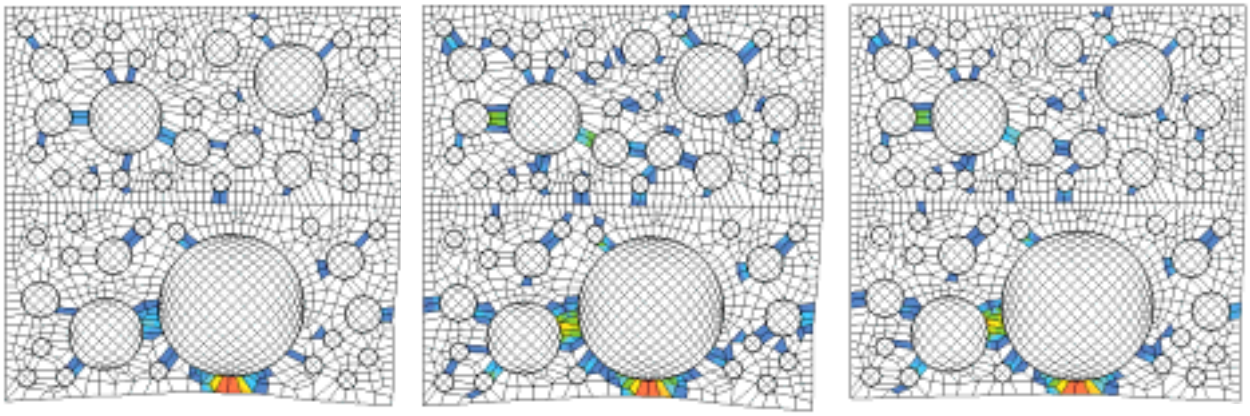

$E_{aggregate}$ = 50 GPa
$\varepsilon_{cr,max} = 0{,}224 \cdot 10^{-3}$

$E_{aggregate}$ = 40 GPa
$\varepsilon_{cr,max} = 0{,}212 \cdot 10^{-3}$

$E_{aggregate}$ = 30 GPa
$\varepsilon_{cr,max} = 0{,}217 \cdot 10^{-3}$

Figure 14: Influence of aggregate stiffness on critical crack strains

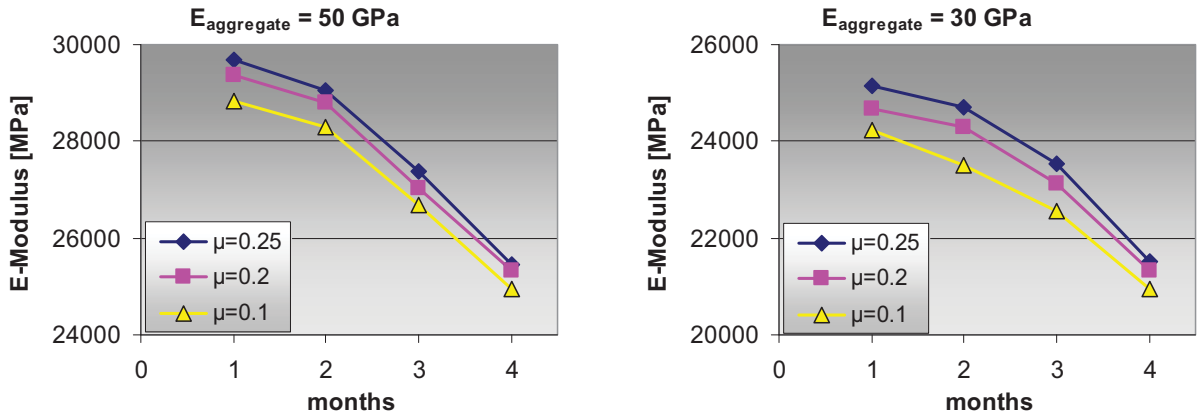

Figure 15: Influence of aggregate stiffness and Poisson's ratio μ on the modulus of elasticity

The influence of the aggregate stiffness on the maximum crack strains is low (Figure 14) and varies by only 6 % for the given elastic moduli of 30 to 50 GPa. It could be expected, that the stiffest aggregates generate the highest strains. However, no clear tendency of a correlation can be observed, because the smallest strains do not arise with the softest aggregates but with the intermediate ones.

The correlation of aggregate stiffness, Poisson's ratio and resulting elastic modulus can be seen in Figure 15. Naturally, stiffer aggregates must result in a higher modulus of elasticity of the concrete. A higher Poisson's ratio generates higher elastic moduli as well because of the partial constraint of lateral strains which counter possible deformations. With a variation of less than 5 % for the examined Poisson's ratios, this effect is fairly low and not of importance for further calculations.

3 Experimental investigations

The own experimental investigations provide the basis to determine the deformation behaviour and the mechanical properties of hardened cement paste subjected to sulphate attack. The obtained results constitute a reference for the calibration of the numerical continuum model and the validation of the prediction model. They provide the essential values for linear expansion, mass change, flexural strength and compressive strength as well as porosity (total porosity, pore distribution).

The prismatic samples are sized 100x40x10 mm^3. Amongst the tested parameters are the water-cement ratio, the age at testing as well as the type and duration of storage (Table 3).

Table 3: Overview on tested parameters of experimental programme

water-cement ratio	**type of storage (T = 20 °C)**	**duration of storage*/ age at testing [d]**	**number of samples**
0.4 and 0.6	sealed	0, 7, 28, 90, 180	2·5·3 = 30
	water	7, 28, 90, 180	2·4·3 = 24
	solution I	7, 28, 90, 180	2·4·5 = 40
	solution II	7, 28, 90, 180	2·4·5 = 40
	total number of samples:		134

* after start of examinations at the age of 3 months

For the first 3 months all samples are cured the same way. After stripping at the age of 7 days, the samples are stored over water in a covered tray at a constant temperature. After 90 days one part of the samples is left sealed in the conditioning chamber whereas all other samples are

immersed in either water or sodium sulphate solution with two different sulphate concentrations (Na_2SO_4 solution with high and low concentration, see Table 3 “solution I” and “solution II”). The samples stored under water are required to specify the volumetric expansion and the difference in strength between sealed and water stored samples, respectively. Together with the sealed samples they serve as a reference and will contribute to a better understanding and interpretation of the test results gained from the samples subjected to sulphate attack.

The sealed reference samples are tested at the age of 3 months, corresponding to a duration of storage of 0 days according to Table 3. Afterwards all samples are tested 7, 28, 90 and 180 days after the beginning of their individual storage condition. The number of samples related to the different storage conditions is given in Table 3. Altogether 134 samples are tested.

4 Overview on research modules and prediction models

The configuration of the model and the interaction of the different modules are shown in Figure 16. The numerical model on the micro level is calibrated with measured material properties and damages of hardened cement paste samples. Combined chemical and mineralogical investigations deliver the necessary transport coefficients and volumetric expansions whereas the crystallisation pressures have to be calculated on the basis of thermodynamic data, because they cannot be measured directly.

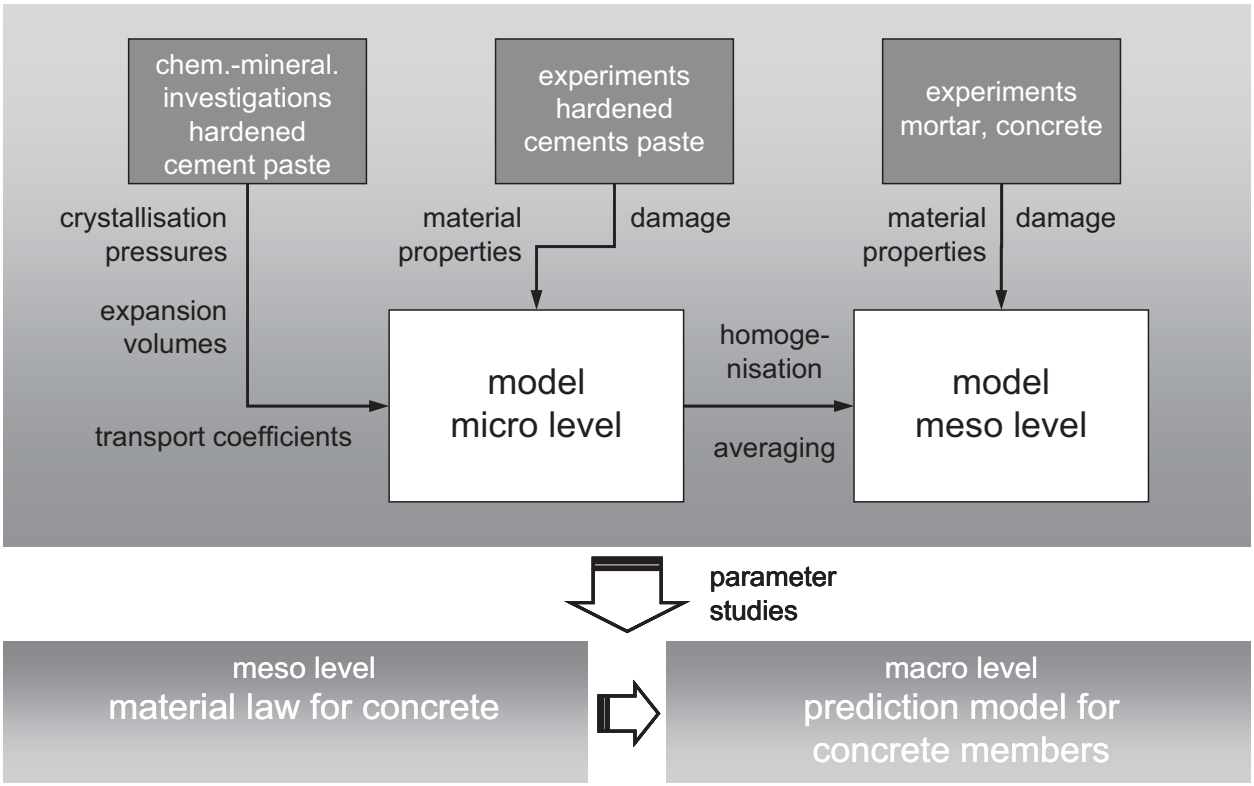

Figure 16: Overview on research modules, parameters and resulting models

In the next step, the calculated expansions and material deteriorations of different micro level models (which consist of hardened cement paste without pores and the pores themselves) are averaged and thus provide the input data for the matrix on the meso level, which is modelled as a heterogeneous continuum. Together with the aggregates and the interfacial transition zone a three-phase model on the meso level is obtained. The experiments on mortar and concrete are used to calibrate and verify the model on the meso level.

Because of the various influencing parameters in the three-phase model (see chapter 2.2.4), their effects and importance are investigated in numerous parameter studies. The derivation of an appropriate material law for concrete and a simplified analytical prediction model for sulphate attack on concrete members complete the research study.

5 Discussion

Within the research study a numerical model on the micro level was developed which is suitable to reproduce the advancing corrosion front due to sulphate attack. Furthermore, the formation of crack paths can be calculated for small to medium sized finite element models. On the meso level, the model is capable of reproducing a sound combined crack formation in hardened cement paste and interfacial transition zone around the aggregates. With experimental data of mortar samples as input for the material parameters of the matrix, the calculated strains and strengths in the overall model are in good agreement with the measured values for concrete samples.

One of the still remaining problems is to find the correct input parameters for the model on the micro level, as they are either complex to measure or cannot be measured with the necessary precision at all. Whereas the relevant transport coefficients of sulphate in concrete can be identified accurately, the relevant increase of the pore pressures due to ettringite formation cannot be determined. This is due to the fact, that the major part of the damage-relevant ettringite formation takes place in very small gel pores which cannot be assessed properly with any measuring device.

Another subject of further research is the multi-scale character of concrete. For geometric reasons, only one order of magnitude of pore sizes can be modelled in one numerical calculation. Thus, a series of convoluted calculations with different orders of magnitudes is necessary, where the overall results of one model (matrix with pores) deliver the input data for the matrix in the next following model. As a result, the final outcome can vary very much and is characterised by a high geometric dependency.

The calculation of crack paths with the finite element code DIANA causes a problem for larger models with many pores and leads to convergence problems with early program termination and very high calculation time. Because DIANA cannot be run on parallel servers with multiple CPU nodes so far, this point is hard to eliminate.

Due to the above mentioned reasons, the original idea to use the numerical results on the micro level as averaged and homogenised input data for the matrix on meso level is not really successive at the actual state of research, because the delivery of correct input parameters is still questionable. However, the model on meso level could prove to be capable of computing sound results if the required input data is given by experiments. This achievement may be considered as a remarkable research progress in view of the state-of-the-art.

6 Conclusion and outlook

Within the research study numerical models on the micro and the meso level could be developed that are suitable to describe the qualitative deterioration processes of concrete subjected to sulphate attack. There is still some effort required to improve the reliability of the calculations and to get a better knowledge of the relevant processes and characteristic parameters on micro level.

Further research study is necessary to derive a simplified analytical prediction model for sulphate attack on concrete members. Such a model can substantially aid in the design and construction of concrete members exposed to sulphate attack and help forecasting the service life of members under such actions. It is a key part of an overall service life design, which will be a part of future code generations.

7 References

[1] Herold, G.: Korrosion zementgebundener Werkstoffe in mineralsauren Wässern. Schriftenreihe des Instituts für Massivbau und Baustofftechnologie, Heft 36, Universität Karlsruhe, 1999.

[2] Skalny, J., Marchand, J., Odler, I.: Sulfate Attack on Concrete. Spon Press, London, UK, 2002.

[3] Bažant, Z. P., Oh, B. H.: Crack band theory for fracture of concrete. In: Matériaux et Constructions, Vol. 16, No. 93, 1983.

[4] Mechtcherine, V.: Bruchmechanische und fraktologische Untersuchungen zur Rissausbreitung in Beton. Schriftenreihe des Instituts für Massivbau und Baustofftechnologie, Heft 40, Universität Karlsruhe, 2000

[5] Atkinson, A., Hearne, J.A.: An assessment of the long-term durability of concrete in radioactive waste repositories. AERE-R11465, Harwell, UK, 1984

[6] Gollop, R. S., Taylor, H. F .W.: Microstructural and Microanalytical Studies of Sulfate Attack – I. Ordinary Portland Cement Paste. Cement and Concrete Research 22 (1992), pp. 1027-1038

Ellen Rigo
Dr.-Ing.

MPA Braunschweig
Braunschweig, Germany

Frank Schmidt-Döhl
Prof. Dr.-Ing.

Hamburg University of Technology
Institute of Materials, Physics and Chemistry of Buildings
Hamburg, Germany

Harald Budelmann
Prof. Dr.-Ing.

iBMB, Department Building Materials and Reinforced Concrete,
Braunschweig, Germany

Probabilistic concept for durability design of cement-based materials exposed to acid, ammonium, and sulphate solution

Summary

The paper presents a probabilistic concept for durability evaluation. It deals with corrosion induced by sulphate solution and degradation by a leaching process. The concept is based on a probabilistic approach and was accomplished by combining the transport-reaction model Transreac with a Monte Carlo simulation. The necessary validation of the simulation models used has been demonstrated. It is evident that simulated and experimentally derived data are in good agreement. Finally the application of the probabilistic concept is demonstrated by a number of examples which deal with corrosion of cement-based materials in sulphate, acid, and ammonium solution. The simulated results agree with practical experience. The excellent results show that the model Transreac in combination with a Monte Carlo simulation is a powerful tool to set up the probabilistic safety concept for durability problems.

Keywords: *Modelling, Monte Carlo simulation, durability, sulphate attack ammonium attack, acid attack*

1 Introduction

Durability is the capability of a building, structural element or material to maintain a requested performance over a specified time under service conditions. The durability design of concrete structures is based on implicit rules for materials, material compositions, working conditions, structural dimension, etc.. Examples of such rules are minimum concrete cover, maximum water/cement ratio, and minimum cement content. Modern building codes for structural design make use of the reliability theory based on a probabilistic approach. Increasingly, these approaches expand into durability design. For example, Corr et al. [1] presented an empirical reliability analysis for sulphate attack on concrete, and Gehlen [2,3] presented a probabilistic design concept for concrete carbonation and penetration of chlorides into concrete. This kind of concept optimizes the cost for construction, maintenance, and repair while considering safety factors.

The aim of this study is to present a probabilistic concept for durability evaluation. Firstly, the theoretical background for the probabilistic concept and the procedure of the durability design is presented. Secondly, this study demonstrates examples for durability design, dealing with chemical attack on different cement-based materials.

The principles of the probability concept are explained below. Structures must be reliable with respect to their life time. In the mathematical sense reliability is the probability of the structure to resist all influences during service life. The probability of failure, which is the complementary value to the probability of reliability, is the commonly used value. The acceptability of low residual risk and a small probability of failure offers the possibility to consider economic aspects as a part of building design.

A designer must be able to calculate the probability of failure for structures under the influence of degradation factors as a function of different design parameters and time. He will then be able to prove the compliance with certain requirements, referring to serviceability limit state and ultimate limit state. With the aid of this model he can make decisions on the required dimensions and material properties.

For this procedure, two models are required. First, a deterministic model showing the degradation over time as a function of an appropriate design parameter is needed. The mathematical model which is needed to calculate the probability of failure used in this study is called the probabilistic model.

In Figure 1 an example of a degradation model as a function of time of attack $\mu(t)$ is shown. The horizontal line asterisked as ‘max’ illustrates the maximum allowable corrosion depth. For reinforced concrete this usually is the depth of the cover. Design parameters, e.g. environmental factors and properties of the building materials, vary greatly. Because of this, the performance of a structure must be treated stochastically. Otherwise the calculated life time t_g is too long if only the medium degradation over time is taken into account. This means that not only the average values, but also distributions or the distribution function ($\Phi_G(t)$) in dependence of time must be considered. For this purpose, a probabilistic model is needed. This model must give reliable information on the variation of the degradation. The degradation itself and the variation of the degradation is affected by the variation of the environmental conditions and the variation of the material properties.

The probability of failure is the black marked area in Figure 1. The probability of failure is the probability of the material not resisting the chemical attack. In most cases the designer can not ensure that the material will resist chemical attack for the whole life time because of the external parameters as a whole. Because of this we must accept a low residual risk and a small probability of failure. Otherwise the designer must choose quite a big depth of cover, which in most cases is not realistic due to the economic aspects. By means of this information, the designer can make decisions on the required dimensions, e.g. concrete cover and type of material, e.g. water to cement ratio and cement type.

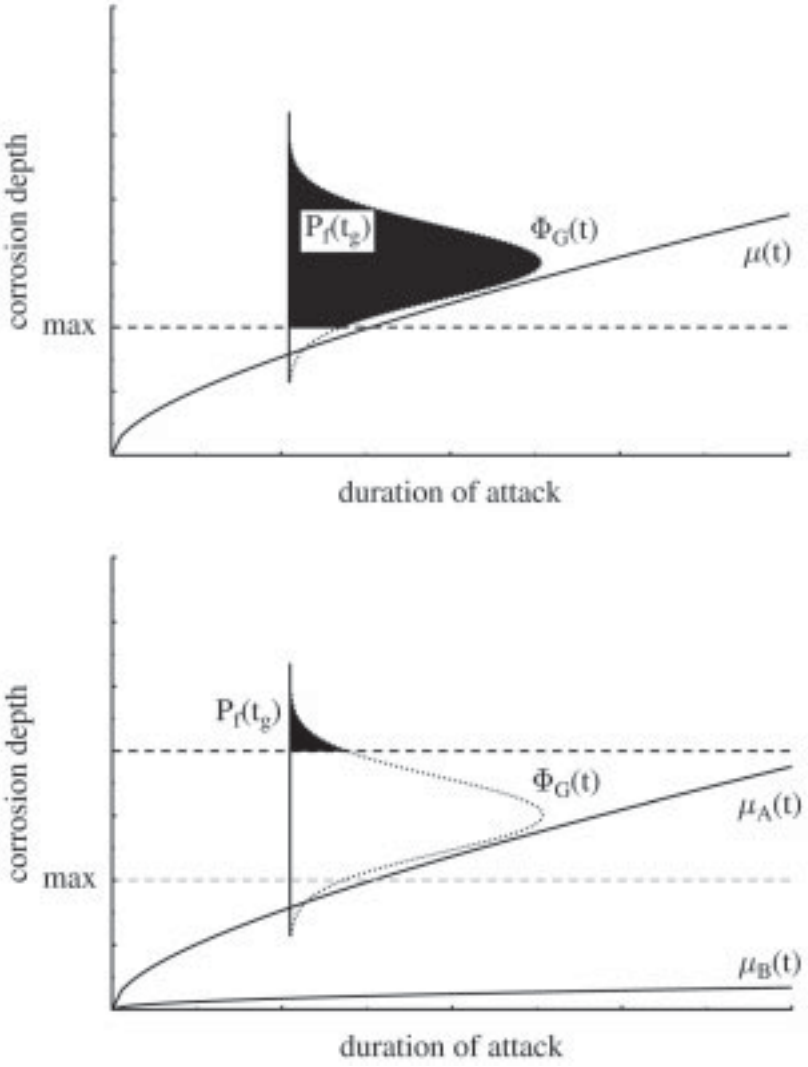

Figure 1: Reliability theory for chemical attack (see also [4]). On the upper the calculation of the probability of failure is shown, and on the lower two arrangements (increase of depth of cover and the use of another material) for maintaining the required probability of failure are demonstrated.

In Figure 1 (lower) the decreasing probability of failure $P_f(tg)$ as the result of increased cover depth is demonstrated. The choice of a more resistant material (degradation model $\mu_B(t)$) to maintain the required probability of failure is also demonstrated in Figure 1 (lower).

The degradation and the probabilistic model offer the possibility to calculate the probability of failure with respect to the life time for different materials and environmental conditions. The design methodology demands that the calculated probability of failure must be lower than the maximum allowable probability of failure during the life time of the structure. So far the maximum allowable probability of failure for chemical attack is not defined in technical standards. In this study the maximum allowable probability of failure for different environmental conditions is suggested.

The probabilistic concept is presented for different aggressive environmental conditions:

-sulphate solution
-acid solution
-ammonium solution.

At first, the deterministic and probabilistic model is introduced. The probabilistic concept must be based on a realistic deterioration model. Because of this, validation of numerous corrosion experiments are demonstrated. These corrosion experiments are taken from the literature. Both, the deterministic and the probabilistic model need a numerousness of input data. Most of the needed data are not mentioned in the literature that deals with the corrosion experiment. Because of this most of the input data must be estimated. For this purpose there are databases compiling the data of a lot of different materials.

The validation of the corrosion experiments are based on data which are extracted by a special procedure from the database which is described in [5].

Before calculating the probability of failure for each attack, the limit state must be defined which is specified in this study.

2 Deterioration model Transreac

The deterministic model used in this study is Transreac, which simulates corrosion effects of building materials caused by the attack of chemical solutions. Transreac is described in [6-8]. This model combines the calculation of chemical reactions with the calculation of transport processes within the structure. The flow chart is demonstrated in Figure 2.

The calculation of chemical reactions is based on repeated determination of the stable phase assemblage (Gibbs energy minimization, Pitzer model, consideration of chemical kinetics).

The transport module covers a large number of different transport processes within porous materials. These are capillary suction, flow by seepage pressure, transport of solved species connected with these processes, diffusion of solved species, diffusion caused by diffusion potential, heat and moisture transfer, and water vapour diffusion.

In addition, modules for calculating corrosion effects were implemented. These corrosion effects include the expansion caused by the formation of ettringite, the loss of material strength and the loss of mass caused by the dissolution of phases. A lot of improvements have been made since the papers [6-8] were published. The accuracy and speed of the thermodynamic algorithm has been increased and the simulation of redox-reactions has been incorporated. All transport processes can now be calculated as 2-D processes. The heat and moisture transport can be now calculated on the basis of the model of Künzel [9]. In addition, the model for transport caused by diffusion potential has been improved.

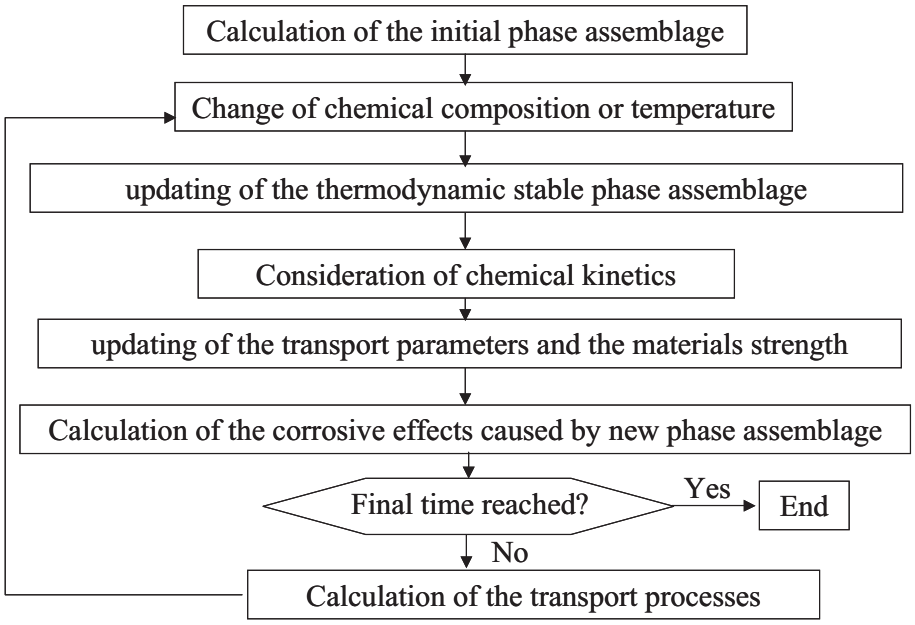

Figure 2: flow chart for the determistic model Transreac.

With this highly flexible model a lot of different simulations were done in the past. The examined materials cover cement mortar, concrete (also with fly-ash and blast furnace slag), sandstone and sorel cement. The aggressive solutions cover sulphate solutions, chloride solutions, acid, seepage water from a landfill, saline solutions characteristic for salt mines, and solutions with different contents of aggressive carbon dioxide (see for example [5-8,10-19].

3 Probabilistic model

Transreac has been extended to a probabilistic model. This was accomplished by incorporating the deterministic model into a Monte Carlo simulation (see [5,18,19]). The Monte Carlo method is a stochastic technique, which means that it is based on the use of random numbers and probability statistics to investigate problems (see [20]). This numerical approach was used to preserve all the features and the full flexibility of the deterministic model. This extension allows the probability of failure to be calculated and the sensitivity to be analysed. Both of them are important for the safety concept. The implementation of Transreac in a Monte Carlo simulation is in principle a multiple calling of the main program of Transreac (see Figure 3).

With every calling, the initial values are changed corresponding to their experimentally derived pattern of distribution. Then the results of the Transreac algorithm produced for changed initial values are recorded. A random generator produces the changed input parameter. At the end there is a statistic analysis of the response. The program offers the possibility to split the calculation on different computers.

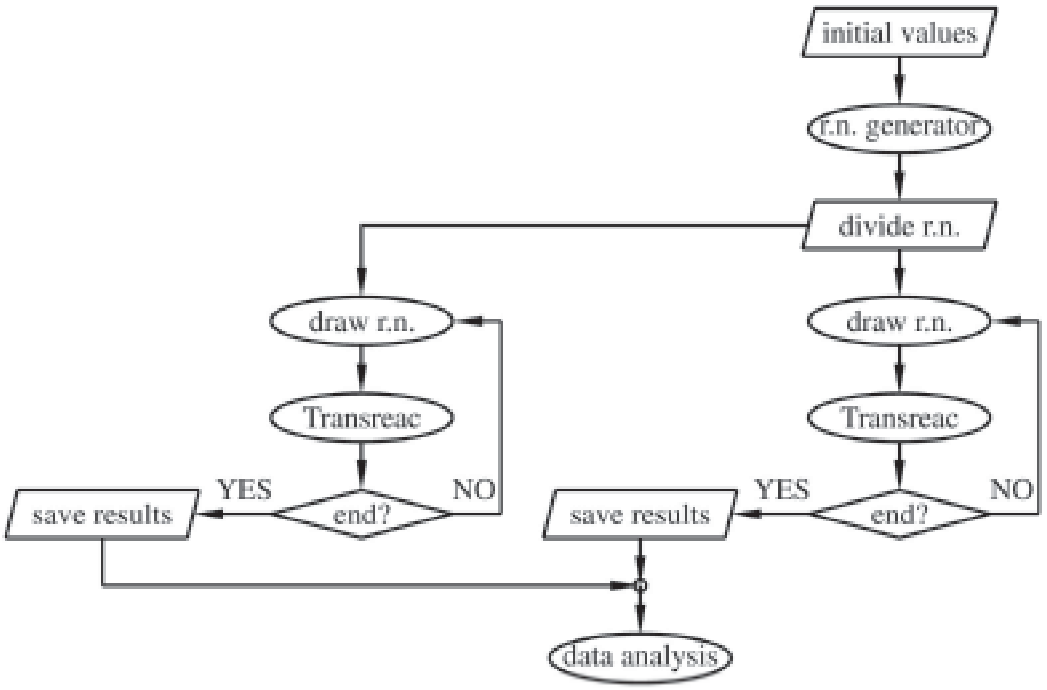

Figure 3: Structure of the probabilistic algorithm, split for two computers (r.n.=random number.) (from [18]).

4 Data records

To use the probabilistic and the deterministic model it is essential to provide a lot of data that deals with the average values and also the distributions of properties of building materials. For this purpose an extensive database is provided in this work. The database contains about 9500 values on:

-pore distribution,
-bulk density
-data to calculate transportation process (e.g. capillary suction, diffusion)
- mechanical data (tensile strain)

This data is available for concrete, mortar and cement stone for different water to cement ratios and different cement types. The data sets were extracted by assembling data from about one hundred publications. The data was analysed by a special stochastic procedure which is described in [5]. Most data from the literature show a strong deviation even on the same material. One example of this phenomenon is shown in Figure 4.

This deviation can be explained by different experimental methods of estimation of diffusion coefficients, different treatment of the samples, or inhomogeneous material. For the use of the safety concept the deviation is only allowed if it can be attributed to inhomogeneous material. To overcome this problem, future data measurements should be more standardized.

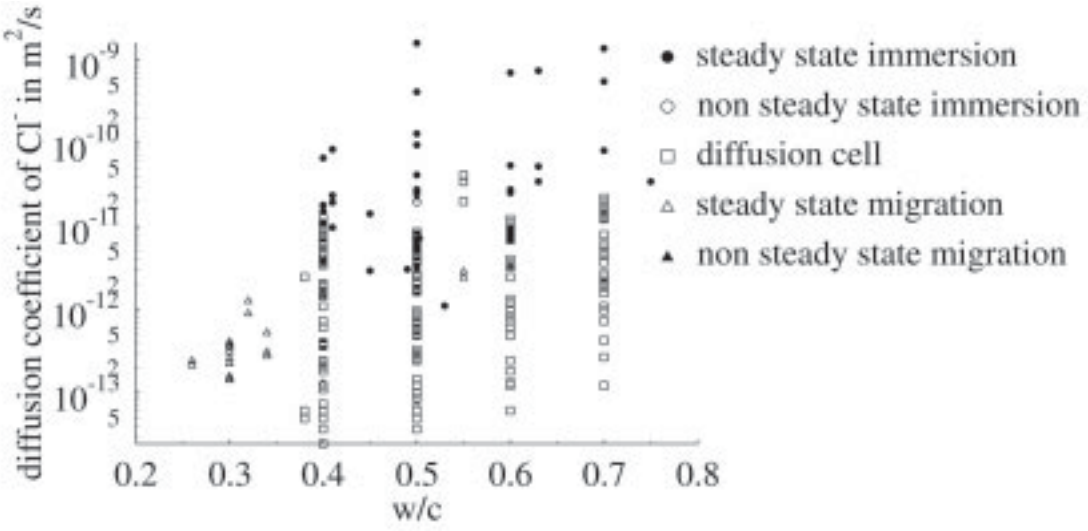

Figure 4: Diffusion coefficient of Cl^- for concrete at various water to cement ratio. Diffusion coefficients are from the sources [17-28]. type of cement: CEM I 32,5 N, CEM II/A-D, CEM II/A-P, CEM II/A-S, CEM II/A-T, CEM II/A-V, CEM II/B-P, CEM II/B-S, CEM II/B-T, CEM II/B-V, CEM II/B-W, CEM III/A 32,5 N, CEM III/B N-NW/HS, CEM IV/B 32,5 N,CEM V/A 32,5 N, CEM V/B 32,5 N

Furthermore, data to calculate chemical reaction must be provided, this is also presented in [5].

5 Validation

The deterministic and the probabilistic model must be validated. The validation of the probabilistic model is also described in [5,18]. This example deals with the formation of ettringite due to sulphate solution attack. Examples of validation of the deterministic model can be found in [6-8,10-17].

Additional examples are presented in [5,19]. Here a certain amount of corrosion experiments from literature are used. The corrosion experiments taken into account deal with corrosion of concrete, mortar or cement stone as a result of nitric acid, hydrochloric acid, sulphuric acid and aqueous ammonium solution attack.

Data needed for the calculation are taken from the data records described in this article.

5.1 Validation of probabilistic model

The validation of the probabilistic model deals with the formation of ettringite. The validation is described in detail in [5,18]. Here is described a summary of the results. The experiment is described in [8]. Mortar specimens with a length of 100 mm were in contact with sodium sulfate solution (44 g/L). Then the formation of ettringite and the induced corrosion effects were investigated (see Figure 5).

During the first phase of the experiments, capillary suction was the main transport process. After saturation of the specimens, the diffusion of dissolved species was the only transport process. The experimental input parameters for Transreac (mean value and standard deviation) are listed in [8]. All these parameters were derived from non-corroded material. Due to the lack of experimental data it is assumed that the initial values have a normal distribution.

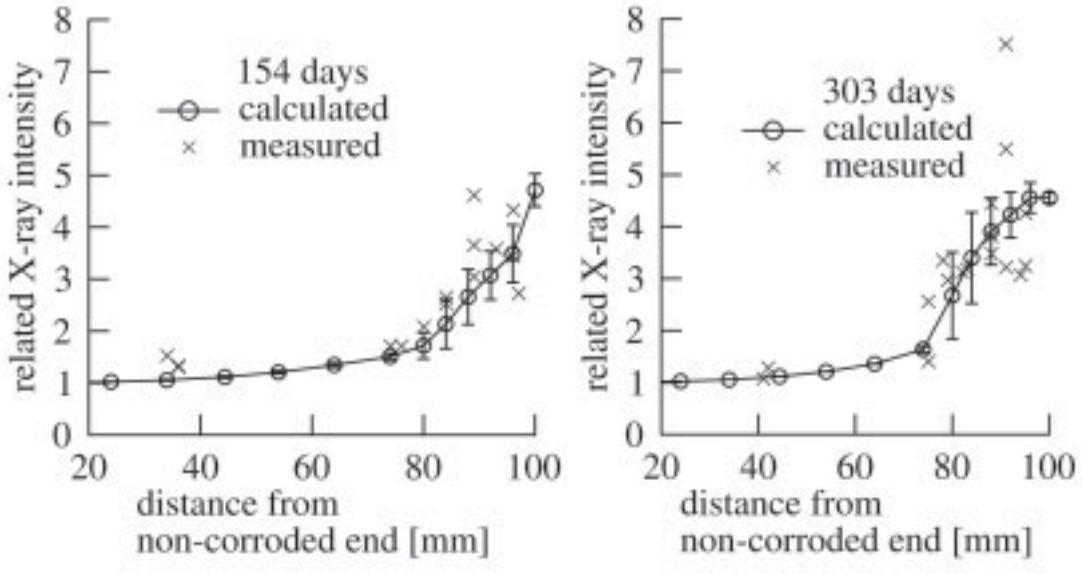

Figure 5: Ettringite profile of corroded specimen after 154 days (left) and after 303 days (right) in contact with Na_2SO_4-solution (from [18]). The X-ray intensity of ettringite is related to the X-ray intensity of non-corroded material.

The measured ettringite profiles (see Figure 5) show an additional formation of ettringite caused by the attack of the sulphate solution. After 303 days it was found that gypsum had also formed on the corroded side of the specimen.

The calculated results are consistent with the experimental data (see Figure 5). The experimentally observed formation of gypsum was also simulated by Transreac. The error bars are the result of the Monte Carlo simulation. They show the standard deviation of the simulated ettringite profile. The Monte Carlo simulation shows an increased standard deviation beginning at 75 mm from the non-corroded end of the specimen. This can also be found in the experimental results. The calculated maximum coefficients of variation are 22 % (154 days) and 31 % (303 days). The experimental measurements show a maximum variance of 24 % (154 days) and 40 % (303 days). Most of the experimentally derived scatter of the ettringite concentration can be predicted by the Monte Carlo simulation. Merely the simulated scatter at 90 mm from the non-corroded end of the specimen is too small.

These excellent results show that the deterministic model (Transreac) in combination with a Monte Carlo simulation is a powerful tool for the application of the probabilistic safety concept to durability problems.

5.2 Validation of the deterministic model

In this paper examples dealing with the attack of nitric acid on cement stone and the attack of ammonium solution on concrete are presented.

5.2.1 Attack of nitric acid on cement stone

An example of corrosion by nitric acid acting on cement stone specimens is shown in Figure 6. Data for calculation are summarized in [5] denoted as Z-0.6-PZ-1084. Within the framework of SPP 1122 have been exchanged experimentally derived data. The whole experiment was made by Carsten Gunstmann (see [21]). Analyses by RFA und IR were also made by Carsten Gunstmann. Examinations by XRD were performed by the first author.

The specimens were prepared with a water to cement ratio of 0.6. After demoulding, the specimens were stored for 28 days under water and then immersed in 30% HNO_3 for 2000 hours. The porosity of the specimens was analysed by a special method described in [21]. By this method the specimen is soaked in resin under vacuum and after that the specimen is cut into slices. Then the porosity is measured by analysing the mass loss due to the combustion of the resin. With this method it is possible to determine the porosity as the function of the distance from the aggressive solution. In addition, the chemical composition at different distances between the contact surface of cement stone and aggressive solution was analysed by RFA and some examinations by XRD and IR were used to detect and confirm mineralogical phases.

As can be seen in Figure 6 after the immersion in nitric acid, 3 mm of the specimen were dissolved. The layer in direct contact with acid solution has turned into different shades of brown, corresponding to different states of deterioration. As can be seen from the CaO-content of the specimen, the brown layer must consist of solid phases containing only a minor CaO-content. The light brown layer in direct contact with the acid solution is fully deteriorated and contains mainly amorphous SiO_2, indicated by XRD and IR. The brown colour indicates the formation of iron-containing hydroxides and oxi-hydroxides. These products and additional aluminium-hydroxide are the corrosion products from the AFt- and AFm-phases. It can be assumed that the pH value of the light brown and dark brown zones is about 2.0-3.0 [22,23]. The medium brown zone shows a cumulation of SO_3, Al_2O_3 and Fe_2O_3 caused by diffusion of sulphate, aluminium and iron ions from decomposed cement paste into this zone [22]. Probably AFt- and AFm- phases are formed and the pH value is approximately 10-11 [23].

The porosity of the brown zone is very high at about 55-90%, as indicated in Figure 6, and the mechanical stability of this layer is very low.

The light grey layer indicates the area where portlandite decomposes. The transition from the brown to the light grey layer is indicated by a sharp decrease of CaO-content and porosity. In the dark grey intact cement stone area, portlandite can be detected by XRD and IR.

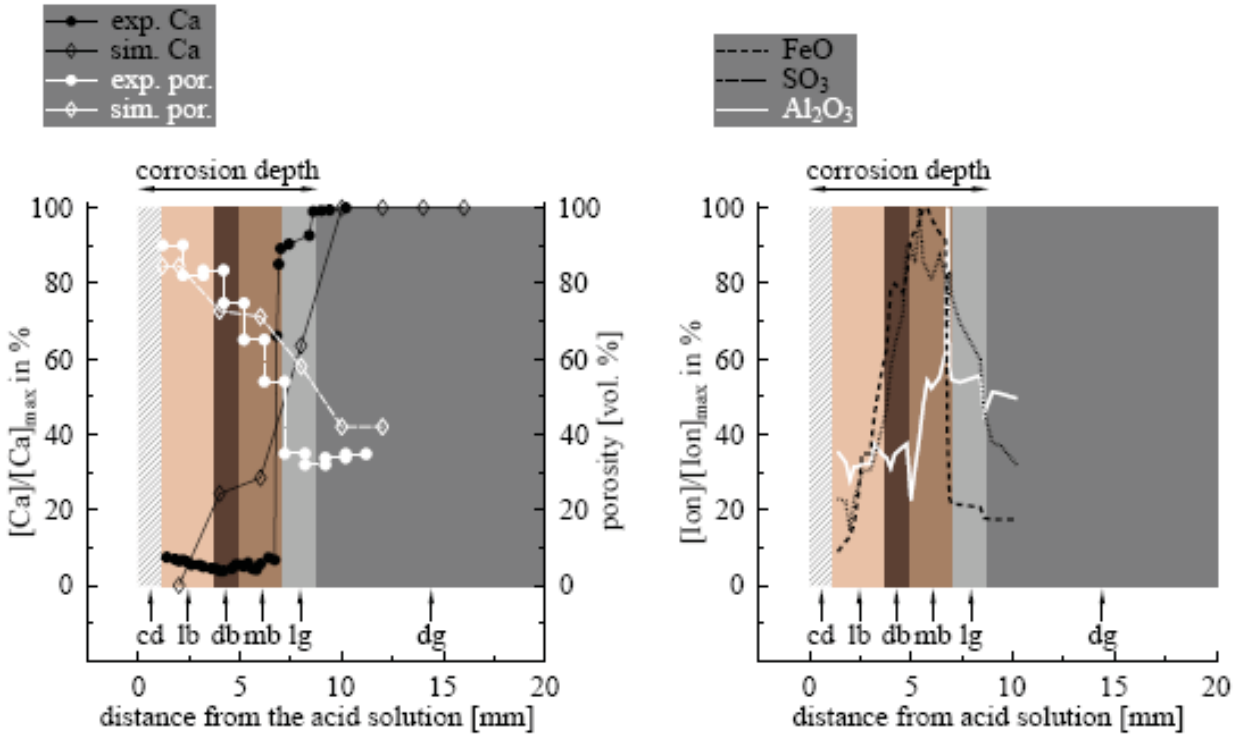

Figure 6: Simulated and experimentally derived Ca-profile and porosity as a result of nitric acid-induced corrosion of cement stone (left). Experimentally derived distribution of FeO, SO_3 and Al_2O_3 by [21] (right). The Meaning of the abbreviation: cd: completely dissolved, lb: light brown, db: dark brown, mb: medium brown, and lg: light grey layer, dg: dark grey uncorroded core

Figure 6 compares data from simulation and data from different experiments. As can be seen, the simulated CaO-content as well as porosity are in good agreement with experimentally derived data. In addition, the simulated phase assemblage at different distances between the contact surface cement stone and acid solution corresponds to experimentally derived findings, as has been mentioned before.

5.2.2 Attack of ammonium solution on concrete

In Figure 7 the loss of weight of concrete specimens in ammonium solution (100 mg/L NH_4Cl) for a period of 9 years is shown. The experimental conditions are described in [24]. The concrete specimens were prepared with Portland cement and fly-ash cement (w/c=0.5). Specimens were demoulded after 24 hours and cured for 7 days in water and afterwards stored at 100 % relative humidity. Data for calculation are summarized in [5] under denotation B-0.5-PZ-400 for concrete made from Portland cement, and B-0.5-FAZ-375 for concrete made from fly-ash ce-

ment. Experimental and calculated data show a minor weight loss. The maximum experimentally derived weight loss of 3 % is equal to a corrosion depth of 0.3 mm. The simulated data are presented as error bars for varied transport and porosity parameters resulting from the Monte Carlo simulation. The assumed variation of the input parameter is based on a wide range of information from literature and is typical of concrete considered here. Within those error bars, simulated and experimentally derived data coincide. It can be calculated that the weight loss of the concrete made from Portland cement is greater than the weight loss of the concrete made from fly-ash cement, just like the experimental results show.

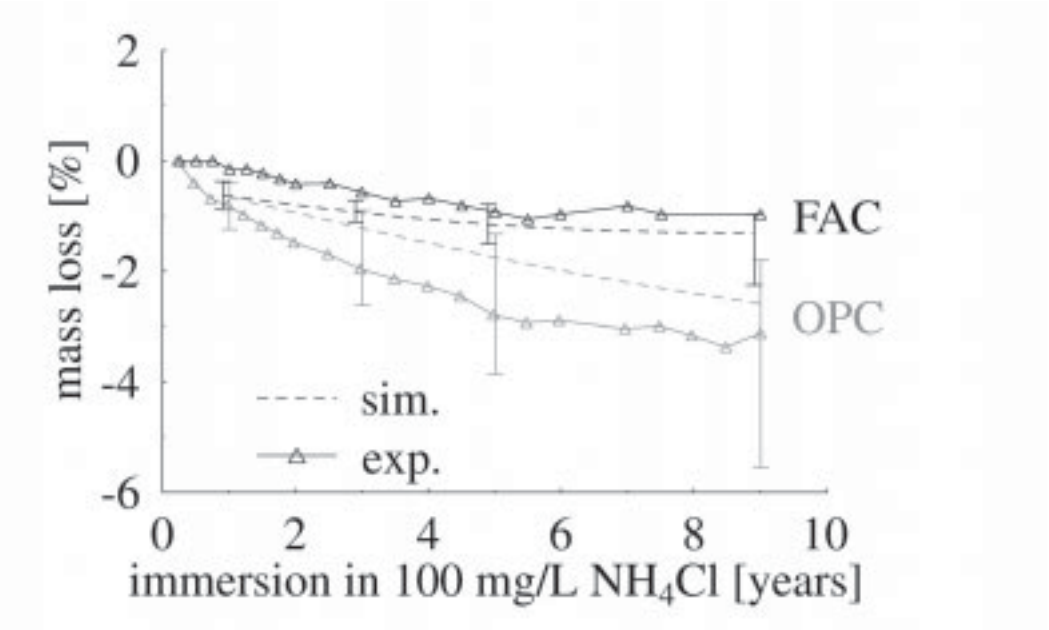

Figure 7: Experimentally derived and simulated mass loss of concrete (w/c=0.5) made from ordinary Portland cement (OPC) and made from fly-ash cement (FAC). The error bars are the results of the Monte Carlo simulation. They show the 33 and 66 % quantile of the simulated mass loss profile.

6 Definition of limit state

The performance must be described with reference to a specified limit state. The limit state concerned in this case is the serviceability limit state. For this limit state, the maximum probability of failure is related to relative cost of safety measures as suggested by Rackwitz [25] (see Table 1). Gehlen [3] used this concept to define the maximum allowable probability of failure for different exposure classes which are described in [26]. Gehlen is concerned with exposure classes which are related to the corrosion of reinforcement by carbonation of concrete (XC) and the corrosion by chlorides produced by de-icing salt (XD) and seawater (XS). The same principle is applied to the exposure class relating to chemical attack (XA). The results of the maximum probability of failure are presented in Table 1.

For the application of the reliability theory, the definition of a limit state is required as indicated in Figure 1.

The definition of the limit state in the case of corrosion by sulphate solution is explained in [18]. The maximum expansion was determined to be 0.5 %.

In the case of degradation by a leaching process, the corrosion mechanism is taken into account. The aggressive reagent reacts with hydrated cement compounds and residues of unhydrated cement. During the attack calcium ions are leached out and corrosion products form a soft and porous corrosion layer. The reduced cross section and the reduced strength of the corrosion products lead to a loss of compressive strength. Another problem is the reduced pH value by leaching out the easily soluble components of cement. During the corrosion reaction, the pH-value is reduced to 2.0. In this region, the reinforcement is no longer protected against corrosion.

At first a corrosion depth must be defined. The brown layers (see Figure 6) are soft and mechanically instable. Furthermore, the high porosity and relatively low pH value (2-10) in the brown layers do not offer adequate protection of the reinforcement. In fact, the corrosion starts with the decomposition of portlandite and takes place in the light-grey layer (see Figure 6). In this layer, the pH value amounts to 12.5 and in this environment the reinforcement is protected. Because of this, the calculated corrosion depth is defined by the boundary between this layer and the uncorroded dark-grey core (see Figure 6).

Table 1: Probability of failure P_f related to serviceability limit states and different exposure classes. Furthermore cover depth as stated in DIN 1045 [27].

Relative cost of safety measure	**Exposure class**	**P_f [%]**	**Cover depth [cm]**	**pH**	**SO_4^{2-} [mg/L]**	**NH_4^+ [mg/L]**
Normal	XA1	6.681	3	5.5-6.5	200-600	15-30
Low	XA2	2.275	4	4.5-5.5	600-3000	30-60
Low	XA3	2.275	4	4.0-4.5	3000-6000	60-100

Secondly, this corrosion depth is to be compared with a maximum allowable corrosion depth as indicated in Figure 1. For this purpose, the cover depth listed in DIN 1045 [27] is chosen as the maximum allowable corrosion depth. DIN 1045 [27] demands a cover depth of 4 cm for exposure class XA2 (related to moderate chemical attack) and 3 cm for exposure class XA1 (related to weak chemical attack). Cover depths, environmental conditions (pH, SO_4^{2-}-content, NH_4^+-content) for different exposure classes are listed in Table 1.

7 Examples of a concept for evaluation of corrosion by sulphate attack

The formation of ettringite caused by sulphate attack on mortar or concrete effects an expansion that can destroy mortar or concrete. Sulphates are found in run-off rain water, ground water or ground. In the following example, a concept for the evaluation of durability is demonstrated. In Figure 8 the probability of failure as a function of time of exposure in 2.1 % Na_2SO_4 is shown. The graph shows the results for mortar made from ordinary Portland cement and the results for mortar from blast furnace slag cement. The water to cement ratio is 0.6 and 0.45. In addition, the maximum allowable probability of failure is marked. Data for calculation are listed in [5]. They are denoted M-0.6-PZ-470 for mortar made from Portland cement and M-0.45-HOZ-500 for mortar made from blast furnace slag cement.

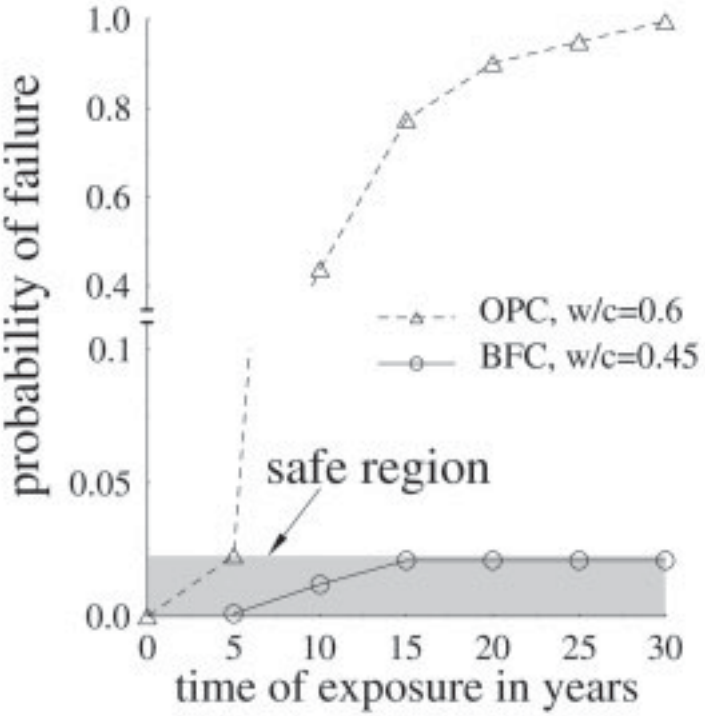

Figure 8: Probability of failure as a function of time of exposure in 2.1 % Na_2SO_4 solution for mortar made from Portland cement (OPC) with w/c=0.6 and for mortar made from slag cement (BFC) with w/c=0.45.

The results of the Monte Carlo simulation show that the Portland cement-based specimens with a water to cement ratio of 0.6 are in the safe region for up to 5 years. On the other hand, the slag cement-based mortar with a water to cement ratio of 0.45 is reliable during its life time. This is in agreement with the practical guidelines which specify that the water to cement ratio of 0.6 and this type of Portland cement is not suitable for the production of concrete or mortar requiring high resistance against sulphate attack. A water to cement ratio of 0.45 and slag cement, on the other hand, is suitable.

8 Examples of a concept for evaluation of corrosion by ammonium attack

Salts of ammonium, especially those of strong acids, react with hydroxide ions in the pore solution and reduce the chemical stability of hydrated cement phases. In addition, the anion of the ammonium salt forms a calcium salt, which leaches out easily.

This example deals with the deterioration of concrete as a result of immersion in ammonium solution. The calculated corrosion depth after 50 years in the concretes (see above denoted as B-0.5-PZ-400, B-0.5-FAZ-375) immersed in NH_4Cl (100 mg/L) is 1.6-4.5 mm for the concrete made from Portland cement, and 0.2-0.7 mm for the cement made from fly-ash cement. The denoted range of values refers to the 33 % and 66 % quantile. After extrapolation of the experimental results of Rechenberg and Sylla [24], the corrosion depth for concrete made from Portland cement is expected to be 1.2 mm, and that of concrete made from fly-ash cement is expected to be 0.7 mm [5] after 50 years. Calculated and extrapolated data are within an acceptable range. The corrosion depth is much smaller than the maximum allowable corrosion depth of 40 mm. Because of this the probability of failure for both types of concrete is 0.0 %, which means that these concretes are suitable for the application in such aggressive environments. This disagrees with the regulation in DIN 1045, according to which concrete is to be protected against the penetration of ammonium solution of this high concentration. On the other hand, the experimental results of Rechenberg und Sylla [24] argue for increasing the maximum allowable concentration of ammonium to an amount of 300 mg/L. An ammonium content of 100 mg/L is in that case classified as a chemically moderate attack (XA2). This exposition class implies a cement content of 320 kg/m^3 and a water to cement ratio of 0.5. Both of the concretes fulfil this requirement and the calculated probability of failure of 0.0 % argue for application in an environment with the denoted ammonium content. From this follows that the practical experience agrees with the calculated results.

9 Conclusions

Currently the design with respect to the durability of concrete structures is based on deem-to-satisfy rules, where the minimum concrete cover, the cement content and a maximum water/cement ratio is specified. In contrast to this, modern building codes make use of a reliability theory based on a probabilistic approach. This means that the ability to fulfil relevant functions can be quantified. Increasingly, these approaches expand into durability design. This study presents a probabilistic concept for the evaluation of durability with respect to corrosion by sulphate attack and corrosion by leaching processes induced by the attack of acids and ammonium solutions. The methodology of a probabilistic concept with respect to durability requires a reliable degradation model to predict the future behaviour of the concrete structure, and the degradation must be described as a probabilistic value. This requirement is achieved by means of the deterministic model Transreac which simulates corrosion effects on building materials caused by the attack of chemical solutions in combination with the Monte Carlo Simulation. To demonstrate the reliability of the deterministic model, numerous comparisons of simulated and experi-

mentally derived corrosion depths based on acid attack and attack of ammonium solution were performed. It was shown that simulated data are in good agreement with experimentally derived data. In this way, a powerful probabilistic safety concept for durability problems with respect to leaching effects and expansion effects is demonstrated. Particularly examples of sulphate attack on mortars made from Portland cement and blast furnace slag cement, examples of acid attack on mortars with different water to cement ratio of 0.45 and 0.6, and examples of attack of ammonium solution on concrete made from Portland cement and fly-ash cement are demonstrated. For all examples it can be shown that the calculated deterioration after the life time are within realistic ranges. The quantified ability to fulfil the serviceability limit state requirement and the consequences for durability design are in agreement with the practical guidelines and practical experience.

The procedure which is presented in this study, i.e. the development and validation of a suitable degradation model and the combination of this degradation model with a Monte Carlo method, can be used for durability design based on the performance concept. Because the degradation model Transreac used here is based on physical - chemical principles, it can be applied to different materials in different environments. By combining the flexible degradation model with the flexible Monte Carlo method, a way is shown of how to apply the performance concept in durability design for structures in different aggressive environments.

10 References

[1] D.J. Corr, P.J.M. Monteiro, K.E. Kurtis, and A.D. Kiureghian: Sulfate attack of concrete: reliability analysis. ACI Materials Journal, 98(2), p. 99-104, 2001.

[2] C. Gehlen: Probabilistische Lebensdauerbemessung von Stahlbetonbauwerken Zuverlässigkeitsbetrachtungen zur wirksamen Vermeidung von Bewehrungskorrosion. Beton, 50(11), p. 652-663, 2000.

[3] C. Gehlen: Probabilistische Lebensdauerbemessung von Stahlbetonbauwerken – Zuverlässigkeitsbetrachtungen zur wirksamen Vermeidung von Bewehrungskorrosion. Doctoral thesis, RWTH Aachen, 2000.

[4] A. Sarja and E. Vesikari: Durability design of concrete structures: report of RILEM Technical Committee 130-CSL. E & FN SPON, London, 1996.

[5] E. Rigo: Ein probabilistisches Konzept zur Berurteilung der Korrosion zementgebundener Baustoffe durch lösenden und treibenden Angriff. Doctoral thesis, TU Braunschweig, 2005.

[6] F. Schmidt-Döhl and F.S. Rostásy: A model for the calculation of combined chemical reactions and transport processes and its application to the corrosion of mineral building materials (I) simulation model. Cement and Concrete Research, 29, p. 1039-1046, 1999.

[7] F. Schmidt-Döhl and F.S. Rostásy: A model for the calculation of combined chemical reactions and transport processes and its application to the corrosion of mineral building materials (II) experimental verification. Cement and Concrete Research, 29, p. 1047-1054, 1999.

[8] F. Schmidt-Döhl: Ein Modell zur Berechnung von kombinierten chemischen Reaktions- und Transportprozessen und seine Anwendung auf die Korrosion mineralischer Baustoffe. Doctoral thesis, TU Braunschweig, 1996.

[9] H.-M. Künzel: Verfahren zur ein- und zweidimensionalen Berechnung des gekoppelten Wärme- und Feuchtetransports in Bauteilen mit einfachen Kennwerten. Doctoral thesis, Universität Stuttgart, 1994.

[10] C. Hof, T. Triantafyllidis, and F. Schmidt-Döhl: Erkenntnisse über den Einfluss von kalklösender Kohlensäure auf das Tragverhalten von Verpressankern. Geolex, 1, p. 31-41, 2002.

[11] F. Schmidt-Döhl, E. Rigo, S. Bruder, and H.Budelmann: Chemical attack on mineral building materials, features and examples of the simulation program transreac. In: Second international conference lifetime oriented design concepts, p. 269-278, Bochum, 2004.

[12] C. Hof, T. Triantafyllidis, and F. Schmidt-Döhl: Über die Abnahme der Tragfähigkeit von Verpressankern unter Angriff kalklösender Kohlensäure. Bautechnik, 81(5), p. 357-363, 2004.

[13] Schmidt-Döhl, F.; Bruder, S.; Budelmann, H.: Monitoring and prognosis of concrete durability under chemical attack. Proceedings of the Second European Workshop Structural Health Monitoring, München, 7.-9.7.2004, p. 285-292.

[14] Schmidt-Döhl, F.: Examination of the long term behaviour of cementitious materials in contact with saline solutions. Internet- research report 2004. www.mpa.tu-bs.de/docpool/reports/report-006.pdf

[15] Budelmann, H.; Hariri, K.; Schmidt-Döhl, F.; Bruder, S.; Rigo, E.: Adaptive prognosis of chemical concrete degradation and probabilistic system analysis as instrument of structural monitoring. In: Advances in life-cycle cost analysis and design of civil infrastructure systems. Proceedings of the 4th International Workshop, Cocoa Beach, Florida, USA, p. 261-270, 2005,

[16] Budelmann, H.; Schmidt-Döhl, F.; Rigo, E.: Adaptives Modell zur Dauerhaftigkeitsprognose im Zuge der Überwachung von Betonbauwerken. Tagungsband des Kolloquiums des SFB 477, Braunschweig, 08.-09.6.2006, p. 39-44, 2006.

[17] Rigo, E.; Schmidt-Döhl, F.; Budelmann, H.: Monitoring, adaptive and probabilistic modelling of chloride ingress in concrete structures. In: Güemes, A. (ed.): Proceedings of the third European Workshop Structural Health Monitoring, Granada, 5.-7.7.2006, p. 73-80.

[18] E. Rigo, F. Schmidt-Döhl, M. Krauß, and H. Budelmann: Transreac: a model for the calculation of combined chemical reactions and transport processes and its extension to a probabilistic model. Cement and Concrete Research, 35, p. 1734-1740, 2005.

[19] Rigo, E.; Schmidt-Döhl, F.; Budelmann, H.: Ein probabilistisches Konzept zur Beurteilung der Korrosion zementgebundener Baustoffe durch lösenden und treibenden Angriff. 16. Internationale Baustofftagung ibausil, Weimar, p. 2-0557-2-0564, 2006.

[20] C.R. Sundarajan: Probabilistic structural mechanics: handbook-theory and industrial applications. Chapmann & Hall, Houston, Texas, 1995.

[21] L. Franke and C. Gunstmann: Beurteilung der Säurebeständigkeit von zementgebundenen Baustoffen. In Beiträge zum 42. DAfStb Forschungskolloquium, p. 51-58, Hamburg, 2003.

[22] V. Pavlik: Corrosion of hardened cement paste by acetic and nitric acids part (II): Formation and chemical composition of the corrosion products layer. Cement and Concrete Research, 24, p. 1495-1508, 1994.

[23] G. Herold: Korrosion zementgebundener Werkstoffe in mineralsauren Wässern. Doctoral thesis, Universität Karlsruhe, 1999.

[24] W. Rechenberg and H.-M. Sylla: Die Wirkung von Ammonium auf Beton. Beton, 26(1), p. 26-31, 1993.

[25] R. Rackwitz: Zuverlässigkeitsbetrachtungen bei Verlust der Dauerhaftigkeit von Bauteilen und Bauwerken. Fraunhofer IRB Verlag, Stuttgart, 1998.

[26] DIN 1045-2: Tragwerke aus Beton, Stahlbeton und Spannbeton; Beton; Festlegung, Eigenschaften, Herstellung und Konformität. Beuth Verlag GmbH, Berlin, 2001.

[27] DIN 1045: Beton und Stahlbeton - Bemessung und Ausführung, Juli 1988.

Carsten Gunstmann
Dr.-Ing.

Lutz Franke
Prof. Dr.-Ing.

Institute of Building Materials, Physics and Chemistry of Buildings
Hamburg University of Technology, Germany

Prediction by numerical simulation of corrosion of hardened cement paste and concrete caused by acid

Summary

The durability of a building material is an important aspect for its range of application. Particularly cement-based materials are often exposed to aggressive environment, e. g. acids. The aim of the project was to create a program for numerical simulation of acid attack to cement-based materials. In this paper a short review of the basics of the simulation program are described. In addition to a model for the mass transport and chemical reactions, a model to calculate the pore structure only on the basis of the chemical composition is presented. Most of the necessary parameters could be taken from the literature. Some had to be won, however, from experimental investigations. For example a procedure for the determination of the diffusion coefficient in the electrical field, inferred from the literature, was partially improved. The proof that the simulation program supplies meaningful results is shown on the basis of comparisons by computational simulation and experimental test results.

Keywords: *acid attack, simulation, mass transport, chemical reactions, pore structure model, diffusion coefficient*

1 Introduction

The durability of a building material is an important aspect for its range of application. Particularly cement based materials are often exposed to aggressive environment, e. g. acids. Today the resistance of the cement based materials to acids has to be tested in laboratories. After an approved method of the Institute of Building Materials, Physics and Chemistry of Buildings of the Hamburg University of Technology (Germany) specimens of the testing material are stored in acid bathes and the damages are compared to established reference material. How much the testing boundaries influence corrosion can only be answered by varying these boundary conditions. Besides the possibility to make a large amount of tests in the laboratory, these parameter studies can be done by numerical simulation. So the aim of the project was to create a program for numerical simulation of acid attack to cement based materials.

2 Basics of simulation

The corrosion process itself can be divided approximately into three parts: mass transport, the field of chemistry reaction and the pore structure alteration respectively the degradation of the material.

2.1 Mass transport

In the literature a multitude of more or less adequate models to simulate the mass transport can be found. All models found are based on the so called extended Nernst-Planck-Model. On the basis of this model it is possible to calculate the concentration of every species subject to the time and position. For every considered species a balance equation must be established.

$$\frac{\partial\left(w\cdot m_i\right)}{\partial t}=\underbrace{\nabla\left(w\cdot D_i\nabla m_i\right)+\nabla\left(m_i\cdot D_{ui}\frac{z_i\cdot F}{R\cdot T}\nabla U\right)-\nabla\left(q_{water}\cdot m_i\cdot k\right)}_{\text{mass transport}}+S_i \qquad (1)$$

Sink/Source for chemical reactions

The mass transport is composed of three various transport mechanisms: diffusion, migration and convection. Which of these mechanisms are the strongest depends on the boundaries of the situation.

Besides the balance equations for the species the balance equation for the electrical field must be solved simultaneously. An electrical field can be induced by an external electrical power or by the different diffusion velocity of the charged species.

$$0=\frac{w}{\tau}\cdot\Delta U+w\cdot\frac{F}{\varepsilon}\cdot\sum_{i=0}^{n}z_i\cdot m_i \qquad (2)$$

The transport parameters D_i and D_{ui} depend on the temperature, the water content, the pore structure and the concentration of the pore solution.

$$D_i=f_T(T)\cdot f_w(w)\cdot f_\phi(\phi)\cdot f_m(m_1,m_2,...) \qquad (3)$$

$$D_{ui}=f_T(T)\cdot f_w(w)\cdot f_\phi(\phi)\cdot f_{um}(I) \qquad (4)$$

The dependency on the temperature is being established by the following polynomial:

$$f_T(T)=a_i\cdot T^2+b_i\cdot T+d_i \qquad (5)$$

The coefficients a_i, b_i and d_i are fitted by experimental data from the literature.

A modified function from the literature is used to indicate the dependency of the two transport parameters D_i and D_{ui} on the water content.

$$f_w(w)=\left(\frac{w-w_{limit}}{w_{sat}-w_{limit}}\right)^h \qquad (6)$$

The dependency on the pore structure a function based on experimental studies is developed. On the basis of these results it could be detected a significant dependency of the diffusion resistance number (W) and the pore volume ($ø_{QG}$) investigated by mercury intrusion. The diffusion resistance number can be calculated by the following formula:

$$W = \frac{\tau}{\phi_{QG}} \tag{7}$$

With this function the pore structure dependency of the transport parameters D_i and D_{ui} can be described:

$$f_{\phi_{QG}} = \frac{1}{p \cdot \left(\frac{1}{\phi_{QG}^{q}} - 1 \right) + 1} \tag{8}$$

The parameters p and q depend on the pore structure of the specimens and will be established by diffusion investigations in the electrical field (will be explained later).

The transport parameters D_i and D_{ui} have in an infinite dilute solution the same value. Experimental data indicate that the influence of the strength of ionic solution on these parameters is not the same. So for each transport parameter two different functions must be implemented in the simulation program. For the migration transport parameter a function based on a model to describe the dependency of the electrical conductivity of a solution from the ionic strength published by SNYDER [1] is integrated into the simulation model.

$$f_{um}(I) = \frac{1}{\left(1 + G_i \cdot \sqrt{I/1000}\right)} \tag{9}$$

The concentration dependency of the diffusion transport parameter is described by the following function:

$$f_m(m_1, m_2, ..) = \left(1 + \frac{\partial \ln \gamma_i}{\partial \ln m_i} \right) \tag{10}$$

The activity coefficient γ_i can be calculated optionally by the model of Pitzer or modified Davies.

2.2 Chemical Reactions

The chemical reactions are considered by sinks or sources in the balance equations (formula 1). The evaluation of the sinks/sources realized in an own algorithm. The basis of the algorithm is that a chemical system composed of several species strives for a state of equilibrium. In this state the free enthalpy has an energy minimum. The free enthalpy is often described as the Gibbs-energy.

$$G_E(T, P, n_i) = Min \tag{11}$$

To calculate the energy-minimum an improved approach of Store/van Zeggeren [2, 3] was implemented in the simulation program.

Since the equilibrium state will sometimes be reached after a long time, the temporal course of the chemical reactions has to be accounted for. Therefore the species are divided into fast and slow chemical reactive ones. All species that reach their equilibrium concentration in 6 minutes are be considered as fast ones. For these species a simplified linear temporal course is assumed. For the slow ones an individual temporal course is supposed. The computation scheme for the chemical reactions is as follows:

1. Calculation of the equilibrium concentration for the fast species **without** the slow ones
2. A new equilibrium computation is done with the first slow species and fast species
3. On the basis of kinetic parameters, reactive surface of the specimen and the reactive volume of the slow species will be calculated how far the last calculated equilibrium will be reached for the slow one.
4. For every slow species step 2 and 3 will be repeated respectively.
5. At the end an equilibrium calculation will be done with all fast species (incl. the reaction products of the slow species). In this calculation not the slow species will be considered but the changing of there reaction products calculated in step 2 and 3. Therefore for this algorithm for every slow species a reaction equation must be established.
6. The difference between the starting concentration of all species and the calculated concentration will be the basis for calculation the sinks/sources in the balance equation (formula 12). The time step Δt_{chem} will be determined as 6 minutes.

$$S_i = \frac{\Delta n_i}{\Delta t_{chem}} \tag{12}$$

Therefore in practise not only fully hydrated cement based materials are attacked by aggressive mediums, it is possible to consider the behaviour of partially hydrated material in the simulation program.

More information about the algorithm to calculate the sinks/sources can be obtained in the dissertation from KIEKBUSCH [4].

2.3 Pore structure model

With the corrosive processes not only the chemical composition of the hardened cement paste or mortar changes, but also to a large extent the pore structure. Since the pore structure, however, has also a large influence on the characteristics of the hardened cement paste, it is important to develop a model which is able to consider these changes. Basis for this developed model is that the hardened cement paste/mortar is a compound material from several components, as the solid phases and the rock granulation (fig. 1).

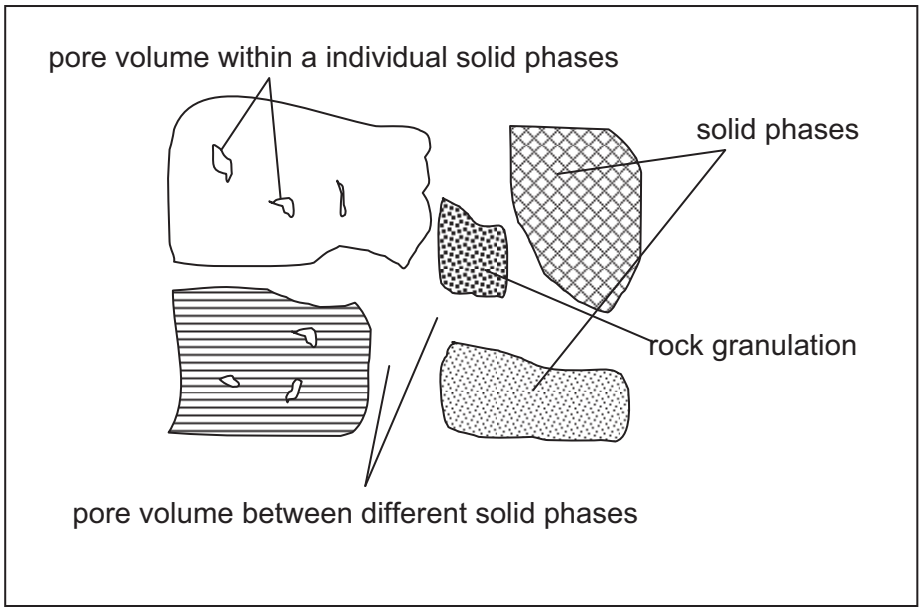

Figure 1: Schematic representation of the pore areas

The pore area is divided in two categories. The first is the pore volume between the different solid phases. This according to formula 13 determined as difference of 100% and the sum of all solid phase concentration c_i multiplied by the molar volume Θ_i (after formula 16) less the inert volume of rock granulation. The molecular volume is determined according to formula 16 and indicates the volume, which the solid phase takes including its assigned porosity parts of $\Theta_{i,gelpores1}$ and $\Theta_{i,gelpores2}$ per mol of solid phase. The second category of pores is within the individual solid phase.

This gel pore volume is also in reality within the individual solid phase and an allocation to this one is also obvious sensible. The gel pore volume was divided within the individual solid phase in two classes (formulas 14 and 15). Both porosity portions are determined as sum of the single porosity portions of the individual solid phases. An allocation of gel pore volume can naturally to be done as above described, however, only with e.g. the solid C-S-H or aluminate phases. The fixed phases CaSO4·2H2O or portlandit do not have a gel pore volume and so the parameter $\Theta_{i,gelpores1}$ and $\Theta_{i,gelpores2}$ must set zero for these solid phases. With this model the computation of a porosity distribution is possible only on the basis of the chemical composition of the material.

$r \geq 10$ nm

$$\phi_{ZW} = 1.0 - \sum_{i=1}^{i<n} c_i \cdot \Theta_i - V_{rock\ granulation} \tag{13}$$

$1{,}8$ nm $\leq r < 10$ nm

$$\phi_{gelpores1} = \sum_{i=1}^{n} c_i \cdot \Theta_{gelpores1,i} \tag{14}$$

$r < 1{,}8$ nm

$$\phi_{gelpores2} = \sum_{i=1}^{n} c_i \cdot \Theta_{gelpores2,i} \tag{15}$$

The computational molecular volume of the solid phase Θ_i in m³/(mol of fixed phase i) results from the molecular pure volume $\Theta_{pure,i}$ and the assigned molecular gel pore volumes $\Theta_{gelpores1,i}$ and $\Theta_{gelpores2,i}$ within the solid phase.

$$\Theta_i = \Theta_{pure,i} + \Theta_{gelpores1,i} + \Theta_{gelpores2,i} \tag{16}$$

3 Experimental investigations and theoretical evaluation

For the verification of the simulation program and for the determination of important material parameters extensive investigations were accomplished.

3.1 Diffusion tests in the electrical field

The relationship of the diffusion coefficient in the porous material to the diffusion coefficient in free solution is accepted for all species equally large and is thereby a material property, which depends on the pore structure of the material. This relationship is called diffusion resistance number (formula 7).

Since the diffusive induced transport of the individual species is very slow, in particular in the cement-based sample test specimens, an accelerated procedure for the determination of the diffusion resistance number was selected here. The charged species are strongly accelerated transported by an electrical field put on from the outside, so that the necessary investigation duration can be substantially reduced. In figure 2 the test range is represented. In order to keep pore structure changes, during the testing, as small as possible a NaOH solution with a pH value of approximate 12.5 is in both vessels.

In the optimal case reproducible results can already be obtained in few hours. The investigation duration depends on the size of the diffusion resistance number and the evaluation method. With the materials examined here investigation duration of 72 hours was sufficient.

The evaluation of the diffusion tests in the electrical field takes place recursively, as the unknown value τ is changed until the electrical current computed after formula 17 corresponds to the measured current.

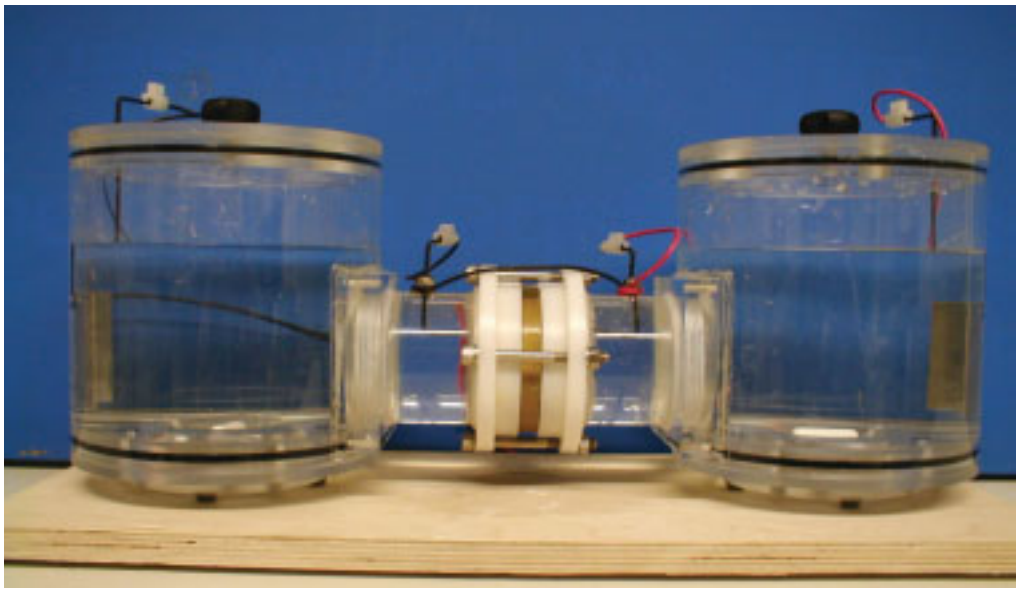

Figure 2: Migration cell

The expiration of analysis is as follows:

1. Numeric solution of the coupled differential equation system of the 1-dimensionalen of material transfer in each time step (formula 1 and 2).
2. Determination of the species flow after the determination of the concentrations of the species m_k and the electrical field U.
3. Computation of the electric current with known sample cross-section area $A_{specimen}$:

$$i_{ber} = \sum_{k=1}^{n} z_k \cdot j_k \cdot F \cdot A_{specimen} \tag{17}$$

Convective transport due to water transportation and the chemical reactions are neglected.

This evaluation technique is an improved one compared to the technique presented in the article [5]. First in this model is considered the different concentration dependence of the transport parameters. The effect can not be neglected. For example at an ionic strength of 0.5 mol/kg NaCl-solution the diffusion coefficient decreases about 9 % compared to infinite dilute solution while the decrease for the electrical mobility is about 26 %. Second in opposite to the technique in [5] the testing solution is only NaOH **without** an additional salt to avoid chemical reaction between the testing solution and the material. This point is very critical because chemical reactions have a big influence on the test results. Further information is described in [6].

The diffusion resistance number W results from formula 7:

$$W = \frac{\tau}{\phi} \tag{7}$$

The aim of these investigations was to develop a function, with which it is possible to compute the diffusion resistance number of a porous material on the basis of the pore volume of the ma-

terial. Therefore the diffusion resistance number of hardened cement pastes and mortars with different bonding agents, pore volume and bonding agents/rock granulation relationship was measured. It turned out that the measured values can be determined with good approaching in dependence of porosity, which is detected with the mercury intrusion.

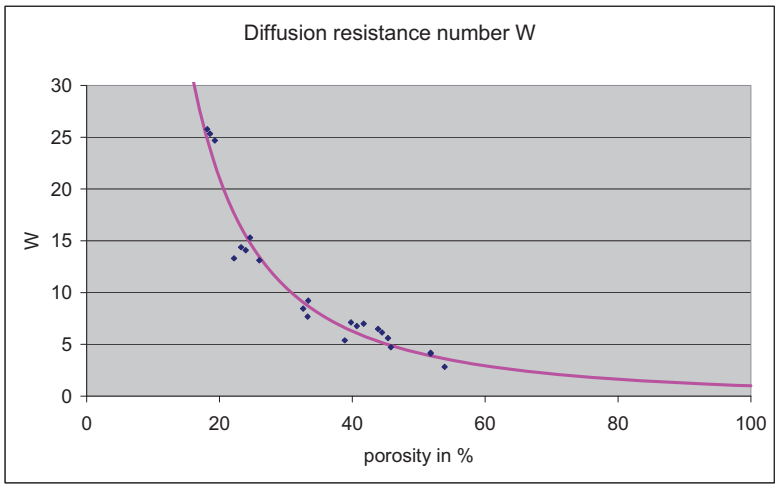

Figure 3: Diffusion resistance number of all hardened cement pastes from CEM I in dependence of the measured cumulative porosity (mercury intrusion) after vacuum drying

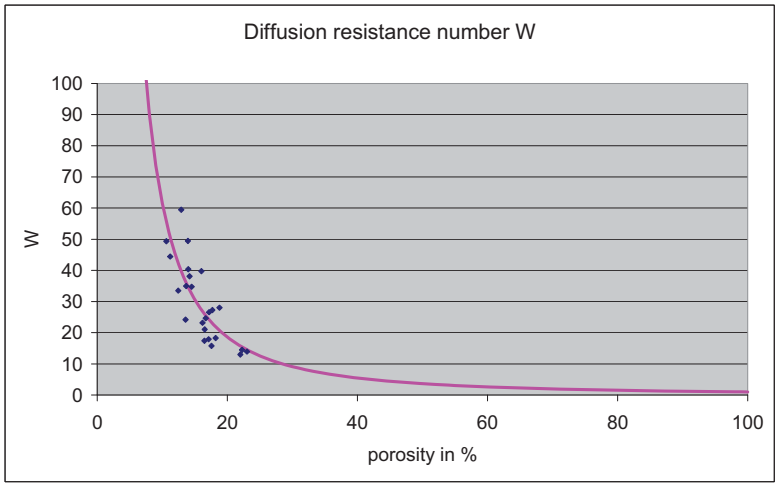

Figure 4: Diffusion resistance of mortars measured in dependence of the cumulative porosity (mercury intrusion) after vacuum drying

With the mortars as bonding agent only CEM I was used. A significant dependence of the diffusion resistance number of the bonding agents/rock granulation relationship was not to be recognized on the basis of the test results. Rather it was possible also with good approaching to determine the diffusion resistance number in dependence of porosity measured with the mercury intrusion.

The measured values for the different materials were approximated with the following formula:

$$W = \frac{p \cdot \left(\frac{1.0}{\phi_{Queck-Gesamt}^{\ q}} - 1.0 \right) + 1.0}{\phi_{Queck-Gesamt}} \tag{18}$$

Table 1: Summary of the parameters for the description of the dependence of the diffusion coefficient on the overall porosity measured with the mercury intrusion

Material	**p**	**q**
Cement paste, CEM I 42.5R-HS/NA und CEM I 52.5	2.6	0.5
Cement paste, CEM III/B 42.5-NW/HS/NA	4.5	1.9
Mortal, CEM I 42.5R-HS/NA und CEM I 52.5, B/G = 1/3 und 1/5	1.4	0.67

3.2 Equilibrium investigations

The computation of the equilibrium of solution was effected via the determination of the minimum of the Gibbs-energy of the system. To the verification and to the determination of measured variables extensive equilibrium investigations were accomplished. In addition suspensions were examined consisting of hardened cement paste powder and solutions of several compositions. The results show that it is possible to describe sufficiently exact with the help of the simulation program the composition of the solution in the equilibrium state. Here, it is referred to the interim reports [7, 8], where a detailed representation of the results is already contained. An extension of the thermodynamic data record regarding the temperature dependence took place.

3.3 Kinetics investigations

Kinetics describes the course of the chemical reactions. In [8] the approach is in detail represented for the description of the chemical reactions. There the computational approach is compared with the extensive test results. Further remarks to kinetics are to be found in [4].

3.4 Reference tests

To the verification of the entire simulation program extensive investigations were accomplished. Therefore sample test specimens from hardened cement paste and mortars were stored into acid baths and the effects on the sample test specimens were documented. Since it comes with different acids to different corrosion processes, four different acids were used: in detail the hydrochloric, nitric, sulfuric and lactic acid. The test specimens were stored for 2000 or 4000 hours in the acid bathes.

During the investigations the pH value in the acid bath was kept constant by a titration plant. The pH value of the attacking solution was depending upon the test about 1.5, 3 or 4.

The ph value and even the concentration of the individual species were ensured by constant agitating. In order to keep the influence of the ions extracted from the sample test specimens during the acid attack as small as possible, at defined times the acid bathes were renewed. On the one hand the decrease in weight and the corrosion depth at the end of the respective investigation were determined and on the other hand the element oxide distribution were ascertained quantitatively to selected sample test specimens with a local dissolved x-ray analysis.

Altogether 31 tests were accomplished.

In figure 5 the experimental setup is represented schematically.

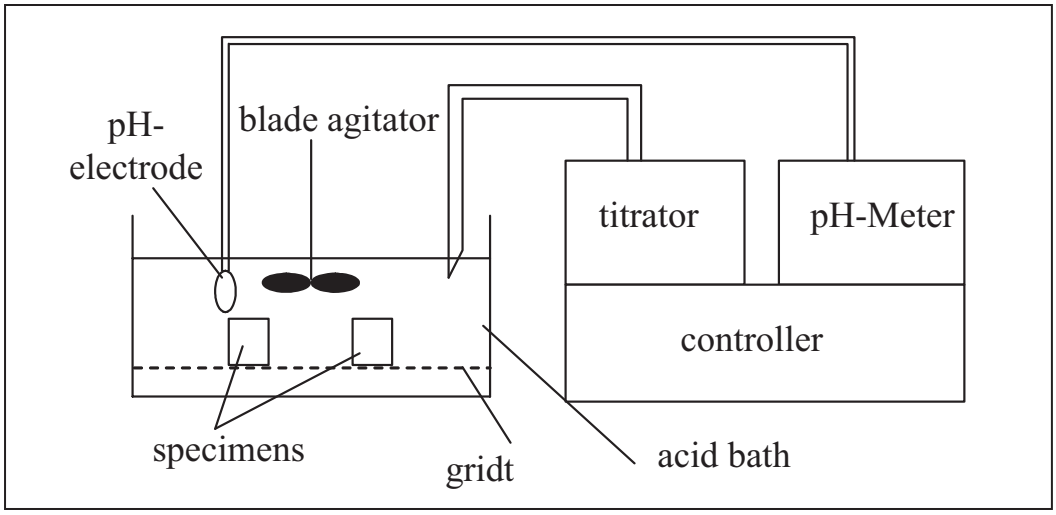

Figure 5: Experimental setup in principle for reference tests

3.4.1 Element distribution

In the following only the results of some investigations are to be represented more nearly. The element oxide distributions in weight percentage at the end of the corrosive attack are represented in the following figures. The weight percentage is related to the material still existing at the respective point.

With the comparison of a nitric acid attack on a hardened cement paste represented in figure 5 the efficiency of the simulation program is very well evident. The CaO-, SiO_2- and Fe_2O_3-courses do not agree as expected accurately but they are, however, very similar. Some differentiates appears with the Al_2O_3-course. In the simulation an increased $Al(OH)_3$ accumulation can be detected in a depth of 7 mm, whereas in the experimental results it cannot be found again. This is due to the too small accepted solubility of the solid phase $Al(OH)_3$.

Also with a hydrochloric acid attack (fig. 6) similar observations are to be made regarding the comparison of the experimental and computational results.

The attack of an organic acid was simulated only on the basis of literature data. The comparison is represented in figure 7. Here still certain differences are to be recognized. In particular the solubility of $Al(OH)_3$ and $Fe(OH)_3$ is too small accepted. An improvement of the thermodynamic data record on the basis experimental investigations appears here still meaningful.

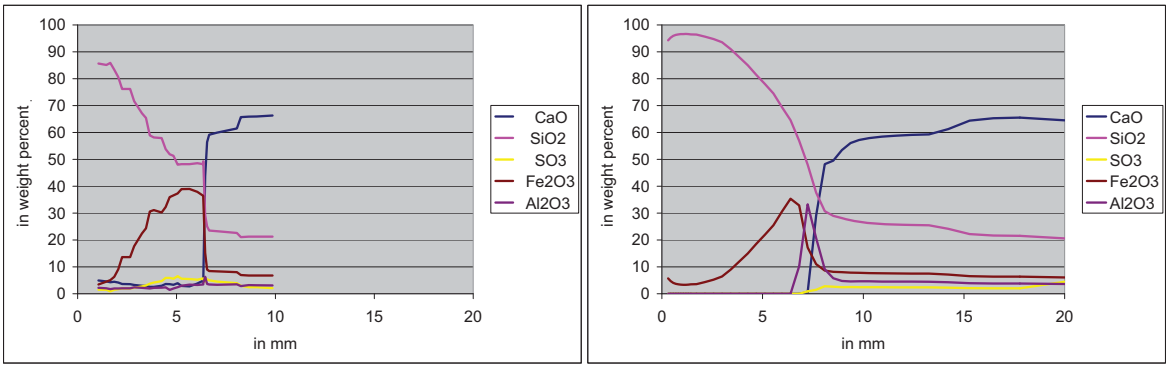

Figure 6: Experimental (left) and computational (right) results of test 3C16, cement paste, CEM I, W/C = 0.6, nitric acid, pH 1.5, Exposition duration 2000 hours

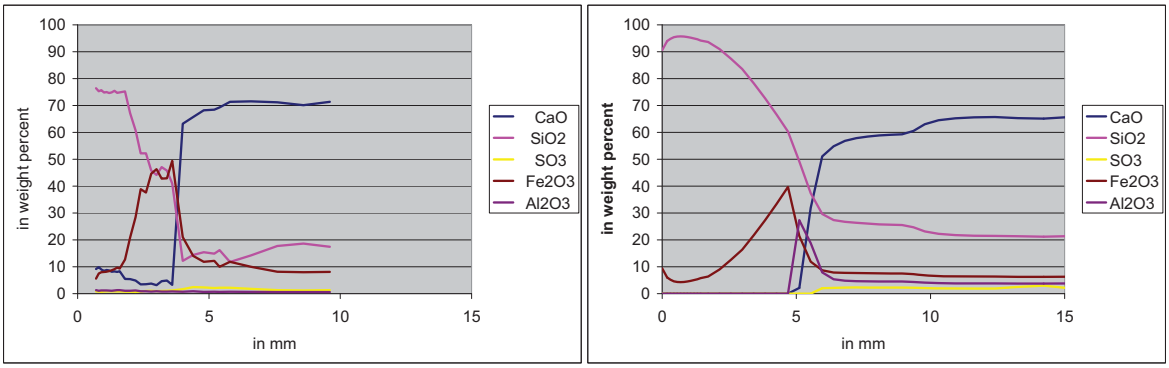

Figure 7: Experimental (left) and computational (right) results of test 3C14a, cement paste, CEM I, W/C = 0.4, hydrochloric acid, pH 1.5, Exposition duration 2000 hours

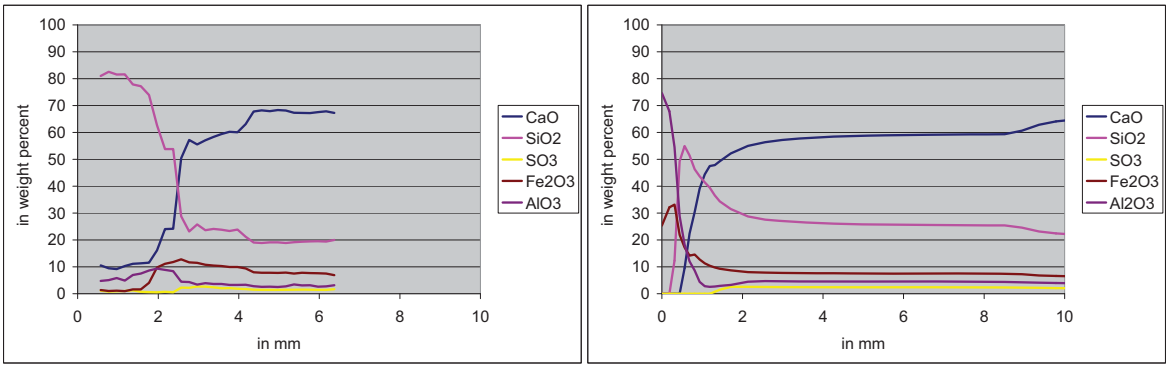

Figure 8: Experimental (left) and computational (right) results of test 4C16, cement paste, CEM I, W/C = 0.6, lactic acid, pH 4.0, Exposition duration 2000 hours

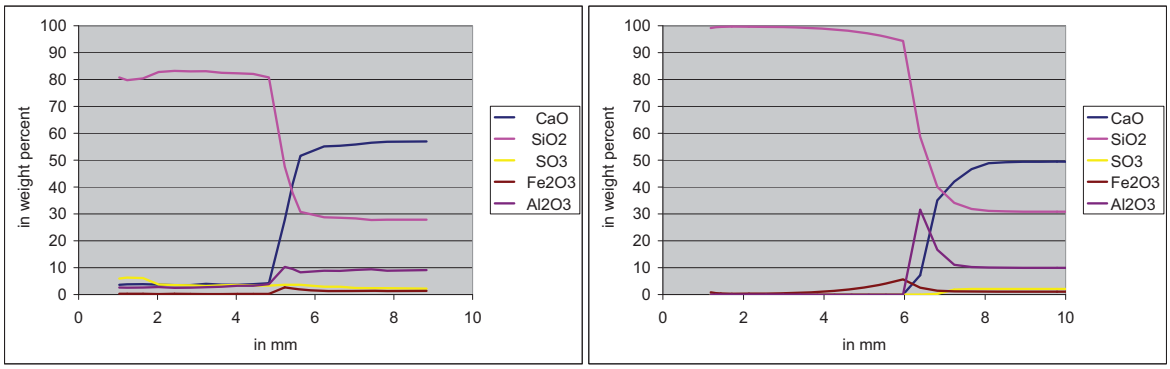

Figure 9: Experimental (left) and computational (right) results of test 3C36, cement paste, CEM III/B, W/C = 0.6, hydrochloric acid, pH 1.5, Exposition duration 2000 hours

The comparison of the results of a hydrochloric acid attack on a hardened cement paste from CEM III/B NW/HS/NA in figure 8 shows also here that the substantial processes can be well illustrated even if the computational corrosion depth are a little larger.

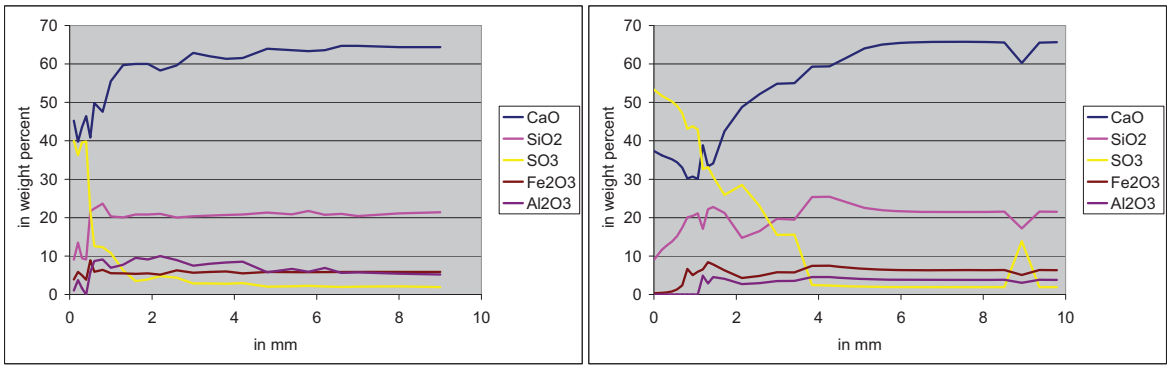

Figure 10: Experimental (left) and computational (right) results of test 2C14, cement paste, CEM I, W/C = 0.4, sulfuric acid, pH 1.5, Exposition duration 2000 hours

The results of a sulfuric acid attack are represented last. Very well, the influence of the clogged pores appears on the corrosion depth.

During a sulfuric acid attack the hardened cement paste matrix is dissolved and simultaneously gypsum forms in the pores, which clogs the pores and impedes the transport of the acid from the bath into the material. From this a clearly smaller damage compared to a hydrochloric or nitric acid attack is the result. The comparison of the results of fig. 6 and fig. 9 shows this very impressively.

In all simulations presented here, fully hydrated materials are postulated. The hydration degree might be rather of smaller importance (starting from a hydration degree of approx. 50%) with the simulation of acid attacks, since the clinker phases are opened with the corrosion and hydrated fairly fast. With other questions the hydration degree should not be neglected, however, and into the simulation program was therefore integrated a module to account for the hydration of the clinker phases during acid attack.

3.4.2 Decreases in weight after acid attack

In fig. 10 a comparison of the computed and experimentally determined decreases in weight is represented. One point is the combination of a reference test and the appropriate simulation at the end of the test. Ideally all points would be on the bisector. Nevertheless the prognosis quality of the simulation program is to be recognized well.

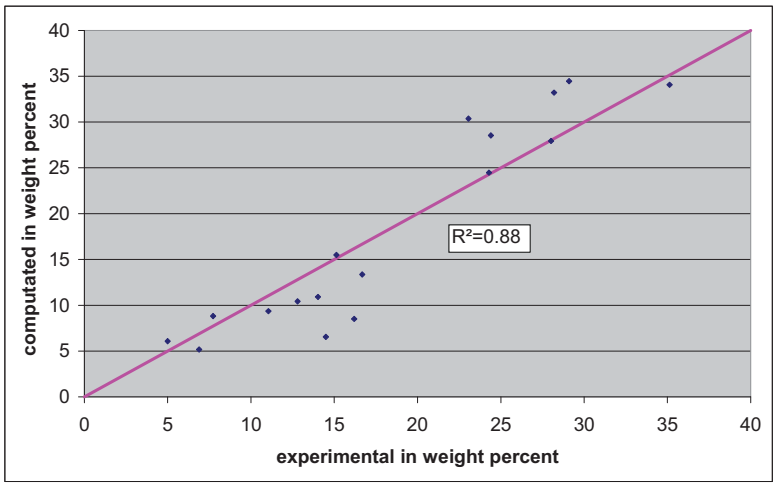

Figure 11: Comparison of computational and experimentally determined decreases in weight of hydrochloric, nitric, and lactic acid attacks at the end of the test

3.4.3 Corrosion depth

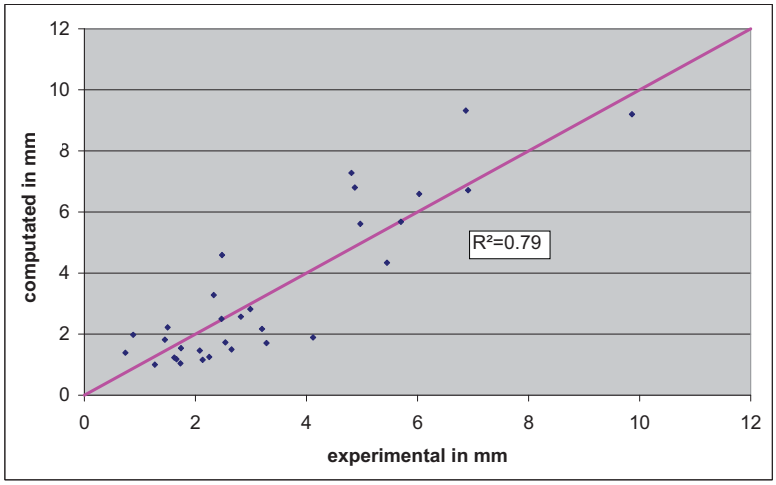

Figure 12: Comparison of computational and experimentally determined corrosion depth at the end of the test

With the corrosion depths a similar view as with the decreases in weight can be identified. Here also is to be recognized that the computed and experimentally determined corrosion depths do not show an exact but a satisfying agreement nevertheless.

4 Conclusion

In order to determine the acid resistance of a material, even today still experimental investigations must be accomplished. Therefore the testing materials are exposed under defined boundary conditions to an acid attack and the damages are evaluated. A possibility is thereby the results with proven materials to compare [9,10]. To what extent, however, the selected boundary conditions have an influence on the results, is difficult to measure and would have to be determined on the basis of extensive experimental parameter studies. This, however, is both time-consuming and cost-intensive. A possible operational area of the simulation program developed here is to be seen in the reduction of the investigations. It is to be stressed that the results also show clearly that in the current stage on experimental investigations to the evaluation of the acid resistance of a cement-based material cannot be done without.

5 References

[1] Snyder, K. A.; Feng, X., Keen, B. D.; Mason, T. O.: Estimating the electrical conductivity of cement paste pore solutions from OH, K and Na concentrations, Cement and Concrete Research , S. 293 - 798, 2003

[2] Storey, S.H.; Van Zeggeren, F. : Computation of chemical equilibrium compositions II, Canadian Journal of Chemical Engineering, Vol. 42, S. 54-55, 1964

[3] Storey, S.H.; Van Zeggeren, F. : Computation of chemical equilibrium compositions II, Canadian Journal of Chemical Engineering, Vol. 48, S. 591-593, 1970

[4] Kiekbusch, J. : Säureangriff auf zementgebundene Materialien – Untersuchung und Modellierung des Zementstein-Säure-Systems und numerische Simulation der chemischen Reaktionen mittels GEM unter Berücksichtigung der Lösungskinetik, Dissertation, Hamburg-Harburg 2007

[5] Samson, E.; Marchand, J.; Snyder, K. A. : Calculation of diffusion coefficients on the basis of migration test results, Materials and Structures, Vol. 36, S. 156-165, 2003

[6] Gunstmann, C. : Rechnerische Simulation von zementgebundener Materialien, Dissertation, Hamburg-Harburg 2007

[7] Franke, L.; Gunstmann, C.; Kiekbusch, J. : Bericht zur 1. Förderungsperiode im Rahmen des SPP 1122, Hamburg-Harburg 2003

[8] Franke, L.; Gunstmann, C.; Kiekbusch, J. : Bericht zur 2. Förderungsperiode im Rahmen des SPP 1122, Hamburg-Harburg 2005

[9] Franke L.; Oly M.; Pinsler F. : Prüfrichtlinie für Mörtel im Sielbau, TIS 97/4

[10] Franke L.; Oly M.; Witt S. : Richtlinie für die Prüfung von Mörteln für den Einsatz im Sielbau, Fassung 2001

6 Formula symbols

τ	Tortuosity	-
ε	Dielectric constant	C/(Volt·m)
$\phi_{gelpores1}$	Porosity from 1.8 nm until 10 nm	-
$\phi_{gelpores2}$	Porosity smaller than 1.8 nm	-
$\Theta_{gepores1,i}$	Molar volume of the gel pores in the solid species i	m³/mol
$\Theta_{gepores2,i}$	Molar volume of the gel pores in the solid species i	m³/mol
γ_i	Activity coefficient of the species i	-
Θ_i	Molar volume of the solid species i incl. the gel pores	m³/mol
$\Theta_{pure,i}$	Pure density	m³/mol
ϕ_{ZW}	Porosity greater than 10 nm	-
$A_{specimen}$	Cross section surface of the specimen	m²
a_i	Temperature polynomial coefficients of species i	m²/(s·K²)
b_i	Temperature polynomial coefficients of species i	m²/(s·K)
c_i	Concentration of the solid species	mol/(m³ Material)
d_i	Temperature polynomial coefficients of species i	m²/s
D_i	Diffusion coefficient of species i	m²/s
dt_{chem}	Time of the chemical reactions	s
D_{ui}	Migration coefficient of species i	m²/s
F	Faraday constant	C/mol
$f\phi$	Function for the consideration of the pores structure influence on D_i and D_{ui}	-
f_m	Function for the consideration of the ionic strength influence on D_i	-
f_T	Function for the consideration of the temperature influence on D_i and D_{ui}	m²/s
f_{um}	Function for the consideration of the ionic strength influence on D_{ui}	
f_w	Function for the consideration of the water content influence on D_i and D_{ui}	-
G_E	Gibbs-energy	J
G_i	Parameter for the influence of ionic strength to the transport parameter D_{ui} of species i	$(mol/kg)^{-0.5}$
h	Parameter for calculation the influence of water content on the transport parameter	-
j_k	Ionic flow of species k	mol/(m²·s)
k	Retardation factor	-
m_i	Concentration of the solved species i	mol/(kg water)
n_i	Amount of species i	mol
p,q	Parameters for calculating the influence of the pore structure on the transport parameters	-
q_{water}	Water flow	kg/(m²·s)
R	Gas constant	J/(mol·K)

S_i	Sinks/Sources of Species i	mol/m³
t	Time	s
T	Temperature	K
U	Voltage	Volt
$V_{rock\ granulation}$	Relationship of the rock granulation volume to the material volume	-
w	Water content	kg/m³
W	Diffusion resistance number	-
w_{sat}	Maximum of water content	kg/m³
w_{limit}	Water content until mass transport occurs	kg/m³
z_i	Charge of Species i	-

Robin E. Beddoe,
Dr. BSc PhD

Harald Hilbig
Dr. rer. nat.

Centre for Building Materials, Technische Universität München, Munich, Germany

Modelling the Evolution of Damage to Concrete by Acid Attack

Summary

A numerical model has been developed for the prediction of concrete corrosion due to acid attack at exposure classes XA1, XA2, XA3 according to DIN EN 206-1. The degree of concrete degradation is characterised by the depth of a porous, corroded surface layer of reduced mechanical strength. The corrosion progress can be simulated for concrete of known composition made with Portland, Portland blast-furnace as well as calcium aluminate cement exposed to organic or mineral acids which attack the concrete surface under static or flowing conditions. The concrete may contain dissolvable or acid resistant aggregate of a given grading. The type of attack is defined by parameters which may obtainable from field observation and chemical analysis of the attacking medium. The main simulation result is the time needed to reach a given depth of corrosion.

Keywords: *acid attack, modelling*

1 Introduction

The service life of concrete structural components in industrial and agricultural use can be considerably reduced by exposure to acidic liquids if their surface is not suitably protected. The variety of media which are able to dissolve concrete is large and ranges from mineral acids, such as sulphuric or hydrochloric acid, through organic acids, such as acetic or lactic acid, to ammonium, see [1, 2]. Acid attack can take place statically (e.g. containers for liquid manure, silage or containers for de-icing agent run-off at airports) or dynamically by flowing liquids (e.g. cooling towers, waste water pipes). The dissolution reaction results in the formation of a porous surface corroded layer of low mechanical strength whose rate of growth determines the service life of concrete structural components. The corrosion rate depends on the composition of the acid, the physical nature of the attack (flowing or static) and concrete composition. Whereas corrosion slows down as the corroded layer becomes thicker, removal of the corroded layer by mechanical action speeds up corrosion.

In the first four years of the present project, a basic mathematical model for acid attack was developed. Rate constants for the dissolution reaction were estimated by observing the corrosion

of thin mortar disks and mortar powder in sodium acetate buffer solutions. The effect of corrosion on the transport of ions was quantified by measuring diffusion coefficients for corroded mortar disks in a diffusion cell. To verify the model, mortar cylinders made with quartz sand and CEM I 42.5 R, CEM III/B 32.5 and CAC were stored in sodium acetate acid buffer solutions for 16 d. Afterwards, the cylinders were turned on a lathe to remove the corroded layer in steps of roughly 0.5 mm. Distributions of total and dissolved Al, Fe, Ca and Na over the depth of the corroded layer into the undamaged material were determined by analysis with ICP OES and compared with the corresponding model results. The last two years of the project concentrated on extending the model to include the effects of practice conditions, in particular, flowing attack, abrasion and the loss of surface aggregate particles. Corrosion experiments were performed under static and flowing conditions for concrete compositions ranging from UHPC through normal concrete compositions to a mix designed for high acid resistance. Acid attack under static conditions was observed in tanks tests with sodium acetate buffer solutions. A specially developed flow test was used to observe corrosion under dynamic conditions.

The present contribution is an overview of the model demonstrating the essential mechanisms. Detailed descriptions of the mechanisms, the determination of the input parameter values as well as the experimental verification of the model components have appeared elsewhere [3, 4, 5, 6] or will be published shortly. Finally, in an application example, the model is used to investigate the effect of concrete composition on the resistance of concrete made with Portland cement to acid attack.

2 Characterisation of the Attacking Acid

In practice, the nature of the attacking acid is either known or, in principle, can be determined by chemical analysis. Attacking media can be broadly divided into (a) weakly dissociating acids whose aggressiveness lies in their ability to form buffer solutions and (b) highly dissociated mineral acids. In the former case, the equilibrium concentrations of protons c_H, acid anions c_X and acid molecules c_{HX} in the acid are determined by the acid constant K_a for the equilibrium reaction $HX \Leftrightarrow H^+ + X^-$.

$$c_H c_X / c_{HX} = K_a \tag{1}$$

For the model calculation, the attacking medium can be sufficiently characterised by its pH value and the total concentration of acid groups in ionic and molecular form (e.g. acetate) at the location of attack, i.e.

$$c_H = 10^{-pH} \text{ and } c_{X,tot} = c_X + c_{HX} . \tag{2}$$

The concentrations of acid anions and molecules are be found by solving (1) and (2). Charge neutrality is satisfied by the concentration c_Y of an appropriate balancing ion of charge z_Y. The ionic product of water $I_p = c_H c_{OH}$ fixes the concentration of hydroxyl ions so that

$$z_Y c_Y + z_X c_X + c_H - I_p / c_H = 0 \quad . \tag{3}$$

For highly dissociated mineral acids, the pH value provides sufficient characterisation if the type of acid is known. At present it is possible to simulate attack by acetic, lactic and propionic acids as well as ammonium (chloride, sulphate and nitrate) and carbonic acid. The action of hydrochloric, nitric and sulphuric acid can also be simulated.

3 Characterisation of the Concrete

The concrete is specified by its cement content, w/c ratio, grading curve and aggregate type (acid resistant quartz, dissolvable calcite or dolomite). The model requires the oxide analysis of the cement (CaO, Al_2O_3 and Fe_2O_3) and the initial capillary porosity P_{ini} of the concrete which may either be specified or calculated following Powers. The effect of silica fume and fly ash on porosity is taken into account by adding them to the cement content at proportions of 100% and 40%, respectively. The total volume fraction of aggregate is used with the grading curve data to estimate values of mean spherical particle radius $R_{A,j}$ and volume fraction $V_{A,j}$ for each grading fraction *j*. The number density of each grading fraction is taken as

$$M_{A,j} = \frac{3V_{A,j}}{4\pi R_{A,j}^3} \cdot \tag{4}$$

To account for the change in aggregate volume fraction when moving from the surface into the depth of the concrete, a geometric description of the spatial aggregate distribution based on the wall-effect for spherical particles is used. Considering a single particle of radius R_j belonging to grading fraction *j* and neglecting inter-particle effects, the probability of finding the particle at any distance $R_j<x<\infty$ from the concrete surface is assumed to be equal. Integration yields a simple distribution of volume $V_j(x)$ over depth x related to the distribution of radius $R_j(x)$.

$$V_j(x) = \pi\left(3R_j - x\right)x^2 \Big/ 3,\ x \le x_{R_j}^{near} \text{ and } V_j(x) = 4\pi R_j^{\,3} \Big/ 3,\ x > x_{R_j}^{near} \text{ where } x_{R_j}^{near} = 2R_j \tag{5}$$

$R_j(x)$ and correspondingly $V_j(x)$ are, in effect, averages of the real distributions at any point on the concrete surface taken over an infinite concrete surface. According to (5), the volume of aggregate increases from the surface until a depth of $x_{R_j}^{near}$ is reached after which it is constant. The surface-averaged distribution of total aggregate volume fraction as a function of depth is

$$V_A = \sum_j V_j M_{A,j} \cdot \tag{6}$$

The initial distributions of Ca, Fe and Al over concrete depth [mol/m^3] are calculated from the distribution V_A and the oxide content of the cement. Thus the initial uncorroded concrete is described by distributions of radius, and therefore volume, of the individual grading fractions together with distributions of Ca, Fe and Al content. In real concrete, the aggregate particles at the concrete/formwork surface are packed - in three dimensions - more effectively than de-

scribed by (5). Thus the distribution (5) moves towards the surface so that the width of the near-surface concrete region is reduced, i.e. $x_{R_j}^{near} = 2R_j\phi$ where, at present, ϕ is taken as 1/3.

4 Static and Flowing Attack

If acid attack takes place under "static" conditions a certain volume of acid of given initial composition is in contact with a given concrete surface area. Owing to the reaction with the concrete, the composition of the acid changes in the course of the corrosion process. Under flowing conditions, the concrete surface is continuously exposed to fresh acid, the amount depending on the rate of flow. In practice, the assessment of corrosion due to acid attack will be confined to a particular region of a structural component. This region can be defined in terms of a flow stretch s_F underneath the attacking medium of depth d_F moving with a velocity v_F. The chemical composition of the medium $c_{Ext,i}$ directly above the flow stretch is determined by (a) species i entering and leaving the concrete surface by diffusion, (b) the advection of species $c_{F,i}$ entering the flow stretch with the oncoming acid and (c) the advection of species $c_{Ext,i}$ leaving the flow stretch with the attacking medium. d_F is also the ratio of the volume of the attacking medium to concrete surface area. The change in concentration of the attacking medium above the flow stretch is given by

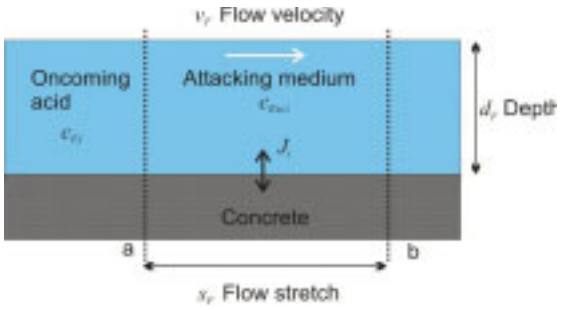

Figure 1: Parameters characterising acid attack under flowing conditions

$$\frac{\partial c_{Ext,i}}{\partial t} = \left(c_{F,i} - c_{Ext,i}\right)\frac{v_F}{s_F} \cdot \tag{7}$$

The boundary condition at the medium/concrete interface is defined such that the concentrations of each individual species in the external acid and in the surface pore solution are equivalent at all times. Charge conservation and the equilibria of the acid species and water are observed. Static conditions with known volume/surface ratio are defined simply by v_F = 0.

5 Simulation of Corrosion

For simplicity, only one dimensional transport is considered. The differential equations describing the mechanisms summarized in Figure 2 are solved by iteration using the conventional difference method where the time increment Δt is calculated for a chosen volume element Δx thickness and the particular mechanisms under consideration.

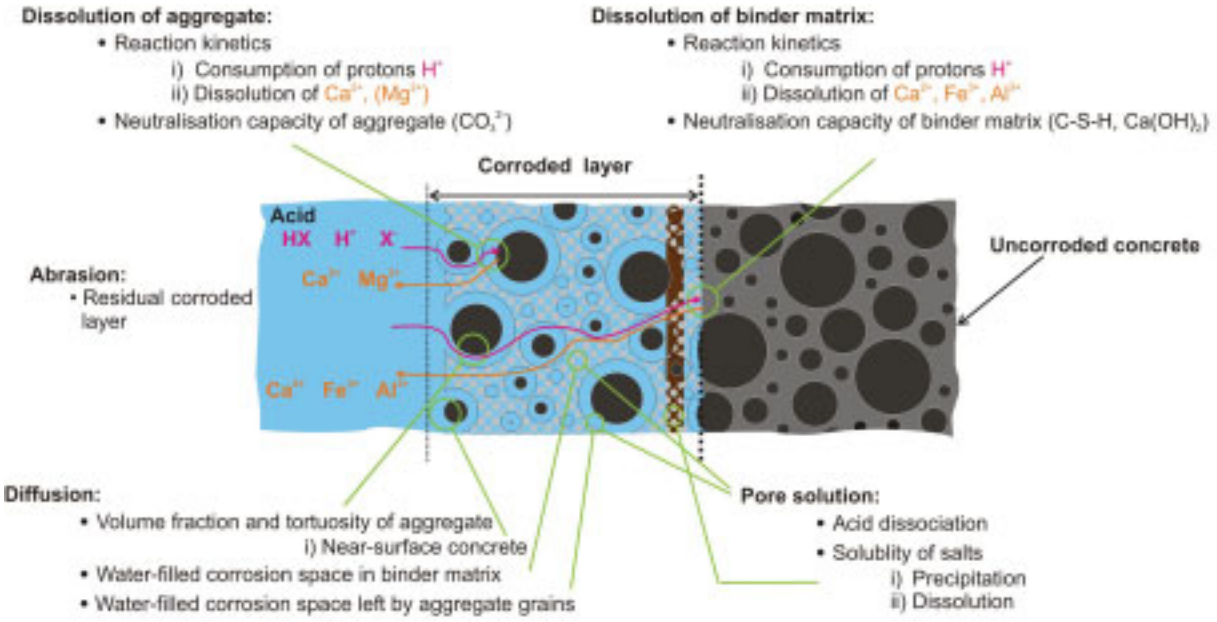

Figure 2: Processes affecting acid attack on concrete

Each volume element is assigned an initial porosity, radius and number density for each aggregate fraction, as well as contents of Ca, Fe and Al. Values for the volume/surface ratio, flow velocity and initial composition of the external acid are set. During the simulation, values of Ca, Fe, Al content as well as dissolved Ca^{2+}, Fe^{3+}, Al^{3+}, Mg^{2+} and acid species (protons, molecules, acid anions and balancing ions for buffer solutions) are calculated for each volume element and the external acid. Precipitate volume and the volumes of water-filled space due to aggregate and binder matrix corrosion are also determined. In the following, the various mechanisms are considered in more detail and illustrated by simulation results.

5.1 Diffusion

It is assumed that the pore system is completely saturated with solution so that the transport of the various species occurs only by diffusion, the rate of corrosion depending primarily on diffusion within the space generated by corrosion. The well-known extended Nernst-Planck equation is used to calculate flux density.

$$J_i = -D_i^{eff} P_C \left(\frac{\partial c_i}{\partial x} + \frac{F z_i}{RT} c_i \frac{\partial \psi}{\partial x} + c_i \frac{\partial \ln \gamma_i}{\partial x} \right) \tag{8}$$

Here the effective diffusion coefficients for the individual species D_i^{eff} are related to the specific values D_i^0 for diffusion in water and the volume fraction of the pore space P_C in which the diffusion takes place.

$$D_i^{eff} = \frac{D_i^0}{\tau} \left[f\left(V_B - V_{CB}\right) + P_C \right] \text{ where } P_C = P_{ini} + V_{CB} + V_{CA} - V_{Pt} \tag{9}$$

As corrosion proceeds, the original volume fraction of the binder matrix V_B is reduced by the solution-filled space V_{CB} produced by the dissolution of the binder matrix. In (9), the first term in the square brackets accounts for the remaining uncorroded binder matrix where f is the ratio of the effective diffusion coefficient of a species in the uncorroded binder matrix to the corresponding specific value. In diffusion experiments, f was estimated at 0.05 [4] so that the effect of diffusion in the uncorroded material on the corrosion process as a whole is relatively small. The porosity P_C increases from the initial value P_{ini} as space is formed by the corrosion of the binder matrix V_{CB} and the aggregate particles V_{CA}. It can also be filled by precipitation V_{Pt}. The diffusion path is lengthened by the tortuosity τ of the aggregate particles. A geometrical approach is used to account for changes in tortuosity caused by aggregate corrosion.

The electric potential ψ in the Nernst-Planck equation arises from the separation of charge due to the different diffusivities of the various ions. The high strength of the resulting potential necessitates, in principle, long computational times for the numerical solution of the differential equation. To avoid this, it is assumed that the electric current produced by the overall motion of all the participating ions of charge number z_i is zero.

$$\sum_i z_i J_i = 0 \tag{10}$$

In this case, the following solution for the local electric field exits if activity is neglected.

$$\frac{\partial \psi}{\partial x} = -\frac{RT}{F} \sum_i D_i z_i \frac{\partial c_i}{\partial x} \Bigg/ \sum_i D_i z_i^{\,2} c_i \tag{11}$$

In the simulation this expression is used with (8) to calculate the flux densities of ions other than H^+ and OH^-. The local concentrations of H^+ - and thus OH^- ions - are found by solving the equations for the zero charge condition.

$$\sum_{i \neq H,OH} c_i z_i + c_H - \frac{I_P}{c_H} = 0 \tag{12}$$

The above approach enabled rapid numerical solution of the Nernst-Planck equation. At present, an extended Debye–Hückel equation with the parameters A, B, a and $\dot{b}$ is used to calculate the activity coefficient γ_i in (8).

$$\ln(\lambda_i) = 2.303 \left[I\dot{b} - A z_i^2 \frac{\sqrt{I}}{\left(1 + B a_i \sqrt{I}\right)} \right] \text{ where the ionic strength is } I = \frac{1}{2} \sum_i z_i^{\,2} c_i \tag{13}$$

5.2 Corrosion of the Binder Matrix

The neutralisation reaction between acid protons in the pore solution and hydroxyl ions in the hydration products results in the transfer of Ca^{2+} from the hydration products into the pore solu-

tion. Reaction kinetics of the second order are used so that the change in calcium concentration of the pore solution is given by

$$\frac{\partial c_{Ca}}{\partial t} = k_{Ca} \; s_{Ca} \; c_H \qquad \text{and thus} \qquad \frac{\partial c_H}{\partial t} = -2\,\frac{\partial c_{Ca}}{\partial t}\,,\; \frac{\partial s_{Ca}}{\partial t} = -\frac{\partial c_{Ca}}{\partial t}\,. \tag{14}$$

Here s_{Ca} is the amount of potentially soluble calcium in concrete with respect to pore solution volume, c_H the proton concentration of the pore solution and k_{Ca} the rate constant. It is assumed that the potentially soluble calcium is, at all stages of corrosion, accessible to the acid. At the beginning of corrosion, s_{Ca} is essentially the neutralisation capacity of the concrete given by the total quantity of calcium calculated from the CaO content of the cement and the cement content of the concrete. The increase in concrete porosity due to the removal of calcium from the binder matrix is related to the increase in calcium concentration c_{Ca} of the pore solution by the experimentally determined coefficient κ_{Ca}, [4, 5, 6].

$$\frac{\partial V_{CB}}{\partial t} = \kappa_{Ca} P_C \frac{\partial c_{Ca}}{\partial t} \tag{15}$$

The effect of Fe^{3+} and Al^{3+} dissolution is treated similarly. Since the dissolution of Fe^{3+} and Al^{3+} in aluminate and ferrite hydrates occurs along with Ca^{2+}, their effect on porosity is not considered separately, but included in (15).

5.3 Equilibrium of the Acid Species

During the simulation, changes in the concentrations of the acid species in the pore solution and the external attacking medium due to diffusion, flow and dissolution result in concentrations $c_{H,0}$, $c_{HX,0}$, $c_{X,0}$ which are no longer in mutual equilibrium. In order to restore equilibrium with concentrations $c_{H,1}$, $c_{HX,1}$, $c_{X,1}$, only the species directly participating in the equilibrium reactions are considered as affecting the final state. Since other ions are present, the charge of the participating species is non-zero and is conserved according to

$$z_X c_{X,1} + c_{H,1} - I_p / c_{H,1} = z_X c_{X,0} + c_{H,0} - I_p / c_{H,0}\,. \tag{16}$$

As well as the equilibrium condition for the acid (1), conservation of the acid group is required.

$$c_{X,1} + c_{HX,1} = c_{X,0} + c_{HX,0} \tag{17}$$

The combination of (1), (16), (17) eliminating $c_{HX,1}$, $c_{X,1}$ yields a polynomial in the equilibrium concentration of protons.

$$\begin{gathered} \sum_k \phi_k c_{H,1} = 0 \\ \phi_0 = -K_a I_p\,, \qquad \phi_1 = K_a\left(I_p / c_{H,0} - c_{H,0} - c_{HX,0}\right) - I_p \\ \phi_2 = I_p / c_{H,0} - c_{H,0} + c_{X,0} + K_a\,, \qquad \phi_3 = 1 \end{gathered} \tag{18}$$

The polynomial is solved for $c_{H,1}$ using the Newton-Raphson method. Expressions are derived for the remaining equilibrium concentrations $c_{HX,1}$, $c_{X,1}$.

5.4 Simulation Examples

A simulation was performed for concrete made with 320 kg/m^3 Portland cement, containing 64.7 wt.% CaO, 5.9 wt.% Al_2O_3 and 2.8 wt.% Fe_2O_3, at a w/c ratio of 0.5 and quartz aggregate with an A16/B16 grading. The initial porosity was set at 10%. Attack by acetic acid initially at pH 4.5 with a total of 168 g/l acetate (1.82 mol/l CH_3COOH, 1.02 mol/l $NaCH_3COO$) was simulated for an exposure period of 17 days. Static tank test conditions at a volume to surface ratio of 275 l/m^2 were assumed. Figure 3 shows the main results of the simulation, i.e. the depth of the corroded layer (5.5 mm) and the distribution of pH of over depth. The results compare well the real tank test behaviour shown in the photograph where the depth of corrosion is given by the colour change of a phenolphthalein indicator solution (pH≈8.5) sprayed on fracture surfaces.

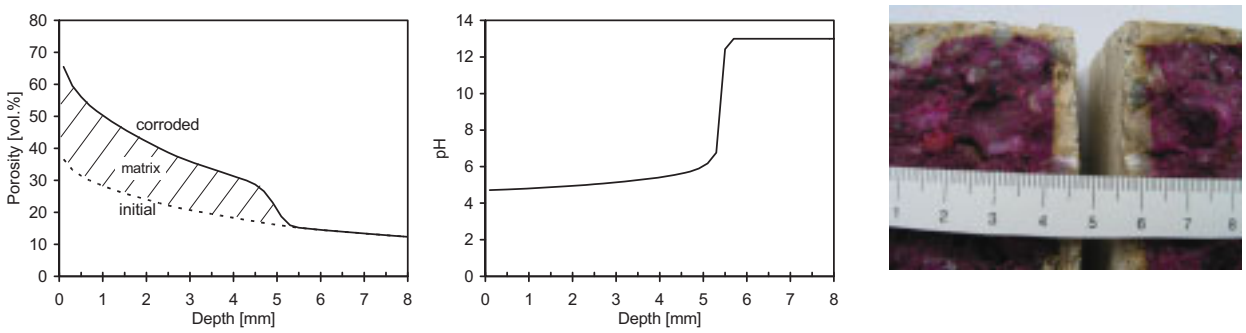

Figure 3: Distribution of porosity and pH over concrete depth from simulation of static acetic attack (17 d). Photograph: concrete with corroded layer after tank test

The consumption of protons by the neutralisation reaction promotes the dissociation of acid molecules increasing the concentration of acetate ions behind the corrosion front, Figure 4. Ca, Fe and Al ions enter the pore solution and diffuse toward the surface. The concentration of sodium supplied by the external acid is only affected by diffusion explaining its flat penetration profile. As opposed to aluminium and iron, the faster dissolution kinetics of calcium means that virtually all the calcium dissolves and diffuses out into the external acid. The correctness of the calculated distributions in Figure 4 has been experimentally verified [6]. Despite the high buffer capacity of the external acid, its pH increased from 4.5 to 4.7 over 17 days as observed experimentally and calculated by the simulation model.

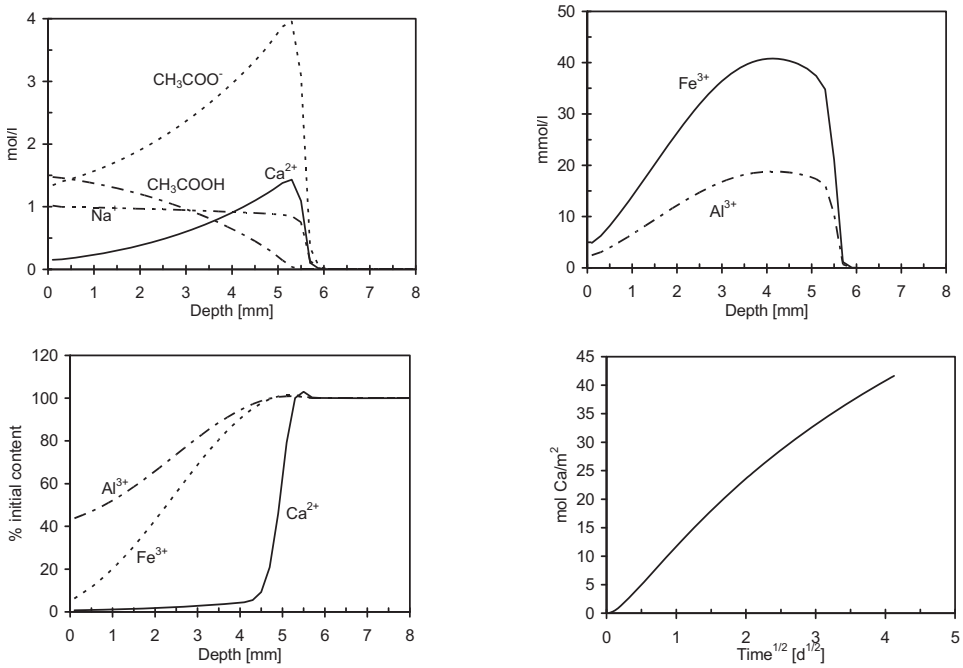

Figure 4: Simulation of acetic acid attack. Top: Distribution of dissolved species over concrete depth. Bottom left: Distribution of residual Ca, Al and Fe over concrete depth. Bottom right: Loss of calcium through the concrete surface during corrosion

As opposed to organic buffer solutions, the pH of mineral acids in contact with concrete surfaces rapidly increases eventually leading to subsidence of corrosion if their acidity is not maintained by flow or replenishment. In the flow test, the acid is pumped just once through an axial hole in a cylindrical specimen, Figure 5, and collected in a container for chemical analysis of Ca, Fe and Al concentrations.

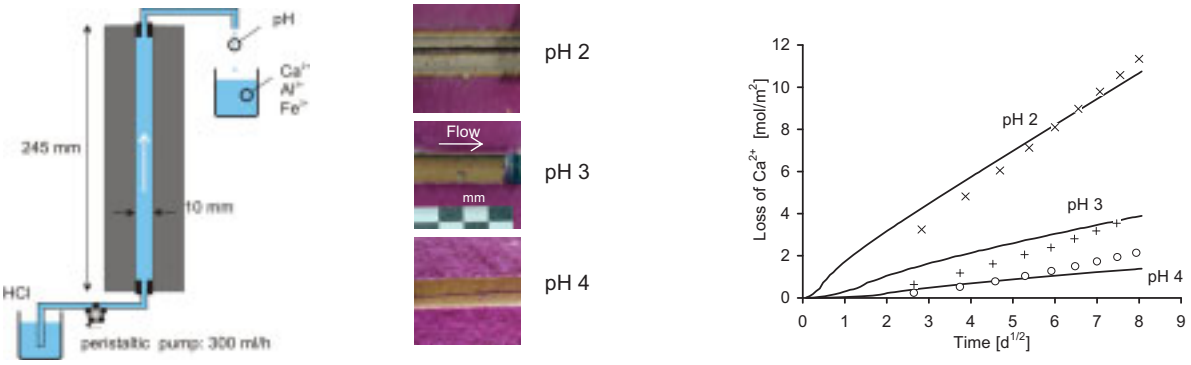

Figure 5: Left: Flow test set-up. Centre: Photographs of corroded layers in mortar after exposure to HCl at different pH values for a period of 64 d. Right: Simulated (curves) and measured (symbols) loss of calcium during corrosion

The flow test was performed for mortar (449 kg/m^3 CEM I, w/c = 0.6, quartz sand) attacked at pH 2, 3 or 4 by slowly flowing hydrochloric acid (v_F = 1.1 mm/s, s_F = 245 mm, d_F = 2.5 mm). The

duration of attack was 64 days. In Figure 5, the measured loss of calcium through the mortar surface is compared with equivalent simulation results. The calculated and experimental corrosion depths, visible in the photographs, are in reasonable agreement.

5.5 Aggregate Corrosion

Aggregate may be separated into acid resistant (e.g. quartz) and dissolvable minerals (e.g. calcite, dolomite) where dissolution of the aggregate particles increases the porosity of the corroded layer. The dissolution process is controlled by surface reactions and the diffusion of the acid species through the diffuse boundary layer, see [7]. During corrosion, smaller aggregate particles tend to dissolve first and be replaced by water-filled holes [8] whereas larger particles diminish in size and acquire a water-filled surface layer. For calcite and dolomite at pH values above approximately 4.0, the surface area normalised dissolution rate for the surface reaction is given by

$$r = k_A c_H{}^n \tag{19}$$

where c_H is the proton concentration adjacent to the mineral surface and k_A the rate constant. The exponent n is the order of the reaction. Since the water-filled space left behind by the dissolved material increases transport in the corroded layer, the molar volume κ_A of $CaCO_3$ or ½Ca½MgCO$_3$ is used to calculate the volume created by aggregate dissolution. The rate of decrease in radius of the aggregate particles is therefore

$$\frac{\partial R_j}{\partial t} = -\kappa_A \, k_A \, c_H{}^n \,. \tag{20}$$

During the simulation, the distributions of radius $R_j(x)$ and thus volume $V_j(x)$ for the grading fractions *j*, change as particle radii decrease according to (20). The space formed in the corroded layer is given by the rate of total aggregate dissolution.

$$\frac{\partial V_{CA}}{\partial t} = -\frac{\partial V_A}{\partial t} \tag{21}$$

At the same time Ca^{2+} and, in the case of dolomite, Mg^{2+} ions enter the pore solution. For limestone aggregate the change in pore solution concentration is

$$\frac{\partial c_{Ca}}{\partial t} = -\frac{1}{\kappa_A P_C} \frac{\partial V_A}{\partial t} \,. \tag{22}$$

A simulation was performed for static acetic acid attack on concrete made with limestone aggregate. The concrete composition and conditions are described in Section 5.4. As expected, aggregate dissolution has less effect at the concrete surface owing to the wall effect of the particles, but increases porosity at greater depths in dependence of the depth of corrosion and the grading curve, Figure 6.

In the model, the aggregate particles are, on average, in different states of corrosion ranging from complete dissolution of the smallest particles near the surface to asymmetrical corrosion of

the largest particles where the amount of dissolved material increases from the front to the back of the particles not yet reached by the acid, i.e. the particles are approximately egg-shaped.

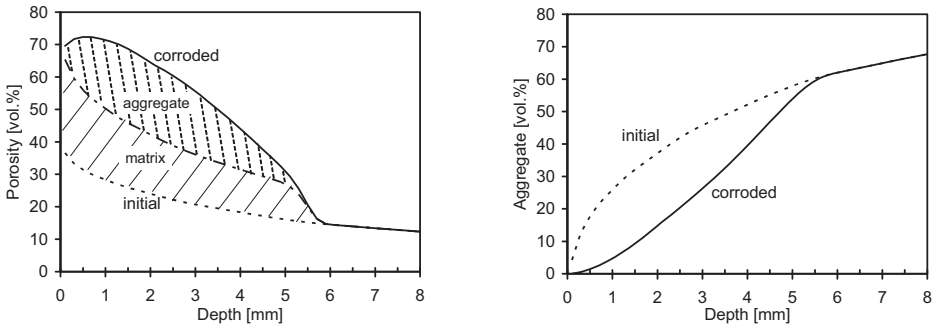

Figure 6: Simulation of static acetic acid attack on concrete with limestone aggregate

The corrosion of the limestone aggregate increased the pH of the external acid by 0.1 to 4.8, but did not exhaust the buffer capacity of the acid solution, cf. Section 5.4. Due to aggregate corrosion, the amount of calcium which entered the external acid increased by 60% and the depth of corrosion by 0.5 mm.

5.6 Abrasion

Figure 7: Example of corrosion with abrasion showing protruding particles and surface cavities (courtesy of Ingenieurbüro Schießl, Gehlen, Sodeikat GmbH)

The extent of removal of corroded surface material depends on the severity of abrasion and the strength of the material. Since accurate modelling of the actual mechanical abrasion process is difficult, loss of surface material is described by setting an upper limit x_{RCL} on the thickness of a residual corroded layer defined to exist between the abraded surface of the corroded concrete and a depth at which a pH value of, for example, 8.5 is reached. In practice, the depth of the residual corroded layer could be determined by application of a phenolphthalein indicator solution to freshly fractured concrete surfaces. In the model, the distance of the abraded surface x_S from the original surface of the uncorroded concrete is given by the conditions

$$x_S = x_{pH\,8.5} - x_{RCL};\ x_{pH\,8.5} > x_{RCL} \qquad \text{and} \qquad x_S = 0;\ x_{pH\,8.5} \le x_{RCL}. \tag{23}$$

Here $x_{pH8.5}$ is the depth at which the proton concentration in the pore solution $c_H(x)$ first exceeds pH 8.5. As abrasion proceeds, the external boundary is moved to x_S, i.e. its position is time dependent, see Figure 8. The relative increase in porosity ϕ with respect to the initial porosity may also be used to define the position of the abraded surface. A relative increase in surface poros-

ity above a given limiting value ϕ_S is deemed not to be possible which causes the position of the abraded surface to move deeper into the concrete as corrosion proceeds.

$$\phi(x_S) = \phi_S(x_S) \text{ where } \phi = \left(V_{CB} + V_{CA} - V_{Pt}\right) / P_{ini} \tag{24}$$

Abrasion also results in the exposure of aggregate particles which, if not firmly embedded, will be removed leaving behind open surface cavities which will tend to increase the rate of corrosion. In the model, the loss of surface aggregate particles is described in terms of its effect on the surface-averaged distributions of particle radius and volume, $R_j(x)$, $V_j(x)$. Depending on the type of aggregate and the severity of abrasion, the loss of particles at the surface ranges from “easy removal” leaving holes with the same diameter as the original particles to “difficult removal” where protruding particles “stick” to the abraded surface. Consequently, a “pop-out” factor p_A is defined as the smallest fraction of spherical particle diameter which may remain embedded in the corroded binder matrix, Figure 8.

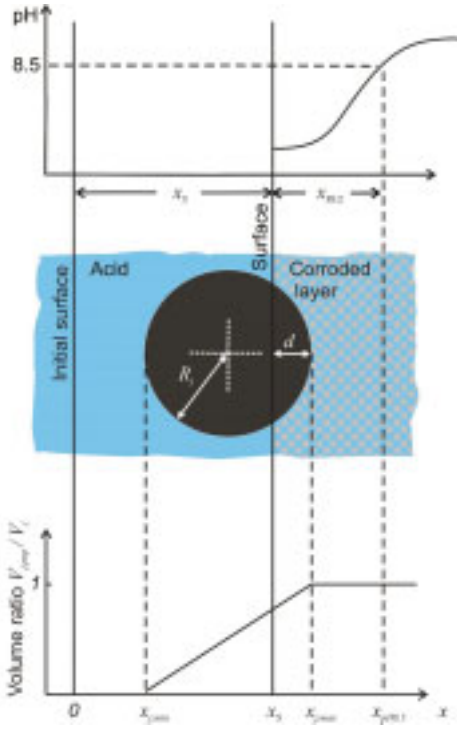

Figure 8: Residual corroded layer and “pop-out” factor

$$0 \le p_A = d/2R_j \le 0.5 \tag{25}$$

Particles at positions such that $d < p_A\ 2R$ are removed whereas those with $d \ge p_A\ 2R$ remain embedded. The largest cavities occur when p_A = 0.5 and most protruding particles when $p_A = 0$. For sake of simplicity, p_A is assumed to be valid for all grading fractions. Depending on the thickness of material lost by abrasion x_S and aggregate particle size, minimum and maximum depths exist under the initial surface below and above which all aggregate particles of a particular fraction are removed or remain, respectively.

$$x_{j,\min} = x_S - 2R_j\left(1 - p_A\right) \text{ and } x_{j,\max} = x_S + 2R_j\,p_A \tag{26}$$

Thus the surface-averaged aggregate volume V_j and hence particle radius R_j are zero at depths below $x_{j,min}$ or are left unchanged at depths above $x_{j,max}$. Between these limits partial aggregate particle removal occurs where a linear relationship is used to calculate the volume of particles $V_{j,pop}$ which remain embedded, i.e.

$$\begin{aligned} &V_{j,pop} = 0,\ \ x \le x_{j,\min};\ V_{j,pop} = V_j,\ \ x \ge x_{j,\min} \\ &V_{j,pop} = V_j \frac{x - x_{j,\min}}{x_{j,\max} - x_{j,\min}},\ \ x_{j,\min} < x < x_{j,\max} \end{aligned} \tag{27}$$

This approach permits the determination of changes in volume and consequently particle radius for the individual grading fractions as surface-averaged values. Complicated particle-based calculations are therefore avoided.

Figure 9 demonstrates the effect of abrasion and pop-outs on the corrosion of concrete by acetic acid for a residual corroded layer thickness x_{RCL} = 1.5 mm and a pop-out factor p_A = 0.15. The conditions of attack and concrete composition are described in Section 5.4. In this case, 7 mm of surface material is removed by abrasion over 17 days. The loss of surface aggregate particles results in a high surface porosity which together with abrasion increases the depth of corrosion from 5.5 mm to 8 mm. The largest aggregate particles removed to leave cavities are 6 mm in diameter; the larger particles still protrude from the concrete surface.

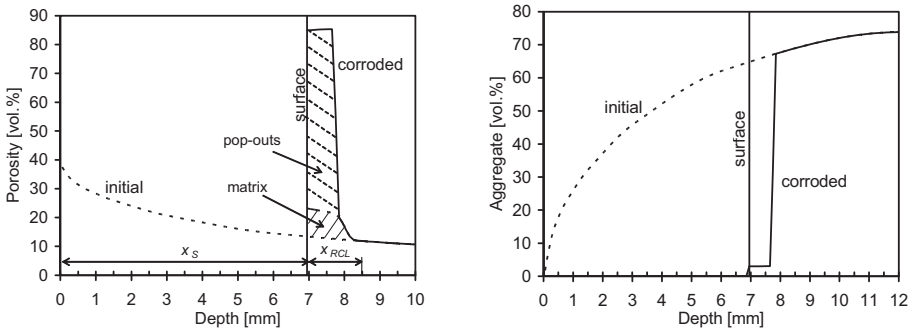

Figure 9: Simulation of abrasion and loss of surface aggregate particles due to static acetic acid attack on concrete. Left: porosity of surface concrete due matrix corrosion and particle loss. Right: volume fraction of aggregate in corroded concrete

5.7 Precipitation

Depending on the composition of the attacking acid and the cement, the precipitation of low solubility compounds such as iron hydroxy salts, brucite, gypsum or gibbsite can reduce the pore space for diffusion and consequently the rate of corrosion. The amount of precipitate is determined by the solubility equilibrium of the compound in question and the dissociation of the acid. In the model, the equilibrium state is calculated using the methodology described in Section 5.3 where the appropriate equilibrium reactions are considered for the acid and the species involved in precipitation. For example, four equilibria are considered in the case of gibbsite precipitation during acetic acid attack.

$$\begin{aligned} Al(OH)_3 + 3H^+ &\Leftrightarrow Al^{3+} + 3H_2O;\ Al^{3+} + 4H_2O \Leftrightarrow Al(OH)_4^- + 4H^+ \\ CH_3COOH &\Leftrightarrow H^+ + CH_3COO^-;\ H_2O \Leftrightarrow H^+ + OH^- \end{aligned} \tag{28}$$

Simulating for example acetic acid attack, Figure 10, left, shows the distribution of precipitated iron hydroxy acetate which, in practice, appears as a narrow brown region in the corroded layer adjacent to the corrosion front. $Fe(CH_3COO)_2OH$ was found to be a suitable model substance to describe the observed behaviour. The ferric ions enters the pore solution at the corrosion front,

precipitate and redissolve on encountering lower pH values as the corrosion front moves deeper into the concrete. However, owing to the small amount of precipitate, the rate of corrosion is virtually unaffected by this precipitation.

In contrast, the performance of calcium aluminate cement under acid attack is explained by the precipitation of alumina hydrate [9] which is stable down to pH values near 4. The precipitation of gibbsite is demonstrated in Figure 10, right, for mortar made with calcium aluminate cement after 7 years exposure to flowing HCl at pH 3.5. During corrosion the volume of precipitate is similar in size to the space formed by the dissolution of the binder matrix. The simulation results indicate that the effectiveness of gibbsite precipitation in reducing the diffusion of the acid species through the corroded layer depends on the initial porosity of the mortar.

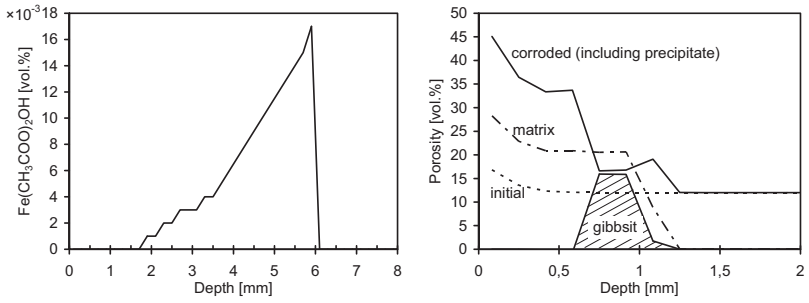

Figure 10: Left: Simulation of static acetic acid attack on concrete with precipitation of iron hydroxy acetate. Right: Precipitation of gibbsite during flowing hydrochloric acid attack on calcium aluminate cement mortar

5.8 Temperature

The effect of temperature on diffusion is taken into account by modifying the specific diffusion coefficient of the participating species with respect to the reference temperature of 293.15 K.

$$D_{i,T}^{0} = D_{i,T_r}^{0} \frac{T}{T_r} \tag{29}$$

The reaction rates for Ca, Al and Fe are changed according to Arrhenius

$$k_{i,T} = k_{i,T_r} e^{-\frac{E_a}{R}\left(\frac{1}{T}-\frac{1}{T_r}\right)} \tag{30}$$

where a value of 54.5 kJ/mol is assumed for the activation energy. At present the ionic product of water, the dissociation of ammonium and carbonic acid are corrected for the effect of temperature using the van‘t Hoff equation.

6 Effect of Concrete Composition on Acid Resistance

6.1 Static Acid Attack

The static attack of organic acids as encountered in agriculture was represented by the attack of an acetic acid buffer solution with a total acetate concentration of 12 800 mg/l and a pH value of 4.0 (i.e. XA3) on Portland cement concrete containing quartz aggregate A16/B16 mm. The acid composition was kept constant thus simulating the worst case situation, i.e. no loss of acid strength during attack owing to the reaction of the acid with the concrete. It should be pointed out that even at high buffer capacities in a tank test, a reduction in the strength of the acid can occur especially when testing concrete with a high cement content, see [10]. The resistance of the concrete to acid attack was characterised by the time need to reach a corrosion depth of 10 mm. Simulations were performed for w/c ratios between 0.4 and 0.6 and cement contents between 240 and 800 kg/m^3. The simulations were repeated including the effect of abrasion for a residual corroded layer thickness x_{RCL} of 4 mm, Figure 11.

The results of the simulation indicate that the corrosion resistance of concrete can be significantly improved by the use of low cement contents and low w/c ratios for the attack scenario simulated.

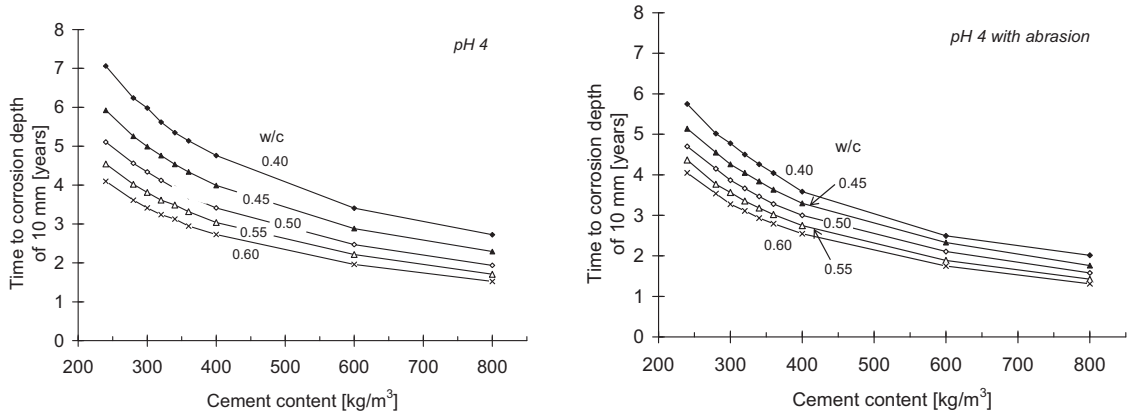

Figure 11: Effect of concrete composition on resistance to static acetic acid attack. Left: without abrasion. Right: with abrasion

To understand the effect of w/c ratio and cement content on acid resistance it should be borne in mind that the rate of corrosion is determined by the transport of the acid through the corroded layer to the uncorroded concrete. Thus factors which affect the porosity of the corroded layer also affect the rate of corrosion. In general, a reduction in cement content has two possible effects on resistance to acid attack.

a) Acid resistance is improved because the volume of dissolvable binder matrix is lower and thus the porosity of the corroded layer is lower as well.
b) The neutralisation capacity of the concrete with respect to the acid is lower and thus, in some scenarios of acid attack, the acid resistance too.

In the case of strong buffer solutions with a high potential concentration of protons in non-dissociated acid molecules, the neutralisation capacity is of secondary importance meaning that low cement contents affect acid resistance positively.

Low w/c ratios improve acid resistance because the contribution of the capillary porosity of the uncorroded concrete to the porosity of the corroded layer is smaller. The corrosion process opens up the pore system of the binder matrix destroying tortuosity [4].

The corrosion of a concrete with an optimized combination of binder and 0/16 mm quartz aggregate particle sizes, such as designed in [11] to be an acid resistant concrete, was also simulated. The particles sizes were optimised according to the extended Fuller-Thompson grading curve [12] and thus well packed. As well as a low Portland cement content of 241.2 kg/m^3 at a w/c ratio of 0.56, the concrete contained fly ash and silica fume (64.3 and 16.1 kg/m^3, respectively) so that the effective water cement ratio w/c_{eff} was reduced to 0.48 ($c_{eff} = c + 0.4\,f + s$). The time needed to reach a corrosion depth of 10 mm was longer for this concrete than normal concrete compositions or a UHPC composition (c = 832, w = 166, s = 135 kg/m^3, w/c_{eff} =0,17, f_{c28d} = 150 MPa) [10].

For the conditions of attack considered, the depth of corrosion d was found, in general, to be described approximately by a root time law.

$$d = a\sqrt{tc_A} \tag{31}$$

Here, c_A is the concentration of the acid. The constant a depends on the composition of the concrete and the conditions of attack. It is assumed that the strength of the acid and the conditions of attack are constant and that the effect of any possible precipitation processes as well as abrasion is negligible.

The significant effect of abrasion on corrosion resistance is demonstrated by Figure 11, right. The time needed to reach a corrosion depth of 10 mm, in this case comprising 6 mm abraded material and 4 mm residual corroded layer, is shortened by abrasion. Whereas the depth of corrosion increases proportionally to $\sqrt{t}$ if the corroded layer remains intact, abrasion causes the depth of corrosion to increase faster then $\sqrt{t}$. Complete and continuous removal of corroded material is expected to cause the depth of corrosion to increase linearly with time.

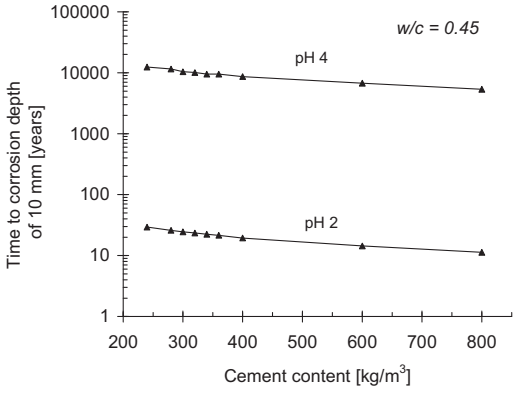

Figure 12: Simulation of flowing sulphuric acid attack on concrete

6.2 Flowing Sulphuric Acid Attack

The attack of flowing sulphuric acid on Portland cement concrete (w/c= 0.45, 200<c<800 kg/m^3) was considered as an example for the degradation of concrete in contact with flowing mineral acids in industrial plants. Corrosion was simulated for CEM I

cement concrete made with quartz aggregate (A16/B16) at pH values of 2 and 4, i.e. exposure class >XA3 and XA3, respectively. Constant acid strength was assumed. Gypsum precipitation and loss of surface material were not considered. The effect of cement content, w/c ratio and pH value on corrosion resistance were found to be generally similar to static acetic acid attack. However, at pH 4 the rate of corrosion due to dissolving attack was negligible for all concrete composition considered. The depth of corrosion depends is given by

$$d = a\sqrt{tc_A} \tag{32}$$

Further details are in [10].

7 Conclusions

The main result of the model presented in this contribution is the time needed for the depth of corrosion of concrete subjected to acid attack under static or flowing conditions to reach a given value. Along with distributions of porosity and pH value over concrete depth, the model provides distributions of calcium, aluminium and iron in solution and solid phases as well as calcium loss through the concrete surface.

The simulation of static acetic acid attack indicates that low cement contents and w/c ratios improve the acid resistance of concrete. Since the capillary porosity of the binder matrix is not significantly reduced by w/c ratios below 0.4, the corrosion resistance of concretes is not expected to be significantly improved by w/c ratios below 0.4. Measures which reduce the capillary porosity of concrete, such as the addition of fly ash and silica fume, or lower the content of dissolvable Ca, e.g. binders with low Ca content, are expected to have a beneficial effect on corrosion resistance. This will be systematically investigated in the future. To meet the requirement of practice better, real field scenarios of acid attack will be considered and compared with model simulations.

Further publications which have appeared or have been submitted by the authors in the course of this research project are to be found in [3, 4, 5, 6, 10, 13, 14, 15]

The authors express their thanks to the German Research Foundation (DFG) for supporting this project financially.

8 References

[1] Zivica, V., Bajza, A.: Acid attack of cement based materials – a review. Part 1. Principle of acid attack. In: Constr. Build. Mater. 15, pp.331-340, 2001

[2] Bertron, A., Duchesne, J.: Attack of cementitious materials by organic acids in agricultural and agro-food effluents – a review. In: Proceedings of workshop on performance of cement-based materials in aggressive aqueous environments, Ghent, Belgium, Sept. 2007 , Ed. Nele De Belie, 15-28

[3] Dorner, H. W., Beddoe, R. E.: Prognosis of concrete corrosion due to acid attack. In: Proceedings 9th Internat. Conf. Durability of Building Materials, Brisbane, Australia, March 2002

[4] Beddoe, R. E., H. W. Dorner: Prognose von Betonschäden bei Säureangriff. In: Proceedings 15. ibausil, Band 2, S.0873-0882, Weimar Sept. 2003

[5] Beddoe, R. E., Dorner, H. W.: Modelling acid attack on concrete: Part I. The essential mechanisms. In: Cem. Concr. 35, pp.2333-2339, 2005

[6]. Beddoe, R. E., Dorner, H. W.: Modelling Acid Attack on Concrete: Part II. Effect of Cement Paste Matrix. Submitted to Cem. Concr. Res.

[7] Morse, J. W., Arvidson, R. S.: The dissolution kinetics of major sedimentary carbonate materials', Earth-Sci. Rev. 58, pp.51-84, 2002

[8] Pavlík, V., Effect of carbonates on the corrosion rate of cement mortars in nitric acid. In: Cem. Concr. Res. 30, pp.481-489, 2000

[9] Scrivener, K. L., Cabiron, J.-L., Letourneux, R.: High-performance concretes from calcium aluminate cements. In: Cem. Concr. Res. 29, pp.1215-1223, 1999

[10] Beddoe, R.E., Schmidt. K.: Säureangriff- Einfluss der Betonzusammensetzung, beton, eingereicht, Feb. 2008

[11] Hüttl, R., Hillemeier, B.: Hochleistungsbeton – Beispiel Säureresistenz, Betonwerk + Fertigteil-Technik 1, S.52-60, 2000

[12] Punkte, W.: Wasseranspruch von feinen Kornhaufwerken. In : beton 5, S. 242-248, 2002

[13] Beddoe, R.E., Hilbig, H.: Acid Attack on Concrete - A New Computer Model. In: Proc. 5th Internat. Workshop, Transport in Concrete, Essen, June 2007

[14] Beddoe, R.E.: Modelling Acid Attack on Concrete Structural Components. In: Proceedings of workshop on performance of cement-based materials in aggressive aqueous environments, Ghent, Belgium, Sept. 2007 , Ed. Nele De Belie, 15-28

[15] Beddoe, R.E., Dorner, H.W., Hecht, M., Rucker, P.: Betonbauteile in Wechselwirkung mit der Umwelt - Modellierung der maßgeblichen Transportmechanismen, In: Festschrift zum 60. Geburtstag von Prof. Dr.-Ing. Peter Schießl, Schriftenreihe Baustoffe, Heft 2 (2003) S. 311-321

Rosa M. Espinosa-Marzal *Dr.-Ing.*
Carsten Gunstmann *Dr.-Ing.*
Jana Kieckbusch *Dr.-Ing*
Lutz Franke *Prof. Dr.-Ing.*

Institute of Building Materials, Physics and Chemistry of Buildings
Hamburg University of Technology, Germany

The program systems CeSa and AStra for cement and salt chemistry and the prediction of corrosion processes

Summary

Prediction of corrosion processes of cementitious materials requires knowledge of several interconnected phenomena. The chemical behavior of the attacking media, of the material as well as their interactions need to be known, particularly regarding possible crystallization and dissolution reactions of soluble compounds. Such corrosive processes need to be quantified to predict the material durability.

To determine the distribution of water content, temperature and concentration of each chemical substance throughout the material, numerical modeling and simulation of coupled transport of heat, moisture, air and species carried in the solution must be realized. This requires the thorough knowledge of the pore solution chemistry, the transport characteristics of the material with respect to the medium as well as the kinetics of chemical reactions and phases changes and its interaction with the transport processes.

The program **CeSa** calculates the equilibrium composition of salt mixtures and their thermodynamic properties. Additionally, the chemical composition of cementitious materials during hydration and after reaction with attacking media can be calculated. CeSa is a tool to calculate chemical processes in equilibrium neglecting transport and reaction kinetics.

The program **AStra** simulates a coupled transport of heat, moisture, air and chemical substances. Within **AStra** simulations some functionalities of the chemistry program CeSa are necessary such as the computation of the properties of salt mixtures and kinetics of chemical reactions. Hence, AStra is capable of simulating and predicting corrosion processes of concrete structures as well as mechanical stresses in inert porous building materials induced by salt crystallization.

Keywords: *acid attack, simulation, mass transport, chemical reactions, pore structure model, diffusion coefficient, salt crystallization, crystallization pressure, damage.*

1 Introduction

Prediction and simulation of corrosion processes in porous building materials require the description of the transport processes in the porous material as well as the chemical reactions of the reactive materials such as cement-based materials. Furthermore, the physical properties of the material, e.g. heat capacity, porosity and pore structure, and the environmental conditions have to be considered in order to describe the chemical processes as accurately as possible. In return, the chemical processes influence the physical and chemical properties of the material since they change the pore structure due to crystallization or dissolution reactions, which has a significant influence on the transport properties and on the moisture retention curve of the material. Thus, the interaction between transport processes and chemical reactions must be taken into account for a reliable prediction of the corrosion processes.

In the last two decades, there have been several efforts to simulate these phenomena using physics-based and/or empirical models [1][2][3][4]. Currently, available computational power permits simulations on both laboratory and field scales.

The coupled advective-diffusive partial differential equations for the transport of moisture and dissolved substances in porous media [5], or its extended version including migration in an electric field based on the Nernst-Plank model [14], are well-known. Within the last decade, our research group has focused on the investigation of the chemical and physical interaction between pore solution and porous material and universal models has been developed. These models have been implemented in two tools - CeSa and ASTra- whose efficiency is shown in this paper through three different experiments.

2 CeSa – Cement and Salt Chemistry

CeSa is a program describing chemical processes, especially the composition and chemical behavior of cement-based materials and salt solutions.

The calculation routines used in this program are mainly based on Pitzer's semi-empirical ion interaction model [6] extended by Steiger et. al. [7] and the Gibbs energy minimisation algorithm [8][9] extended by Schmidt-Döhl [10] and Kiekbusch [11]. These algorithms are used for advanced functionalities described below.

CeSa includes two databases that are optimized for the main fields of application: (1) calculation of compositions of salt mixtures and their properties and (2) calculation of compositions of cementitious materials and their chemical behavior.

The salt database includes a consistent parameter set for SO_4, NO_3, Na, K, Cl, Mg and Ca [7]. The cement database is based on available data from the literature [6]. Both databases can be extended with additional data or even substituted with own databases, which allows a wide application field. Thus, given an ion mixture of known composition, it is possible to determine

which salts are thermodynamically stable at each temperature and relative humidity and therefore which salts might have lead to damage of the material in a particular site.

CeSa provides an intuitive and user-friendly graphical interface. The structure and design of the user interface is based on the main fields of application and allows problem oriented user input (figure 1). In the following, CeSa is applied to determine the equilibrium chemical composition of two different cement pastes exposed to acid attack.

2.1 Application of CeSa for acid corrosion of cementitious material

The chemical composition of a cementitious material changes with time due to hydration processes, which depends on environmental conditions. Therefore, an algorithm was developed to calculate the chemical composition of a material at different hydration states. Cementitious materials consist of four components of known mass fraction: cement, admixtures, aggregates and water. Cement, admixtures and water are included in the equilibrium calculation, while the aggregates are assumed to be chemically inert and therefore they do not influence the equilibrium. The equilibrium calculation gives the composition of a completely hydrated material for a sufficient amount of water. The algorithm for partial hydration subdivides the reactive parts cement and admixtures, into temporary reactive (hydrated) and non-reactive (unhydrated) parts. This partition is dependent on the degree of hydration and it is applied to the total amount of admixtures and to each clinker phase, C_3S, C_2S, C_3A and C_4AF-C_2F, for cements. Kiekbusch [11] describes in detail the theory and applications of the partition algorithm. This algorithm was implemented in CeSa to describe the composition of cementitious material for different hydration states.

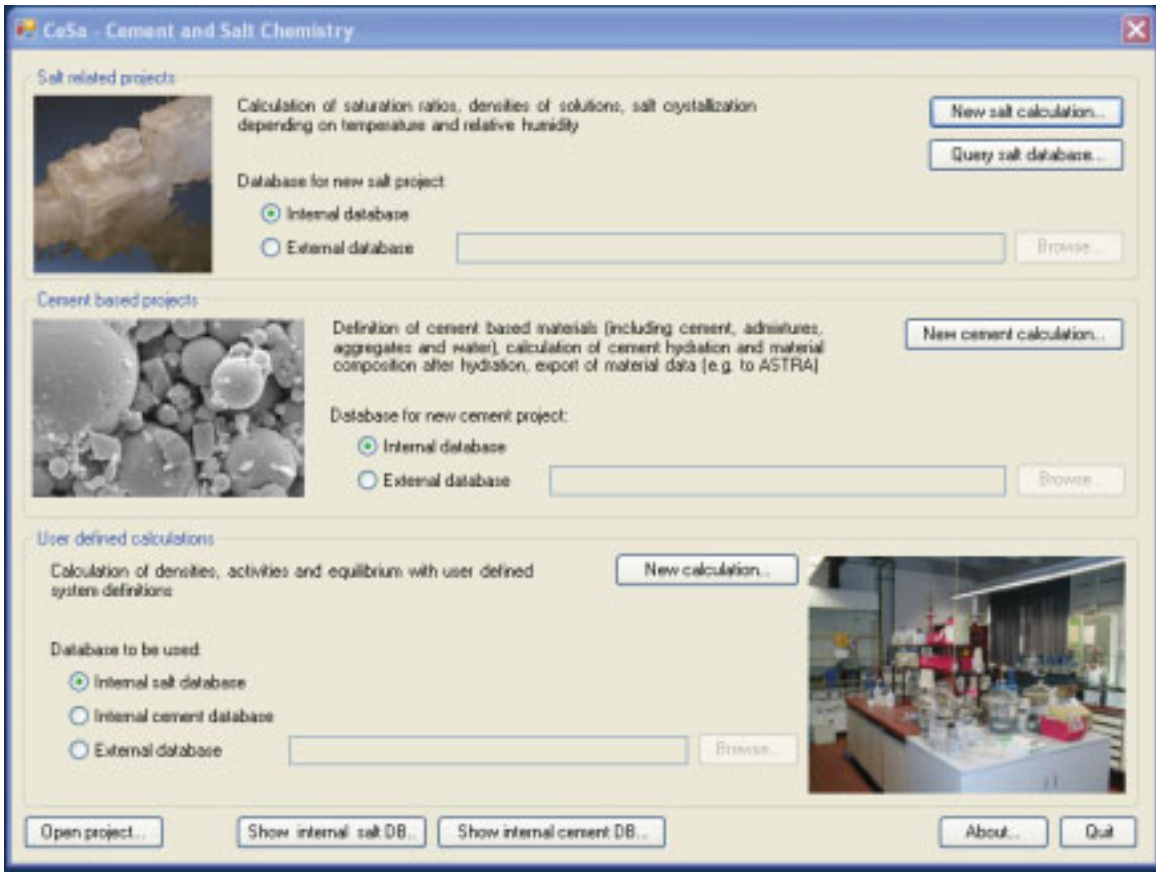

Figure 1: Main user interface of CeSa representing the three main application fields for salt solutions, cement chemistry and the usage of the main algorithms.

After defining the material, the chemical behavior can be calculated using the equilibrium algorithm. CeSa provides three different modes of attack: **carbonation, mineral and organic acid corrosion and salt corrosion**.

The internal database was verified for modelling corrosion processes of hydrochloric [11], sulphuric acid and lactic acid [12] by comparison of calculated and experimental results.

To experimentally simulate the corrosion process, identical suspensions of saturated $Ca(OH)_2$ solution and cement paste powder of known composition with a mass ratio of 100 to 1 were prepared. These suspensions were shaken for one day prior to the addition of 1 molar hydrochloric acid. A range of acid addition was investigated. After shaking for three weeks, the suspensions were filtered and the resulting filtrates analysed for pH and dissolution products (Ca, Si, Al, Fe and Mg).

Two different cement paste powders were used: a Portland cement CEM I 42.5 R – HS/NA and a blast furnace slag-blended cement CEM III/B 42.5 HS/NW/NA. The amount of chemical bound water of the cement pastes after complete hydration was determined thermogravimetrically to be 18.54 % and 14.57 % for CEM I and CEM III based cement paste, respectively.

The **chemical model** contains the cement phases $CaSO_4$, Na_2O, K_2O and MgO and the clinker phases mentioned above in addition to hydrated phases including:

- the hydroxides Portlandite, Brucite, Gibbsite and $Fe(OH)_3$
- the C-S-H phase described by Kulik et al. [13] with an ideal mixture of Jennite and Tobermorite for calcium-rich CSH(II) and a second ideal mixture of Tobermorite and Silicate for silicon-rich CSH(I)
- the AFm phase described by an ideal mixture of pure Aluminium-containing and Iron-containing phase and the AFm phase containing chloride, the Friedel's salt
- the calcium aluminate and ferrate hydrates C_4AH_{13}, C_3AH_6 and C_4FH_{13}, C_3FH_6 as well as M_4AH_{10}
- the silicious aluminium hydrates C_2ASH_8 and $C_3AS_nH_{6n-2}$, the latter being described as an ideal mixture of C_3AH_6 and C_3ASH_4
- the aluminate silicates CAS_2 and AS_2H_2 for the advanced corrosion process

The experimental and simulated compositions of the solutions as a function of the amount of acid added are shown in figure 2 for both cement pastes. The results for Portland cement paste show a good agreement between experimental and calculated values for all elements, except for calcium at a small degree of corrosion and the pH values at higher acid addition.

The calcium concentration in the solution corresponds to the most stable calcium-containing phase. In the initial range (< 5 mmole H+/ g cement paste), the stable phase is portlandite (see fig. 2). However, $Ca(OH)_2$ solutions in contact with CO_2 tend to form carbonate very quickly resulting in a reduction of the calcium concentration. Although we attempted to minimize the carbonation process during the experiment, contact of the solution with air during filtration was impossible to avoid. Portlandite was detected in the solid using Fourier transformation infrared spectroscopy. Hence, carbonation affected the experimental results but was neglected in the simulation, causing a discrepancy between experimental and simulated calcium concentrations. Therefore, in equilibrium, the predicted calcium concentrations are higher than those measured.

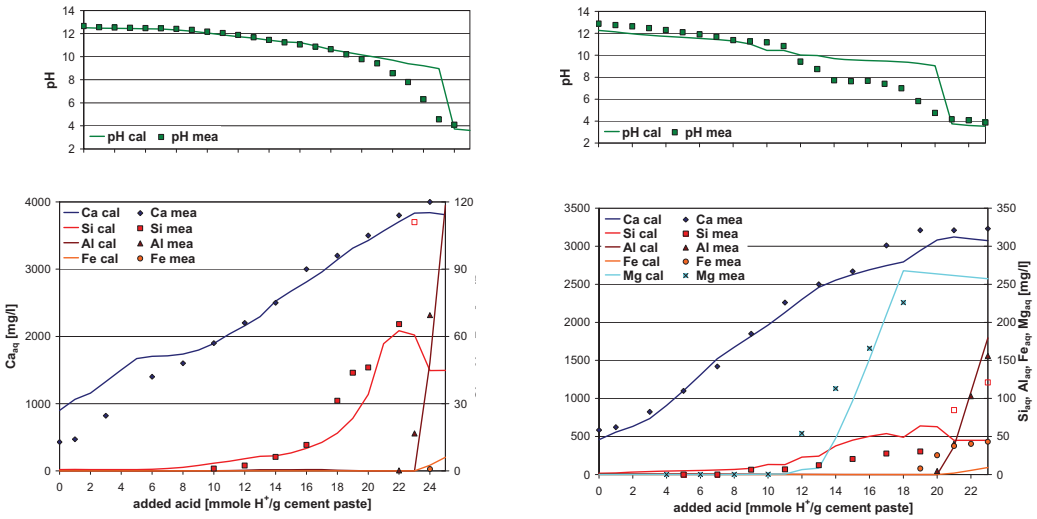

Figure 2: Comparison of calculated (cal) and measured (mea) solution compositions dependent on the degree of corrosion for Portland cement paste (left) and blast furnace slag blended cement paste (right).

The differences between experimental and simulated pH values result from the C-S-H model of Kulik et al. [13]. The model is in agreement with the calcium and silicon concentrations for the calcium-rich C-S-H phase. However, for the silicon-rich C-S-H phase, the pH value is overestimated due to the formation of tobermorite at small calcium concentrations. The corresponding pH value for solution in equilibrium with tobermorite is approximately 9. Discrepancies occur in the range where CSH(I) is stable (see fig. 2, left). After complete dissolution of these phases, the experimental and simulated pH values are in agreement.

Identical issues with pH simulation occur with the blast furnace slag blended cement paste. However, the effect occurs over a wider range (see fig. 2, right). In this cement paste, portlandite is not present during the complete corrosion process. Therefore, experimental and simulated calcium concentrations are in agreement during initial additions. For this material the gradient of the calculated slope of magnesium is too large, suggesting an over-prediction of solid dissolution. This discrepancy is reflected in the calcium concentration over this range. Furthermore, simulated increases in iron concentration are lagging relative to experimental results. Thus, amorphous $Fe(OH)_3$ is not the stable iron-containing phase. Most likely, an amorphous phase consisting of iron, aluminium and silicon formed during these solution conditions.

Figure 3 shows the simulated phase compositions with respect to the degree of corrosion. Due to the smaller amount on silicon in Portland cement paste, the amount of the C-S-H phase is smaller in comparison to the blended cement paste. Furthermore, the chloride-containing Friedel's salt, AFm (Cl), is stable over a wider range for Portland cement paste whereby the silicious calcium aluminate phases are stable over a wider range in the blended cement paste.

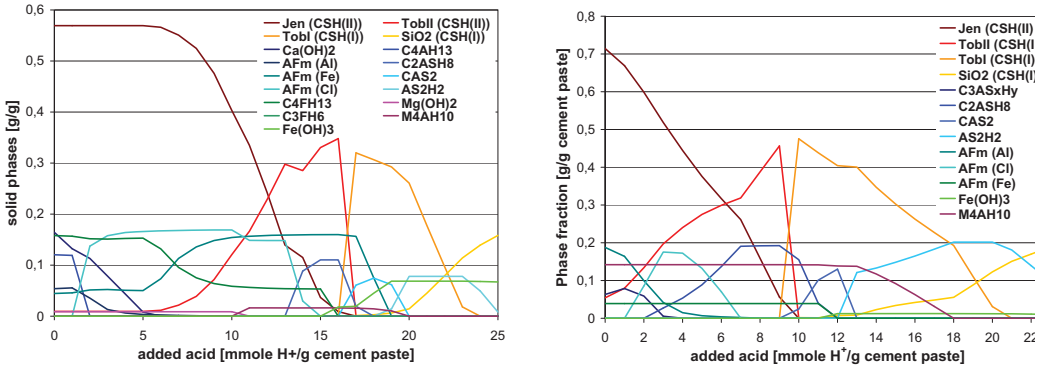

Figure 3: Composition of cement paste with respect to the corrosion state for Portland cement paste (left) and blast furnace slag blended cement paste (right).

Thus, the model reproduces the experimental results well for Portland cement paste. Considering the small knowledge about the phase formation processes in blended cement paste, the agreement between experimental and simulated results is satisfactory. Due to the open and extendible concept of CeSa's database, optimized data sets can be incorporated easily by the user.

3 AStra – Coupled heat, moisture and mass transport including chemical reactions and mechanical stress

AStra is a simulation tool for the two-dimensional coupled transport of heat, moisture, air and chemical substances including corrosion processes in both, inert and reactive porous materials.

If an attacking media (a solution) goes into a porous material and is transported through the pore system, material corrosion can take place. The corrosive process depends on moisture content, temperature and concentration of the dissolved particles. Furthermore, the art of the dissolved particles and the flow velocity have a significant influence on the kind and intensity of corrosion. In addition, dissolution and precipitation processes affect strongly the transport process through the change of the porosity and pore-blocking.

AStra consists of a user interface for pre- and post-processing and a computation module (solver), which contains the necessary algorithms for the simulation of corrosion processes. A detailed description of the solver can be found in Franke et. al [1].

By means of the user interface the geometry of the system is firstly defined, the system is discretised and materials, initial and boundary conditions are assigned to each element of the system. An exemplary construction is shown in figure 4. The different colors used in the graphics indicate the components of the construction: concrete in blue, brick in yellow and mortar in green.

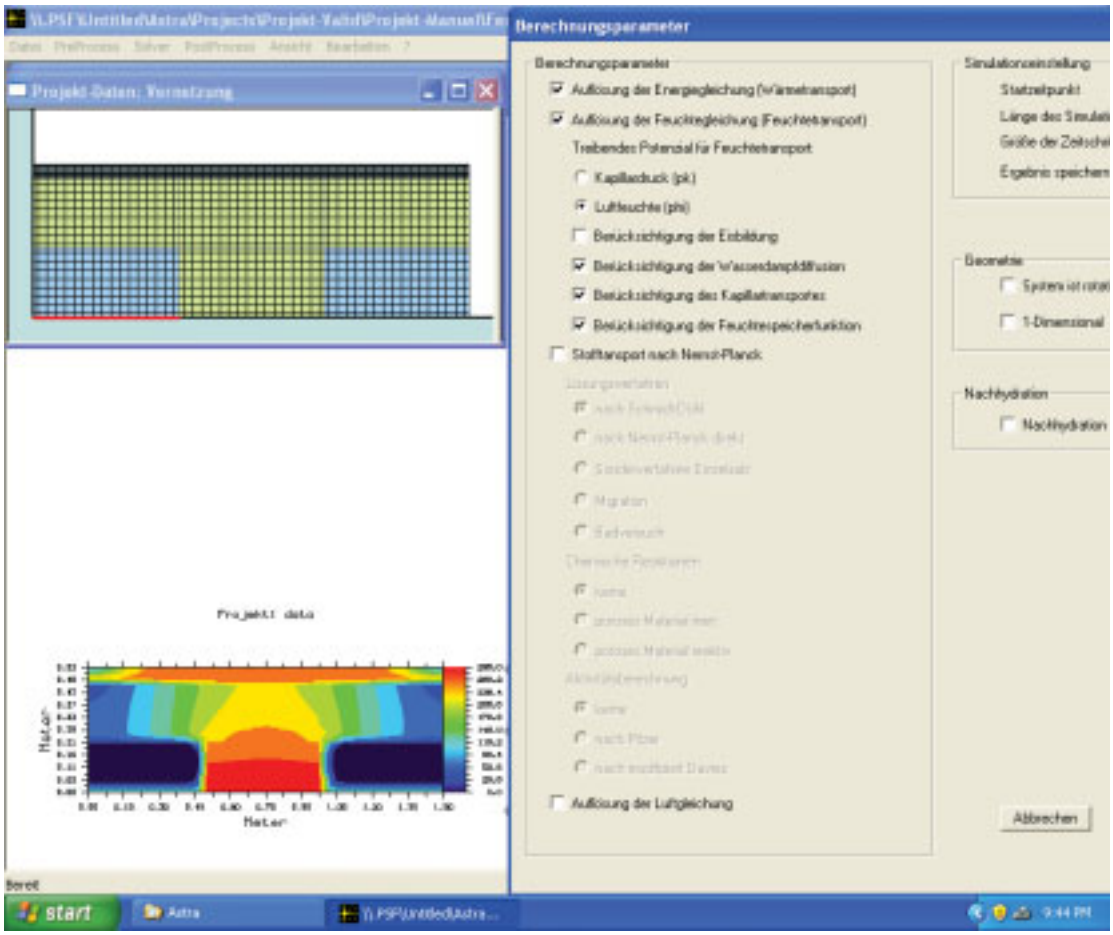

Figure 4: User interface of AStra with four selected windows: discretised system (left, top), moisture distribution at a selected time point (left, bottom) and input parameters for the simulation (right).

Figure 5 shows the main computation modules implemented in the solver of AStra.

The post-processing tool generates three kinds of diagrams for the results of the simulation, thus, for the computed state variables (temperature, water content, relative humidity, content of each chemical substance, crystallization pressure etc.):

- time-dependent course of each state variable in a selected element
- a two-dimensional projection of the distribution of each state variable at a selected point of time (see the moisture distribution in graphic on figure 4 on the bottom, left)
- three-dimensional distribution of each state variable at a selected point of time.

For the prediction of the corrosion of inert and reactive material, it is necessary to solve a system of coupled (non-linear) balance equations, which consists of a conservation equation for the energy and one for the mass of each substance (including water and air), whose content can change within the simulated period of time. This change can be induced either by transport, by a phase change or by chemical reactions.

Actually, it can be distinguished between degradation of reactive and of inert materials. In the former case, degradation takes place due to chemical reactions between the pore solution and the solids contained in the pores and the material compounds. Hereby, AStra uses the experiences and calculations in modeling chemical processes of CeSa.

Kinetics of phase changes of salt and water in porous materials have been already investigated, modeled [15][16] and implemented in AStra [1]. Damage in capillary inert porous materials can result from the action of the crystallization pressure that is required for a confined crystal in a pore to remain in a supersaturated solution. The resulting mechanical stress in capillary porous material has been intensively investigated experimentally in [17][18] and in current experiments.

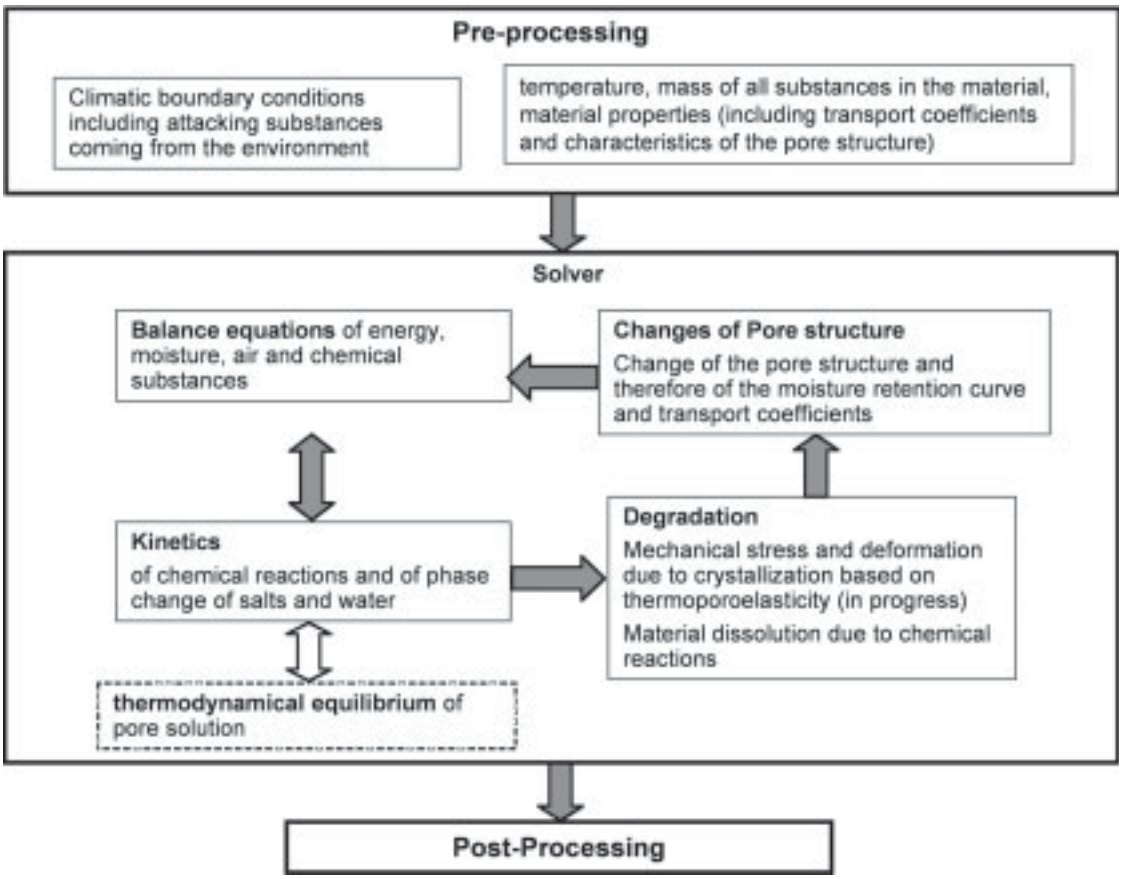

Figure 5: Main computation modules of the AStra-solver

A further important characteristic of the simulation tool AStra is the hysteresis model for the moisture retention curve of nano porous materials, as hardened cement paste and concrete, which has to be considered for a reliable prediction of the water content and finally, of the material corrosion. The IBP-method was developed to calculate the Scanning-isotherms that results from the hysteresis between adsorption and desorption isotherms [19] and implemented in AStra. Results in [19] show a very good agreement with experimental results.

3.1 Model for the time-dependent corrosion

The amount of each single species is determined by using the extended Nernst-Plank model [14]. Thus, the mass balance of each single chemical substance is set up and the resulting set of coupled equations is solved.

$$\frac{\partial\left(w \cdot c_i\right)}{\partial t} + S_i = \nabla\left(w \cdot D_{i,Diff} \cdot \nabla c_i + w \cdot D_{i,Mig} \cdot \frac{z_i \cdot F}{R \cdot T} \cdot c_i \cdot \nabla V - k \cdot c_i \cdot q_w \right) \tag{1}$$

where w is the water content, c the concentration, D_{Diff} and D_{Mig} the diffusion and migration transport coefficient, respectively, z the charge, R the gas constant, T the temperature, V the electrical potential, F the Faraday constant, k a retardation factor for the convective transport of the species, q_w the flux velocity of the solution and i the species index. Thus, the time-dependent change of the species molar mass is caused by the transport as well as by the sink/sources S_i due to chemical reactions and/or phase changes.

Three driving forces are considered for the transport of the species (right side of eq. 1). The first term gives the diffusive transport and includes the influence of the activity coefficient on the transport. The activity coefficients are calculated by means of either the theory of Pitzer or the modified model of Davies. The second term describes the migration. Thereby, charged substances (or, ions) are transported in order to provide for an electrical neutrality of the solution at each position. The transport potential „the electric field“ is defined by means of a Poisson equation, which is coupled with the mass balance and must be solved iteratively. The last term gives the advective transport term of each movable substance. Thus, the ions are carried by the liquid water flow. The water flow is obtained by solving the mass balance of water in the porous material. Here, the dissolved ions affect the density and the viscosity of the pore solution and with it, the moisture transport. A detailed description of the implemented Nernst-Plank model in AStra, as well as of the experimental investigation of the diffusive transport involved in the corrosion of cement-based materials can be found elsewhere [20][21].

Indeed, the equilibrium concentration of some species may be reached only after a long time and therefore a kinetics model is required. The sinks/sources S_i. i.e. the transformation rates of the involved species, are calculated with an enhanced version of CeSa, implemented in ASTra [11].

The following example shows the corrosion of a hardened cement paste specimen with the W/C-value of 0.6 that was exposed to nitric acid for 2000 hours. The pH-value was kept constant at 1.5 and the temperature was averaged at 25°C. After 10, 100 and 1000 hours the bath conditions were renewed.

The measured element distribution (given as mass fraction) after 2000 hours is shown in the left diagram of figure 6. The measured corrosion depth is c. 7 mm. On the surface in contact with the acid, the material consists mainly of SiO_2 and of Fe_2O_3, while all other elements are nearly leached by the acid attack as the abrupt increase of the CaO-concentration indicates. In the corroded zone, the mass fraction of SiO_2 decreases with increasing depth, while the mass of

fraction of Fe_2O_3 increases. The right diagram in figure 6 shows the results of the simulation performed with AStra. Although there are still discrepancies between simulation and experiment, the tendency of the computed and measured distributions of the oxide concentration is similar and even the abrupt increase of the CaO-concentration is obtained by simulation. The calculated corrosion depth is c. 9 mm.

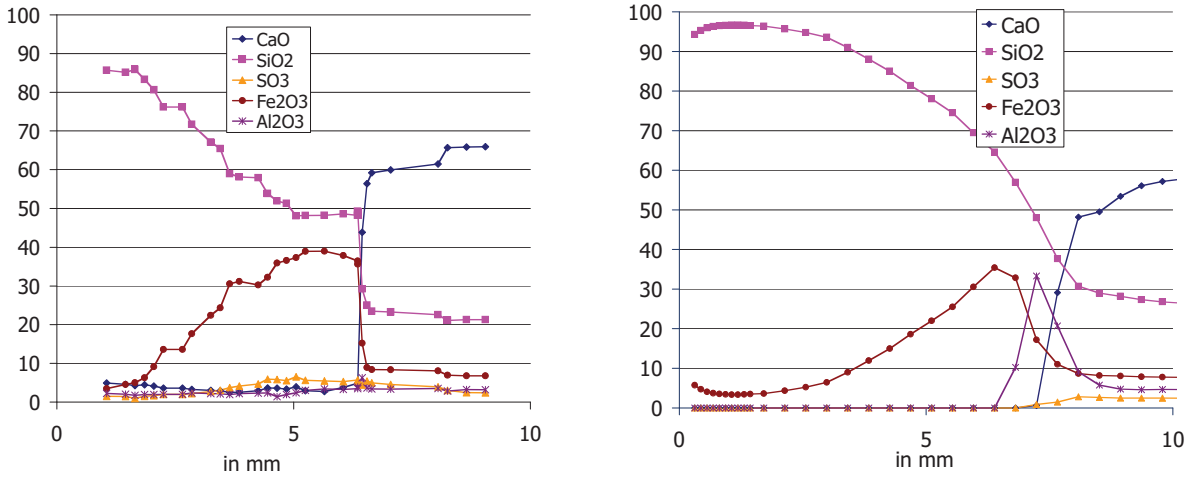

Figure 6: Time-dependent course of the weight loss of a hardened cement paste specimen during a nitric acid attack.

At the end of the experiment the predicted weight loss has increased up to 34%, while the measured value reaches c. 29%. Indeed, this result is good considering the complexity of the chemical reactions. Further experiments and simulations are discussed in [20][21].

3.2 Simulation of salt crystallization in capillary porous materials

According to Espinosa et al. [15], the rate of deliquescence, hydration/dehydration, dissolution and crystallization in capillary porous materials is given by:

$$S_i = K_i \left(U_i - 1\right)^{g_i} \quad \text{for } U_i > U_{i,start} \tag{2}$$

where K_i and g_i are kinetic parameters for each phase change and salt, also dependent on the porous material and $U_{i,start,}$ is the required thermodynamic supersaturation for nucleation to start. Thus, eq. (2) describes the rate of transformation considering that the difference of chemical potential between the start and the end phase, the supersaturation ratio, is the driving force for each phase change. The supersaturation is calculated in ASTra according to [7].

The crystallization pressure Δp in capillary porous materials is calculated according to [17][22][23]:

$$\Delta p = \frac{R \cdot T}{V_m} \cdot \ln U_a \tag{3}$$

where V_m is the molar volume of the precipitated salt. The simplest method to convert the microscopic crystallization pressure into an average stress in each representative elementary volume (REV) $\Delta\sigma_{REV}$ is to use the partial volume of salt crystals $\theta_{S,REV}$ in that REV:

$$\Delta\sigma_{REV} = \Delta p \cdot \theta_{S,REV} \tag{4}$$

Experiments carried out at the University of Munich [24] were provided for the validation of these models with ASTra. Sander sandstone samples (height=140 mm, edge=1.5 mm) were exposed controlled temperature and relative humidity in a climatic chamber. The relative humidity oscillated between 20 and 100 % and the temperature remained approximately constant at 28 °C. The conditions of six dry-wet-sequences are depicted in figure 7. The goal was to compare the hygric and mechanical behavior of salt-free and with sodium sulphate contaminated samples (1.3 weight per cent, i.e. 1.3 wt%).

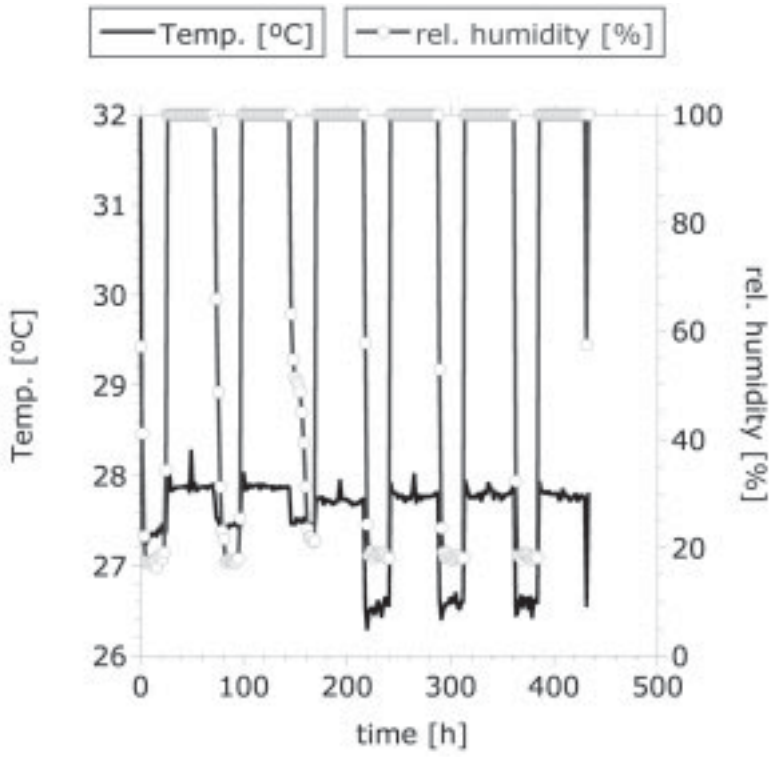

Figure 7: Measured relative humidity and temperature in the climatic chamber during six wetting-dry-cycles.

The time-dependent dilatation of the samples was recorded automatically, while the weight change of the samples was measured by means of an accompanying experiment exposed to the same climatic conditions.

Figure 8 shows the measured total water content (squares) in a sample with 1.3 wt% sodium sulfate, during various successive dry-wet-sequences, while the curve gives the moisture content in the sample computed with ASTra. Indeed, the presence of salts in the porous materials

affects significantly the water content, mainly due to the hygroscopic properties of the salt and to the precipitation of hydrates, but also through hydration and dehydration processes. Thus, the agreement between experiment and simulation is satisfactory.

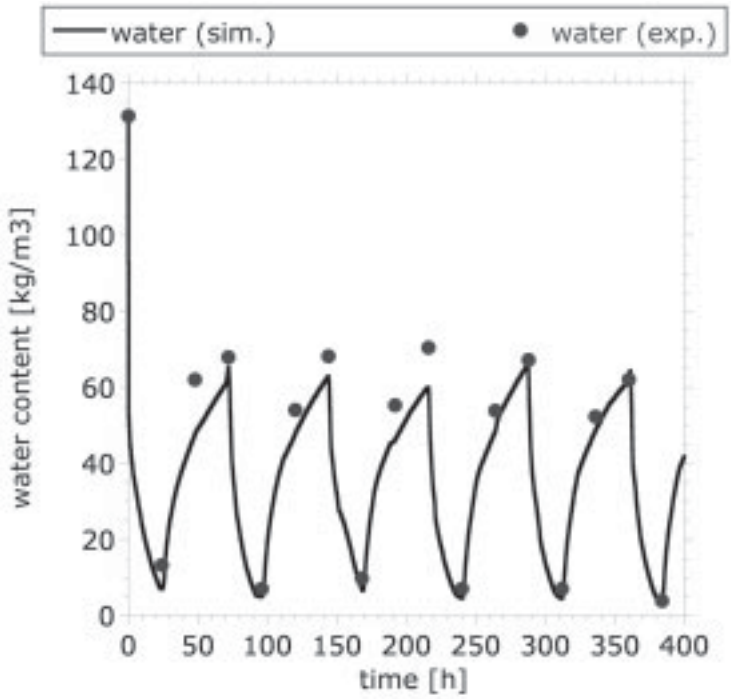

Figure 8: Measured and calculated water content with ASTra in a sample of sandstone with 1.3 wt% sodium sulphate.

The evolution of the total amount of mirabilite (line) and thenardite (dotted line) in the stone during one wet-dry-sequence is depicted in figure 9. Firstly the humidity drops from 100 to 20 % leading to the drying of the sample. This induces a supersaturation of the solution with respect to mirabilite that is the stable salt at 28 °C. When the start-supersaturation for crystallization is reached (about 1.8 [-]), mirabilite crystallizes and the confined mirabilite in the pores is likely to exert a pressure on the pore wall. If drying continues, mirabilite dehydrate and as a consequence, thenardite starts to appear slowly in the pores. The dehydration of mirabilite does not lead to a mechanical stress but it induces a relaxation of the system.

During the following wetting period, the water content increases, and consequently thenardite dissolves in the unsaturated solution. Then, the solution becomes supersaturated with respect to mirabilite, which precipitates as the required start-supersaturation is reached. A mechanical stress may also result from it.

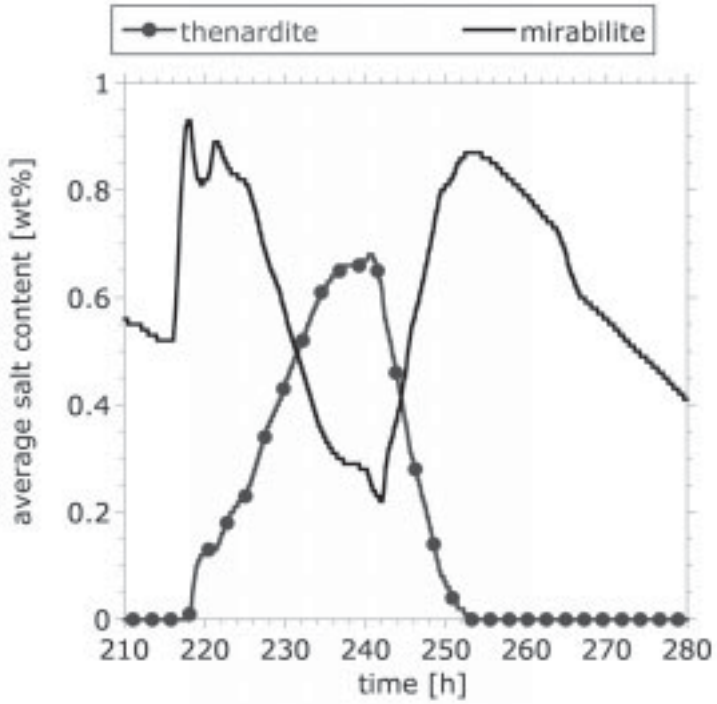

Figure 9: Average mass of mirabilite and thenardite in the sandstone sample during one wetting-cycle period predicted with ASTra.

During the following wetting period, the water content in the sample increases and the solution becomes unsaturated. Thus, mirabilite dissolves according to the corresponding kinetics. And simultaneously the deliquescence of mirabilite and with it an additional water uptake take place. Interestingly, both salts are present in the material at the same time and even in the same REV according to this kinetics model.

The computed mechanical stress $\Delta\sigma_{REV}$ induced by the crystallization pressure of the confined mirabilite crystals is depicted in figure 10. Each curve gives the computed time-dependent course of the stress in an elementary volume along the vertical axis. Indeed, the simulation clearly shows the more significant stress during the periods, in which mirabilite crystallizes and a relaxation of the system during the dehydration of mirabilite and formation of thenardite.
The result of the simulation shows an oscillating stress with a maximal value of 0.4 MPa. The tensile strength of this material is larger (about 2 MPa). However, a damage caused by fatigue might be expected after enough wet-dry-sequences or in samples with a higher salt content.

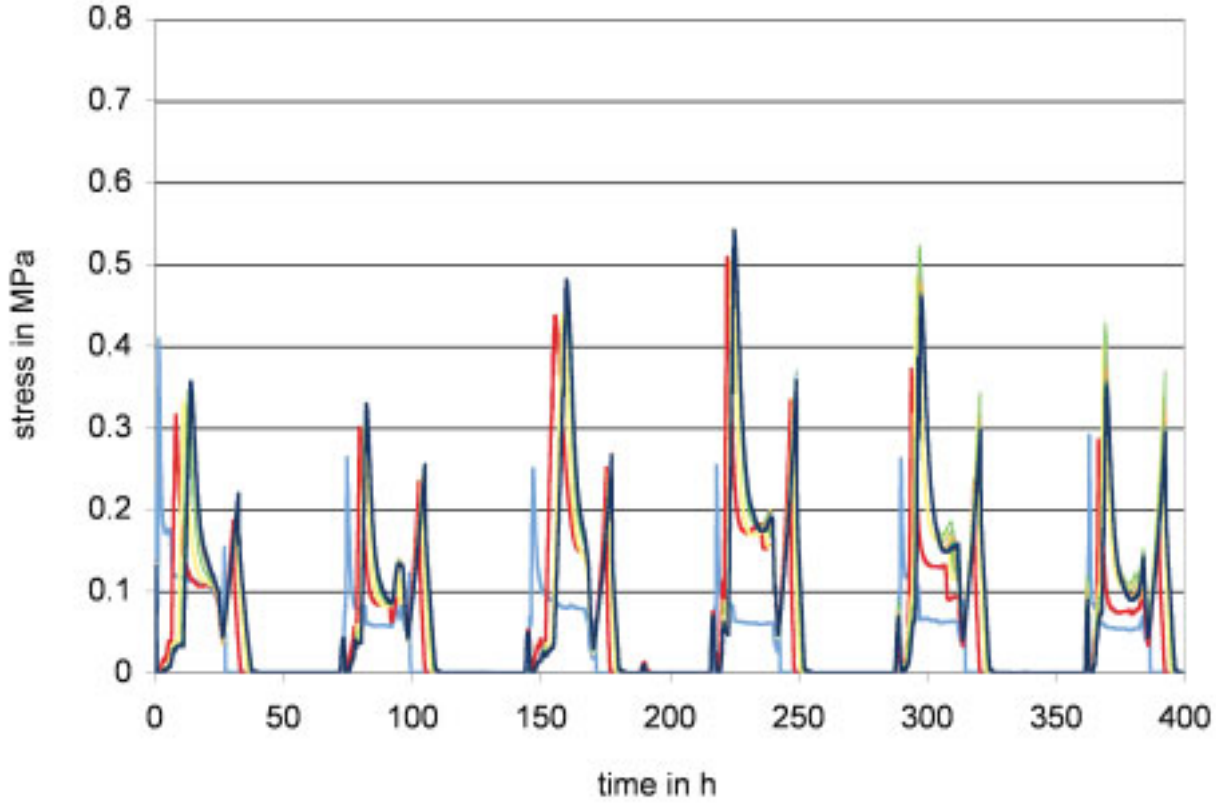

Figure 10: Predicted stresses in different REV along the vertical axis. The simulation was performed with the software AStra.

Figure 11 shows the measured strain of two similar samples (in blue), both with 1.3 wt% Na_2SO_4, reflecting the scattering of the measurement. The red curve gives the calculated length change on the surface and the green one gives the length change along the Y-axis. The computed strain consists of hygric strain and deformation caused by the action of the crystallization pressure and assuming an elastic behavior. The maximal value of the strain is about 900 µm/m, but only about 15 % of the total strain is caused by the crystallization pressure. Although there are still differences between simulation and experiment, this example demonstrates that a correct tendency of the mechanical stress caused by the crystallization pressure can be predicted with AStra.

Indeed, eq. (4) is a very rough estimation of the mechanical stress. In [25], a thermoporoelastic model has been deduced to describe the stress induced by crystallization and freezing considering the action of pore pressures (crystallization pressure, capillary pressure) to the porous material in alignment to Thermodynamics and the interaction between solution transport and pressure. This model has been implemented in AStra and applied to evaluate single crystallization experiments [26][27] leading to very satisfactory results.

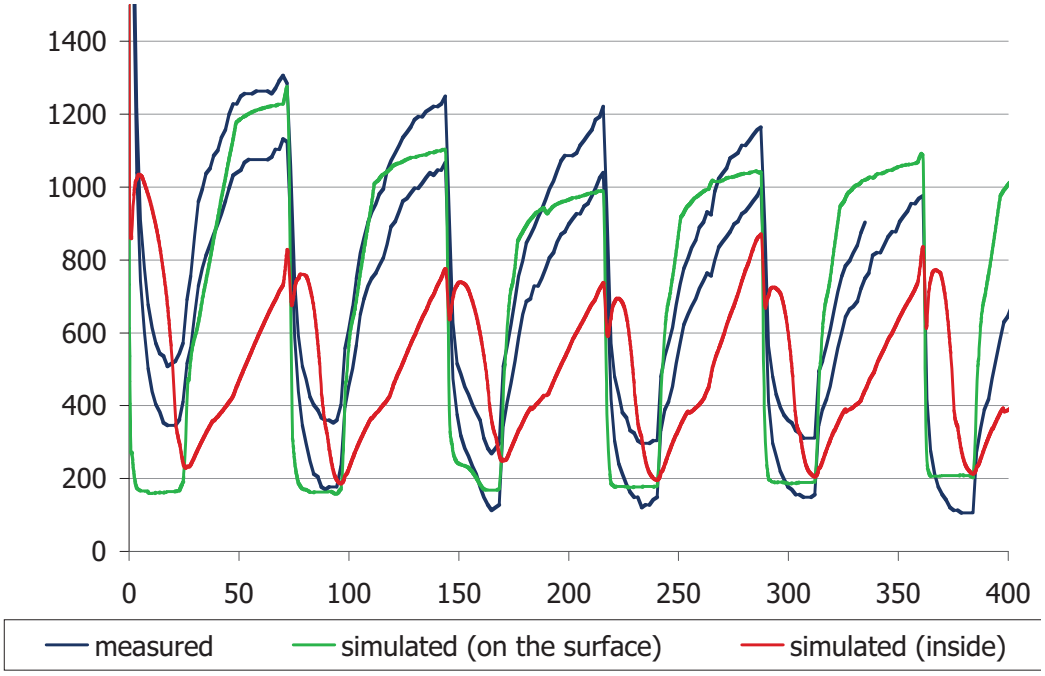

Figure 11: Measured length change of samples of sandstone [23] and predicted deformation on the surface of the specimen and along the Y-axis (center of the sample). Simulation performed with the software AStra.

4 Conclusions

CeSa and AStra are two engineering and research tools with rich functionality regarding the description of chemical and physical processes involving salts and cement-based materials.
AStra is an engineering level program designed for practical application in building engineering. It combines the simulation of a coupled transport of heat, moisture, air and chemical substances in the porous material with the calculation of changes of the material matrix and its pore structure due to chemical reactions and phase changes of the involved substances. In contrast to other transport programs, physic-chemical based models for sorption hysteresis, for kinetics of chemical reactions and phase change of salts have been implemented in AStra and therefore a satisfactory agreement between simulation and experiment is obtained and demonstrated in this paper with thee examples. In addition, mechanical stress caused by salt crystallization and frost and the resulting deformation of the material can be determined by means of a simplified model.

Moreover, AStra uses several functionalities of CeSa, as the computation of supersaturation ratio of each solid in the pore solution, thermodynamical equilibrium and density of the pore solution.

CeSa is a research-oriented tool with application for salt related problems and cement chemistry. The tool can be used to calculate thermodynamic properties and chemical equilibrium of ion mixtures. For cementitious materials CeSa includes the functionality of determining the chemi-

cal composition of such materials caused by partial or total hydration and the chemical equilibrium under the action of chemical attack. The design of the program allows extending the database to user-defined problems.

Recently, improved models for the mechanical stress caused by salt crystallization and frost have been developed on the bases of the thermoporoelasticity and the first simulations with AStra give very good results.

5 References

[1] Franke L., Espinosa R., Deckelmann G., Gunstmann C., Bandow D. AStra - Ein neues Berechnungswerkzeug zur Simulation des gekoppelten Wärme-, Feuchte- und Stofftransports einschließlich der Korrosionsprozesse in porösen Baustoffen. Bauphysik 3/2007, Nr. 607.

[2] Cerny R., Pavlik Z., Jirickova M., Fiala L., Madera J. Modeling coupled moisture and salt transport in porous materials, Proceedings of the seminar October 2006, Thermophysics 2006.

[3] Derluyn, H., Moonen, P., Carmeliet, J. 2008. Modelling of moisture and salt transport incorporating salt crystallization in porous media, Proceedings of CONMOD'08, Delft, The Netherlands, 28-30 May 2008.

[4] Nicolai, A. Modeling and Numerical Simulation of Salt Transport and Phase Transitions in Unsaturated Porous Building Materials, PhD. Thesis, Syracuse University 2007.

[5] Bear J. Dynamics of Fluids in Porous Materials, Dover Publications Inc. 1972.

[6] Pitzer, K.S.: Ion interaction approach: Theory and data correlation In: Pitzer, K.S.: Activity Coefficients in Electrolyte Solutions. CRC Press, Boca Raton, 1991, pp. 75-153.

[7] Steiger, M. Kiekbusch, J., Nicolai, A. An improved model incorporation Pitzer's equations for calculation of thermodynamic properties of pore solutions implemented into an efficient program code, doi:10.1016/j.conbuildmat.2007.04.020.

[8] Storey, S.H.; Van Zeggeren, F. Computation of Chemical Equilibrium Compositions. In: The Canadian Journal of Chemical Engineering 42, pp. 54-55, 1964.

[9] Storey, S.H.; Van Zeggeren, F. Computation of Chemical Equilibrium Compositions II. In: The Canadian Journal of Chemical Engineering 48, pp. 591-593, 1970.

[10] Schmidt-Döhl, F.: Ein Modell zur Berechnung von kombinierten chemischen Reaktions- und Transportprozessen und seine Anwendung auf die Korrosion mineralischer Baustoffe. Dissertation TU Braunschweig, 1996.

[11] Kiekbusch, J.: Säureangriff auf zementgebundene Materialien – Untersuchung und Modellierung des Zementstein-Säure-Systems und numerische Simulation der chemischen Reaktionen mittels Gibbs-Energie-Minimierung unter Berücksichtigung der Lösungskinetik. Dissertation TU Hamburg-Harburg, 2007.

[12] Kiekbusch, J., Schmidt, H., Franke, L. Chemical modelling of mineral and organic acid corrosion at Portland and blended cements using the calculation program CeSa, in progress.

[13] Kulik, D.A.; Kersten, M.: Aqueous Solubility Diagrams for Cementitious Waste Stabilization Systems: II, End-Member Stoichiometries of Ideal Calcium Silicate Hydrate Solid Solutions. In: Journal of the American Ceramic Society 84, pp. 3017-3026, 2001.

[14] Samson, E.; Marchand, J. : Numeric Solution of the extended Nernst-Planck Model, In: Journal of colloid and interface science 215, pp. 1 – 8, 1999.

[15] Espinosa R. M., Franke L., Deckelmann G. Phase changes of salts in porous materials, Construction and Building Materials, 22, 1758–1773, 2008.

[16] Hinniger A. Numerical Simulation of the Frost Resistance of Masonry, in “Simulation of Time Dependent Degradation of Porous Materials”, in print, Franke et al., Cuvillier Verlag, 2009.

[17] Espinosa R. M., Franke L., Deckelmann G. Model for the mechanical stress due to the salt crystallization in porous materials. Construction and Building Materials, 2007, 22, 1350–1367, 2008.

[18] R. M. Espinosa Marzal, G.W. Scherer. Study of sodium sulfate salts crystallization in limestone, Env. Geo. DOI 10.1007/s00254-008-1441-7.

[19] Espinosa R., Franke L., ‘Inkbottle Pore-Method: prediction of hygroscopic water content in hardened cement paste at variable climatic conditions‘, Cement and Concrete Research 36, pp. 1954-1968, 2006.

[20] Gunstmann, C. Rechnerische Simulation von Säurekorrosionsprozessen zementgebundener Materialien. Dissertation TU Hamburg-Harburg 2007.

[21] Gunstmann C., Franke L. Prediction by numerical simulation of corrosion of hardened cement paste and concrete caused by acid, in “Simulation of Time Dependent Degradation of Porous Materials”, in print, Franke et al., Cuvillier Verlag, 2009.

[22] Steiger, M. Crystal growth in porous materials I-: The crystallization pressure of large crystals, Journal of Crystal growth 282, pp. 455-469, 2005.

[23] Steiger, M. Crystal growth in porous materials II-: Influence of crystal size on the crystallization pressure, Journal of Crystal growth 282, pp. 470-481, 2005

[24] Rucker, P. Versuchsergebnisse zum Dehnungsverhalten salzdotierter Sandsteinproben. TU München, 2006, unpublished.

[25] Coussy O. Deformation and stress from in-pore drying-induced crystallization of salt. Journal of the Mechanics and Physics of Solids 54 1517-1547, 2006.

[26] R. M. Espinosa-Marzal, A. Hamilton, M. R. McNall, K. Whitaker, and G. W. Scherer. The chemomechanics of sodium sulfate crystallization in thenardite impregnated limestones during re-wetting, submitted to Journal of Geophysical Research - Earth Surface in November 2008.

[27] R. M. Espinosa-Marzal and G. W. Scherer. Crystallization pressure exerted by in-pore confined crystals, accepted by The Fourth Biot Conference on Poromechanics in December 2008.

Rosa M. Espinosa-Marzal *Dr.-Ing.*
Gernod Deckelmann *Dr.-Ing.*
Lutz Franke *Prof. Dr.-Ing.*

Institute of Building Materials, Physics and Chemistry of Buildings
Hamburg University of Technology, Germany

Model for the mechanical stress due to the salt crystallization in porous materials

Summary

This work deals with the experimental investigation and the mathematical modelling of crystal growth in porous materials and resulting mechanical stress due to the crystallization pressure.

Crystallization of different salts was induced in two bricks by cooling down at constant rate. As it was described in the first part of this project, the measured temperatures describe indirectly the crystallization and the dissolution rates and with it the time-dependent course of the supersaturation ratio of the pore solution. In addition, the sample strain was measured continuously during crystallization. The results show that the mechanical stress due to the salt crystallization depends on both salt and pore structure.

A model for the mechanical stress due to crystallization pressure was developed based on crystal growth kinetics considering the influence of pores with different size (called pore classes). The model considers that nucleation and crystal growth take place in large and small pores simultaneously and calculates the distribution of salt crystals in pores of different size and the resulting load surface of the crystals under stress. The estimation of two model parameters (the number of pore classes and the amount of nuclei in the smallest pore) is necessary for the proposed computation model.

It is assumed that the mechanical stress is caused by the crystallization pressure that crystals exert on the pore wall when growing in a supersaturated solution. Thus, the crystallization pressure is calculated as a function of the solution supersaturation. It was demonstrated that the crystallization pressure can reach high values in a non-equilibrium state, even with a lack of small pores.

The results show that the material strain owing to the salt crystallization can be approximately estimated in the selected bricks by means of this new model. An improvement of the model is necessary for a better prediction of the mechanical stress, e.g. at drying conditions or for the simulation of the re-allocation of salt crystals from pores under stress into stress-free pores.
In this work, the required properties of the salt solution are calculated using a thermodynamic model according to Steiger [15], which is based on the Pitzer model.

Keywords: *salt crystallization, supersaturation ratio, crystal growth, crystallization pressure.*

1 Introduction and backgrounds

Worldwide the destruction of valuable building materials causes substantial economic damages. A significant part of the damage is due to the salt crystallization in the material pores. Forecast models, i.e. used in simulation programs are necessary to avoid or to limit the material damages.

According to [1] [14][17] a salt crystal can exert a pressure on the pore wall due to:

- the linear crystal growth from a supersaturated solution,
- the hydrostatic pressure owing to the increase of the total volume consisting of solution and salt crystals compared to the volume of the supersaturated solution before crystallization occurs,
- the hydration pressure caused by the increase of the salt volume induced by hydration.

In practice, the pore system is partially filled with solution. Therefore, the hydrostatic pressure due to the volume increase after salt precipitation (max. 1% according to [16]) can be simply released by pushing the solution into the empty pores. In previous works the hydration mechanism was used to explain the severe material damage induced by mirabilite. However, in several recent works the hydration of thenardite to mirabilite could not be observed (e.g. [1][3][9][12]). Instead of this, dissolution of thenardite followed by precipitation of mirabilite (and thenardite in small pores) takes place. Thereby, the linear crystal growth pressure (generally known as crystallization pressure) is the main reason for the damage of building materials under normal climatic conditions.

Correns and Steiborn [2] derived an equation for the maximum stress as a function of the supersaturation of the solution. They defined the supersaturation of the solution as the quotient between the solute concentration in the supersaturated and in the saturated solution. This implies that the influence of the ion activity coefficients and of the water activity on the supersaturation are negligible, which is false from thermodynamic point of view.

Everett [4] considered the effects of crystal size on crystallization pressure. Thermodynamics of salt crystals says that large crystals are more stable than small crystals since they have a smaller chemical potential. Based on this fact, this model assumes that crystallization must take place firstly in the large pores.

According to the Everett model, when a large pore is completely filled, a salt crystal can continue growing in this pore if the neighbour pores (which are filled with the same solution) are small enough. In this case, the crystal growth causes a crystallization pressure, which can be calculated with the radii of the large and the neighbour small pores.

Based on thermodynamics, it follows that an equilibrium pressure Δp is necessary for the stability of a crystal in a supersaturated solution [5][22][18], which also means, the solubility of a salt crystal under stress is higher than the one of a stress-free crystal.

According to Steiger [23], the crystallization pressure Δp is given by:

$$\Delta p = \frac{R \cdot T}{V_m} \cdot \ln U_a - \gamma_{cl} \cdot \frac{dA}{dV} \qquad (1)$$

V_m =mol volume of crystal
A =interface between crystal and solution
V =crystal volume
γ_{cl}=crystal-solution surface energy

The first term in this equation says that the crystallization pressure depends on the supersaturation ratio. The influence of the crystal size (given by the second term) can be neglected if crystals are larger than 0.1 µm.

In a non-equilibrium state, eq. 1 indicates that a high mechanical stress may arise due to high supersaturation ratio even if there is a lack of small pores. Hereby, if a local large supersaturation ratio cannot be reduced enough rapidly in the small pores by way of ion diffusion or solution transport, the resulting mechanical stress can become considerable and even cause a material damage.

2 Description of experiments

The following building materials were selected for the investigation of the mechanical stress induced by crystallization of salts in porous materials:

- Brick A with a total porosity equal to 30 ± 2 Vol.-%. The pore size distribution (measured by MIP) has two maxima at 10 µm and at 0.7±0.1 µm. Its pore surface area is equal to 0.6 m²/g. The tortuosity of the pore structure of brick A measured by MIP is equal to 6 [-].
- Brick B with a total porosity equal to 33 ± 2 Vol.-%. The pore size distribution (measured by MIP) has only one maximum at 0.8±0.1 µm. Its pore surface area is equal to 5 m²/g. The tortuosity of the pore structure of brick B is equal to 35 [-].

The porosity of brick B is clearly finer than the one of brick A. 13 % of the total porosity of brick B consists of pores smaller than 0.1 µm, while in case of brick A only 3 % of the pores are smaller than 0.1 µm. The mechanical properties are given in the next table:

	Elasticity moduli in MPa	thermal expansion coefficient in [µm/m·K]	tensile strength in MPa
Brick A	6700	13.5	1.95
Brick B	5000	6	1.01

Table 1: Mechanical properties of brick A and B (average values)

For the salt crystals it was assumed an elasticity moduli equal to 15000 MPa and a thermal expansion coefficient equal to 38 [µm/m·K].

2.1 Difference temperature and strain measurements during crystallization

Kinetics of salt crystallization in the material pores as well as the resulting mechanical stress were investigated experimentally by means of a self-constructed device for measuring temperature and strain differences simultaneously.

A sample (cube, l=3 cm) was impregnated with salt solution at a known molality m_0, sealed and put in a container (the reaction container), which is filled with a mixture of water and glycerine. Glycerine is used to avoid the formation of ice at low temperatures. A similar sealed sample was impregnated with water (water content $m_{w,0}$) and located in a reference container. Both containers were placed in a water bath whose temperature was controlled during the experiment. Indeed, the bath is also filled with a mixture of water and glycerine.

Firstly, the samples were cooled down from a maximal temperature to 0 °C at constant cooling rate (0.1 K/min to 0.01 K/min). Then, the temperature was maintained constant at 0°C for at least 10 hours. Afterwards the samples were warmed up to the maximal temperature at a constant rate and finally the temperature was maintained constant about 10 hours. Each temperature cycle was repeated at least for two times with each sample.The maximal temperature depends on the used salt and on its concentration. It was varied between 40 °C and 60 °C.

The purpose of this experiment is to cause a supersaturation of the salt solution by cooling down the sample and consequently the limitation of this analysis is that only salts, whose solubility depends on temperature, can be evaluated.

It must be pointed out that this evaluation method for the crystalline salt content induces a maximal error of $\pm$0.05 g. The maximal error is reached at constant temperature (0 °C). Hereby, the error involves a very pronounced variation of the supersaturation ratio (about $\pm$0.5 [-]). Thus, the supersaturation ratio calculated at 0 °C, when crystallization has taken place, is submitted to a significant error.

Four strain gages were stuck on the sample faces with a special water-resistant adhesive in order to measure a two-directional strain. The sample strain is measured continuously during the temperature cycles and registered in a data logger. Thus, information about the mechanical stress is obtained continuously during the crystallization.

Unfortunately, salt crystals often grew against the DMS during the measurements causing their damage. On this account, several experimental results could not be evaluated and experiments had often to be repeated.

3 Experimental results

The next examples show the measured strain induced by cooling down a sample impregnated with potassium nitrate as well as the reference strain. In [7] it was reported about the results obtained for other salts.

The reference strain is only caused by the temperature change (thermal strain). The reaction strain is caused additionally by the crystallization pressure. The influence of the salt crystals on the total thermal expansion coefficient of the sample is calculated by using the Nielsen-Larsen model [10]. Hereby, the resulting thermal expansion coefficient depends on porosity, salt content as well as on elasticity moduli and thermal expansion coefficients of both salt and salt-free porous material. The measured strain of the reference sample (impregnated with water) gives the thermal expansion coefficient of the salt-free porous material.

A sample of brick A impregnated with potassium nitrate solution (molality=6.32 mol/kg) was cooled down at a constant rate equal to 0.1 K/min from 50 °C to 0°C. The next diagram shows the time-dependent course of the crystalline salt content (right y-axis), determined by means of the evaluation method described in the first part of this work and [6]. The measured reaction and reference strains are depicted in the same diagram (left y-axis).

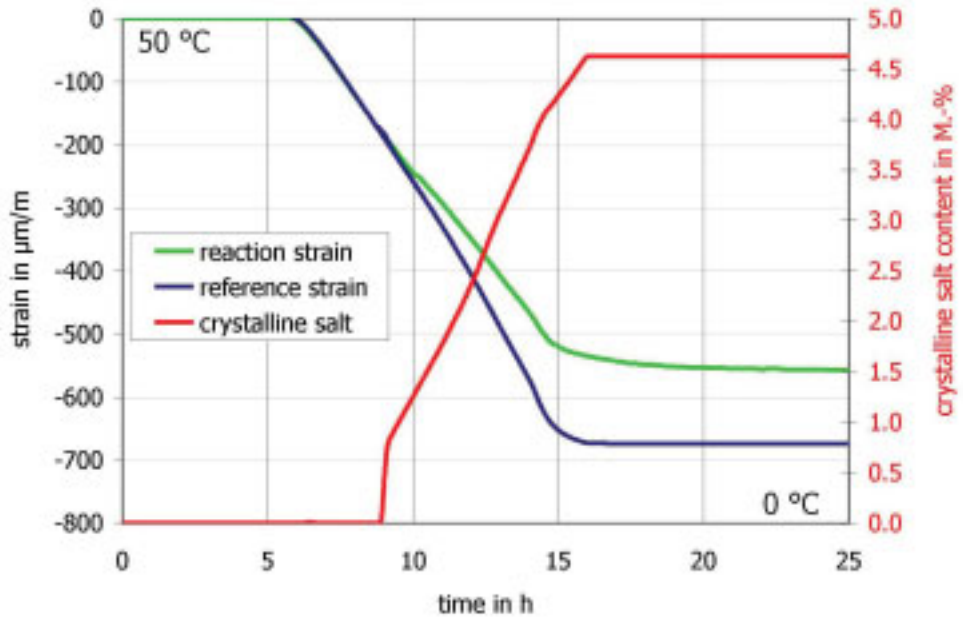

Figure 1: Time-dependent courses of the measured reaction and reference strains of brick A (left y-axis) and of the crystallized KNO3-amount (right y-axis) by cooling down from 50 °C to 0 °C at a constant cooling-rate of 0.1 K/min.

The crystallization of KNO_3 in brick A begins at 34.7 °C. Therefore, the necessary supersaturation ratio for the crystallization of KNO_3 to start in brick A is 1.135 [-] (calculated with m=6.32 mol/kg, ϑ=34.7 °C). Figure 1 points that the crystallization proceeds almost simultaneously with the temperature decrease up to 0°C. It takes approximately 7 hours to be completed. At the end of the crystallization process, at (0.27 °C), the pore solution is nearly saturated.

The corresponding course of the *calculated* supersaturation ratio as well as the difference between reaction and reference strain are shown in figure 2. The strain difference arises just after crystallization begins and can only be induced by the crystallization pressure.

The strain difference is visible. Its maximal value reaches 125 µm/m (related to an absolute strain of 700 µm/m). Thus, the mechanical stress during the crystallization of KNO3 in brick A is significant. At the end of the crystallization process, the residual strain difference is equal to about 100 µm/m, thus crystal are still exerting a pressure on the pore wall, which indicates that the supersaturation of the thin film between crystals an pore wall must be higher than the supersaturation of the pore solution.

The mechanical stress during the crystallization of KNO_3 in brick B is also significant (see figure 3). The maximal strain difference is about 400 µm/m. The start supersaturation ratio is equal to 1.038[1]. That means, the pore solution is nearly saturated, as the crystallization of KNO_3 in brick B begins.

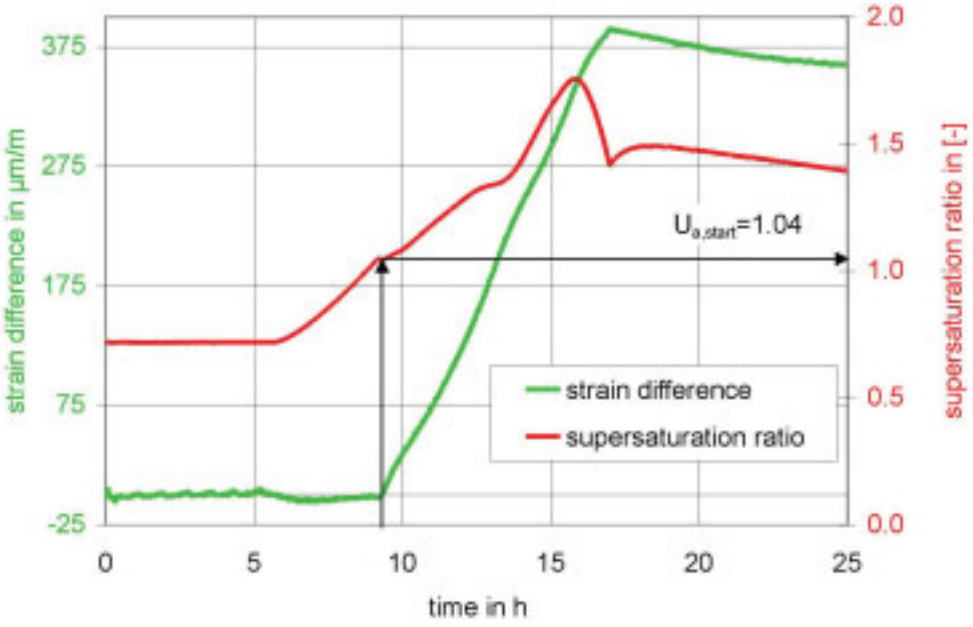

Figure 2: Measured strain difference of brick A due to the crystallization of KNO_3 in its material pores (left y-axis) and calculated supersaturation ratio of the pore solution (right y-axis).

[1] Supersaturation ratio calculated with m=7 mol/kg, ϑ=41.91 °C

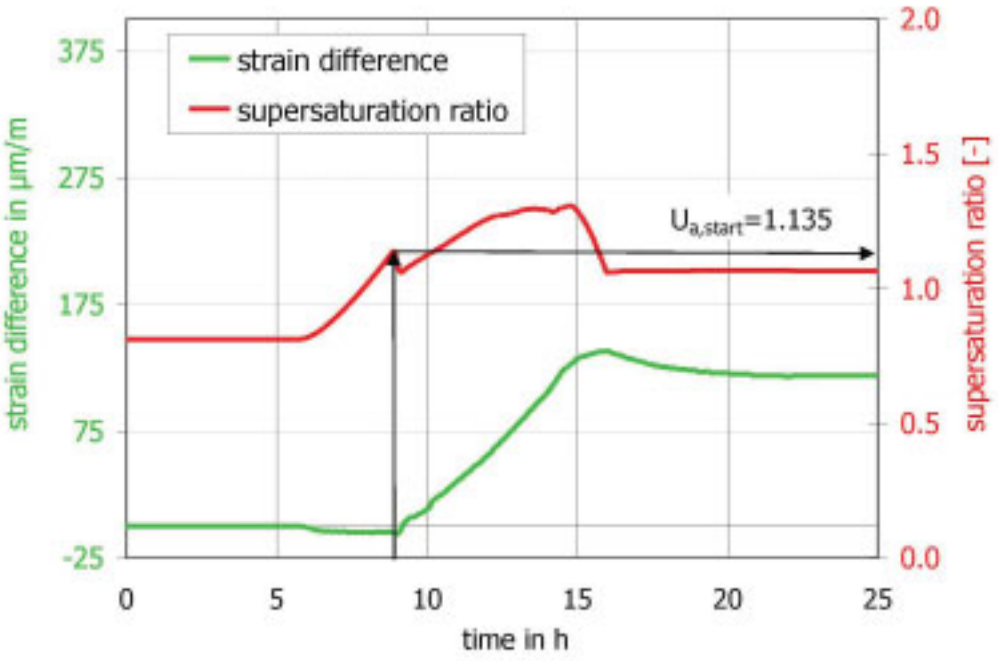

Figure 3: Measured strain difference of brick B due to the crystallization of KNO_3 in its material pores (left y-axis) and calculated supersaturation ratio of the pore solution (right y-axis).

Taking into account, that crystallization kinetics depends strongly on the supersaturation ratio [6], the crystallization of KNO_3 in brick B proceeds firstly more slowly than in brick A because of the low start-supersaturation. Since a simultaneously cooling-down is taking place at the same time, the supersaturation becomes higher in brick B than in brick A. On this account, a major crystallization pressure is expected in brick B.

A very slowly relaxation, i.e. a decrease of the strain of brick B, is observed up to 17 hours, which is partially caused by the decrease of the supersaturation ratio during crystallization proceeding at constant temperature of 0 ºC. Moreover, if the solution is supersaturated, the non-stressed surface of the crystals will continue growing and consequently the supersaturation will decrease. Therefore, the stressed-surface of crystals is not stable any more and they dissolve leading to a decrease of the crystallization pressure. In addition, small crystals are not stable if the supersaturation decreases and they dissolve to precipitate in larger pores. Thus, a re-distribution of crystals from small to larger pores takes place, since the system tends to reach equilibrium. This involves also a relaxation of the stress. If the re-distribution takes place slowly because of the slowly ion diffusion from pore to pore a high transient stress can be expected for a long time, as it seems in case of brick B. In equilibrium (after waiting enough time), the pores are expected to be filled with a saturated solution at 0 ºC and unstressed crystals.

Afterwards the sample was heated up to 60 °C and the salt crystals dissolved completely in the solution. The residual strain after the first temperature cycle can be neglected (16 µm/m). However, after two temperature cycles a progressive increase of the residual strain was measured. This points an irreparable damage of the brick B, due to the formation of cracks as caused by fatigue, which could be observed at the end of the experiment.

The experiments were repeated with different samples and the results are reproducible.

4 Crystal growth model

The mechanical stress during the investigated cooling-induced crystallization in a porous material is due to the crystallization pressure Δp, which is exerted by a crystal on the pore wall when it is growing from a supersaturated solution. In a porous material there are numerous crystals that grow at the same time and exert a pressure. Thus, by means of developed approach, the total (macroscopic) mechanical stress of the porous material is estimated by considering a distribution of crystals in the pores and calculating the load surface and the crystallization pressure of each of them.

For it, the system is discretised into small representative elementary volumes (REV). The representative length of the REV must be larger than the maximal pore size ($l_{REV}>R_{max}$). The time-dependent temperature, water content, crystalline salt content, solution concentration and supersaturation ratio must be known in each REV. A detailed description of the model can be found in [6].

The simplest assumption is to consider a pore model consisting of cylindrical pores. Thus, the real pore structure is simplified by considering a discrete number of pore sizes, called pore classes. Each pore class is characterised by its radius R_i (R_1, R_2, R_3, …R_N). It will be assumed that the porous material is isotropic and each of its pores is located along one of the three Cartesian directions (x,y,z).

The pore size distribution of the material is measured by means of the mercury porosimetry. The number of pore classes n_{Pk} is given by the number of measured pore radius R_i. The corresponding volume of each pore class $V_P(i)$ is given by the measured pore size distribution and with it, the length and the amount of pores $N_P(i)$ of each pore class.

If the solution is supersaturated, nuclei form in the solution. From the overall excess free energy of solution and crystal results a minimal nucleus size (called critical size r_{cr}). Nuclei, which are smaller are unstable and dissolve. Larger nuclei are stable and go on growing up. In order to simplify the mathematical model, we choose a spherical geometry for the crystals. The maximal amount of nuclei N_s is obtained assuming an initial radius equal to the critical radius r_{cr}.

The nucleation in the porous material is heterogeneous, since the pore wall can be regarded as a contaminant or foreign body in the solution. Therefore, a uniform distribution of nucleation sites on the pore surface is assumed. On this account, the number of nuclei in each pore class

is proportional to the pore surface of the considered pore class and the nuclei are allocated uniformly in each pore class.

The increase of salt content Δm_s which is given by the measured or computed crystallization rate [6] is distributed between the existent nuclei or salt crystals proportional to their crystal surface. A spherical growth will be considered before either a contact between nuclei or between nuclei and pore wall takes place. In this case, the increase of salt content is distributed uniformly between all crystals: ($\Delta m_s/N_s$) and the new crystal radius can be calculated from a mass balance.

Considering this model for the crystal growth, nucleation and crystal growth take place equally in pores of different size. However, the contact between crystal and pore wall occurs firstly in the small pores. The pore wall avoids a radial growth and the crystals can only keep on growing in axial direction adjusting their geometry to the pore geometry. Simultaneously, crystals exert a pressure in the supersaturated solution Δp that can be calculated by means of (1).

There may be more than one crystal placed in a pore, so that each crystal can come into contact with adjoining crystals and convert into a single growing crystal (cylindrical crystals with hemispherical ends, also called here “cigar-geometry”). Thus, the described crystal growth model is a rough approximation of the real mechanisms but it yields to satisfactory results, as it will be shown in section 5.

The value of the contact area between crystal and pore wall is necessary for the calculation of the resulting mechanical stress. Evidently, the contact area $A_{\Delta p}$ depends on both, crystal and pore geometry. Taking into account the geometry of a cigar-crystal, it follows for the contact length $d_s(i)$ and the loading surface $A_{\Delta p}(i)$, i.e., the contact area between crystals and pore surface in the pore class i:

$$A_{\Delta p}(i) = d_s(i) \cdot 2 \cdot \pi \cdot R_P(i) \cdot N_s(i) \text{ mit } d_s(i) = \frac{\Delta m_s(i) / \rho_c - 4/3 \cdot \pi \cdot R_P^3(i)}{\pi \cdot R_P^2(i)} \tag{2}$$

This calculation proceeds iterative, since the amount of salt Δm_s in each pore class cannot be calculated a priori if a contact between crystal and pore wall takes place. Two model parameters are required: the number of pore classes and the amount of nuclei in the smallest pore class.

From the microscopic distribution of the crystallization pressure to a macroscopic mechanical stress

By means of the previous assumptions, both the distribution of crystallization pressure and of loading surface are computed in each REV.

Firstly, crystals exert a pressure on the pore walls of the smallest pore classes. Progressively, larger pore classes are filled with crystals, which exert a pressure on the pore wall. The highest

radius of pores submitted to crystallization pressure depends on the amount of salt in each pore class. However, some of the exerted forces compensate themselves inside the material. Thus, it is necessary to determine a resulting *macroscopic* stress from the *microscopic* distribution of crystallization pressure in the discretised porosity.

Hereby, a uniform **section force** in the REV is deduced, from which the macroscopic tensile stress results. The goal is to obtain an adequate material section-cross. The method developed in [9] was used for this purpose. Thus, the macroscopic stress results from the addition of the crystallization pressure that acts in the pores located in a defined volume. The section width (t) was assumed as the diameter of the largest pore class filled with salt crystals under stress. The total section force or load F within t and perpendicular to the section is given by:

$$F = t / L_{REV} \cdot \sum_{k} \Delta p_k \cdot 2 \cdot R_k \cdot d_k \cdot N_s(k) \tag{3}$$

where k is the index of the pore classes filled with crystals under stress located in the selected volume, R_k the radius of the pore class, d_k the length of the load surface between crystal and pore and $N_s(k)$ the number of crystals in each pore class k. The corresponding fraction of pores, which are located in this selected volume is obtained by considering an isotropic REV, thus multiplying by t/L_{REV}.

Finally, the resulting mechanical tensile stress follows:

$$\sigma = \frac{F}{a \cdot b} = \frac{F}{L_{REV}^{\,2}} \tag{4}$$

With a, b the dimensions of the REV, perpendicular to t. This assumption leads to satisfactory results as it will be shown in the next section.

5 Simulation of the mechanical stress during the crystallization in porous materials by means of the new model

The new model was implemented in a simulation program (in C++ programming language). The time-dependent courses of water content, crystalline salt content, solution concentration, sample temperature and supersaturation ratio of the pore solution are the necessary input data for the simulation. In [6] it was explained how to deduce them from the DTS-experiments.

For the numerical simulation, the material samples were discretised in cubical cells (edge length=1μm). A uniform distribution of salt concentration, water and temperature in the sealed sample as well as isotropic properties were assumed. Thus, the simulation of the material strain during the described temperature changes can be carried out in a cell and in one of the three Cartesian directions.

The time-dependent course of the material strain due to the crystallization pressure is determined from the macroscopic stress by means of the elasticity modulus. Actually, the elasticity

modulus may decrease because of micro cracking induced by the crystallization pressure and may be influenced by the crystals in the pores but these changes have been neglected as yet.

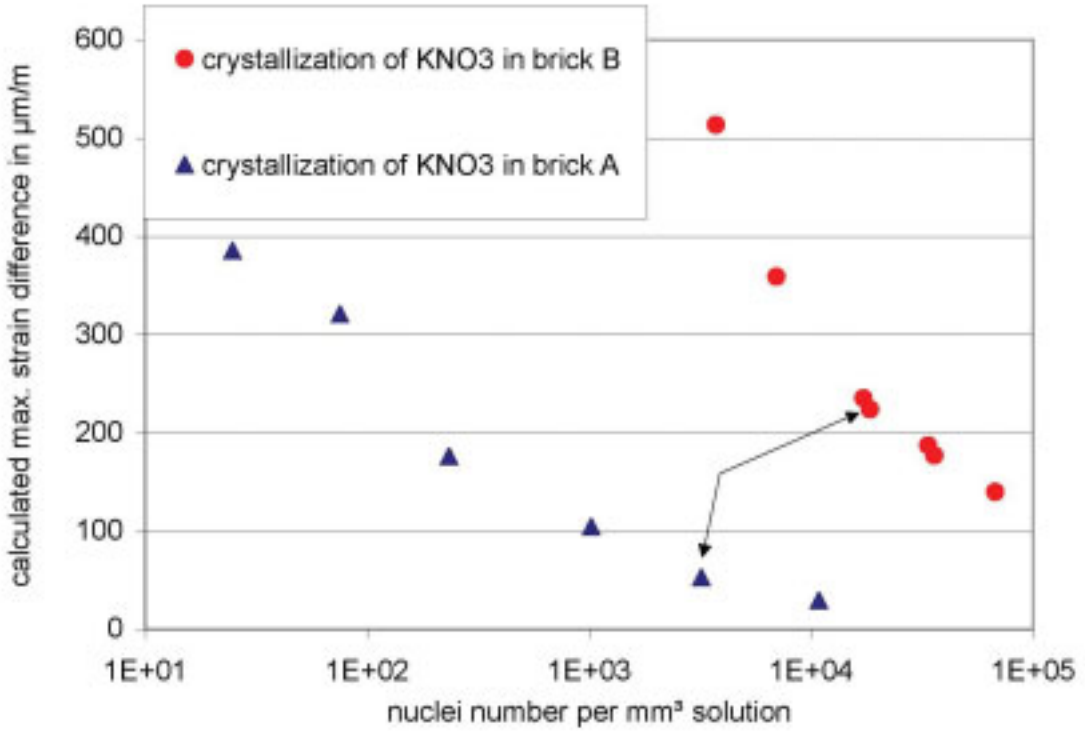

Figure 4: Calculated maximal strain induced by the crystallization of KNO_3 in the pores of bricks A and B by assuming different amounts of nuclei.

Actually, the influence of the total amount of nuclei on the resulting mechanical stress is significant. Figure 4 shows the maximal strain during the crystallization of KNO_3 in brick A and B calculated with different amounts of nuclei N_s (x-axis in logarithmic scale). The arrows in the diagram point the best approximation between simulation and measurement.

KNO3 starts in both bricks at a similar supersaturation ratio (1.1 [-] in brick A and 1.03 [-]) in brick B). The best results were obtained by considering a larger amount of nuclei in brick B than in brick A. This seems to be correct, since the pore surface of brick B (5 m^2/g) is larger than the one of brick A (0.6 m^2/g), whereby a larger amount of nuclei is expected to form in the pores of brick B.

The diagram clearly accentuates the necessity for a correct estimation of the amount of nuclei. Therefore, the goal of a future work shall be the experimental investigation of the nucleation on mineral surfaces.

5.1 Crystallization of KNO_3 in brick A

The time-dependent course of the strain of brick A by cooling down the sample with simultaneous crystallization of KNO_3 was computed. The diagram shows the results when assuming 63 pore classes and 5 nuclei in the pore class with the smallest pore surface. That means that 155 nuclei per mm^3 solution forms at 35 °C.

All pore classes, whose size is smaller than 3.25 µm, are subjected to the action of the crystallization pressure. Crystals placed in larger pores are stress-free.

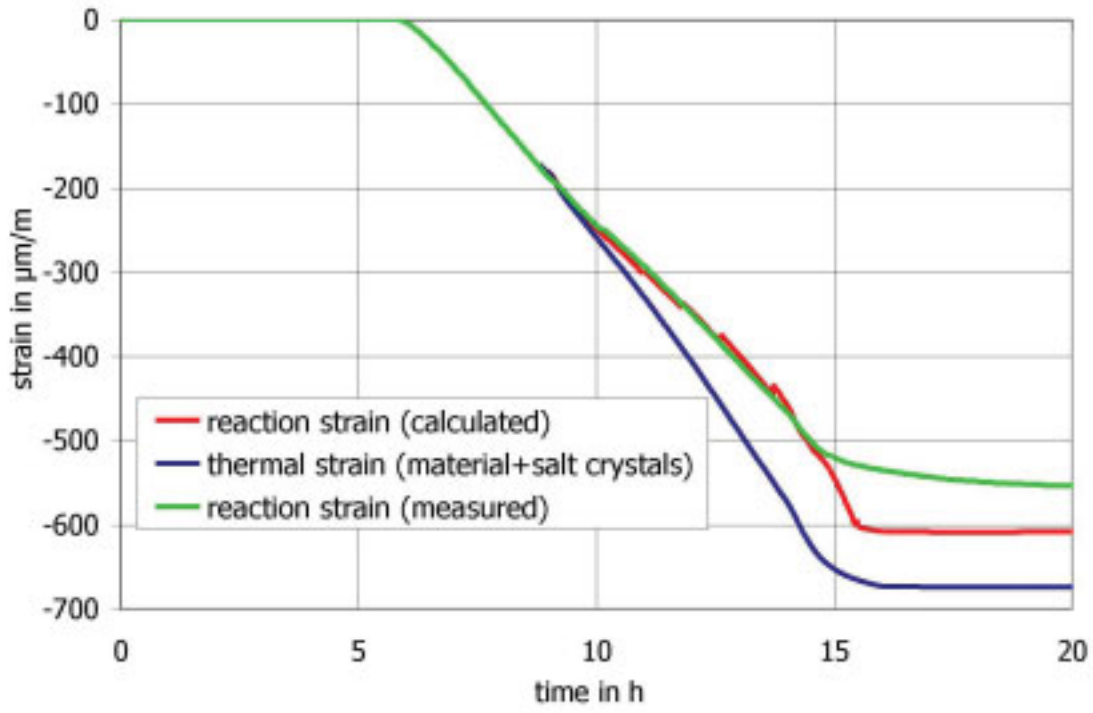

Figure 5: Computed and measured reaction strains of brick A induced by cooling down from 50 to 0 ºC and by the simultaneous crystallization of KNO_3 in its pores.

The maximal crystallization pressure (at a maximal supersaturation ratio equal to 1.27) reaches 10.7 MPa, according to:

$$\Delta p = \frac{R \cdot T}{V_m} \cdot \ln\left(U_{a,\max}\right) = \frac{8.314 \cdot (11.2 + 273.15)}{4.75 \cdot 10^{-5}} \cdot \ln\left(1.27\right) = 10.7 \text{ MPa}$$

However, the maximal macroscopic stress (in each direction) obtained by means of the distribution of crystals in the pore system and the contact area between crystals and pore wall is smaller than the tensile strength of the material, (σ^{calc}_{max}=0.812 MPa, (σ_{exp}= 1.95 MPa,). This stress causes a visible difference between the reaction and the reference (or thermal) strain. The correlation between calculated and measured strain is satisfactory.

5.2 Crystallization of KNO_3 in brick B

Figure 6 shows the measured and computed reaction strains as well as the thermal (or reference) strain of brick B induced by cooling down and by the simultaneous crystallization of KNO_3 in its pores.

As it was shown in figure 4, several simulations were done by changing the model parameters: the number of pore classes was varied between 20 and 86 and the number of nuclei in the pore with the smallest pore surface between 5 and 200.

The significant influence of the total nuclei number ($N_{s,1}$ $N_{s,2}$ and $N_{s,3}$) on the resulting strain of brick B is shown in the next diagram.

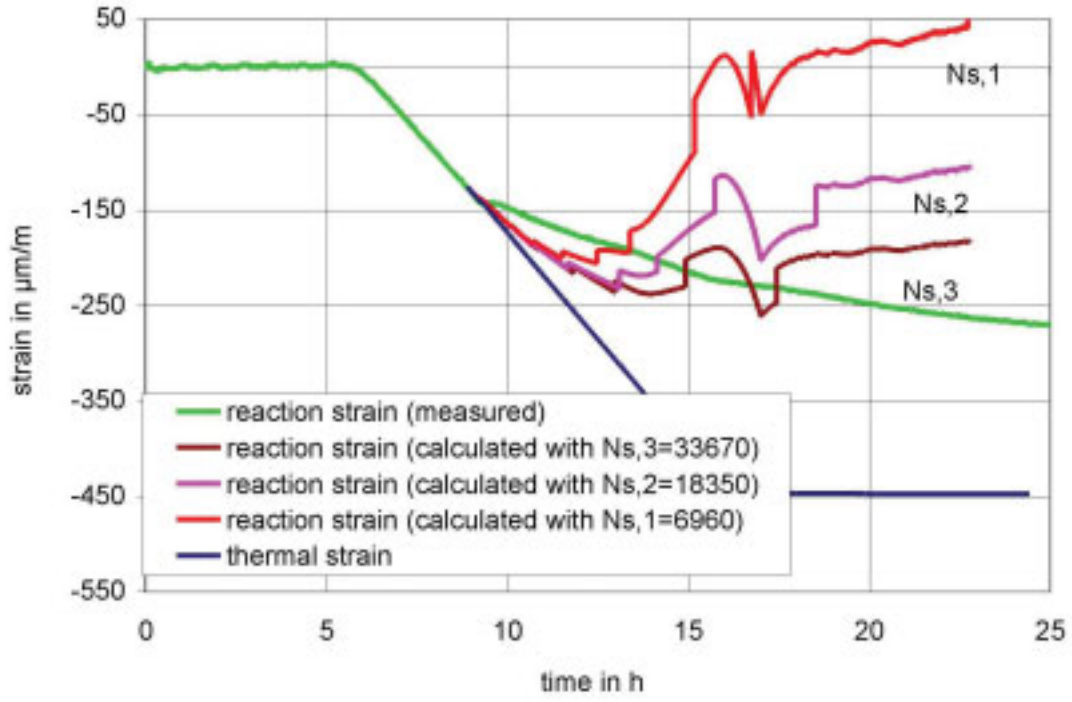

Figure 6: Computed and measured reaction strains of brick B induced by cooling down from 60 to 0 ºC and by the simultaneous crystallization of KNO_3 in its pores.

There are two main reasons for the considerable decrease of the simulated mechanical stress by increasing the nuclei number.

a) The larger is the nuclei number, the less increases each crystal radius. Thus, the contact between pore wall and crystals takes place later, i.e. at a larger amount of crystallized salt. On this account, the stress of the material takes place later, too. Therefore, the course of the reaction strain moves towards the right by increasing the nuclei number.
b) The larger is the nuclei amount, the nearer are the nuclei in a pore, whereby the collision between crystals is more likely to take place. If two or more spherical crystals grow together, a cigar-crystal forms. Considering a surface-forced crystal growth as explained in section 4,

the increase of the radius of the cigar-crystal ($r_1+\Delta r_2$) is smaller than the increase of the radius of each spherical crystal ($r_1+\Delta r_3$), if the length of the cigar-crystal (d_s) is assumed to remain constant as in case of a radial crystal growth.

Therefore, three spheres growing far away from each other will contact with the pore wall much faster. Then, they will turn into cylinder-crystals, the contact area will increase progressively and the stress of the material will take place. Eventually, they will grow together and form an only cylindrical-crystal, too.

The higher supersaturation ratio during the crystallization of KNO3 in brick B involves a higher maximal crystallization pressure than in brick A, as the following equation shows:

$$\Delta p = \frac{R \cdot T}{V_m} \cdot \ln\left(U_{a,\max}\right) = \frac{8.314 \cdot (2.91 + 273.15)}{4.75 \cdot 10^{-5}} \cdot \ln\left(1.75\right) = 24.44 \text{ MPa}$$

On the other hand, the effect of the curvature of small crystals on the crystallization pressure is considerable in brick B due to the large amount of small pores (<0.1µm). On the contrary, this effect can be neglected in brick A.

According to eq. 1 the crystallization pressure in small pores (0.010 µm) results: $\Delta p = 24.44 - 0.1 / 0.010 = 14.44$ MPa , while in pores with a radius equal or lager than 0.133 µm, the effect of the curvature of the crystals on the crystallization pressure is negligible: $\Delta p = 24.44 - 0.1 / 0.133 = 24.44 - 0.75 = 23.69$ MPa .

Thus, by taking a nuclei amount $N_{s,1}$=1060[2] per mm³ solution, the macroscopic stress in each direction reaches a maximal value of 1.94 MPa. That computed stress is similar to the tensile strength of brick B. In comparison, if the nuclei number is assumed to be $N_{s,3}$=223 per mm³ solution [3], the maximal macroscopic stress is about 3.4 MPa, i.e., much larger than the tensile strength (=1.10 MPa), which means that a damage of the material might be expected.

Further, figure 6 shows a discrepancy between the computed strain and the measured strain. This can be explained by the existence of a high supersaturated thin film between crystals and pore wall in contrast to the low supersaturation of the pore solution. Due to the concentration gradient, an ion diffusion takes place between thin film and pore solution, whose efficiency depends on the tortuosity of the porosity of each material and the solution properties (i.e. diffusion coefficient) as well as on the pore filling with crystals. Current investigations are focused on that topic.

[2] total nuclei amount=1060 per mm^3 solution for $z_{s,min}$=30 and nPk=86 (formed at 42 °C)

[3] total nuclei amount=223 per mm^3 solution for $z_{s,min}$=10 and nPk=86 (formed at 42 °C)

6 Conclusions

The mechanical stress during the crystallization of different salts in the pores of two bricks with different porosity was analysed by means of strain measurements. The crystallization was induced by cooling-down a sample, which was impregnated with salt solution. The hydrostatic pressure due to the volume increase after salt precipitation (max. 1% according to [20]) can be simply released by pushing the solution into the empty pores. Thus, the resulting strain difference is only due to the crystallization pressure.

It was shown that tendencies of the mechanical stress induced by the crystallization (induced by a temperature change) can be estimated by means of this new model and simulation modul.

The experimental results indicate that the stress due to crystallization depends on both, salt and pore structure. Thus, a higher start-supersaturation is necessary for the crystallization of mirabilite than for the crystallization of potassium nitrate, as shown in [7]. When comparing the porosity of the selected bricks, it is found that the porosity of brick B is clearly finer than the one of brick: one third of the pore volume of brick B consists of pores smaller than 0.1 µm, while so small pores are not present in brick A. Assuming that crystals grow uniformly in small and large pores, crystals will exert a pressure on the pore wall firstly in the smallest pores. Thus, if the pores are larger, the load surface is expected to be smaller and with it the resulting stress. This explains the higher stress of brick B compared to brick A.

Furthermore, the results calculated by mean of the new crystal growth model point out the mechanical stress can be estimated by means of the supersaturation ratio of the pore solution, confirming the validity of eq. 1 in a non-equilibrium state. This stress can be high enough to cause damage, even in absence of small pores. It must be remarked that the load surface of the crystals has also to be accounted which means that the distribution of crystals in the pores has a significant influence on the resulting mechanical stress.

The resulting mechanical stress depends strongly on the nuclei amount. Thus, the increase of the amount of crystals involves a decrease of the mechanical stress. Currently experimental investigations [7] by using the combination of the differential mechanical analyzer and the differential mechanical analysis confirm this result.

Surface-induced nucleation and crystal growth lead to good results. It is important to remark that in contrast to the majority of theories the nucleation and the crystal growth are assumed to take place uniformly in all pores classes, whose radius is larger than the critical radius (1 nm).
An average supersaturation of the pore solution was assumed. The consequence of this assumption is that the supersaturation ratio is equal overall and a re-distribution from the small into the large pores as well as a re-adjustment of the crystal form cannot be computed. Thus, the material relaxation cannot be simulated. This simplification is supposed to be the main reason for the discrepancy between computed and measured strains and is the objective of a current work.

7 References

[1] Benavente D. et al.: Role of pore structure in salt crystallization in unsaturated porous stone. Journal of Crystal Growth 260, pp. 532-544, 2004.

[2] Correns, C.W., and W. Steinborn, Experimente zur Messung und Erklärung der so-genannten Kristallisationskraft. Zeitschrift für Kristallographie 101, Heft 1/2, pp. 117-133, 1939.

[3] Doehne E.: In Situ Dynamics of Sodium Sulfate Hydration and Dehydration in Stone Pores: Observations at High Magnification Using the Environmental Scanning Electron Microscope. The Conservation of Monuments in the Mediterranean Basin pp. 143-150, 1994.

[4] Everett, D.H. J. Chem. Soc. Faraday Trans. 57, pp. 1541, 1961.

[5] Espinosa, R. M., Franke L., Deckelmann, G: Model for the mechanical stress due to the salt crystallization in porous materials. Construction and Building Materials 22 pp. 1350–1367, 2008.

[6] Espinosa, R. M., Franke L., Deckelmann, G: Phase changes of salts in porous ma-terials: Crystallization, hydration and deliquescence. Construction and Building Ma-terials 22, pp. 1758–1773, 2008.

[7] Espinosa R.M., Scherer G.W. Study of sodium sulphate salts crystallization in limestone with the dynamic mechanical analyzer and the differential scanning calorimetry. Accepted by Environmental Geology, 2008.

[8] Flatt, R. J.: Salt damage in porous materials: how high supersaturations are generated, Journal of Crystal Growth 242, pp. 435-454, 2002.

[9] Kiencke, S.: Beanspruchungsmechanismen und kritischer Gehalt von Salzen in porösen Materialien, Dissertation, Hamburg University of Technology, 2005.

[10] Larsen, E.S, Nielsen, C.B.: Decay of bricks due to salt, Materials and Structures, 23, pp. 16-25, 1990.

[11] Mutaftshiev, B.: Nucleation Theory, handbook of Crystal Growth, Vol. 1, Chapter 4, 1993.

[12] Rodriguez-Navarro C., Doehne E.: Salt weathering: influence of evaporation rate, supersaturation and crystallization pattern. Earth Surface Processes and Landforms, 24 pp. 191-209, 1999.

[13] Scherer, G. W.: Stress from crystallization of salt, Cement and Concrete Research 34, pp. 1613-1624, 2004.

[14] Scherer, G.W.: Factors affecting crystallization pressure. International Sulphate Attack: Proceedings of RILEM Workshop on Delayed Ettringite Formation, Paris 2004.

[15] Steiger, M, Zeunert, A.: Crystallization Properties of Salt Mixtures: Comparison of Experimental Results and Model Calculations. In: J. Riederer (ed.), International congress on deterioration and conservation of stone – proceedings, Möller Druck und Verlag GmbH, Berlin, pp. 535–544, 1996.

[16] Steiger, M.: Crystallization pressure: What is the effect of changes in total volume during phase transitions? 6th International Conference on Materials Science and Restoration, MSR VI. Aedificatio Publishers, pp. 43-52, 2003.

[17] Steiger, M.: Crystal growth in porous materials I-: The crystallization pressure of large crystals, Journal of Crystal growth 282 , pp. 455-469, 2005.

[18] Steiger, M.: Crystal growth in porous materials II-: Influence of crystal size on the crystallization pressure, Journal of Crystal growth 282 , pp. 470-481, 2005.

Stefan Kiencke
Dr.-Ing.

Tewis Ingenieurbüro
Hamburg, Germany

Lutz Franke
Prof. Dr.-Ing.

Institute of Building Materials, Physics
and Chemistry of Buildings
Hamburg University of Technology, Germany

Prediction of stress due to crystallization in a porous material and calculation of the damaging salt concentration

Summary

It is already known that low contents of salt can cause damage within a porous material due to the crystal growth pressure. The force that a crystal could exert on a porous wall is given by the thermodynamic equilibrium between the pressure on the crystal face and the supersaturation of the surrounding solution. But even if these values are known it is not possible to calculate the stress resultant on the material.

Therefore a model was developed to estimate the macroscopic stress in a cross section caused due to the microscopic crystallization pressure. Furthermore the estimation of a damaging salt concentration was possible.

Keywords: salt crystallization, supersaturation ratio, crystal growth, crystallization pressure.

1 Introduction

The literature often deals with the question of how high the crystallization pressure could be and if this force could cause the damage of a porous material. Many authors attempted to the estimate of the crystal growth pressure [2], but only a few authors tried to calculate the stress resultant on the basis of the microscopic crystallization pressure of a growing crystal [6], [11]. But till now no satisfiable solution was found.

Because there was no proper approach to this problem an own model was created to calculate the stress by the crystallization pressure. Therefore many experiments were arranged for its verification. In these experiments the expansion of the samples were measured during the crystallization of salt within their porous bodies. Furthermore the amount of crystallized salt and the degree of supersaturation was determined at every point of time to get a correlation between the microscopic crystallization pressure and the expansion.

2 Measurement of expansion in the difference temperature measuring device

The principle of the difference-temperature-measuring-device is based on the measurement of very little changes in temperature when a salt is crystallizing or dissolving. In these experiments the used samples were soaked up with saline solution which has a high solubility, depending on the temperature to get a high amount of crystallized salt by changing the temperature [4]. Furthermore the expansion of the samples were measured to estimate the strain, with the known stress-strain-characteristics of the material.

Therefore we used samples of brick material of dimension 30 x 30 x 30 mm. On the two opposite faces strain gauges were applied and in the middle of the sample a hole was drilled to fix a temperature sensor. Afterwards the whole sample was soaked in saline solution and sealed by silicon. Every sample was combined with another water filled sample to determine the difference in temperature. All the samples were put into a bath, whose temperature was controlled exactly by a program.

In these experiments the salts KNO_3 and Na_2SO_4 were used because of its high solubilities depending on the temperature. The experiments started at a temperature of 40° / 50° C and then the bath was cooled down slowly (0.02 / 0.01 K/min) till 0° C.

By measuring the difference in temperature between the water and the solution containing the sample, with an accuracy of 0.01 K, it was possible to estimate the beginnig of crystallization by the released enthalpy.

Furthermore at every point of time the amount of crystallized salt was determined by integration of the generated heat. Therefore the energy balance of the salt containing sample was drawn [4].

The concentrations of the saline solutions used for these experiments are given in Table 2.1.

Table 2.1: Concentrations of the saline solutions in the experiments * Mirabilite

Salt	**Saturation at T [°C]**	**Concentration at the beginning - m_1**		**Concentration at T=0° C - m_0**	
		[mol]	**[%]**	**[mol]**	**[%]**
KNO_3	40	6.32	39.0	1.31	11.7
Na_2SO_4	30*	2.82	28.6	0.35	4.7

The second column in Tab. 2.1 gives the temperature at which the saturation of the solution is reached during the cooling down of the samples. This means for sodium sulfate the solubility of mirabilite is reached compared to the thenardite which is still undersaturated.

For all experiments the samples were first put in to the gadget and the temperature was held for long as constant at 40 °C (Na_2SO_4) / 50 °C (KCl), as there was no difference measured between all samples. Then the bath was cooled down with a velocity of 0.1 / 0.02 K/min. Reaching the minimum of 0° C the temperature was held untill no more change of expansion was measured. After this the bath was heated up to the initial value of 40° / 50° C. This was repeated several times depending to the expansion behavior of the samples and a possible damage.

2.1 Results of the experiments with the difference temperature measuring device

The measured values of **brick-4** with saline solution of **KNO_3** during the first cooling down period shows that there is a rising difference in temperature between the water and the solution containing sample after starting the cooling down process (section 1 in Fig.2.1). Because the solution is still undersaturated only a local crystallization in special areas of the pore volume is possible.

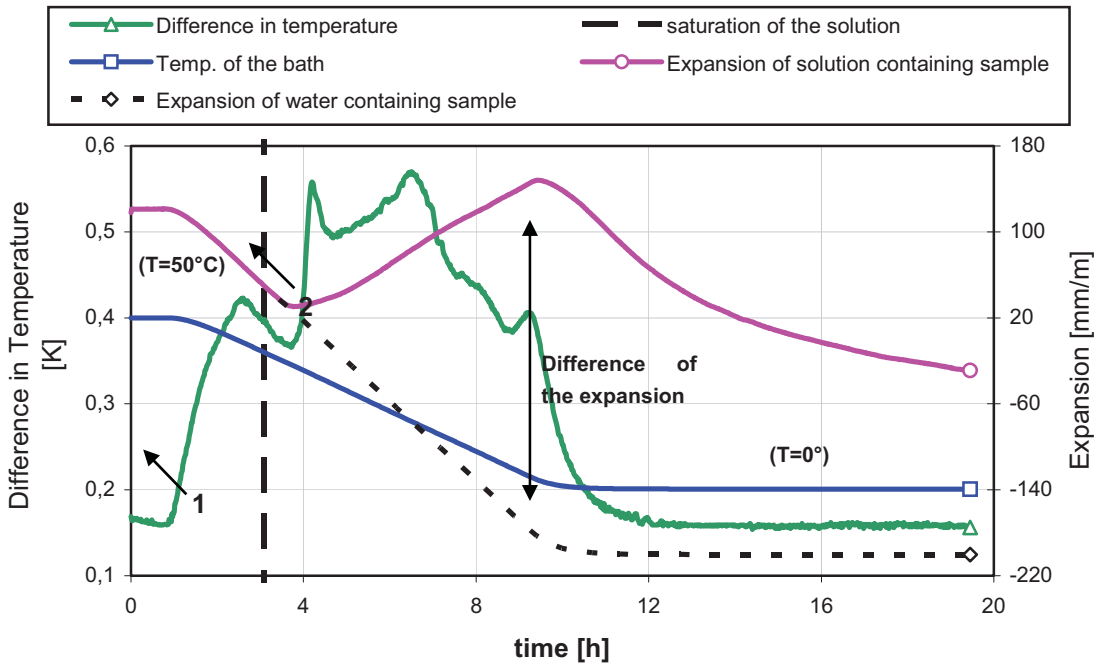

Figure 2.1: Measured values, brick-4 with solution of KNO_3

Primarily the second rise of the difference in temperature (section 2 in Fig. 2.1) shows the principal crystallization because the solution has been supersaturated before.

This is also the time were a difference between the thermal expansion due to the cooling and the expansion as a result of the crystallized salt could be measured. When the temperature reaches the minimum value of 0° C this difference in expansion gets maximum with a value of about 335 $\cdot 10^{-6}$. This is more then the ultimate strain of tension of this material and so that a

damage is likely to be caused. After a time of 72 hours there could be noted a constant expansion which argued for an irreversible deformation and caused a damage of the sample.

When the experiment was stopped and the sample was removed several cracks of the brick material were visible, which clearly proved that an actual damage had occurred.

Fig. 2.2 shows the results of the same experiment. In this case the amount of crystallized salt which was calculated by the difference in temperature as well as the degree of supersaturation is demonstrated. This indicates that immediatly after the beginning of the crystallization, an expansion could be measured due to the accumulated salt within the pores.

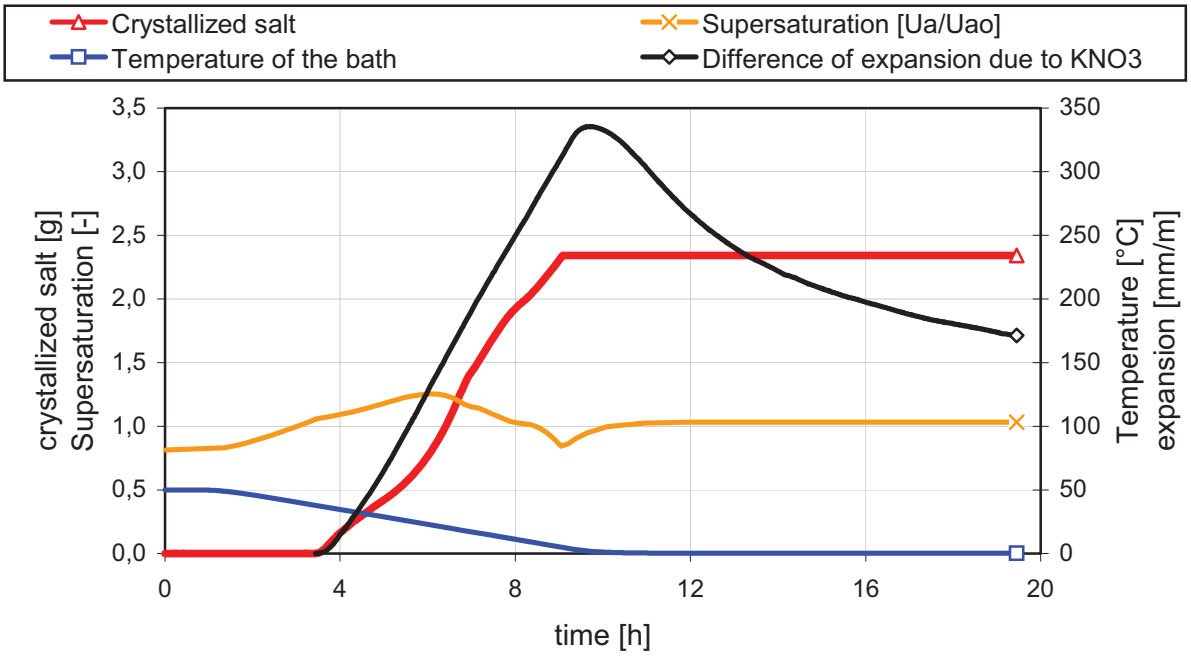

Figure 2.2: Evaluated values, brick-4 with solution of KNO_3

The calculated degree of supersaturation of this experiment was low. At the beginning of the crystallization is was about 1,05 and then rised up to 1,25. By taking this maximum value we could estimate a crystal growth pressure of 11 N/mm² [4].

Fig.2. shows the measured values of **brick-4** with saline solution of **Na_2SO_4** which had a cooling rate of 0.02 K/min. It can be seen that the maximum degree of supersaturation with a value of about 10, is much higher than in the case of KNO_3. At the point of time when the crystallization occurred, a great part of the salt crystallized immediately, which lead to a sudden load. After a maximum expansion of 200 μm/m this value fell to 125 μm/m when the temperature reached 0° C. A further relaxation did not take place, due to which a damage of the sample was assumed.

After another three loops of changing the temperature the lasting expansion was rising from step to step which was a certain sign for damaging the sample.

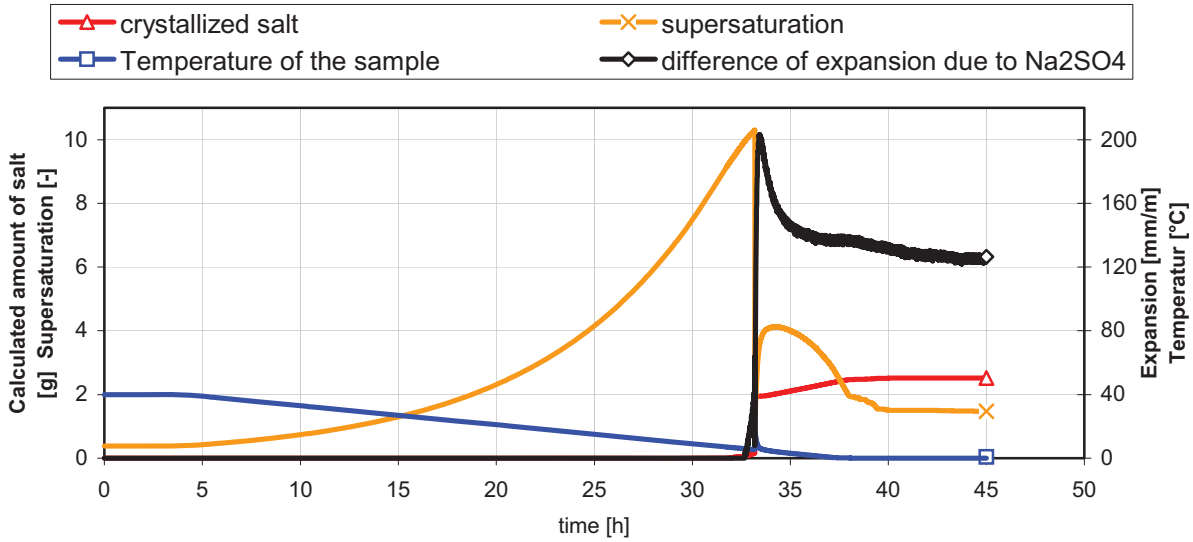

Figure 2.3: Measured values, brick-4 with solution of Na_2SO_4

Taking the maximum degree of supersaturation of about 10, we can calculate a thermodynamic crystal growth pressure of 25 N/mm².

The following table resumes the results of these experiments.

Table 2.2: results of the experiments with solution of KNO_3

Material	**Filling degree with solution [vol.-%]**	**Supersaturation U_a**		**Maximum expansion [µm/m]**	**Maximum Filling degree with crystals [vol.-%]**
		at the point of nucleation	**maximum value**		
Brick-1	84	1.15	1.20	37	18
Brick -2	95	1.20	1.31	16	16
Brick -4	88	1.05	1.25	335	16
MWS-1	75	1.27	1.28	-	14

Table 2.3: results of the experiments with solution of Na_2SO_4

Material	**Filling degree with solution [vol.-%]**	**Supersaturation U_a**		**Maximum expansion [µm/m]**	**Maximum Filling degree with crystals [vol.-%]**
		at the point of nucleation	**maximum value**		
Brick -2	90	4,16	8,67	90	45
Brick -4	97	8,84	10,30	202	49
MWS-2	90	(no crystallization!)		-	(45)

In the experiment with the synthetic material and a saline solution of Na_2SO_4 (Tab.2.3), no crystallization was determined by a measurable difference in temperature. On the other hand it is unlikely that no crystallization had occurred even with a very high degree of supersaturation about more than 18 at a temperature of 0° C. But with regard to the experimental datas no other conclusion could be given.

2.2 Analysis of the experimental datas and results

First of all these experiments demonstrated that already little amounts of crystals caused a measurable load. Especially in the case of the brick-4 it could be seen that immediately after KNO_3 began to crystallize an expansion of the sample was detectable. The other samples indicated a similar behaviour.

Hence, the expansion at the beginning of the crystallization has to be lead back on the crystallizing salt within the little pores, because in the greater pores a higher content of salt would be necessary to cause a load. As a result of this, the sample-4 showed an expansion caused by a very little volume of salt, because this material contains the finest pores.

It also makes clear, why a high amount of crystals did not create a load within the synthetic material. These materials only contain a very close pore size distribution which could be seen as a pore volume with pores of a constant radius. In this case, if salt crystallizes uniformly within the pores, they will reach the pore walls at the same point of time. This situation represents a high filling degree with crystals, which could not be reached in the experiments.

Concerning the different results between the salts KCl and Na_2SO_4 the experiments showed that a higher amount of salt and a higher crystal growth pressure are not an inevitable lead to a higher load.

In addition to the load due to the crystallization, these experiments demonstrated the different behavior of the dissolution of the salt when the pressed cyrstall faces became undersaturated due to a reduction of supersaturation during the crystallization.

All samples showed a maximum expansion at a temperature of 0° C although at that point of time there was no supersaturation and, thus the crystal growth pressure reached 0 N/mm². This can be explained by the lower kinetic of dissolution compared to the kinetic of crystallization. Also the parameter of the transport of the ions in the thin layer of solution between the crystal face and the pore wall is responsible that a sudden dissolution could not occur.

Dissolution of the pressed crystal face can only occur, if ions dissociate into the solution film between crystal and pore wall. The temporary increase of the activity has to be reduced by the transport of the ions. If this transport is hindered or prevented the effective load can be maintained over a period of time.

In the case of the experiments with Na_2SO_4 it is possible that, the high filling degree of the pores could have hindered this transport of the ions. Another point could be the absence of solution after the cysrallization which also could inhibit the compensation of different concentrations.

Comparing the different behavios of the salts KNO_3 and Na_2SO_4 it is noticeable that the degrees of supersaturation differ greatly. In the case of KNO_3 supersaturations between 1.2 and 1.3 were measured, whereas Na_2SO_4 shows values betwenn 8 and 10. These high degree of supersaturation originates from the different solubilities of thenardite and mirabilite. Because of the higher solubility of thenardite, it is posible to create a thermodynamic metastable solution which means a high degree of supersaturation in regard to mirabilite.

A dependance between the maximum reachable supersaturation and the material of the sample could not be determined because of the variation of the experimental datas.

3 Simulation of the stress due to salt action and estimation of a damaging salt concentration

3.1 Model for calculating the stress resultant

To calculate the load due to the crystallization within a porous material, firstly it is necessary to describe its porosity. In this case we reduce the continous pore size distribution got by mercury intrusion to pore classes each with a constant pore radius. The procedure is described in chapter 3.2.

An assumption had to be made to estimate the number and distribution of the seed crystals in the pore system. The numer of seed is described in chapter 3.3. Based on the fact that a heterogeneous nucleation is possible, the seed were distributed proportional to the inner superface of the pores.

In the case that several crystals reach the pore walls and exert a load, a stress resultant should be calculated referring to the cross section of the material containing the pores, because normally the strength of the pure material without the pores is unknown.

We made the assumption that crystallization takes place in all classes of pores. These crystals grow uniformly up to that point of time when some crystals (in the smaller pores) first reach the pore walls and exert a load on the material.

The example shows a porous material with three different classes of pores which are all parallel. At a view point of time there are crystals in all of these pores but only the salt in the smallest and the medial pores exert a pressure on the material, because the crystals in the largest pore do not reach the walls.

Now it should be carried out on an applicable section to get the stress resultant as a sum of the crstystall pressure in the cut.

Therefore it is necessary to find the controlling section. However an arbitrary direct cut (Fig. 3.1a) leads to an underestimation of the stress, because the real cut crosses the areas of the highest loads and minimum resistance (Fig. 3.1b).

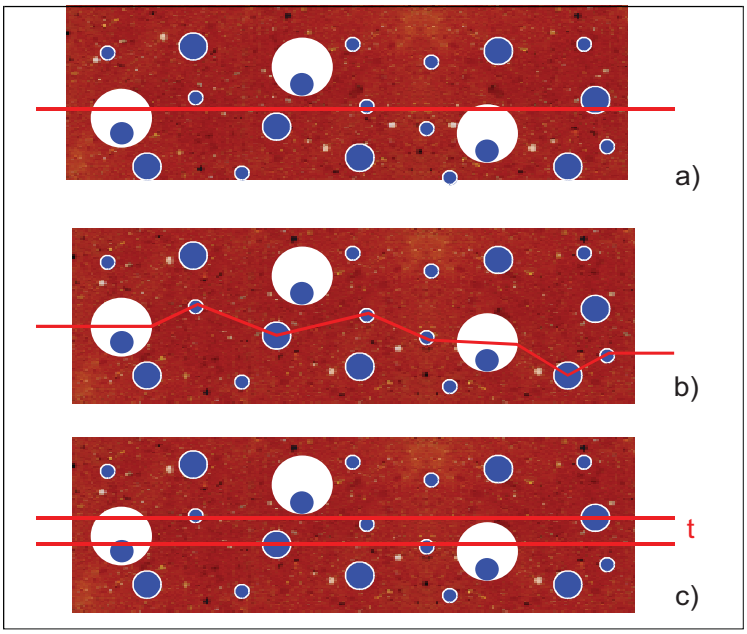

Figure 3.1: Design model for the calculation of the stress resultant

As this section is not practicable for a calculation, we left the imagination of a cross section in favour of using a sliced volume with the width t (Fig.3.1c). The value for t is taken as the pore diameter of the greatest pores where the crystals produce a load on the pore walls. Because of this, the sliced volume width t is not constant during the crystallization.

Inside the sliced volume, all crystals producing a load were cut in the middle to sum the crystal pressures which were effective in these sections. This is simplified for two crystals in two different pores in Fig. 3.2.

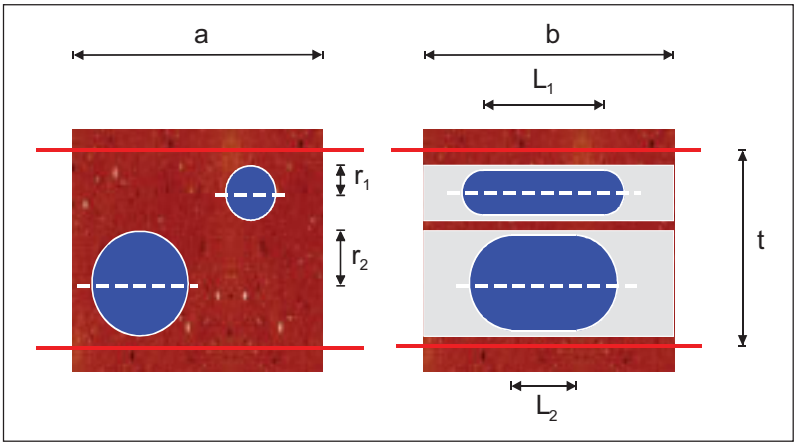

Figure 3.2: Calculation of the section force from the loaded pores

The section force which is oriented normal to the section, can be calculated with the sum of all cut crystals exerting a pressure:

$$F = \sum^{i} p_{kr,i} \cdot n_i \cdot 2r_i \cdot L_i \qquad (3.1)$$

$p_{kr,i}$ - crystal pressure in the pore class i
n_i - number of crystals in the pore class i inside the sliced volume with the width t
r_i - pore radius of the pore class i
L_i - length of the loaded crystal face in the class i

Taking this section force, the stress resultant can be calculated as follows:

$$\sigma = \frac{F}{a \cdot b} \qquad (3.2)$$

a,b - length, width of the observed volume
σ - tensile stress of the material

Taking this calculated tensile stress it is posible to estimate the damaging salt concentration of the material. Furthermore the elastic expansion can be calculated with the known module of elasticity.

3.2 Simplification of the porosity

The porosity of a porous material is characterized by its volume, the number and shape of the pores and their connectivity. For the calculation the most important datas are the size of the pores and their volume fraction. These datas can be taken by the use of mercury intrusion, which assumed a cylindrical shape of the pores.

For the calculation we reduced the continous pore size distribution got by mecury intrusion to pore classes each with a constant pore radius. Thus the whole porosity is represented by the number of pore classes, whereas every class is defined by its median pore radius and their volume fraction.

To do this first, the number of classes and the borders of each class had to be arranged. Therefor the limiting radius of each class was determinded by the following formula:

$$r_{\lim it,i} = r_{\min} \cdot \left[\left(\frac{r_{\max}}{r_{\min}} \right)^{\left(\frac{1}{n}\right)} \right]^{i} \qquad (3.3)$$

$r_{border,i}$ - limiting radius between two adjacent classes
$r_{max/min}$ - max./min. value got by mecury intrusion
n - number of classes
i - class limit (0 up to n)

By using this formula, all class limits have the same width in a lograthmic scale (Fig.3.4).

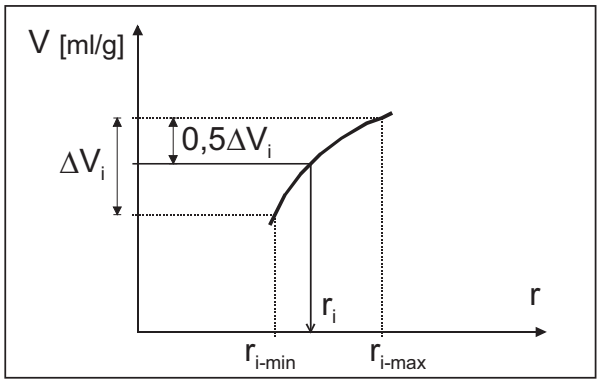

Figure 3.3: Definition of the characteristic pore radius of a pore class

The characteristic pore radius of a spacial class was defined as the radius which is appendant to its median pore volume (Fig. 3.3). Thus the whole porosity is now represented by the numer of classes and the values r_i and ΔV_i of every class.

Using this proceedings, it was possible to vary the accuracy by varying the numer of classes. The maximum number of classes were only limited by the amount of datas got by mercury intrusion.

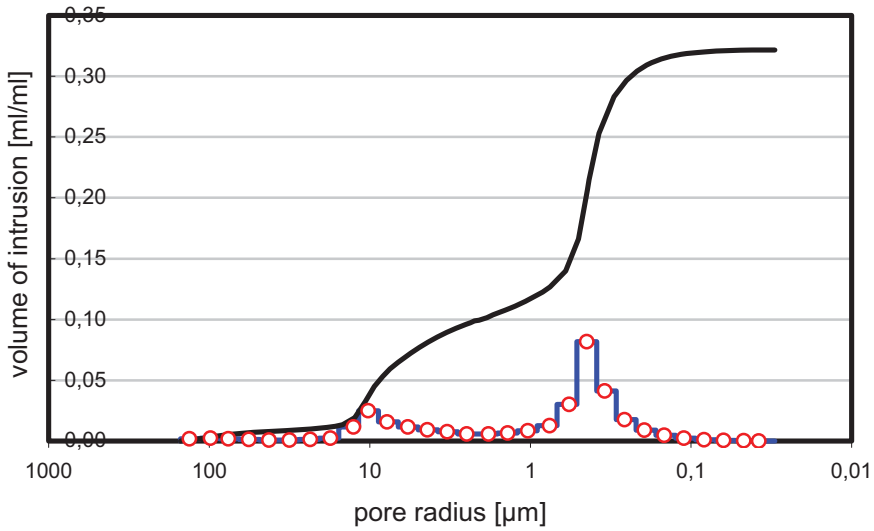

Figure 3.4: Porosity of the brick-2 by the use of 30 pore classes

After the classification we had to form single pores to distribute them in the examined volume. Therefore firstly, the geometry of the pores was arranged by the proportion of length to diameter. This value was varied between 2 up to 10 depending on the shape of the pores, estimated by electron microscope. This value was taken for all pores independently from their size. The number of single pores of each class was then calculated with the known fractal volume.

The spacious distribution of these single pores had to be adapted to the regarded pore system. In general it is unlikely to assume a uniform distribution in all directions of the space coordinates. Due to the fabrication by an extrusion press, the formation of textures is possible. Like it could be seen in the used bricks that every material contains areas with unidirectional pores.

For the load due to crystallization pressure within the pore system the stress in these areas of the material is the controlling one. Because of this we primarily assume that all cylindrical pores are unidirectional inside an area. That means that we get a maximum stress in a direction normal to the axes of this plane. This assumption, what signify the “worst case” was presumed for all brick materials because of the observation that all materials contain areas of unidirectional pores.

3.3 Number and distribution of the crystal seeds within the pores

Important for the calculation of a load due to salt, is the number of crystals as well as their distribution in the pore volume.

However the nucleation rate is mostly unknown for a pure solution and varies over many orders of magnitude. Thus the number of seeds had to be estimated for the calculation. Because of the insecurity of depending on the dimension of this value, the number of crystal seeds was also varied over many magnitudes. This value was defined as the number of seeds per mm³ of the solution. In adjacent, a sensitivity analysis was arranged to estimate the influence.

The seeds were distributed proportional to the inner surface of the pores because a heterogeneous nucleation was assumed [4]. Depending on the pore size distribution and the number of pore classes the number of seeds per single pore was defined. This value can be < 1, which signifies that there are empty pores. For values > 1 there is the possibility that several crystals within one single pore can grow together generating a single crystal. To consider this, the seeds were evenly distributed on the inner surface of the pore. If the growing crystals get in contact to each other, the formation of one single crystal was presumed.

In the case that not the whole pore volume is filled with saline solution we have to distribute the amount of solution on the different pore classes. Because of the higher (negative) capillary pressure in the smaller pores, we assume that initially the smallest pores get filled, followed by a successive filling of the next pore class with the larger pores.

3.4 Presumptions and simplifications for the calculation

For the calculation of the stress resultant due to the salt growth, a given amount (volume) of crystals was simulated and the load was calculated assuming the model described in chapter 3. For this the following presumptions and simplifications were made:

- a kinetic of crystal growth was not considered
- changes in volume during the crystallization were not considered

- differences of the activity in the solution were adjusted immediately, thus every pore contains solution with the same activity
- crystal growth takes place proportional to the free surface of the crystals, to consider the different growth velocity between crystals with a varying size
- The shape of the crystals is spherical up to the point of time when the pore wall is reached. After that the crystal grows only at its sides by having hemispherical ends. If the pore gets filled completely, the crystals can grow into free adjacent pore.
- If there is more than one crystal within a single pore they can grow together forming one single crystal when they get in contact with each other.

The algorithm of the simulation is exactly described in [7].

3.5 Comparison between the simulation and the experimental data's

First of all we compared the results of the simulation with the experimental data's of the difference temperature measuring system. For that the following parameters were needed:

- filling degree of the pores with solution, concentration of the solution, amount of crystals after the crystallization
- number of crystal seeds
- processing of the crystal growth pressure during the crystallization

The filling degree with saline solution and the amount of formatted crystals were known and directly adopted for the simulation.

As the number of crystal seeds was unknown (chapter 3.3) several calculations were made by varying this parameter.

Basic principle for assuming the crystal growth pressure was the processing of the variable degree of supersaturation during the crystallization got by the experiments. This is described more exactly in the following chapter.

3.5.1 Thermodynamic equilibrium pressure vs. effective pressure

In the experiments the degree of supersaturation was determined at every point of time during the crystallization. By using the formula to calculate the crystal growth pressure [4] the pressure was known at every step of the crystallization.

Assuming that the gradient of activity in the solution and the solution film between the crystal and the pore wall is adjusted immediately, the pressure had to be reduced completely after the crystallization had taken place, because there does not exist a crystal growth pressure at a supersaturation of 1,0. Because of this all reversible expansions also had to be reduced to the point of origin. The experiments showed that this relaxation did not take place, or only took place marginally because after the crystallization always a remaining expansion was visible (Fig. 2.4).

The matter is that the dissolution of the loaded crystals face did not occur immediately and obeys a kinetic which depends on the degree of undersaturation as well as the transport of the ions in the solution film between the crystal face and the pore wall. In [1] it is already described that dissolution of a loaded crystal face is much slower that the crystallization of a free face. This effect yields to the persisting load and has to be considered for the calculation.

Due to the fact that the kinetic of the dissolution of the crystals inside the pores is unknown, we made the following assumptions.

When a crystal reaches the pore wall, the exerting pressure equals the crystal growth pressure depending on the supersaturation at that point of time. If the degree of supersaturation rises subsequently, the pressure also rises because the same degree of supersaturation is assumed in the solution film between crystal and pore wall.

But if the supersaturation (and with it the crystal growth pressure) falls, the effective pressure remains preserved because a sudden dissolution does not take place. The lower crystal pressure is applied for the crystals which reach the wall at that point of time.

3.5.2 Evaluation of the experiments

On one hand we calculate the maximum stress resulting was calculated to compare this value with the one got by the experiment. On the other hand the time-dependent process of tensile stress was calculated for a comparison with the experimental data's. As the simulation did not consider a kinetic of the crystallization, the process of tensile stress and the expansion respectively was described against the crystallized amount of salt.

For the calculation, all unknown parameters had to be varied in a reasonable range to compare the result with the experimental data's.

The different materials were simplified by taking 30 pore classes, of different pore shapes. From the images taken by SEM for the brick-1 and -2, we assumed a proportion of L/D = 2…3 whereas for the brick-4 we took 3…5 because its pores are more slit-like.

The number of crystal seeds was varied in a range of 10^4…10^{12} / mm³ solution.

3.5.2.1 Simulation of the experiments with KNO_3

The following table shows the input parameters used for the simulation. In Fig.3.5 the results of the best corresponding simulation were opposed to the values measured in the experiments without making an optimal adaptation.

Table 3.1: input parameters for the simulation of the experiment with brick-4 and KNO_3

Simulation	Number of pore classes	L/D	Filling degree with solution	Number of seeds [1/mm³ solution]
1	30	5	84%	10^8
2		3		

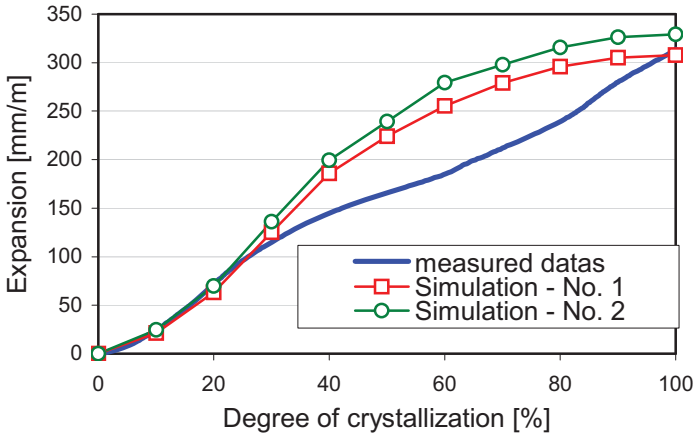

Figure 3.5: Process of expansion, Brick-4 with KNO_3

In the following simulation the expansion of brick-1 with saline solution of KNO_3 was calculated to compare the results with the experimental data's.

Table 3.2: input parameters for the simulation of the experiment with brick-1 and KNO_3

Simulation	Number of pore classes	L/D	Filling degree with solution	Number of seeds [1/mm³ solution]
1	30	3	95 %	10^9
2		2		

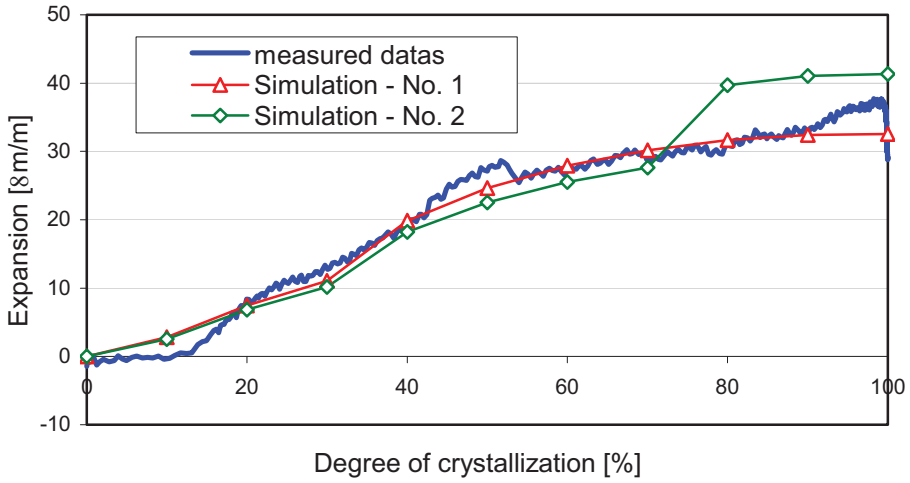

Figure 3.6: Process of expansion, Brick-1 with KNO_3

Different from the expansion of the other samples due to crystallization of KNO_3, the measured values of brick-2 were significantly less. Because of the low expansion the accuracy of the measured values is also very less.

Table 3.3: input parameters for the simulation of the experiment with brick-2 and KNO_3

Simulation	Number of pore classes	L/D	Filling degree with solution	Number of seeds [1/mm³ solution]
1	30	2	88 %	10^{10}
2		2		

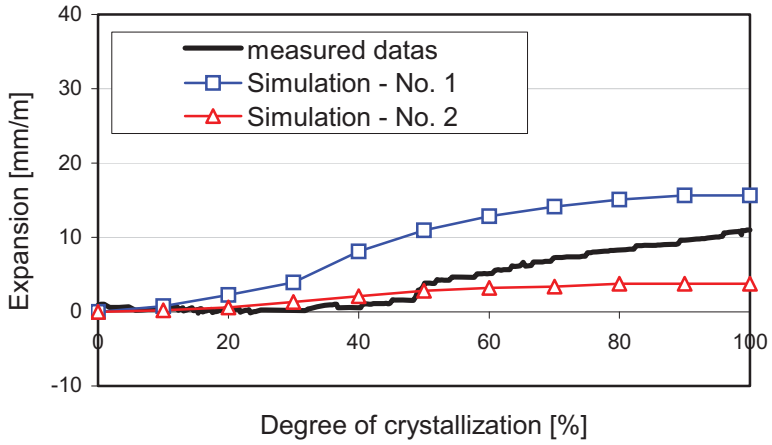

Figure 3.7: Process of expansion, Brick-2 with KNO_3

In the case of the brick-1 the number of seeds has to be in several dimensions higher to get a consistent result by simulation.

3.5.2.2 Simulation of the experiments with Na_2SO_4

For the simulation of this experiment, only the result of one parameter set is shown. By using the number of seeds and varying the proportion of the pores (L/D), the calculated expansions diverged extremely from the measured values.

Table 3.4: input parameters for the simulation of the experiment with brick-2 and Na_2SO_4

Simulation	Number of pore classes	L/D	Filling degree with solution	Number of seeds [1/mm³ solution]
1	30	3	90 %	10^9

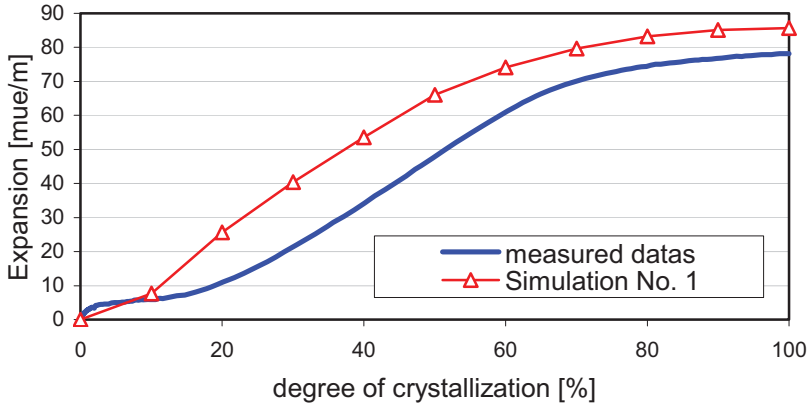

Figure 3.8: Process of expansion, Brick-2 with Na_2SO_4

3.5.3 Evaluation of the simulation of the experiments

By simulating these experiments it could be shown that, it was possible to calculate the expansion by using the right input parameter set. Referring to this the number of seeds was the parameter with the greatest influence. A comparison between measured and calculated values demonstrated that a best adaptation could be achieved using a number of seeds between 10^8 up to 10^{10} / mm³ solution.

If we examine the number of seeds of the different simulations with KNO_3 it is obvious that in the case of brick-4 it had to be assumed the least, whereas in the case of the brick-2 the highest number of seeds had to be taken. Fig.3.9 demonstrates the correlation between the degree of supersaturation and the assumed number of seeds at the point of time when the nucleation takes place.

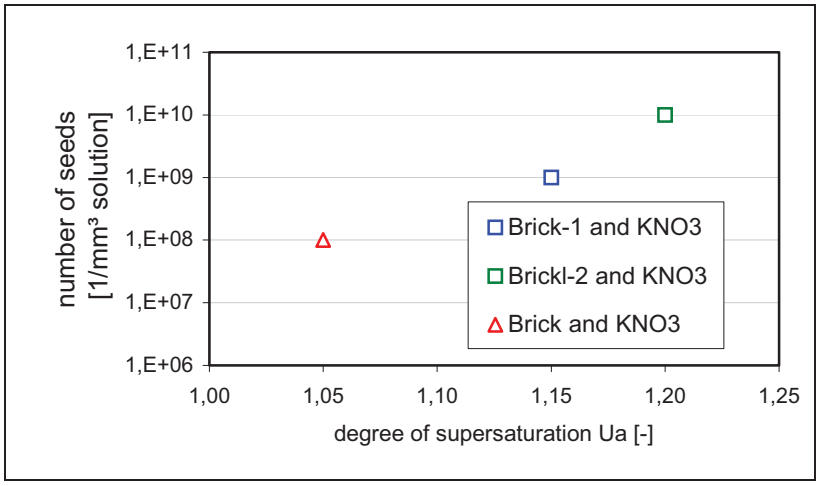

Figure 3.9: correlation between the degree of supersaturation and the assumed number of seeds

It is obvious that an increasing degree of supersaturation corresponds to a higher number of crystal seeds, which is an available fact. This justified the number of seeds which were assumed for the simulation of the experiments.

3.6 Estimation of a damaging salt content

To estimate a critical salt concentration which is damaging the material we used the model described in chapter 3. In this case it was the aim to estimate a limiting amount of salt, below which no damage of the material would occur.

Assuming that the crystallization begins in the smallest pores before they are filled completely with salt, the whole pore system is gradually filled up by salt up to the point, where the calculated stress resultant exceeds the tensile strength of the material. This amount of salt gives the critical concentration below which no damage is expected.

Therefore we did not use simplification of the pore system by classes but instead used the continuous pore size distribution got by mercury intrusion.

To estimate the critical amount of salt, the stress resultant was calculated at every point of time during the gradual filling of the pores, starting at the smallest ones.

For the calculation of the crystal growth pressure we used the maximum degree of supersaturation which was ever measured in the difference temperature measurement system. Therefore we also used the results of the experiments done within the scope of „Modellierung, Software-Implementierung und Verifikation des Feuchte- und Salztransportes, der Salzkristallisation und -schädigung in kapillar-porösen Mauerwerksstoffen“[5]. (“Modelling, Software Implementation and Verification of the salt transport moistening, of the salt crystallization and damage in capillary porous brick-work materials”).

For the salt KNO_3 a crystal growth pressure of 20.6 N/mm² was calculated, depending on the maximum degree of supersaturation of 1.5. This value for the crystal growth pressure was maintained constant, during the filling of the pores by crystals, assuming the worst case.

Doing this the stress resultant can be calculated by,

$$\sigma = 2r_{i,\max} \int_{r=0}^{r_{i,\max}} p_{kr} \cdot 2r_i \cdot L_i \qquad (3.4)$$

p_{kr} - crystal growth pressure [N/mm²]
$r_{i,max}$ - pore radius of the greatest salt-filled pore
L_i - total length concerning to the pore with the radius r_i per volume [mm/mm³]

Fig. 3.10 shows the results of this calculation for the salt KNO_3 and all the used materials. It has to be regarded that the assumed model is limited by the tensile strength of the material. In the diagram the maximum stress resultant of 5 N/mm² is demonstrated even though the tensile strength of the most materials is much lower.

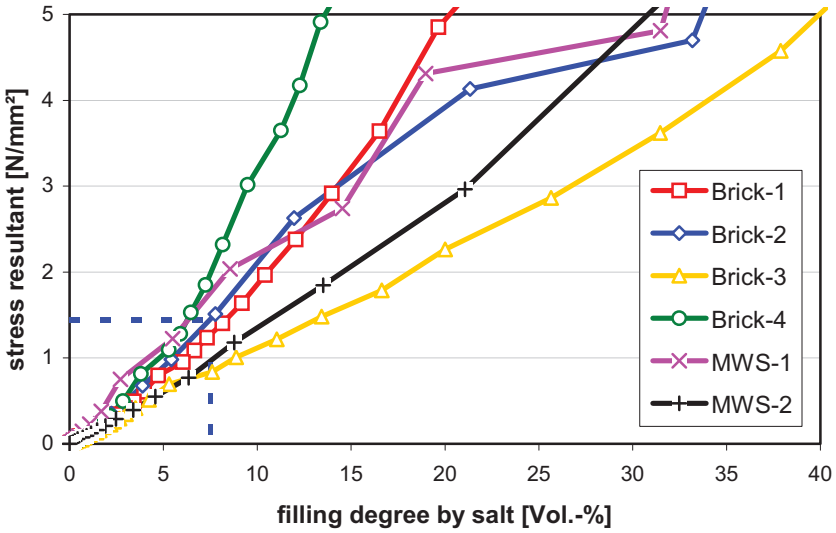

Figure 3.10: load as a result of a crystallization pressure of p=20,6 N/mm² by gradual filled pores

The critical damaging salt content could be read off by knowing the resistance of the material. This is demonstrated for the brick-2 which has a tensile strength of about 1.45 N/mm² which is reached at a filling degree of 7.5% by volume.

The following table presents these limiting salt concentrations for the salts KNO_3, KCl, Na_2SO_4 and the used brick materials.

Table 3.5: limiting salt contents of KNO_3, KCl and $Na_2SO_4 \cdot 10H_2O$ for the used brick materials
*) interfacial tension between crystal and its solution
**) concerning to the anhydrous phase

salt	γ_{cl} *) [N/m]	max.-U_a [-]	max.-p [N/mm²]	material	Filling degree [vol.-%]	crit. salt content [% by weight]
KNO_3	0.015	1.5	20.6	brick-1	7.5	2.6
				brick -2	10.4	3.0
				brick -3	> 40.0	> 6.5
				brick -4	4.8	1.8
KCl	0.020	1.6	30.5	brick-1	5.4	1.8
				brick -2	7.7	2.1
				brick -3	> 29.6	> 4.6
				brick -4	3.3	1.2
$Na_2SO_4 \cdot 10H_2O$	0.010	9.8	25.2	brick-1	9.0	0.8*)
				brick -2	6.3	0.7*)
				brick -3	> 34.5	1.8*)
				brick -4	3.7	0.5*)

The result shows that the damaging amount of salt varies greatly between the different bricks. By contrast the values differ little between the different kinds of salt because the assumed crystal growth pressures were very similar.

Noticeable is the fact that the limiting salt concentrations are very little and only about 1 to 2 percent by weight in consequence to the assumption of the worst case. Thus it is likely that the damaging amounts of salt are higher in practice. It also has to be recognized that the calculated values refers to a concentration of a local part of the pores system and not to the whole pore volume of the material.

All calculated values show that these were always below the damaging concentration which was estimated in the experiments [4] and also with a reasonable limit. Furthermore the calculated values have the same dimension like the damaging concentrations determined in practice. In [9] a global limiting salt content about 3% is given for easily soluble salt which also has the same dimension.

4 Conclusions concerning the processes of damage

By the experiments it could be shown that, the load of a material due to salt depends on the characteristics of the porous material and the salt, and also on the settings of the crystallization. Precondition for every crystallization is the formation of a supersaturated solution under one of the following conditions:

- Evaporation of water
- Change of temperature
- Reaction with other ions by mixing different solutions

During the crystallization, a growing crystal can exert a pressure while the solution is supersaturated in respect to the crystal face under pressure. During further crystallization, the unloaded crystal faces will grow by decreasing the degree of supersaturation. Because of the fact that the solubility of a crystal face under pressure is lower than a free one, there does not exist an equilibrium state between the loaded and the unloaded crystal faces which are surrounded by the same solution. Thus there is a point during the formation of crystals where the crystal faces under pressure would dissolute in favour of the free crystal faces as long as both are in contact with the same solution.

Even if the aspired equilibrium state could not be reached or is reached after a long period of time it is possible, that a mismatch state is relevant for the load. Because the solution within the pore system is the determining factor for an adjustment between the loaded and the free crystal faces, it had to be differentiated between the following cases:

1.) Crystallization in a solution filled pore system
2.) Crystallization as a result of drying or loss of resolvent

The basic differences as a result of these different settings were described in the following chapters.

4.1 Crystallization in a solution filled pore system

If nucleation takes place in a supersaturated solution it is likely that crystallization occurs in pores of all size, whereas the pore radius has to exceed the minimum radius of the crystal seed. The examined brick materials generally contain pores which were lager than the minimum radius of the seed crystals appending to the determined degrees of supersaturation, thus this consideration could be neglected. But if the considered material contains a relevant fraction of pores with a radius smaller than 10 nm, like cement based materials, it is necessary to deal with it.

Additional to the assumption that crystallization takes place in pores of all sizes we presumed a heterogeneous nucleation because of the great inner surface of the pore system and the presence of particles in the solution.

Assuming a steady crystal growth, the crystals will first reach the pore wall of the smallest pores. After that further crystal growth could only take place at the side faces because the shape of the crystal is limited by the pore wall at the other faces. To hinder the crystal to grow at these faces a pressure is necessary. The value of this pressure depends on the degree of supersaturation of the solution and corresponds to the crystal growth pressure acting on the pore wall (Fig.4.1b, c).

A continued crystallization could also occur within the greater pores, presuming that the solution is still supersaturated (Fig. 4.1d).

Because of the different solubility between the loaded and the unloaded crystal faces there does not exist an equilibrium state that is valid for the whole system if all crystal faces are connected with the same solution. If the degree of supersaturation decreases during the crystal growth, firstly the pressed crystal face would dissolve when they are getting undersaturated and lead to a deterioration of the load. The increasing activity of the solution will be decreased by further growth of the free crystal faces. Finally an equilibrium state is aspired were no pressure is produced on the pore walls (Fig. 4.1e).

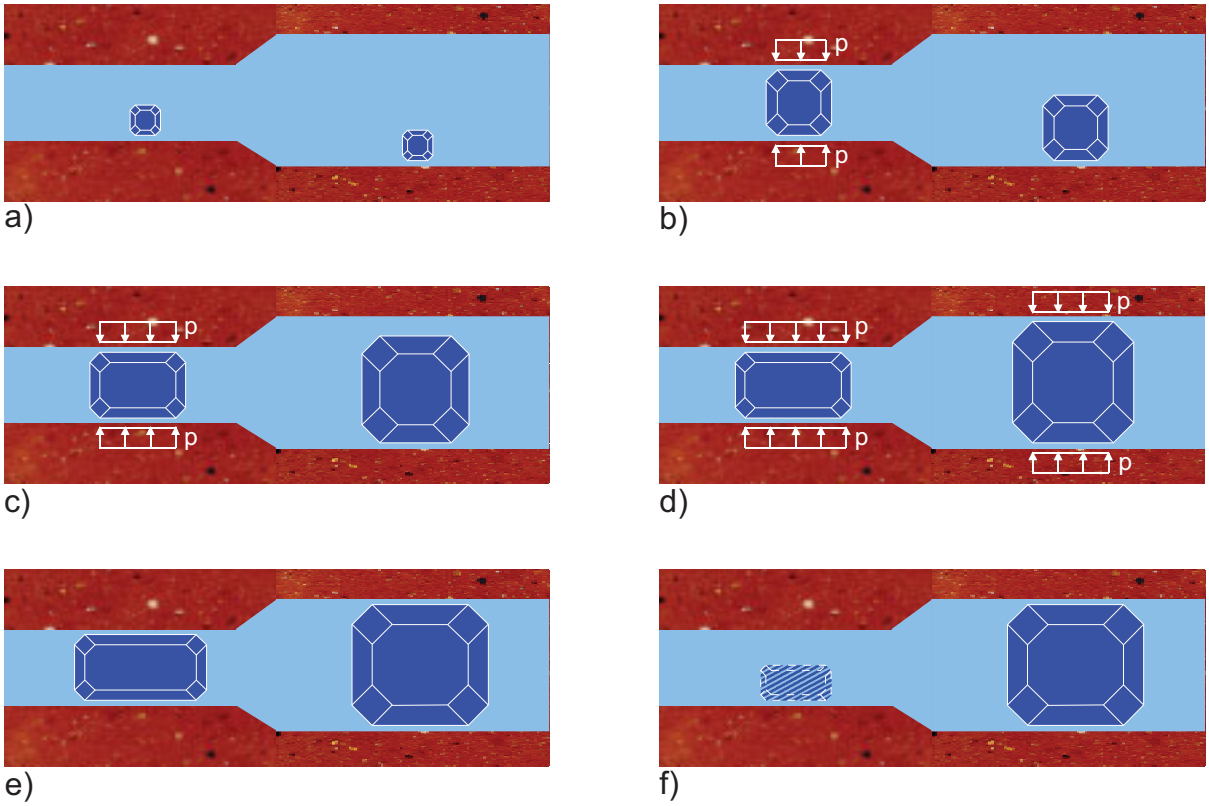

Figure 4.1: crystal growth in pores of different size

Because of the influence of the crystal size on the solubility is important in the case of very little crystals (< 10 nm) it has to be considered when the pores have a similar size. This would lead to the dissolution of the smallest crystals in favour of the larger ones (Fig. 4.1f).

A thermodynamic equilibrium state is reached when all crystals have the same size, because their chemical potentials depend on its sizes. Because of this effect the literature is referred to as the “preferred crystal growth in the greater pores” [12], [10]. Many citations said, that crystal growth only occurs in the greater pores supplied by the dissolving salt in the smaller ones, like it is demonstrated in Fig. 4.1f [12], [3].

This thermodynamic reflection which only regards the equilibrium state is not relevant for the load of a material due to crystallization. In the case of brick material the fraction of pores where this effect has to be considered is normally negligible. Furthermore, only regarding the equilibrium state (concerning the whole pore system) would ignore the local (temporary) stress such as in the smallest pores, thus the damaging potential of a salt would be underestimated.

Regarding the case of crystallization in a porous system with different pore sizes, it is important to note which equilibrium- or disequilibrium-state could develop and how long it could persist. Therefore some assumptions have to be made, like in the case above, were an instant diffusion of ions, which yields an equal activity in the solution at every point of time was estimated. The real behaviour can vary considerably depending on the transport parameter given by the pore system and the amount of solution. It is possible that a disequilibrium state gets relevant and persists without reaching the equilibrium state because the transport of solution is hindered seriously. This effect was mentioned by the experiments with sodium sulphate in the difference temperature measuring system.

4.1.1 Crystallization in a solution filled porous system in practice

In practice there are several possibilities that crystallization can take place in a solution filled porous system.

Normally the solubility of every salt depends on the temperature whereas in the most cases the solubility increases with an increasing temperature. Because of this dependency it is possible that a change in temperature could cause crystallization in practice, if a porous material is filled with solution.

This was simulated by the experiments in the difference temperature measuring system.

Another case occurs when a porous material in soaked in solution permanently and the water evaporates at the surface of the construction element.

This could take place when a wall without a sealing is in contact with a humid ground. If it is soaked in water permanently, then crystallization could occur without drying of the material.

In the experiment [FRA-2005] this was reached by hydrophobizing the surface of the samples, where the bottom was put into saline solution. Thus the whole sample was saturated with the solution up to the upper area which was hydrophobized. Like in the case, the crystallization would take place in all pores, were the solution gets supersaturated (under the hydrophobized zone, were the water evaporates) and firstly exerts a pressure on the pore walls of the smallest pores. So the same mechanism of load is obtained here.

But in this case it is possible that the whole pore system is filled with salt because of the continued transportation of solution. This represents the worst case, because in this case it would be possible that all crystals could exert a pressure on the pore walls.

In practice this observation could be made when gypsum crystallizes within a brick material. Normally it takes years for a coating of gypsum to accumulate under the surface of the material. Because of the low sizes of the crystals, a pressure could only be exerted when a great part of the pore volume is filled up by salt. Because of this, a damage will occur not until the amount of gypsum is extremely high. This effect could also be demonstrated by experiments [4], [7].

4.2 Crystallization in a solution filled porous system by drying

If salt crystallizes within a porous material due to drying, besides the crystallization in the different pores, the transport of solution between them also has to be regarded.

Krischer described in [8] a mechanism of drying of a material with a capillary porosity. He simplified a porous material with a pore size distribution, by two connected cylindrical pores with different radius. These two pores are initially completely filled up with water. It could be demonstrated that in case of drying them, the greater pore empties first because of the higher capillary suction of the smaller pore. The effect is also valid for a pore system with a continuous pore size distribution.

This has to be considered if crystallization occurs in a porous material with different pore sizes in case of drying.

Assuming that at the beginning, if the whole pore volume is filled up with saline solution it is likely that nucleation also takes place in the pores of all sizes (Fig. 4.2a). The water lost due to evaporation leads to the transport of solution from the bigger to the smaller pores (Fig. 4.2b). Thus the biggest pores dry up first and the crystal growth will stop in these parts of the pore volume. In this case the biggest pores are keeping supplies for the smaller ones.

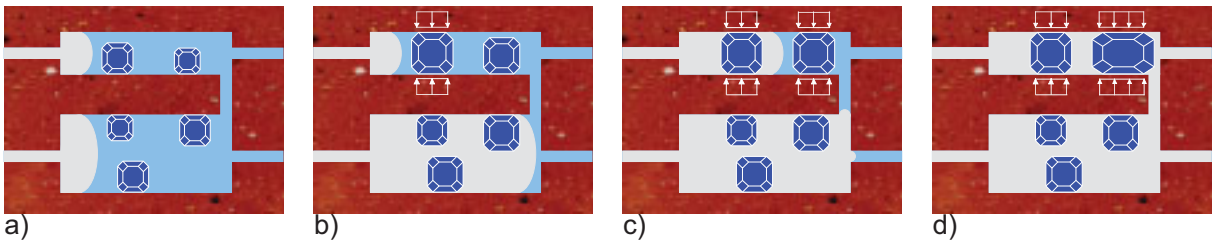

Figure 4.2: crystal growth due to evaporation of water (drying)

Because of the drying of the bigger pores the crystallized salt gets insulated and they are no longer in contact with the solution. Thus on the one hand the crystals which are not yet exerting a pressure could not exert a load during the further crystallization because their growth has stopped completely. On the other hand a crystal which is already exerting a pressure cannot

dissolve as long as it is not in contact with water or solution. Thus a load case persists up to the moment, when the material is moistened again (Fig. 4.2c).

In practice we get this mechanism when a porous material is moistened (e.g. due to sprinkling) followed by drying at its surface. A change of the moisture content could also occur because of a change of the relative humidity, particularly when the pore system already contains salt which could take up water by vapour to form a solution.

Due to an alternating load due to crystallization and dissolution, it is possible that a material is damaged by fatigue.

5 References

[1] B. Brehler; *Über das Verhalten gepresster Kristalle in ihrer Lösung*, Neues Jahrbuch für Mineralogie, (1951)

[2] C.W. Correns, W. Steinborn; *Experimente zur Messung und Erklärung der sogenannten Kristallisationskraft,* Zeitschrift für Kristallographie, Bd. 101, Heft 1/2, S. 117–133, (1939)

[3] B. Fitzner, D. Basten ; *Gesteinsporosität - Klassifizierung, meßtechnische Erfassung und Bewertung ihrer Verwitterungsrelevanz,* Jahresbericht Steinzerfall – Steinkonservierung, (1994)

[4] L. Franke, R. Espinosa, G. Deckelmann; *Die zeitliche Abhängigkeit der Phasenumwandlung von Salzen in kapillarporösen Baustoffen*, Feuchtetag 2004, DGfZP Berichtsband 91, (2004)

[5] J. Grunewald, G. Deckelmann, C. Kaps, M. Steiger; *Modellierung, Software-Implementierung und Verifikation des Feuchte- und Salztransportes, der Salzkristallisation und -schädigung in kapillarporösen Mauerwerksstoffen,* DFG-Zwischenbericht (SSP 1122), (2005)

[6] A. La Iglesia, V. Gonzalez, V. Lopez-Acevedo, C. Viedma; *Salt crystallization in porous construction materials I.Estimation of crystallization pressure*, Journal of Crystal Growth, Bd. 177, S. 111-118, (1997)

[7] S. Kiencke; Beanspruchungsmechanismen und kritischer Gehalt von Salzen in porösen Materialien, Dissertation, GCA-Verlag, 2006

[8] O. Krischer; *Die wissenschaftlichen Grundlagen der Trocknungstechnik*, 3. Ausgabe, Springer, (1978)

[9] H. C. Kühne; *Untersuchungen zum Einfluß der Porenstruktur auf die Dauerhaftigkeit baukeramischer Produkte bei Einwirkung von Salzen oder Frost,* Dissertation TU Hamburg-Harburg, (1997)

[10] J. D. Neisel; *Rasterelektronenmikroskopische Untersuchung der Gefügemerkmale von ungeschützten und imprägnierten Sandsteinen nach Verwitterungsbeanspruchung,* Dissertation RWTH Aachen, (1995)

[11] F.S. Rostásy, F. Schmidt-Döhl, S. Linnenberg, *Materialschädigung durch Phasenneubildung in mineralischen Baustoffen*, Abschlußbericht zum Forschungsprojekt der DFG, (2001)

[12] R. Snethlage; *Steinkonservierung, Forschungsprogramm des Zentrallabors für Denkmalpflege,* Bericht für die Stiftung Volkswagenwerk, (1983)

Maren Heidmann
Dipl.-Min.

Frank Schmidt-Döhl
Prof. Dr.-Ing.

Ellen Rigo
Dr. Ing.

Hamburg University of Technology
Institute of Materials, Physics and
Chemistry of Buildings, Germany

iBMB MPA Braunschweig
Germany

Extension and Application of the Simulation Program Transreac to Investigate Debonding of Gypsum Plaster and Concrete

Summary

The title of the paper describes the aim of the research project. It consists of the following parts: 1: Necessary extension of the simulation program Transreac. 2: Debonding experiments in laboratory to examine if Transreac is able to simulate this type of damage. 3: Determination of material properties of gypsum and concrete, necessary for the simulations, for example diffusion coefficients in the unsaturated state. 4: Transreac simulations considering the influence of carbonation, moisture conditions of the concrete at the time of plastering and the chemical composition of concrete and gypsum will give us a more detailed insight into the damage process and strategies to avoid it. The research project is not finished until now. Preliminary results are presented.

Keywords: *debonding of gypsum plaster on concrete, dissolution of gypsum, syngenite formation, simulation, K^+ diffusion coefficient of unsaturated materials, Transreac*

1 Introduction

Debonding of gypsum plaster on concrete surfaces is a frequent type of damage. Until the first falling down of pieces some weeks or some years will elapse. It seems that the number of such damages is increasing over the last years. The damages are not restricted to certain gypsum producers or concrete surfaces with or without contact to the formwork and also application of a bond coat will not prevent such damages. The state of the art was comprised in [1]. Examinations in the past showed, that the typical damage, bulging in the middle of a structural component, must be caused by a former loss of adhesion between gypsum and concrete. Only if the debonding has occurred, the plaster is deteriorated due to a loss of stability by shrinkage or other deformations. But our knowledge about this process and the traditional rules to avoid a loss of adhesion, like a period of 60 days without frost between concrete placement and plastering, are insufficient.

In most cases it can be shown that the drying out of excess water from the concrete through the contact plane between concrete and gypsum must be very important for the process.

In such cases a formation of syngenite ($K_2Ca(SO_4)_2\ H_2O$) can be analysed at the contact surface of the plaster. Syngenite can only by detected by X-ray diffraction when the surface of gypsum specimens is analyzed directly without any preparation and mechanical treatment and is not detectable in the gypsum itself. This shows that the transport of potassium from the concrete pore solution to the contact plane is a precondition of syngenite formation. Syngenite is also not detectable if the concrete had enough time to dry out before plastering and is detached by another process like constraint. In same cases instead of syngenite ettringite will be detected. This new formation of a solid phase may be a possible cause for the loss of adhesion. Another possible process causing the loss of adhesion may be the dissolution of gypsum at the contact with concrete. This is an interesting point, because the solubility of gypsum in a concrete pore solution with high pH is much higher than in water. After plastering of a non carbonated concrete with high residual water content the alkaline concrete pore solution is in contact with the gypsum. It was not clear, which of the two processes is of more importance.

2 Aims of the research project

It is the aim of the research project described here to extend the simulation program Transreac in such a way, that the software can be applied to the problem of gypsum plaster detachment. Therefore it is necessary to treat the diffusion coefficients of solved species as functions of the moisture content of the material. The simulation of capillary transport of water and solved species in unsaturated materials must be improved too. Then the simulation program should be used to examine if the dissolution of gypsum or the new formation of solid phases are the cause for the loss of adhesion, and which influence the climatic conditions and the composition of the gypsum and the concrete have on the process.

The calculations are accompanied by experimental investigations. The aim of the experimental part of the project is to determine material properties, necessary for the simulation, and to examine if the program is able to simulate a damage of gypsum plaster on concrete at laboratory conditions.

This ongoing research project started with the beginning of the third period of the priority program 1122. It was not finished until the deadline of the paper. So only preliminary results can presented.

3 Structure of the simulation program Transreac

Figure 1 shows the basic structure of the simulation program Transreac, complemented by additional features that are possible in some transport or reaction models in principle. In the main, Transreac is a combination of a reaction model, a transport model, modules for the actualization of transport parameters in corroded areas and modules to simulate corrosive effects, like expansion in the case of a sulphate attack. The development of Transreac started in 1991. The algorithm is in practical use since 1997. Examples for the application of Transreac are shown in [2]. During the priority program 1122, Transreac was extended to a probabilistic model (see paper of Rigo, Schmidt-Döhl and Budelmann and [3]).

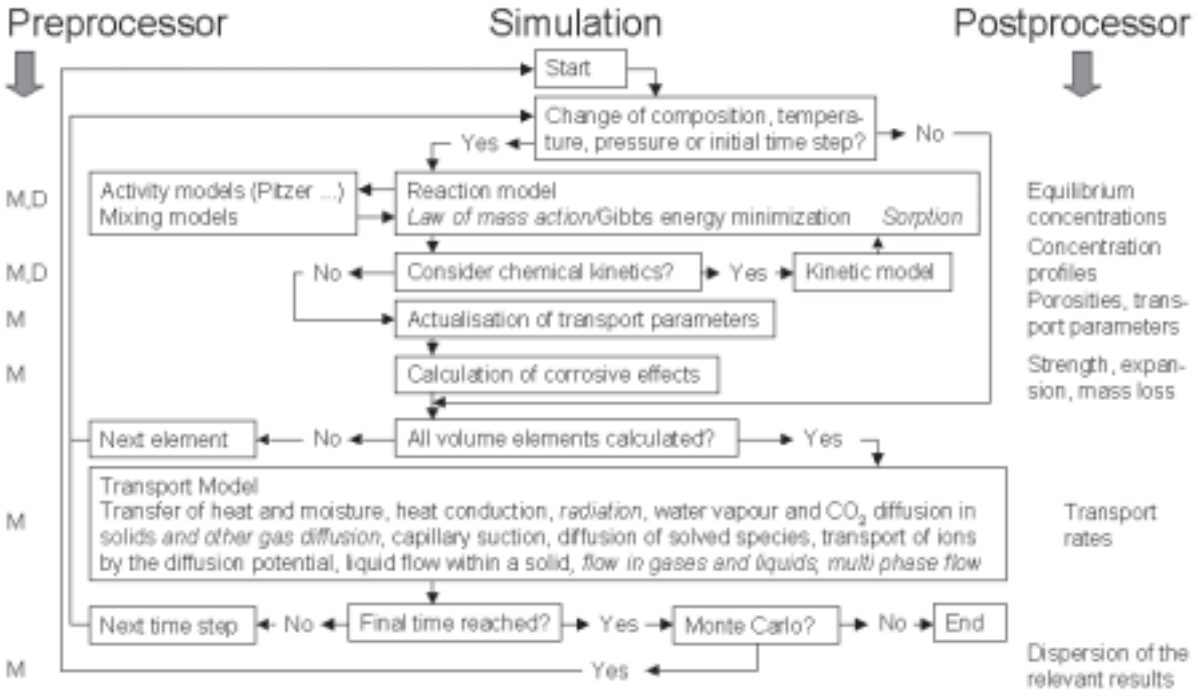

Figure 1: Basic structure of a transport-reaction model. Modules in italics are not incorporated in Transreac. M – input data about materials, environment and the structural member, D –material independent input data. From [2].

4 Debonding experiments

Debonding experiments were planned to test the simulation program Transreac with data measured under defined environmental conditions and material properties. For these tests compound samples made of concrete with a height of 11 cm and gypsum plaster with a height of 1 cm were used. The width of the samples was 20x20 cm (see figure 2). The concrete was made with cement CEM I 32,5 R, a cement content of 312 kg/m^3, a water/cement ratio of 0,69 and a maximum grain size of 8 mm. The gypsum plaster (Knauf MP75) was spray applied on the surface of the concrete samples after two different very short hydration times (7 and 21

days). In addition specimens with and without a bond coat were produced. All sample sides were sealed with the exception of the gypsum plaster to get one dimensional and reality like drying conditions. The specimens were then stored at 20° C and 65 % relative humidity and tested regularly for debonding by sounding and pull off strength tests.

In addition, cylindrical compound samples with concrete and gypsum plaster with a diameter of 5 cm were tested at the Fraunhofer Institute für Bauphysik Holzkirchen by NMR, to get information about the moisture profiles as function of time.

Compound specimens with a mortar and the gypsum plaster were examined with X-ray computer tomography (CT), to get information with a non destructive test about structure changes in the contact zone between mortar and gypsum plaster. For this examination small specimens with 8 mm diameter and 12 cm height (1 cm gypsum, 11 cm mortar) must be used to get a high resolution of about 10 micrometers (1/1000 of the diameter). The compound specimens for the CT-investigations were made with the same cement, water/cement ratio and gypsum like the concrete specimens. The CT examinations were prepared by the Bundesanstalt für Materialforschung und -prüfung (BAM), Berlin.

Unfortunately the specimens do not show any debonding even at an age of two years. So these debonding experiments can not be used to test the simulation program up to now. We then decided to store some of the specimens at 23° C and 80 % relative humidity, because it is possible, that the relative humidity of 65 % is too low to get remarkable transport rates of solved species by diffusion. Some of the specimens were stored further on in contact with water to get a capillary suction from the rear. The side with gypsum plaster is stored at 80 % relative humidity. We hope we will get a debonding of the compound specimens in future.

4.1 Pull off strength tests

The compound specimens with concrete and gypsum plaster were tested for their pull off strength at different times. Different to DIN 18555 part 6 we used a squared test field of 50 x 50 millimetres. This squared test fields were prepared with a diamond saw. This is more gentle for the bond as drilling (fig. 2, right side).

Table 1 shows the results of these pull off strength. No remarkable change of the pull off strength can be observed until 24 months.

Table 1: Results of pull off strength tests

Storage time	**Without bond coat**		**With bond coat**	
Hydration time before plastering	**7 days**	**21 days**	**7 days**	**21 days**
3 month	0.61 ± 0.15	0.59 ± 0.09 N/mm^2	0.62 ± 0.06 N/mm^2	0.50 ± 0.06 N/mm^2
24 month	-	0.50 ± 0.08 N/mm^2	0.55 ± 0.03 N/mm^2	0.53 ± 0.07 N/mm^2

- not measured

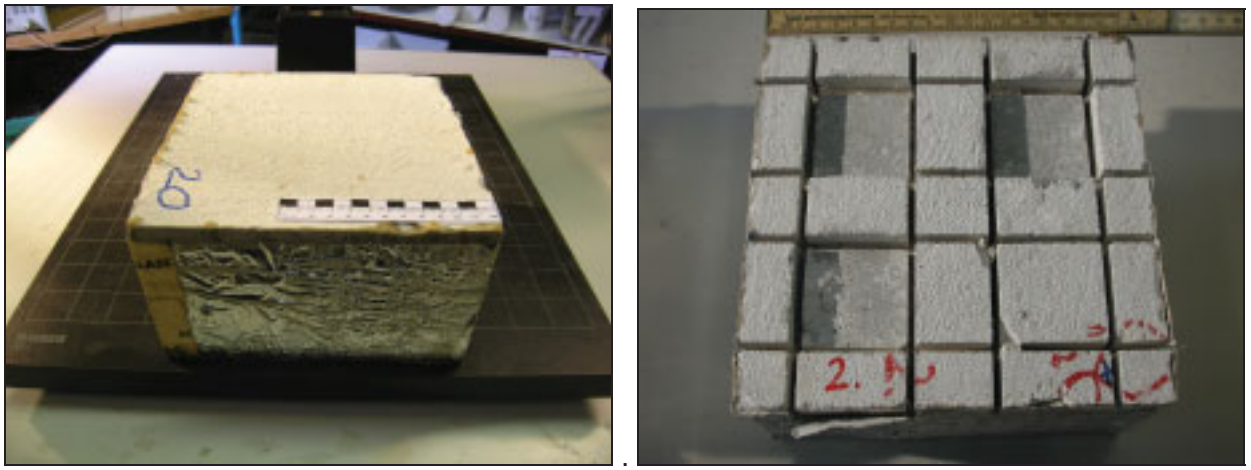

Figure 2: Compound sample before (left) and after (right) pull off strength test

4.2 X-ray computer tomography (CT)

The aim of these experiments was to see any structural changes near the contact surface of plaster and concrete. In particular the solution of gypsum will result in a decrease of the density of the contact zone. For this part of investigation compound samples of mortar and plaster within a cylindrical plexiglas mould with an inner diameter of 8 millimetres were prepared. The height of the CT-samples and the storage conditions were like the compound specimens with concrete and gypsum. The samples are measured after storage for 3, 5, 14 and 24 months. Figures 3 and 4 show CT-pictures of one sample, taken after 5 and 24 months storage. No remarkable density changes can be seen, in particular no mineral dissolution.

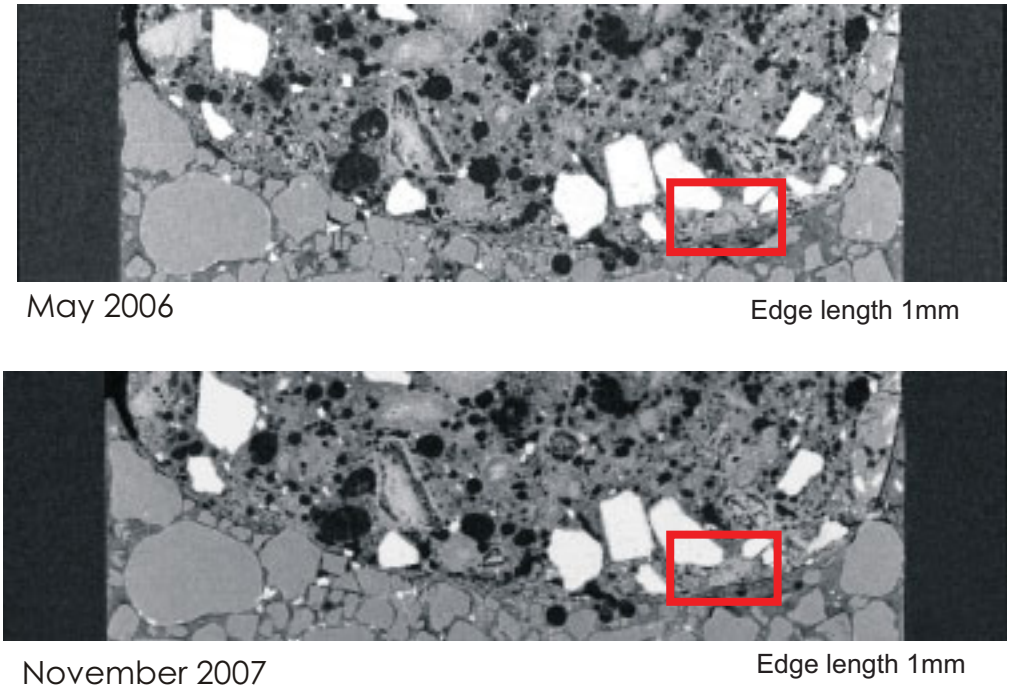

Figure 3: X-ray CT examinations after 5 (May 2006, top) and 24 (November 2007, below) months storage, top: gypsum plaster, bottom: mortar.

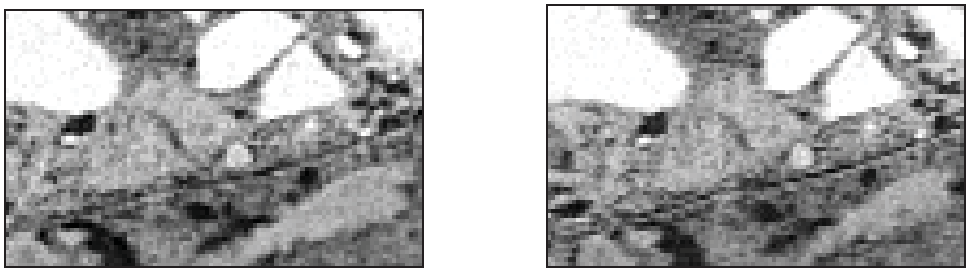

Figure 4: X-ray CT examinations – detail of field marked in red in figure 3.
Left: May 2006; right: November 2007. Width of the pictures: 1 mm.

4.3 Moisture profiles measured by NMR

Beside biology, chemistry and medical science Nuclear Magnetic Resonance Spectroscopy (NMR) is a laboratory method to measure moisture profiles with high resolution. NMR uses the spin of positive charged protons and their resultant magnetic moments due to the fact that the protons are not equally distributed. In an applied magnetic field the hydrogen nuclei behave like magnetic dipoles. There are two possible energy levels of the protons. They are related to the orientation of their magnetic moments – parallel or anti parallel to the orientation of the applied magnetic field, due to the effect of an alternating magnetic field with a certain frequency vertical to the constant field, changes between the different energy levels are induced. The absorbed energy of a sample depends on the number of the protons in the sample and can be used to

determine the moisture content of a sample, because in building materials hydrogen protons occur commonly as water.

Figure 5 shows NMR moisture loss profiles (drying from the left side) of concrete gypsum plaster compound specimens with a hydration time before plastering of 7 days, with bond coat at different times spans after plastering. This moisture profiles will be used to test the simulation program.

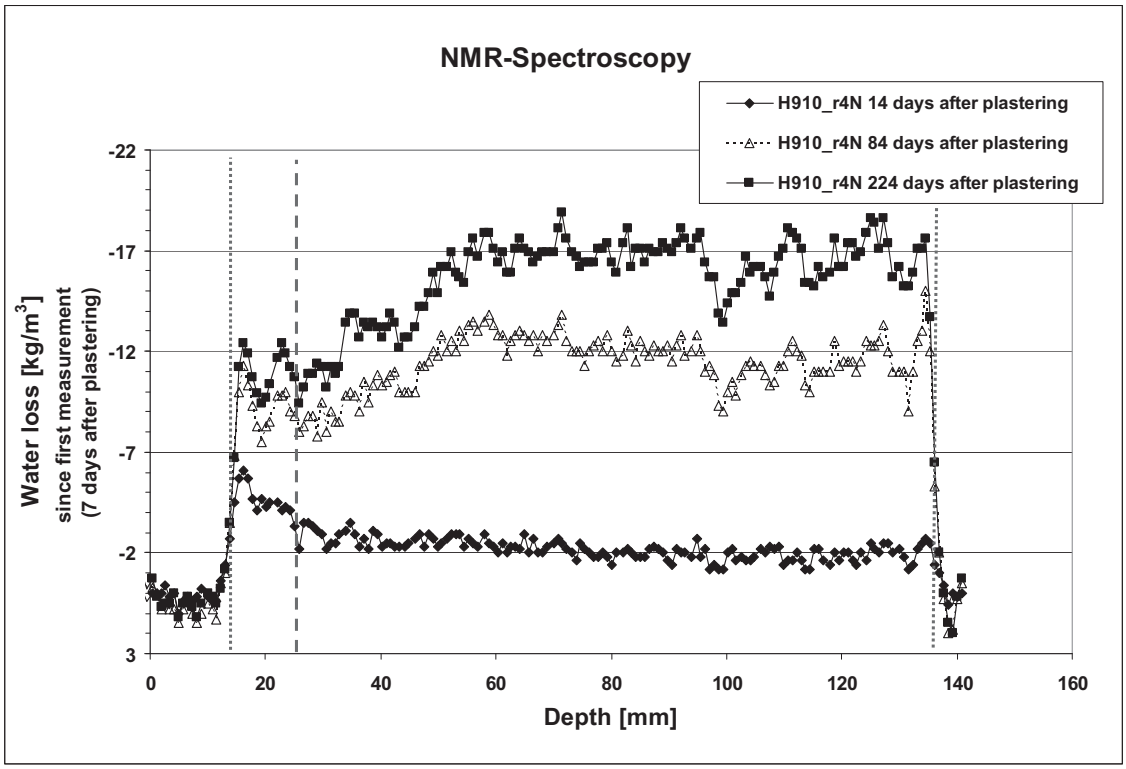

Figure 5: Time dependent moisture loss profiles of compound sample made of gypsum plaster (left) and concrete (right) determined by NMR spectroscopy. The vertical dotted lines indicate the beginning (left) and the end (right) of compound specimen. The dashed line indicates the contact between gypsum plaster and concrete.

5 Experimental examination of initial material data for simulations

To investigate debonding of gypsum plaster and concrete by computer simulation with the software Transreac some material specific initial data are needed. We determined these data for the concrete and the gypsum plaster used in the debonding experiments.
These data used for Transreac simulations are:

- The reactive initial phase assemblage: see tables 2 and 3
- The concentration of non-reactive material in the concrete (aggregates and the unhydrated cement): 1807 kg/m^3
- Pore radius distribution determined by mercury intrusion porosimetry: see figures 6 and 7. Mean value of total porosity by mercury intrusion: gypsum 436.88 mm^3/g, concrete 73.772 mm^3/g.
- Diffusion coefficients of solved species as a function of moisture content: see chapter 5.1
- Bulk density of the dry material: gypsum 1119 kg/m^3, concrete 2083 kg/m^3
- Water uptake in vacuum: gypsum 53.13 vol.-%, concrete 20.97 vol.-%
- Water uptake without pressure: gypsum 34.08 vol.%, concrete 18.93 vol.-%
- Water desorption isotherms: see figure 8
- Air void content of concrete: 2.60 vol.-%
- Water vapour diffusion resistance factor (dry): gypsum 8.3, concrete 115.5
- Rate constants to simulate chemical kinetics of gypsum solution, syngenite formation and ettringite formation: not clear if necessary and not determined until now
- Water absorption coefficient: gypsum 5.63 kg/m^2 h$^{0.5}$, concrete 2.53 kg/m^2 h$^{0.5}$
- Parameters to describe capillary transport without contact of the material with free water. These parameters will be determined by analysis of time dependent moisture profiles in concrete and gypsum determined by NMR, see fig. 9.
- Maximum porosity in case of chemical attack: gypsum 100 vol.-%, concrete 31.55 vol.-%

For the following material specific and material independent parameters, estimations were used for Transreac simulations, based on literature data:

- Specific heat capacity 850 J/kg K
- Heat conductivity as a function of moisture: gypsum 0.2 W/m K, concrete 1.4 W/m K, increase of 8 % per m.-% moisture increase
- Solar absorptance: gypsum 0.7, concrete 0.7
- Heat transfer coefficient: 8 W/m^2 K
- Moisture transfer coefficient: $2.2 \cdot 10^{-8}$ kg/m^2 s Pa
- Mean density of non-reactive material in the concrete (aggregates and the unhydrated residual of the cement): 2640 kg/m^3
- Temperature dependence of anion diffusion (activity coefficient, reference temperature 296.15 K): gypsum 22.8 kJ/mol, concrete 45.3 kJ/mol [4, 5]
- Temperature dependence of cation diffusion (activity coefficient, reference temperature 296.15 K): gypsum 20.8 kJ/mol, concrete 56 kJ/mol [4, 5]
- Temperature dependence of neutral species diffusion (activity coefficient, reference temperature 296.15 K): gypsum 17.5 kJ/mol, concrete 17.5 J/mol [4, 5]

Table 2: Reactive initial phase assemblage of gypsum plaster used in Transreac simulations

Phase	Concentration in mol/m^3
Anhydrite	474.16
Water	31854
Calcite	429.96
Gypsum	6939.3
Bassanite	444.73

Table 3: Reactive initial phase assemblage of concrete used in Transreac simulations

Phase	Concentration in mol/m^3
CO_2 gas	92.75
C_3A	110.03
C_4AF	58.95
C_2S	148.66
C_3S	788.35
Anhydrite	116.73
Water	11934.21
Na_2O	4.02
K_2O	38.04

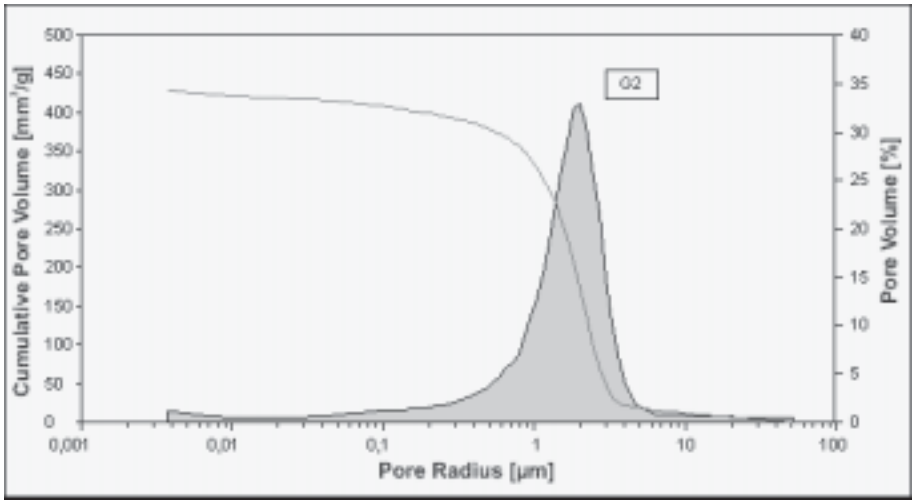

Figure 6: Pore radius distribution of gypsum used in Transreac simulations

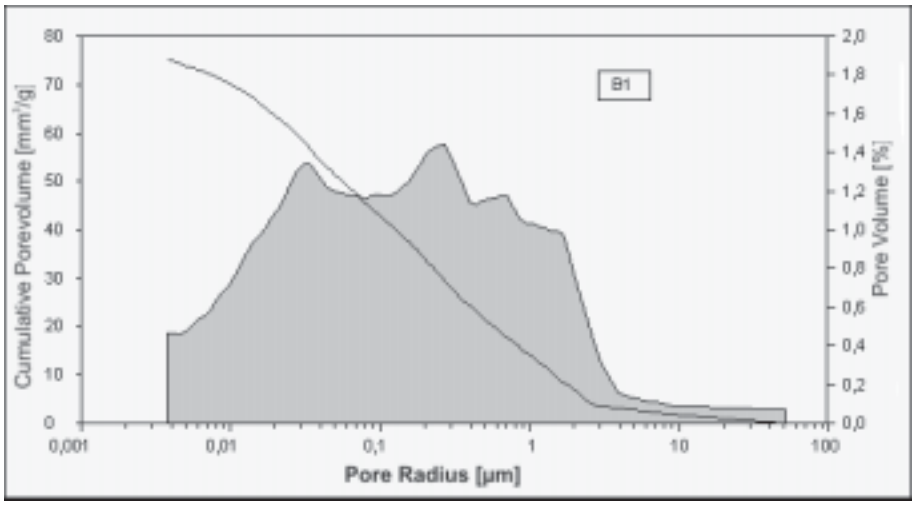

Figure 7: Pore radius distribution of concrete used in Transreac simulations

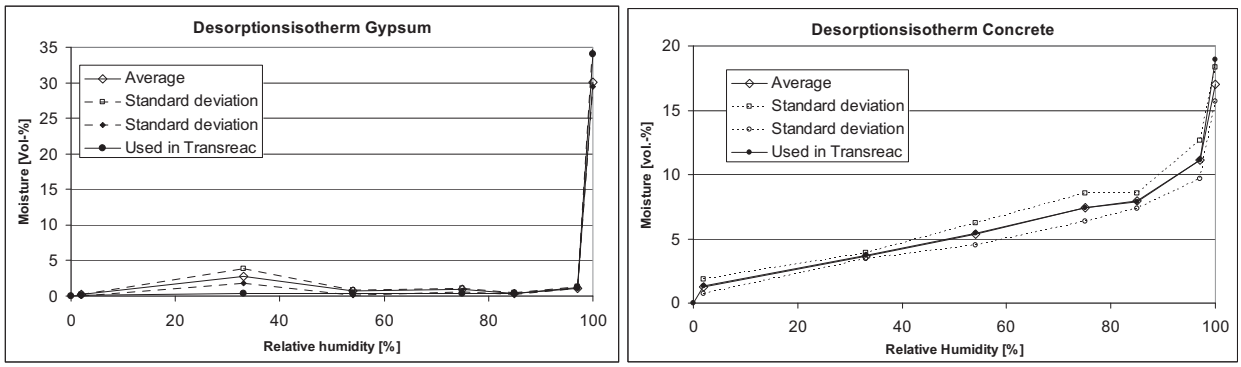

Figure 8: Left: water desorption isotherm of gypsum plaster. In Transreac simulations we are ignoring the maximum at 33 % r.h.
Right: water desorption isotherm of concrete used in Transreac

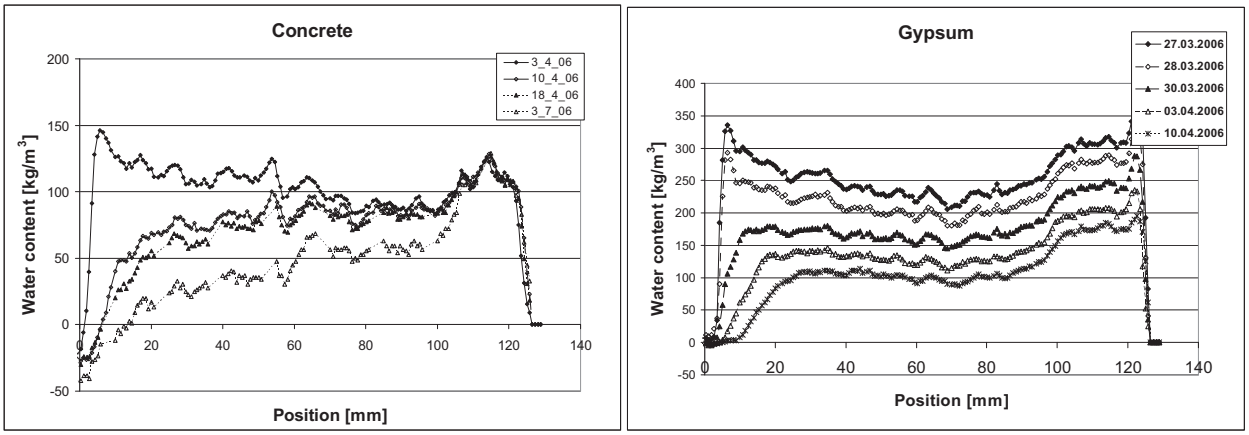

Figure 9: NMR moisture profiles of concrete (left) and gypsum plaster (right) to determine capillary transport parameters without contact of the material with free water. After hardening, the samples (diameter: 50 mm) were stored for about four months at 65 % relative humidity and 23°C, then stored in water with one open face (left side, concrete 14 days, gypsum plaster 7 days). The measurement started after restorage at 65 % relative humidity and 23°C.

5.1 Diffusion of solved species in gypsum and concrete as function of moisture content

To simulate the new formation or dissolution of phases in the system gypsum plaster and concrete, diffusion coefficients of solved species in the unsaturated state must be known. For the experimental determination we decided to use non steady state isothermal diffusion experiments with potassium, because potassium can be analyzed by X-ray fluorescence very well. Small prisms of concrete and plaster with a base area of two squared centimetres were stored at 23°C in 51% and 75% relative humidity as well as in water or gypsum saturated solution resp., until weight constancy. Adjacent they were sealed with epoxy except one squared surface (fig. 10). On this open area we applied a concentrated potassium hydroxide solution.

Figure 10: Sketch of KOH application

After application the samples were dried back to the weight they had before to reduce the influence of capillary water transport. So an area with a KOH-saturated pore solution or very high KOH-concentration was produced at one end of the specimens. After application and drying to the original weight all samples were stored back in their relative humidity they had before, and saturated samples were sealed completely. After time intervals of 24 h, 7 d, 14 d, 28 d, 56 d, 120 d and 180 d the distribution of potassium concentration was analyzed by the X-Ray Analyti-

cal Microscope Horiba XGT-7000 (μ-XRF). The measurement conditions we used were 15 kV excitation voltage, 1.0 mA current intensity and a capillary tube with 1.2 mm diameter. To protect the capillary tube and due to the moisture content of the samples we used a partial vacuum during the measurements.

Because the samples – particularly the concrete samples – were so inhomogeneous, we did not determine the penetration depth of potassium by individual measurement points because it was not possible to discriminate definitely between very small aggregates and cement matrix. The $CaO:SiO_2$ ratio did not help to eliminate satisfactorily the influence of the aggregate to the measurements. Therefore we took mappings of the specimens. Out of the received mappings we took line-scans ignoring whether there were aggregates or not – except aggregates with remarkable high potassium content. The high number of line scans reduced the effect of aggregates to the determination of the diffusion front more than individual point measurements did.

For estimation of the diffusion coefficient we used the profile after 24 h as origin to eliminate possible influence of capillary transport mechanisms. Figure 11 for example shows two concentration profiles determined from a concrete sample stored in 51% (left) and 75 % (right) relative humidity for 24 h and 28 and 180 days after KOH application, respectively.

The diffusion coefficient of K was determined by simulation of the experiments with Transreac and variation of the diffusion coefficient until optimal correspondence of the form of the profile with the experimental data occurs. As an example the following preliminary diffusion coefficient was determined for concrete at 23 °C and 51 % r.F.: $8.6 \cdot 10^{-14}$ m^2/s.

All other diffusion coefficients were determined by multiplying these experimental values with constant factors which approximately describe the different velocity of solved species in aqueous solutions in proportion to the K^+ diffusion ([4, 5]).

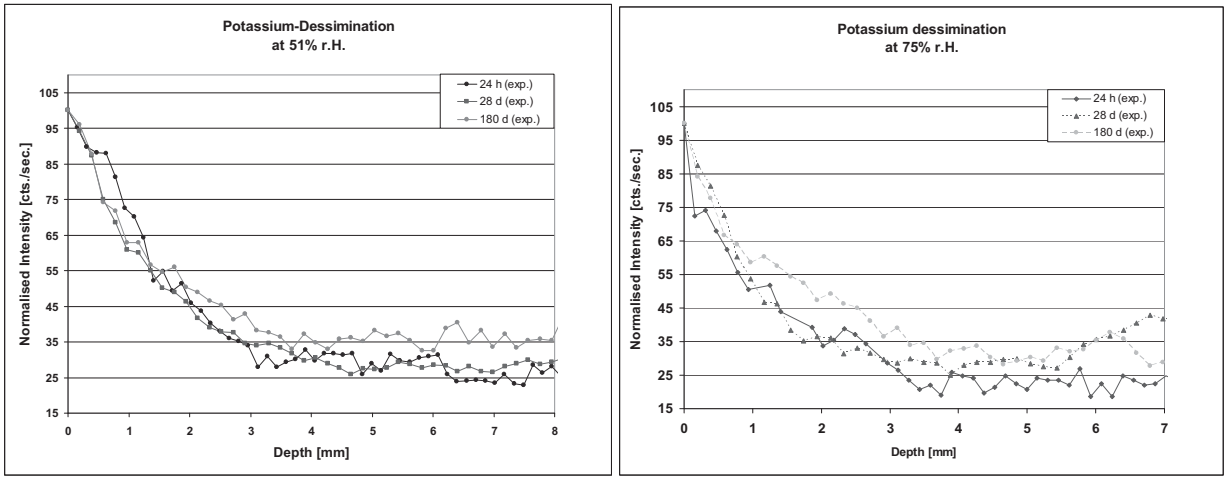

Figure 11: K-concentration profile of a concrete sample stored at 51 % (left) and 75 % (right) relative humidity, 24 h, 28 d and 180 d after KOH application.

6 Simulation

To simulate the transport processes and chemical reactions in a gypsum plaster concrete compound we are using one dimensional models. Figure 12 depicts such a model. The point of interest within this system is the contact surface between the gypsum plaster and the concrete. So we are using rather small elements near this surface, about 0.5 mm thick. The boundary conditions, for example temperature, relative humidity and heat and moisture transfer coefficients, are defined by an air element.

At the moment we only can present preliminary results of such calculations. Figure 13 shows an example of such a test simulation, in this case with approximated and not moisture dependent diffusion coefficients. Figure 13 depicts plastering after 30 days hydration time compared to plastering after 60 days hydration time of the concrete, at 51 % relative humidity and 20 °C, respectively. The displayed concentrations are certainly too high. But it can be seen, that the simulation is able to calculate a new formation of syngenite at the gypsum side of the contact surface, like in reality. There is also gypsum dissolving at this area, but only a small amount. Also it could be seen that with plastering after 60 days no syngenite is crystallised.

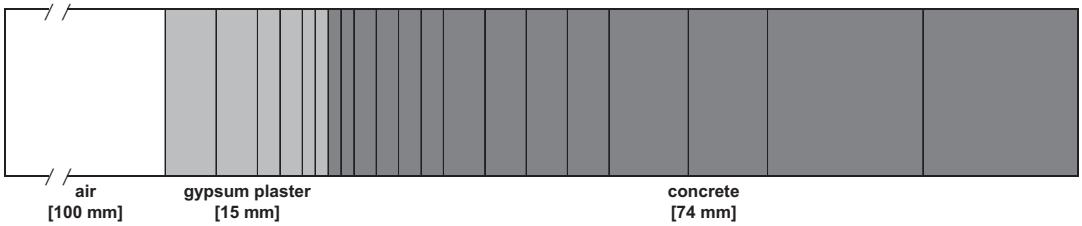

Figure 12: A compound sample made of gypsum plaster (grey) and concrete (dark grey), created for simulation with Transreac.

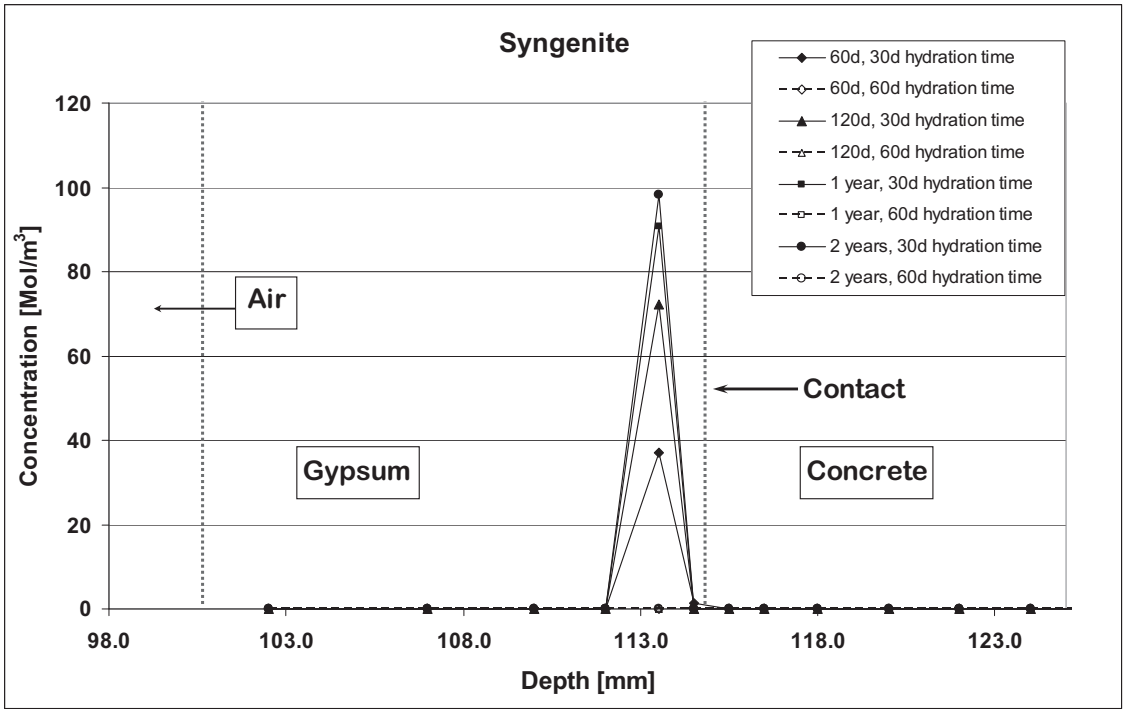

Figure 13: Syngenite new formation at the gypsum side near the contact surface between gypsum plaster and concrete at a function of time. The diffusion coefficients are approximated and not moisture dependent at the moment. So the calculated concentrations are certainly wrong. But the process of syngenite formation can be simulated. $8.6 \cdot 10^{-14}$ m^2/s diffusion coefficient for potassium cations.

7 Discussion

Unfortunately the compound specimens do not show any debonding up to now. So at the moment these experiments can not be used to test the simulation program. It seems that a relative humidity of 65 % is too low to get remarkable transport rates of solved species in the area of the contact surface between concrete and gypsum. We hope that the storage of the specimens in 80 % r.h. and the storage of some specimens in contact with water at the rear will produce a damage, which can be used to test the simulation program under laboratory conditions.

Preliminary simulations show a new formation of syngenite on the gypsum side of the contact surface between concrete and gypsum plaster, like in reality. There is also gypsum dissolving at this area, but only a small amount.

Further results of the ongoing project based on simulations of mass-transport- und reaction processes in multilayered non-saturated building components and considering the influence of carbonation, moisture conditions of the concrete at the time of plastering and the chemical composition of concrete and gypsum will give us a more detailed insight into the damage progress and strategies to avoid it.

8 References

[1] Schmidt-Döhl, F.; Lampe, J.; Schrenk, J.: Causes of detachment of gypsum plaster on walls made of normal weight concrete and lightweight aggregate concrete to DIN 4219. Concrete Plant + Precast Technology, Vol. 68, p. 54-62, 2002.

[2] Schmidt-Döhl, F.; Rigo, E.; Bruder, S.; Budelmann, H.: Chemical attack on mineral building materials, features and examples of the simulation program Transreac. In: Stangenberg, F.; Bruhns, O.T.; Hartmann, D.; Meschke, G. (ed.): Proceedings of the Second International Conference Lifetime-Oriented Design Concepts, 1.-3. März 2004, p. 269-278, Bochum 2004.

[3] Rigo, E.: Ein probabilistisches Konzept zur Berurteilung der Korrosion zementgebundener Baustoffe durch lösenden und treibenden Angriff. Doctoral thesis, TU Braunschweig, 2005.

[4] Schmidt-Döhl, F.; Rostásy, F.S.: A model for the calculation of combined chemical reactions and transport processes and its application to the corrosion of mineral building materials. I. Simulation model. Cement and Concrete Research, Vol. 29, p. 1039-1046, 1999.

[5] Schmidt-Döhl, F.; Rostásy, F.S.: A model for the calculation of combined chemical reactions and transport processes and its application to the corrosion of mineral building materials. II. Experimental Verification. Cement and Concrete Research, Vol. 29, p. 1047-1054, 1999.

Jens Kruschwitz
Dr.-Ing.

Max J. Setzer
Univ.-Prof. rer. nat. Dr.-Ing. habil.

University of Duisburg-Essen, Institute of Building, Physics and Material Science, Essen, Germany

Multi phase and multi scale modelling of frost attack on cementitious materials

Summary

Surface physics and chemistry acting in the nano-scale affect fundamental properties of concrete such as strength, ductility, creep and shrinkage, fracture behaviour and here highlighted the durability against freeze-thaw. Recent data prove that the characteristic properties of both solid gel matrix and of pore water are essentially changed by surface interaction in the nano-scale. It is crucial to handle hardened cement paste as a linked system of both components characterised by naming 'Solid-Liquid Gel System' (SLGS). The model comprises the nano-effects in a smeared microstructure. On this basis the findings of Powers, Feldman and Sereda or the Munich model - can be improved essentially. In this contribution the properties of the sub-microscopic SLGS model are embedded in a macroscopic multi-phase and multi-scale model. At the macroscopic scale transient conditions with long relaxation times must be handled e.g. water-uptake and heat transport. The macroscopic aspects are processed by a thermome-chanical model based on the Theory of porous Media (TPM) consisting of a mixture of five interacting constituents. The TPM is a combination of the Theory of Mixtures and the concept of volume fractions. This multiscale model describes the characteristic freeze-thaw phenomena of cementitious materials like frost shrinkage, frost heave and artificial saturation during melting, been obviously two to three times greater than isothermal capillary suction. The methodology can be adopted to other properties.

Keywords: *frost shrinkage, water-uptake, modelling, Solid-Liquid Gel System, porous Media*

1 Introduction

It is well established that frost damage in porous materials is linked to the generation of internal pressures induced by the progressive formation of ice and the transfer of liquid water within the material's pore structure. During a freeze-thaw cycle a transient heat transport takes place with essential temperature gradients. This leads to transport of liquid to ice during freezing, trapping of water at the micro-ice-lenses and suction of external water into the concrete during heating as described in the micro-ice-lens model e.g. [22]. Litvan reported a convincing evidence of the subsequent migration of unfrozen water to the freezing sites [14]. The driving force for this ice

accretion phenomenon was linked to the existence of a free energy gradient between ice and unfrozen water. The existence of unfrozen water is due to high surface forces. If a critical degree of saturation is reached by this frost suction the damage sets in rapidly. So, when modelling durability aspects of cementitious material it is essentially to distinguish three size scales: A macro-, micro- and nanoscopic scale. For distinction here the temperature changes and their typical time constants are used.

The **microscopic** area is the easiest to handle - as a rule with typical dimensions between 0.1 µm and some millimetre. It comprises unhydrated cement and calcium hydroxide crystals. The capillary pores of this region are filled under normal environmental conditions with air or with water. Transport phenomena of both liquid - water and dissolved mater – and of gas - vapor and CO_2 - become increasingly important with growing pore diameter. Furthermore, on one hand the natural laws well known for usual macroscopic physics and chemistry are dominant. On the other hand thermal and thermodynamic equilibrium or at least a metastable state can be assumed. That means that water dries out near 100 % r.h. and during cooling below the freezing point ice is formed. Supercooling effects might take place, which are ended by heterogeneous nucleation.

The **macroscopic** scale starts at least above some millimetres. Subsequently, the relaxation time, especially for transport phenomena become larger as well as the usual observation time and the transient phenomena becomes dominant. This is the main domain of the numerical model. However, the values found in the microscopic scale are vital. They deliver the parameters for the modelling, e.g. transport coefficients for diffusion, liquid and heat transport.

The **nanoscopic** gel region smaller than 0.1 µm is characterised by the calcium-silicate-hydrate (CSH) gel, gel pores and adsorption layers on surfaces of gel particles. Here surface physics and chemistry become increasingly dominant with decreasing size. The gel pores are mostly filled with gel-pore water which deviates in its characteristic properties from bulk water; see e.g. [10]; [11]; [16]; [18]. For example, it freezes definitely below bulk freezing point and its density calculated by Powers is with 1.15 g/cm^3 higher than bulk water. Our findings, newly compiled in [23], do not correspond with this statement. In the Munich model [19]; [26]; [30] surface energy and disjoining pressure were discussed. Subsequently in at least a semi-quantitative correlation between the macroscopic properties and the nanoscopic surface effects was possible.

2 Concept of Theory of porous media

The basis of the averaging model is the Theory of porous Media (TPM). It is a combination of the concept of volume fractions in connection with the saturation condition. Furthermore, the kinematics, the balance equations and the entropy inequality are used in view of the derivation of restrictions for constitutive relations.

2.1 The concept of volume fraction and the saturation condition

Using the mixture theory implies a statistically distribution of pores over the porous solid B_S. By this restriction the mass of all constituents is distributed over the whole solid volume V so that all constituents occupy it simultaneously.

$$V = \int_{B_s} dV = \int_{B_s} \sum_{\alpha}^{\kappa} dV^{\alpha} = \sum_{\alpha}^{\kappa} V^{\alpha} \qquad , \qquad \sum_{\alpha}^{\kappa} n^{\alpha} = 1 \tag{1}$$

Since all constituents κ occupy all the volume available the porous medium is called saturated. Hence, $(1)_2$ is the so-called saturation condition. The 'smeared' substitute continua show the same properties as a mixture body. For modelling, it is essential that these partial bodies of a porous medium can be 'identified' at any time during a thermodynamic process. This identification will be done with the help of the concept of volume fractions. At each point **x** at any time t the real (physical) density $\rho^{\alpha R}(\mathbf{x}, t)$ as well as a volume fraction $n^{\alpha}(\mathbf{x}, t)$ are defined. From these parameter the apparent (partial) density $\rho^{\alpha} = n^{\alpha} \rho^{\alpha R}$ can be calculated. Moreover, the total mass M of the porous medium of actual placement of the mixture at time t will be introduced as the sum of the partial masses of the constituents.

$$M = \sum_{\alpha=1}^{\kappa} M^{\alpha} = \int_{B_s} \sum_{\alpha=1}^{\kappa} \rho^{\alpha R} dV^{\alpha} = \int_{B_s} \sum_{\alpha=1}^{\kappa} \frac{\rho^{\alpha}}{n^{\alpha}} dV^{\alpha} \int_{B_s} \sum_{\alpha=1}^{\kappa} \rho^{\alpha} dV \tag{2}$$

In (2) M^{α} are the partial mass of the constituents and dV^{α} are there unit partial volumes.

2.2 Balance equations and entropy inequality

In order to derive the balance equations of the mixture theory, balance equations for each constituent have to be established, where interaction or supply terms, respectively, are used for the description of chemical and physical exchange processes between the different phases. Then, the sum of the balance equations of mass, momentum, moment of momentum and energy of the constituents results in the corresponding balance laws of the mixture, which, formally, must be equivalent to the conservation laws of a one-component material. With respect to the volume element dv, the local statements of the balance equations of mass

$$\frac{\partial \rho^{\alpha}}{\partial t} + \operatorname{div}\left(\rho^{\alpha} \mathbf{v}_{\alpha}\right) = \hat{\rho}^{\alpha} \tag{3}$$

the balance equation of momentum and angular momentum,

$$\operatorname{div}\boldsymbol{\sigma}^{\alpha} + \rho^{\alpha}\left(\mathbf{b} - \mathbf{a}_{\alpha}\right) = \hat{\rho}^{\alpha}\mathbf{v}_{\alpha} - \hat{\mathbf{p}}^{\alpha} \qquad , \qquad \boldsymbol{\sigma}^{\alpha} = \left(\boldsymbol{\sigma}^{\alpha}\right)^{T} \tag{4}$$

and the balance equation of energy,

$$\rho^{\alpha}\left(\frac{\partial u^{\alpha}}{\partial t}+\nabla u^{\alpha}\cdot\mathbf{v}_{\alpha}\right)-\rho^{\alpha}r^{\alpha}+\operatorname{div}\mathbf{q}^{\alpha}-\boldsymbol{\sigma}^{\alpha}\cdot\mathbf{D}_{\alpha}=\hat{u}^{\alpha}-\hat{\mathbf{p}}^{\alpha}\cdot\mathbf{v}_{\alpha}-\hat{\rho}^{\alpha}\left(u^{\alpha}+\frac{1}{2}\left(\mathbf{v}_{\alpha}\cdot\mathbf{v}_{\alpha}\right)\right) \tag{5}$$

are determined for each individual constituent. In these equations, the interaction or supply terms (..ˆ..) denote the exchange between the constituents of the mixture, $\boldsymbol{\sigma}^{\alpha}$ is the partial Cauchy stress tensor, **b** is the external acceleration of the constituent, $\mathbf{D}_S$ is the symmetric part of the spatial velocity gradient. Furthermore r^{α} herein is used for the internal heat supply and $\mathbf{q}^{\alpha}$ for the external heat supply. In addition, “div” is the divergence. For the interaction or supply terms of mass, momentum and energy the following conservation relationships are applied:

$$\sum^{\kappa}\hat{\rho}^{\alpha}=0 \quad , \quad \sum^{\kappa}\hat{\mathbf{p}}^{\alpha}=\mathbf{o} \quad , \quad \sum^{\kappa}\hat{e}^{\alpha}=0 \qquad . \tag{6}$$

In order to gain restrictions for constitutive relations like heat flux or partial stress tensors, the second law of thermodynamics (entropy principle) is a helpful tool. The local entropy inequality for the mixture with different temperatures of the constituents is defined as

$$S\geq\sum_{i}^{\kappa}\left[\frac{1}{T^{\alpha}}\rho^{\alpha}r^{\alpha}-\operatorname{div}\left(\frac{1}{T^{\alpha}}\mathbf{q}^{\alpha}\right)\right] \qquad . \tag{7}$$

Readers interested in the foundation of the governing equations of the TPM are referred to [32]; [33]; [34].

3 Conceptual model

In view of the numerical simulation of frost suction in porous media, in this section a concept will be derived to handle the essential scaling problem. Therefore a ’smearing’ microscopic model consisting of a Solid-Liquid Gel System and a ’smearing’ macroscopic model consisting of the matrix, the freezable liquid and vapour phase is derived. It is assumed, that the solid skeleton φ^{s}, the ice φ^{i} and the microscopic model φ^{gel} follow the same motion. Hence, the volume dilatation of 9 % due to the phase change from bulk water φ^{l} to ice is balanced by the empty pore volume φ^{v} close to the ice.

3.1 Microscopic scale

The total mass of the Solid-Liquid Gel Structure enclosed in a r.e.v. |V| is

$$\left|V\right|m^{gel}=\int_{V_{gel}}\rho^{gel}dv \tag{8}$$

and its variation reads

$$\frac{dm^{gel}}{dt} = \frac{1}{|V|}\int_{V_{gel}} \frac{\partial \rho^{gel}}{\partial t} + \mathrm{div}(\rho^{gel}\mathbf{v}_s) + \frac{1}{|V|}\oint_{\partial V_{gel}} \rho^{gel}\mathbf{v}_s \cdot n_s da \quad . \tag{9}$$

Therein the first term expresses the mass conservation at the microscopic level of the cementitious matrix; while the second term refers to the mass flux at the boundary of the microstructure ∂V_{gel}. Furthermore, for a cube of 120 µm length at least thermal or thermodynamic equilibrium is established under normal conditions [21]. Subsequently it is helpful to postulate that the local temperatures of all constituents are equal. At constant temperature, the non-freezing interlayers and films are in equilibrium with ice and vapour. Their existence was proved by [29]. The temperature of the bulk ice governs the pressure and by this the equilibrium. Of course, the location of this surface must be defined with care especially for non-flat interphases. The synonym interfaces is here used in the manner of the Gibbs theory [7]. To this interphase excess mass and energy are attributed. The interaction of surface forces of two interfaces is covered by the disjoining pressure Π [8]; [4]. The thickness of the interfacial zone - in Gibbs theory treated as zero – has now to be attributed to the distance h of two surfaces. In a thermodynamic treatment the Gibbs free energy defines the disjoining pressure. Three different types of interaction forces generate the disjoining pressure: dispersive or molecular Π_m which are attractive, electrostatic Π_e and structural forces Π_s which are as a rule repulsive. Their absolute value decreases rapidly with distance h. However, the sign can be positive - repulsive - and negative - attractive. For our considerations it is important that on one hand the dispersive part of disjoining pressure is always negative i.e. attractive and on the other hand the dispersion forces increases by a factor of app. 5.6 when the medium within the pores changes from water to air. For the electrostatic interaction the interphase must be a liquid. Here the surfaces are charged and an electric double layer is generated. If the two layers superimpose a disjoining pressure is generated. This term is in our case i.e. equivalent surfaces positive i.e. repulsive. Finally the structural term is if the surfaces are not hydrophobized always positive or repulsive.

Otherwise, experiments have shown that the ice freezes in situ [28]. That means the motion of the pore water to the ice is highly dynamic. However, the response time for movement from gel to ice and the flow distance is rather small. Nevertheless, the pressure gradient is extremely high. The driving force of a phase transition is the chemical potential. At triple point the chemical potentials of liquid, vapour and ice are equal and the changes of the chemical potential are related to this. A calculation of the chemical potential following the non-constant entropy of the constituents is in [20]; [21]. The chemical stability criterion simply states that in equilibrium the chemical potential must be equal in all phases. Following this its temperature term must be balanced by its pressure term. In concrete and hardened cement paste several phase transitions have been observed between 273 and 210 K [27]; [2]; [13]. They can be attributed to two simultaneous effects nucleation or depression of freezing point by surface interaction. Heterogeneous or homogeneous nucleation leads to a supercooling even of bulk liquid. In nanoporous systems surface interaction both hinder the progress of existing ice into smaller pores (percolation) and enforces melting below bulk freezing point in these pores. Progress or percolation during cooling is a metastable system while the

premature collapse of nano-ice during heating is the thermodynamic stable process. Both cooling and heating are separated by a factor of approximately two in the reduction of transition temperature, which explains the hysteresis corolated to a radius freezing point relation [17]. So the mass supply of the gel structure per time to ice and vice versa

$$\hat{\rho}^{gel} = \frac{1}{|V|} \oint_{\partial V_{gel}} \rho^{gel} \mathbf{v}_s \cdot \mathbf{n} \, da \tag{10}$$

is taken into account via a flux at the boundary of the micro scale driven by the chemical potential. As mentioned before, attention should be paid to the different timescales of transports. The ice traps pore water very fast and the ice melting and the return transport is rather slow. Due to the mass transport and the disjoining pressure a volume change of the Solid-Liquid Gel System is demand but its size is can be determine by helium pycnometry. Subsequently it is possible to measure the pure volume of liquids and solids exclusively all pores even in the nanoporous range since helium enters the pores even below 1 nm. Therefore, the combined thermal and hygral phenomena during frost were regarded separately. The description of the pure thermal process is well known. Consequently, the influence of the isolated hygral phenomenon was observed by sorption experiments. Since the specimens were weighed simultaneously the pure density of the Solid-Liquid Gel System can be determined without any modification [24]. It is possible to detect the density during a desorption-adsorption cycle. Simultaneously the sorption isotherm is evaluated from the measured mass.

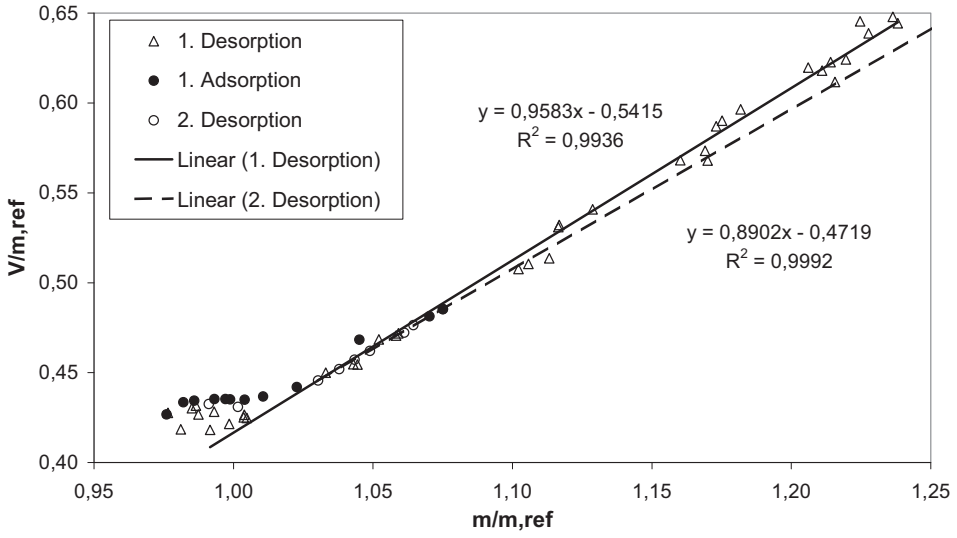

Figure 1: Volume change of hardened Portland cement paste specimen stored at different rel. humidity as function of their mass. The plot in both axis is normalised by dividing the mass of each individual specimen reached when dried to 33 % r.h. in the first desorption branch [25].

Only water is evaporating during desorption and adsorbed or condensed during adsorption. The density of the solid (> 2.3 g/cm^3) is distinctly higher than the density of bulk water – 1 g/cm^3 -

and data following Powers 1.15 g/cm^3. Our own measurements, outlined in [25], would allow a maximum density of pore water of 1.29 g/cm^3. Therefore, the density of solid-liquid gel system should increase with a loss of water. Of course, inherently it is assumed that the density or volume of the solid is unchanged. However, in contrast to all data known to the author and in contrast to the expected behaviour the density is decreasing below a rel. humidity of 33 % even if a steady loss of water is still found. In figure 1 the pure volumes of the solid-liquid gel-system are plotted as a function of the specimens mass. Since different specimens were measured both volume and mass were normalized by dividing them by the respective mass reached at 33 % r.h. in the first desorption branch. Since the mass changes are related to loss or gain of water the slope of the curve represents the specific volume - i.e. the inverse of the density - of gel pore water under the assumption that the solid volume is constant. From the graph it can be concluded that in the region above 33 % r.h. a nearly constant slope is found. For the first desorption it is near to 1 cm³/g i.e. equivalent to bulk water. In [25] it is shown that it depends slightly on the type of binder. After the first desorption i.e. loss of the condensed water the situation has changed. The water uptake during adsorption is dramatically reduced. Again we can calculate a specific volume or density of the condensed water in the upper vapour pressure region. The densities are now significantly higher and similar to the values reported by Powers.

3.2 Macroscopic scale

On the macroscopic scale we have to model transient condition that means at this scale the thermodynamic processes need a larger time span to reach equilibrium. Therefore, dynamic effects will be neglected. Furthermore, it will be postulated that the motions of solid and ice are the same, i.e. the ice lenses are assumed to be trapped to the solid phase. There is no flow of ice through the pore structure opposed to the liquid phase. Also a mass supply from the liquid phase and the gel structure to the ice phase is taken into account. The balance equations of the microscopic model are solved for each (GAUSS) point of the macroscopic model. Mass exchanges with the vapour are neglected. The vapour fraction just has one function: To realize the distinction between a critical filled pore system [31] and a non-critical filled pore system following observations of [1].

4 Field equations and constitutive relations

In view of the numerical simulation of freeze-thaw characteristics of cementitious materials, in this section the field equations and constitutive relations for a simplified model will be derived. Considering the aforementioned averaging microstructure, assumptions and provided that all components are incompressible, the field equations are a combination of the balance equations of mass,

$$\frac{\partial n^{si}}{\partial t} + \operatorname{div}\left(n^{si}\mathbf{v}_s\right) = \hat{\rho}^{gel}\left(\frac{1}{\rho^{pR}} - \frac{1}{\rho^{iR}}\right) - \frac{\hat{\rho}^{l}}{\rho^{iR}} \tag{11}$$

$$\frac{\partial n^{l}}{\partial t} + \operatorname{div}\left(n^{l}\mathbf{v}_{l}\right) = \frac{\hat{\rho}^{l}}{\rho^{lR}} \tag{12}$$

$$\frac{\partial n^{v}}{\partial t} + \operatorname{div}\left(n^{v}\mathbf{v}_{v}\right) = 0 \tag{13}$$

and the balance equations of momentum for the merged solid and ice phases, the liquid and the vapour phase,

$$\operatorname{div}\left(-n^{si}p\mathbf{I} + \boldsymbol{\sigma}_{E}^{si}\right) + \rho^{si}\mathbf{b} = -\hat{\rho}^{l}\mathbf{v}_{s} + \hat{\mathbf{p}}^{l} + \hat{\mathbf{p}}^{v} \tag{14}$$

$$\operatorname{div}\left(-n^{l}p\mathbf{I}\right) + \rho^{l}\mathbf{b} = -\hat{\rho}^{l}\mathbf{v}_{l} - \hat{\mathbf{p}}^{l} \tag{15}$$

$$\operatorname{div}\left(-n^{v}p\mathbf{I}\right) + \rho^{v}\mathbf{b} = -\hat{\mathbf{p}}^{v} \tag{16}$$

as well as the balance equation of energy for the mixture, due to the assumption of equal local temperature,

$$\begin{aligned}&\rho^{si}\left(\frac{\partial u^{si}}{\partial t} + \nabla u^{si}\cdot\mathbf{v}_{s}\right) + \rho^{l}\left(\frac{\partial u^{l}}{\partial t} + \nabla u^{l}\cdot\mathbf{v}_{l}\right) + \rho^{v}\left(\frac{\partial u^{v}}{\partial t} + \nabla u^{v}\cdot\mathbf{v}_{v}\right) + \operatorname{div}\mathbf{q} + \left(n^{si}p\mathbf{I} - \boldsymbol{\sigma}_{E}^{si}\right)\cdot\mathbf{D}_{s} + \\ &+ n^{l}p\mathbf{I}\cdot\mathbf{D}_{l} + n^{v}p\mathbf{I}\cdot\mathbf{D}_{v} = -\hat{\mathbf{p}}^{l}\cdot\mathbf{w}_{ls} - \hat{\mathbf{p}}^{v}\cdot\mathbf{w}_{vs} - \hat{\rho}^{gel}\Delta u^{gel} - \hat{\rho}^{l}\left[\Delta u^{li} - \frac{1}{2}\left(\mathbf{v}_{l}\cdot\mathbf{v}_{l}\right)\right] \quad .\end{aligned} \tag{17}$$

The material time derivative of the saturation condition along the trajectory of the solid is

$$\frac{\partial n^{si}}{\partial t} + \nabla n^{si}\cdot\mathbf{v}_{s} + \frac{\partial n^{l}}{\partial t} + \nabla n^{l}\cdot\mathbf{v}_{l} + \frac{\partial n^{v}}{\partial t} + \nabla n^{v}\cdot\mathbf{v}_{v} - \nabla n^{l}\cdot\mathbf{w}_{ls} - \nabla n^{v}\cdot\mathbf{w}_{vs} = 0 \quad . \tag{18}$$

Furthermore, in (11) - (17) the saturation condition, the relations for partial densities and the restrictions for the supply terms have been used. The quantities $\mathbf{w}_{ls} = \mathbf{v}_{l} - \mathbf{v}_{s}$ and $\mathbf{w}_{vs} = \mathbf{v}_{v} - \mathbf{v}_{s}$ are the velocities of liquid and vapour relative to the solid matrix. As a first approximation the effective stress tensors of the liquid and the vapour phase are neglected. For the so-called effective stress tensor $\boldsymbol{\sigma}_{E}^{si}$ of the phases following the solid trajectory an assumption is made analogue to de Boer et al. (2003). Furthermore, in these equations the abbreviations

$$\mathbf{q} = \sum^{\kappa}\mathbf{q}^{\alpha} \quad , \quad n^{si} = n^{s} + n^{i} \quad , \quad \rho^{si} = \rho^{s} + \rho^{i} \quad , \quad u^{si} = u^{s} + u^{i} \tag{19}$$

have been used. In connection with the dissipation mechanism of the entropy inequality, the relations for the heat flux, the supply terms of momentum and the mass supply terms are determined. The relation for the heat flux vector

$$q = -\alpha_{\partial T}\nabla T - \alpha_{\partial \mathbf{w}_{ls}}\mathbf{w}_{ls} \tag{20}$$

is a function of the temperature gradient and of the difference velocities. Also, it can be derived for the supply terms of momentum of the liquid phase

$$\hat{\mathbf{p}}^{l} = p\nabla n^{l} - \gamma^{l}_{\partial T}\nabla T - \gamma^{l}_{\partial \mathbf{w}_{ls}}\mathbf{w}_{ls} - \gamma^{l}_{\partial \mathbf{w}_{vs}}\mathbf{w}_{vs} \tag{21}$$

and for the supply term of momentum for the vapour phase

$$\hat{\mathbf{p}}^{v} = p\nabla n^{v} - \gamma^{v}_{\partial T}\nabla T - \gamma^{v}_{\partial \mathbf{w}_{ls}}\mathbf{w}_{ls} - \gamma^{v}_{\partial \mathbf{w}_{vs}}\mathbf{w}_{vs} \tag{22}$$

and for the supply terms of mass

$$\hat{\rho}^{l} = -\beta^{l}_{\mu^{gel}{}^{i}}\left(\mu^{gel} - \mu^{i}\right) - \beta^{l}_{\mu^{l}{}^{i}}\left(\mu^{l} - \mu^{i}\right) \quad , \quad \hat{\rho}^{gel} = -\beta^{gel}_{\mu^{gel}{}^{i}}\left(\mu^{gel} - \mu^{i}\right) - \beta^{gel}_{\mu^{l}{}^{i}}\left(\mu^{l} - \mu^{i}\right) \tag{23}$$

The phenomenological coefficients in (20)-(23) are based on the Onsager assumption of relations between fluxes and corresponding gradients. The symmetrical coefficients characterize the direct effects: motions and thermal heat flux. The cross coefficients are linked by the symmetry restrictions of the Onsager relationships. To consider the heat of fusion at the phase transition a non-linear function for the second derivative of the Helmholtz energy functions ψ^{α} of the constituents are used. Furthermore, the hysteresis from freezing to melting of the pore solutions is taking into account. By evaluation of the radius-freezing point relation and the radius-melting point relation it can be shown that a hysteresis exists between the freezing point T_{0g} and the melting point of the pore solution T_{0s} [35]. Freezing is a metastable process (percolation). The interface of the non-wetting phase (ice), is penetrating the pore along the matrix interface. The melting process is a stable process. The formation of the wetting (liquid) phase results from the collapse of the non-wetting (ice) phase in the pore. These requirements are fulfilled by the function

$$\sum_{i}^{\kappa}\frac{\partial^{2}\psi^{c}}{\partial T^{2}} = \frac{H_{s0,i}}{\sqrt{\pi}}\, e^{-\left(\frac{T-T_{0\beta,i}}{\sigma}\right)^{2}} \quad . \tag{24}$$

Herein $H_{s0,j}$ is the heat of fusion of the water fraction j, $T_{0\beta,j} = T_{0g,j}$ is the freezing point of the solution j and $T_{0\beta,j} = T_{0s,j}$ is the melting point of the solution j. Freezing and melting are distinguished in the model by evaluating the material time derivative of the temperature to time along the trajectory of the solid. σ is a standardization factor.

5 Example

As an application of the model frost suction due to ice formation in a capillary saturated porous cement specimen will be simulated by using the finite element method. The test specimen is a cuboid with a side length of 15 cm and a height of 7.5 cm. It is assumed that all surfaces are adiabatic to the environment; therefore, it is sufficient to analyze the middle surface of the cuboid. Furthermore, it will be postulated that a mixture of macroscopic water and vapour fills the capillary pores. Its degree of saturation is a function of height as predicted by physics (capillary rise). At the border area a degree of saturation of 70 % is adopted. The capillary rise is 0.6 cm in dependence on the measurements. The solid-liquid gel system is saturated with water. For

description of the anomalous water density a function is used. The empty pore volume close to the ice balances the volume dilatation of 9 % due to the phase change from water to ice. The phase change starts in larger pores following the radius freezing point relation and advances into the smaller pores with decreasing temperature. In the smaller pores the freezing point of water is lower due to high surface interactions of the surrounding pore walls. The heat of fusion is evaluated from data of the melting curve in low temperature DSC for specimens pre-stored under different rel. humidity [13]. An evaluation shows a dramatic reduction of the heat of fusion with respect to bulk water. By X-ray it has been proved that the pore ice is ice Ih the changes must be attributed to the changed entropy of pore water [36]. The heat of fusion and the existing energetic hysteresis from freezing to melting are modelled by an additional function. For the dynamic viscosity of the bulk water η^L data measured by Poiseuille are interpolated [12]. The capillary permeability B_0 of the hardened cement matrix [15] is also approximated. By the help of these equations a Darcy approximation for the viscous flow is made. The additional material parameters of the initial configuration are given in the table 1.

Table 1: Initial configuration of the example.

	Solid	**ice**	**liquid**	**vapour**
Lamé constant μ^α in N/m²	1.25e+10	1.25e+10		
Lamé constant λ^α in N/m²	8.33e+9	8.33e+9		
Heat dilatation coefficient in α_T^α in 1/K	1e-5	1e-5	3.13e-5	
Heat capacity c^α without fusion in J/kg	800	2100	4000	
Heat conduction coefficient α_T in W/mK	2.3	2.3	0.5724	1
Real density $\rho^{\alpha R}$ in kg/m³	2300	1000	900	1

For the stresses of the solid and ice phase a linearized law of Hookean type will be adopted. For solving this frost problem the linearized weak forms of the balance equations of mass, momentum of the involved phases and energy of the mixture, and the rate of saturation condition are implemented in the finite element program FEAP. The elements were discretized by the Galerkin method. The Newmark method will be used for the time discretisation. Furthermore, the following boundary conditions are restricted. The bottom of the specimen will be lowered from the initial temperature (293 K) in 4 hours with a constant cooling rate of 10 K/h. Then it is kept constant for 3 h at 253 K and increased in 4 h with a constant heating rate of 10 K/h. At the end it is kept constant for 1 h at 293 K. As mentioned earlier, the other surfaces are adiabatic.

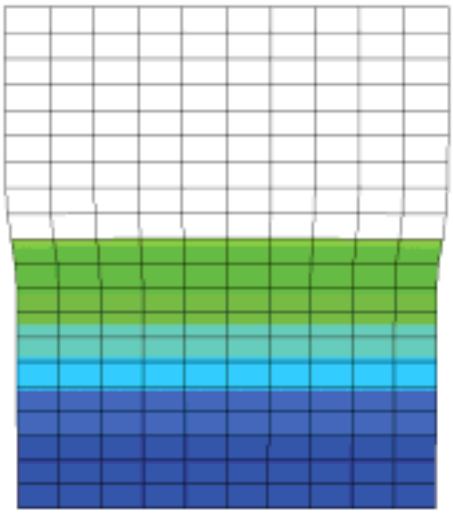

Figure 2: calculated deformation of the matrix during penetration of the frost front (larger than in reality). The frost dilatation is covered by frost shrinkage.

6 Conclusion

As predicted by the micro ice lens model during cooling, frost-shrinkage could be modelled. The mass of the gel water reduces while the quantity of macroscopic ice filled pores increases. Due to the pressure difference between liquid and solid phase of water the matrix contracts. During heating the pressure difference decreases. See figure 2. Furthermore, the moisture uptake of normal concrete specimens during the first freeze-thaw cycles increasing significantly. This artificial saturation process, illustrated in figure 3, only takes place during thawing. This is the only possible significant water transport considering vapour diffusion, viscous flow of adsorbed water and capillary suction. The water is sucked into the expanding gel efficiently. In the left figure the filter velocity $\mathbf{w}_{ls}$ of the external water vs. the local body temperature T is shown. The calculated mass uptake - the integral of additional partial volume over the control space multiplied by the real liquid density - is comparable to measured data [1]; [3], etc. In the second figure the filter velocity vs. the height of the specimen is shown. The strong increase in speed difference is clearly shown if liquid water in the outermost layer of the matrix is available. At that time, the pressure gradient result of the triple phase condition on the largest. As a consequence of the movement and the resulting balance of chemical potential, the flow rate decrease quickly. So the available external water is sucked in during the movement of the melting front. The flow rate decreases with increasing flow distance, equal to the specimen height.

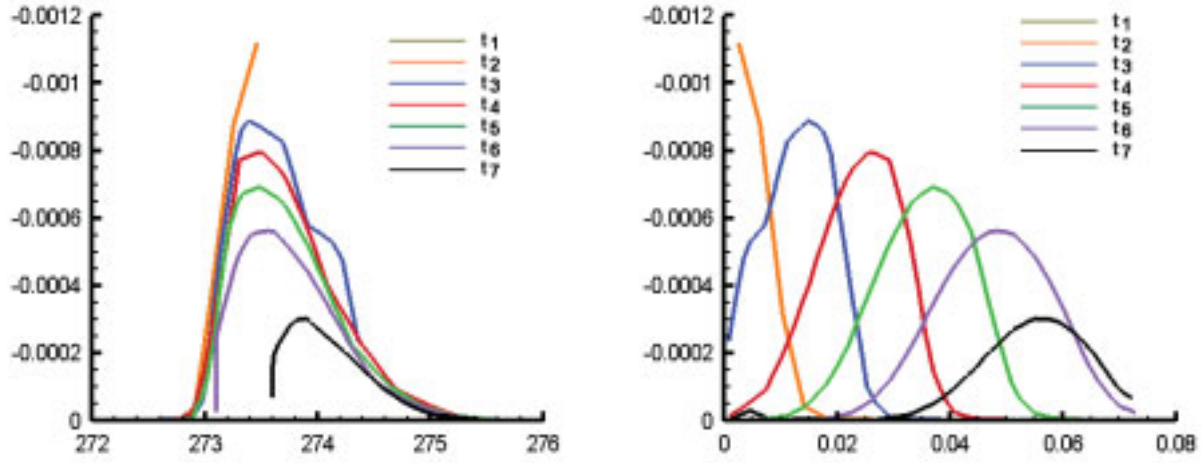

Figure 3: 1) Calculated filter velocity of the moving liquid water phase versus the local temperature in the range of the phase transition at different time steps (t_1 to t_7 with Δt = 2 min.) during the heating period. 2) Calculated filter velocity of the moving liquid water phase versus the height of the specimen at different time steps (t_1 to t_7 with Δt = 2 min.) during the heating period.

The figure $(3)_2$ also demonstrates the width of the phase transformation zone which is widening during penetration of the melting front. As a result of this it has been shown that a combination of TPM and a micromechanical theory of surface forces is an applicative tool describing artificial saturation due to frost attack in cementitious material.

7 Acknowledgements

Financial support was provided by the Deutsche Forschungsgemeinschaft DFG (German Research Foundation) in the project Se336/ 53. This support is gratefully acknowledged.

8 References

[1] Auberg, R.: 1999, Zuverlässige Prüfung des Frost- und Frost-Tausalz-Widerstands von Beton mit dem CDF und CIF-Test., Diss., Universität-GH Essen.

[2] Beddoe, R.E. & Setzer, M.J.: 1990, Phase transformations of water in hardened cement paste - a low-temperature DSC investigation., Cement & Concrete Research, 232 – 242.

[3] Bevanda, I. & Setzer, M. J.: 2006, Untersuchungen zur Feuchteverteilung während des Frostangriffs., in: Beiträge zur 6. CDF/ CIF Fachtagung, Mitteilungen aus dem Institut für Bauphysik und Materialwissenschaft, Band 10, pp. 121 – 131.

[4] Churaev, N. V.: 2000, Liquid and vapor flows in porous bodies - surface phenomena, Vol. 13 of Topics in chemical engineering, Gordon and Breach science publishers.

[5] de Boer, R.: 2000, Theory of Porous Media - highlights, Springer-Verlag.

[6] de Boer, R., Bluhm, J., Wähling, M. & Ricken, T.: 2003, Phasenübergänge in porösen Medien., Bericht FB Bauwesen, 98, Universität Duisburg-Essen.

[7] Defay, R., Prigogine, I. & Bellemans, A.: 1966, Surface tension and adsorption.

[8] Derjaguin, B. V., Churaev, N. V. & Muller, V. M.: 1987, Surface forces.

[9] Ehlers, W.: 1989, Poröse Medien – ein kontinuumsmechanisches Modell auf der Basis der Mischungstheorie., Bericht FB Bauwesen, 47, Universität-GH Essen.

[10] Feldman, R. F.: 1968, Sorption and length-change scanning isotherms of methanol and water on hydrated Portland cement., Proceedings 5th International Symposium Chem. Cem., pp. 53 – 66.

[11] Kondo, R. & Daimon: 1974, Phase composition of HCP., 6th International Symposium on Chemistry of Cement.

[12] Kruschwitz, J.: 2008, Instationärer Angriff auf nanostrukturierte Werkstoffe — eine Modellierung des Frostangriffs auf Beton., Diss., Uni Duisburg-Essen

[13] Liebrecht, A.: 2006, Phasenübergänge, Frostschwinden und Schrumpfvorgänge in Zementstein., Diss., Uni Duisburg-Essen.

[14] Litvan, G. G.: 1973, Frost action in cement paste, Material and Structures 34(6), 293 – 298.

[15] Powers, T. C.: 1958, Structure and physical properties of hardened Portland cement paste., Journal of the American Ceramic Society, 41(1), 1 – 6.

[16] Powers, T. C. & Brownyard, T. L.: 1948, Studies of the physical properties of hardened Portland cement paste. - in nine parts. Bulletin of the Research Laboratories, Portland Cement Association 18.

[17] Prigogine, I. & Defay, R.: 1973, Chemical Thermodynamics. Longmans, London.

[18] Sereda, P. J., Feldman, R. F. & Ramachandran, V. S.: 1980, Structure formation and development in hardened cement paste., Proceeding of the 7th International Symposium on the Chemistry of Cement, pp. VI–1/ 3–44.

[19] Setzer, M. J.: 1972, Oberflächenenergie und mechanische Eigenschaften des Zementsteins., Diss., Technische Universität München.

[20] Setzer, M. J.: 2001, Mechanical stability criterion, triple phase condition and pressure differences of matter condensed in a porous matrix., Journal of Colloid Interface Science, 235(1), 170 – 182.

[21] Setzer, M. J.: 2005, Mechanisms of frost action., in: T.-j. Zhao, F. H. Wittmann & T. E. Ueda (eds), Proceedings of the International Workshop on Durability of Reinforced Concrete under Combined Mechanical and Climatic Loads, Aedificatio Publishers, Freiburg, Qingdao, China, pp. 263 – 274.

[22] Setzer, M. J.: 2008a, Frost-attack on concrete – modelling by the micro-ice-lens model - evaluating by RILEM CIF test, in: Proceedings of CONCREPP 8.

[23] Setzer, M. J.: 2008b, The Solid-Liquid Gel-System of hardened cement paste, in: Proceedings of CONCREEP 8.

[24] Setzer, M. J., Kruschwitz, J. & Liebrecht, A.: 2006, Bestimmung der Porenwasserdichte von Zementstein - modifizierter Versuchsaufbau, in: J. E. Stark (ed.), Proceedings 16th international Baustofftagung, Vol. 1, F.A. Finger-Institut, Weimar, Germany, pp. 543 – 550.

[25] Setzer, M. J., Liebrecht, A., Duckheim, C. & Kruschwitz, J.: 2006, The solid-liquid gel system of hardened cement paste, in: Proceedings 2nd international Symposium on advances in concrete through science and engineering, Quebec City, Canada.

[26] Setzer, M. J. & Wittmann, F. H.: 1974, Surface energy and mechanics of hardened cement paste., Applied Physics 3, 403 – 409.

[27] Stockhausen, N.: 1981, Die Dilatation hochporöser Festkörper bei Wasseraufnahme und Eisbildung., Diss., TU München.

[28] Stockhausen, N. & Setzer, M. J.: 1980, Anomalien der thermischen Ausdehnung und der Gefriervorgänge in Zementstein., Tonindustrie Zeitung 104(2), 83 – 88.

[29] Vignes, M. & Dijkema, K. M.: 1974, A model for the freezing of water in a dispersed medium., Journal of Colloid and Interface Science, 49(2), 165–172.

[30] Wittmann, F. H.: 1977, Grundlagen eines Modells zur Beschreibung charakteristischer Eigenschaften des Betons., Deutscher Ausschuss für Stahlbeton, 290.

[31] Fagerlund, G.: 1997, Internal frost attack - state of the art, in: Setzer & Auberg (eds), Proceedings of the International RILEM Workshop. Frost Resistance of concrete, Vol. 34, E & FN Spon, London, pp. 321 – 338.

[32] Bowen, R. M.: 1980, Incompressible porous media models by use of the theory of mixtures. International Journal of Engineering Science 18, 1129 – 1148.

[33] Ehlers, W.: 1989, Poröse Medien – ein kontinuumsmechanisches Modell auf der Basis der Mischungstheorie. In Forschungsbericht aus dem Fachbereich Bauwesen, Volume 47, Essen. Universität-GH Essen.

[34] de Boer, R. (2000). Theory of Porous Media – highlights in the historical development and current state., Volume 2. Berlin, Heidelberg, New York: Springer-Verlag.

[35] Setzer, M. J.; Auberg, R.: 1997, Basis of testing the freeze-thaw resistance: Surface and internal deterioration., in: Setzer and Auberg (eds), Frost resistance of concrete — Proceedings of the International RILEM Workshop – Frost Resistance of concrete., Vol. 34, E & FN Spon, London.

[36] Badmann, R.: 1981, Das physikalisch gebundene Wasser des Zementsteins in der Nähe des Gefrierpunkts., Diss., Technische Universität München.

Arne Hinniger
Dipl.-Ing.

Institute of Building Materials, Physics and Chemistry of Buildings
Hamburg University of Technology, Germany

Numerical Simulation of the Frost Resistance of Masonry

Summary

The frost resistance of brick masonry is simulated including coupled heat and moisture transport. Phenomena like supercooling and freezing point depression by pore structure and pore solution are taken into account as well as moisture transport processes with ice present in the material. The resulting stresses from crystal formation are calculated, making it possible to conduct a service life analysis of existing masonry as well as to predict the frost resistance of new micro porous materials.

The main material properties considered in the simulation are the water absorption and the pore size distribution of the material since they are main parameters for the maximum water content and the maximum stress in material. The change of water absorption with the change of free pore space is also calculated, which allows the simulation of water absorption of partially frozen material, for instance when only the surface is warmed by radiation.

When calculating pore solutions in masonry, both ion transport and the changes of solution density and heat capacity are taken into account.

The maximum local stress is calculated based on the supersaturation of ice in the viewed pore size class and is homogenized to calculate the average stress in the material.

Different results of calculations can be shown, allowing to evaluate the influence of different material properties on the frost resistance of inert porous media.

Keywords: *frost, frost resistance, masonry, brick, pore radius distribution, tension, stress, microstructure*

1 Introduction

Frost damage of buildings is not only an optical problem, but may lead to severe damage of the material, because the surface may be changed to its disadvantage. The damaged surface may contain cracks and will become very uneven as the damage becomes more severe and parts of the surface fall off. This may result in even higher water content of the material, which in turn leads to more severe damage.

The frost resistance of masonry is normally determined by experimental survey according to DIN 52252 standards [1]. The methods of examination differ from Part 1 to Part 3 and show mostly different results. It is very difficult to extract enough brickware from existing buidlings to conduct these tests, so the on site analysis of existing buildings is time consuming and complex. As shown in [2], the number of freeze-thaw-cycles required by DIN 52252 are too low. Sveda [4] also shows that even bricks with a low frost resistance can withstand a much larger number of freeze-thaw-cycles than DIN 52252 requires. The main problem is that these methods do not allow to do a lifetime analysis of existing materials taking into account the location of the buidling. There were approaches to simulate freezing in building materials [3], but stress of the material was not calculated, and the transport coefficients used for the simulation were not verified.

The aim was to be able to determine the frost resistance by numerical simulation, representing the heat and moisture transport and the stress in the material. It should also be possible to consider the influence of naturally occurring variations in the material properties as well as the influence of the location where the material is used.

We will show which material properties are needed to simulate the durability of masonry exposed to freeze-thaw stress.

2 Theoretical Background

2.1 Transport processes

The simulation is done based on finite volume elements. The transport processes are driven by gradients in concentration of water or vapour for moisture transport and by temperature gradients for heat transfer. Sources or sinks of heat and moisture (e.g. melting ice) also have to be taken into account.

If we consider the energy balance, we obtain:

$$\frac{\partial(\rho_s \cdot C_{v,s} \cdot T)}{\partial t} + \frac{\partial(w \cdot C_{v,l} \cdot T)}{\partial t} + \frac{\partial(c_d \cdot C_{v,v} \cdot T)}{\partial t} + \frac{\partial(e \cdot C_{v,i} \cdot T)}{\partial t} = -\nabla \cdot (h_L \cdot \dot{m}_L + h_v \cdot \dot{m}_v) - \nabla \cdot \left(\lambda(l,i) \cdot \nabla T\right) + \dot{Q}_{i,l,v} \quad (1)$$

Where T ist the actual temperature, w is the mass of liquid water and index for water, c_d is the vapour concentration, d the index for vapour, e the mass of ice and the index for ice, C is the heat capacity of the considered phase. The heat flux is represented by the gradient of enthalpy in liquid (l) and vapour (v) phase as well as the heat conduction λ depending on the content of water and ice and heat sources Q resulting of phase changes between water, ice and vapour.
If we calculate vapour and liquid water in one mass-balance, the moisture balance results in:

$$\frac{\partial}{\partial t}\left(\frac{p_d}{R_d \cdot T} \cdot \left(\psi - \theta_l - \theta_i\right)\right) + \frac{\partial w}{\partial t} = -\nabla \cdot \dot{m}_v - \nabla \cdot \dot{m}_l + \dot{S}_{i-v} + \dot{S}_{i-l} \tag{2}$$

The flux of vapour can be described as:

$$\dot{m}_d = -D_v(\varphi, l, i) \cdot \nabla p_v - \left(\psi - \theta_l - \theta_i - \theta_\tau\right) \cdot \rho_d \cdot K_g(l, i) \cdot \frac{p_v}{R_v \cdot T}(\nabla p_{surr} + \nabla p_{\Delta V}) \tag{3}$$

with D_d as the transport coefficient for vapour flux driven by vapour pressure gradient ∇p_v, θ the volumes of the considered phases, Ψ the total pore volume and $K_g(l,i)$ the permeability for air of the materiel in dependence of water and ice content. This part of the equation describes the convective flux induced by air pressure gradients ∇p_{surr} resulting from surrounding pressure differences and $\nabla p_{\Delta V}$ resulting of volume changes resulting phases changes.

The flux of water can be described as:

$$\dot{m}_l = -K_l(l, e) \cdot \left(\nabla p_k + \nabla p_{\Delta V} + \nabla p_{surr}\right) \tag{4}$$

where K_l is the water permeability oft the material in dependence of water and ice content and ∇p_k is the gradient of capillary pressure.

To be able to calculate convective transport induced by change of volume, the air in the pores also has to be taken into account:

$$\frac{d}{dt} g = -K_g(l, i) \cdot \left(\nabla p_{\Delta V} + \nabla p_{surr}\right) \tag{5}$$

To be able to calculate the transport processes with ice present in pore system, there has to be a model for the dependence of transport coefficients of ice content for air, water and vapour (e.g.[5]).

2.1.1 Liquid Water Flux

To be able to describe the dependence of liquid water transport by the amount of ice in the porous media, we analyzed the water uptake of different materials with increasing ice content. The measured dependency is shown for a chosen material in figure 1.

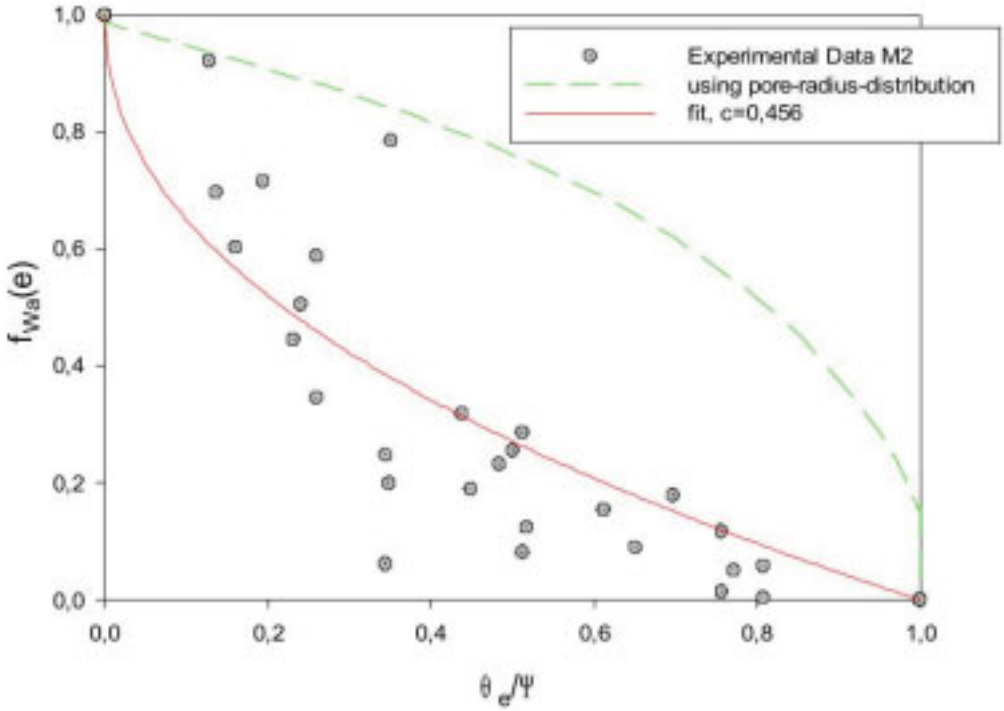

Figure 1: Dependence of the water-uptake coefficient $f_{Wa}(e)$ of ice content $e/(\rho \times \psi)$ with ψ the pore volume an e the content in kg/m³ material.

The approach to calculate these dependencies while using the pore radius distribution for calculating the change of permeability, when proposing, ice fills the pores starting with the biggest pores is shown as dashed curve in figure 1. The approach didn't lead to satisfying results, so we have to use the following empiric dependency:

$$f(e) = 1 - \frac{\theta_e^c}{\Psi} \tag{6}$$

Where c is the coefficient, which has to be derived experimentally.

2.1.2 Water Vapor Flux

The water vapor transport as well is affected by ice crystals in porous media. Standard experiments (dry-cup, wet-cup) were not suitable to derive the influence, because they are done at

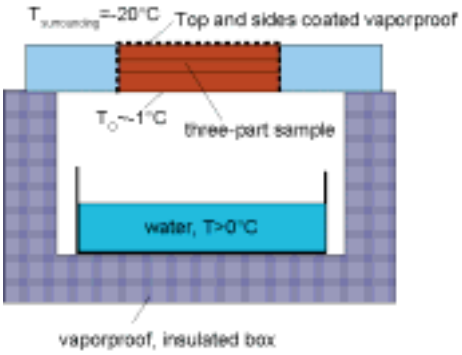

Figure 2: Assembly for measuring vapor transport in porous media containing ice.

above freezing point temperatures. Tries to change conditions to below freezing point temperatures showed no usable results, because the ice in porous media sublimated parallel to the vapor flux, so no influence of ice content could be calculated.

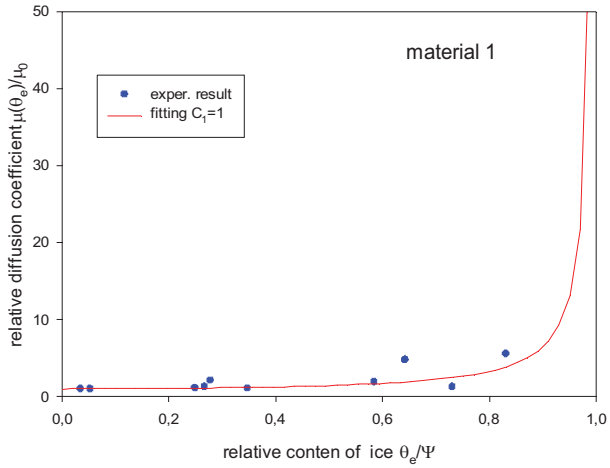

Figure 3: Influence of ice content on diffusion coefficient for a chosen material

This leads to an experiment, where the vapor transport was induced by temperature difference following [5]. The vapor transport is measured trough the amount of ice accumulated in the material after the analyzed element (s. Fig. 2).

The influence of ice content on the vapor diffusion could be calculated and led for a chosen material to the experimental results shown in Figure 3. To obtain the real influence for every material, it is necessary to measure it, to obtain the parameters. The equation shown below (7) can nevertheless be used for simulations with only very little error with the parameters C_0=0,75,

C_Ψ=0,35 an C_1=1,0, where vapor diffusion is not the only water flux which has to be taken into account.

$$\mu(e) = \mu_0 \frac{\left(\Psi - (C_0 + C_\Psi \left(\frac{\theta_e}{\Psi}\right)^3\right) \cdot \theta_e}{\Psi - \theta_e} \cdot C_1^{\frac{\theta_e}{\Psi}} \tag{7}$$

Calculations of real constructions with real climate conditions showed only little influence on changes of the possible parameters, but for lab conditions, it can be usefull to know the exact parameters, because differences may be huge.

2.2 Ice formation

Ice formation starts in view of thermodynamic equilibrium when the temperature drops below the freezing point of a given solution. In addition, the temperature where first nucleation takes place depends on kinetic parameters such as the temperature gradient and material parameters like the water content. This phenomenon is called supercooling. Following Kolasa [6] freezing point depression and supercooling can be added for the first nucleation.

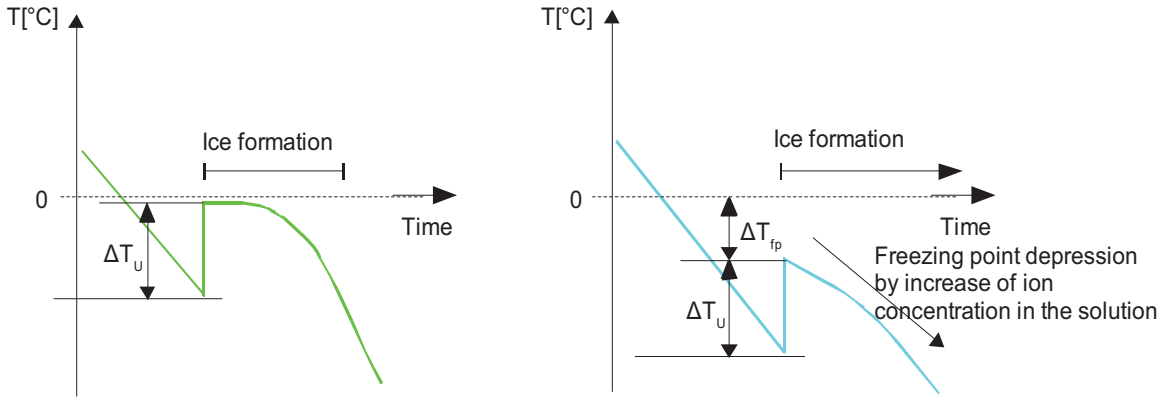

Temperature in a pore system containing *pure water*, when cooled down

Temperature in a pore system containing *salt solution*, when cooled down

Figure 4: Freezing point depression (ΔT_{fp}) and supercooling (ΔT_U)

Supercooling can be described with empiric equations which depend on the temperature gradient, the type of pore size distribution an the radius of the biggest pore filled with solution. They can be found in [6] .

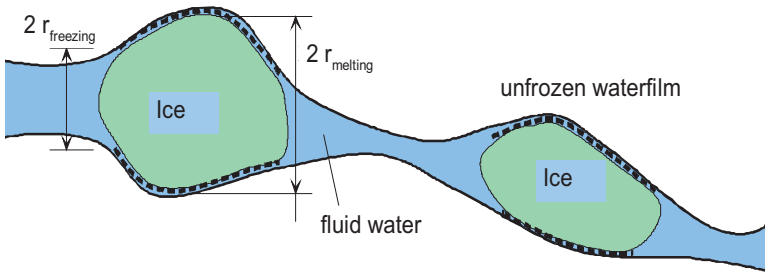

Figure 5: Influence of pore geometry on freezing point depression

Freezing point depression is a result of interaction with the pore walls, the radius of the surface in capillaries and of the ion concentration in solution.

Freezing point depression resulting of pore structure can be described with the empiric equations by Matala [8] (Equations 8 and 9), which take into account that the equilibrium temperature is controlled by the pore entry during freezing and by the maximum pore size during melting.

$$\text{Freezing:} \quad (\dot{T} < 0) \quad r_{freeze} = 0,584 + 0,0052 \cdot \vartheta - \frac{63,46}{\vartheta} \text{ [nm]} \tag{8}$$

$$\text{Melting:} \quad (\dot{T} > 0) \quad r_{melt} = 0,757 + 0,0074 \cdot \vartheta - \frac{33,45}{\vartheta} \text{ [nm]} \tag{9}$$

Freezing point depression by solutes is calculated via activity calculation as shown by Steiger in [8]. We use a Pitzer algorithm to calculate the solutes' freezing temperature by determining at which temperature the activity a_w of water– depending on supersaturation caused by temperatures below 0°C – equals the solute. This calculation has to be done in every time step because we always consider equilibrium at the onset of nucleation.

2.3 Internal pressure and stress

2.3.1 Hydrostatic Pressure

The increase of volume parallel to the the phase change from water to ice of 9% results either in transport of moveable phases like water and ice as shown in 2.1. or in stress to the material. The resulting hydraulic pressure, presuming an enclosed volume in the moment of ice formation, can be calculated as follows:

$$\frac{d}{dt}p = \frac{1}{V_{compressed}} \cdot \frac{dV}{dt \cdot \beta} = \frac{1}{\Psi} \cdot \frac{\left(1 - \frac{1}{\rho_e}\right)\frac{de}{dt}}{\beta(\theta_d, \theta_w, \theta_e, E_S)} \tag{10}$$

If there is still enough air in porous media, the air will be compressed resulting in a transport of moveable media and, given sufficient pressure, melting of ice until equilibrium is reached. Masonry rarely exhibits water contents of more than 90% of the pore volume, so we can assume that the volume change does not result in material damage.

2.3.2 Crystallization Pressure

According to Scherer [9] and Steiger [8], every crystal builds up pressure between the crystal an the pore walls when supersaturation is present. In porous media the freezing temperature is always below the freezing temperature of free water and the radius of the pore entry is usually different from the one of the ice crystal in the middle of the pore, so we can speak of local supersaturations.

The resulting pressure can be calculated as follows:

$$\Delta\sigma = \frac{RT}{V_{mol.e}} \cdot \ln\frac{a_w}{a_{w,fp}} = \frac{RT}{V_{mol.e}} \cdot \ln(U_e) \tag{11}$$

with a_w the actual activity of water depending on solutes and $a_{w,fp}$ the activity in equilibrium. U_e describes the supersaturation concerning ice. The resulting medium pressure can be described as:

$$\frac{\partial}{\partial t}\sigma_m = \frac{\partial}{\partial t}\sigma_{cryst} \cdot \int A_{cryst}(\theta_e)\,dt \tag{12}$$

Assuming that ice fills biggest pores first, and with the knowledge of the pore radius distribution, we are able to determine the stressed pore area in every volume for each amount of ice.

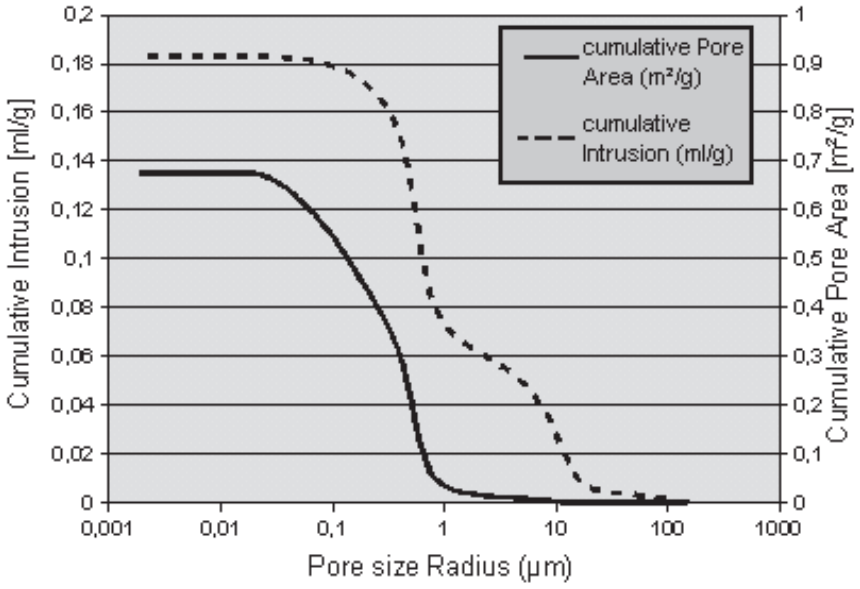

Figure 6: Pore radius distribution and pore area distribution of a selected material

In the material shown in Figure 3, it is obvious that for the first 30 % of pore volume filled with ice (approx. pores bigger than 1µm), the pore area loaded with crystallization pressure is very small. This result is also seen in experimental survey, where recognizable expansion resulting from ice formation was seen only when the ice content exceeded 40 % of pore volume.

All these proposals led to the calculation of am medium material pressure for assumed cylindrical pores as shown in equation 13, where σ_{pore} is the maximum stress calculated for a given period of time an $r_{pore,press,med}$ is the medium pore radius of pores influences by that stress, $\Delta\theta_e$ change of ice content and ΔA_{press} the pore surface of the considered cylindrical pores.

$$\sigma_{med} = \sigma_{pore} \cdot \frac{4 r_{pore,press,med}}{\pi} \cdot \frac{\Delta\theta_e}{3 \cdot \Delta A_{press}} \tag{13}$$

If a material is clearly anisotropic in pore structure, the equation has to be modified to take into account, that resulting pressure will differ for each direction as well.

2.3.3 Experimental verification

The calculation basics discussed before were implemented in the model for numerical simulation and experiments were uses to verify them. One of them was the measurement of tension while samples with different water contents were set out in freeze-thaw-cyles in a climatic chamber.

The result of calculated strains for a freeze-thaw-cycle from 20°C to -30°C and back to 20°C is shown in figure 7.

A significant result, which was also recognized by Kühne [13] before, is that the biggest relative tension, meaning the difference between ice-free and material with ice, can be seen at the beginning of the melting process. This has been verified in simulation, as well as measured in experiments. It results from different temperature strain of brick and ice and shows starting of freezing at lower temperatures due to the effect of supercooling.

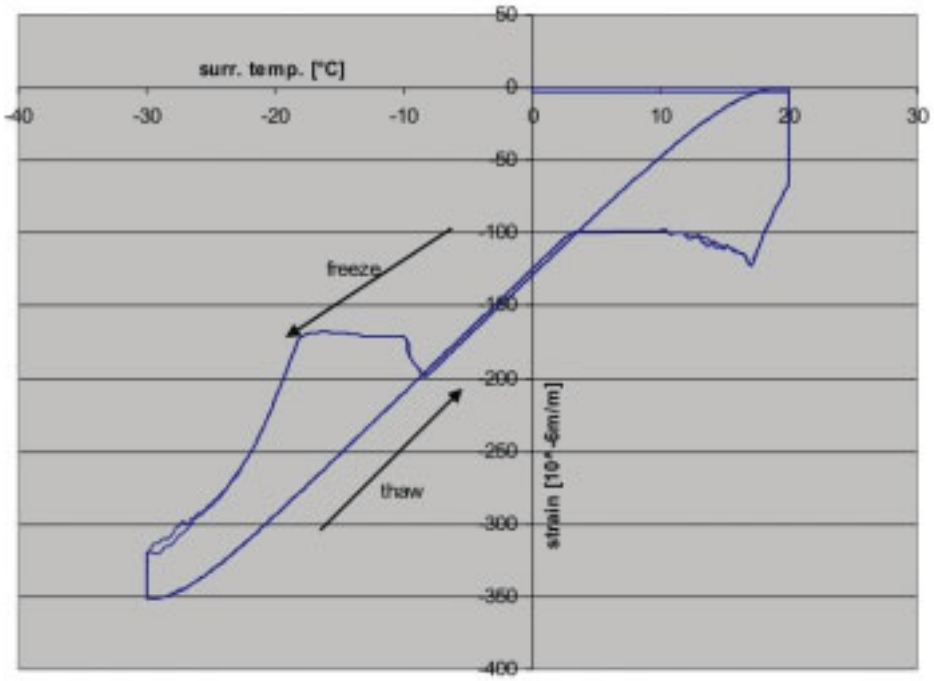

Figure 7: Calculated strain of a 4x4x16cm sample in a freeze-thaw-cycle

More calculations of different climatic situations showed the good approach of the simulation model, so from our opinion, it is a reasonable utility to analyze material properties regarding frost resistance.

3 Example Calculation

3.1 Base of Calculation

Using the relations shown in Chapter 2, we did some calculations to show the capability of the simulation model. We used real weather data from Hamburg in February 2006 for different types of construction to show that the durability of a given material may depend on surrounding conditions as well as on structural data.

The geometry used corresponds to figure 4.

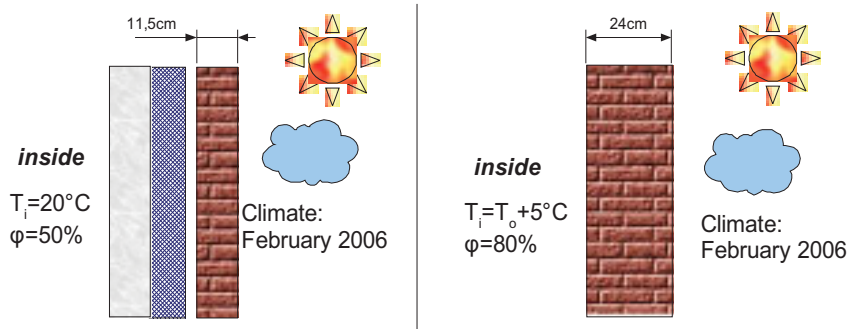

Example1: Modern Building with 10cm insulation

Example2: Historical Building without insulation

Figure 8: Brickwork constructions used for numerical simulation

3.2 Calculation results

Calculated ice, moisture content and temperature are shown in Figure 5 to 7.

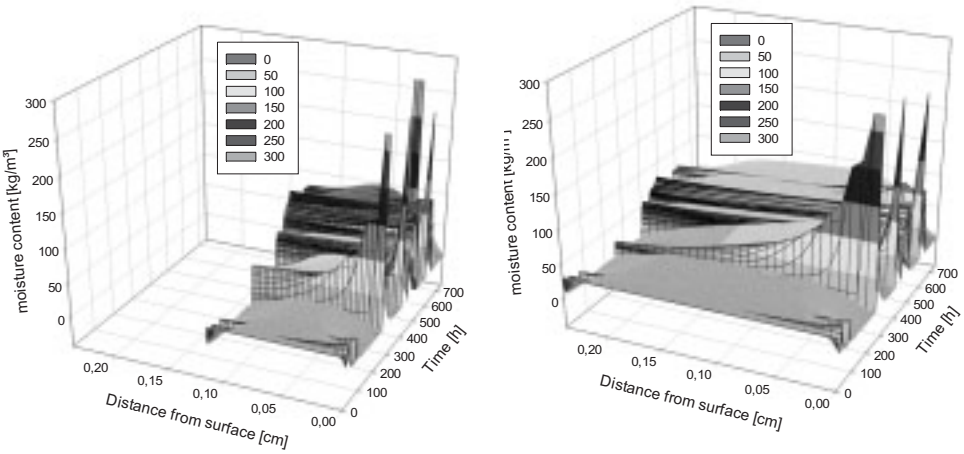

Example 1 Example 2

Figure 9: Moisture content for the calculated peroid of time

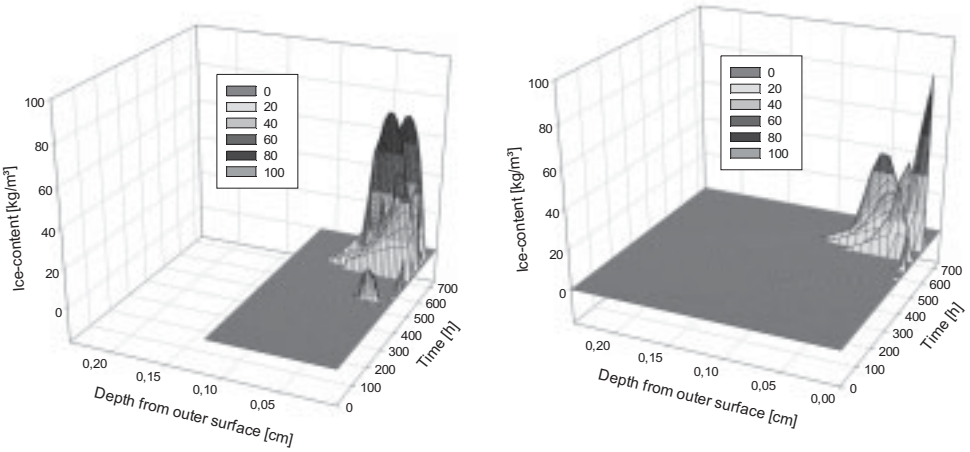

Example 1 Example 2

Figure 10: Ice content for the calculated period

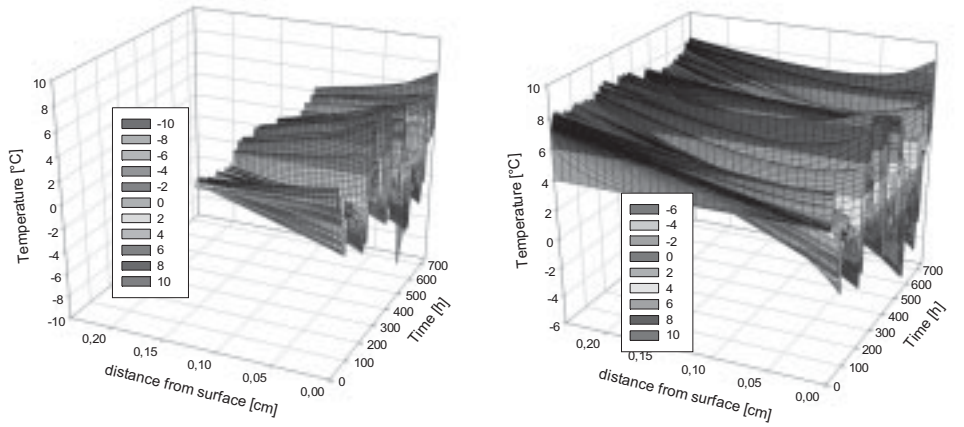

Example 1 Example 2

Figure 11: Temperature for the calculated peroid of time

The calculation shows, that moisture content, ice content and of course temperature profiles differ for the chosen constructions. For example1 the maximum stress was found 10 mm below the surface, for example 2 it was 1mm below the surface. Stress is not shown here, because it did not reach significant values.

4 Conclusion

It was shown, that freezing in the pores of bricks can be calculated for different situations by numerical simulation. With the knowledge of short-time and long-time strength it is possible to predict service life time of existing constructions as well as of newly designed masonry. It is possible to extend the material models to lime stone and sand stone as well as to cement based materials. For cement based materials additional mechanisms like micro-ice-pump [14] have to be taken into account.

5 Reference

[1] DIN 52252: Prüfung der Frostwiderstandsfähigkeit von Vormauerziegeln und Klinkern, Beuth Verlag 1986

[2] Bentrup, H.: Untersuchung zur Prüfung der Frostwiderstandsfähigkeit von Ziegeln in Hinblick auf die Lebensdauer, Dissertation TU Hamburg-Harburg 1992

[3] Xu: Numerische Simulation der Eisbildung in kapillarporösen Baustoffen unter Berücksichtigung der gekoppelten Wärme und Feuchtetransportprozesse, Dissertation TU Dresden 2002

[4] Sveda, M. Frost resistance of brick, American Ceramic Society Bulletin, (80) (2001), 46-48

[5] Auracher: Wasserdampfdiffusion und Reifbildung in porösen Stoffen, VDI Forschungsheft 566, 1974

[6] Kolasa, P. Kinetics of freezing in porous media, Dissertation TU Hamburg-Harburg, 2007

[7] Zuber, Marchand: Modeling the detoriation of hydrated cement systems exposed to frost action, Part 1 Description of the mathematical model, Cement & Concrete Research 30 (2000), 1929-1939

[8] Steiger, M. Influence of Salts on the freezing temperature of water: Implications on frost damage to porous materials, Proceedings of the 10th International Congress on Detoriation and Conservation of Stone, ICOMOS, Stockholm, (2004); 179-186

[9] Scherer, G. Internal stress and cracking in stone and masonry 16th European Conf. Fracture, Alexandroupoulis, Greece, 2006

[10] Franke, Espinosa: Aktuelle Entwicklung der theoretischen Vorhersage nicht stationärer Stofftransport- und Korrosionsprozesse in Bauteilen aus mineralischen Materialien, Festschrift TU-Harburg 2001

[11] Künzel: Verfahren zur ein- und zweidimensionalen Berechnung des gekoppelten Wärme- und Feuchtetransportes in Bauteilen mit einfachen Kennwerten, Dissertation Universität Stuttgart 1994Kühne, H.: Untersuchung zum Einfluss der Porenstruktur auf die Dauerhaftigkeit baukeramischer Produkte bei Einwirkung von Salzen oder Frost, Dissertation TU Hamburg-Harburg, 1997

[12] Stockhausen, N.: Die Dilatation hochporöser Festkörper bei Wasseraufnahme und Eisbildung. Diss. TU München 1981

[13] Kühne, H.-C.: Untersuchungen zum Einfluß der Porenstruktur auf die Dauerhaftigkeit baukeramischer Produkte bei Einwirkung von Salzen oder Frost, Dissertation TU-Hamburg-Harburg, 1997

[14] Setzer, M.: Micro-Ice-Lens Formation in Porous Solids,Journal of Colloid and Interface Science, (243) (2001), 193-201

Thomas Mansfeld
Dipl.-Ing.

Bauhaus-Uni, FIB, Weimar, Germany

Development of a Simulation Program for the Prediction of a possible ASR-Damage

Summary

It is the aim of this research project to find a way of simulating an ASR-damage. Since this damage mechanism is not yet sufficiently clear, in a first step several experimental approaches were taken to gain base values for a simulation. Unknown factors for a simulation are the provision of the starting materials for an ASR (kinetics, amount) and the behavior of the reaction products.

The following investigations were carried out:

- Investigations on the swelling behaviour of synthetic gels
- Investigations on the solubility of different silica modifications

The first successful steps were the simulation of the solubility of silica in dependence of the pH-value and the rock type, as well as the successful simulation of a pore solution in dependence of the cement type, the amount of cement and the added water.

This was followed by the development of a user interface for the simulation program. This interface enables the user to integrate partial simulations. The presently existing simulation program makes it possible to predict a probable ASR-damage for selected starting materials.

Keywords: *alkali-silica reaction, simulation, damage prediction*

1 Measuring Data from Swelling Experiments

Figure 1 shows the experimental setup for the swelling measurements. This setup enables a continuous water or solution supply to the sample.

Figure 2 shows the swelling behaviour of selected synthetic alkali-silica gels. The gels differ in their C/S-ratio and their amount of bounded alkalis. It can be recognised that the sample without calcium, i. e. a pure alkali-silicate, has no swelling capacity but it dissolves in the course of the measuring. With the calcium content rising, the expansion stress rises, too.

Figure 1: Test Arrangement

Table 1: Sample Composition

Nr.	Na_2O [M%]	K_2O [M%]	CaO [M%]	SiO_2 [M%]	SiO_2-carrier/ remark
G1	10	35	0	55	Microsilica
G2	10	35	10	45	Microsilica
G3	10	35	20	35	Microsilica
G4	10	35	30	25	Microsilica
G5	10	35	40	15	Microsilica
G6	5	2.5	0	77.5	Microsilica
G7	5	2.5	10	67.5	Microsilica
G8	5	2.5	20	57.5	Microsilica
G9	2.5	9	0	88.5	Microsilica
G10	2.5	9	10	78.5	Microsilica
G11	2.5	9	20	68.5	Microsilica
G12	12.5	42.5	0	45	Microsilica
G13	12.5	42.5	10	35	Microsilica
G14	12.5	42.5	20	25	Microsilica
G15	20	25	0	55	Microsilica
G16	20	25	10	45	Microsilica
G17	20	25	20	35	Microsilica
G18	35	10	0	55	Microsilica
G19	35	10	10	45	Microsilica
G20	35	10	20	35	Microsilica

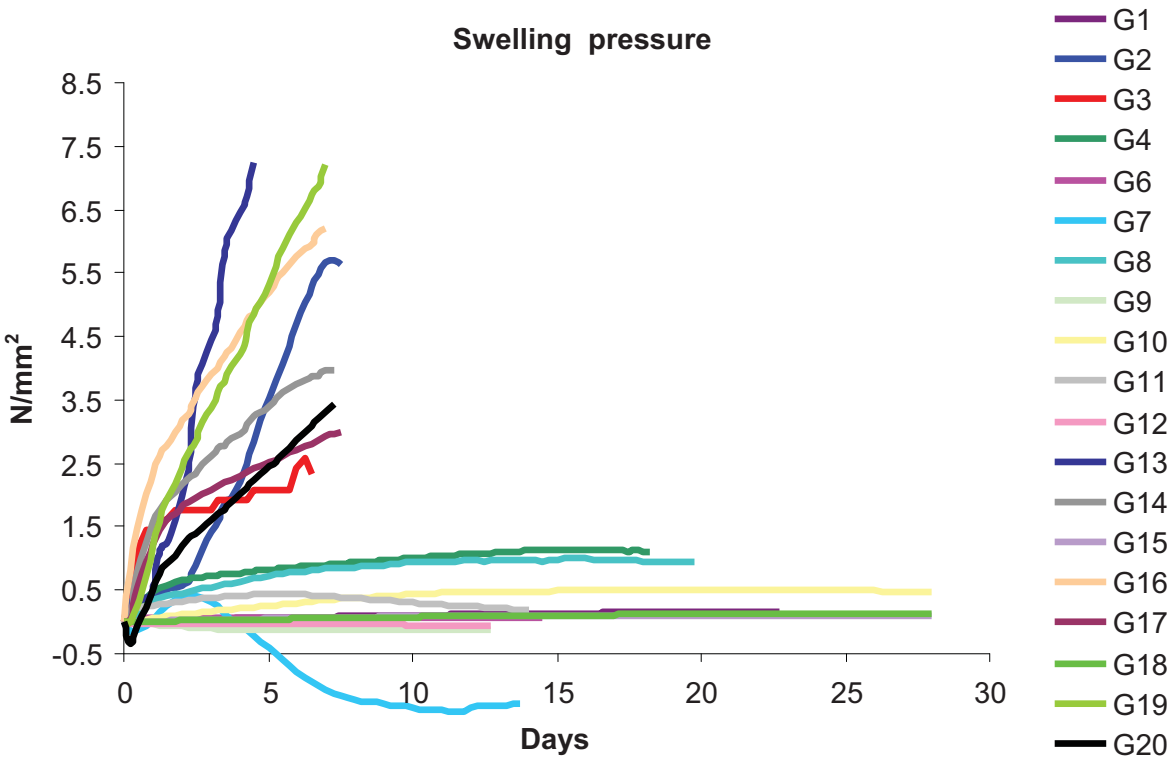

Figure 2: Swelling pressures of selected synthetic alkali-silica gels

It is easy to recognise that the calcium content has a strong influence on the stability of the gels. With the calcium contents rising, the solubility decreases and swelling becomes possible. In the case of the samples G6 to G11 the alkali content was decreased step by step in comparison to the samples G1 to G4, and the calcium content was varied as with the samples G1 to G4. These measurements show that with the alkali content in the gel decreasing, the swelling capacity decreases as well. The calcium content for its part has influence on the stability of the gels. The samples G12 to G14 were produced with especially high alkali and calcium contents of 0, 10 and 20 % by mass. Here again, one can see the dependence on the calcium content in the samples. In the samples G15 to G20 the alkali content was varied but this has no recognisable influence on the swelling behaviour of the samples.

2 Inves*tigation*s on the Solution Mechanism of SiO_2

In the second support period we began to determine the solubility of silica-containing rock and to simulate this solubility in dependence of the pH-value /01/. In view of the low dissolution velocities, data could only be determined for two silica modifications which can also be simulated successfully. Dissolution tests will follow for further rocks in order to determine material parameters by which one can derive a simulation.

Figure 3 shows the solution course of different SiO_2- modifications and the corresponding simulated solution curves.

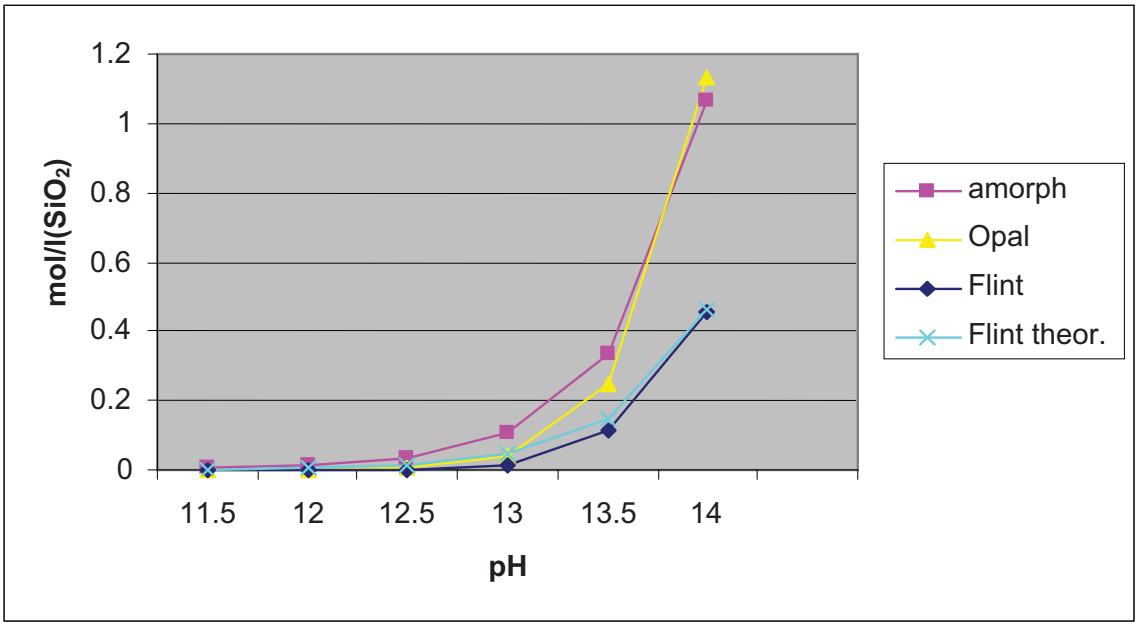

Figure 3: Comparison between measured and calculated solubility curves for different SiO_2-modifications

Corresponding to the literature the solubility of the different SiO_2-modifications only increases strongly at pH-values of 13 and beyond. The simulated curves follow those of the measurements very well.

The calculations were carried out using the equilibrium constant determined by means of test results. For amorphous silica $K= 6.9*10^{-5}$ whereas for flint $K= 3*10^{-5}$.

3 Development of the User Interface

The next step that was taken in the second support period was the programming of a user interface which is illustrated in Figure 4. This interface is designed to enable the user to evaluate a concrete mixture by entering the relevant data. Necessary data are: the cement manufacturer, the cement type, the amount of cement, the w/c-ratio, the rock type and its supplier, and lastly the planned location of the concrete element.

After having entered these data a calculation is carried out consisting of several steps. For this calculation, databases are used which are integrated in the program. The output that the user gets at the time being consists of a swelling-form-related simulation of the possible course of expansion or tension caused by ASR in the construction element to be produced and used at the planned location.

In the individual calculation steps, not only information from the databases are used but also established control values such as the Na_2O- equivalent of the used cement are integrated. The databases include cement analyses of the cements selectable on the user interface (ordered by manufacturer), equilibrium constants for the simulation of the solubility of the silica-modifications and the measuring data from the swelling experiments. Based on the data entered by the user a theoretical pore solution composition of the concrete (depending on its age, according to /05/) is calculated. This composition provides several pieces for the theoretical alkali-silica gel to form. The calculated pH-value of the pore solution is then integrated into the solubility simulation of the used aggregate. From these data a theoretical composition of an alkali-silica gel can be calculated. When this is brought together with the data on the environmental conditions at the construction element's location, a prediction as to the swelling behaviour of this gel becomes possible. The physical dimensions of the construction element have not yet been taken into account.

As illustrated in Figure 4 it is the user's first step to select a cement manufacturer from a menu. All cements available in the database coming from this manufacturer will be shown and ready for further processing. As illustrated in Figure 5 the cements coming from the selected manufacturer can be specified. This selection enables the program - based on integrated cement analytical data - to calculate the composition of a theoretical pore solution at a given w/c-ratio for a given concrete age. At the time being the concrete age is set to a value of 84 days but shall be made available as selection parameter. The next selection to make is the grain size, as illustrated in Figure 6. Presently there are only two types of rock available. These are embedded into the program only symbolically. The calculations are presently carried out using the already determined solubility data of opal and flint from /01/. The diabase serves as example for non-reactive material.

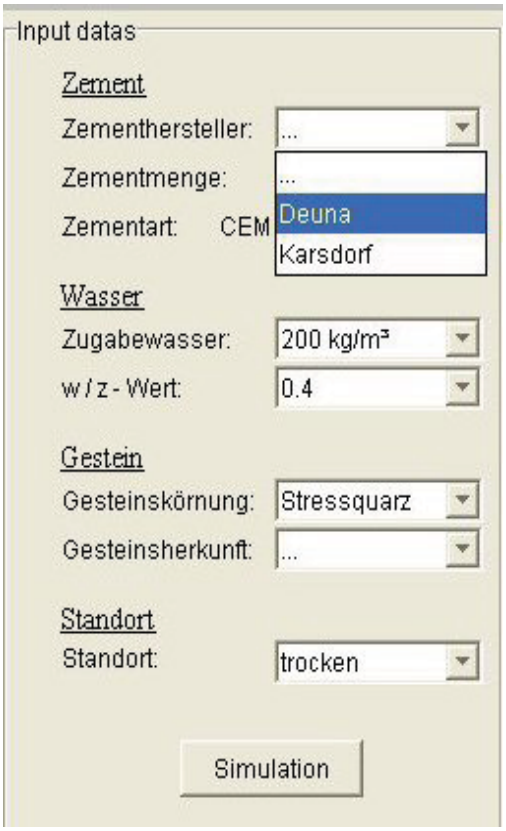

Figure 4: Menu bar of user interface, step 1

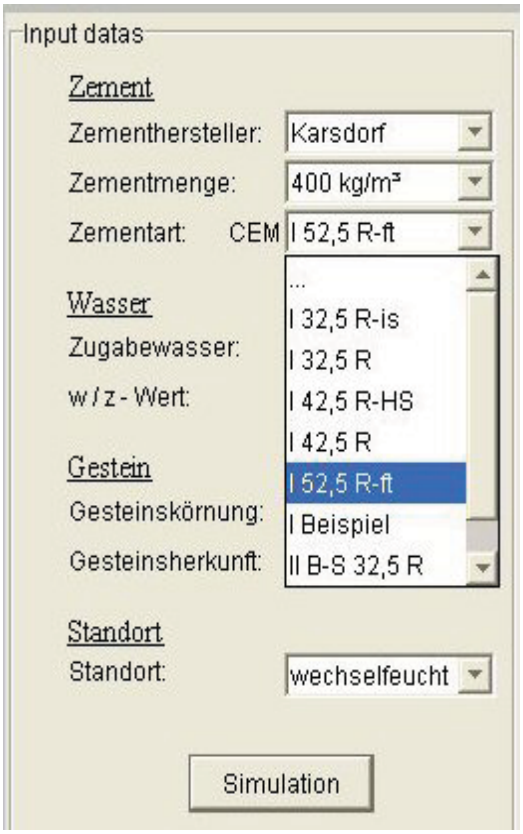

Figure 5: Menu bar of user interface, step 2

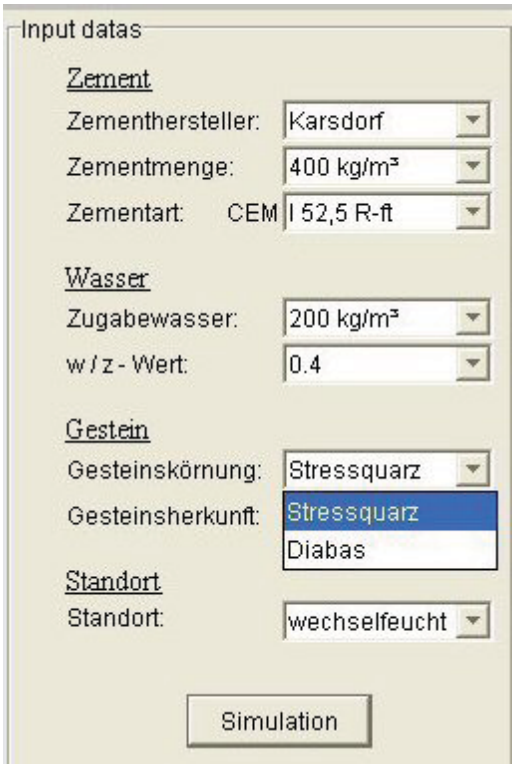

Figure 6: Menu bar of user interface, step 3

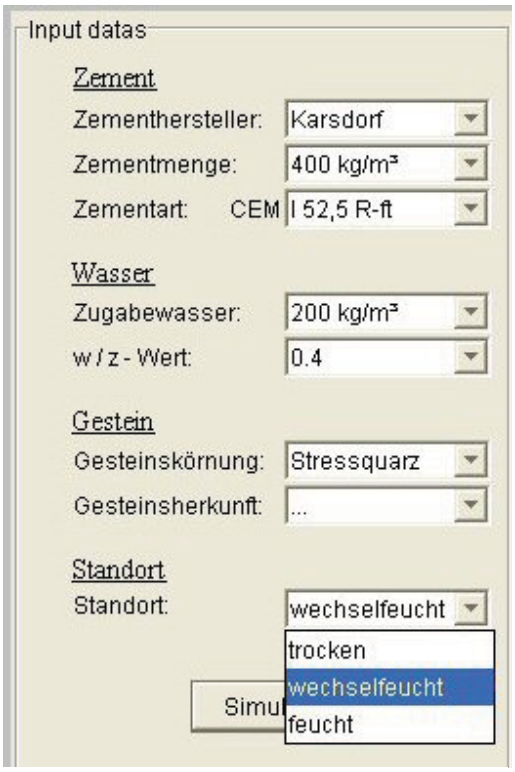

Figure 7: Menu bar of user interface, step 4

After the selection of the grain size - using the existing pH-value - the solubility of the selected grain size is simulated according /01/.

The presently last step, as can be seen in Figure 7, is the selection of the environmental conditions. An external alkali supply is a planned selection parameter.

When this last selection has been made it becomes possible to calculate a composition of an alkali-silica gel by means of the theoretical pore solution and the soluble silica therein.

By means of the entered environmental conditions the simulation of the swelling behaviour of the calculated gel starts after activating the start button. The output, as illustrated in Figure 8, is presently a swelling curve. This curve shows a simulated course of the swelling forces to be expected in the construction element. The output does not give dimensions at the time being. The measured swelling curves which are the groundwork for the data are given in N/mm^2 per time unit. In the course of further improvements an appropriate definition of the axes and the introduction of a threshold value shall be worked out.

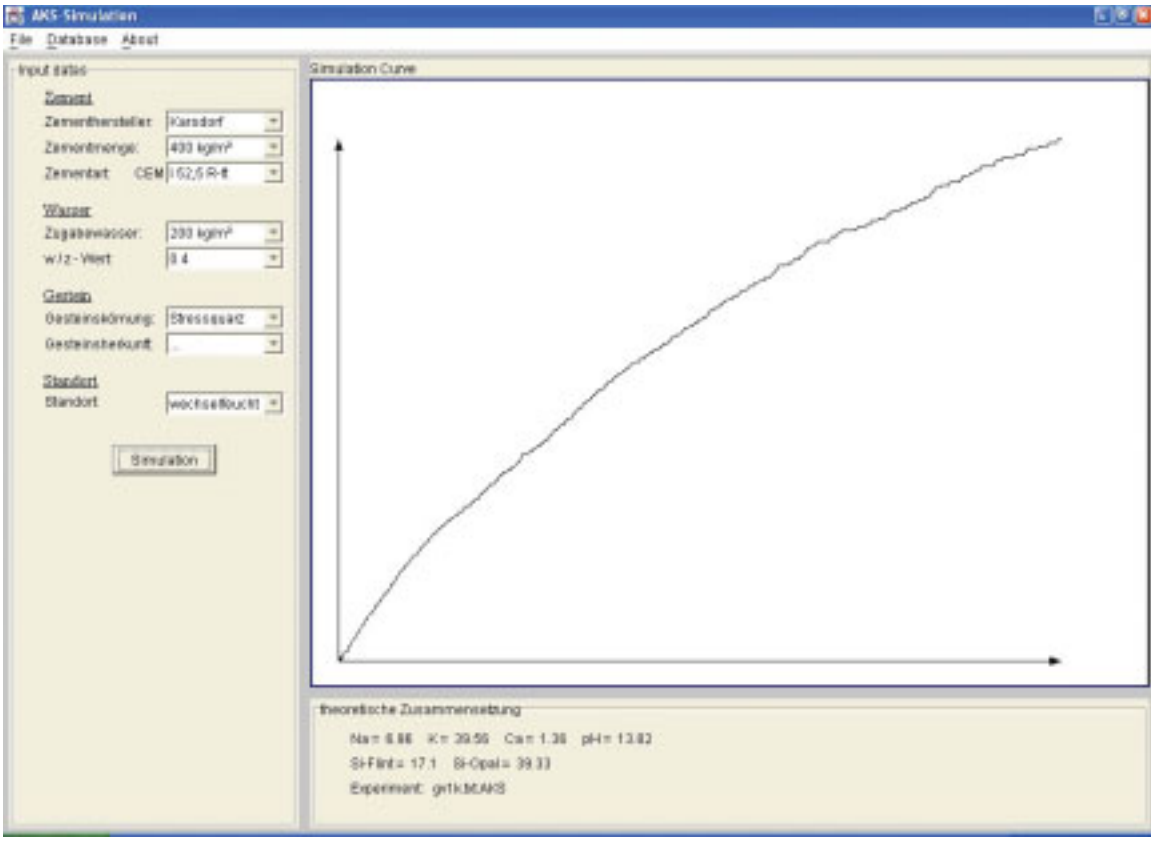

Figure 8: User interface, step 5

The basic structure of the program consists of the following 3 components

- the Graphical User Interface (GUI)
- the Algos component
- the Data component

The GUI gives the graphical user interface its appearance and steers the event treatment whereas the Algos component contains and implements the subject specific algorithms, e.g. the determination of the chemical composition and the correct linking to a corresponding laboratory test. In addition, all necessary data while the program is running are administrated in the class "DataSet". The groundwork of the application is a persistently stored data file in ASCII-format to be found in folder "Database". The administration of these data is done by the component Data.

On the one hand, the folder "Database" contains all laboratory tests. These tests are all single files designated with a name and the file ending "AKS". A linking to individual tests with their corresponding composition is done by the program in the file "Database.dat" that consequently administrates the tests with the corresponding characteristic values.

On the other hand the cements are stored by their names as files having the file-ending "CEM". They are ordered in individual folders carrying the name of the cement manufacturer.

The project-oriented programming language Java in the version 1.2 was used for this project. In light of future improvements of the program Java 1.2 offers in addition to its programming-technical advantages comprehensive capabilities to integrate databases.The complete structure with its intermediate steps of simulation is illustrated schematically in Figure 9. A pH-value-dependent simulation of the solubility of existing silica is carried out, as well as the simulation of the composition of a theoretical pore solution in dependence of the cement, the cement manufacturer and the w/c-ratio.

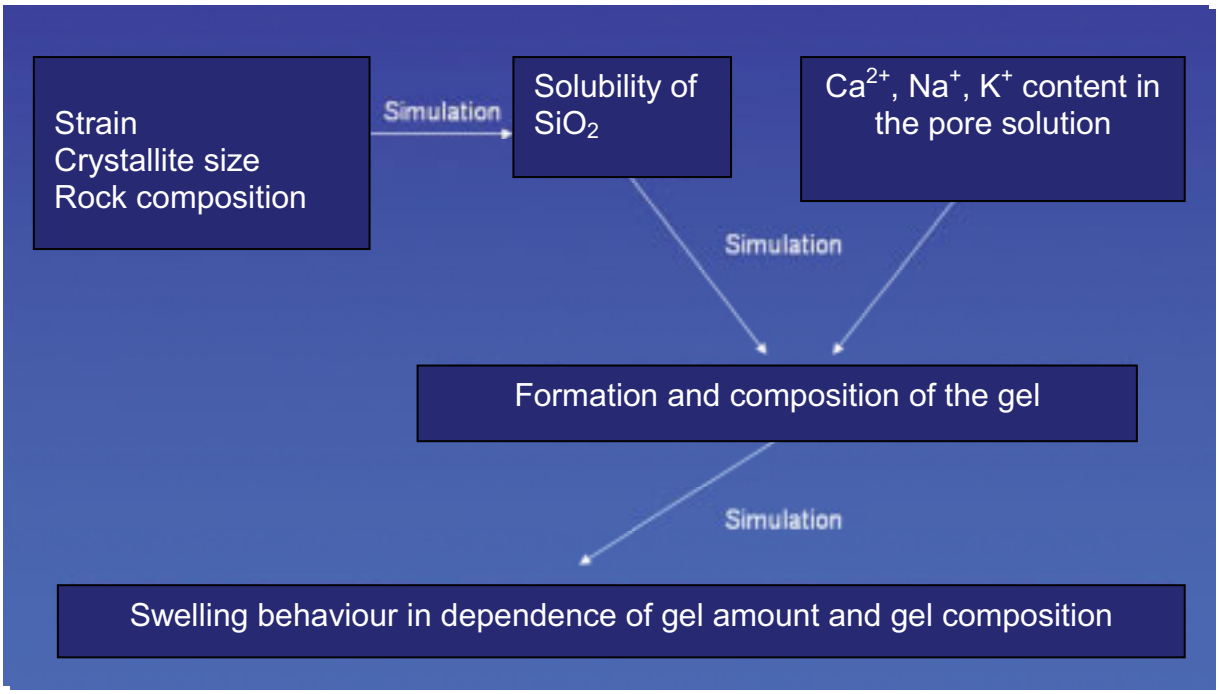

Figure 9: Schematic illustration of the program's working steps

Through the gained data it becomes possible to calculate a theoretical composition of an alkali-silica gel.

By means of the composition of the gel and the gained data from the expansion measurements, it becomes possible to derive an evaluation as to the swelling behaviour of the theoretical alkali-silica gel.

4 References

[1] Berninger, A.M.: Mikrostrukturelle Eigenschaften von Quarz als Bestandteil spät reagierender, alkali-empfindlicher Zuschläge. Dissertation, Fakultät Bauingenieurwesen, Bauhaus–Universität Weimar, Weimar, 2004.

[2] Wen, Zi-yun; Yin, Qi: Study of expansion mechanism of A.S.R. using Sol-Gel Expansion Method. In: Proc. 12th ICAAR 2004 Bejing, page 226-229, China 2004.

[3] Wen, Zi-yun, Yin, Qi: Sol-Gel Expansion Method: a new way for testing aggregate alkali reactivity. In: Proc. 5th International Symposium on the Cement and Concrete, Shanghai, China, 2002.

[4] Kawamura, M.; Iwahori, K.: Some theoretical considerations on expensive pressure of ASR gel. In: Proc. 12th ICAAR 2004 Bejing, page 135-142, China 2004.

[5] Reardon, E.J.: Problems and approaches to the prediction of the chemical composition in cement/water systems. In: Waste management Vol. 12 pp. 221-239, New York, 1992.

[6] Carrazedo, R.; de Lacerda L.A.: A parametric model discussion for the concrete expansion due to AAR. In: Proc. 12th ICAAR 2004 Bejing, S. 79-86, China 2004.

[7] Fairbairn, E.M.R.; Ribeiro et all, F.L.B.: Smeared cracking FEM simulation of alkali silica expansion using a new macroscopic coupled model. In: Proc. 12th ICAAR 2004 Bejing, S. 104-114, China 2004.

[8] Capra, B.; Sellier et all, A.: Modeling of alkali-silica reaction in concrete, part 2: influence of water on ASR. In: Proc. 12th ICAAR 2004 Bejing, S. 185-189, China 2004.

[9] Capra, B.; Bournazel, J.-P.: Modeling of inducted mechanical effects of alkali-aggregate reaction. In: Cement and Cencrete Research, Vol. 28, No. 2 pp., 251-260, 1998.

[10] Léger, P.; Coté, P.; Tinawi,R.: Finite element analysis of concrete swelling due to alkali-aggregate reactions in dams. In: Computers and Structures, Vol. 60, No. 4 pp., page 601-611, 1996.

[11] Bazant, Z.P.; steffens, A.: Mathematical model for kinetics of alkali-silica reaction in concrete. In Cement and Concrete Research, Vol. 30, page 419-428, 2000.

[12] Moranville-Regourd, M.: Modeling of Expansion Induced by ASR – New Approaches. In: Cement and Concrete Composites, Vol. 19, page 415-425, 1997.

[13] Thomas, M.: The role of calcium hydroxide in alkali recycling in concrete. In: Proc. Material Science of Concrete by The American Ceramic Society, Anna Maria Island / Florida, 2000.

[14] Tang Ming-Shu and Co-authors: Alkali Reactivity of Glass Aggregate. In: Durability of Building Materials [4], page 377-385, 1987.

[15] Wieker W. and Co-authors: Bedeutung der relativen Feuchtugkeit für die Alkali-Kieselsäure-Reaktion (AKR) an einem chemischen Modell für diese Reaktion. In: DGZfP-Berichtsband BB 69-CD, 1999.

[16] Cong, X.-D. and Co-authors: ^{29}Si MAS NMR Spectroscopic Investigations of Alkali-Silica Reaction Product Gels. In: Cement and Concrete Research Vol. 23 [4], page 811-823, 1993.

[17] Tapper, A. and Co-authors: Procedure of Preparation of a crystalline Sodium Layer Silikate with Kanemite structure. In: EP 0627383, April 1994.

[18] Wieker W. and Co-authors: Recent Results of Solid-State NMR Investigations and their Possibilities of Use in Cement Chemistry. In: Proc. 10th ICCC Gothenburg / Sweden, 1997.

[19] Locher, F.W.; Sprung S.: Einflüsse auf die Alkali-Kieselsäure Reaktion im Beton. In: Zement-Kalk-Gips, Vol.28 [4], page 162-169, 1975.

[20] Sideris, K.: Theorie des Mechanismus der Alkali-Kieselsäurereaktion. Dissertation, Rheinisch-Westfälische Technische Hochschule Aachen, 1974.

[21] Wieker, W.; Hübert, C.; Heidemann, D.; Ebert, R.: Zur Reaktion von Alkaliverbindungen mit Kieselsäure und Silicaten im Hinblick auf betonschädigende Dehnungsreaktionen. In: Proc. 14th ibausil, page 911-929, Weimar, 2000.

[22] Deutscher Ausschuss für Stahlbeton (DafStB): Vorbeugende Maßnahmen gegen schädigende Alkalireaktion im Beton. Richtlinie, Fassung Mai 2001.

[23] Thaulow, N.; Jakobsen, U.H., Clark B.: Composition of AlkaliSilica Gel and Ettringit in Concrete Railroad Ties: SEM-EDX and X-Ray diffraction analyses. In: Cement and Concrete Research Vol. 26 / 2, page 309-318, 1996.

[24] Freyburg, E.: Betonschäden durch Alkali-Kieselsäure-Reaktion (AKR): petrographische Ursachen und mikroskopische Diagnosen. In: Presentation Dyckerhoff-Forum, Wiesbaden, 1998. (Not. ZKG International Vol. 51, page 8, 1998.)

[25] Urhan, S.: Alkali Silica and Puzzolanic Reaktions in Concrete. Part 1: Interpretation of Published Results and a Hypothesis Concerning the Mechanism. In: Cement and Concrete Research, Vol. 17, page 141-152, 1987.

[26] Tschegg, E.K. et al.: Alkali Aggregate Reaktion in Mass Concrete State-of-the-Art Experimental Study Report. Schriftenreihe der Forschung im Verbund Wien, page 142, 1998.

[27] Andersen, K.T., Thaulow, N.: The Application of Undulatory Extinction Angles (UEA) as an Indication of Alkali-Silica Reactivity of Concrete Aggregates. In: R&H Bulletin No.: 15 Alakli-Silica Reactions in Concrete, page 1-6, 1990.

[28] Sprung, S.; Sylla, H.-M.: Beurteilung der Alkaliempfindlichkeit und Wasseraufnahme von Betonzuschlagstoffen. In: ZKG International, Vol. 50, page 63-74, 1997.

[29] Siebel E.; Reschke, T,; Sylla, H.-M.: Alkali-Reaktionen mit Zuschlägen aus dem südlichen Bereich der neuen Bunderländer. Untersuchungen an geschädigten Bauwerken. In: Beton, Vol. 46, page 298-301 and 366-370, 1996.